PhD-FSTM-2021-90
The Faculty of Science, Technology and Medicine

DISSERTATION

Defence held on 26/11/2021 in Luxembourg

to obtain the degree of

DOCTEUR DE L'UNIVERSITÉ DU LUXEMBOURG

EN PHYSIQUE

by

Thibaut GALLET
Born on 25 May 1992 in Arras (France)

CO-EVAPORATION AND SCANNING PROBE MICROSCOPY CHARACTERIZATIONS OF HYBRID HALIDE PEROVSKITE THIN FILMS FOR SOLAR CELLS

Dissertation defence committee

Dr. Alex Redinger, dissertation supervisor
Associate Professor, Université du Luxembourg

Dr. Thomas Unold
Deputy Head, Dept. Structure and Dynamics of Energy Materials, Helmholtz Zentrum Berlin

Dr. Mael Guennou, Chairman
Assistant Professor, Université du Luxembourg

Dr. Philip Schulz
Research Director, Institut Photovoltaïque d'Ile de France

Dr. Phillip Dale, Vice Chairman
Professor, Université du Luxembourg

Contents

Abstract

Hybrid organic-inorganic perovskites (HOIPs) are the trending materials when discussing solar cells. Their power conversion efficiency went from 3.8% to 25.5% in twelve years, making them extremely promising, especially when combined with silicon in a tandem configuration. This improvement has been achieved by finding the best candidates for charge extraction and by interface engineering, compositional engineering and surface passivation. However, the surface of the HOIPs is still not well understood, and the role of grains boundaries for example is still highly debated. Determining the intrinsic surface properties of HOIPs is therefore crucial to find the best passivation strategies or fabrication designs to limit the surface and interfacial losses, and further improve solar cell efficiencies. Currently, solution-based processes are the most used techniques for fabrication, even though their upscalability towards commercialization is highly unlikely, and the use of solvents, sometimes toxic, considerably alters the perovskite surface, which makes the interpretation of their characterization challenging and sometimes misleading.

The aim of this thesis is to clarify the intrinsic surface properties of HOIPs, and mainly $CH_3NH_3PbI_3$ (or $MAPbI_3$), by using surface-sensitive techniques such as scanning tunneling microscopy and spectroscopy (STM and STS) and Kelvin probe force microscopy (KPFM). To that end, HOIP thin films are mainly fabricated by thermal co-evaporation to achieve pristine surfaces, and inert-gas transfer is used to avoid contamination before their characterization.

The lateral variations of the local density of states of $MAPbI_3$ and mixed halide HOIPs are investigated. The grain-to-grain and facet variations are linked to different density of surface states that pin the Fermi level at the surface, and different workfunctions (WF), which are both attributed for $MAPbI_3$ to different surface terminations, and for the mixed HOIPs to an additional degradation of the perovskites.

The effect of varying the methylammonium iodide (MAI) content, via the partial pressure, in co-evaporated $MAPbI_3$ is studied and the excess of MAI proves to be detrimental, as it introduces low-dimensional perovskites and stacked perovskite sheets that considerably reduce its intrinsic stability. Therefore near-stoichiometric conditions are preferred and yield films more stable to light and heat and without photostriction.

Nevertheless this intrinsic stability is still not optimal, and the continuous variations of the WF measured by KPFM upon prolonged illumination is investigated. Combined with X-ray photoelectron spectroscopy (XPS), the photo-induced degradation of $MAPbI_3$, and evaporation of I_2 are revealed as the causes of these variations. Besides, by combining KPFM and photoluminescence (PL) techniques for different thicknesses and substrates, energy band diagrams can be drawn and unveil a bending of the bands in the bulk.

Lastly, the surface sensitivity of HOIPs is investigated when they are intentionally put in contact with extrinsic factors such as oxygen and solvents, and the surface properties are shown to be considerably altered. In addition, passivation strategies are used to demonstrate how surfaces can be improved.

Introduction

The latest Intergovernmental Panel on Climate Change (IPCC) report was published in August 2021 [1]. It showed that since 1850-1900, the emission of greenhouse gases from human activities has led to a warming of approximately 1.1°C. Additionally, it estimates this temperature to reach 1.5°C in the next 20 years, and warns that if no immediate and rapid action is undertaken to cut down green houses gases at a global scale, there will be no way to limit the warming below 2°C. This will result in more intense rainfall, flooding and droughts as well as melting of glaciers, ice sheets, loss of seasonal snow cover and reduced oxygen levels [1]. This drastic and imminent reduction of greenhouse gases, such as CO_2, can already be performed through energy transition. More than 80% of the energy produced in the world comes from fossil fuels, such as burning coal, oil and gas, which release billions of tonnes of carbon dioxide and are the biggest driver of climate change [2]. Using renewable energies such as wind and solar would help in getting closer to the required 40% emission cuts needed to reach climate goals [3]. In 2020, only 3.7% of the total energy consumed was generated by solar or photovoltaic (PV) energy [4], which was around 845 TWh coming from a solar energy capacity of 707.5 GW (+34% between 2010 and 2020 [5]). PV is one of the fastest-growing renewable energy technologies and the cost of manufacturing solar panels has drastically decreased in the last 10 years, which often makes solar energy the cheapest energy in the market [6]. The solar PV power generation is estimated to increase radically and reach around 3270 TWh in 2030 [7].

In 2020, silicon technology accounted for 95% of the total solar energy production [5], with the remaining 5% coming from thin-film technologies such as cadmium telluride (CdTe) and copper indium gallium di-selenide (CIGSe). Solar panels and cells made of silicon have a record efficiency of 26.7% [8] but are compact and therefore hard to integrate into flexible electronic devices or for building integrated photovoltaics (BIPV) applications. On the other hand, CdTe and CIGS can be made in a flexible configuration but the highest solar cells efficiencies are 22.1% and 23.4% respectively [8]. More recently, a new material, **perovskite**, has been intensively studied in the PV community. Its physical and lightweight properties, flexibility, ease of fabrication at low cost and its conversion efficiency make it a promising candidate for the PV industry. The efficiency obtained from hybrid halide perovskite solar cells fabricated in laboratories has increased from 3.81% in 2009 [9] to 25.5% in 2021 [8], making it the fastest improvement in efficiency from all PV technologies. Combined with silicon, perovskite is one of the materials of choice for the fabrication of tandem solar cells (two stacked solar cells), which yield even higher efficiencies (29.5% [8]). Since then, many start-up companies have been created for the manufacture and commercilization of perovskite or tandem solar panels, such as OxfordPV, CubicPV, Saule Technologies, Evolar, Microquanta Semiconductor, Swift Solar... Companies and research groups all over the world are still trying to understand the properties of this material system (perovskite) and how to further improve its efficiency.

The surge in the performances of solar devices made from perovskites has several origins. For a long time, the studies were mainly based on one type of composition, $CH_3NH_3PbI_3$, also called $MAPbI_3$ or MAPI. This configuration is hybrid as it consists in organic and inorganic elements. The fist improvement came from optimizing the fabrication processes and the layers surrounding this material and which are part of the solar cell [10, 11]. However stability issues have quickly been encountered [12] and therefore new material compositions were found, by multiplying the number of cations and anions in the structure, which both improved the stability and the efficiency [13]. Another important route to improve the two latter criteria is the control of the surfaces and interfaces of the layers used in the solar cell. The surface is the termination of a film and therefore implies the introduction of structural variations, such as dislocations, defects or grain boundaries in the case of thin-film poly-crystalline perovskites. Therefore investigating the surface properties is crucial in order to find ways to optimize them such that they produce minimum efficiency losses. Research works have been mainly focused on the improvement of the solar cell efficiency, and much less on the surface properties of the perovskite itself. Atomic resolution has been achieved using scanning tunneling microscopy (STM) on single-crystals to reveal different phases at different surface terminations [14], or to investigate the surface stability of perovskite when substituting elements [15, 16]. Similarly, scanning tunneling spectroscopy (STS) was used on perovskite thin films and demonstrated passivation effects and photo-induced transfer of charge [17]. Grain boundaries were also analyzed by a few groups, and most of the time showed, using Kelvin probe force microscopy (KPFM), electronic variations compared to the grains, which were linked to either the improvement or deterioration of the solar cell efficiencies, which still make them highly debated [18, 19, 20, 21].

It is therefore extremely important to understand whether grain boundaries, and to a greater extent the surface of perovskites, are detrimental or beneficial in perovskite solar cells. Besides, energetic variations from grain to grain are an important information to retrieve in order to quantify the homogeneity of the surface and find routes for optimization, such as passivation strategies [22]. However most, if not all, of the literature related to the investigation of the perovskite surfaces consist in either perovskites fabricated using solution-based processes, or the measurements of their surface properties after contamination or in an ambient environment. The use of solvents in these fabrication methods, and the oxygen and water contained in an ambient environment both alter the intrinsic surface properties of perovskites. Therefore there is a clear need to understand the pristine surface properties of perovskites. Only then should extrinsic factors be used to study how perovskite films interact with them. That way, design rules and strategies could be found in order to yield higher solar device efficiencies in a systematic and rigorous way.

This introduces the SUNSPOT (Surface and interface science on photovoltaic materials) project and the idea behind this PhD thesis. The latter has two goals, with the first one being the synthesis of $MAPbI_3$ perovskite thin films for solar cells using a technique that does not alter their surface: physical vapor deposition (PVD). The second goal of this thesis is to investigate the intrinsic surface of these perovskites, which requires to avoid contamination from extrinsic factors such as oxygen and exposure. To that end, nitrogen-filled gloveboxes, inert-gas transfer suitcases and a scanning probe microscope (SPM) in an ultra-high-vacuum (UHV) environment will be used. The SPM will enable the use of STM/STS in conjunction with KPFM to acquire a full picture of the surface energetics of hybrid halide perovskites. In the following, the structure and content of the thesis will be presented.

The thesis will start with an introduction of perovskites and more specifically hybrid organic-inorganic perovskites that are used in solar cells. The semiconductor basics will be given and the properties of $MAPbI_3$, which has been synthesized and investigated during this thesis, will be discussed, as well as the stability and degradation issues and the losses occurring when it is used in a solar cell. This first chapter will end with a detailed review of the surface properties of $MAPbI_3$ films.

Chapter 2 will then introduce the main characterization techniques used, namely STM, STS and KPFM. Their working principles, the SPM machine and the important parameters will be thoroughly described, followed by a review of the SPM literature on perovskite solar cells.

Chapter 3 will present the technique used to grow the samples, physical vapor deposition, and how it differs when evaporating $MAPbI_3$. The physics behind PVD and the machine will be detailed as well as the characterization method that was used to determine the quality of the films made: photoluminescence (PL). A brief working principle of PL will be given followed by the ways to determine the PL quantum yield (PLQY), the effective lifetime and doping densities of $MAPbI_3$ films using calibrated and correlative PL and time-resolved PL (TRPL).

Chapter 4 will investigate the surface properties of solution-based $MAPbI_3$ using STM and STS. More precisely, electronic variations at the surface, between grains and within single grains, will be demonstrated at the nanometer scale, and computations will be used to quantify the density of surface states. This chapter will discuss how these observed variations translate into different densities of surface states but also different local surface dipoles related to the workfunction. The origin of these surface variations will be suggested. Chapter 4 will end with the investigation of solution-based mixed halide perovskites by comparing them to solution-based $MAPbI_3$.

Chapter 5 will dive into the co-evaporation of $MAPbI_3$ and how the change of the MAI partial pressure affects their properties. KPFM in conjunction with X-ray diffraction (XRD), scanning electron microscopy (SEM), PL and TRPL will be used to understand how a change in composition can drastically alter the surface as well as the structural and optoelectronic properties of $MAPbI_3$. More precisely, the excess of MAI inside the $MAPbI_3$ crystal structure will be shown to introduce low-dimensional perovskites and stacking faults, that are guilty of decreasing the solar cell performances, by reducing the intrinsic stability of $MAPbI_3$ against heat and light.

Chapter 6 will look in details into the observed fast and slow transients in the workfunction (WF) signal of $MAPbI_3$ when measuring them in KPFM upon prolonged light exposure. Combined with X-ray photoelectron spectroscopy (XPS), the KPFM measurements will demonstrate that photo-induced degradation occurs, which contaminates the SPM environment. The second part of the chapter will use KPFM, surface photovoltage (SPV) measurements, calibrated PL and TRPL to draw energy band diagrams of $MAPbI_3$ for different substrates and show how the energy bands in a semiconductor differ from flat band conditions.

Chapter 7 will present the sensibility of the $MAPbI_3$ surface when exposed to extrinsic factors such as oxygen exposure or solvents, before comparing them with mixed halide perovskites, that proved to yield much higher efficiencies. Despite their much greater performances, their surfaces will prove to be imperfect, and the use of passivation strategies will be carried out to show their effects on the surface of mixed halide perovskites, and how they annihilate their imperfections.

The thesis will end with a summary of the main results and will offer outlooks as well as a large appendix, in which supporting information are given as well as detailed studies that are outside of the scope of this thesis but interesting for any reader working in a perovskite field.

Chapter 1

Fundamentals and review

In the following review chapter, an introduction to perovskites, the basics of semiconductors, the use of perovskites in solar cells and the surface of perovskites will be given.

To that end, the chapter is split into three parts, with the first section 1.1 introducing the concept of perovskites, and more precisely the structure and properties of hybrid organic-inorganic perovskites used for solar cells.

The second section 1.2 first explains the basics of semiconductors, important to understand the concept of a solar cell. The second part of this section discusses hybrid halide perovskite solar cells and introduces the prototypical thin film $CH_3NH_3PbI_3$ ($MAPbI_3$), which will be studied throughout this thesis. Its structure, properties and the related efficiency losses and stability issues of the solar cells made of this material will be briefly presented.

The last section 1.3 focuses on the surface properties of $MAPbI_3$, as its surface characterization is the main topic of this thesis.

1.1 General aspects of hybrid perovskites

1.1.1 Perovskite structure

In 1839, Gustav Rose, a German mineralogist discovered a new mineral consisting of calcium titanium oxide, $CaTiO_3$ [23], which he named *perovskite* in honor of the Russian mineralogist Lev Perovski. The first description of its crystal structure came then in 1926 by Victor Goldschmidt [24] and later on the term *perovskite* was used to classify all compounds having the same type of crystal structure as $CaTiO_3$. The latter structure consists in corner-sharing TiO_6 octahedra in three dimensions and Ca in the cuboctahedral cavity in each unit cell (Figure 1.1) [25].

Since the discovery of $CaTiO_3$, many more compounds with the same crystal structure were found, such as $CaRbF_3$ and $SrTiO_3$. For simplification, the denotation ABX_3 was used to identify the perovskite structure, with A and B two cations and X the anion bonding the two latter cations. Even if originally the X anion used was an oxide, leading to a multitude of insulating materials, several perovskite were found to form without oxygen, such as fluoride perovskites (ABF_3), metallic perovskites (ABM_3), halide perovskites... More recently, machine-learning has been used to discover and screen feasible perovskite compounds, which produced hundreds or thousands of possibilities [26, 27, 28]. The stoichiometry of ABX_3 compounds is linked to the charge neutrality formula as represented in equation (1.1):

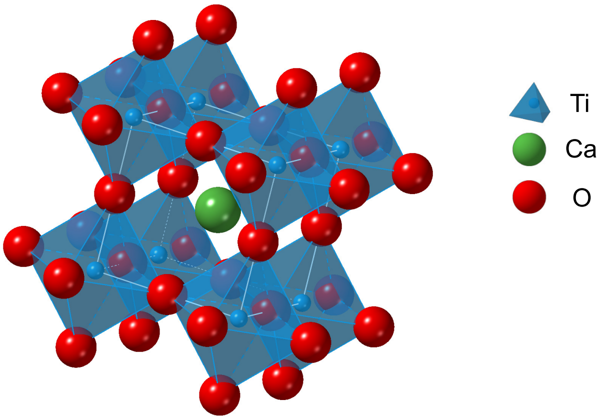

Figure 1.1: $CaTiO_3$ cubic structure, generated using CrystalDiffract®: a powder diffraction program for Mac and Windows. CrystalMaker Software Ltd, Oxford, England (www.crystalmaker.com).

$$q^A + q^B + 3q^X = 0 \tag{1.1}$$

q represents the charge, and A, B and X are representative of the elements of the ABX_3 material. From this equation, the possibility of forming a variety of materials with the same chemical structure can be imagined. In the case of metal oxide perovskite (ABO_3), combining elements with oxidation states of I, II, III, IV and V can be possible as follows: I-V-O_3, II-IV-O_3 and III-III-O_3, because $3q^O = -6$ for $q = -2$. Besides the abundance of elements that one can use to form a perovskite compound, the crystal structure can also vary. The cubic structure is rarely encountered and the orthorhombic and tetragonal phases are more common [25]. Several external effects can in addition tune the phase of the perovskites, such as temperature, pressure, magnetic or electric fields, which are attributed to the tilting and rotation of the BX_3 polyhedra in the lattice [29]. Since the discovery of the perovskite structure, researchers have been looking into ways of forming it using different combinations of elements, which has led to the discovery of materials for a wide range of applications: supercondutivity [30], magnetoresistance [31], dielectrics [32], microelectronics [33], telecommunications [34], light-emitting diodes [35], solar cells [36]...

1.1.2 Halide perovskites

When the X element of the ABX_3 structure is chosen to be an halide element (halogen with a negative charge) from the group 17 of the periodic table, then the charge balancing equation becomes $q^A + q^B = -3q^X = 3$ and the requirements to fulfill the latter limit elements to the ones with oxidation states of I and II. For most halide perovskites (HPs), the B cations being divalent and the A ones being larger monovalent cations, this translates into the following ternary compound I-II-X_3, which can give for example $CsSnI_3$ or $CsPbI_3$, as Cs is the most common monovalent alkali metal [37]. The most commonly used halides for perovskite compounds are F^-, Cl^-, Br^- and I^-. Considering solely inorganic element, one fluoride perovskite, $KMgF_3$ exists in nature and has a cubic structure ($Pm\bar{3}m$) [38] but when using heavier halides, the crystal structure of these fully inorganic HPs change due to a disordered lattice.

Several other subgroups of halide perovskites exist such as the ones with an "A-site vacant BX_3" crystal structure, the ordered perovskites or "double perovskites" and the vacancy-ordered perovskites [37]. They can exhibit different crystal structures, which can also vary along the applied temperature. The three-dimension (3D) structure of the perovskite itself can also be altered. The A site in the ABX_3 structure is in that matter extremely important, as its size relates to the stability of the perovskite. If it is either too small or too large, the framework of the HP collapses and so does the stability of the crystal structure. The Goldschmidt tolerance factor is in that way an indication of the stability of the perovskite structure with respect to the A cation size [39, 40], which will be discussed further in this thesis. When an ABX_3 perovskite cannot form into a stable structure, it deviates towards either a one-dimension (1D) or two-dimension (2D) edge-sharing crystal lattice or 1D face-sharing crystal lattice. However, as mentioned before, annealing at temperatures around 200-300 °C can lead to the transition of stable perovskites. In that case, the term "post-perovskites" is used as the structure crystallizes into a 3D lattice after thermal treatment (this is the case of $CsPbI_3$ and $FAPbI_3$ which will be introduced after) [41]. Zero-dimension (0D) perovskite can also exist as well as layered halide perovskites ("Ruddlesden-Popper perovskites") where 2D layers of halide octahedra are separated by a layer of A atoms. However perovskites have seen a surge in popularity due to one sub-group of the halide perovskites, namely the hybrid organic-inorganic metal halide perovskites (HOIPs).

1.1.3 Hybrid organic-inorganic halide perovskites

In the HOIPs or hybrid perovskites, the A site of the ABX_3 structure is occupied by an organic cation, which is coming most of the time from the alkyl ammonium group. The choice of the latter is strongly linked to the aforementioned Goldschmidt tolerance factor [40] and additionally the octahedral factor [39]. The latter introduces the concept of stability of the BX_6 octahedron, where for instance small cations coordinating with larger anions would prefer tetrahedral coordination. The Goldschmidt tolerance factor t enables the prediction of the stability of a perovskite, based only on the chemical formula and the ionic radii, r_i of each ion of the ABX_3 structure, following the equation (1.2).

$$t = \frac{r_A + r_X}{\sqrt{2}(r_B + r_X)} \tag{1.2}$$

This equation has direct consequences on the organic molecules that can be used to form HOIPs. It explicitly limits the organic cations to small pseudo spherical cations such as methylammonium (MA) and formamidinium (FA) and simultaneously induces restriction on the B cation to Pb^{2+} and Sn^{2+} [42]. As an example, the $APbI_3$ structure was taken and the Goldschmidt tolerance factor was calculated by varying the A site from Na to guanidinium (GA) (Figure 1.2). The ionic radius given by Shannon et al. [43] and Kieslich et al. [44] were used for the calculations. From these empirical calculations of lattice distortion and crystal structure stability, the tolerance factor for stable and fully-formed perovskites, also called *black-phase* perovskites, is found to lie between 0.8 and 1.08. Therefore only Cesium (Cs), MA and FA can be used and are known to be within the established perovskites. Additionally, the $APbI_3$ structure at the edge of the tolerance factor exhibit a slightly distorted lattice and can be distinguished by a non-perovskite yellow-phase at room temperature [45], but can also be referred to "post-perovskites" as they transition to a black-phase perovskite upon annealing ($CsPbI_3$ and $FAPbI_3$).

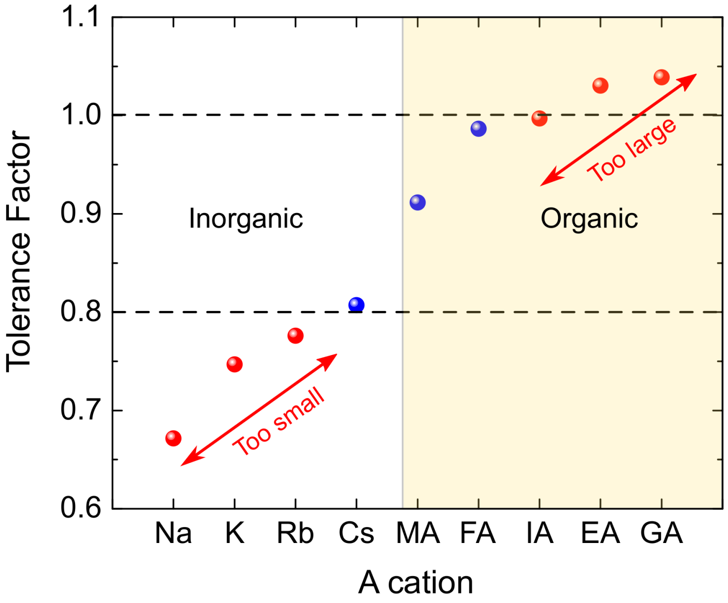

Figure 1.2: Tolerance factor of the $APbI_3$ perovskite structure. Sodium (Na), Potassium (K), Rubidium (Rb) have a too small ionic radius to form a stable perovskite. Imidazolium (IA), etyhlamine (EA) and guanidinium (GA) gave on the other hand a too large ionic radius. Cesium (Cs), Methylammonium (MA) or Formamidinium (FA) can be used to achieve a stable perovskite.

However, the Goldschmidt tolerance factor has its limits and recently Bartel et al. have showed that it can correctly distinguish between perovskite and nonperovskite for only 74% of materials, and with an even worse precision for halides (51% for chlorides, 56% for bromides and 33% for iodides) [40].

For the last decade, HOIPs have been the center of attention in one specific community, the photovoltaics one. Most HOIPs are insulating but hybrid perovskites having tin(II) iodide or lead(II) iodide framework are electrically conductive. Mitzi et al. have been pionneers in studying the properties and use of the HOIPs. In 1995, they revealed with Hall measurements a Hall mobility at room temperature of 50 $cm^2/V{\cdot}s$ for a $MASnI_3$ perovskite [46]. The first report of the use of a halide perovskite to fabricate a potential solar cell appeared in 1980, with the $KPbI_3$ structure [47], which presented an optical absorption range attributed to the direct energy bandgaps between 1.4 and 2.2 eV. HOIPs have been therefore largely studied for a variety of applications. Density functional theory (DFT) calculations predicted that they could have a narrow bandgap and good charge carrier mobility, giving them a chance to compete in the sectors of light-emitting diodes (LED) or thin film transistors [48], which were initially the domains in which they were most studied. It was only in the spring of 2009 that organometal halide perovskites reappeared in the solar cell literature with Kojima et al. [9], who fabricated the first HOIP solar cells using mesoporous TiO_2 photoanodes as the substrate of the device.

The combination of HOIPs' ideal properties such as their bandgap range, optimum for the absorber layer in a solar cell, high carrier mobility, long diffusion length and low non-radiative recombination rates made them the center of attention in the solar cell community and led to one of the highest photovoltaic conversion efficiencies of thin-film technologies. The next section will therefore discuss the structure and the working principle of a solar cell, before exploring the main differences for perovskite solar cells.

1.2 Perovskite solar cells

This section will discuss the specific and basic working principle of a perovskite solar cell, without going into the details of the working principle of the commonly-used solar cell, made of a p-n junction. However, the reader is directed to section A.1 of appendix Chapter 1 for a comprehensive discussion about the physics of a solar cell made from a p-n junction. In addition, a textbook such as [49] is an appropriate reading material for that matter. The last part of this section will further introduce the concept of defects and stability issues in perovskites and will present the most used HOIP throughout this thesis: the methylammonium lead iodide perovskite $\mathrm{MAPbI_3}$.

1.2.1 Semiconductor basics

Unless explicitly stated otherwise, the following explanations have been based from textbooks such as [49] and [50].

The solar panels that are often seen on top of buildings, houses or in fields are a combination of electronic components and a multitude of solar cells. The solar cell is the core of the solar panel as it is the part that converts the incoming light from the sun into the electricity that will be delivered from the solar panel. In order to convert photons to electrons and holes, called charge carriers, and that generate the electrical power, the solar cell requires a wide range of materials for different functions such as absorbing photons efficiently, generating and transporting the charge carriers and collecting these charges at external contacts. Semiconducting materials, or semiconductors, are the materials that correspond best to the needs of a solar cell. Semiconductors lie between metals and insulators and the transport of charge carrier (conduction) can occur upon excitation above a certain energy due to their band structure (Figure 1.3a). A semiconductor exhibits a forbidden energetic zone, called the bandgap, where no electronic states can exist. The energy range below the gap is called the valence band (VB) and at zero Kelvin, it is entirely occupied by electrons. On the other hand, the energy range above the gap is called the conduction band (CB) and is unoccupied. The highest energy of the valence band, E_V, is called the valence band maximum (VBM) and the lowest energy of the conduction band, E_C, is called the conduction band minimum (CBM).

Upon excitation, which could be for example temperature-, light- or voltage-driven, an electron can get excited from the VB to the CB and the resulting unoccupied state in the VB is then called a hole and ultimately contributes to the transport of charges together with the excited electron. Figure 1.3b depicts an excitation caused by an incoming photon with an energy $\hbar\omega$. If this energy is larger than the bandgap energy, then an electron from the VB is excited into the CB at a certain energy state, leaving a hole in the VB at another energy state. Then the electron relaxes towards the CBM, losing an energy ϵ_t to the system, in a process called thermalization. The similar thermalization process occurs for holes when they are excited in a lower energy state than the valence band maximum, except that they relax towards higher energy states.

The density of electrons $\mathrm{d}n_e$ with an energy E_e distributed over an energy range $\mathrm{d}E_e$ can be calculated within a certain cavity volume, by taking into account the density of states in the CB $D_e(E_e)$ and the way the electrons are distributed along these states, defined by the Fermi-Dirac distribution function $f_e(E_e)$ by the following equation 1.3:

$$dn_e(E_e) = D_e(E_e)\, f_e(E_e)\, dE_e \tag{1.3}$$

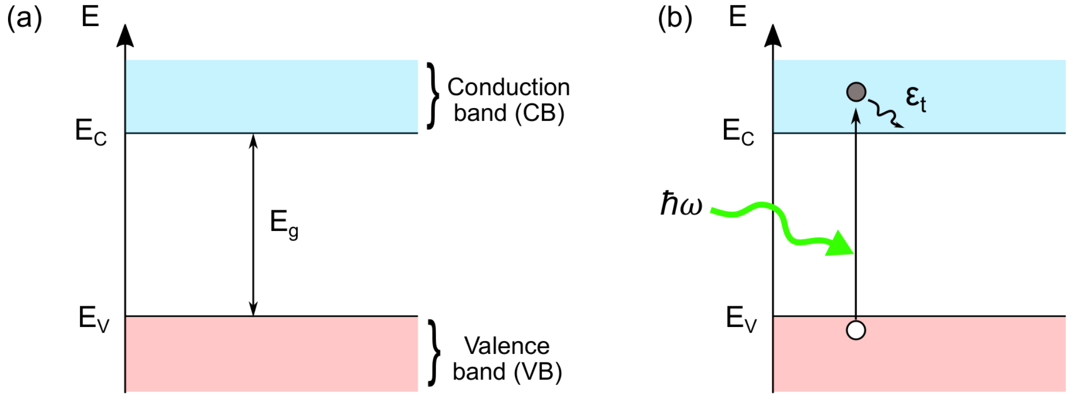

Figure 1.3: (a) Energy band diagram of a semiconductor with E$_V$ the energy of the valence band maximum, E$_C$ the energy of the conduction band minimum, E$_g$ the bandgap energy. (b) Excitation of an electron from the valence band to the conduction band by the absorption of a photon with an energy $\hbar\omega$ and the following loss of an energy by thermalization ϵ_t.

where $f_e(E_e)$ can be calculated by using equation (1.4):

$$f_e(E_e) = \frac{1}{exp(\frac{E_e - E_F}{kT}) + 1} \tag{1.4}$$

E_F is denoted as the Fermi energy level and is characteristic of the top boundary of the collection of electron energy states at absolute zero Kelvin, suggesting that at this temperature no electron should exist above this Fermi level. For the states E_e extremely lower than E_F, the distribution of electrons over these states approaches 1 as depicted by Figure 1.4a. Contrarily, for E_e much higher than E_F the distribution approaches 0. The density of states (DOS) $D_e(E_e)$ is defined as the proportion of states occupied by the system at each energy. The density of states in the CB as a function of the number of electron states dN_e per volume V per energy interval dE_e at the energy E_e for a three-dimensional crystal can be described by the equation (1.5).

$$D_e(E_e) = \frac{1}{V}\frac{dN_e}{dE_e} = 4\pi\left(\frac{2m_e^*}{h^2}\right)^{3/2}(E_e - E_c)^{1/2} \tag{1.5}$$

m_e^* is the effective mass of the electrons and h the Planck constant. An example of a DOS representation is given in Figure 1.4b using the semiconductor germanium. Using the previous equations, it becomes possible to access the density of free electrons n_e in the CB by integrating equation (1.3) over the CB energy range, that is:

$$n_e = \int_{E_c}^{\infty} D_e(E_e) f_e(E_e)\, dE_e \tag{1.6}$$

In the case of a semiconductor where the Fermi energy level lies between the CBM and the VBM, also called non-degenerate semiconductor, at thermal equilibrium, the Fermi-Dirac integral can be approximated via Boltzmann statistics to an exponential function and therefore the electron concentration, denoted n_0 becomes:

$$n_0 = N_C \exp\left(-\frac{E_C - E_F}{k_B T}\right) \text{with } N_V = 2\left(\frac{2\pi m_e^* kT}{h^2}\right)^{3/2} \tag{1.7}$$

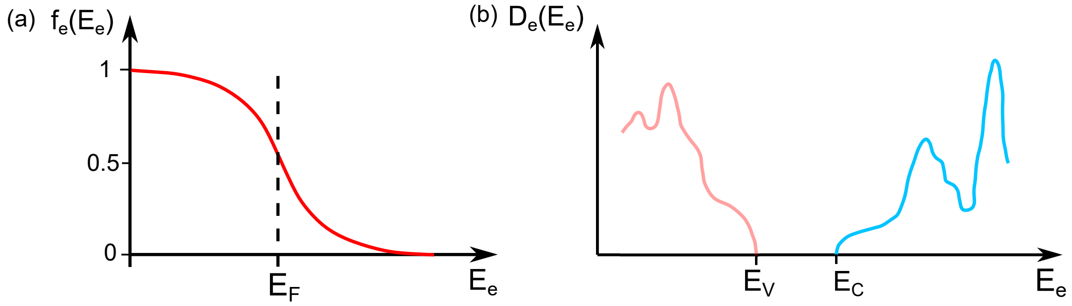

Figure 1.4: (a) Fermi distribution function and (b) density of states for electrons in the conduction and valence bands of the semiconductor germanium. Adapted with permission from [49]. Copyright John Wiley and Sons 2005.

N_C is the effective density of states of the conduction band. Similarly, the concentration of holes in the valence band p_0 is given by:

$$p_0 = N_V \exp\left(-\frac{E_F - E_V}{k_B T}\right) \text{ with } N_C = 2\left(\frac{2\pi m_h^* kT}{h^2}\right)^{3/2} \tag{1.8}$$

N_V is the effective density of states of the valence band and m_h^* the effective mass of the holes. The product of the electron and hole concentrations is independent of the Fermi energy but depends solely on the effective densities of states of both type of carriers. In a pure semiconductor, also referred to as intrinsic, electrons and holes densities are equal to the intrinsic concentration n_i and:

$$n_0 p_0 = n_i^2 = N_C N_V \exp\left(\frac{-E_g}{k_B T}\right) \tag{1.9}$$

As previously stated, E_g is the bandgap energy and is also equal to E_C-E_V. From the previous equations, the position of the Fermi energy can be deduced, and is situated close to the middle of the bandgap energy but not exactly, due to the differences in effective masses of the electrons and holes. Therefore E_F can be expressed for an intrinsic semiconductor following equation (1.10):

$$E_F = \frac{1}{2}(E_V + E_C) + \frac{1}{2}\ln\frac{N_V}{N_C} \tag{1.10}$$

Since intrinsic semiconductors have relatively low conductivity and low concentrations of charge carriers, introduction of impurity atoms within the semiconductor can be used to modulate its electrical, optical and structural properties such as conductivity, charge mobility... This phenomenon is called extrinsic doping and can be performed using both atoms with an excess of valence electrons (donors) or with a deficiency of valence electrons (acceptors) with respect to the semiconductor doped. As an example, for the silicon (Si) semiconductor, atoms of phosphorus (P) can be used as donors and atoms of boron (B) can be used as acceptors. This ultimately leads to a semiconductor doped with a higher concentration of electrons compared to holes (referred to as an n-type semiconductor) or reciprocally, a semiconductor doped with a higher concentration of holes compares to electrons (p-type semiconductor). It stems out that in an n-type semiconductor, the electrons are called majority charge carriers, and the holes minority charge carriers, whereas in a p-type semiconductor, the opposite is true. As doping leads to the occurrence of a majority carrier concentration within a semiconductor (either of electrons or holes), the

Fermi energy level varies depending on the type of doping (donor or acceptor), the concentration (in cm^{-3}), the impurity energy level and the lattice temperature. In order to have a doped semiconductor, the introduced impurities need to be ionized, or electrically active. Most of the time the ionization energy is such that at room temperature almost all impurities (donors and acceptors) are already ionized. n_D and n_A are the concentrations of donors and accepors respectively. In an n-type semiconductor, $n_0 \approx n_D$ and $p_0 = \frac{n_i^2}{n_0} \approx \frac{n_i^2}{n_D}$ and in a p-type semiconductor $p_0 \approx n_A$ and $n_0 = \frac{n_i^2}{p_0} \approx \frac{n_i^2}{n_A}$. Therefore the Fermi energy can be defined the following way:

$$\begin{aligned} E_F &= E_C - kT \ln \frac{N_C}{n_D} \\ E_F &= E_V + kT \ln \frac{N_V}{n_A} \end{aligned} \tag{1.11}$$

It results that for an n-type semiconductor, the Fermi energy level is closer the CBM and for a p-type semiconductor, the Fermi energy level gets closer to the VBM. Doping of semiconductors is the starting point of the working principle in electronic and optoelectronic devices, such as a solar cell.

1.2.2 The n-i-p case of perovskite solar cells

The first perovskite solar cell was differently structured compared to the classic p-n junction of solar cells (see section A.1 of appendix Chapter 1). In 2009, Myasaka and coworkers used the organometal halide $MAPbI_3$ (MAPI) perovskite as a visible-light sensitizer in a photovoltaic, more precisely photoelectrochemical, solar cell [9]. In their work, they used their know-how of dye-sensitized solar cells (DSSC) and used MAPI to sensitize a mesoporous layer of TiO_2, which enabled efficient absorption of light by the perovskite nanoscrystals and excitations of electrons in the conduction band of the TiO_2 layer. The working principle and role of the transport layers are depicted in Figure 1.5 with a simplified version where the recombination mechanisms have been omitted on purpose as they will be discussed later in this chapter. After illumination and generation of charge carriers, the charge collection is made possible due to the low band offsets or energy differences created between an electron transport layer (ETL) at the cathode and a hole transport layer (HTL) at the anode, acting sort of like the n- and p-side of a generic p-n junction for solar cells. The band diagram resembles the combination of two type II heterojunction (staggered bandgap). The ETL has its CBM aligned such that electrons can flow easily into it but also presents a large VBM offset with the perovskite layer so that the holes are repelled and cannot access the ETL. The HTL on the other hand has its VBM, also often called highest occupied molecular orbital (HOMO), aligned with the VBM of the perovskite to efficiently extract holes and a large CBM, or lowest unoccupied molecular orbital (LUMO), band offset with the perovskite to repel electrons. However charge collection is also made possible due to an inherent property of perovskites as well as the probability of charges not to recombine, which depends on the diffusion lengths of the charge carriers, the perovskite thickness and others parameters, which will be discussed after.

The first working perovskite solar cell was then created, with an efficiency of 3.81% [9]. The nature of the HTL and ETL were different as an electrolyte was originally used for the HTL. But later on, in 2012, Park et al. replaced the liquid electrolyte by a solid HTL, namely 2,2',7,7'-tetrakis(N,N-di-p-methoxyphenylamine)-9,9'-spirobifluorene

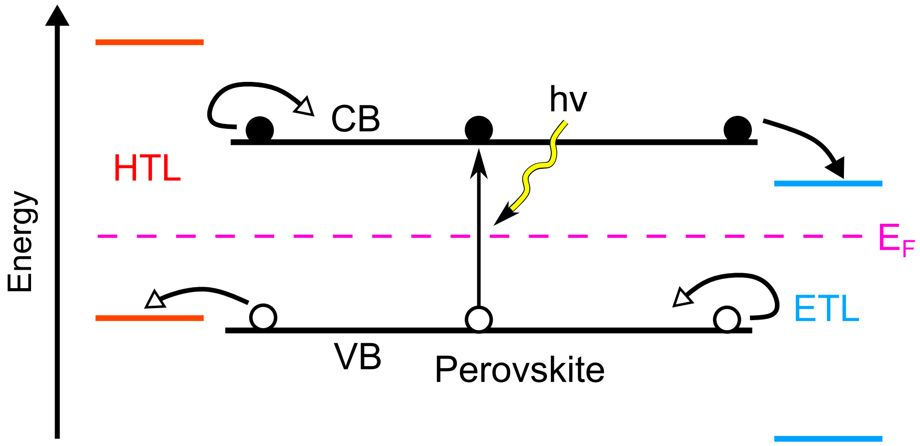

Figure 1.5: Working principle and role of the transport layers. CB represents the conduction band (minimum) and VB the valence band (maximum). HTL its the hole transport layer while ETL is the electron transport layer. E_F is the bandgap of the perovskite semiconductor.

(spiro-MeOTAD) (Figure 1.6a), and reported a perovskite solar cell of 9.7% [51]. The need to use DSSC-like solar cells was based on the assumption that perovskite had a relatively short diffusion length. However starting in 2013, reports came out stating that perovskite had both diffusion length exceeding 1 µm [52, 53] as well as ambipolar transport properties [53, 54]. This implied that the differences in the holes and electrons effective masses were quite balanced compared to other semiconductors. What stemmed out from such properties was that perovskites could transport both eletrons and holes in a much more efficient ways than commonly-used semiconductors for solar cells, and additionally planar perovskite of a few hundreds of nanometers could sustain charge generation and transport. The concept of built-in potential created by the differences in energetic alignment between the HTL and ETL was therefore questionable. Recently Sandberg et al. looked into this phenomenon and concluded that even though charge carrier collection is mostly diffusion-controlled due to the perovskite behavior, there is still need of a built-in potential arising from the sandwich of the perovskite between the ETL and HTL, to avoid the formation of reverse electric fields inside the perovskite layer, which induces hysteresis and loss of stability [55].

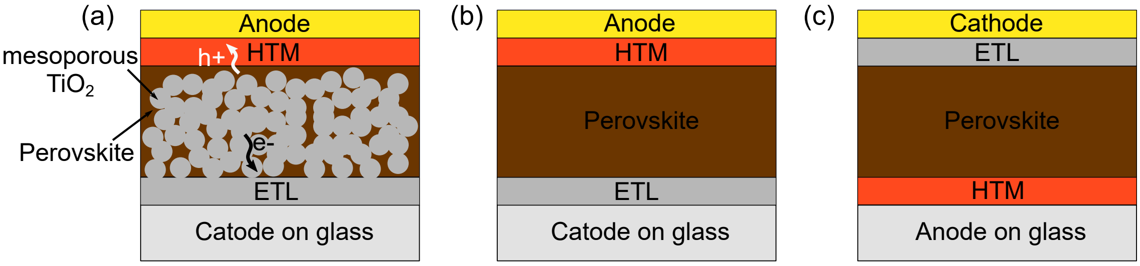

Figure 1.6: The evolution of perovskite solar cells. (a) n-i-p mesoporous structure, (b) n-i-p planar structure, (c) p-i-n planar structure.

Due to the aptitude of the perovskite to be able to absorb photons and transport charges by itself, the first planar perovskite solar cell was demonstrated in late 2012 by Snaith and co-workers [56] with a PCE of 1.8% (Figure 1.6b), which they directly improved the year after to achieve over 9% in efficiency with an internal quantum efficiency approaching 100%, implying an almost full conversion of the absorbed photons into collected charge carriers. During the same year, Jeng et al. reported the first p-i-n perovskite planar device with a PCE of 3.8% [57] (Figure 1.6c). Up until then, the solar cells were solution-based, but later in the year, Liu et al. demonstrated the fabrication of a n-i-p perovskite solar cell using physical vapour deposition (PVD) with an efficiency of 15.3% [58].

The first ever certified perovskite solar cell made its appearance in the NREL best-research solar cell efficiency chart in 2014 [8] by EPFL with a PCE of 14.1%. Since then, the efficiency of the devices kept on increasing year after year, as depicted in Figure 1.7 and the highest efficiency is now at a record 25.5% held by the Ulsan National Institute of Science and Technology, in Korea. The improvement of the perovskite PCE throughout these years has been made possible by working on different optimization of the full device. The quality of a solar cell relies on first, a proper absorption of the photons by the active layer, i.e, the perovskite, and with minimum absorption from the other layers. Secondly, increasing the PCE is correlated with improving the generation of electrons - hole pairs that will be extracted towards the electrodes, which results in two optimization processes: improving the material intrinsic properties, which is basically defect-related, and improving the transport of the charge carriers towards the electrodes, which is the role of the charge transport layers.

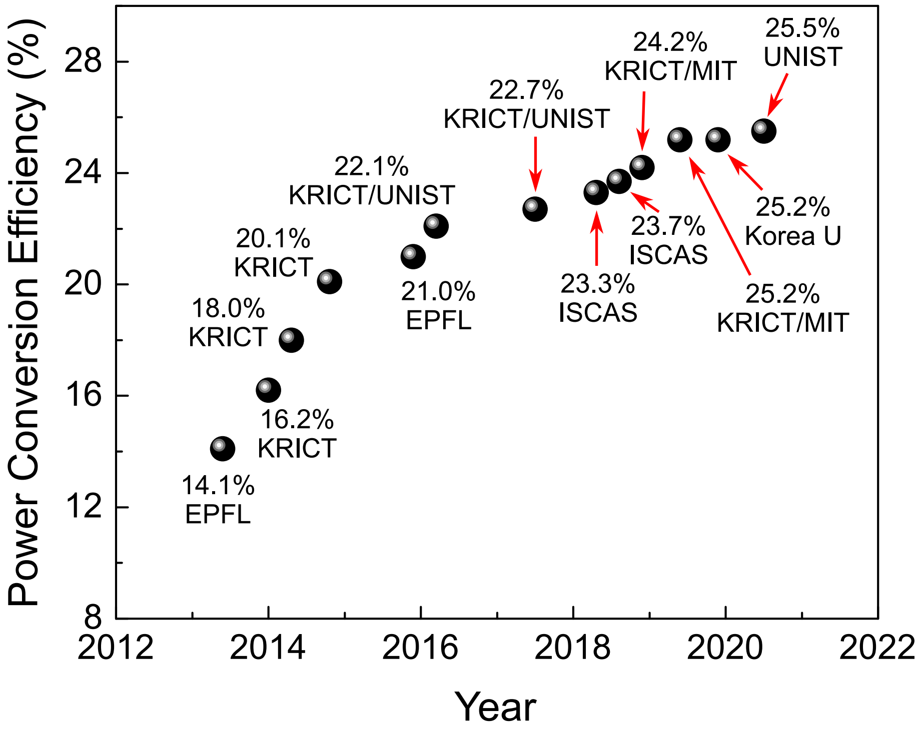

Figure 1.7: Power conversion efficiency of perovskite solar cells as function of the years. EPFL is the acronym of Ecole Polytechnique de Lausanne, KRICT for Korean Research Institute of Chemical Technology, ISCAS for Institute of Semiconductors, Chinese Academy of Sciences, MIT for Massachusetts Institute of Technology and UNIST for Ulsan National Institute of Science and Technology. The data presented come from the NREL efficiency chart [8].

Therefore efforts have been put into place to find the perfect transport layers for the perovskite absorber, as charge separation and collection require a suitable adaptation of the energy levels of these transport layers with respect to the perovskite one. In addition, charge carrier selectivity should be taken in consideration when choosing these layers, that is finding ETL with high conductivity for electrons and low conductivity for holes, and vice versa for the HTL. Combining these properties, reports have come out finding a multitude of suitable transport layers. For the ETL, metal oxides such as TiO_2, SnO_2, ZnO and organic fullerene-based materials such as C60 and [6,6]-phenyl-C61-butyric acid methyl ester (PCBM) have shown to be the best candidates [10]. For the HTL, the main materials are organic-based like Spiro-MeOTAD or poly [bis (4-phenyl) (2,4,6-trimethylphenyl) amine (PTAA), but metal oxides such as NiO have also proven to work. A shortlist of the most used ETL and HTL is depicted in Figure 1.8 with the electron affinities and ionization potentials used from [10, 59, 60, 61].

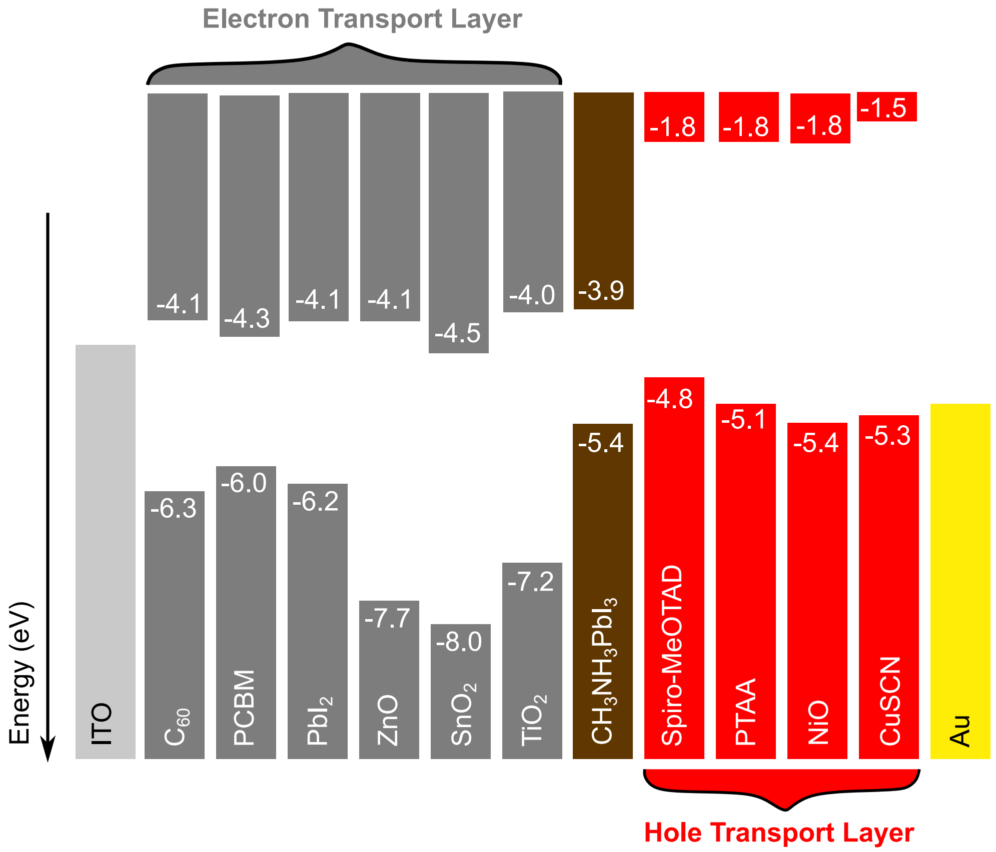

Figure 1.8: Band diagram of the most used ETL and HTL for the perovskite solar cells. Adapted from [62].

Other improvement routes consisted in growing better-quality material systems, more stable by the substitution of the halogen X anion. Chlorine (Cl) and bromine (Br) have similar properties and suitable atomic radius for the tolerance factor discussed previously and have been reported to improve the overall stability of the device but with an increased bandgap, limiting the device efficiency [63]. A solution came from inter-mixing the different halogens and forming mixed halide hybrid perovskites such as $CH_3NH_3PbI_{3-x}Cl_x$. In addition to the variation of the anions, substitution of the A cation was also investigated. As previously observed with the Goldschmidt tolerance factor, a few cations can be used for the A site in order to form a stable perovskite that can be used for solar cells. The goal of this substitution is to gain in stability by getting closer to a cubic phase and the appropriate position of the conduction and valence bands, crucial for improving device efficiencies and stability [64]. To that end, organic formamidinium ions (FA^+) and inorganic cesium ions (Cs^+) have been used to replace the methylammonium ions (MA^+). The incorporation of FA^+ induced a lower bandgap compared to $MAPbI_3$ and a much better overall stability of the devices [65, 66]. Cs^+ ions have also been reported to improve the stability of the perovskite solar cells [67, 68] and therefore partial substitutions of multiple cations were reported to be more effective. Therefore inter-mixing of cations has also been one of the solutions to improve device efficiencies and stability in solar cells, and ultimately, mixed-anions mixed cations hybrid halide perovskites have been the most studied material systems in PV these last few years. As an example, Figure 1.9 depicts the composition of the different record certified solar cells through the years. As can be observed, the latest devices are using mixtures of several anions and cations.

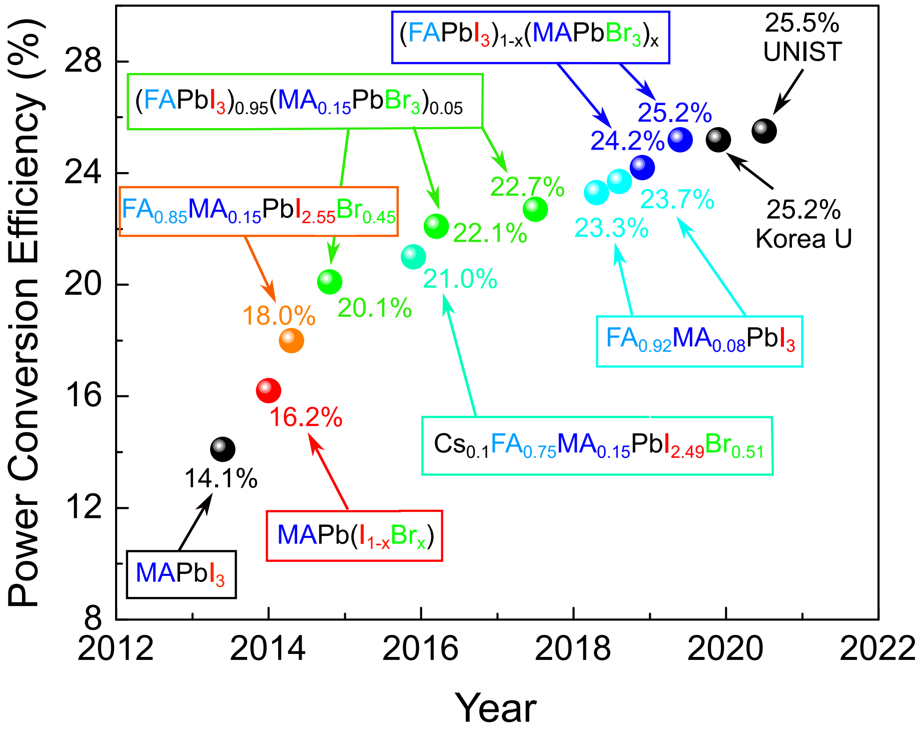

Figure 1.9: Certified PCE throughout the years with the associated composition. Adapted from [69] and completed using [70, 71].

Varying the composition and the transport layers are not the only effective ways to increase a device efficiency. Proper selection and optimization of the electrodes to reduce series resistance and light management are amongst other routes that are used for that matter. However, this thesis will focus on one aspect of device optimization that is also crucial, the surface of the absorber and the interfaces that are induced with such surfaces. As most of the work of this thesis will focus on $MAPbI_3$ perovskite, the next sections will summarize the properties of this material and the mechanisms that introduce efficiency losses in a solar cell made of such a perovskite.

1.2.3 The prototypical absorber: MAPI

$CH_3NH_3PbI_3$, MAPI or $MAPbI_3$ was used in the first certified solar cell reported in the NREL best-research solar cell efficiencies chart [8]. In addition, the thin films fabricated during this thesis were based on this material as it still yields the highest efficiencies when using thermal evaporation. Its full name is methylammnonium lead iodide and its crystal structure is composed of lead sites, iodine sites and MA sites as depicted in Figure 1.10. The latter organic cations have been reported to rotate within their cages and give rise to a higher lattice symmetry [72, 73]. Therefore, even if the ideal form for the crystal structure would be the cubic one, $MAPbI_3$ has three temperature-dependent phases: orthorhombic when the temperature is below 165 K, tetragonal when the temperarure lies between 165 and 327 K, and cubic when the temperature goes above 327 K [74]. Therefore at room temperature, the crystal structure of $MAPbI_3$ is tetragonal and the lattice parameters are $a = b = 8.81$ Å and $c = 12.71$ Å [75]. There, the molecular cations are no longer in a fixed position and the molecular disorder increases [72]. As also represented in Figure 1.10, the iodine sites form the VBM and the lead sites form the CBM.

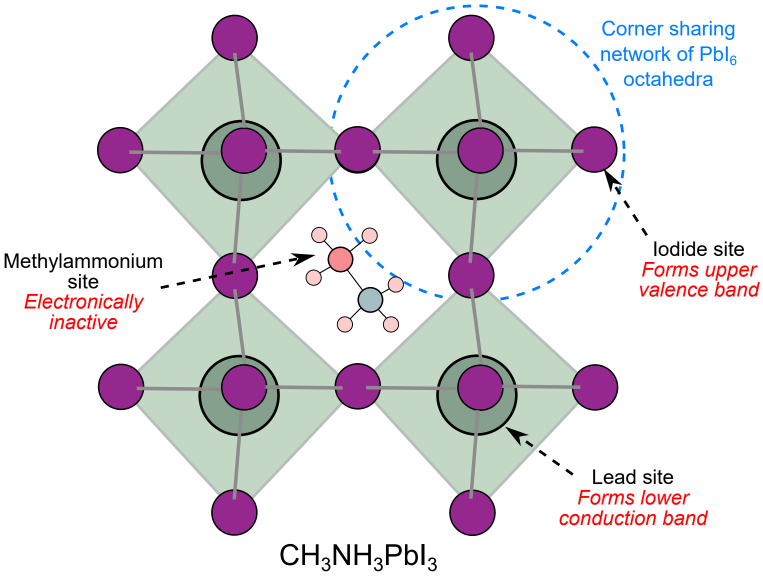

Figure 1.10: Schematic representation of the $CH_3NH_3PbI_3$ crystal structure, reproduced and adapted from [76] under a Creative Commons license.

In Figure 1.11, the electronic band structure of $MAPbI_3$ is represented by Umari et al. [77] and used to calculate a direct bandgap of $\sim 1.67 \pm 0.1$ eV. In addition, both the tetragonal and orthorhombic phases display a similar direct bandgap at the center of the Brillouin zone. As already stated, the CBM is mostly composed of Pb p orbital with some negligible coupling with I, whereas the VBM is composed of antibonding states derived from hybridization of the I 5p- and Pb 6s states [78, 79]. There is therefore no contribution of the organic cation in the band population close to the bandgap. This material also presents a strong s-p antibonding coupling which induces comparable small hole and electron effective masses, which gives its ambipolar transport properties that suit the p-i-n or n-i-p device architecture.

In addition, $MAPbI_3$ presents a sharp absorption edge and a large absorption coefficient above its bandgap, for instance above 10^5 cm^{-1} at $\sim$ 500 nm or $\sim$ 2.5 eV as measured by Xing et al. and displayed in Figure 1.12 [53]. The steepness of the absorption edge is used to determine the Urbach energy, which is representative of the structural disorder and imperfection in stoichiometry amongst other phenomena [80]. This slope has been measured to be around 15 meV [81], which ranges between the values of GaAs (12 meV) [82] and amorphous silicon (a-Si, 50 meV) [83]. One of the additional factor that makes $MAPbI_3$ a suitable absorber for a photovoltaic device is its diffusion length, mobility and

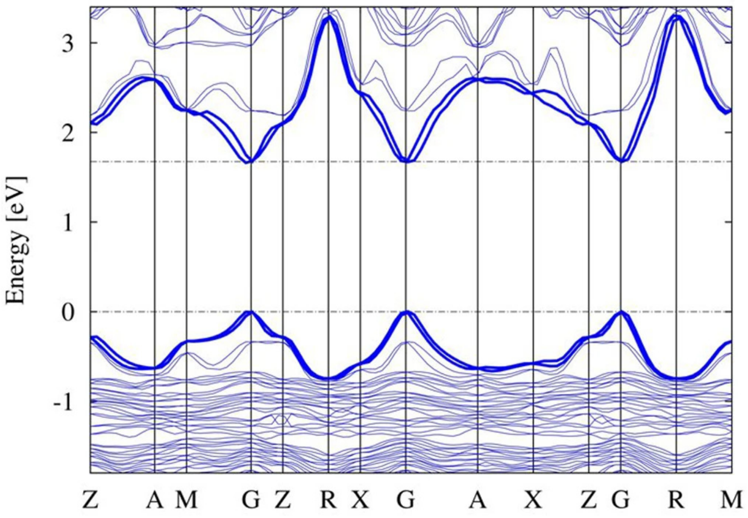

Figure 1.11: Electronic band structure of $MAPbI_3$ along the directions $\Gamma(0,0,0) \rightarrow$ M (0.5, 0.5,0); $\Gamma \rightarrow$ Z (0,0,0.5); $\Gamma \rightarrow$ X (0,0.5,0); $\Gamma \rightarrow$ A (0.5,0.5,0.5); $\Gamma \rightarrow$ R (0,0.5,0.5), as calculated by SOC-GW. Reprinted from [77] under a Creative Commons Attribution-NonCommercial-NoDerivs 3.0 Unported License. Copyright Springer Nature.

defects properties. Stranks et al. were one of the firsts to report diffusion length of ~ 100 nm for $MAPbI_3$ which was within the absorption depth of the absorber itself and therefore not good enough with a typical absorber thickness of 300 - 500 nm [52]. Later on however, Li et al. reported diffusion lengths which varied with the thickness of the perovskite film. As an example, for a 95nm-thick $MAPbI_3$ thin film, they calculated a diffusion length of 270 nm for the electrons and 460 nm for the holes, whereas when they used a thicker thin film of 390 nm, they calculated diffusion lengths of 1.7 µm and 6.3 µm for the electrons and holes respectively [84]. These reported thickness-dependent diffusion length in $MAPbI_3$ still remained longer than the thickness of the absorber and made it suitable for thin film solar cells.

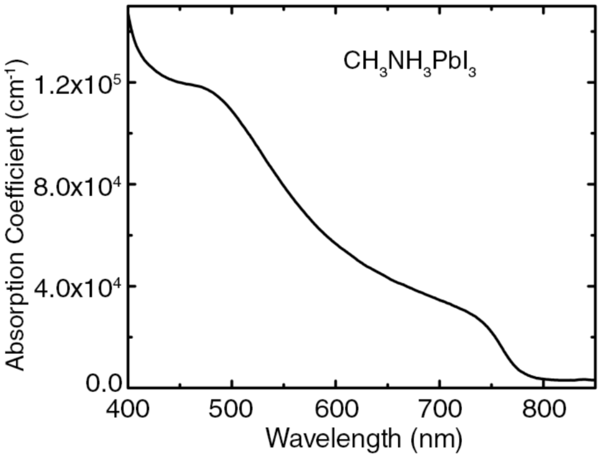

Figure 1.12: Room-temperature absorption coefficient of polycrystalline $MAPbI_3$ as a function of wavelength by [53]. Reprinted with permission of the American Association for the Advancement Science.

Another aspect of the $MAPbI_3$ absorber is that even though they present an ambipolar transport behavior, they still can have a predominant doping, p- or n-type. The tuning of the weakly intrinsic doping can arise from the stoichiometry of the perovskite. Wang et al. have for example reported that depending on the ratio lead iodide (PbI_2) / methylammnoium iodide (MAI) in the precursor solution, different doping could be obtained. With a stoichiometric ratio, $MAPbI_3$ would come as n-type whereas when reducing the PbI_2/MAI ratio, it would be possible to tune it to p-type. Annealing was also observed to convert p-type doping into heavily n-type doping. Therefore PbI_2-rich MAPI would be more n-doped due to more iodine (I^-) vacancies as elemental defects and PbI_2 deficient (or MAI-rich) MAPI would become more p-doped due to Pb^{2+} vacancies [85].

1.2.4 Efficiency losses in MAPI solar cells

Many phenomena and mechanisms cause a solar cell to not fully convert light to energy. The first major losses are discussed in every solar cell textbook and a brief summary is given for the reader in section A.2 of appendix Chapter 1. They can be described as Carnot, emission, thermalization losses and non-absorption of photons below the bandgap. This gives a first theoretical efficiency limit, the Shockley-Queisser (SQ) limit (see section A.2 of appendix Chapter 1) which gives a theoretical efficiency of 30.14% for $MAPbI_3$ [86]. However the highest efficiencies obtained for this perovskite composition still lie within the 21-22% [87, 88], which shows that other phenomena are present that considerably reduce the theoretical PCE. The first one is related to light-management. When photons come in contact with a solar cell, there is absorption but also reflection. The photons reflected are lost and therefore contribute to the reduction in the efficiency. Before a photon can be absorbed by the active layer, it passes through different layers (including the first one being the top contacts). Depending on the absorption coefficients of these layers, additional photons can be lost in this process, by either parasitic absorption or reflection. These losses already account for a certain amount but can also be minimized, by for example using anti-reflection coatings, surface texturing, light trapping... Additionally, when a photon is absorbed by the perovskite layer and generates an electron-hole pair, these charge carriers need to be extracted by the different transport layers towards the electrodes. Again here, collection losses can occur, further reducing the power conversion efficiency (PCE) compared to the SQ limit.

However, not all electron-hole pairs generated by an absorbed photons recombine radiatively (by emitting a photon). Non-radiative recombination also exist, namely defect-assisted recombination or Shockley-Read-Hall (SRH) recombination and Auger recombination (excitation of a third electron). A schematic representation of all the different recombination types is depicted in Figure 1.13. R_{rad} represents the radiation recombination (rate), R_{SRH} the SRH rate, R_{Aug} the Auger recombination rate and $R_{s,h}$ the surface/interface recombination (rate) at the HTL/$MAPbI_3$ interface, which is defect-driven. R_I represents the front recombination at the ETL/$MAPbI_3$ interface. As these recombination mechanisms are not the main focus of this thesis but intervene in one of the characterization techniques used, they have been detailed in section A.3 of appendix Chapter 1 to give an idea on what parameters they depend on.

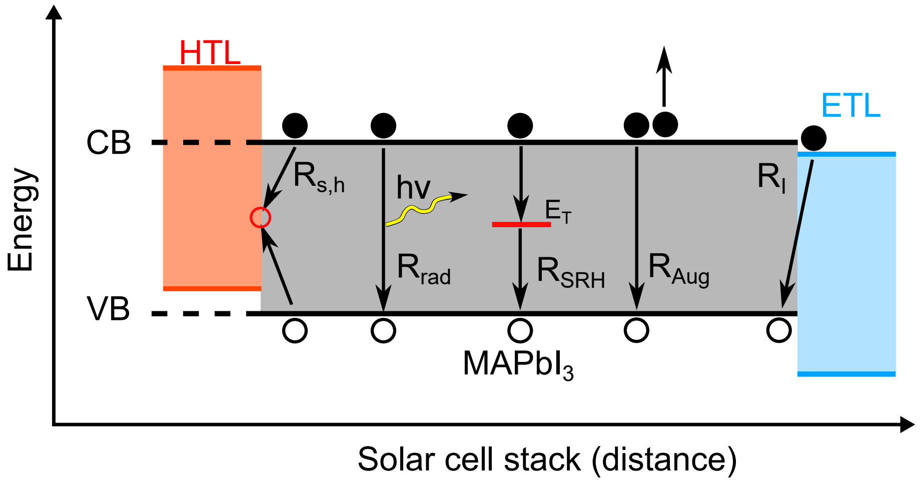

Figure 1.13: Different recombination mechanisms. R_{rad} represents the radiation recombination (rate), R_{SRH} the Shockley-Read-Hall recombination (rate), R_{Aug} the Auger recombination (rate), and $R_{s,h}$ the surface/interface recombination (rate) at the HTL/$MAPbI_3$ interface, which is defect-driven. R_I represents the front recombination at the ETL/$MAPbI_3$ interface.

All these recombination mechanisms are linked to a lifetime, which is a characteristic time before a specific recombination process occurs: τ_{rad} for radiative recombination, τ_{Aug} for Auger recombination, τ_{SRH} for the SRH recombination. These three processes form the bulk recombination lifetime τ_{bulk} such that:

$$\frac{1}{\tau_{bulk}} = \frac{1}{\tau_{rad}} + \frac{1}{\tau_{SRH}} + \frac{1}{\tau_{Auger}} \tag{1.12}$$

In addition to the bulk lifetime, a surface lifetime τ_s also exists (see section A.3 of appendix Chapter 1) and therefore the total lifetime, which takes into account both bulk and surface lifetimes can be written as follows:

$$\frac{1}{\tau_{tot}} = \frac{1}{\tau_{bulk}} + \frac{1}{\tau_s} \tag{1.13}$$

To minimize efficiency losses in solar cells, recombination mechanisms should be reduced, which also means that lifetimes should be increased. Most of the time one of the non-radiative recombination mechanisms is limiting the solar cell performances (SRH or surface recombinations).

1.2.5 Stability issues and degradation of MAPI solar cells

Stability in solar devices is key as they are intended to be used for long times and in order to be made into solar modules, they need to have a guaranteed lifetime and stability of 25 years required by the IEC 61646 testing standards [89]. Besides, these encapsulated solar cells need to perform under different weather conditions like various humidity levels and temperatures and therefore stability is one of the key parameters to monitor in perovskite. However currently, $MAPbI_3$ solar cells can only retain their efficiencies for a few months and are strongly affected by external environmental stimuli such as moisture and water, light and temperature but also by intrinsic properties such as structural changes and ionic motion.

Temperature and thermal annealing

One of the first stability issues comes from the structural changes. As previously explained, a phase transition occurs for $MAPbI_3$ from a tetragonal phase to a cubic one at $\approx$ 327 K (or 54 °C). This transition changes the ordering of the MA^+ ions and further displacements in the PbX_6 octahedron, which changes the structure volume and can alter the recombination dynamics, the bandgap but also the band alignment. It can also induce additional ferroelectricity [90, 91] and thermal stress leading to decomposition [92, 93]. This can be a problem as the solar cell itself can easily reach operating temperatures above 54 °C depending on the combination of the outside temperature and the incoming illumination. Annealing at temperatures above 80 °C for a long heating time has also been shown to induce decomposition towards the PbI_2 complex [94], which is irreversible compared to the tetragonal-cubic phase transition. X-ray photoelectron spectroscopy (XPS) even measured the loss of the MA organic cation (or MAI complex) at temperature above 100 °C [95]. To counter the phase transition at operating temperatures, incorporation of FA and Br in a $(FAPbI_3)_{0.85}$ $(MAPbBr_3)_{0.15}$ mixture has proven to be successful [96], and in general, the use of mixed perovskites was identified as a way to improve stability [97, 98].

Water, moisture and humidity exposure

In addition, $MAPbI_3$ has been reported to degrade upon prolonged exposure to water, humidity or moisture by transitioning from a black to yellow color. This is indicative of a decomposition towards PbI_2, where the perovskite undergoes first intermediate phase decomposition, in the hydrous form such as water-intercalated iodide perovskite $MAPbI_3\_H_2O$ and monohydrated phase $MAPbI_3{\cdot}H_2O$ [99]. The polyhedral representation of these intermediate phases is depicted in Figure A.6 of appendix Chapter 1A.5. This implicates the formation of defects such as the partial Schottky PbI_2 vacancy complex (V_{PbI_2}) and point defects like V_I and V_{MA} which are linked with the decomposition of $MAPbI_3$ into CH_3N_2 and HI. It has however been reported that growing in I-rich conditions can improve the stability of this compound against humidity exposure [99]. It has to be noted that even though prolonged water exposure decomposes $MAPbI_3$, a small amount of moisture has been proven to improve the film quality due to larger grain sizes and consequently fewer grain boundaries [100, 101, 102].

Light-induced degradation

As solar cells are bound to spend their life under cyclic illumination, it is important that they stay stable upon prolonged light exposure and under various environments. However, $MAPbI_3$ has been reported to degrade differently depending on the environment and the illumination time. Many studies have first demonstrated how light soaking could improve the performance of solar cells, which could be linked to re-arrangement of ions in the crystal lattice, inducing a spontaneous p-i-n homojunction within the absorber [103], or by the neutralization of the bulk and interfacial defects by the photogenerated defects [104]. Nevertheless the prolonged effect of the light on $MAPbI_3$ is controversial and different groups have reported its effects on the photophysical and electronic properties of methylammonium lead triiodide, such as the motion of the methylammonium ions and rotation of its CH_3 and/or NH_3 groups around the C-N axis [105], or a light-enhanced structural deformation [106]. But the degradation state depends on the environment used. In ultra-high vacuum (UHV, pressure lower than 10^{-9} mbar), a direct evidence of the degradation comes from the change in colour from black to gray upon illumination as reported by Tang et al. [107], which is linked to the formation of metallic lead (Pb^0) and PbI_2 within 6 hours of white light illumination. Several reports based on XPS have shown such decomposition pathways where $MAPbI_3$ would first decompose into PbI_2 and other gaseous compounds and then PbI_2 would futher get reduced to Pb^0 and I_2 [108, 107, 109, 110]. The decrease of the N/Pb and I/Pb ratios also suggested that N and I from the MAI complex are lost to the UHV, indicating also a decomposition of the MA cation. The nature of the volatile products are however difficult to identify and could be one of the following compounds: CH_3NH_2, HI, I_2, H_2 or NH_3 [111]. In inert atmosphere, like in nitrogen (N_2), negligible changes were noticed by several reports [107, 112] where no Pb_0 formation or decomposition was noticed, which is promising for encapsulated devices. However, degradation would occur on a much greater and faster scale under ambient conditions where oxygen acts as a catalyst and induces the deprotonation of $CH_3NH_3^+$ resulting in the formation of the gaseous CH_3NH_2 and H_2 [113]. Other reports noted the rapid change of color from black to either yellow or transparent when illuminated under continuous illumination [107, 112, 114], indicating a decomposition towards PbI_2 and then into lead salts such as PbO, $PbCO_3$ or $Pb(OH)_2$ [107]. The following decomposition pathways can occur:

$$MAPbI_3 \xrightarrow{h\nu \geq E_g} MAPbI_3^* \tag{1.14}$$

$$MAPbI_3^* + O_2 \rightarrow MAPbI_3^+ + O_2^{\cdot -} \tag{1.15}$$

$$MAPbI_3^+ + O_2^{\cdot -} \rightarrow 4CH_3NH_2 + 4PbI_2 + 2I_2 + 2H_2O \tag{1.16}$$

Equation 1.14 shows that $MAPbI_3$ is in an excited state after the photons excite carriers into the conduction band. Upon oxygen exposure, deprotonation of the MA cation occurs as well as oxidation of iodine (equation 1.15). In the end, decomposition into multiple compounds (solid and gaseous) happens (equation 1.16) [115]. Lastly, other groups have reported that the adsorption of H_20 on the $MAPbI_3$ surface and incorporation in the bulk was made easier upon illumination due to a giant photostriction effect, that is a light-induced expansion of the $MAPbI_3$ lattice. This structural change upon illumination would lead to a decrease in bandgap and therefore more absorption, resulting in a self-accelerated photostriction process, that would speed up the decomposition process of $MAPbI_3$ under moisture exposure and be detrimental for devices [116, 117].

Hysteresis and ion migration

One common issue concerning $MAPbI_3$-based solar cells is that upon current-voltage characterization, a shift between the forward (negative to positive voltages) and reverse (positive to negative voltages) sweeps would occur, which is called hysteresis and is depicted in Figure 1.14.

It has been initially reported that this hysteresis depended on the type of the contact material (p- or n-type) and was strongly dependent on the scan rate, as a slow sweep would increase the degree of hysteresis. Snaith et al. [118] gave three possible origins from this effect: firstly, the defects within the perovskite absorber would act as traps and depending on the sweep direction, detrapping would occur resulting into poorer performance. Consequently using fast scan rate would speed up the trapping/detrapping effect. Secondly, the ferroelectricity behavior of $MAPbI_3$ could induce favorable collection depending on the sweep. And lastly, the excess ions could migrate in the films, screening

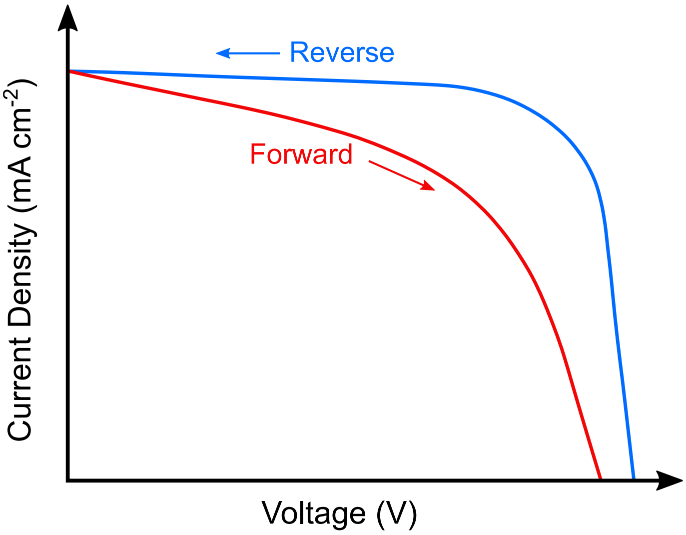

Figure 1.14: Sketch of the hysteresis effect observed during JV measurements.

the space charge buildup, giving rise to better charge collection depending on the sweep direction [118]. Later on, it was demonstrated that the strong dependence on sweep rate and time was related to the migration of ions that then accumulate at the interfaces of the electrodes and screen the applied field, reducing the built-in potential and therefore varying the efficiency to collect carriers [76, 119]. The variation of the hysteresis degree with different device architecture was explained by a change of the defect density, for instance by efficiently passivating trap states at the surface of the absorber, which can also contribute to the hysteresis but is not the dominant factor [120]. However some studies clearly state that both ion migration and interface recombination are required to observe this hysteresis [121, 122]. There is therefore still a debate on the nature of the ionic species that are responsible for the ion migration, causing hysteresis and which is further discussed in section A.6 of appendix Chapter 1.

Lastly, other degradation routes exist in perovskite, due to an applied bias [123, 124], X-rays exposure [125, 126], electron beam [127, 128], degradation of the charge transport layers or interfaces [129, 130] and the degradation of the bare surface of perovskite, which will be discussed thereafter.

This section clearly highlights how the stability of $MAPbI_3$ can be altered by internal and extrinsic factors and where the losses are situated. In order to improve perovskite solar devices, optimizing the bulk material is crucial. However, the optimization of the surface of $MAPbI_3$ and the direct interfaces that follow is equally important. In order to improve a perovskite device efficiency and stability, non-radiative recombination, degradation and ion migration have to be controlled. Surfaces and interfaces in solar cells can be in that matter the limiting factors to achieve the highest efficiencies and therefore, they need to be thoroughly investigated, which is the focus of the next section.

1.3 The surface of MAPI solar cells

It has been previously shown that surfaces and interfaces were the key parameters to control in order to improve device efficiencies and get closer to the SQ limit. Even though a perfect perovskite absorber layer with the minimum defect density could be grown, interfaces could still limit in the end the PCE. Therefore, characterizing the surface of $MAPbI_3$ under different environment and stimuli is the first step to understand how to optimize the interfaces that will be formed later, which will also need careful scrutiny.

1.3.1 Surface terminations

The surface is the termination or interruption of the atomic periodicity of the crystal lattice. All surfaces are therefore energetically unfavorable as the bonds are broken and they have a positive surface free energy (surface tension) of formation. In order to reduce this unfavorable contribution, and access the most favorable surface configuration, one can reduce the amount of surface exposed, expose surface planes with low surface free energy or alter the unfavorable planes such that it results in a reduction of their surface free energy. A surface with low surface free energy is the most energetically favorable as it will enable the creation of bonds with layers deposited on top, creating energetically favorable interfaces with less defects, less recombination and therefore less device performance losses [131].

The interruption of the atomic periodicity induces either specific intrinsic or extrinsic surface states that are different from the ones present in the bulk. Depending on the nature of these surface states or terminations, the quality of the material will vary due to the changes in band structure and electron behaviour. The surface terminations of $MAPbI_3$ can therefore either be the PbI_6^- units or the organic cations. Taking into account the most energetically favourable surface of $MAPbI_3$ (001) [132], three surface terminations can be kept, which are depicted in Figure 1.15 and are MAI, PbI_2-flat and PbI_2-vacant. Surface terminations are also more or less energetically favourable depending on the lattice orientation. But in tetragonal $MAPbI_3$, (110) and (001) surfaces are assumed to be more stable than (100) and (101) for example. Also X-ray diffraction measurements present them as the predominant surfaces in $MAPbI_3$ [132].

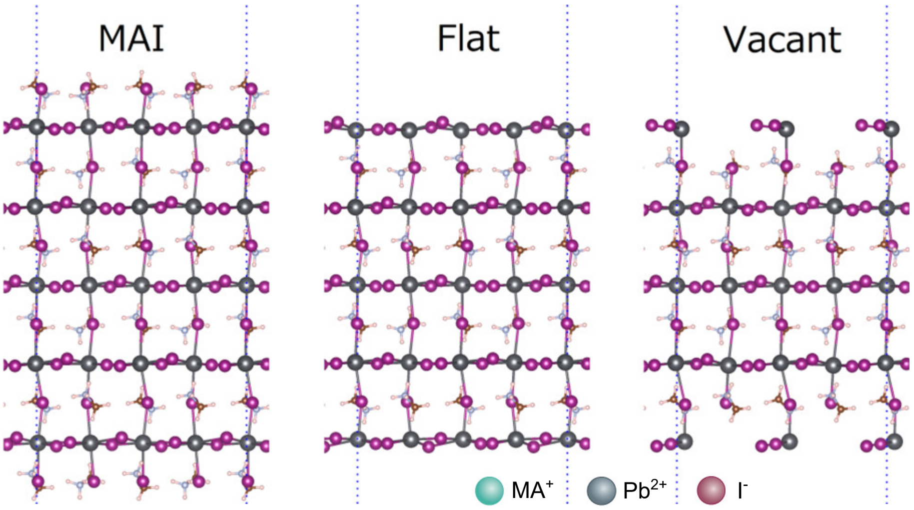

Figure 1.15: Crystallographic side views of three representative surface terminations in $MAPbI_3$: MAI, PbI_2-flat and PbI_2-vacant. Adapted from [132] by permission of ACS, further permissions relating to the material excerpted should be directed to the ACS.

These terminations are strongly dependent on the synthesis method and composition used, as for instance PbI_2-rich conditions would induce a higher probability of obtaining PbI_2-flat terminations [133], but still some terminations are more energetically favourable compared to others. A PbI_2-vacant termination has for example been reported to be more stable than a PbI_2-flat termination [133, 134] whereas other reports showed MAI-rich terminations to be more thermodynamically stable than PbI_2 flat-terminated surfaces [135]. In addition, one type of termination can sometimes be more desirable depending on the layer deposited on top of the perovskite, in order to have a more favourable energy level alignment [135]. Knowing the terminations at the surface is of great use to further elucidate the type of surface defects that can be encountered. However $MAPbI_3$ presents additional surface disorder owing to the dynamic rotations of the MA^+ cations and the weak binding of the ionic lattice. This translates into a varying surface composition and structure, resulting in changes at the surface and possible reconstruction, for example upon external stimulation [136].

1.3.2 Surface defects

Similar to the bulk, interstitial, antisite defects and vacancies can exist at the surface of $MAPbI_3$ and have been represented by Xue et al. [136] in Figure 1.16. The dominating point defects in $MAPbI_3$ are shallow defects and the deep defects have high formation energies. However, due to the different environment between the bulk and the surface, the energetic properties of the surface defects can vary from the bulk ones. The chemical surrounding stemming from the different terminations also plays a role in the deviations between bulk and surface defects. Surface states arising from the different surface terminations can only result in small variations in bandgap, where perovskites with a PbI_2-terminated surface show slightly smaller bandgap than with MAI-terminated surfaces [133, 134].

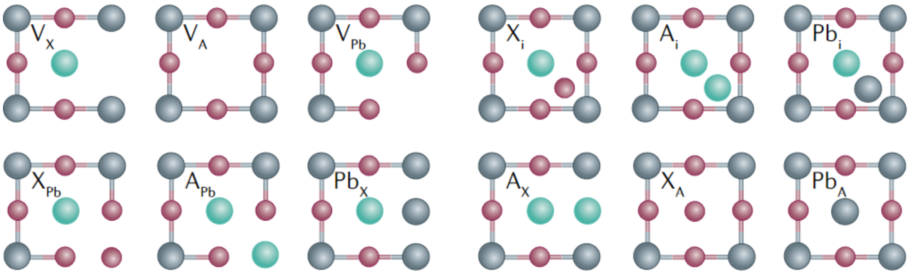

Figure 1.16: The 12 types of native point defects found in metal halide perovskites. V_Y denotes a Y vacancy, Y_i denotes an interstitial Y-site and Y_Z denotes a Z-site substituted by Y, where Y and Z represent an ion of $APbX_3$ (where A^+ is a monovalent cation and X^- a halide). Reprinted by permission from Springer Nature, [136], Copyright (2020)

Uratani et al. have calculated the formation energies of surface defects when taking into consideration different fabrication conditions: I-rich, moderate and Pb-rich where the chemical potentials of I, Pb and MA were varied accordingly in the calculations [132]. The types of surface defects with their respective formation energies depending on the fabrication conditions are listed in Table 1.1.

From these calculations, they observed for instance that on an MAI-terminated surface, only V_{MA} has a low formation energy but no deep defect states, whereas both PbI_2-flat and vacant have several surface defects with low formation energies and close midgap defect states. If I-rich conditions (excessive I atoms) are taken, only I_i combines both a low formation energy and deep defect states. Under Pb-rich condition (excessive Pb atoms and I atom vacancies), Pb_i generates deep defect states and has low formation

Termination	Defect	I-rich [eV]	Moderate [eV]	Pb-rich [eV]
MAI	V_I	2.38	1.77	1.15
MAI	V_{MA}	0.32	0.91	1.54
MAI	Pb_i	4.69	3.45	2.24
MAI	Pb_{MA}	2.35	1.70	1.13
MAI	Pb_I	5.97	4.14	2.31
PbI_2-flat	I_i	-0.03	0.57	1.19
PbI_2-flat	V_I	4.55	3.94	3.32
PbI_2-flat	Pb_i	2.94	1.71	0.50
PbI_2-flat	V_{Pb}	-0.13	1.10	2.31
PbI_2-vacant	I_i	-0.12	0.48	1.10
PbI_2-vacant	V_I	1.76	1.15	0.54
PbI_2-vacant	Pb_i	2.71	1.48	0.26
PbI_2-vacant	V_{Pb}	-1.40	-0.17	1.04

Table 1.1: Considered types of surface defects and their formation energy (in eV) under different conditions. Reprinted from [132] with the permission of ACS. Further permissions relating to the material excerpted should be directed to the ACS.

energies, making it the most favourable surface defects, in complement with V_I on PbI_2-vacant surfaces. Therefore both I-rich and Pb-rich conditions induce carrier-trapping surface defects but Pb-rich conditions are more desirable due to higher formation energies compared to I-rich conditions. Therefore fabrication with an excess of PbI_2 (an excess of Pb compared to the iodine in $MAPbI_3$) would in that sense be beneficial, and has been reported to increase PCE in $MAPbI_3$ solar cells [137, 138, 139]. However, the fabrication of $MAPbI_3$ under moderate conditions (stoichiometric composition) does not induce carrier-trapping surface defects and therefore, combined with the most favourable MAI-terminations, would minimize carrier trapping and non-radiative recombination, leading to higher efficiencies [132].

1.3.3 Surface and extrinsic factors

$MAPbI_3$ is known to have a metastable surface, which therefore can change upon external stimuli in order to attain a more favourable energetic state. The complexity of perovskite therefore arises from external factors that induce extrinsic surface disorders. Xue et al. [136] and Schultz et al. [140] discussed these phenomena in more details in their respective review papers. Multiple extrinsic factors can lead to changes at the surface, such as passivating layers, diffusion of elements from metallic electrodes, transport layers that alter the surface of the perovskite or again environmental factors such as O_2 and H_2O exposure.

Some adsorbates for instance only interact (and adsorb) onto specific surfaces. Torres et al. have studied the impact of anisole on the (001) surface of $MAPbI_3$ to better understand the interaction with the spiro-MeOTAD HTM, and they observed that adsorption would only occur on MAI-terminated surfaces [141]. Water and moisture can be detrimental to the performance of $MAPbI_3$ and even more when light comes into play. It is therefore essential to look at the interaction of species such as H_2O and O_2 with different surfaces. Koocher et al. have demonstrated that water adsorption by the (001) surface of

$MAPbI_3$ was happening differently depending on the polarization of the MA^+ cation. For an MAI-terminated surface, water adsorption would be more favourable when -NH_3^+ was pointing towards the surface compared to -CH_3 pointing towards the surface, whereas opposite dependence would occur for a PbI_2-terminated (flat) surface. Mosconi et al. have demonstrated using DFT calculations that MAI-terminated surfaces are more prone to interact with and adsorb H_2O molecules at the Pb sites, giving rise to a dissolution of the MAI unit. The PbI_2-terminated surfaces on the other hand have been reported to be more stable as the water molecules infiltrate the perovskite lattice leading to a perovskite hydrated phase, which does not show electronic or structural disorder [142]. Water incorporation through the surface does not alter significantly the structural or electronic properties of the $MAPbI_3$ thin-film, but the addition of light will induce the degradation towards PbI_2 as already discussed. Apart from the environmental factors, additional layers such as HTM and ETL, that need to be deposited on top of the perovskite to make a solar cell, are extrinsic factors that can have either negative or positive effect on the $MAPbI_3$ surface. Depending on the deposition process, some layers can damage it or can induce diffusion of elements at the interface or within the bulk. However, other layers can help passivate the dangling bonds or the non-favourable terminations and therefore reduce or suppress the recombination centers. In any case, it is crucial to know the surface energetics and morphology of $MAPbI_3$ before depositing a layer on top in order to properly understand the effects of the latter.

1.3.4 Surface grains and grain boundaries

As previously discussed, surface terminations and defect states depend on the orientation of the lattice and therefore can be different on the (001) and (110) surfaces. Polycrystalline perovskites are made of thousands of grains with different crystallographic orientations. This ultimately results in different properties between different grains of the same absorber as deQuilletes et al. have demonstrated using photoluminescence mapping, where some grains display worse non-radiative recombination rates than others [143]. Bischak et al. have also used cathodoluminescence to resolve spatially an heterogeneous surface in terms of charge carrier recombination [144]. But the discrepancy in surface terminations has not only been observed at grains but also within one grain. Grains are actually made of a multitude of facets that have different orientations. Leblebici et al. have demonstrated through the use of scanning probe microscopy techniques a striking intra-grain heterogeneity, which they attributed to variations of trap state density at different crystal facets within a single grain [145]. The large difference of short-circuit current coming from the different facets or grains are problematic and ultimately limits the overall efficiency of the device. Therefore it is suggested to try to control the growth direction of $MAPbI_3$ grains as well as the orientations of the facets in order to facilitate and improve the interface with either the hole or electron transport layer. For example, one can choose correct Lewis base solvents and annealing times for modulating the nucleation mechanism of $MAPbI_3$ [146], or transform the (100) and (112) facets into (110) and (002) facets by means of solution-mediated secondary growth [147]. It has however to be noted that recent reports have also demonstrated that grain orientations had no influence on device performances [148].

Another type of interface important to investigate in polycrystalline solar cells is the one separating two adjactent grains, which is called a grain boundary. The previously displayed disparity of grains introduce regions with atomic mismatch and disorder in the lattice, which are called grain boundaries (GBs) and are depicted Figure 1.17. These GBs, which are typically two-dimensional structures [149], have high energy and strongly influence the mechanical and electronic properties of a material.

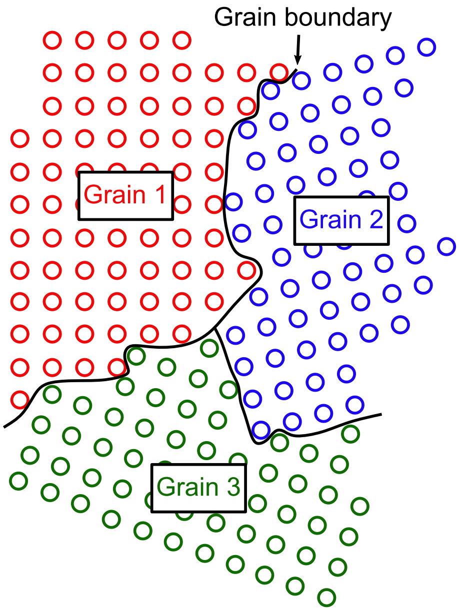

Figure 1.17: Schematic of grain boundaries dividing three grains of different orientations.

The GBs in $MAPbI_3$ and their influence on device efficiencies are still highly debated. Early studies and calculations by Yin et al. showed that grain boundaries were, contrarily to their thin-film counterparts (see section A.7 of appendix chapter 1 for a brief discussion), benign [150, 151]. In their work, they computed the density of states at the grain boundaries, taking the structure of the $SrTiO_3$ perovskite and the $\Sigma3$ (310) GB which has typical features such as dangling bonds. The DOS analysis led to the conclusion that the GB did not generate states in the bandgap of $MAPbI_3$ but rather shallow point defects created by dangling bonds such as I-I and Pb-Pb bonds. They however later found out that the defect level close to the VBM could still act as a shallow hole trap state. Yang et al. have examined the differences in photoluminescence between grains and grain boundaries and concluded that even if the GBs displayed lower luminescence, which they attributed to the reduced area of the grain boundary compared to the grain interiors, the carrier lifetimes were similar at the grain interiors (GIs) and at the GBs, suggesting that GBs were not the dominant non-radiative recombination centers [152]. Chu et al. have also observed that GBs exhibit photo-responses comparable to the GIs and that they were not nucleation centers in the degradation process of $MAPbI_3$, even though they initially reported that growing larger grains perovskite induced better efficiencies, suggesting that GBs were detrimental [153]. Yun et al. went even further and demonstrated using different scanning probe techniques that the GBs were beneficial in $MAPbI_3$, by efficiently separating and collecting the charge carriers [18].

On the other hand, a large amount of reports have found that GBs had a negative and detrimental role in getting high-efficiency perovskite solar cells. First of all, many studies have reported that increasing grain size led to an improvement in PCE [154, 155, 156] with the explanation that the number of GBs, possible recombination centers, is reduced, leading to a direct increase in performances. deQuilettes et al. have reported,

using confocal fluoresence microscopy, that carrier lifetimes were different from one grain to another and much worse within the GBs, suggesting a much higher non-radiative recombination rate [143]. Long et al. have used calculations to show that GBs could accelerate the non-radiative recombination in $MAPbI_3$, by reducing the bandgap and increasing the electron-phonon coupling [157] before later demonstrating in 2019 that GBs can actually have a positive effect by seperating charge carriers and were not necessarily accelerators of charge recombination [158].
Sherkar et al. drew a slightly more moderate vision of the GBs, linking them to the compactness of the film. According to them, $MAPbI_3$ solar cells act differently from inorganic solar cells where trap states lying at the GBs are neutral and then become negatively charged when filled by photogenerated carrier, inducing a barrier for electron transport, which reduces the efficiency (Figure 1.18a). For $MAPbI_3$, traps are very well present at the GBs but they are positively charged due to accumulated iodine vacancies and then become neutral when photogenerated charge carriers fill these trap states, which ultimately results in high-efficiency solar cells, as the electron transport is not influenced (Figure 1.18b).

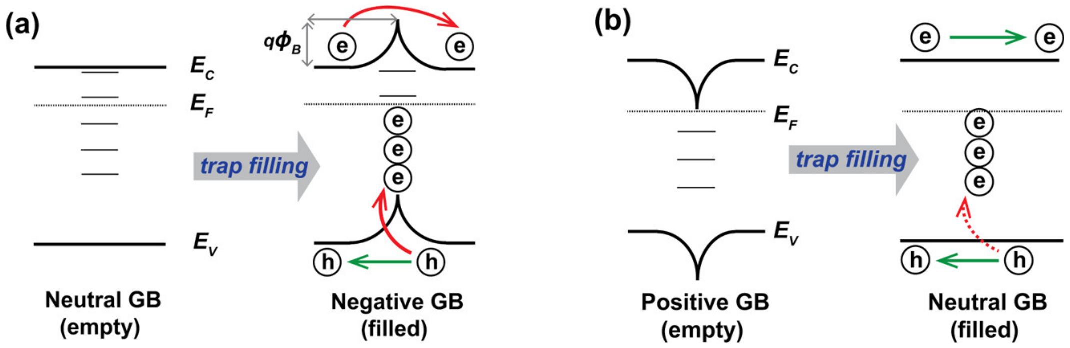

Figure 1.18: (a) Representation of grain boundaries in an inorganic solar cell: traps are neutral when empty and charged when filled with photogenerated carriers, inducing a barrier that reduces efficiency. (b) Representation of grain boundaries in $MAPbI_3$ solar cells: traps are positively charged due to accumulated iodine vacancies and neutral when photogenerated carriers fill the trap states, leading to unaffected electron transport. Adapted with permission of [159] under CC-BY-NC-ND 4.0 license. Copyright 2017, American Chemical Society.

However, depending on the compactness of the film and nature of the GBs, the sign of the traps (charged or neutral) and the trap density will have different effect on the performances. They have demonstrated that non-compact films with open GBs and high trap density (Figure 1.19a) are quite sensitive to the sign of filled traps, leading to faster SRH recombination, whereas compact films with fused GBs and low trap density (Figure 1.19b) do not seem to be sensible [159]. Their conclusions could be linked to the work of Shao et al., who showed that compact films were much less sensitive to light-soaking effect due to lower trap-assisted recombination, compared to non-compact films [160].
Several review papers and essays with additional information concerning grain boundaries and their impact on different aspects of perovskite solar cell efficiencies can be found in the literature [161, 162].

The main takeaway message from this subsection is that the role of grain boundaries in $MAPbI_3$ solar cells performances is still highly debated but it is strongly linked to the fabrication process used and composition of the $MAPbI_3$ films (either Pb-rich or I-rich

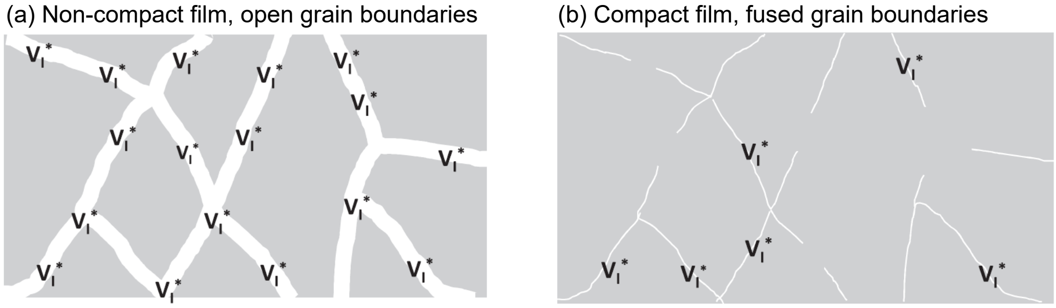
(a) Non-compact film, open grain boundaries
(b) Compact film, fused grain boundaries

Figure 1.19: Representation of (a) open grain boundaries in a non-compact perovskite film and (b) fused grain boundaries in a compact perovskite film. Reprinted, with permission, from [160]. Copyright 2014 John Wiley and Sons

for instance), leading to different surface terminations, trap densities, and defect states.

1.3.5 Surface energetics, interfaces and surface passivation

As the surface of $MAPbI_3$ can introduce local variations in surface terminations, surface states at the grain facets and at the GBs, it will induce different recombination mechanisms when an interface comes into play, whether it is a hole or an electron extraction layer. Interfaces are therefore one of the limiting factors when discussing solar cell performances and research has been going on to look into layers that would be suitable energetically with $MAPbI_3$ but also that could passivate the different surface states, synonym of unwanted recombination.

It is however essential to define beforehand the relevant energetic quantities that can help position electronic levels of two solids in contact. The Fermi level (E_F), which was already defined in this thesis, is one of them and can be seen as the levels separating filled from empty electronic states. Another important surface-related quantity is the vacuum level E_{VAC}, which is defined as the minimum energy needed for an electron to escape from the solid into vacuum. The value of the vacuum level is set locally as the surface is composed of local electrostatic dipoles that will induce different vacuum levels [163]. It then becomes clear that the composition at the surface, as well as extrinsic factors altering the latter, for example the adsorption of molecules, will condition the position of E_{VAC}. As these two quantities have been defined, the energy difference between them can be introduced as follows:

$$\Phi = E_{\mathrm{VAC}} - E_F \tag{1.17}$$

Equation 1.17 introduces the workfunction (WF) Φ which gives the position of the Fermi level of a solid with respect to the vacuum level (Figure 1.20). It can additionally be defined as the energy required to remove an electron situated at the Fermi level and place it outside of the surface. As E_{VAC} is positioned at rest within a few nanometers to micrometers outside the solid [164], the closest available electrons at rest lie in the VBM as doping and thermal stimuli are neglected (which would enable electrons to be excited in the CBM). The few nanometers to micrometers distance is a vague definition that refers to the distance sufficient for the electron to experience the full impact of the surface dipole, which will be defined after. In order to escape from the solid, electrons in the VBM require beforehand an energy to be removed from the system, which is called ionization energy

(IE) (Figure 1.20). On the other hand, when an electron gets inside the system, it drops onto the lowest unoccupied state, which is the CBM and the energy gained from that action is called the electron affinity (EA). The electron affinity in solid state physics and semiconductors is defined differently than in chemistry and atomic physics. Commonly-used semiconductors have IE and EA between 4.5 to 6.5 eV and 2 to 4 eV, respectively. It stems from these definitions that the difference between the IE and the EA is defined as the bandgap E_G. The quantities depicted in Figure 1.20 are therefore the essential ones in order to define the electronic structure of an interface, between the surface of a material and an environment, but also an interface between different materials. These energetic positions are the core parameters to understand and picture the processes of charge transport within a solar cell. However, it has to be noted that E_{VAC}, WF, IE and EA are solely defined at the surface of the material, as removing electrons from a semiconductor, or gaining one from the outside can only happen via the surface of this semiconductor.

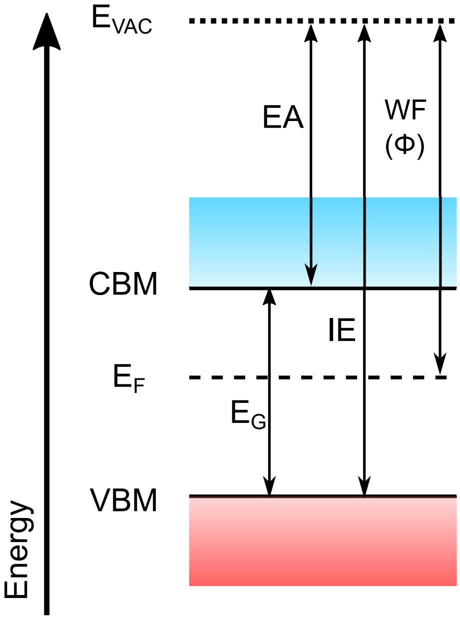

Figure 1.20: Energy diagram of a semiconductor representing the relevant electronic levels position: bandgap (E_G), electron affinity (EA), ionization energy (IE), and workfunction (WF, Φ)), with respect to the vacuum level E_{VAC}.

It is now interesting to look at what affects these different quantities. The WF depends on two parameters: the position of the Fermi level and the vacuum level. E_F is defined using the density of states, temperature, carrier density and doping concentration in a semiconductor as discussed in the equations 1.7 to 1.11 of sub-section 1.2.1. The WF can be seen as an energy barrier which electrons need to overcome in order to escape the solid. It consists in a bulk and a surface component and measuring the WF means measuring the convolution of both [140]. The bulk component is linked to the chemical potential derived from the density of states and density of charge carriers and is therefore strongly influenced by fabrication processes and composition of the bulk material. The surface component on the other hand depends on the charges at the surface of the semiconductor, as well as physical effects present at the surface, and can also be referred to as the surface dipole component. The dipole arises from surface termination. In an ideal semiconductor, the electron density in the bulk along the z direction (z being from the rear to the surface) is the same but as the lattice terminates at the surface, a negative "layer" will be formed outside of the solid due to evanescent electrons. This will directly result in the formation of positive ions at the surface. This double layer creates a potential a few nanometers away from the surface, altering E_{VAC} and thereby the WF [164]. It then becomes clear that depending on the surface terminations and surface states, the WF will vary considerably. Strayer et al. have for example demonstrated a WF of 4.47 eV for an atomically clean (111) single crystal tungsten compared to a WF of 5.25 eV for the (110) surface [165]. It also stems from the dependence of the surface on the dipole, that the environment as well as extrinsic factors such as adsorbates and molecular orientations will alter E_{VAC} and the WF. However, compared to metal surfaces, the surface dipole in semiconductors is less prominent in the contribution of the WF as the electron density is lower there but the environment will definitely change the EA, IE, and WF. Deposition of a layer on top of the surface will affect differently these quantities, depending on the nature of the latter. A layer with acceptor-like species will result in an increase of the E_{VAC}, WF, IE and EA, whereas one with donor-like species will do the opposite [164]. Therefore surfaces of a semiconductor will vary depending on the layer on top and it is evident that knowing the energetics of both layers can help in the determination of the interface and thereby the charge transfer.

Figure 1.20 however only displays flat bands, which is the ideal case of a semiconductor with a perfectly clean surface. In reality, bending of the bands (vacuum level, CBM and VBM) can occur, either with the bands going down from the bulk to the surface, called downward band bending, or with the bands going up from the bulk to the surface, called upward band bending (Figure 1.21). Band bending can be induced via an interface with another material (metal, semiconductor, oxide), by an internal or external electric field but also due to the surface states present at the surface [166]. The surface terminations and the resulting dangling bonds form electronic states at the surface, which lead to a continuum of localized energy states, that can either be occupied by electrons or empty.

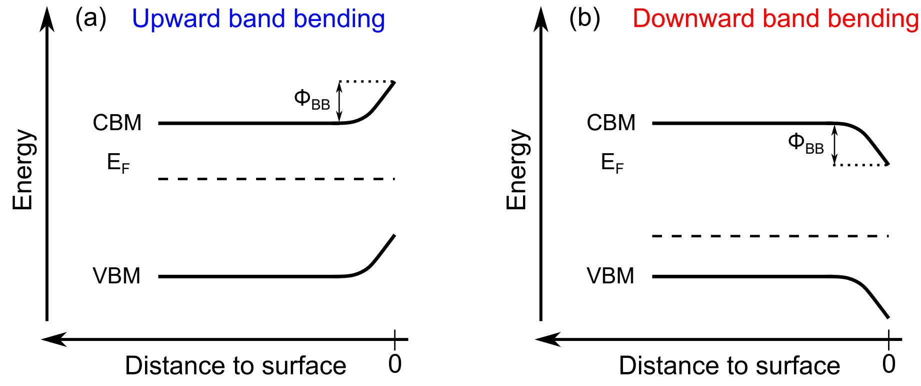

Figure 1.21: Schematics of (a) upward band bending and (b) downward band bending. Φ_{BB} = qV_{BB} where V_{BB} refers to the band bending potential.

This introduces the concept of charge neutrality level (CNL) which lies between the VBM and CBM and induces charge neutrality in the near-surface region if the states below the CNL are filled and the states above the CNL are empty. Reciprocally, if the states above the CNL are filled or the states below the CNL are empty, then the surface states are negatively charged or positively charged respectively. The charging or neutrality of these states depend therefore on the position of the CNL with respect to the bulk E_F. Surface states are therefore divided into two classes: donor-like or acceptor-like surface states.

Donor-like are neutral when filled and positively charged when empty, while acceptor-like are neutral when empty or negatively charged when filled [131, 167]. The CNL is therefore used to separate acceptor-like from donor-like states.

Let's now consider an n-type $MAPbI_3$ with both donor and acceptor surface states, separated by the CNL and with a Gaussian distribution, as depicted in Figure 1.22a. Ideally, all the donor states below the CNL should be filled and all the acceptor states above should be empty in order to have charge neutrality. However with the current flat bands and since the CNL is below E_F, all the states are filled which therefore induces a net negative charge Q_{net} at the surface, which is against the principle of charge neutrality. Therefore, in that specific situation, the bands have to bend upward (Figure 1.22), which creates a depleted (of electrons) space charge region at the vicinity of the semiconductor surface, also called depletion region. This depletion region has a positive charge Q_{SC} and the bending of the bands will move the CNL closer to E_F, resulting in the partial neutrality of the acceptor-like states (empty, above the CNL). This band bending will adjust such that the positively charged space charge region compensates the new net negative surface states charge Q_{SS}. The charge neutrality at the surface is therefore fulfilled as $Q_{SS} + Q_{SC} = 0$. The surface upward band bending in that situation solely originate from the acceptor states as the donors are neutral.

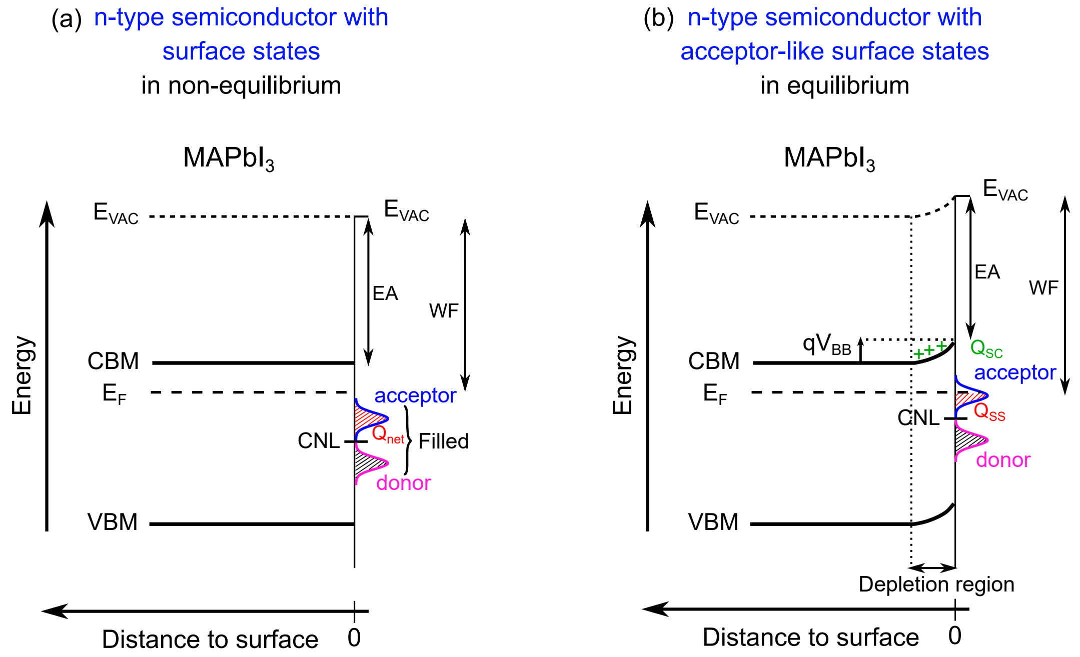

Figure 1.22: Band energy diagram of an n-type semiconductor with surface states in (a) non-equilibrium and (b) thermal equilibrium, where upward band bending occurs and acceptor-like surface states are formed.

In the specific situation of an n-type semiconductor with only acceptor-like states, downward band bending would not have been possible as an accumulation of electrons (instead of depletion) could not have been obtained. Indeed, this would have led to a negatively-charged space charge region resulting in a total net negative charge, not fulfilling the charge neutrality equation. However downward band bending could be possible with a weak n-type doping (close to intrinsic) and with a certain energy position of the donor-like surface states. For the case of a p-type semiconductor, where the majority carriers are the holes in the valence band, and with a CNL above E_F, downward band bending would occur at the surface, with the formation of surface donors. These surface donors are positively charged and compensated by a negatively charged depletion layer (depleted of holes in the VBM). If both acceptor- and donor-like surface states are present at the surface, surface band bending will occur and this irrespective of the doping (n or p) and the induced space-charge region will always be depleted.

Coming back to the Figure 1.22, one can observe that the net charge of the surface state had to be compensated by the upward band bending to have charge neutrality. One of the consequences is that E_F had to cross the surface state distribution and was positioned slightly above the CNL. If the surface state density at the CNL is high enough, about 10^{12} cm^{-2} eV^{-1} for a commonly-used semiconductor, E_F will stay close to the CNL and this irrespective of the bulk doping, temperature change and potentially applied bias. This phenomenon is called Fermi level pinning because the Fermi level is pinned at a specific position [168]. From the discussion about surface states and band bending, several conclusions can be drawn:

- The net charge of the surface states contributes to the position of the Fermi level at the surface, i.e., the workfunction (WF).
- Therefore the surface E_F can be completely different from the bulk E_F, and an inversion can happen at the surface (n-type bulk doping and p-type at the surface).
- The surface states are defined by the atomic structure and terminations of the semiconductor surface, and therefore, different surface terminations on the same semiconductor will yield different band bending magnitude and different WF (and potentially different IE / EA see Figure 1.22).
- The WF will therefore have a contribution from the band bending, in addition to contributions from surface dipoles and chemical potential [163].
- The density of surface states defines if there is Fermi-level pinning at the surface.
- Adsorption of molecules on the semiconductor surface may induce a change of the band bending magnitude.

For $MAPbI_3$, two critical interfaces can obviously be defined: the one at the rear surface of the perovskite, which is sometimes just with the substrate, and the one with a layer deposited on top of the surface of the perovskite.

The bottom interface plays an essential role in the growth of the perovskite as the terminations and orientations of the grains of the substrate (or transport layer) at the rear of the perovskite will structure the perovskite lattice and growth conditions (grain orientation and size, roughness. . .). The selection of the bottom layer undergoes strict criteria, as it should be compact, with limited-to-no absorption, highly conductive and finally should be such that they align energetically with the $MAPbI_3$ absorber. Due to the different device structures, the bottom layer can either be the ETL or the HTL, with a n-i-p or a p-i-n structure respectively. Evidently, improvements were achieved by filling out the aforementioned conditions but some ETL and HTL introduced an additional passivation due to the chemistry of their surface (see section A.8 of appendix Chapter 1 for more details).

Apart from its influence on the charge extraction efficiency and the non-radiative losses at the interface, the bottom layer also plays a role in the formation of the perovskite as well as its properties. Olthof et al. have reported a clear change in the chemical reactions at the interface bottom layer/$MAPbI_3$ where metal oxides such as MoO_3 and ITO would initially lead to formation of volatile product before the start of the growth, which led to different effective absorber thicknesses as well. Besides, the stoichiometry can also be altered, as different intermediate compounds can be formed [169]. In addition, changing the bottom layer can vary the doping of the $MAPbI_3$ absorber, where WF variations of 500 meV were reported by solely changing the substrate from ITO to PEDOT:PSS for instance [169]. Miller et al. and Schulz et al. have also both demonstrated a shift of the Fermi energy level E_F depending on the substrate type, which followed the doping properties of the latter [170, 171]. By using spin-coating and XPS, Miller et al. have calculated VBM and vacuum energy values for $MAPbI_3$ on different substrates and have reported large changes in the energy band diagrams, as depicted in Figure 1.23 [170]. Likewise, Schulz et al. demonstrated that on a TiO_2 substrate, $MAPbI_3$ would be n-doped but slightly p-doped on a NiO substrate [171]. The origin of such a change in the doping of the perovskite could arise from several origins, such as [140]:

- The different initial formation of the perovskite, resulting sometimes in non stoichiometric phases acting as self-dopants, as previously described.
- Forced alignment of the energy levels due to the substrate workfunction.
- Pinning of the Fermi level due to a highly-doped substrate, such as TiO_2.

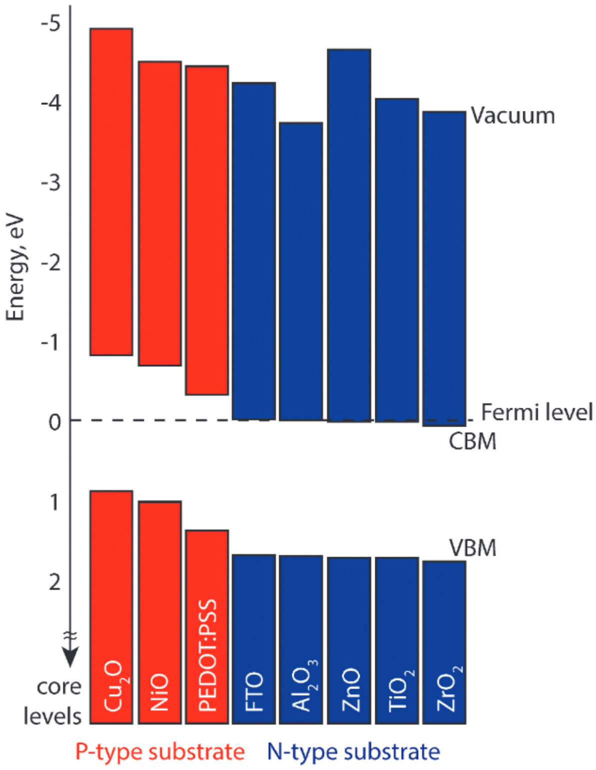

Figure 1.23: CBM, VBM and vacuum energy values for $MAPbI_3$ grown on different substrates. Both the VBM and the vacuum energy values were determined via XPS and the CBM value was derived using the calculated bandgap of 1.7 eV. Reproduced with permission from [170]. Copyright 2014 Royal Society of Chemistry.

The top layer, either ETL or HTL depending on the device structure, also undergoes strict criteria, but mainly related to suitable energy alignment, good conductivity and also processability of the deposition, as the top layer should not damage the underlying perovskite absorber, which are sensible to temperature and high-energy electrons. It then becomes evident that the surface energetics of the bare $MAPbI_3$ perovskite absorber, which are already different from the bulk ones, will be potentially altered depending on the layers and fabrication processes used, as they can undergo structural and chemical changes. Besides, the large ionic mobility in $MAPbI_3$ can additionally change the top interface as layers that accept ions, like polymers, will cause either halide depletion or enrichment [172, 173, 174]. Transparent conductive oxides are therefore often less used for ETL top layers as deposition techniques such as sputtering can be quite destructive to the perovskite layer. Therefore the already discussed C_{60} and PCBM fullerene-based layers are the most used and suitable for an ETL top layer both in terms of energy alignment and ease of deposition, with an additional passivation effect [175]. As for HTL, top and bottom layers are most of the time interchangeable as spin-coating is the commonly used technique, and therefore the aforementioned layers work for a top HTL as well.

Besides the interlayer engineering, the potential defective surface of the perovskite can also be passivated by a multitude of other techniques. Review papers on that matter are numerous and give extensive but non-exhaustive lists [176, 177, 178, 179, 180]. Some example of surface passivation techniques are listed below:

- during the growth via incorporation of alkali elements [181, 182, 183],
- via a self-induced passivation due to a surface enriched with PbI_2 or MAI for instance [137, 184],
- via post-deposition treatments such as annealing [185], treatments with additives [186, 187], Lewis bases and acids [188, 189, 190], organic and inorganic molecules [191, 192] or salts [70, 193],
- via the deposition or formation of one- (1D) or two-dimensional (2D) perovskites on top of the three-dimensional (3D) perovskites [194, 195, 196],
- via capping the surface with a wide band-gap material [197, 198, 199].

The aforementioned non-exhaustive list can however affect the surface of the perovskite differently. Some techniques were therefore reported to passivate the surface defect states, others to passivate the grain boundaries and another category would induce a better interface alignment, acting more as an intermediate energetic layer rather than a passivation effect.

1.3.6 Surface photovoltage

The previously discussed surface properties were assuming dark conditions, but the surface energetic quantities are affected by illumination, due to the effect of photo-generated carriers on the surface states. Let's consider an n-type semiconductor with surface states in the dark. As previously explained, acceptor-like surface states will have a net negative charge and in order to reach charge neutrality, surface band bending (upward) will occur, which will define the workfunction WF_{dark} (Figure 1.24a). If this semiconductor is illuminated with supra-bandgap photons, charge carriers will be photogenerated near the surface and holes will get trapped in these negatively charged surface states while electrons will go towards the conduction band. The holes will therefore reduce the net negative charge of these surface states, like a screening process. This will ultimately result in a reduction of the surface band bending in order to reach charge neutrality, inducing a reduction of the workfunction WF_{light}. This process is known as surface photovoltage (SPV) and $\mathrm{SPV} = \mathrm{WF}_{light} - \mathrm{WF}_{dark}$. The magnitude of the SPV, and therefore the flattening of the bands, depends on the illumination intensity. If upon a certain illumination, the bands become completely flat, the illumination will be called saturation illumination and result in a SPV_{sat}. The SPV will be positive in case of initial downward surface BB and negative in case of initial upward BB. The sign of the SPV can therefore be helpful in determining the type (n- or p-) of simple semiconductors but it can be more challenging to draw a conclusion for more complex ones, such as perovskites [200]. SPV can be measured using photoluminescence, capacitive pick-up techniques, X-ray photoelectron spectroscopy or Kelvin probe force microscopy (KPFM) as demonstrated later in this thesis [166]. When the illumination is switched off, the carriers will recombine and the SPV will therefore relax. The relaxation of the SPV signal can be studied by transient SPV measurements which can give information about the carrier dynamics: charge separation, recombination, drift, diffusion, de-trapping... [201].

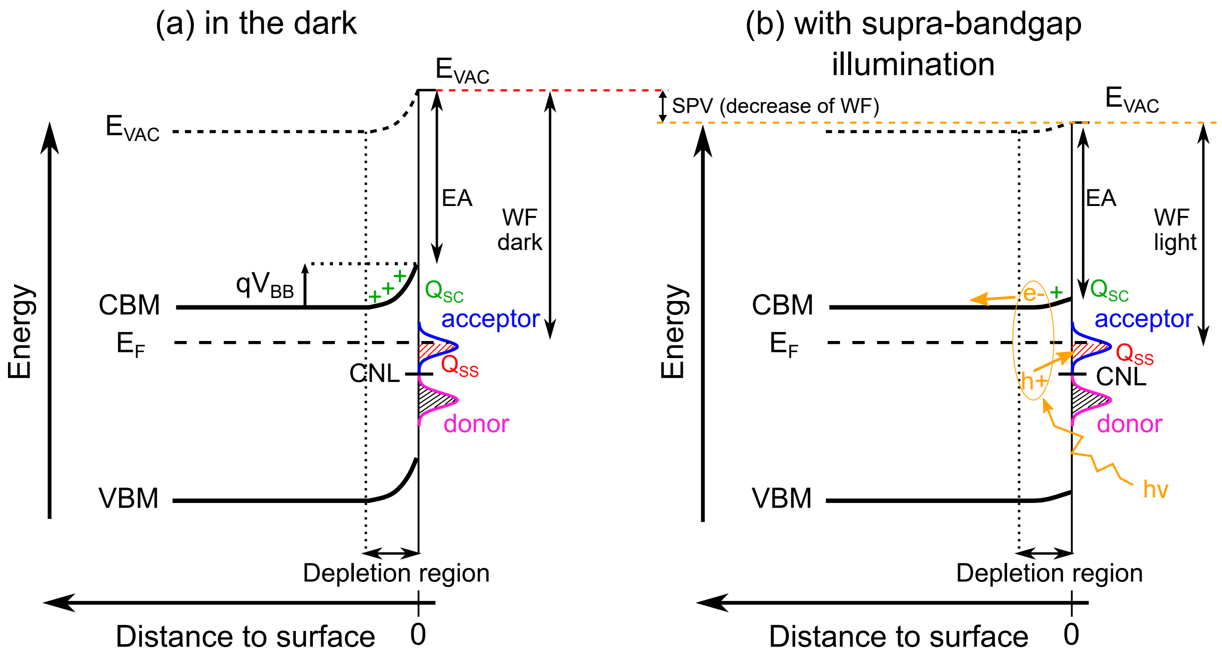

Figure 1.24: (a) Energy band diagram of a semiconductor with surface states in the dark: donor-like are neutral, acceptor-like have a net negative charge, compensated by the surface band bending. (b) Same semiconductor with supra-bandgap illumination. The charge carriers photo-generated close to the surface (holes) partially screen the net negative charge of the acceptor-like surface states, which induces a reduction of the surface band bending and therefore a reduction of the workfunction. This effect is called surface photovoltage.

When using KPFM on perovskites, the photo-induced changes in the measured SPV do not solely reflect the reduction of the band bending but can be related to effects such as heating and charging, variations of the measurement environment, photochemical processes or the occupation of defect states [200]. These can result in reversible or non-reversible variations of the WF upon illumination in timescales varying from seconds to hours [202, 203, 204, 205, 206, 207]. Reshchikov et al. have studied the effect of illumination on n-type GaN and showed that depending on the light intensity, the SPV could increase relatively fast or slowly, and that the magnitude was intensity-dependent. Additionally, they demonstrated that the SPV was dependent on the environment used (air and vacuum), due to the difference in surface states which induce the surface band bending. The different fast and slow rise or decay of the SPV before and after illumination were explained by three mechanisms: the accumulation of photogenerated carriers, the fast redistribution of charge and the slow photo-adsorption and desorption processes after illumination [204]. On the same material, Winnerl et al. have reported that the slow response of the SPV and its slow recovery were caused by localized shallow trap states [207]. In $MAPbI_3$ this phenomenon was also observed and correlated to a combination of interfacial trap states and ionic migration [202, 203, 208, 209, 210]. Almadori et al. have reported the occurrence of fast and slow transients when light was shone on the sample, which they attributed to the SPV effect followed by ionic migration [202], which were however on a small timescale (less than a minute). Garrett et al. also claimed to have encountered light-induced reversible ion migration, which was responsible for a long transient and an equilibrium reached only after a few minutes [203]. Toth et al. have also observed different components in the SVP signal of perovskite upon illumination (fast and slow) which they associated to different physical phenomena such as generation of charge carriers at the surface, ion transport or migration and charge accumulation [211].

The previous discussions on the surface properties, energetics and alteration of the perovskite surface indicate how important the understanding of the surface is in order to achieve record-efficiency solar cells. Determining the surface structure (terminations, surface states, defects, dipoles...) and energetics (WF, EA, IE,...) is crucial in order to understand where potential losses come from. A multitude of instruments and techniques can be used for that matter, such as scanning electron microscopy (SEM), X-ray and ultraviolet photoelectron spectroscopy (XPS/UPS), secondary ion mass spectroscopy (SIMS)... A summary of most of the techniques used to study the surface of semiconductors, their resolution and some limitations is available in section A.9 of the appendix Chapter 1. From these techniques, scanning probe microscopy (SPM) stood out as a useful way to access different important aspects of the surface of perovskites, such as the local density of states, the surface bandgap, the density of surface states, the WF and the grain boundary band bending. The techniques related to scanning probe microscopy will be discussed in the next chapter, as most of them were used during this thesis.

Chapter 2

Scanning Probe Microscopy

Scanning probe microscopy (SPM) refers to a broad range of techniques which use a probe, or a tip, to scan the surface of a sample in order to image different properties of this surface. Insulating, conductive and semi-conducting materials can be measured using these techniques and in different environments, such as in air, in inert gas, in vacuum (high and ultra-high as well) but also in liquid environments [212, 213, 214]. The first SPM technique was invented in 1981 by Rohrer, Binnig and Gerber at IBM Zürich [215] where they used an atomically sharp metallic tip to locally measure the current from a metallic surface. This technique was called scanning tunneling microscopy (STM) and will be detailed in the first section as it is one of the characterization methods used throughout this thesis. Section 2.2 will then describe the working principle of AFM and KPFM while section 2.3 will introduce the SPM machine and the important parameters used during STS and KPFM measurements. Finally, section 2.4 will review some of the SPM work on perovksite available in the literature.

2.1 Scanning Tunneling Microscopy/Spectroscopy

Scanning tunneling microscopy (STM) is based, as its name indicates, on the principle of tunnel effect. Figure 2.1 represents a particle wave function ψ. In classical mechanics, if such a particle encounters a potential barrier U_b and does not have sufficient energy to surmount it, the particle will not be able to reach the other side of the potential barrier. However, due to electrons (and holes) being known to have a wave-particle duality, quantum mechanics demonstrated an alternative to this problem where, if the barrier is sufficiently small, i.e. within a few nanometers, the probability for a particle to exist on the other side of the potential barrier is non-zero. The stationary Schrödinger equation was used firstly by Friedrich Hund to describe how the wave function changed when passing through and after the potential barrier. As represented in Figure 2.1, when both the width (L) and the height (U_b) of the barrier are finite, there is a probability that the wave penetrates, or tunnels through, the barrier where it will be gradually attenuated (almost exponentially). Depending on the width L and height U_b, there will a probability for the wave to emerge on the other side of the barrier in a form of a transmitted wave. After tunneling through the barrier, the wave function of the particle will therefore be changed and will depend on the transmission probability, which is based on the initial energy of the incident particle and the width and height of the potential barrier.

STM uses an atomically sharp and metallic tip which is brought within a few nanometers of a sample's surface. Using the same analogy as the one explained for the tunnel

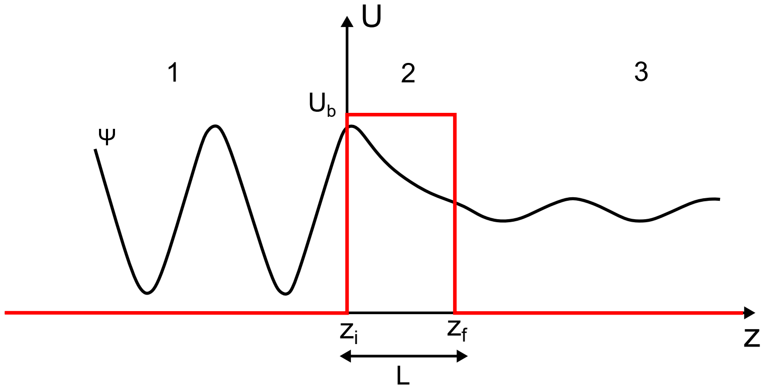

Figure 2.1: Sketch of the tunnel effect where a wave function of a particle exponentially decays when tunneling through a potential barrier, of width L and height U_b.

effect, the density of electrons (or holes), which have wave-particle duality, does not drop to zero at the surface of a material, but it will decay exponentially on the outside (ambient, inert atmosphere or vacuum), which can be seen as the potential barrier. When the metallic tip is approached within a few angstroms or nanometers of a conductive material (Figure 2.2a), the electron clouds that surround the atoms at the surface of this material will overlap with the electron clouds surrounding the atoms of the tip, as depicted in Figure 2.2b. Therefore, applying a voltage between the tip and the sample will induce the tunneling of electrons, from the sample's surface to the metallic tip, or the other way around, creating a tunneling current, which will be a measure of the wave function overlap of sample and tip and which will depend on different parameters.

In quantum mechanics, an electron with an energy E > U can be described by a wave function ψ, which satisfies the one-dimensional Schrödinger equation. In the allowed regions, the solutions of this equation are given by [216]:

$$\psi(z) = \psi(0)e^{\pm ikz}, k = \sqrt{\frac{2m_e(U_b - E)}{\hbar^2}} \tag{2.1}$$

k is called the wave vector. In addition, as previously discussed, quantum mechanics demonstrate that electrons can penetrate the energy barrier U_b even with an energy E < U, but in that case the wave function will decay exponentially with the width of the barrier.

Therefore in this forbidden region (region 2 of Figure 2.1), the solution of Schrödinger equation will be:

$$\psi(z) = \psi(0)e^{-\kappa z}, \kappa = \sqrt{\frac{2m_e(U_b - E)}{\hbar^2}} \tag{2.2}$$

κ is called the decay constant and describes the penetration of electrons through the potential barrier. Equation 2.2 only represents the tunneling from region 1 to region 3 (Figure 2.2), but there is also a probability for electrons to tunnel from region 3 to 1. Therefore the total wave function ψ(z) has for solution [218]:

$$\begin{cases} \psi(z) = \psi_1(z) = Ae^{ikz} + Be^{-ikz} & \text{for z} < \text{z}_i \\ \psi(z) = \psi_2(z) = Ce^{-\kappa z} + De^{\kappa z} & \text{for z}_i < \text{z ¡ z}_f \\ \psi(z) = \psi_3(z) = Fe^{ikz} & \text{for z} > \text{z}_f \end{cases} \tag{2.3}$$

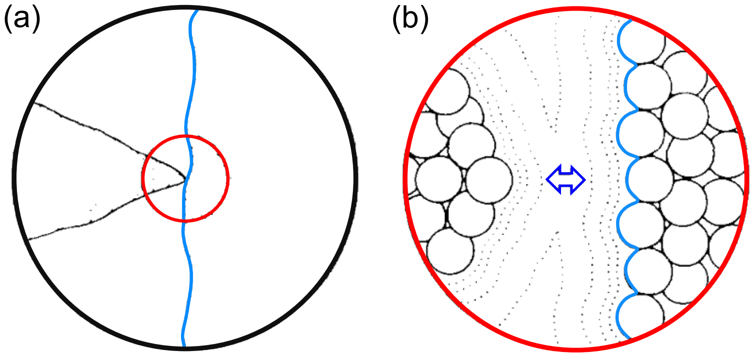

Figure 2.2: (a) Sketch of the STM tip scanning the surface of a conductive sample. (b) Zoom of the red circle of (a) where atoms are depicted as circles and which represents the overlap of the electron cloud surrounding the tip and the surface of the sample. Adapted from [217], Copyright (1985), with permission from Elsevier.

A, B, C, D and F are all complex numbers. A represents the amplitude of the incoming wave, B is linked to the amount of reflected wave, C refers to the coefficient linked to the wave function that tunnels through the barrier, D a reflection of the latter at the position z_i and F is linked to the amount of transmitted wave. The probability density of an electron being at a certain z position is proportional to $|\psi(0)|^2$. The ratio of the probability density of the transmitted (ψ_t(z)) wave over the incident wave (ψ_i(z)) can therefore be deduced by solving the equation with a computer algebra system and is written as follows [218]:

$$T = \frac{|\psi_i(z)|^2}{|\psi_t(z)|^2} = \frac{|F|^2}{|A|^2} = \frac{4k^2\kappa^2}{(k^2+\kappa^2)^2 sinh^2(\kappa z_f) + 4k^2\kappa^2} \tag{2.4}$$

T represents the probability for an electron to be transmitted from the region 1 to region 3, or to tunnel through the barrier, and can be called the transmission factor. T is also equal to ratio of transmitted current (I_t) over incident current (I_i). Several theories can be used to model the current but the most widely used is based on Bardeen's first order perturbation theory [219], which was later extended by Tersoff and Hamann [220] and Chen [221].

From now on, region 1 will be considered to be the surface of the conductive sample, region 2 vacuum and region 3 the tip. Taking this into consideration, the barrier that electrons, at the surface of a conductive sample, face in order to be removed from the solid into a vacuum is the WF ϕ, which was defined before as E_{VAC} - E_F, and where E_{VAC} is the vacuum energy level and E_F the Fermi energy level. Considering that the WF of the sample and the WF of the tip are different, the Bardeen model considers first a separability of the system sample-vacuum-tip in the case of the tip being far away from the sample and where both wave functions (tip and sample) will vanish in vacuum. However, when brought close together, a one-dimensional tunnel junction can be used and is represented in Figure 2.3.

U_s and U_t are the potential functions of the sample and the tip respectively. $E_{F,s}$ and $E_{F,t}$ are the Fermi energy level of the sample and the tip respectively when isolated. ρ_s and ρ_t represent the density of states at an energy E at the surface of the sample and at the surface of the tip. When the tip and sample are in close vicinity and when a positive voltage **V** is applied to the tip (or negative to the sample), there is an increase of the density of filled energy states in the sample that can tunnel through vacuum towards

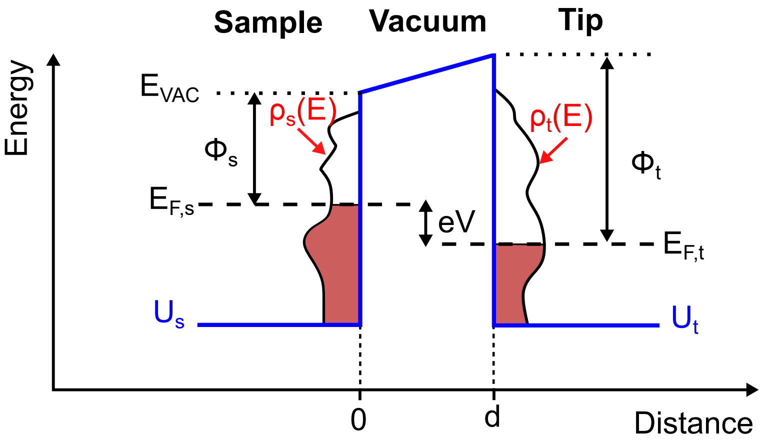

Figure 2.3: Energy band diagram representing the model of a one dimensional tunnel junction. U_s and U_t are the potential functions of the sample and the tip respectively. $E_{F,s}$ and $E_{F,t}$ are the Fermi energy level of the sample and the tip respectively when isolated. ρ_s and ρ_t represent the density of states at an energy E at the surface of the sample and at the surface of the tip.

the empty states of the same energy of the tip, which is called elastic tunneling. The tunneling current, which depends on the applied voltage, can therefore be determined. In the first version of the Bardeen approach, the time-dependent perturbation theory and the Hamiltonian model are used. The tunneling current can be calculated as a sum of different components: a tunneling matrix element M, which depends on the WFs of the tip and of the sample, and the Dirac delta function [218].

Bardeen's model then includes an energy dependent approximation which introduces the density of states of the tip and the sample (ρ_t and ρ_s in Figure 2.3), which are linked to the Dirac delta functions. Therefore, considering an energy state ϵ between 0 and eV (V being the potential applied), the tunneling current can be written as follows:

$$I = \frac{4\pi e}{\hbar} \int_0^{eV} \rho_t(\epsilon - eV)\rho_s(\epsilon)|M(\epsilon)|^2 \, d\epsilon \tag{2.5}$$

where M is the matrix element discussed above, which depends on the WFs of the tip and the sample amongst other things [218]. Considering a one-dimensional barrier, the matrix element can be simplified and the tunneling current becomes:

$$I = \frac{4\pi e}{\hbar} \int_0^{eV} \rho_t(\epsilon - eV)\rho_s(\epsilon)T(\epsilon, V, d) \, d\epsilon \tag{2.6}$$

This brings back the transmission factor which can be written as follows:

$$T(\epsilon, V, d) \propto exp\left[-2d\sqrt{\frac{2m}{\hbar^2}\left(\frac{\phi_t + \phi_s}{2} + \frac{eV}{2} - \epsilon\right)}\right] \tag{2.7}$$

Equation 2.6 is the Bardeen equation for a one-dimensional barrier in the low temperature case, which considers that all levels below the Fermi level are filled and all levels above are empty, which is also called the Fermi step function. However, the actual distribution of the Fermi distribution is not a step function and therefore other equations exist for a better approximation of the tunneling current [218]. Compared to equation 2.6, an additional term, linked to the Fermi-Dirac function would be added in the integral, and the limit of the integral would be from minus infinity to infinity.

In addition to Bardeen's equation of the tunneling current, the Tersoff-Hamann's approximation is generally used to simplify the equation. The latter stipulates that the applied voltage used for tunneling is considered so small that both the energy dependence of the matrix element and the energy dependence of the densities of states can be neglected, and that the tip wave function is approximated to be a spherical s-shape (or that the tip states in tunneling are mostly s-orbitals) with a radius of curvature R centered at r_t. In addition, they described the wave function of the sample's surface with a plane wave Fourier expansion. This led to the following simplification at small voltages:

$$I \propto \rho_s(E_F, r_t) \tag{2.8}$$

They therefore demonstrated that the tunneling current was proportional to the local density of states (LDOS), which is just the density of states at a specific local position, for example around a specific atom. Lastly, they compared their approximation at small voltages to a large voltage approximation by considering the limit of very small voltages. This brings the following equation, with z_0 the distance between the center r_t and the sample's surface [218]:

$$\rho_s^{\text{Ters}-\text{Ham}}(E_F, z_0) = LDOS(E_F, z_0) = \rho_s^{\text{large volt. appr.}}(\epsilon = 0) \times T(\epsilon = 0, V = 0, d = z_0) \tag{2.9}$$

However the Tersoff-Hamann's model only considers s-wave tip, which is not essentially the case for the apex of the STM tip and depends on the type of materials used (d-p orbitals for transition metals for examples) [218]. Therefore Chen [221] expanded the Tersoff-Hamann's approximation for different types of orbitals, which will not be discussed further in this thesis. As expressions of the tunneling current and ways to calculate them have been displayed, the principle of STM can be discussed.

STM consists in a conductive tip which is brought within a few nm or angstroms of a conductive surface. As previously described, a voltage is applied, to the tip or the sample, and electrons from the filled states of one side tunnel through vacuum to the empty states of another side, which forms the tunneling current. Therefore, STM can access the local density of states at the surface of a sample, either the filled or empty states depending on the voltage applied. In order to move the tip in the three directions (x, y and z), and image the properties of the surface of a conductive sample, the tip, often made of tungsten (W) or platinum-iridium (Pt-Ir) alloy, is attached to a piezodrive that consists in three perpendicular piezoelectric transducers (Figure 2.4). Therefore, voltages are applied on the x, y piezo transducers to move around the surface and coarse controller will be used for the z piezo to bring the tip and the sample within a distance of a few nanometers or a fraction of a nanometer. This will generate a tunneling conductance and by applying a voltage between tip and sample, a tunneling current will be created [216].

STM can operate in two modes: constant-height or constant-current mode. In the constant-height mode, the tip is maintained at a certain height and is scanned over the surface while the tunneling current is monitored. This method can be used to measure the LDOS of an atomically flat conductive surface as the Tersoff-Hamann's approximation demonstrated that the tunneling current was proportional to the LDOS at E_F. However thermal drift and piezo creep are predominant in constant height-mode at room temperature and above, which results in difficulties to acquire LDOS with a precise resolution.

Thermal drift refers to the distortion of images due to the heating of the components of the microscope, and therefore is not only linked to the heating of the piezo elements. Piezo creep is the delay time it takes the piezo transducer to respond from a sudden jump in voltage from the electronics linked to a fast change of the electric field. For example, at the end of a line scanned in the +x direction, a piezo extension still remains while the voltage has changed to scan in the -x direction, which induces a slight displacement as a function of time. In addition, rougher samples with atomic steps or deeper grain boundaries will result in either a change of tip-sample distance, which will change the tunneling current by several orders of magnitude, or undesirable tip-sample interaction, which can alter, damage or break the tip. Therefore this mode is mostly used for measuring atomic flat samples at low temperatures.

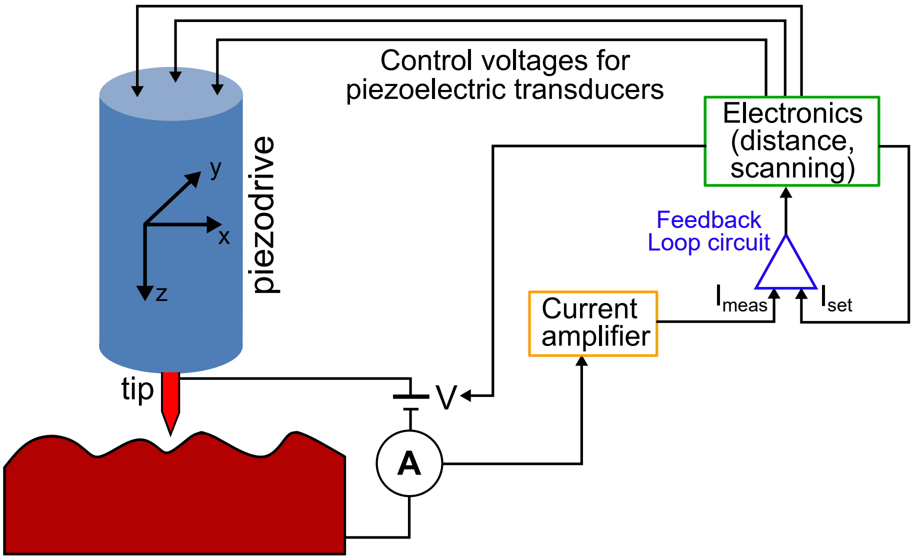

Figure 2.4: Sketch and working principle of a scanning tunneling microscope.

The constant-current mode, which will be used for this thesis, consists in maintaining a constant tunneling current between tip and sample to image a sample. The constant current will result in a continuous adjustment of the tip height (z piezo) while the tip-sample distance will remain constant, as it is proportional to the tunneling current. The working principle is depicted in Figure 2.4. In order to keep a constant current, a value for the current is first set by the user through the computer interface, which the electronics will translate in a certain voltage applied to the z piezo electrode. The electronics, via an auto-approach loop, will gradually reduce the tip-sample distance until the measured current (via an ammeter) matches the set value. Then the scan will start in the x and y direction. At each (x,y) position, the tunneling current will be measured (I_{meas}) and compared to the set current (I_{set}). Using a proportional–integral–derivative (PID) controller (see section B.1 of appendix Chapter 2 for a short description), the electronics will adjust the tip-sample distance, by applying a voltage on the z piezo, to nullify the difference I_{meas}-I_{set}. This is also referred to as the feedback loop.

Therefore STM using the constant-current mode is more suitable with polycristalline thin films such as perovskite films where the surface roughness is relatively large (tens to hundreds of nanometers for example) and where steep height steps exist, for instance grain boundaries. Due to these conditions and the low bandwidth of the feedback loop, scanning rough films is much slower than the fast scan of atomically flat surfaces using constant-height mode. Using these techniques, the contour of the topography and the atoms at the surface of a sample can be acquired in the three dimensions (x,y,z), which is however a simplified vision of the interpretation of an image acquired using STM. As discussed previously, the tunneling current is calculated using the density of states of the sample (and the tip). Therefore if a perovskite sample is considered, atoms that are supposedly at the same height in a specific grain but have different chemical elements will induce different density of states, which will result in different tunneling current and therefore different apparent height in the constant-current mode. In addition, depending on the applied voltage, the acquired image will represent either the filled states or the empty states at the surface of the samples, which will also change the apparent height.

STM is not only a useful technique to image the surface of a conductive sample with atomic resolution, it can also be used to spatially resolve the electronic properties of the latter using scanning tunneling spectroscopy (STS). In STM, acquiring an image with the constant-current mode is performed at a specific voltage, which also means a finite density of states of the sample. A small increase of the voltage (dV) will shift some of states down and lead to a change of the tunneling current by *dI.* The principle of STS is therefore to measure the tunneling current as a function of a range of voltages at a specific position, which will result in the acquisition of an I-V curve as depicted in Figure 2.5 for the case of $MAPbI_3$.

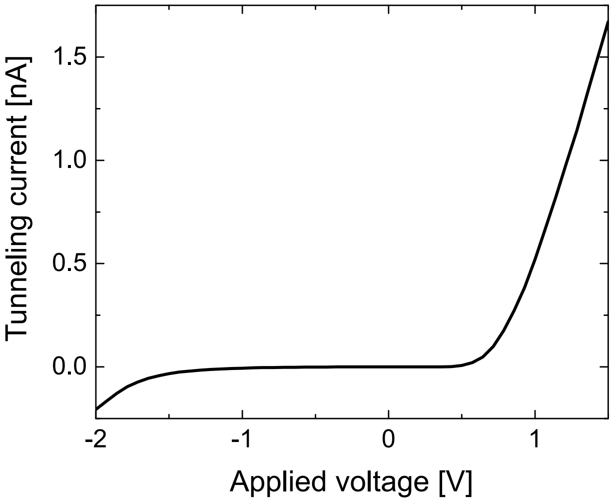

Figure 2.5: Tunneling current of a $MAPbI_3$ sample as a function of the applied voltage, acquired using STS. The voltage is applied to the sample.

As previously discussed, the tunneling current is a convolution of the DOS of the tip and the DOS of the sample (2.6). Using this equation 2.6 and assuming a constant density of states for the tip (which is usually unknown), the differential conductance, dI/dV, is calculated as follows [218]:

$$\frac{dI}{dV} = \frac{4\pi e}{\hbar}\left[e\rho_t\rho_s(eV)T(eV,V,d) + \rho_t\int_0^{eV}\rho_s(\epsilon)\frac{\partial T(\epsilon,V,d)}{\partial V}\,d\epsilon\right] \tag{2.10}$$

By further assuming that the transmission factor T is constant, equation 2.10 becomes:

$$\frac{dI}{dV} \approx \frac{4\pi e^2}{\hbar}\rho_t\rho_s(eV)T(eV,V,d) \tag{2.11}$$

A last assumption that the transmission factor is voltage-independent leads to the conclusion that the differential conductance, in its simplest approximation, becomes proportional to the LDOS of the sample, $dI/dV \propto \rho_s(eV) \equiv LDOS(eV)$. This approximation is often used in STS as it enables to access the LDOS of a sample by only measuring dI/dV at different voltages. However, the transmission factor strongly depends on the applied voltage as presented in equation 2.4 and cannot be taken as constant. T actually induces an exponentially increasing background signal in the dI/dV spectra, which can be neglected when normalizing dI/dV by I/V as shown by Feenstra et al. [222]. Using their calculations, they obtained the following equation:

$$\frac{dI/dV}{I/V} \propto \rho_s(eV)T(\epsilon = eV, V, d) \propto LDOS \tag{2.12}$$

The normalized conductance (dI/dV)/(I/V) therefore brings a closer approximation of the LDOS and does not diverge for large voltages compared to the conductance dI/dV. However for the case of semiconducting materials with a bandgap and forbidden states, the normalized conductance diverges near zero voltage when the current is supposedly zero. Feenstra et al. however demonstrated that by broadening the I/V, a broadened and normalized (dI/dV)/$\overline{I/V}$ would be best to approximate the LDOS and the surface band gap [223], but this broadening will be discussed in Chapter 4. For all the previous approximations, the DOS of the tip were assumed to be constant, but this is usually not always the case. As STS and the dI/dV originally contained a dependence on the tip DOS, STS measurements should ideally be measured with different tips in order to observe the influence of the tip DOS on the dI/dV [218].

Besides the single point spectroscopy of the STS which is useful to have an approximation of the LDOS at a specific point or atom, the scan stage of the STM can be used together with the spectroscopy to acquire an image of the LDOS at the surface of the sample. The method is called current-imaging tunneling-spectroscopy (CITS) or grid spectroscopy and consists in creating a grid where each point or pixel will be used for a STS. This process results in an image of the LDOS at the surface of the conductive sample.

2.2 Atomic and Kelvin Probe Force Microscopy

STM however only works for (semi-)conducting samples and as explained in the previous section, the contour of the topography that STM depicts is rather a map of either the local filled or empty states at the surface of the material. In 1986 Binnig, Quate and Gerber invented the atomic force microscope (AFM) [224], which consisted in measuring the inter-atomic forces between a tip and a sample, which could be insulating, compared to measuring the tunneling current in STM. Several forces exist between a tip and a sample, which can be classified as long-range and short-range forces. The van der Waals force contributes to the long-range forces, and is a force acting between neutral atoms or molecules without a permanent dipole moment [218]. Even though atoms are electrically neutral, their electron density can temporarily shift greatly to one side of the nucleus, inducing a spontaneous dipole which can either attract or repel other atoms. Therefore van der Waals forces include both attraction and repulsion force between atoms, molecules and surfaces. These forces are the weakest of the weak chemical forces with very low energy per bond and therefore vanish rapidly when the tip is far away from a sample [218]. If the shape of a tip is approximated with a sphere of radius R and the sample by a semi-infinite solid, which is at a distance D of the tip, the van der Waals interaction energy can be described as follows [225]:

$$U_{dvW} = -\frac{HR}{6D},\ H = \pi^2 C \rho_A \rho_B \tag{2.13}$$

H is the Hamaker constant which is a property of a material that represents the strength of the van der Waals force, C is a coefficient resulting from the calculation of the atom-atom pair potential and ρ_A, ρ_B are the atom densities of the tip and the sample respectively [218]. From equation 2.13, the van der Waals force between tip and sample can be calculated and is:

$$F_{vdW} = -\frac{HR}{6D^2} \tag{2.14}$$

For tip-sample distance up to 1 nm, the van der Waals force is the predominant force but below this limit, short-range forces, either repulsive or attractive, exist due to the overlap of the electron wave functions of the sample and the tip, as already discussed in the previous STM section. When the tip and the sample are approached such that the overlap of the electron wave functions of their outer shell (chemical bonds) reduces the total energy, then the short-range force is attractive. However, when the tip-sample distance becomes too small, there will be a repulsion force caused by the repulsive interaction between the electron wave functions of the inner shells of the tip and the sample. This repulsive interaction is also composed of the Pauli exclusion principle that states that two electrons cannot occupy the same energy state. The long-range van der Waals interaction and the short-range interactions between a tip and a sample can be expressed by the Lennard-Jones potential [218]:

$$U_{LJ}(r) = 4 * U_0 \left[\left(\frac{R_a}{r} \right)^{12} - \left(\frac{R_a}{r} \right)^{6} \right] \tag{2.15}$$

U_0 is the depth of the potential well, corresponding to the area where the total force changes from a predominance of the attractive force to a predominance of the repulsive force. r is the distance between the atoms and R_a the distance at which $U_{LJ} = 0$. The term in $-1/r^6$ corresponds to the attractive contribution while the term in $1/r^{12}$ to the repulsive contribution. The corresponding total force between tip and sample as a function of the tip distance can be accessed with the partial derivative $F = \frac{\partial U}{\partial r}$ and can be visualized in Figure 2.6. In addition to the previously described forces, another long-range force exists, which is the electrostatic interaction. If a conductive sample with a certain WF or a sample with trapped electric charges at the surface are approached to a conductive tip with another WF, the system tip-sample can be considered as a capacitor where the capacitance depends on the tip-sample distance. The electrostatic force that results from this distance-dependent capacitance C(z) can be defined as follows:

$$F_{el}(z, \Delta V) = -\frac{1}{2} \frac{\partial C}{\partial z} \Delta V^2 \tag{2.16}$$

ΔV is the potential difference between tip and sample that will change the energy of the capacitor and can be expressed by:

$$\Delta V = V_{bias} - \frac{\Delta \Phi}{e} \tag{2.17}$$

V_{bias} is the bias applied between the tip and the sample and $\Delta\Phi$ is the WF difference between tip and sample. If no voltage is applied, $V_{bias} = 0$, then ΔV is only equal to the WF difference between the tip and sample, divided by the elementary charge, which is called the contact potential difference (CPD), and the electrostatic force only results from this CPD.

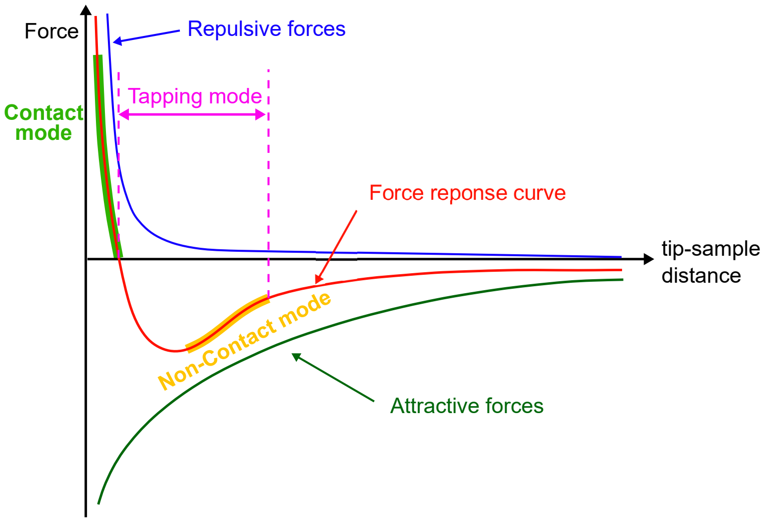

Figure 2.6: Derivative of the Lennard-Jones potential as a function of the tip-sample distance. Force response curve between tip and sample in AFM, with the regions of the different modes (contact, non-contact and tapping modes).

After discussing the different forces that occur between the tip and the sample, the concept of atomic force microscopy will be explained. Contrarily to the STM which requires a conductive tip mounted on a tip holder, AFM requires the use of a cantilever with a tip at its end. The cantilever holder is, similarly as to STM, mounted on a piezodrive with three piezo transducers (x, y and z). As the tip, attached to the cantilever, approaches the surface of the sample, it senses the long-range force and the tip will be attracted, which bends the cantilever towards the sample, until the tip touches the sample (called snap-to-contact). If the distance is further increased, the tip still touches the surface of the sample but this time the repulsive forces make the cantilever bend towards the opposite direction of the sample. While in constant-current STM, the electronic, with the help of the feedback loop circuit, monitors and compares the tunneling current to a certain set value, AFM on the other hand monitors the deflection of the cantilever and uses it as the feedback signal. To that end, a beam-deflection detection method (Figure 2.7) is used where a laser beam is focused on the end of the back side of the cantilever, which will be reflected into a split photodiode (two photodiodes separated by a small slit). Therefore, a change in height on the sample's surface will lead to a variation of the forces between tip and sample, resulting in the deflection of the cantilever and a variation of the signal intensity measured by the photodetector.

Due to the different forces occurring between the tip and the sample, different scanning methods exist for AFM. Contact mode is used when the tip touches the sample's surface and when only repulsive forces deflect the cantilever. The cantilever is not excited and therefore does not oscillate, as the force applied due to the direct interaction between the sample and the tip is enough to deflect the cantilever. This mode is often used for robust samples that can handle high applied forces from the tip or for samples in liquid. It is also the basis of conductive AFM (c-AFM) to measure the current between the

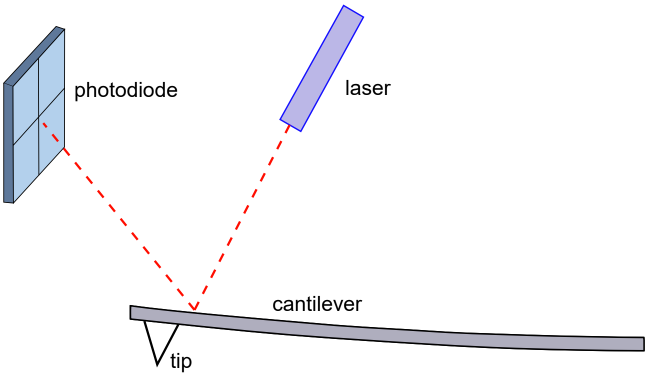

Figure 2.7: Sketch of the beam-deflection detection method used in AFM.

tip and the sample. In the second mode, intermediate or tapping mode, the cantilever is externally oscillated at a driving frequency near its resonance frequency. This is the most used mode when performing AFM in ambient conditions and it consists in using large oscillation amplitude such that the tip comes into intermittent contact with the sample's surface and therefore the short-range interactions prevail in that mode. For each oscillation cycle, the large oscillation will make the tip touch then detach from the sample. Lastly, contrarily to the two previous modes, the non contact (NC) mode uses the attractive force between the tip and sample and enables the tip to not purposely touch the surface of the sample, which could potentially damage it. These AFM modes are also tightly linked to the feedback signal used to image the topography of a sample. The cantilever deflection leads to a change of its oscillation frequency and/or its oscillation amplitude. Therefore the AFM electronics can either use the change in frequency or amplitude in its feedback loop to regulate the tip-sample distance, therefore the detection modes are called amplitude modulation (AM) and frequency modulation (FM).

In AM-AFM (Figure 2.8a), the driving frequency (ω_{drive}) is fixed, near the resonance frequency (ω_0), and a fixed driving amplitude (A_{drive}) is set. The measured value for the feedback is the oscillation amplitude (A), which is different from the driving amplitude due to the environment damping. Due to the dependence of the force gradient on the tip sample distance and the resonance frequency [218], any change in the topography height (increase or decrease in tip-sample distance) will change the force gradient, inducing a change of ω_0, which in turn will change the oscillation amplitude A (and the phase). The feedback loop circuit measures the variation (error) ∂A and the AFM electronics changes the tip-sample distance such that A comes back to its original value. The dependence of the amplitude is generally accepted to be dependent on the force while the resonance frequency depends on the gradient of the force [226]. In FM-AFM (Figure 2.8b) on the other hand, the cantilever oscillates at its resonance frequency and the amplitude is kept at a constant value. A change in the topography height will induce a shift of the resonance frequency, and ultimately a shift of the oscillation frequency. The feedback loop circuit will measure this frequency shift (error) and the electronics will change the tip-sample distance in order to come back to the initial frequency [218].

Several other parameters are important in AFM beside the driving and oscillation frequencies and amplitude. The force constant k of the cantilever gives an indication of its stiffness and whether it is suitable to use this cantilever for certain samples. The quality factor Q of the cantilever depends on the cantilever as well but also on the operating environment (ambient or vacuum) and is a measure of the energy loss of the oscillation due to damping, by calculating the ratio $\omega_0/\Delta\omega$. Ambient conditions therefore reduce considerably the Q factor, which can be of a few hundreds, while it is of a few tens of thousands in ultra-high-vacuum (pressure lower than 10^{-9} mbar) [226].

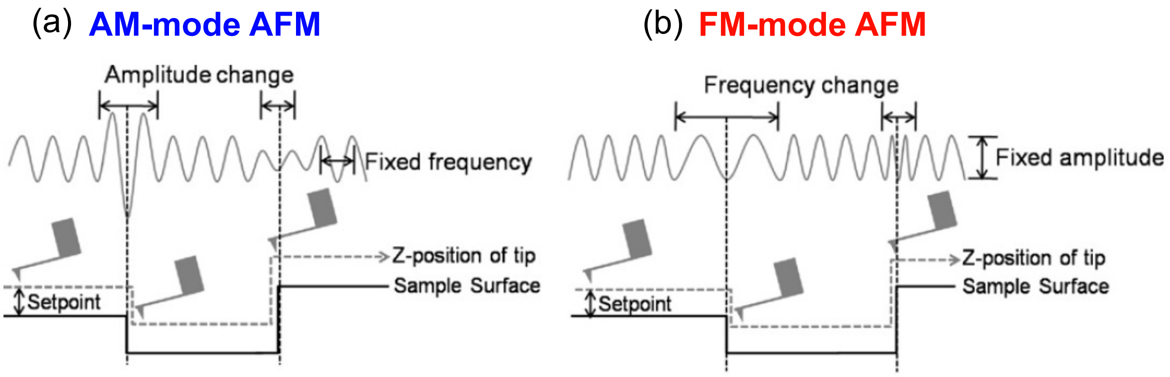

Figure 2.8: Representation of the (a) AM-mode AFM and (b) FM-mode AFM. Reprinted from [226], Copyright (2011), with permission from Elsevier.

While tapping (intermittent) mode always uses the AM feedback loop, the non-contact mode can either use the AM in ambient pressure or FM feedback loop in vacuum environment. This is mainly due to the damping in ambient conditions which inhibits the use of FM (low Q factor and therefore broad resonance frequency) and due to the lack of damping in vacuum environment which results in very slow change in the oscillation amplitude upon tip-sample interaction (high Q factor). As the aim of this thesis is to study the pristine surface of perovskite absorbers, which are relatively rough and made of both organic and inorganic compounds, the method of choice is FM-AFM in ultra-high-vacuum (UHV) where the contamination of the sample can be kept to the minimum. The end of this section will focus on the FM-AFM setup and FM Kelvin probe force microscopy (FM-KPFM) which is depicted in the schematic diagram of Figure 2.9.

In FM-AFM (left part (with blue lines) of Figure 2.9), the cantilever is mechanically oscillated at its resonance frequency f_0 with a set-amplitude A_0. Any change in height due to the topography will induce a deflection of the cantilever oscillation frequency and amplitude which will induce a variation of the reflection of the laser beam on the position sensitive detector (PSD). The signal is then amplified and the measured oscillation amplitude A_{meas} is compared to the set value A_0 and the amplitude regulation system (composed of a positive feedback amplifier, band-pass filter and phase shifter) keeps the amplitude oscillation constant. In addition, a phase-locked-loop (PLL, or FM demodulator) measures the frequency f_{meas} and compares it with f_0 with $\Delta_f = f - f_0$. Initially a certain Δ_f is set by the user through the computer, which corresponds to a certain tip-sample distance, and the frequency feedback loop varies the Z piezo in order to keep that set Δ_f value constant, which will give the topographic signal.

As previously explained, there is an existing electrostatic force between tip and sample defined by equation 2.16, which is generated by the differences in WF between tip and sample (Figure 2.10a). Therefore there is a need of a method to measure this WF difference separately from the topography mapping which relies on the regulation of the Z piezo using the feedback loop of the frequency shift. To that end, FM-KPFM uses, in addition to the mechanical oscillation of the tip at its resonance frequency, an applied AC bias (V_{AC}) to create an electrical contact between tip and sample and which induces a modulation of the electrostatic force [226]. This electrical contact will cause the sample

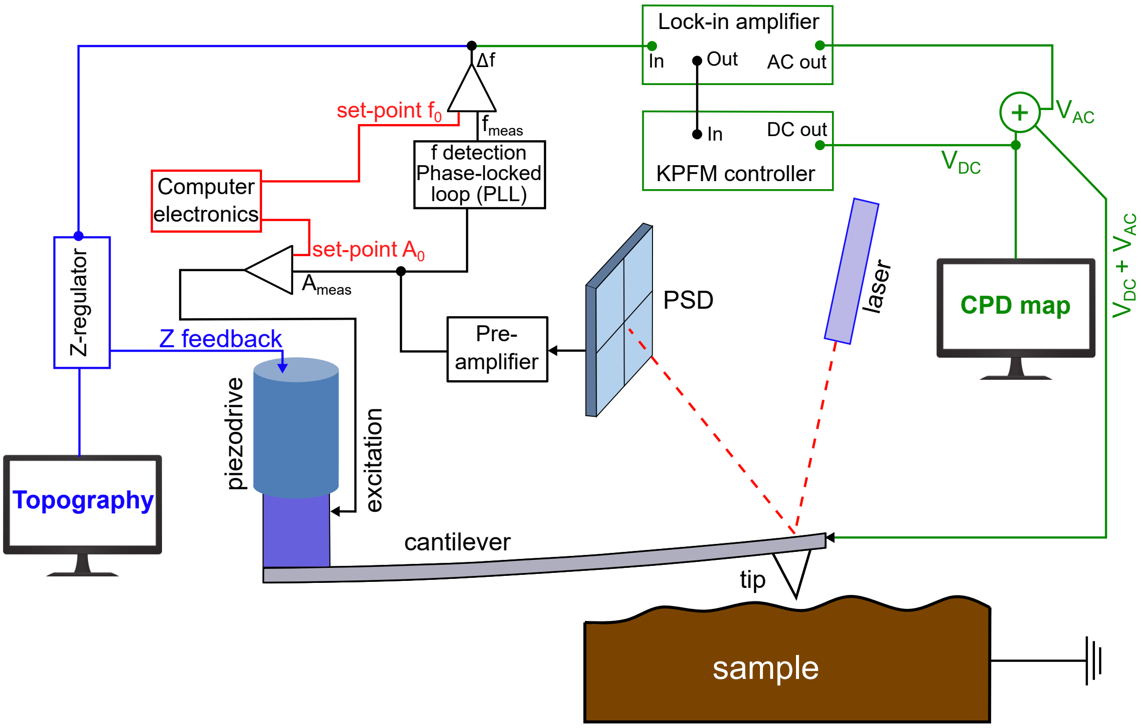

Figure 2.9: Schematic diagram of FM-KPFM. The left blue part represents the FM-AFM for acquiring the topography and the right green part the FM-KPFM for acquiring the CPD map. PSD refers to position sensitive detector.

and tip to be charged, inducing an equilibrium through the alignment of the Fermi energy levels (Figure 2.10b). This will result in a creation of a contact potential difference (CPD) between the vacuum levels of the tip and the sample, that can be defined by equation 2.18 if the bias is applied to the sample:

$$CPD = \frac{\phi_s - \phi_t}{e} \tag{2.18}$$

The modulated electrical force induced by the applied V_{AC} and the resulting CPD can be nullified by using an external DC bias (V_{DC}) applied between the tip and the sample with the same magnitude as the CPD (V_{CPD}) but in the opposite direction (Figure 2.10c). Therefore by monitoring the change of V_{DC} at the surface, a mapping of the CPD can be acquired.

Furthermore, if the WF of the tip is known, a map of the WF of the sample can be retrieved. The additional equipment required for FM-KPFM is represented in Figure 2.9. First an AC bias is applied between the tip and sample. As already discussed, the frequency feedback loop measures Δ_f, which is used for the topography regulation, but the Δ_f signal can be fed into the lock-in amplifier which will then go into the KPFM controller. The KPFM controller acts as a feedback loop by applying continuously a V_{DC} that will nullify the lock-in output signal. The V_{DC} will be monitored in order to map out the CPD of the sample.

In addition to avoiding oxygen contamination by using KPFM in UHV, FM-mode has a higher spatial resolution than AM-KPFM and is less prone to topography-induced artifact because in FM-KPFM, the gradient of the electrostatic force is detected which means that the electrostatic interaction mainly occurs between the tip apex and the sample surface, while in AM-KPFM the force is detected, resulting in a greater contribution from the

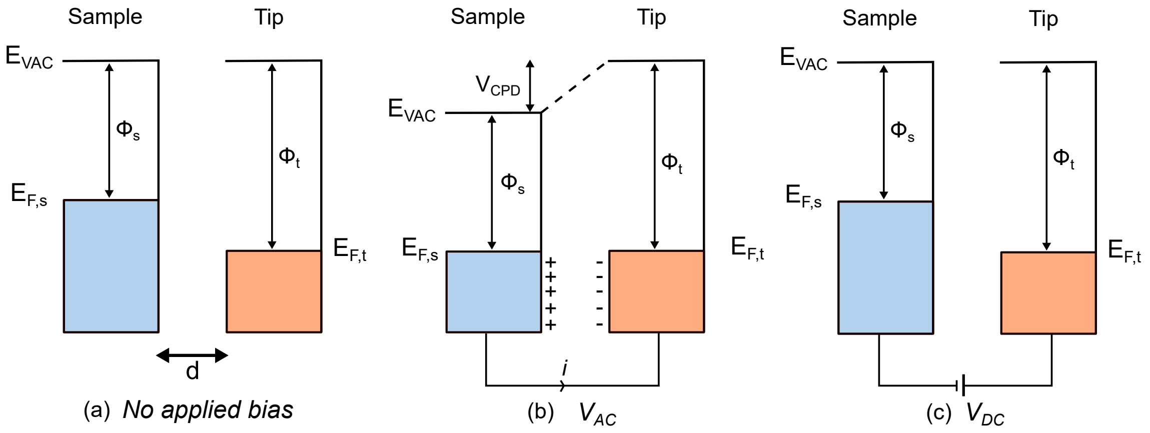

Figure 2.10: Sketch of the energy band diagrams between tip and sample for three cases: (a) the tip and sample are at a distance d of each other and no electrical contact is made, typically the case of FM-AFM. The Fermi energy levels are not aligned. (b) The tip is brought close to the sample and an AC voltage (V_{AC}) is applied between them, which make them in electrical contact. The Fermi energy level are aligned, which creates a contact potential difference (CPD) between the vacuum energy levels. (c) a DC voltage (V_{DC}) is applied to nullify the CPD and therefore the previous AC voltage, which enables the measure of the CPD.

cantilever [226, 227]. However, the energy resolution in AM-KPFM is generally better than in FM-KPFM [226]. Besides, the resolution of both the topography and CPD signals depends on the quality of the tip, such as its Q factor, its shape, its coating...

Besides the previous quantities that STS and KPFM can measure, these two techniques can enable further characterization of the surface's properties. For example, instead of measuring the tunneling current for a range of voltages, which gives the LDOS, the tunneling current can be measured while the tip-sample distance is varied, which can result in the extraction of the local WF [218]. The capacitance of the sample's surface can also be monitored by using the electrostatic force already used by KPFM, a technique commonly called as scanning capacitance microscopy (SCM). Besides STM, STS, AFM or KPFM, SPM regroups a multitude of other techniques. Conductive-AFM (c-AFM) is used to map out local I-V curves using contact AFM and conductive samples. Magnetic force microscopy (MFM) can retrieve the magnetic structure of a sample surface while piezoresponse force microscopy (PFM) can identify the different ferroelectronic domains at the surface of a sample. Many other techniques exist and are used to determined different properties of perovskite's surface [213].

2.3 Measurement setup

As previously discussed, scanning probe microscopy is the method of choice to characterize the surface properties of the perovskite absorbers in this thesis. Sections 2.1 and 2.2 focused on the working principle and state of the art of SPM, and more precisely STM, STS, AFM and KPFM, so this section will go into the details of the machine and the important parameters when carrying out STS and KPFM. The scanning probe microscope is a Variable Temperature-AFM (VT-AFM) from Scienta Omicron and is depicted in Figure 2.11. The machine runs in an ultra-high-vacuum (UHV) environment with pressures that range from 10^{-11} to 10^{-10} mbar. In order to get down to such low pressures, a turbo pump (connected to a rotary vane pump), an ion getter pump (analysis chamber) and a titanium sublimation pump (TSP) are used. In order to keep a very good UHV despite the introduction and annealing of new samples, the titanium filaments of the TSP have to be heated (high current) periodically, which reduces the gas pressure in the chamber.

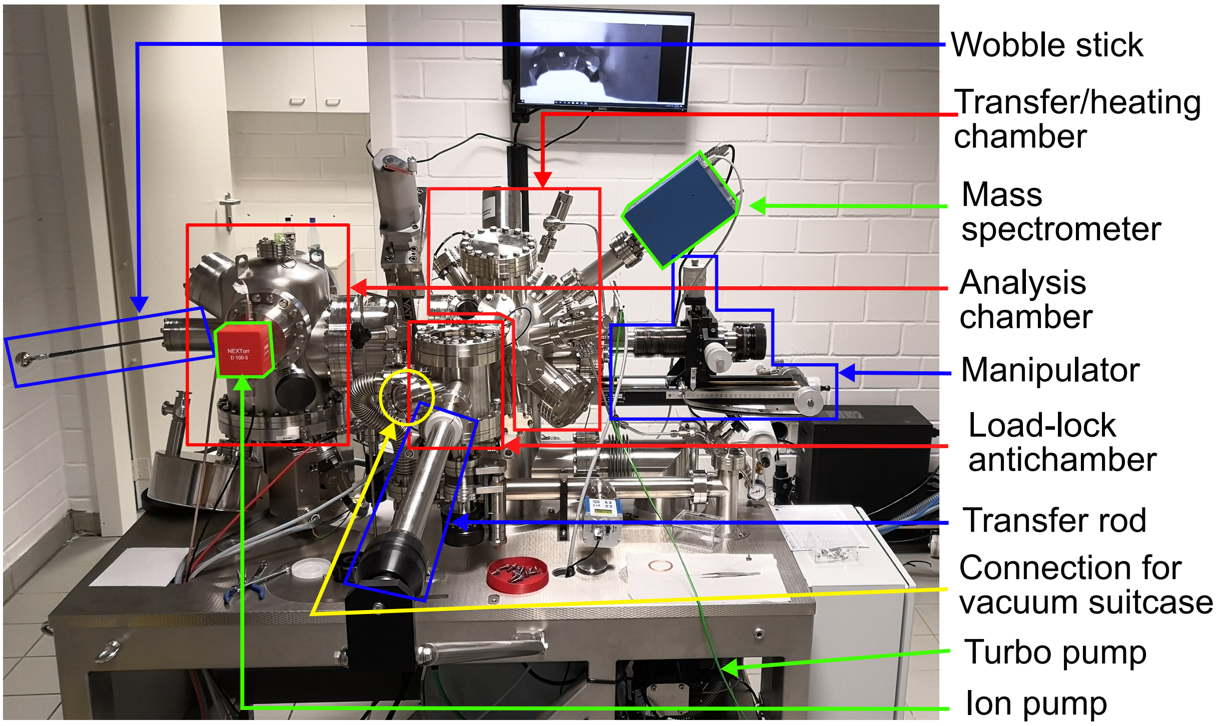

Figure 2.11: Picture of the VT-AFM from Scienta Omicron and description of some parts and components.

The mechanical noise is reduced using a high-quality vibration decoupling system (soft springs + damping mechanism). The samples were introduced inside the SPM using a vacuum suitcase (Figure 2.12a).

The latter was previously connected to the back of the nitrogen glovebox and the samples were taken inside this suitcase using a wobble stick in a nitrogen environment. The vacuum suitcase was then pumped and connected to the load-lock antichamber (Figure 2.11), which was then also pumped. When reaching a low enough pressure, the gate valve of the vacuum suitcase was opened and the samples were transferred on the carousel of the load-lock. The antichamber was left pumping until reaching pressures of 10^{-7} mbar and the gate valve between the antichamber and the tranfer/heating chamber was opened. Using the transfer rod and the manipulator (Figure 2.11), the samples were brought close

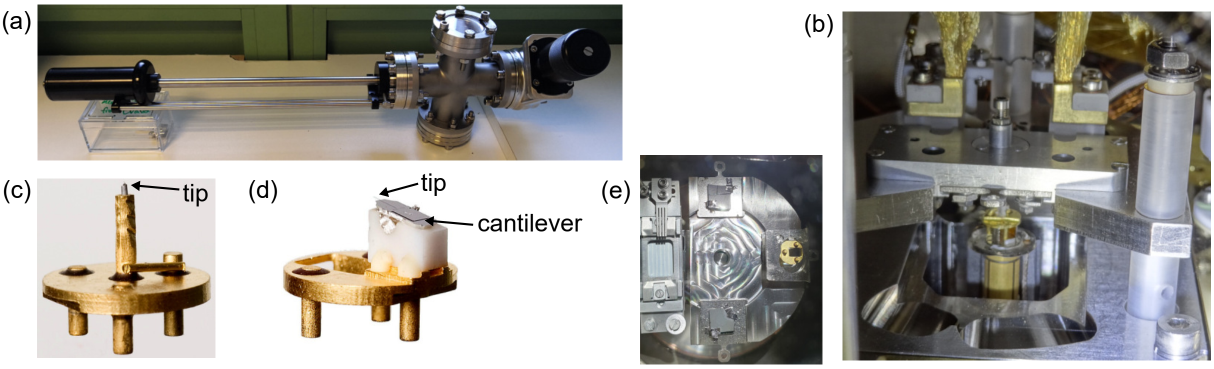

Figure 2.12: Pictures of (a) the vacuum suitcase, (b) the analysis stage from [228], (c) STM tip, (d) KPFM tip from [229], (e) load lock carousel with two samples on their sample holder and one KPFM tip on its holder, courtesy of Evandro Lanzoni.

enough such that the wobble stick could take a sample and place it on the analysis stage (Figure 2.12b). The samples (maximum 10×10 cm^2) were placed and fixed on a sample holder (Figure 2.12e) using conductive clamps. The tip of the STM were made in-house using a tip preparation tool (Scienta Omicron) and introduced in the STM tip holder (Figure 2.12c), while the KPFM cantilevers and tips were bought (Nanoworld) and glued on a cantilever holder (Figure 2.12d) using a UHV-friendly glue (Epoxy Technology).

2.3.1 Scanning Tunneling Spectroscopy

In order to carry out STM and STS measurements, a tungsten (W) wire was etched to form a sharp metallic tip which was mounted on an STM tip holder (Figure 2.12c). The tip was then approached close to the sample using a remote control and by monitoring the tip-sample distance through the reflection of the tip on the sample. As soon as approaching the tip to the sample became challenging due to uncertainties of touching the sample's surface, the tip approach became automatic and driven by the electronics of the SPM. As the STM mode used was constant-current (see section 2.1), a positive or negative gap voltage was applied between the tip and sample and a value for the tunneling current (in the order of pA to nA) was set. Two modes could be used for the tunneling current, either low- or high-current mode. For the low-current mode, the electronics would limit the measured current to 3.33 nA while it would be 333 nA for the high-current mode. For this thesis, only the low-current mode yielded satisfactory results. The gap voltage depended on the sample, but for semiconductors it is necessary to have voltages above the bandgap in order to sense a tunneling current from the empty or filled states of the samples.

Once the auto-approach was finished (see section B.2 of appendix Chapter 2 for a brief description), the scan size was then set, which could vary from a few square nanometers to maximum 8x8 μm^2. The scan speed was also set by adjusting the raster time (time between each pixel) and was usually between 80 to 300 nm/s, which was relatively low. Lastly the loop gains (P and I) were set but adjusted during imaging. During this PhD thesis, STM on perovskites found itself to be rather challenging and required the samples to have very good conductivity. As an example, imaging co-evaporated $MAPbI_3$ was not possible while it was the case for solution-based $MAPbI_3$. Therefore the varying intrinsic properties, such as doping, between samples from different fabrication methods are important. In addition, large negative voltages (applied to the sample, synonym of filled valence states of the sample) were in general the best conditions in order to measure a sufficient and stable tunneling current which resulted in stable images, as also reported by Ohmann et al. [230].

For current imaging tunneling spectroscopy (CITS), more parameters were required and explained in section B.3 of appendix Chapter 2. CITS enables the acquisition of tunneling current maps at different voltages, which can then be extracted pixel by pixel, area by area on in average in order to access the I-V curve and thereafter the LDOS.

2.3.2 Kelvin Probe Force Microscopy

As previously discussed in section 2.2, the mode used for this thesis is frequency modulation KPFM (FM-KPFM). To that end, Si cantilevers with a tip coated with Pt/Ir (PPM-EFM tip from Nanosensor) were used. They have a high mechanical Q-factor which is important to get higher sensitivity in UHV and a resonance frequency between 60 kHz and 90 kHz. Similarly to STM, the cantilever was approached manually with a remote control until the human eye was not sufficient enough to avoid interaction between the tip and the sample. Then a continuous-wave laser with a wavelength of 830 nm and a maximum output power of less than 7 mW was switched on and positioned (using a remote control) at the center of the cantilever and close to its edge in order to get the maximum intensity on the PSD and the highest tip sensitivity but still not lose optical contact due to the sample's roughness. Then by adjusting a mirror, the position of the secondary beam on the PSD can be centered. A normal force moves the reflected beam vertically while a lateral force moves it horizontally across the PSD. An excitation amplitude was then set and the measured amplitude from the position sensitive detector (PSD) was measured as a function of the frequency (amplitude-frequency curve) in order to find the first resonance frequency of the tip and determine its Q factor. The phase was then adjusted to be close to zero and the phase-locked-loop (PLL, see 2.2) was turned on, which brought the Δf value to be zero. As FM-AFM runs on monitoring the change in Δf, a value of Δf was then set, synonym of a certain required tip-sample distance. An auto-approach similar to the one in STM could be started, except than instead of the tunneling current, the system tried to reach the set Δf value by expanding and moving the z-piezo step by step. Once the set Δf value was reached, the laser beam position and the first resonance frequency could be re-adjusted and the loop gains, scan speed and number of pixels (resolution) were set to values matching the surface corrugation. The AFM topography was then measured as explained in 2.2.

As explained in section 2.2, in order to get the CPD signal, FM-KPFM had to use a lock-in amplifier (Signal Recovery, Figure 2.13). The latter had an internal oscillator that generated an AC voltage with a frequency of 1.250 kHz, which was within the PLL bandwidth but far away from the resonance frequency of the tip to avoid topography crosstalk. The amplitude of the AC signal could be adjusted depending on the sample, but was most of the time set to 0.4 V. The modulated force from the applied AC voltage was then detected by the PSD and the detected error signal (Δf) was used as an input for the lock-in amplifier. The output of the lock-in amplifier was used as feedback signal for the Kelvin controller, which had for output the compensation DC voltage, which was recorded by the electronics and the computer and used for the CPD map of the sample. The important parameters of the lock-in amplifiers were the time constant, which went from 10ms to lower values, and the sensitivity, which went from 20 mV to lower values when measuring the perovskite samples (usually 1 ms and 10 mV). Setting up the lock-in amplifier and KPFM regulator was performed after making sure that the topography signal was stable.

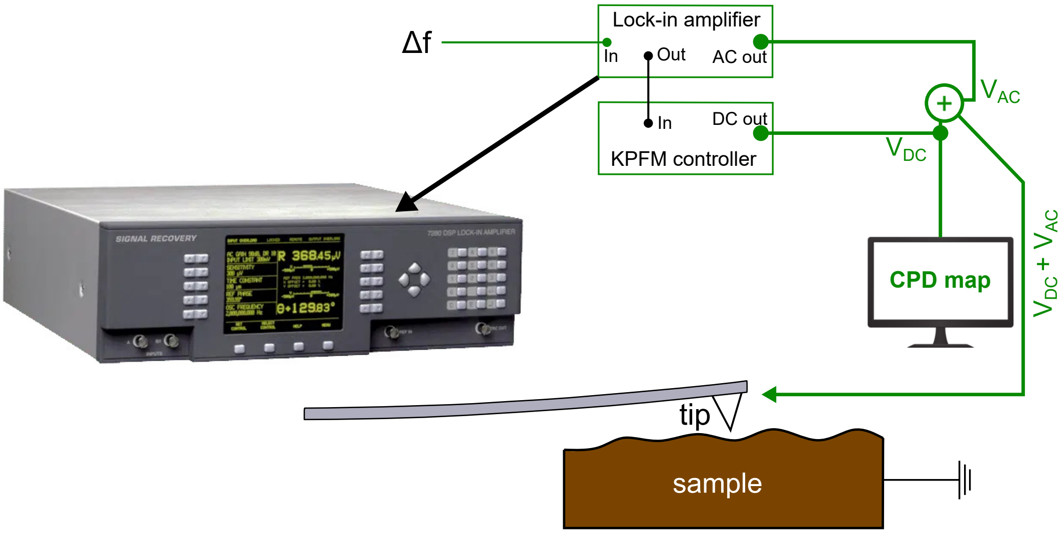

Figure 2.13: Picture of the lock-in amplifier and the sketch of the FM-KFPM part.

The KPFM tip was slightly retracted by solely using the Z-piezo and the AC voltage was then applied. Thereafter, a gap voltage of +1 V was applied to the sample and the phase of the lock-in amplifier was adjusted automatically to maximize the signal. The gap voltage was set back to 0 V and the KPFM regulator was switched on while the I and P gains of the latter were adjusted accordingly to the sample's corrugation. A CPD map was then acquired and the CPD signal was equal to:

$$CPD = \frac{\phi_s - \phi_t}{e} \tag{2.19}$$

ϕ_s and ϕ_t are the WF of the sample and tip respectively while e is the elementary charge. In order to access the WF of the sample, the WF of the tip had to be known, which was done by measuring a highly-oriented pyrolytic graphite (HOPG) sample before and after the perovskite sample. The WF of the HOPG was 4.6 ± 0.1 eV and therefore the WF of the perovskite samples could be estimated with a certain error originating from the HOPG itself, the variations of the tip WF due to tip-sample interactions and the potential degradation of the perovskite.

2.4 SPM on perovskite for solar cells

The following section will review some of the SPM literature related to perovskite solar cells.

Obtaining atomic-scale morphology of polycrystalline perovskite thin films is very challenging due to the roughness of the surface, but also due to the contamination by solvents and air exposure. Therefore, the atomic structure of $MAPbBr_3$ has been experimentally resolved for the first time in 2015 by Ohmann et al. using low-temperature STM on UHV-cleaved single-crystals [230]. Besides the observation of the reconstructed (010) plane of the orthorhombic structure, they also imaged the MA cation, revealed its strong interplay with the Br anion, identified ferroelectric and anti-ferroelectric domains and imaged dislocations lines and defects (Figure 2.14).

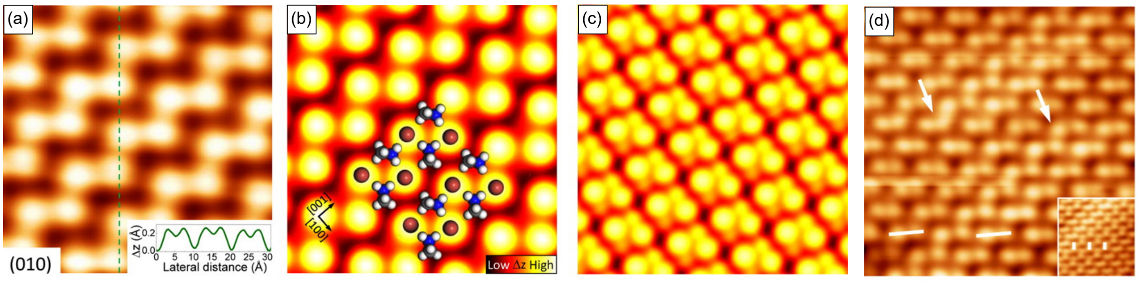

Figure 2.14: (a) Atomic resolution of $MAPbBr_3$ using low-temperature STM where the (010) plane can be observed. (b) Simulated STM image of the same plane with surface reconstruction while the Br and MA ions are overlaid. (c) Calculated STM image with the MA molecules. (d) Disolation rows indicated by the white arrows. Reproduced with permission [230]. Copyright 2015, American Chemical Society.

Similarly, the atomic structure of smooth $MAPbI_3$ on Au(111) was imaged with STM by She et al. where the dimmer phase and the zigzag phases were found on MAI-terminated (001) surfaces (Figure 2.15). In addition, they performed STS on both phases and determined dI/dV spectra and extracted the surface bandgap for different regions. In correlation with DFT calculations they also studied the rotation of the MA cations and its interaction with iodine [14].

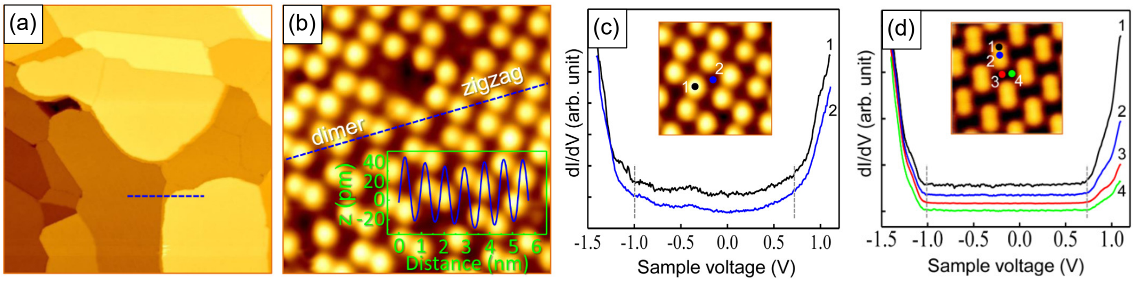

Figure 2.15: (a) Large-scale STM image of $MAPbI_3$ on Au(111). (b) STM images of the two co-existing dimmer and zigzag phases. (c,d) dI/dV spectra for (c) the zigzag structure and (d) the dimmer structure. Reprinted with permission from [14]. Copyright 2016 American Chemical Society.

Other STM studies on single-crystals or flat surfaces were carried out on the same materials. Hieulle et al. have for example investigated, using STM, the atomic structure and stability of $MAPbBr_{3-y}I_y$ by varying the amount of iodine and also by replacing it with chloride [15] or MA by Cs [16], while Liu et al. have used STM measurements combined with STM simulations and DFT calculations to determine the type of surface defects of $MAPbBr_3$ single crystals, which are the Br and the Br-MA double vacancies [231]. Hsu et al. on the other hand have mapped out the dipole orientation of cross-sections of $MAPbBr_3$ single crystals as well as the electrostatic potential in the dark and under illumination using STM, STS and simulations [232] while Murali et al. have demonstrated the restructuring of aged $MAPbBr_3$ single crystals which led to compositional changes compared to pristine cleaved single crystals [233].

For thin films, Shih et al. were some of the first ones to perform STM on solution-based polycristalline $MAPbI_3$ films, where grains of several hundreds of nanometers could be discerned (Figure 2.16a). In addition, they carried out STS mapping in the dark and observed a PbI_2 passivation layer with a larger surface bandgap surrounding $MAPbI_3$ grains (Figure 2.16(b to e)). They also used light to study the photo-induced transfer of charges, band bending and carrier generation and concentration or carrier types [17].

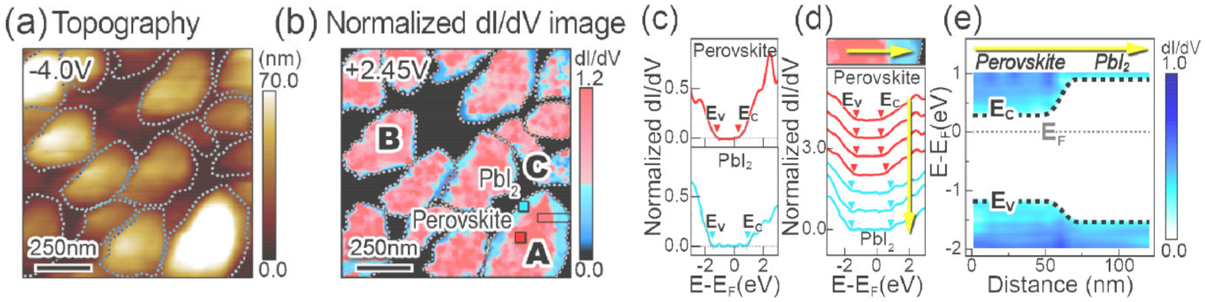

Figure 2.16: (a) STM topography of a $MAPbI_3$ thin film. (b) Corresponding normalized dI/dV image with a sample bias of +2.45 V. (c,d) Normalized dI/dV curves of perovskite and PbI_2. (e) Sketch of the surface bandgap at the interface perovskite/PbI_2. Reprinted with permission from [17]. Copyright 2017 American Chemical Society.

Azulay et al. have on the other hand focused their study on solution-based mixed (both cations and anions) perovskite thin films using a combination of STM, STS, photoconductiviy and steady state photocarrier grating measurements. In their work, they found a correlation between the energy distribution of in-gap states and their manifestation in the photo-transport properties of the perovskite, and determined the role of shallow defects in the bandgap as recombination centers [234]. More recently Wieghold et al. have explored the effects of electric fields on mixed cation Pb-based perovskites using STM and STS, among other techniques, and have found that the valence and conduction bands at the surface would shift depending on the sweep direction of the applied bias, inducing a reduced extracted surface bandgap. In addition, the iodine environment was altered depending on the polarity of the bias [235].

Besides the review papers on STM and STS related to perovskite solar cells [236, 237, 238], several review papers discussed the works related to perovskites using KPFM [237, 239, 240, 241, 242]. Studies based on only AFM will not be discussed in this review section as they essentially concern topography, grain size, film homogeneity, roughness and secondary phases, which can also be measured for most of them by scanning electron microscopy for example, which can however damage the perovskite film. One of the first works using KPFM was by Bergmann et al., where the WF along a cross-section of a $MAPbI_3$ solar cell was measured in the dark and under illumination in order to map the CPD response (Figure 2.17) at different positions. This enabled the observation of an accumulation of holes and a presence of traps in the perovskite layer reducing the short-circuit current, and it permitted to also draw an energy band diagram [243].

Similarly, Dymshits et al. have measured the CPD of a cross section of $MAPbI_3$ using different stacks (nc-TiO_2 and nc-Al_2O_3 for ETL) to estimate the energy band diagrams and measure the depletion width between the extraction layers and the perovskite. They also measured a 25 meV upward band bending between grains and grain boundaries, which led them to say that GBs played a minor role in the solar cell performances (Figure

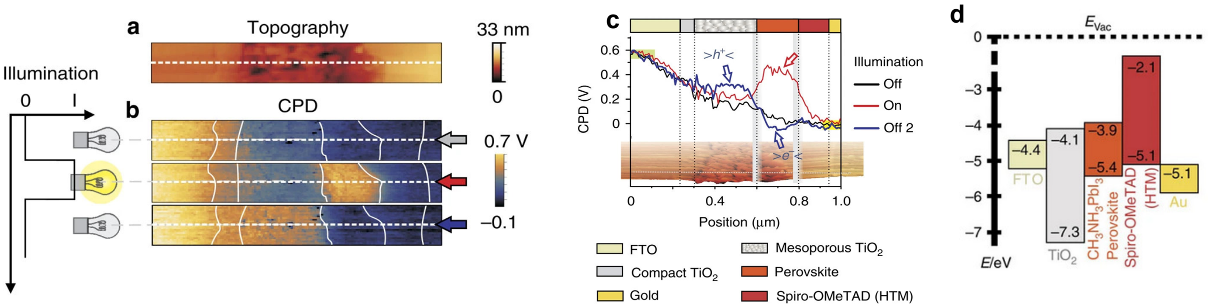

Figure 2.17: (a) Topography of the $MAPbI_3$ device cross-section. (b) Corresponding CPD map in the dark, upon illumination and in the dark after illumination. (c) Extracted line profiles of (b) for the different conditions. (d) Energy band diagram of the device stack. Reprinted by permission from [243], Copyright 2014 Springer Nature.

2.18) [244]. Several other cross-sectional studies of perovskite solar cells using KPFM exist in the literature [21, 245, 246, 247, 248, 249]. Li et al. have used it to observed the effects of the migration of Li^+ ions on the device performance [245], while Cai et al. investigated the different potential drops occurring in the device stack in order to control the position of the diode junction and improve the device performances [246].

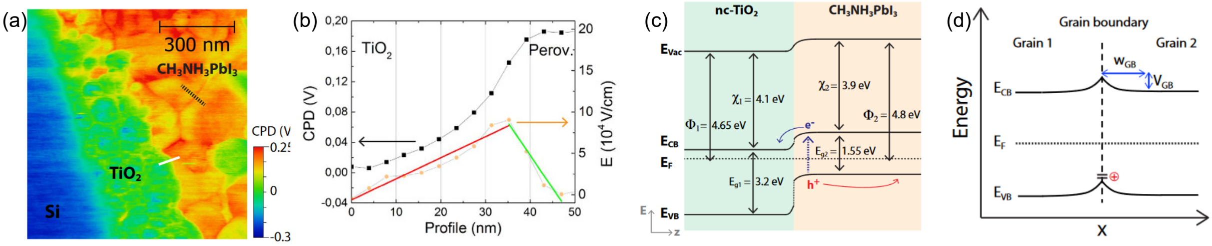

Figure 2.18: (a) KPFM images of the Si/nc-TiO_2/$MAPbI_3$ stack. (b) CPD profile and corresponding electric field for the same stack. (c) Calculated energy band diagram using the KPFM measurements. (d) Grain boundary band bending depicting an upward band bending from grains to grain boundaries. Reprinted from [244] under a Creative Commons Attribution BY license. Copyright 2015 Springer Nature.

The first KPFM studies were also focusing on the effects of grain boundaries as they are often the cause of efficiency losses, even if in perovskites their role is highly debated (see section 1.3.4 of Chapter 1). Yun et al. have for example used KPFM as well as c-AFM to prove that GBs can be beneficial for solution-based $MAPbI_3$ solar cells as they form a potential barrier and more short-circuit current can be collected via them compared to grains, which resulted in a better separation and collection of charges at the GBs (Figure 2.19) [18].

A year later, Yun et al. performed KPFM, in both contact and non-contact modes, this time on solution-based mixed perovskite (cations and anions), by applying positive and negative voltages and they additionally studied the influence of illumination (Figure 2.20) on the surface properties. They observed a large accumulation of ions at negative voltages, with a long CPD recovery when the voltage was turned off, which was in coherence with ion migration, found to be faster at the GBs than at the grains. In addition, they reported a larger surface band bending at the GBs than at the grains, favoring the carrier collection at the GBs [19]. Later on, they studied the impact of humidity on the perovskite surface

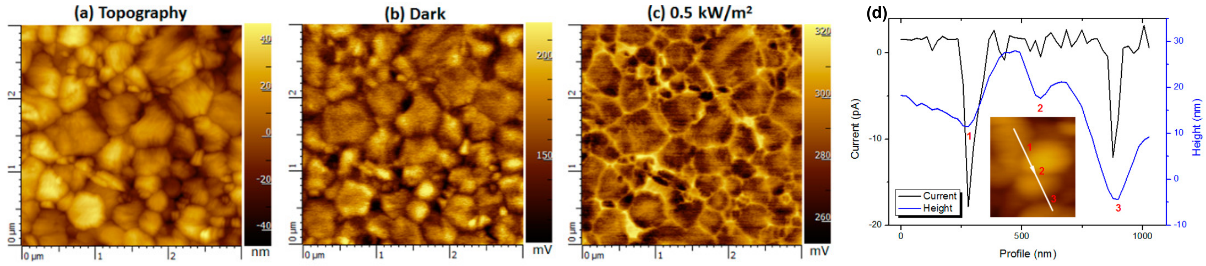

Figure 2.19: (a) AFM Topography of $TiO_2/MAPbI_3$. (b) CPD map in the dark. (c) CPD dark under a 0.5 kW/m^2 illumination at a wavelength of 500 nm. (d) Current (from c-AFM) and height profile at the grains and grain boundaries. Reprinted with permission from [18]. Copyright American Chemical Society.

and observed a degradation via the GBs where non-perovskite phases formed and where ion migration was greatly enhanced compared to grain interiors [250].

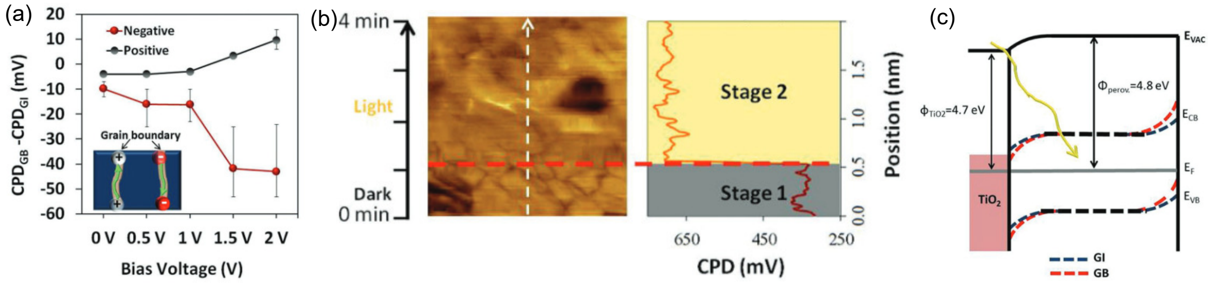

Figure 2.20: (a) Grain boundary band bending as a function of different positive and negative voltages. (b) CPD map and extraction of line profiles in the dark and upon illumination. (c) Energy band diagram taking into account the grains and the GBs. Reproduced with permission from [19]. Copyright 2016 Wiley-VCH Verlag GmbH & Co. KGaA.

On the other hand Li et al. have reported, using KPFM, that downward band bending existed between grains and grain boundaries for a $MAPbI_3$ absorber spin-coated on a PEDOT:PSS extraction layer. They furthermore combined these measurements with c-AFM to show the predominant flow of current happening at the grains and not at the grain boundaries when no voltage was applied but which was reversed when the voltage applied overcame the GBs barrier. Similarly to Yun et al., they said that GBs were efficiently separating the charge carriers as well as they were preferred pathways for these carriers (Figure 2.21) [20].

The combination of KPFM and c-AFM was also used to investigate the ion migration at the grain boundaries for solution-based $MAPbI_3$. Shao et al. have for example reported a faster ion migration at the GBs than within the grain interiors leading to a stronger visible hysteresis at the GBs [251]. A multitude of other work focused on using KPFM and other SPM techniques to study the differences between grains and grain boundaries and determine whether the GBs were really detrimental or beneficial [21, 211, 252, 253, 254, 255].

Besides grain boundaries, KPFM was used to examine the homogeneity of the surface energetics, as well as the existence of secondary phases or other materials at the surface. Gratia et al. have for example linked higher WF (lower CPD) grains in a

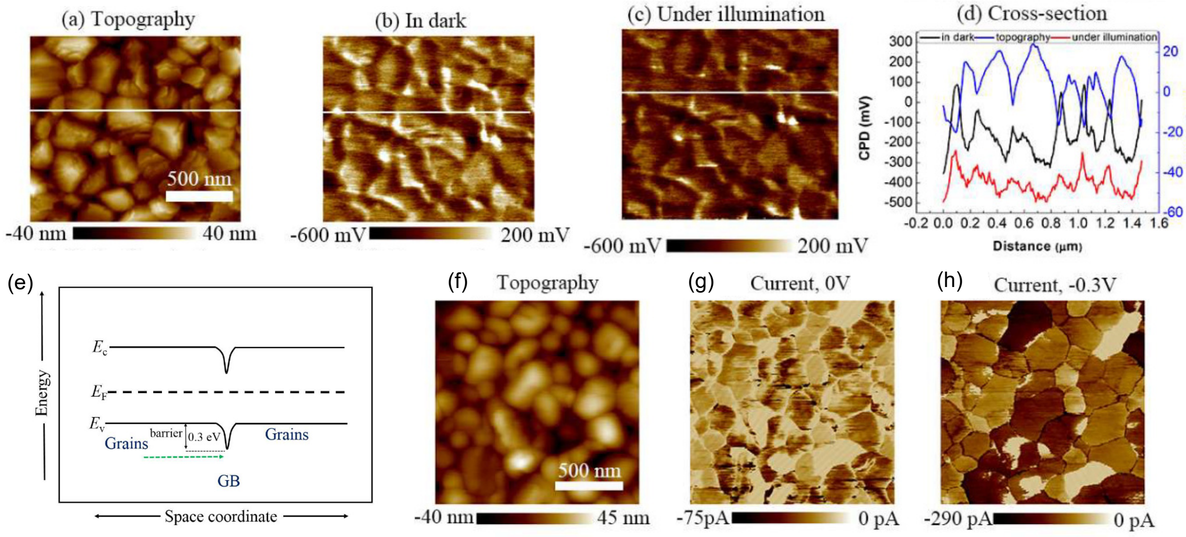

Figure 2.21: (a) AFM topography of $MAPbI_3$ on PEDOT:PSS. (b,c) Corresponding CPD maps in the dark and under illumination. (d) Extracted line profiles (white line on previous maps) to represent the grain boundary band bending. (e) Sketch of the downward band bending from grains to GBs. (f) c-AFM topography of the sample with (g) and (h) the current maps at 0V and -0.3 V respectively presenting a greater current at the GBs when the voltage is around the GB potential barrier. Reprinted with permission from [20]. Copyright 2015 American Chemical Society.

$(FAPbI_3)_{0.85}(MAPbBr_3)_{0.15}$ absorber with $FA_xMA_yPbI_3$ rich domains by combining the KPFM measurements with Helium ion microscope coupled with a secondary ion mass spectrometer (HIM-SIMS) (Figure 2.22a) [256]. Shao et al. have measured large WF inhomogeneities between different grains which they revealed had different crystallographic orientations using transmission electron microscopy (Figure 2.22b) [251]. Collins et al. have reported that the heterogeneous variations of the CPD of their fabricated $MAPbBr_3$ film was most likely due to different effects including local doping, chemical segregation or defect states (Figure 2.22c) [206]. Intra-grains variations could also be discerned in the solution-based mixed perovskite of Lin et al. (Figure 2.22d) [257].

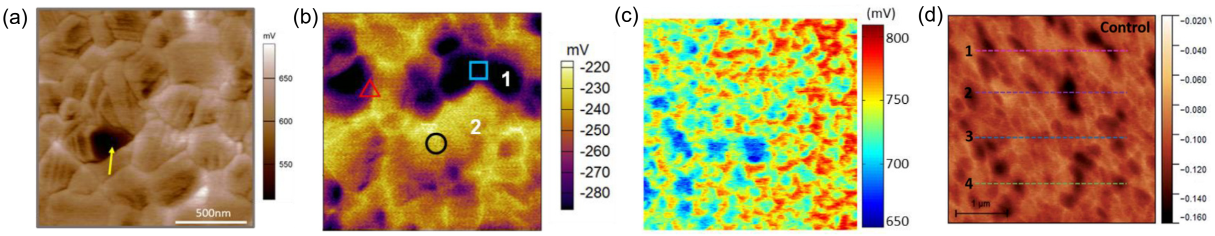

Figure 2.22: (a) KPFM measurements in the dark of $(FAPbI_3)_{0.85}(MAPbBr_3)_{0.15}$. Reprinted with permission from [256]. Copyright 2016 American Chemical Society. (b) KPFM image of $MAPbI_3$. Reprinted from [251] with permission from Royal Society of Chemistry. (c) CPD map of a $MAPbBr_3$ thin film. Reprinted from [206] with permission from IOP Science. (d) KPFM of $Cs_{0.05}(FA_{0.85}MA_{0.15})_{0.95}Pb(Br_{0.15}I_{0.8}$. Reprinted from [257] with permission from the Royal Society of Chemistry.

KPFM is therefore a great tool to investigate how these variations change when post-treating the sample with either surface-treatment techniques or doping strategies. Lin et al. have for example observed that the previous grain inhomogeneities in the CPD map of Figure 2.22d reduced drastically after using a bulk recrystallization process by applying FACl on the preovskite to remove the excess PbI_2 [257]. Xiao et al. have studied the impact of lithium (Li) dopants in the perovskite absorber through diffusion from the hole extraction layer. They observed an increase of the surface potential with an inhomogeneous distribution between grains and grain boundaries [258] while Tennyson et al. have used KPFM to shine light on the effects of introducing additives such as KI during the sample synthesis [259]. Many other work have used KPFM for that matter [260, 261, 262].

Lastly, KPFM can be used to measure the surface photovoltage (see sub-section 1.3.6) of perovskite samples. Almadori et al. have used KPFM for $MAPbBr_3$ single crystals to investigate the response of the CPD upon illumination. They observed different components arising from the illumination, occurring at different times, with first a fast increase of the CPD, linked to the surface photovoltage, and screening of surface states by photogenerated carriers, followed by charge separation and redistribution and ion migration. As soon as the light would be switched off, the carriers would recombine and ion migration would occur again until equilibrium [202]. Similarly, Toth et al. have investigated the response of the open-loop signal of the KPFM to a single light pulse. They observed different components in the signal, which they associated to different physical phenomena such as generation of charge carriers at the surface (SPV), ion transport or migration and charge accumulation and they attributed them to extracted time constants. In the dark, the ions and trapped charges would relax and recombine [211]. A large amount of publications studied the response of the CPD upon illumination [18, 203, 206, 208, 263, 264, 265, 266].

As can be observed by the literature review of section 2.4, a large amount of SPM studies on halide perovskites is already available. However, most of these reports either investigated solution-based halide perovskites, single crystals or halide perovskites in which the surface had already been altered with by solvents, air exposure, thermal annealing or post-deposition treatments. Therefore there is a clear need to understand the intrinsic properties of pristine halide perovskite thin-films, which are the most commonly-used for solar cells (compared to single-crystals). Only then, exposure to extrinsic factors can be used to determine their effects on the surface of halide perovskites. To that end, physical vapor deposition (PVD) is the fabrication technique of choice as it only uses precursors from the chemical composition, in a high-vacuum environment and can be embedded in a nitrogen-glovebox to avoid air exposure. The following chapters will mostly investigate, via SPM, the surface properties of pristine $MAPbI_3$ grown using PVD as this halide perovskite is the most simple configuration and still yield the highest efficiencies when using PVD compared to mixed halide perovskites (see section 3.1). The next chapter will therefore focus on the working principle of PVD and more specifically co-evaporation of $MAPbI_3$, the machine used and the main characterization technique used to determine the film quality: photoluminescence.

Chapter 3

Growth and quality control

A large number of techniques exist to fabricate lab-scale perovskite solar devices, the most common one and the one that yields the highest efficiencies being based on solution processes such as spin-coating. However such techniques require the use of solvents, that alter the surface, and commercialization of these methods is highly unlikely due to the difficulty of obtaining homogeneous layers on a large-scale (see section C.1 of appendix Chapter 3). Perovskite solar panels require homogeneous absorber layers, as pin-holes could result in short-circuit current losses and inhomogeneous grains could yield different electronic properties, inducing local variations of the device performances. Physical vapor deposition (PVD) is a technique that is carried out in vacuum, only uses the compounds from the chemical formula of perovskite and can be up-scaled for large-area fabrication. Therefore the study of perovskite absorbers fabricated with that technique is of great importance for the rapid commercialization of perovskite solar panels. This chapter will describe the main fabrication technique used in this thesis, namely thermal co-evaporation, as well as the characterization methods and instruments used for investigating the quality of the $MAPbI_3$ films fabricated. Section 3.1 will give a brief summary of physical vapor deposition and thermal evaporation before discussing in details the thermal co-evaporation of $MAPbI_3$. It will be shown that due to the organic compound MAI in $MAPbI_3$, the MAI partial pressure will replace the evaporation temperature of MAI as a control parameter. The last section 3.2 will give a basic introduction to photoluminescence (PL) characterization, the set-up used, as well as ways to determine doping densities using PL and time-resolved PL.

3.1 Fabrication of perovskite solar cells

3.1.1 Solution-based fabrication

The most common methods to fabricate perovskite thin films are the so-called one-step, two-step solution-based methods (Figure 3.1). For the one-step technique, perovskite precursors, for example lead iodide (PbI_2) and methylammonium iodide (MAI) for $MAPbI_3$, are mixed in a single solution and deposited by spin-coating on the substrate. Therefore, they often required a post-annealing treatment [267]. For the two-step deposition, a first solution with one precursor is spin-coated on a substrate, followed by a second solution with a different precursor, which can be spin-coated [268] or used as a dipping solution [269]. This requires a post-annealing treatment for the total formation of the perovskite phase [270]. These two techniques are simple to implement in a laboratory and can rapidly yield high-efficiency solar cells but have however been replaced by a solvent-engineering approach (Figure 3.1). The latter is an optimization of the one-step process, where an antisolvent treatment is used between the spin-coating and the annealing steps to facilitate the removal of the host solvent and enable a better crystallization of the perovskite film [271, 272]. This technique is so far the most commonly used one to fabricate high-efficiency perovskite solar cells [273].

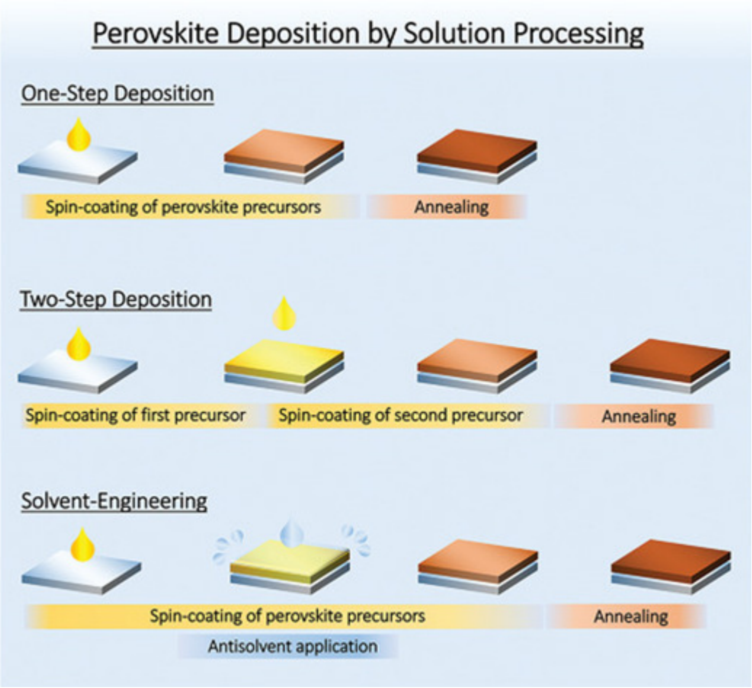

Figure 3.1: Sketch of the different solution-based techniques to fabricate perovskite thin films. Reprinted from [273] under a Creative Commons CC BY license. Copyright 2020 John Wiley and Sons.

In comparison to these primary fabrication methods, a variety of techniques exist, which have been reviewed by Swartwout et al. [274] and mainly consists in inkjet printing [275], spray-coating [276], flash evaporation [277], slot-die coating [278], blade coating [279], chemical vapor deposition (CVD) [280], physical vapor deposition (PVD) [58] and a combination of solution-based techniques and vapor deposition [281]. The use of PVD over solution-based processes and most of the other techniques has several advantages. First, toxic solvents, which can alter the perovskite structure, are not used and the perovskite films can be preserved from air exposure if the PVD is implemented in an inert environment (glovebox). Secondly, no post-annealing is required which is useful for flexible devices. The evaporation of perovskite can also be incorporated in a fully-evaporated solar device, suitable for industry-scale fabrication. Additionally, as no annealing is required, there is no risk of damaging the bottom cell of a tandem solar cell when the perovskite is used as the top cell. Lastly, large-area deposition (for solar panels) is possible and is known to yield much more homogeneous films compared to spin-coating (see section C.1 of appendix Chapter 3) [273]. In addition to these advantages over the solution-based processes, at the time of the beginning of this thesis, few to no studies had been carried out to investigate the surface properties of evaporated $MAPbI_3$, whose morphology and properties are very different from solution-based $MAPbI_3$ [273]. Therefore combining PVD to fabricate $MAPbI_3$ and SPM to study their nanoscale intrinsic surface properties was of great interest and importance for the future optimization and commercialization of perovskite solar panels.

3.1.2 Physical vapor deposition

Physical vapor deposition (PVD) is one of the most used techniques to deposit thin films on a substrate. It can be divided into different parts: sputtering, ion plating, pulsed laser deposition and thermal evaporation, the latter being the one used in this thesis. The concept of thermal evaporation is rather simple and is depicted in Figure 3.2a. In a high-vacuum (10^{-3} to 10^{-7} mbar) chamber, the desired precursor material (powder or crystals for example) of the final film composition is inserted into a ceramic crucible, which can be heated to very high temperatures by a DC power supply (1). A temperature will be set on the crucible such that the material goes from its initial condensed phase to a vapor phase either by sublimation or evaporation [282] (2). This solid-vapor phase transition depends on the triple point of the vapor pressure curve of the material which is derived from the Clausius-Clapeyron equation [283], and therefore the evaporation temperature used is material-dependent. The vapor, made of the material's molecules, will expand into the chamber towards the substrate due to thermodynamic equilibrium (3). Due to the lower temperature of the substrate, the vapor will condense back onto the substrate to form the film (4).

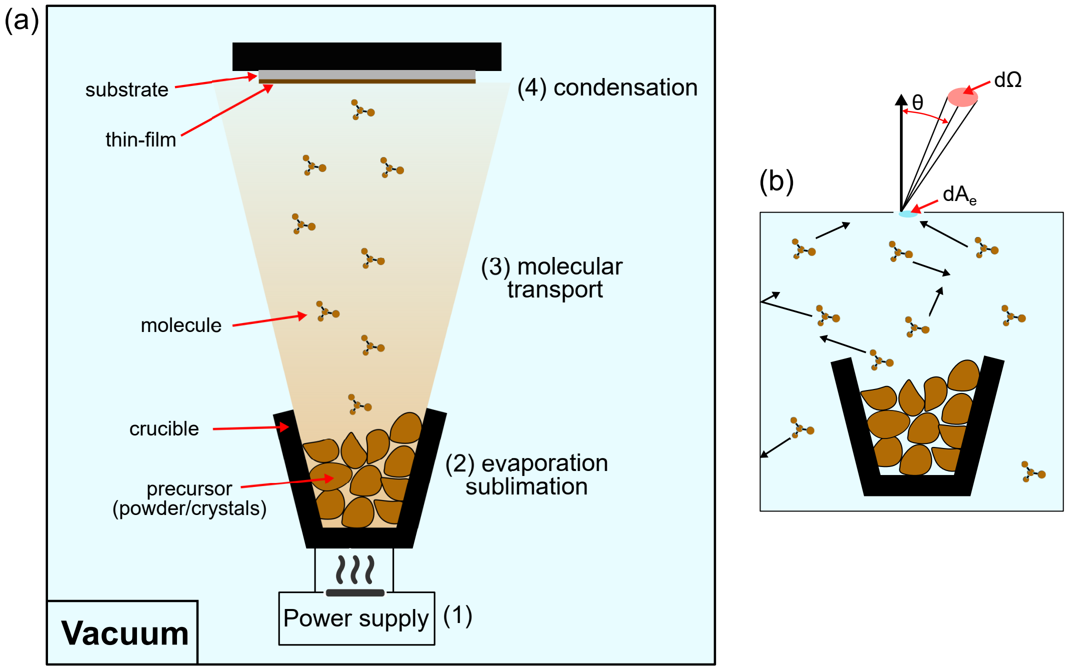

Figure 3.2: (a) Schematic presentation of physical vapor deposition. (b) Representation of a Knudsen cell or effusion cell.

The pressure inside the chamber depends on the vapor pressure of the elements used in the material that will be evaporated or sublimated, as well as the temperature applied to the evaporation source [282]. Diagrams of the vapor pressures of chemical elements as a function of their temperature can be found in [284]. Following this, the net evaporation flux directly at the evaporation source can be described by the Hertz-Knudsen equation 3.1:

$$j = \frac{p_{vap} - p}{\sqrt{2\pi m k_B T}} \tag{3.1}$$

p_{vap} is the equilibrium vapor pressure of the evaporant at the temperature T derived from the Clausius-Clapeyrib equation, p is the ambient chamber pressure which acts upon the evaporant in a condensed phase and m is the mass of the particle. Additionally, Knudsen discovered that the evaporation flux at the solid/vapor interface was different from the one at the surface of the substrate and particles could be reflected back. This introduces α the sticking coefficient (collision probability) of the gas molecules onto a surface. Therefore the evaporation flux on the surface can be defined as follows:

$$j = \alpha \frac{p_{vap} - p}{\sqrt{2\pi m k_B T}} \tag{3.2}$$

It stems from equation 3.2 that the lower the chamber (base) pressure at rest, the higher the evaporation rate, which justifies the need of a deposition under a high vacuum. As presented in Figure 3.2a, the material precursor is set in a crucible and ideally the evaporation should be oriented and maximized only towards the substrate to avoid losses of material and increase the evaporation rate there. However, in vacuum, the free evaporation from the surface of the evaporant is isotropic. Therefore in 1909 Knudsen invented the Knudsen cell, which is depicted in Figure 3.2b. Using the Knudsen cell, the evaporation through an orifice of size dA_e is referred to as effusion and is directional following a cosine law [283]. The use of an orifice suppresses the reflection of incident vapor molecules, resulting in a $\alpha = 1$. The flow of N molecules in dt time emitted through this orifice into a solid angle of $d\Omega$ with an exit angle θ (Figure 3.2b) can be expressed by:

$$d_{j,effusion} = j_{effusion} \frac{cos\theta d\Omega}{\pi} = A_e \frac{p_{vap} - p}{\sqrt{2\pi m k_B T}} \frac{cos\theta d\Omega}{\pi} \approx A_e \frac{p_{vap}}{\sqrt{2\pi m k_B T}} \frac{cos\theta d\Omega}{\pi} \tag{3.3}$$

The cosine dependence using an effusion cell induces a thickness inhomogeneity of the film deposited on the substrate. If a substrate, which is considered a wafer of radius r_s, has its center at a distance r_0 of the effusion cell, the edges will be at a distance r_e defined by the angle θ (Figure 3.3). The ratio of the thickness at the edge d_{edge} to the thickness at the center of the wafer can be defined by:

$$f_r = \frac{d_{edge}}{d_{center}} = \frac{r_0^2}{r_0^2 + r_s^2} cos\phi cos\theta = \frac{1}{\left[1 + \left(\frac{r_s}{r_0}\right)^2\right]^2} \tag{3.4}$$

f_r is the reduction factor and gives an indication on the differences in thicknesses at different positions of the wafer. As the evaporation sources or cells are often not centered with respect to the substrate, inhomogeneities between center and edges can be important and therefore the use of a rotating substrate is of great use to reduce this issue.

The substrate-source distance is not the only determining factor of the evaporation rate in a PVD chamber. The molecular interactions between the base pressure and the vapor phase introduced by the evaporant sources, play an important role. Molecules can collide elastically and be either re-directed or bind chemically with other species. This introduces the mean free path quantity λ (equation 3.5) that reflects the distance before which a particle will change its direction due to collisions [283].

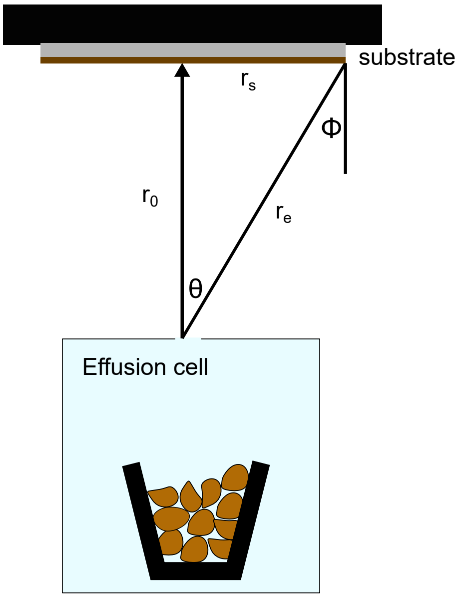

Figure 3.3: Sketch of the direction of the evaporation using an effusion cell, and the difference in thickness at the center and at the edge.

$$\lambda = \frac{k_B T}{\sqrt{2}\pi p d^2} \tag{3.5}$$

where p is the pressure induced by the evaporating material and d is the diameter of the particle. As the diameter of different molecules vary, λ can be expressed with multi diameter [283]. The mean free path should be the highest possible and also depends on both the base pressure and the vapor pressure of the evaporants. This again proves why very high-vacuum is necessary in order to maximize the amount of molecules reaching the substrate. Additionally, the mean free path gives a limit on the source-substrate distance that should be respected. All of the previous effects make the prediction of the evaporation rate and deposited thickness on the substrate challenging. Therefore PVD uses quart crystal microbalance (QCM) sensors, which consist in quartz piezoelectric material which oscillate at a certain frequency when an AC bias is applied. The whole sensor is placed in the way of the vapor phase, which results in a deposition of the source material on the QCM, altering the oscillation frequency of the quartz material, that can be linked to the mass of the deposited material and later by its thickness depending on the material properties. Therefore QCMs give an indication of the evaporation rate as well as the thickness but at the distance of the QCM, which can however be adjusted by a tooling factor to obtain the evaporation rate and deposited thickness on the substrate.

Once the molecules condense on the substrate due to its lower temperature, several phenomena can occur. First, the molecule can be reflected towards another direction, or adsorption can occur followed by direct desorption or the molecules are adsorbed at the surface and stay there. Therefore the rate of the condensed particles on the substrate is different from the incident rate such that $j_{condensation} = \alpha_{sticking} j_{incident}$. The sticking coefficient $\alpha_{sticking}$ depends on the physisorption and chemisorption mechanisms occurring between the molecules and the surface of the substrate [285]. The adsorbed molecules will then merge into clusters and further into crystal nuclei which will nucleate and form grains separated by grain boundaries, which will result in the formation of a film. However the film growth is slightly more complicated and depends on a multitude of parameters such as the type of the substrate (crystal structure, adhesion), its temperature, the evaporation rate and the ambient pressure during the thermal evaporation [286]. Three main growth mechanisms exist: island growth (Volmer Weber), layer-by-layer growth (Frank-van der Merwe) and mixed growth (Stranski-Krastanov) (Figure 3.4) [286] and are explained as follows:

- **Volmer Weber**: when the binding energy of the evaporated atoms is stronger than the one between the atom and the substrate's surface, there is a formation of localized clusters, which can be referred to as island growth. Each island will continue to nucleate until the substrate is covered by a layer of the evaporated material, and then the islands will merge with each other to form a continuous film.

- **Frank-van der Merwe**: on the contrary, if the binding energy between the surface and the atoms is stronger than the inter-atomic binding energy, a sequential formation of layers will occur.

- **Stranski-Krastanov**: for this mixed mode, the growth is initially started by a layer-by-layer mechanism which will be transformed by an island growth at a later stage.

Therefore the binding energy between the surface and the molecules from the vapor phase is very important to understand the growth mode.

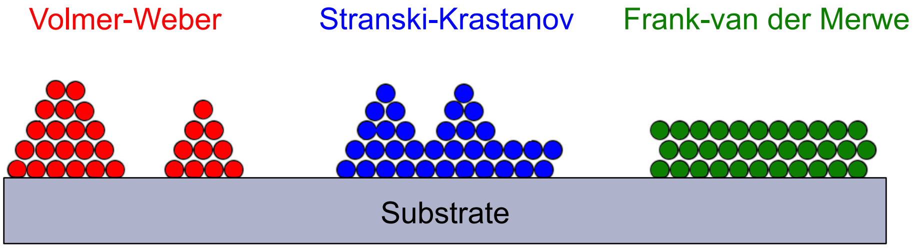

Figure 3.4: The different growth mechanisms of thermal evaporation.

3.1.3 PVD of MAPI

In order to deposit a perovskite thin film using thermal evaporation, several routes can be used, such as single-source evaporation, where a perovskite precursor or crushed perovskite crystals are placed into a single crucible [287, 288]. Another way is to sequentially evaporate the different precursors one after the other but this technique requires post-annealing treatments in order to fully form a perovskite film [289]. The most commonly-used technique, and the one carried out during this thesis, is called co-evaporation and relies on filling up the different precursors in multiple crucibles and co-evaporating them all at the same time. The advantage of this technique is that it usually does not need thermal treatments after the evaporation.

For the co-evaporation of $MAPbI_3$, the precursors used are powders of small crystals of lead iodide (PbI_2) and methylammonium iodide (MAI). The first thermal evaporation of perovskite thin films was performed by Mitzi et al. in 1999 [290] while the first report of vacuum-deposited $MAPbI_3$ using co-evaporation was in 2013 by Liu et al. [58] where a 15.4% planar perovskite heterojunction solar cell was fabricated. Later in 2016 Momblona et al. managed to reach efficiencies of 16.5% and 20.3% by using p-i-n and n-i-p configurations respectively [291]. Since then the power conversion of co-evaporated $MAPbI_3$ has not increase much, staying around 20-21% [292, 293, 294]. Co-evaporation or multi-source evaporation were also used for other types of materials with similar success. Roß et al. demonstrated the co-evaporation of 20.4% $FAPbI_3$ [295] while Chiang et al. fabricated a 18.2% $FA_{0.7}Cs_{0.3}Pb(I_{0.9}Br_{0.1})_3$ solar cell [296]. Even if co-evaporated $MAPbI_3$ lead to similar power conversion efficiencies (PCE) than other techniques for polycrystalline $MAPbI_3$ [297, 298, 299] or $MAPbI_3$ single-crystals [300], the PCE for co-evaporated mixed perovskite are far behind the now commonly achievable 22-24% for solution-based perovskites and the record PCE of 25.5% [301]. Interestingly thermal evaporation focuses mainly on single-cation perovskite and more preceisely on MA-based perovskites such as $MAPbI_3$, $MAPbI_{1-x}Cl_x$ while solution-based processes have moved towards mixed cation mixed anions perovskites [273]. Vaynzof et al. have described these large differences between evaporated and solution-based perovskites with several hypothesis. First, evaporated films lead to much smaller grains resulting in more grain boundaries which are potential defective regions and recombination centers. Secondly compared to solution processes, thermal evaporation cannot introduce additives that have proved to improve device efficiencies [273]. In terms of large-area evaporated perovskites, mini-modules with a 21 cm^2 active area of $MAPbI_3$ reached a 18.13% efficiency [292], while 14.2% efficiencies were demonstrated for $FAPbI_3$, with an active area of 64cm^2. The PCE for the evaporated mini-modules are relatively close to the 20.1% record PCE for perovskite mini-modules [301], which proves that thermal evaporation is a promising technique for commercialization and needs to be further investigated.

Despite the ease of use and good controllability of thermal evaporation, co-evaporation of $MAPbI_3$ was reported to be challenging and to lead to non-reproducible processes when using the standard control parameters which are the temperatures of the evaporation sources (crucible), due to the instability and difficulty of controlling the evaporation rate of MAI [302, 303, 304, 305, 306]. Contrarily to the evaporation of PbI_2 which can be described as effusion [307] and therefore a directional evaporation, the vapor pressure of the organic MAI [274, 308] is high, which induces not only an effusion process but a second non-directional process. Several groups have reported MAI to have both an effusive component and a chemical vapor deposition (CVD) component as depicted in Figure 3.5 [307, 309, 310, 311] which resulted in complications when calibrating and using the QCM to monitor the MAI evaporation rate. Besides, as explained by Abzieher et al., the combination of effusive process from the PbI_2 source and the CVD-like process from the MAI source induces more molecular reactions in the chamber than the one that should occur only at the surface of the substrate. The PbI_2 and MAI molecules can for example react to form perovskite on their way to the substrate, or form perovskite and be deposited onto the QCM (Figure 3.5), which can lead to difficulties in monitoring the evaporation rate of PbI_2 during co-evaporation as well. Besides, even if a substrate shutter is used to end the deposition of a perovskite film, the CVD-like component of MAI can further introduce MAI molecules sticking at the surface of the grown perovskite films, which can result in the introduction of secondary phases at the surface. In addition to these issue, Borchet et al. also reported that the concentration of impurities in the MAI precursor was critical in order to potentially control the evaporation rate and have reproducible processes [303] and MAI has been demonstrated to have a low sticking coefficient and to deprotonate into CH_3NH_2 and HI upon evaporation [312] or decompose into CH_3I and NH_3 [313].

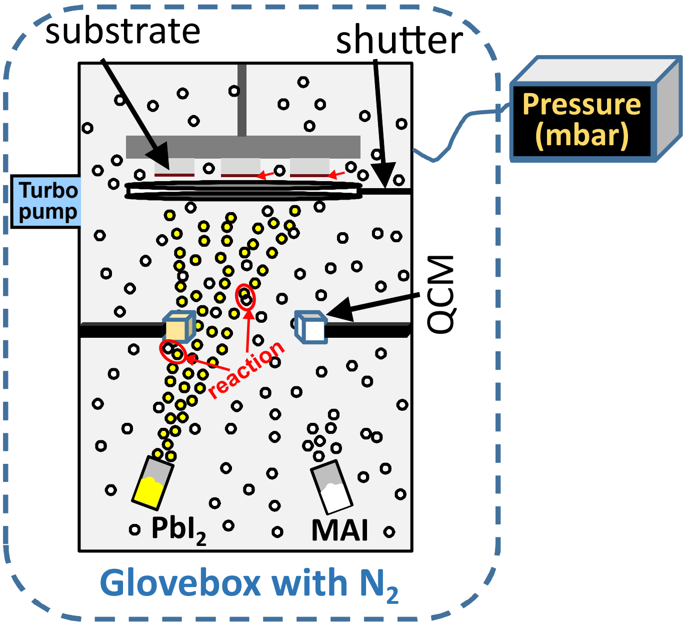

Figure 3.5: Schematic representation of a PVD for the co-evaporation of $MAPbI_3$ using MAI and PbI_2 as material sources. QCM refers to the quartz crystal monitor sensors.

Therefore the temperature of the MAI source cannot be trusted as a control parameter for reproducible deposition, even if some groups have managed to work with it, either by changing the type of crucible used [314, 315], determining the correct acoustic impedance ratio and density of MAI [316] or by modelling the film growth and correcting the evaporation of MAI with its complex adsorption properties [317]. As the evaporating MAI induces a CVD-like component, several groups have instead controlled the deposition of $MAPbI_3$ by using the MAI partial pressure, which is measured by a pressure gauge (as the PbI_2 partial pressure has almost no influence on the total pressure) [307, 309, 310, 311]. This technique is the one used in this thesis to fabricate $MAPbI_3$ absorbers and the growth process will be discussed in the next sub-section together with the experimental set-up.

3.1.4 PVD set-up and growth control of MAPI

In order to not expose the grown samples directly to air, a PVD embedded in a nitrogen glovebox from MBraun was used as depicted in Figure 3.6a. The oxygen and water levels inside the glovebox were below 0.5 ppm almost all the time (around 0.4 ppm of H_20 and <0.1 ppm of O_2). The PVD (Figure 3.6b) consisted in two evaporation sources (Knudsen cells) in which ceramic crucibles of MAI and PbI_2 powders were introduced. These sources had shutters such that thermal evaporation could be stopped rapidly by closing the shutter. Two quartz crystal microbalance (QCM) sensors were installed in the evaporation pathway of the sources, between the sources and the substrate, and were shielded by a metallic cylinder to avoid cross-contamination from the neighboring evaporation source. A custom-made substrate holder (Figure 3.7) was built with screws in order to have a variety of substrate sizes. A shutter was positioned in front of the substrate holder such that it could quickly stop the deposition on the substrate, to a certain extent due to the previously-discussed CVD-like component of MAI.

The high-vacuum inside the PVD chamber was obtained by the use of a Leybold turbo pump (Figure 3.7c), which was not in direct contact with the output of the PVD

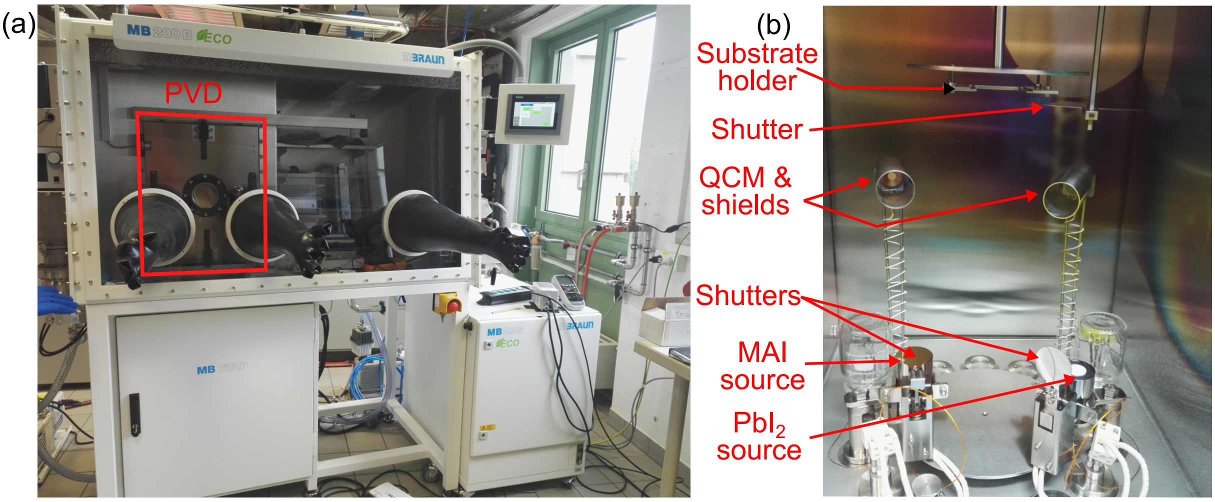

Figure 3.6: Pictures of (a) the PVD embedded in the glovebox and (b) the inside of the PVD.

chamber. In between, a protective baffle from HSR was installed (Figure C.1 of appendix Chapter 3C.2) to protect the turbo pump from the deposition of MAI or species such as HI, CH_3I or NH_3 due to the decomposition of MAI, which could lead to corrosion inside the turbo pump and its malfunction. The protective baffle was cooled down to temperatures ranging from -10 to -20°C by means of a refrigerating machine in order for the molecules to condense on the protective walls. This protection increased the durability of the turbo pump. In addition, a rotary vane pump was installed behind the turbo pump and connected to an exhaust. This set-up enabled to reach a base pressure of 2-3$\times 10^{-7}$ mbar.

An Inficon SQC-310 controller (Figure 3.7b) was used to save deposition recipes, start and stop the deposition processes with the saved parameters and monitor the evaporation rates and thicknesses calculated by the QCMs. For the PbI_2 QCM to give a good indication of the evaporation rate of PbI_2, the density, acoustic impedance and other material properties were set using already-existing values from the literature.

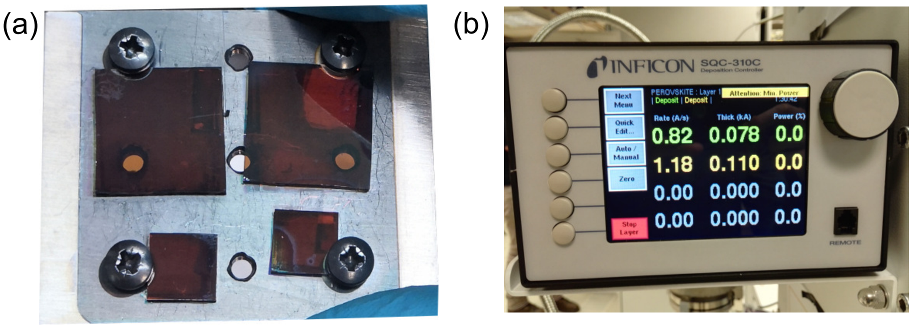

Figure 3.7: Pictures of (a) the sample holder and (b) the Inficon controller to control the deposition.

A pressure gauge was used to measure the variations of the pressure inside the PVD chamber, but in order to get a precise value of the pressure (and not the round values given from the glovebox screen), the voltage from the pressure gauge was extracted with a multi-meter apparatus and a voltage-pressure calibration curve was determined. Using this technique, variations of pressure down to 10^{-8} mbar could be detected.

The procedure to grow $MAPbI_3$ absorber was as follows: first, the substrates were cleaned using a standard cleaning procedure [318]:

- the substrates were placed in a 2% Helmanex III (Ossila) solution, which was introduced in an ultrasonic bath (UB) for 10 minutes at 50°C.
- the substrates were rinsed in 2 beakers of deionized water and placed in an isopropanol (IPA) solution in a UB for 15 minutes at 50°C and were then placed in an acetone solution in a UB for 15 minutes at 50°C.
- the substrates were then individually rinsed with acetone and then IPA and blow-dried with nitrogen.
- The substrates were then ozone-treated for 15 minutes in a UV ozone cleaner (Ossila).

Then the substrates were placed in the substrate holder. The crucibles were filled with a set mass (always the same) of MAI and PbI_2 powders to improve reproducibility and the PVD was pumped until it reached its lowest base pressure of 2-3×10^{-7} mbar. The refrigerating machine was switched on and a temperature range of [-20,-10°C] inside the protective baffle was obtained. The growth process was then started as depicted in Figure 3.8.

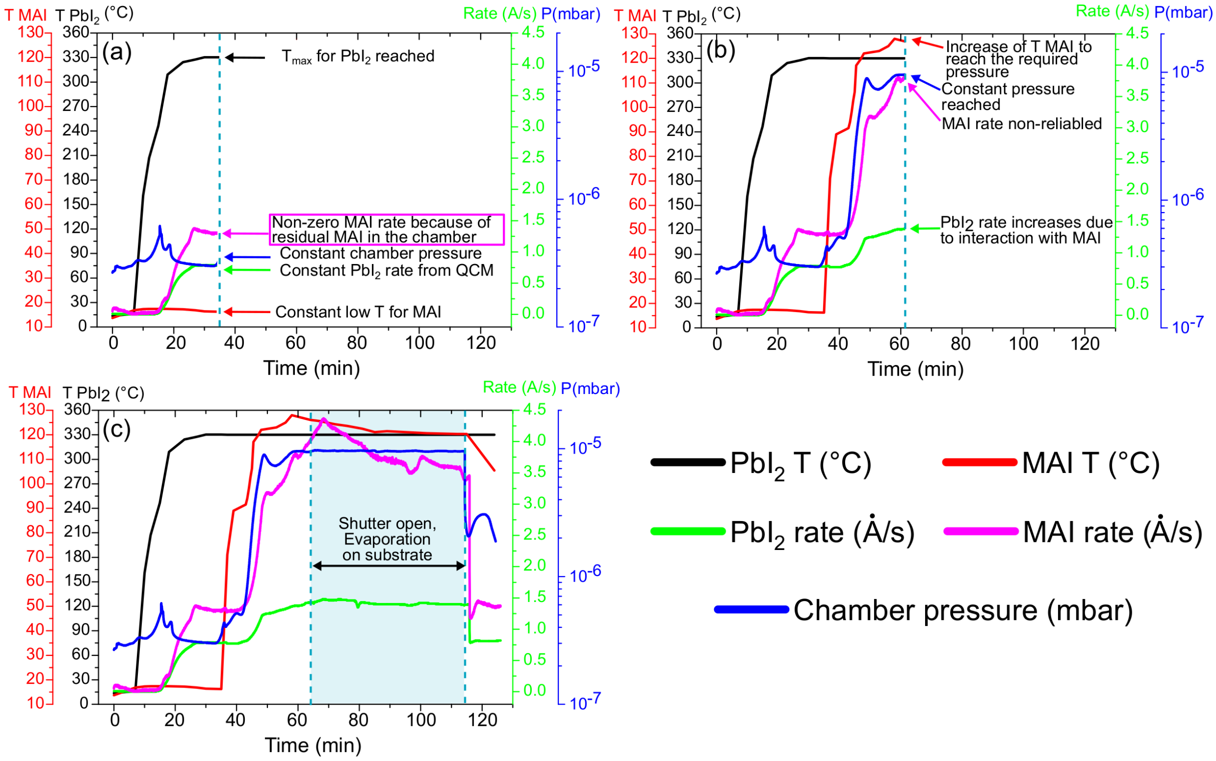

Figure 3.8: Evolution of different growth parameters. (a) Increase of the temperature of the PbI_2 evaporation source until it reaches its required value. (b) Increase of the temperature of the MAI evaporation source until the required pressure is reached. (c) Evaporation of MAI and PbI_2 on the substrate to form $MAPbI_3$ for a certain time.

First (Figure 3.8a), the temperature of the PbI_2 evaporation source was set to a certain value, synonym of an attributed evaporation rate, with a set temperature slope.

The temperature of the MAI source was not changed and the shutter of the MAI source was closed. An increase of the chamber pressure was observed, due to the degassing of the PbI_2 powder and the increase of the temperature inside the chamber, that induced the already present MAI molecules in the chamber (walls, PVD parts...) to desorb from where they had previously condensed. This was also visible with the non-zero MAI evaporation rate, which was however non-reliable. Once the set PbI_2 temperature was reached, all parameters were kept at their values for a few minutes to wait for a constant PbI_2 evaporation rate (Figure 3.8a). A usual temperature was of 330°C which led to an evaporation rate of ~ 0.4 Å/s.

Upon reaching a constant and stable PbI_2 evaporation rate, the temperature of the MAI evaporation source was increased and its shutter was opened until the desired pressure was reached, as the pressure is the control parameter and not the MAI evaporation rate (Figure 3.8b). When closing out on the required pressure, the temperature of the MAI was manually increased or decreased in order to reach the needed pressure (sort of a manual feedback loop). The PbI_2 evaporation rate increased due to the interaction of MAI molecules and PbI_2 molecules at the PbI_2 QCM due to CVD-component of MAI.

Once the desired pressure was reached, the substrate shutter was opened and the evaporation on the substrate started for the desired time, synonym of thickness. In order to maintain a constant chamber pressure, or MAI partial pressure, during the whole evaporation time, the temperature of the MAI evaporation source had to be manually adjusted, i.e. decreased. If this was not done, the chamber pressure would continue to increase due to the constant production of a set MAI partial pressure brought in addition to the already existing MAI molecules everywhere in the chamber, but also due to the desorption of MAI from the substrate's surface or PVD walls and parts. Typical pressures during deposition were between 1×10^{-6} mbar to 1×10^{-5} mbar, depending on the required $MAPbI_3$ composition (see chapter 5). Near the end of the PhD thesis, the MAI powder was renewed from a new container of the exact same manufacturer. This exchanged led to a complete change of the pressure used. A pressure of 1×10^{-5} mbar with the previous powder would lead to an MAI-rich $MAPbI_3$, while with the new powder it would lead to a PbI_2-rich $MAPbI_3$. Therefore both the PbI_2 evaporation temperature and the MAI partial pressure had to be re-adjusted and care must be taken when exchanging the powders.

At the end of the time set for evaporating on the substrate, the substrate's shutter and the MAI shutter were closed, the temperature of the MAI evaporation source was set to zero and the PbI_2 was monitored to see if it reflected the initial value. Then the temperature of the PbI_2 evaporation source was set to zero and the system was left to cool down and reach a lower pressure.

3.2 Photoluminescence

In addition to the characterization of the perovskite surface using scanning probe microscopy, other techniques were used to determine the absorber quality, such as X-ray diffraction (XRD), scanning electron microscopy (SEM), energy-dispersive X-ray spectroscopy (EDX), X-ray photoelectron spectroscopy (XPS), photoluminescence (PL) and time-resolved photoluminescence (TRPL). However, the last two techniques were used systematically for all samples and throughout this thesis. Therefore, their working principle will be briefly presented before introducing the measurement setup and explaining how data such as the PL yield, the lifetime or the doping, were extracted using these two techniques.

3.2.1 Brief working principle

Luminescence is the emission of light from any form of matter. Photoluminescence is the emission of light after the absorption of photons from any form of matter. For a perovskite semiconductor, defined by a bandgap E_g and deposited on a simple glass substrate, photons with energy larger than E_g will be absorbed in the perovskite and hole-electron pairs will be generated. As explained in 1.2.4 of chapter 1, these photo-generated charge carriers will then thermalize such that they reach the CBM, for electrons and VBM, for holes, and then recombine either radiatively or non-radiatively. In photoluminescence spectroscopy at room temperature, which is what was used in this thesis, only the radiative recombination processes are detectable, if the generated photon is not re-absorbed in the perovskite absorber. When the absorber is excited by a photon flux Φ_0, usually by a continuous-wave laser at a specific wavelength, it derives from its thermal equilibrium where the generation $G_{ext,0}$ of electron-hole pairs is equal to their radiative recombination rate $R_{rad,0}$. If the surface is considered to be at a position $x = 0$, then the photon flux density that penetrates the perovskite absorber is defined by Lambert-Beer's law:

$$\Phi(x) = \Phi_0(1 - R(E))^{-\alpha(E)x} \tag{3.6}$$

R(E) is the surface reflectivity and $\alpha(E)$ is the absorption coefficient, which are energy-dependent and characteristic of the perovskite properties (bulk and surface). The generation rate of the carriers is then propotional to the change of the flux density through the film and can be described as follows:

$$G_{ext}(x) = -\frac{\partial \Phi}{\partial x} = \alpha(E)\Phi_0(1 - R(E))e^{-\alpha(E)x} \tag{3.7}$$

Under illumination, and if the re-absorption probability is taken as zero, the net spontaneous radiative recombination rate will be given by (see section A.3 of appendix Chapter 1):

$$R_{net}^{rad} = k_{rad}(np - n_i^2) = k_{rad}\, n_i^2 \left(exp\left(\frac{\Delta\mu}{k_B T}\right) - 1 \right) \tag{3.8}$$

k_{rad} is the radiative recombination coefficient, and $\Delta\mu$ the quasi Fermi level splitting. The emitted photon flux density from the material Φ_{em} is linked to the previous radiative recombination rate, and can be derived from Planck's generalized law and can be described as follows [49]:

$$\Phi_{em}(E) = \frac{1}{4\pi^2\hbar^3 c^2} \frac{\alpha(E)E^2}{exp\left(\frac{E-\Delta\mu}{k_B T}\right) - 1} \tag{3.9}$$

Equation 3.9 describes the spectral dependence of the photoluminescence from the perovskite material under illumination, which can be experimentally measured and is depicted in Figure 3.9. The acquisition and fitting of this curve can enable the extraction of the optical bandgap, as well as the quasi Fermi level splitting but is also necessary to determine the external PL quantum yield (PLQY, η_{ext} or Q_{ext}) of a material, which is defined as the number of photons emitted Y_{em} as a fraction of the number of photons absorbed Y_{abs} [319]:

$$PLQY = \eta_{ext} = Q_{ext} = \frac{Yem}{Y_{abs}} = \frac{\int \Phi_{em}(E)dE}{p_{laser}\frac{\lambda}{hc}(1 - exp(-\alpha d))} \tag{3.10}$$

p_{laser} is the power density of the laser used for measuring the PL, λ is its wavelength, α is again the absorption coefficient of the perovskite absorber at the wavelength λ and d is the thickness of the perovskite film. The PLQY is an important metric to determine the quality of a perovskite film as it directly gives an indication of the photoluminescence efficiency of a sample. When measuring perovskite samples deposited on glass substrates, a higher PLQY will mean that a higher quasi-Fermi level splitting and therefore V_{OC} can be reached when making a solar cell [320], which will usually be translated into higher solar cell efficiencies. However, comparing PLQY of perovskite films deposited on extraction layer can sometimes be misleading due to the multiple transport mechanism occurring at the interface [321].

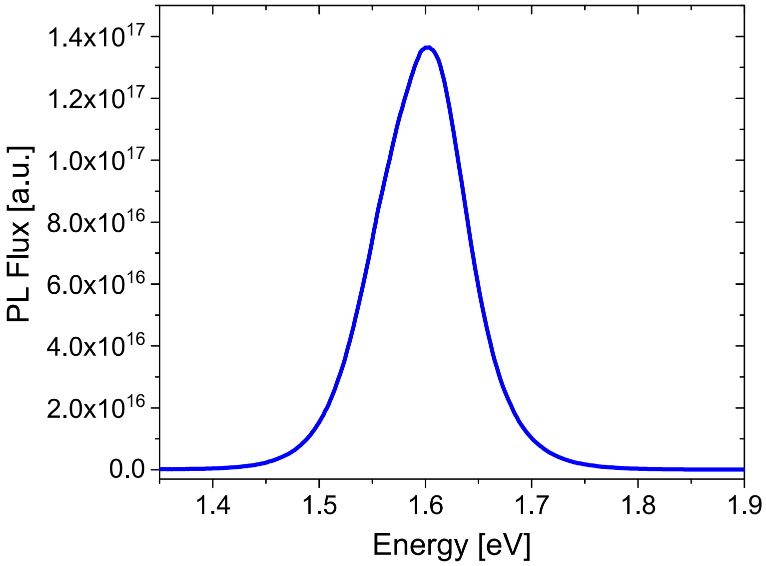

Figure 3.9: PL spectrum of $MAPbI_3$ co-evaporated on an FTO substrate.

In addition to room-temperature PL (steady-state) and the possibility of extracting the bandgap, the PLQY and other data from this technique, time-resolved photoluminescence (TRPL) is a useful technique to additionally quantify and compare the quality of perovskite thin films through the determination of the lifetime (see section 1.2.4). It can further be used to identify the different radiative and non-radiative components of the lifetime when mathematical models are used, combined with power-dependent measurements for example [321]. In TRPL, a pulsed-laser with a specific wavelength is used to excite a perovskite absorber periodically which depends on the frequency used from the pulsed-laser (kHz to MHz). A detector, with single-photon sensitivity like a photo-multiplier tube or a charge-couple-device camera, monitors the emitted photoluminescence at a time T, which is before the next laser pulse. Depending on the type of setup used, different working principles exist. When using a single-photon detector and the time-correlated single photon counting (TCSPC), the laser pulse will correspond to a start signal and the detection of an emitted photon from the perovskite thin film to a stop signal. The measurement will then be stopped and the electronics of the TCSPC will record the time between the start and stop signals. The same procedure will be repeated several thousand or millions of time, depending on the frequency used, and the recorded times will be plotted in an histogram where the time bin corresponds to a defined time difference between the start and stop signal (Figure 3.10). In the case of an imaging setup, as it is for this thesis, a laser pulse is directed on the sample, and the number of emitted photons are detected by the camera at different times after the pulse. By an increment of that detection time, which should not exceed the inverse of the frequency of the laser pulses, and by averaging over sampling, the decay curve of the photoluminescence can be constructed.

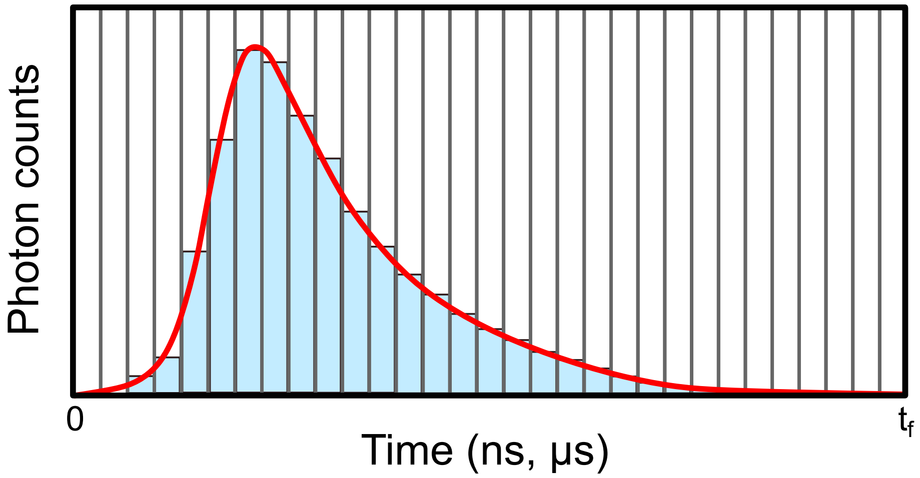

Figure 3.10: Schematic representation of the TCSPC principle for TRPL. t_0 is the start signal corresponding to the laser pulse while t_f is either set by the user or should not exceed the inverse of the frequency used for the laser pulses.

If a laser pulse excites a perovskite absorber, it will generate $\Delta n_0 = \Delta p_0$ electrons and holes such that the density of electrons and holes at $t=t_0$ of the pulse will be $n = n_0 + \Delta n_0$ and $p = p_0 + \Delta p_0$ respectively. Following the pulse, the density of electrons and holes will decrease with time such that:

$$\begin{aligned} n(t) &= n_0 + \Delta n(t) \\ p(t) &= p_0 + \Delta p(t) \end{aligned} \tag{3.11}$$

As previously discussed, TRPL measures the PL emitted (radiative recombination) from the perovskite absorber as a function of time, which depends on the product np as follows [322]:

$$PL(t) = k_{rad}(1 - p_r)(n(t)p(t) - n_i^2) \tag{3.12}$$

p_r is the re-absorption probability. Therefore in order to understand the physical mechanism that govern the PL decay over time, expression of the density of electrons and holes have to be found through the continuity equations [321]:

$$\begin{aligned} \frac{dn(t)}{dt} &= G_{ext}(x,t) + G_{int}(x,t,n,p) - R(x,t,n,p) + D_n\frac{d^2n(x,t)}{dx^2} + F\mu_n\frac{dn(x,t)}{dx} \\ \frac{dp(t)}{dt} &= G_{ext}(x,t) + G_{int}(x,t,n,p) - R(x,t,n,p) + D_p\frac{d^2p(x,t)}{dx^2} + F\mu_p\frac{dp(x,t)}{dx} \end{aligned} \tag{3.13}$$

x is the position normal to the sample's surface, $D_{n,p} = \mu_{n,p}kT/q$ are the diffusion constants for electrons and holes with $\mu_{n,p}$ their respective mobility, F is the electric field, R the recombination rate, G_{ext} the generation of electron-hole pairs and G_{int} the generation of electrons due to photon-recycling (re-absorption). If the drift and diffusion terms (last two terms in both equations) are neglected and the density of electrons is uniform along the thickness of the perovskite absorber (no gradient so no dependence on x), simplifications can be made and analytical solutions can be obtained for two regimes called low and high injection. If a p-type perovskite is assumed with a doping p_0, a high injection corresponds to an injection or injected carrier density (from the laser pulse) higher than the doping p_0 of the material such that $\Delta_p \gg p_0$ and therefore $n = p$. The simplification of the continuity equations in high injection, when Auger recombination (see section 1.2.4) is neglected, can be expressed as follow [321]:

$$-\frac{dn}{dt} = \left[k_{rad}(1-p_r)n^2 + \frac{n}{(\tau_p+\tau_n)}\right] \tag{3.14}$$

τ_n and τ_p are the Shockey-Read-Hall lifetimes for electrons and holes respectively, which were already defined in section 1.2.4. Therefore in high injection, a solution for the density of electrons and a simplification of PL decay over time are [321]:

$$\begin{aligned} PL(t) &= k_{rad}(1-p_r)(n(t)^2 - n_i^2) \\ n(t) &= \frac{n_0\, exp\left(\frac{-t}{\tau_p+\tau_n}\right)}{1+\frac{\tau_p+\tau_n}{\tau_{rad}}\left[1-exp\left(\frac{-t}{\tau_p+\tau_n}\right)\right]} \end{aligned} \tag{3.15}$$

with $\tau_{rad} = 1/(k_{rad}(1-p_r)n_0$ the radiative lifetime. On the other hand, a low injection regime corresponds, in the case of a p-type perovskite absorber, to an injected density of carriers lower than the doping p_0, such that $p(t) = p_0$ with n ≪ p. In that case, the continuity equation becomes (Auger recombination neglected) [321]:

$$-\frac{dn}{dt} = \left[k_{rad}(1-p_r)np_0 + \frac{n}{(\tau_n)}\right] \tag{3.16}$$

Following equation 3.16, a solution for the density of electrons and a simplification of PL decay over time in low injection are [321]:

$$\begin{aligned} PL(t) &= k_{rad}(1-p_r)(n(t)p_0 - n_i^2) \\ n(t) &= n_0\, exp\left(-t\left(\frac{1}{\tau_{rad}}+\frac{1}{\tau_n}\right)\right) \end{aligned} \tag{3.17}$$

For this thesis, low injection conditions were always assumed due to the low injected carriers (from 1.2×10^{14} cm^{-3} to 3.5×10^{15} cm^{-3}) and later demonstrated to be true with the determination of the doping density. Therefore the TRPL transients measured were fitted with exponential decay curves and the effective lifetime measured τ_{eff} was such that:

$$\frac{1}{\tau_{eff}} = \frac{1}{\tau_{rad}} + \frac{1}{\tau_n} \tag{3.18}$$

The previous equation should also take into consideration the surface recombination velocity and the associated surface lifetime τ_s but will not be further discussed in this thesis as determining the latter requires specific thickness-dependent and power-dependent studies, which was however part of the Master thesis work of Joé Seil [323]. Throughout this thesis, effective lifetime values will be given and were extracted from a mono-exponential fitting of the curves. Depending on the appearance of the curve, the fitting was more or less challenging and even in low injection, a first fast decay would sometimes occur, which was neglected for the fitting as can be depicted in Figure 3.11b. Kirchartz et al. have reported this initial fast decay to be caused by radiative recombination, which is dominant at early times, whereas SRH recombination dominates at later times. In addition, increasing the carrier injection will induce a stronger initial fast decay [321]. However, as the measurements were essentially carried out at low injection, the fast initial decay might well be due to a different phenomenon, such as a slow in-depth diffusion of the carriers [324] or electrons filling the trap states, which can happen in a medium injection regime (between high and low) [325], or due to a built-in field at the electrode junction when an electrode is used instead of glass [326].

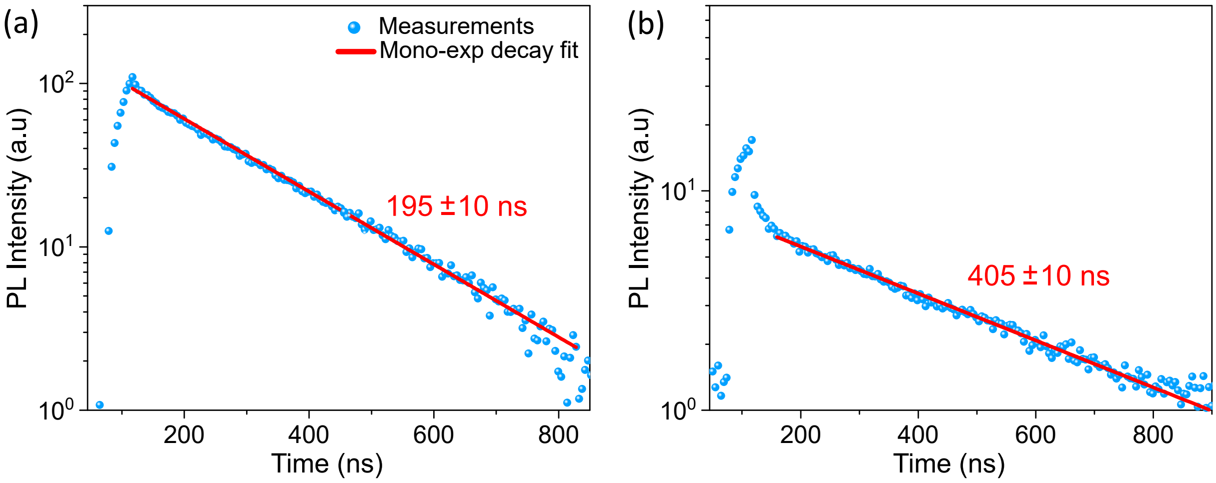

Figure 3.11: TRPL measurements and mono-exponential fit for (a) a clear mono-exponential decay and (b) a multiple-exponential decay with a fast first decay.

The fitting of the curves always induces an error in the estimation of the effective lifetime, which depends on the fitted range, background removal, but also on other parameters set by the user to fit the curve. This error will increase with the lifetime, ranging from a few nanoseconds when lifetimes of a few tens of nanoseconds are obtained and error of a few tens of nanoseconds when lifetimes of a few hundreds of nanoseconds are reached.

3.2.2 Measurement setup

The PL and TRPL measurements were carried out in a custom-made set-up depicted in Figure 3.12 and embedded in a black box. The laser used was not continuous-wave but a pulsed laser from PicoQuant, and its frequency (repetition rate) could be varied from tens of kHz to tens of MHz (maximum 80 MHz). An optical fiber was connecting the laser source to a beam homogenizer (Bayerisches Laserzentrum GmbH) to yield more uniform beam profiles. Additionally, focusing lenses were sometimes used in front of the homogenizer to reduce or increase the laser spot and therefore reduce or increase the power density. The sample was placed in a nitrogen-filled box with a transparent top glass, which induced some illumination losses due to reflection and diffraction but did not alter the PL profile. The PL yield dropped by about 12% when using the nitrogen-filled box compared to when the samples were exposed to air without a glass window. However, as perovskites are oxygen-sensitive and degradation is known to happen fast when air exposure is combined with illumination (see section 1.2.5), theses boxes were necessary to determine the intrinsic optoelectronic properties of the perovskite absorbers.

The samples with or without the box were then placed in an x-y stage that could be moved in order to measure different areas of the sample.

The emitted luminescence of the sample was captured by an intensified charged-coupled device (ICCD), which is a camera from Princeton Instruments (PI-MAX4:1024i). The latter could detect wavelengths from 200 to 900 nm and the working principle is explained in the Master thesis of Ricardo Poeira [327]. Each emitted photon will charge and accumulate at the pixels of the camera, which will be translated into a voltage by an on-chip amplifier and converted into grey values in the x and y direction. Therefore an image of the luminescence of the perovskite sample with an intensity of arbitrary unit is generated on the software. The setup in that configuration can enable to observe the homogeneity of the sample's luminescence and can be used to quickly compare samples between each other using the same illumination parameters.

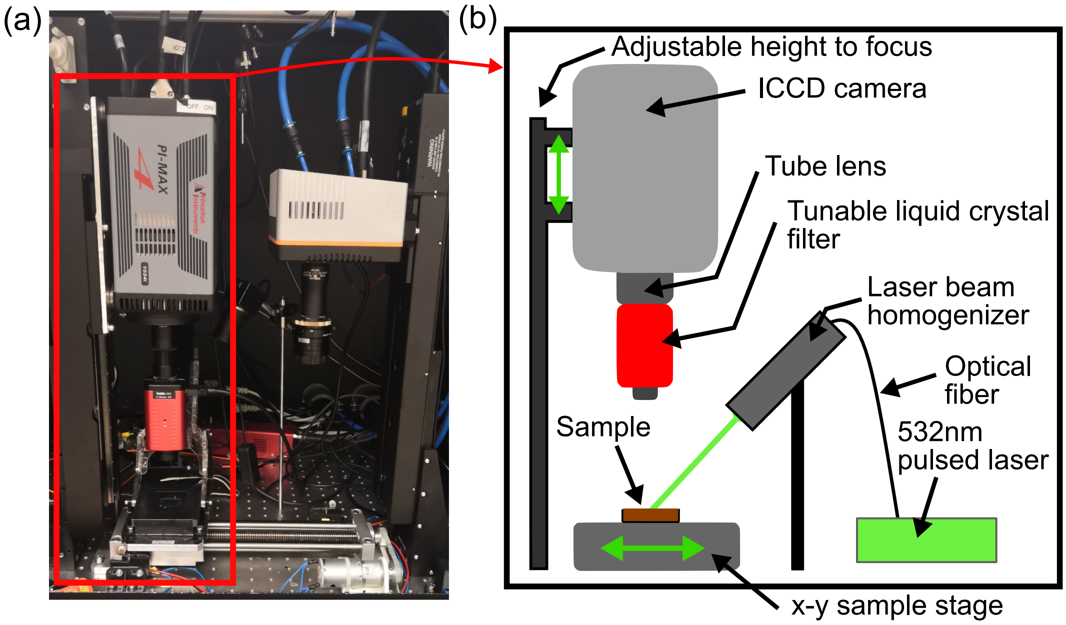

Figure 3.12: (a) Picture and (b) schematic representation of the PL and TRPL set-up

To acquire a PL spectrum of the perovskite thin film, a tunable liquid crystal (LC) band-pass filter (KURIOS-XE2 from Thorlabs) is used to filter the emitted luminescence at a desired wavelength from 650 to 1100 nm. Using the trigger parameters of both the camera and the filter, the camera acquired an image at a specific wavelength then triggered the LC filter to change its wavelength (minimum step size of 1nm), which triggered the camera to acquire a new image. This procedure was automated such that the camera would acquire images at each wavelength for a certain wavelength range and with a set wavelength step size. This iterative measurement was performed in the dark and upon illumination of the pulsed laser to later remove the background originating from the dark conditions. Usually the wavelength range would be [650-900 nm] due to the limit of the camera and the step size of 3 nm, which led to the acquisition of 84 consecutive images. A python program was then used to subtract the background images to the illuminated images and choose the region of interest among the whole map. From this technique, a rudimentary PL spectrum can be obtained by averaging the intensity of the chosen region for each image, but the shape of the spectrum is then odd, due to the unequal response of the camera for different wavelengths. In addition, the given intensity from the PL spectrum is arbitrary and cannot be used for the determination of the PL yield.

Therefore, spectral and intensity calibrations had to be carried out, which are well-known procedures and were already reported in the Master thesis works of Joé Seil and Ricardo Poeira [323, 327]. Briefly, for the spectral calibration, a calibrated white light (Thorlabs) is shone into an integrating sphere, whose role is to diffuse the light into a specific profile. This profile is compared with the profile observed by the camera and the LC and a calibration function is calculated and can be used to obtain the real shape of the PL spectrum. The intensity calibration consists in using a laser diode with a known intensity into the same integrating sphere, which will emit a light that will be measured first by a powermeter and then by the PL setup. This results in a counts-to-photons conversion factor that can be used to obtain the PL spectrum in a quantitative unit: photons/(cm^2 s nm) that can be used to calculate the PLQY. For the TRPL measurements, either the LC filter was removed or it was kept and a specific wavelength was set, usually the one yielding the highest intensity from the PL spectrum. Then the triggering parameters between the camera and the laser were used and the working principle is depicted in Figure 3.13 and will be briefly explained.

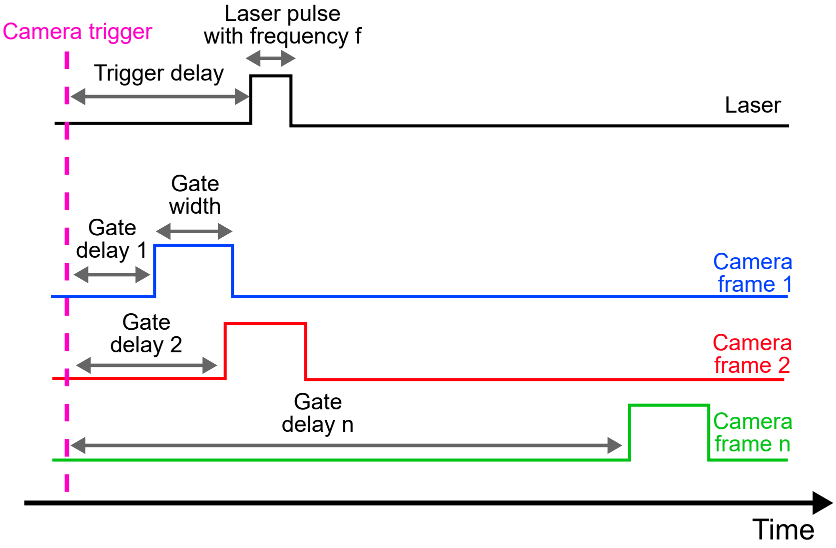

Figure 3.13: Working principle of TRPL using the ICCD camera.

When the recording starts from the software, a trigger signal is sent to the camera and the laser and after a delay time (trigger delay), a laser pulse is made, also sending a trigger signal to the camera to start acquiring the photoluminescence after a certain gate delay and for a certain amount of time (gate width). The larger the gate width, the higher the intensity of the signal but the poorer the resolution of the TRPL transient. By an increment of this gate delay, the acquisition of the PL for a time defined by the gate width will move from before the laser pulse to well after the excitation (during relaxation) and before the next laser pulse. The procedure can be carried out multiple times for each gate delay and averaged in order to get better statistics and resolution. Most of the time, the frequency used was 1 MHz, with a gate width of 3 ns and 200 frames between 50 ns and 1000 ns, yielding a resolution between 4 and 5 ns.

3.2.3 Determination of yield, lifetime and doping

The PLQY was already expressed in equation 3.10 by:

$$PLQY = \eta_{ext} = Q_{ext} = \frac{Yem}{Y_{abs}} = \frac{\int \Phi_{em}(E)dE}{p_{laser}\frac{\lambda}{hc}(1 - exp(-\alpha d))} \tag{3.19}$$

The absorption coefficient at 532 nm (laser wavelength) used was $\alpha = 1.65 \times 10^5 cm^{-1}$ from Ball et al. [328] and the thickness of the absorber was either measured with a profilometer or calculated proportionally to a previously measured thickness. The power density of the pulsed laser was measured with a powermeter and averaged over a certain time due to fluctuations in the power. The laser spot was calculated using the detected Gaussian profile from the camera. The PL spectrum was integrated over its wavelength range and PLQY ranging from 10^{-3} to below 10^{-1} were calculated depending on the composition of the perovskit absorber. A 5% error was assumed in the estimation of the PLQY caused by the fluctuations in the laser intensity and human errors from spectral and intensity calibrations. As explained previously, the effective lifetime was extracted from a mono-exponential decay fit function of the PL decay transient due to the use of low injection conditions and the error on the estimation of the lifetimes varied depending on the decay curves.

If the calculated or extracted PLQY and effective lifetime were carried out using the same excitation intensity (laser power density) with the same PL setup, which was the case in this PhD thesis, the doping density can be calculated. First, Schnitzer et al. have linked the PLQY or external quantum yield with the internal quantum yield (Q_{int}) as follows [329]:

$$PLQY = Q_{ext} = \frac{\frac{Q_{int}}{4n^2}}{\frac{Q_{int}}{4n^2} + (1 - Q_{int})} \tag{3.20}$$

Here n is the refractive index of the perovskite and only one direction is considered to contribute to the Q_{ext}, thus the factor 4 instead of 2 of their original formula. Additionally, Akrenkiel et al. have linked the Q_{int} with the radiative and non-radiative lifetimes (τ_{rad} and τ_{nr}) such that [330]:

$$Q_{int} = \frac{\tau_{nr}}{\tau_{rad} + \tau_{nr}} \tag{3.21}$$

As previously shown, the radiative lifetime can be expressed by $\tau_{rad} = 1/[k_{rad}(1-p_r)p_0]$ for a p-type perovskite absorber in low-injection conditions. From this equation and if photon re-absorption p_r is taken as 0, a relationship between the doping density p_0, the PLQY and the non-radiative lifetime is obtained as presented by Redinger et al. [319]:

$$p_0 = \frac{4n^2}{k_{rad}\,\tau_{nr}}\left(\frac{1}{Q_{ext}} - 1\right) \tag{3.22}$$

Using the refractive index of $MAPbI_3$ of 2.4 [328] and the radiative recombination coefficient of 4.8×10^{11} cm^3/s [322], the doping density can be calculated with the calculated and extracted values of the PLQY and the effective lifetime, which is assumed to be limited by non-radiative recombination. The measurements and fitting errors of both quantities are also used to estimate an error for the doping density, which will be given throughout this thesis. On a side note, the PLQY is usually calculated by using a continuous-wave laser and the formula that governs the PLQY makes use of such a laser. Therefore it is not entirely sure how a pulsed laser affects the PLQY. However, power-dependent (or injection-dependent) PL measurements were carried out and presented in the Master thesis work of Joé Seil [323] to determine the doping density, which is situated at the intersection of the linear (low injection) and quadratic (high injection) dependence of the PL intensity on the carrier injection [322]. The doping density extracted from this method matched the doping density calculated from the combination of the effective lifetime and the PLQY, therefore confirming that a pulsed laser could be used to determine the PLQY of a perovskite absorber.

3.3 Summary of growth and photoluminescence

The growth of hybrid halide perovskite is important, as it is the root of the surface, which is only the breaking point of the thin-film. Co-evaporation of $MAPbI_3$ has been presented in this chapter and proved itself to be more challenging than the original concept of PVD, mainly due to the volatility of the organic compound MAI. However, by carefully controlling its partial pressure, absorbers for solar cells have been made and will be the topic of discussion of Chapter 5. Co-evaporation has the advantage of minimizing the modification of the intrinsic surface properties of $MAPbI_3$ compared to solution-based processes. Nevertheless, obtaining a solid fabrication baseline takes time and also brings some challenges. One of them was that the co-evaporated $MAPbI_3$ films proved themselves not suited for the study of their surfaces via scanning tunneling microscope. Therefore, solution-based halide perovskites were also investigated during this thesis in Chapter 4 and 7. It is therefore useful to draw a clear picture of the samples studied in the different chapters and the techniques used. Figure 3.14 represents the investigated samples, with their fabrication methods, where they were fabricated, and the main techniques used to characterize them. Two chapters discuss the surface properties of co-evaporated $MAPbI_3$ using mainly KPFM and X-ray photoelectron spectroscopy (XPS). One chapter analyzes the surface states of solution-based $MAPbI_3$ and the last chapter evaluates the surface sensitivity and surface passivation of co-evaporated $MAPbI_3$ and mixed halide perovskites.

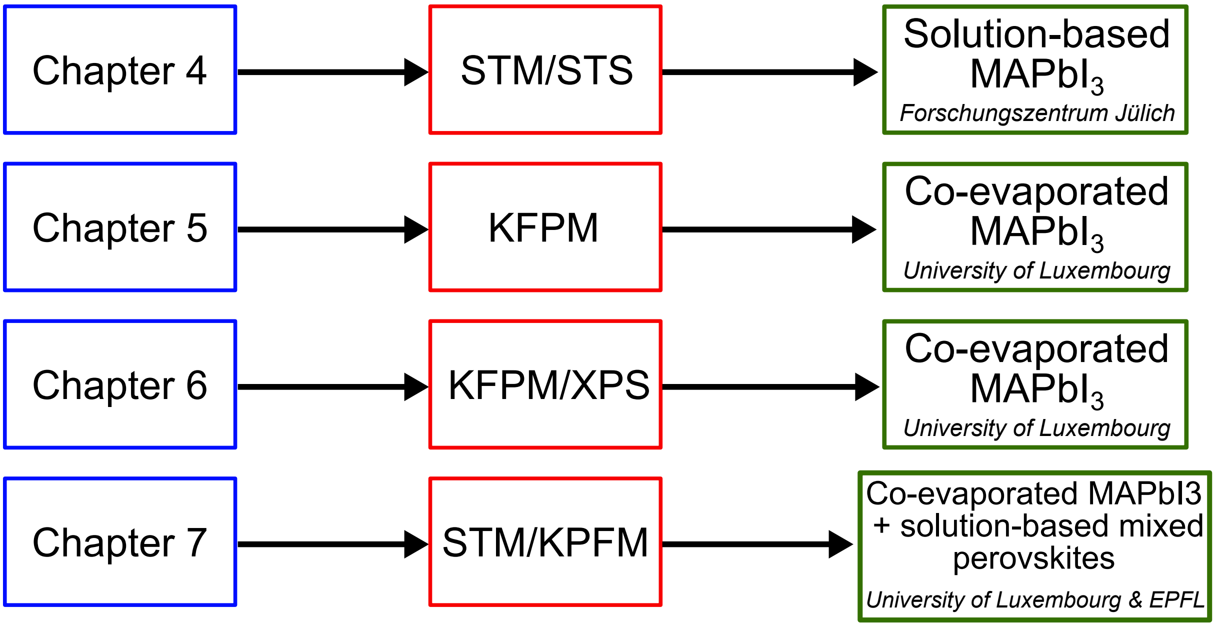

Figure 3.14: Representation of the samples investigated in this thesis, with their fabrication methods and the main characterization techniques.

Chapter 4

Local density of states in solution-based perovskites

An important aspect of polycrystalline semiconductors is the multitude of features that can be observed at their surface, such as different grain orientations, facets and boundaries leading to different surface terminations and thereby surface states [133, 134]. In addition, the grain boundaries do not exist in single-crystal semiconductors. As an example, epitaxially-grown GaAs solar cells are still the best performing single-junction devices to date and it is therefore important to determine if $MAPbI_3$ aborbers are suffering from their polycrystalline nature, and the existence for example of grain boundaries, which have often been reported to be non-radiative recombination centers [143, 154, 155, 156]. Additionally, as the use of perovskite absorbers results in high-efficiency devices, it is interesting to determine whether their surface is free of defects or not. To that end, scanning tunneling microscopy and spectroscopy (STM and STS) will be used, without being exposed to air, to analyse the electronic properties at the surface of grains and grain boundaries for $MAPbI_3$ and mixed halide perovskites. Additionally, simulations will be used to quantify the lateral variations of the densities of surface states, workfunctions and bandgaps.

This chapter is largely based on the work of [331]. The first section 4.1 explains how the local density of states (LDOS) can be used to determine distinct features of the surface such as the surface bandgap. It shows how using dI/dV for the extraction of the surface bandgap is not sufficient and how it has to be normalized by a broadened I/V. The second section 4.2 goes through the process of simulating the LDOS and the observation of Fermi level pinning. The results there suggest a density of surface states for $MAPbI_3$ of about 1×10^{13} cm^{-2} eV^{-1}. Section 4.3 and section 4.4 discuss the occurrence of local variations of the surface states, WFs and surface bandgaps. These measurements reveal that grains and grain facets have different densities of surface states and different surface dipoles (WF) but that the grain boundaries are not different from the grains. Section 4.5 considers some potential origins of the facet-dependent surface states, which is not linked to degradation of $MAPbI_3$ but to the intrinsic properties of the material. Lastly, section 4.6 and 4.7 further investigate the electronic properties of mixed halide perovskite absorbers. The results show variations of the density of surface states and workfunction between grains and of grain facets, which are linked this time to an additional degradation of the mixed halide perovskites.

4.1 Conductance, local density of states and surface bandgap determination

STM and STS on the co-evaporated $MAPbI_3$ absorbers fabricated throughout this thesis have been found to be particularly challenging, potentially due to the low doping and low conductivity, therefore for the purpose of this study, $MAPbI_3$ absorbers were grown on ITO substrates by a solution-based method, which is described in the Appendix Chapter 4D.1. The devices made using this absorber yielded efficiencies comparable to established $MAPbI_3$ high-efficient solar cells at the time, making the absorber suitable to be studied. As previously stated, oxygen and moisture can alter the surface properties of perovskite and therefore the measurements were performed in UHV and the surface contamination was kept to a minimum by using an inert gas transfer suitcase. In addition all measurements were performed in the dark to avoid any light-induced surface change. The measurement parameters for the STM and STS can be found in the Appendix Chapter 4D.2. Large negative tip bias had to be used to carry out the measurements and access the local density of states, due to the relatively low doping and conductivity of the absorbers. Measuring the tunneling conductance of the surface of the $MAPbI_3$ absorbers was made possible by STS, where the current I was measured upon the local variation of the voltage V. As previously discussed in section 2.1, at low voltages, the tunneling conductance dI/dV can be expressed as:

$$\frac{dI}{dV} \propto \rho_s T \equiv LDOS \tag{4.1}$$

ρ_s and T are the density of states at the surface of the sample and T is the transmission coefficient. From the previous equation 4.1, the surface bandgap cannot be extracted due to the exponential voltage dependence of T, which can be bypassed by normalizing dI/dV by I/V, which works well for small surface bangap materials. However, if the current approaches zero much faster than the conductance in large surface bandgap materials such as $MAPbI_3$, the (dI/dV)/(I/V) ratio diverges at the band edges. To circumvent this issue, some amount of broadening of the I/V values can be used. In this case, the broadening method presented by Feenstra et al. [223] was used and the resulting normalized and broadened curves were then referred to (dI/dV)/$\overline{I/V}$. Briefly, the divergent I/V near zero voltage is convoluted with an exponential function, using a certain broadening width ΔV which should be in the order of the bandgap of the semiconductor. This suppresses the noise in the middle of the gap and produces a smooth I/V function with non-zero values throughout the bandgap, that can be used to normalize dI/dV [223].

Figure 4.1 represents the topography by imaging the occupied states of the solution-based $MAPbI_3$ as the image was acquired with a negative gap voltage of -2 V and a current setpoint of 200 pA. Grains of different sizes, separated by clear grain boundaries were observed. Current imaging tunneling spectroscopy (CITS, see section 2.1) was then used on a smaller portion of that image to extract a spectroscopic image. A grid of 100 x 100 points is defined on a 4 μm^2 area and on each pixel of the grid, the current is measured as the voltage is ramped from -2 V to +1.5 V. Figure 4.2 displays the topography and its associated current I(V) image and conductance (dI/dV) image. Multiple electronic features can be discerned, suggesting a non-homogeneous surface either in terms of surface states, density of states or WFs. The difference of current or conductance at the surface will be discussed in the next sections.

From the I(V) spectroscopy, which has been primarily smoothed to get rid of the

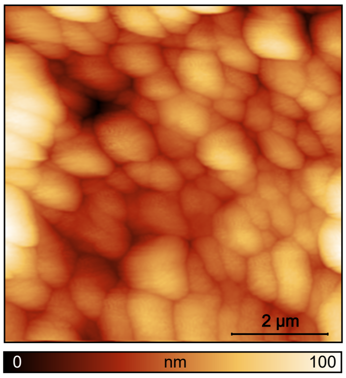

Figure 4.1: STM topography of the solution-based $MAPbI_3$ acquired with negative gap voltage applied to the sample. Parameters: gap voltage = -2 V, tunneling current = 2 pA.

high current curves, an average I(V) spectrum was extracted and the broadening method previously described to further access the average $(dI/dV)/\overline{I/V}$ was used. Clear defined bandgap and valence (VB) and conduction bands (CB) onsets (Figure 4.3b) could be observed. The Fermi level position E_F is found when the voltage equals zero, which clearly shows here an n-type doped surface as E_F is closest to the CB. Previous works, based for instance on photoemission measurements, have already reported such n-type behavior at the surface [332, 333].

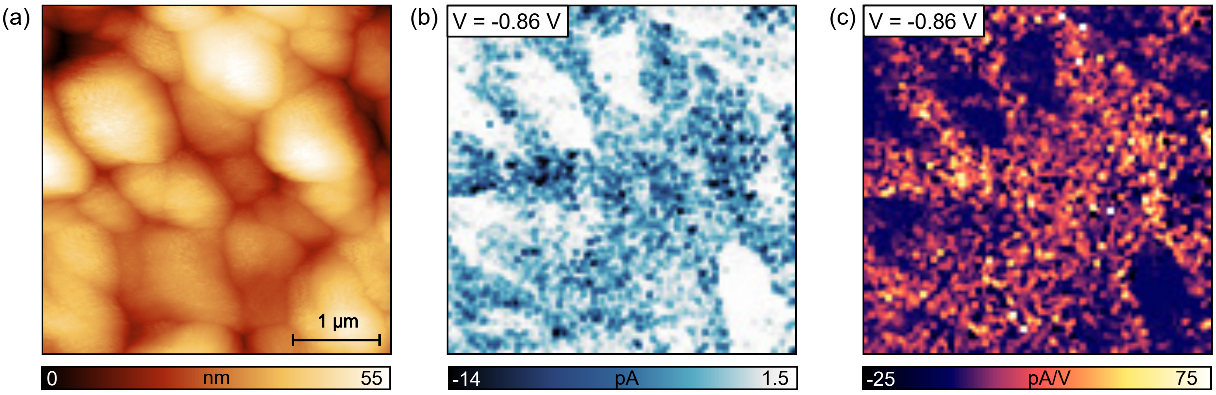

Figure 4.2: (a) Zoom of the STM topography of Figure 4.1. (b) Associated CITS (I(V)) image at the specific gap voltage of -0.86 V and (c) associated conductance image (dI/dV (V))

The observed n-type behavior at the surface can be the result of surface band bending due to surface states, and not specifically driven by an n-type bulk doping. Of course the surface doping type is absorber- and composition- dependent as previous reports already showed that the Fermi level depends on the ratio of MAI to PbI_2 [85, 334]. Besides, it was already discussed in section 1.3.1 of Chapter 1 that depending on the composition, the surface terminations (MAI-terminated or PbI_2-terminated) are different, inducing different surface defects and therefore different doping or band bending magnitude. Extrapolation of the bandgap was made possible using the zoom-in region of the $(dI/dV)/\overline{I/V}$ (Figure 4.3b) and a value of 1.62 ± 0.5 eV was extracted. Note that this is a rough estimate of the surface bandgap as the value depends on how the extrapolation is performed, but it is however in good agreement with the optical bandgap measured with photoluminescence

(Appendix Chapter D.4) and the estimation errors are reduced due to the broadening method used to bypass the divergence issue near zero voltages. The following section concerning simulation will however give a more elaborate estimation of the surface bandgap.

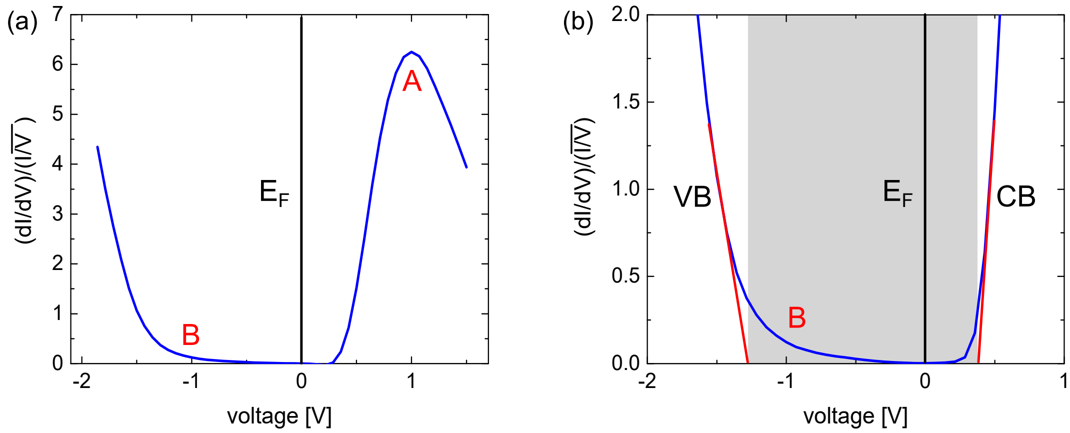

Figure 4.3: (a) Averaged (dI/dV)/$\overline{I/V}$ curve from the CITS perfomed on Figure 4.2a. The A and B letters denote two features that will be further discussed. (b) Zoom-in of (b) where the band onsets are determined via extrapolation. VB and CB refer to the valence and conduction band onsets.

Two letters (A and B) were used in Figure 4.3 to refer to two distinct features of the LDOS. A represents a peak in the positive voltages which can be attributed to the band structure of $MAPbI_3$ and has already been observed in previous DFT calculations, and was linked to the (001) and (110) surfaces and their Pb-6p orbitals [134]. The second feature, denoted B, highlights a larger conductance in the tail of the VB compared to the tail of the CB, i.e., the edge of the VB is less sharp than the one of the CB. This feature will be used in the following sections as it fluctuates at the surface and is linked to different surface state densities.

4.2 Simulation of density of surface states and Fermi level pinning

To understand the dI/dV spectra as well as the features that can be observed in such a curve, modelling becomes a crucial tool. Feenstra and co-workers [335] have previously developed a numerical tool to simulate the tunneling current between tip and sample combined with an electrostatic potential computation of the tip induced band bending (TIBB). In their model, the studied material (semiconductor) is treated as an effective mass approximation (envelope function). The tunnel current from the STM tip to the sample is simulated using the Bardeen method, which uses multiple approximations that are described in details by Bardeen [219]. Essentially, the tunneling current is described as a one-particle process and the interaction between tip and sample, which could induce the formation of coupled electronic states, is neglected. The simulation tool also includes solutions of the coupled Poisson and Schrödinger's equations used for the situation of charge accumulation at the surface. The theory behind the computation, based on the Bardeen formalism, is explained in details in the work of Feenstra et al. [336].

Their computing tool was used in their work on n-type GaAs(110) surfaces and they successfully managed to fit their dI/dV curve in order to access electronic parameters at the surface such as the density of surface states. As for surface states, they modelled acceptor-type surface states with a Gaussian density distribution in energy within the CB. One of the conclusions they drew was that the TIBB at negative voltages is limited by the Fermi level pinning (see section 1.3 of Chapter 1), caused by the surface states. The same fitting routine was therefore used in the previously presented data, in order to access the density of surface states of the solution-based $MAPbI_3$.

To that end, two different approaches were tried out, as depicted in Figure 4.4. The first approach consisted in neglecting the intrinsic surface states of this assumed n-type $MAPbI_3$. When the STM tip approaches the surface of the absorber but no bias is applied to the tip, the Fermi levels at the surface of the sample and of the tip are flat and are aligned (Figure 4.4a). As soon as a positive voltage is applied to the tip (negative to the sample), TIBB induces downward bending of the CBM and VBM bands, such that an accumulation of electrons occurs. The second approach was to assume a perovskite surface with a high density of surface states (Figure 4.4b). As already discussed in sub-section 1.3.5, both acceptor-like and donor-like surface states were considered, separated by the charge neutrality level (CNL) and with a gaussian distribution. Due to the negatively-charged acceptor surface states, equilibrium and charge neutrality impose the VBM and CBM bands to bend upward towards the surface, causing a positively-charged space charge region beneath the surface. Note that here the donor surface states do not contribute to the band bending as they are never occupied with holes (donors are charge-neutral when occupied with electrons). Due to the high density of surface states, the Fermi level is pinned and therefore, applying a voltage does not change the bending of the bands, so no TIBB is induced under positive tip bias.

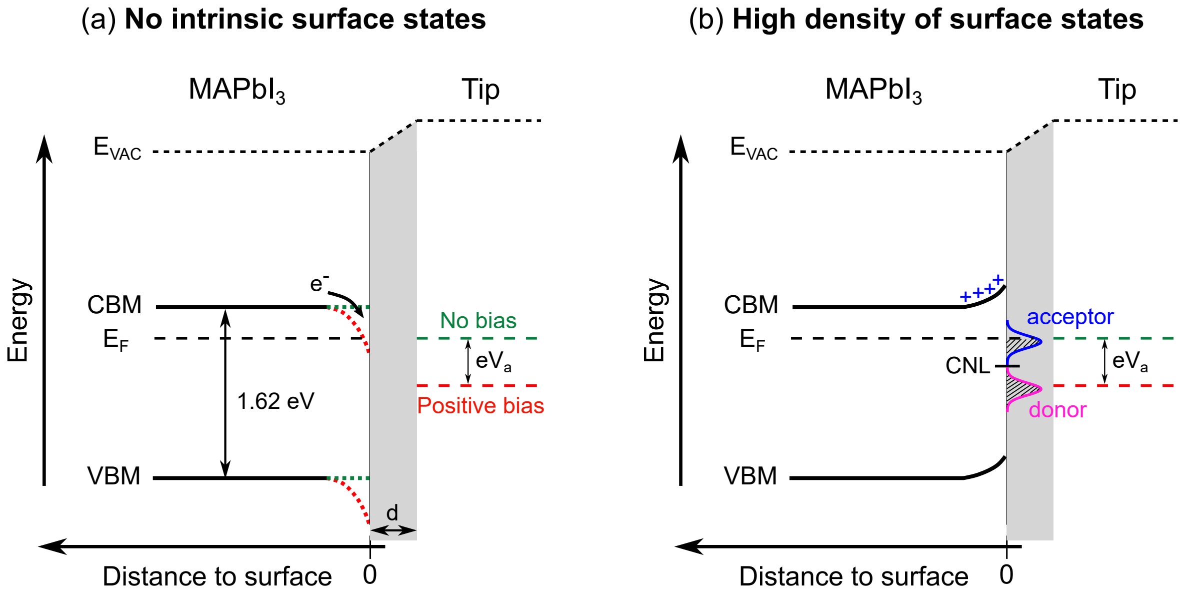

Figure 4.4: Schematic of the tunneling junction between the surface and the tip in the case of (a) no intrinsic surface states at the $MAPbI_3$ surface and (b) high density of surface states. V_a is the applied bias to the tip, and the workfunction of the tip is drawn in green when no tip bias is applied and red when a positive bias is applied to the tip. The CNL in (b) represents the charge neutrality level, dividing the acceptor to the donor surface states. The dashed regions in the Gaussian distribution of the acceptor and donor surface states denote them as filled with electrons, which yields negatively charged acceptors and neutral donors.

These two approaches were then modelled using the model from Feenstra and co-workers [335]. To simulate the first approach with no intrinsic surface states, the parameters presented in table 4.1 were used with a negligible density of surface states of $N_D = 1\times10^{11}$ cm^{-2}eV^{-1}. The simulated dI/dV curve together with the experimental one are represented on a linear and semi-logarithmic scale in Figure 4.5 with the green curve and the blue dots respectively. At positive voltages, the fit to the experimental data was satisfactory and optimized via an adjustment of the contact potential difference between the tip and the sample, the sample-tip distance and the doping level in the bulk.

Parameter	Value	Unit
Tip-sample distance	0.48	nm
Tip radius	16.5	nm
Contact potential difference	-0.55	V
Donor Concentration	1×10^{12}	cm^{-3}
Bandgap	1.62	eV
Donor binding energy	6	meV
Acceptor binding energy	28	meV
Dielectric constant	26	
Temperature	300	K
Charge neutrality level	0.1	eV
FWHM Gaussian distribution	135	meV
Centroid energies for the distribution	1.5	eV
Electron affinity of the sample	4.07	eV
Fermi energy of the tip	5.0	eV

Table 4.1: Parameters used in the simulation of the dI/dV curves.

Ideally, the CPD should be extracted from the variation of the tip-sample distance and the simultaneous measurement of the tunneling current or by KPFM using the same tip. However, at negative voltages, the fit to the experimental data did not match, as a large conductance was observed for the simulated case, which was not the case for the measured dI/dV spectrum of this $MAPbI_3$ absorber. This large conductance at negative voltages in the fitted curve with no density of surface states can be traced back to TIBB, where the accumulation of electrons, as discussed previously, induces a large amount of filled localized surface states, dominating the conductance in the bandgap at low negative voltages.

Therefore, to fit the experimental data at negative voltages, the density of surface states had to be optimized such that it reached a high density of $N_D = 1\times10^{13}$ cm^{-2}eV^{-1}, located at 1.4 eV relative to the CNL (0.1 eV above the VBM) and with a Gaussian distribution of 135 meV (table 4.1). The parameters may not be the most accurate for this specific sample, which makes the simulation and its interpretation more qualitative-based. The assumption of n-type doping was however justified by the resulting dip in the dI/dV curve at small negative voltages, which would occur at small positive voltages if p-type doping was to be chosen. However, the most determining factor was still the density of surface states. Without a relatively high value, the fit to the experimental data would not be possible, which proved that the studied $MAPbI_3$ absorber had a high intrinsic density of surface states, that pinned the Fermi-level and bypassed the TIBB, observed in the former case of no intrinsic surface states at negative voltages.

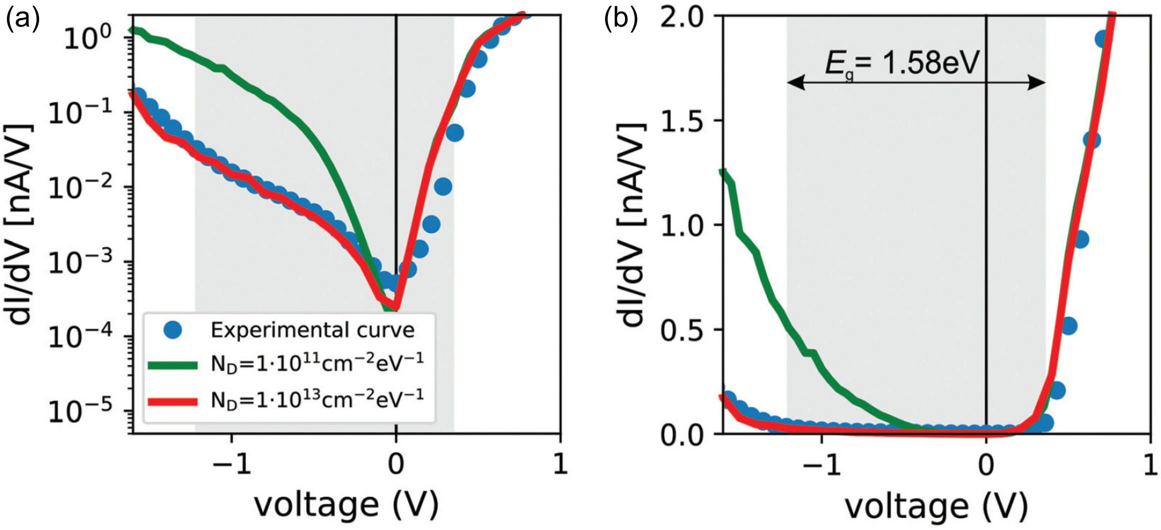

Figure 4.5: Measured and simulated average dI/dV curve on (a) a semi-logarithmic scale and (b) a linear scale for the two cases of no intrinsic surface state (green) and high density of surface states (red), discussed in Figure 4.4. Courtesy of Alex Redinger.

4.3 Local fluctuation of surface states, workfunctions and bandgaps

The distribution of the surface states was then studied by using lateraly resolved dI/dV images. To that end, the grain boundaries were manually defined with black lines for clarity as represented in the topography in Figure 4.6a. From the dI/dV maps, derived from the CITS, regions at two specific voltages were extracted, at -0.86 V (Figure 4.6b) and +0.36 V (Figure 4.6c), to represent negative voltages and positive voltages, which previously showed completely different behaviors. There, the grain boundaries are represented with white lines.

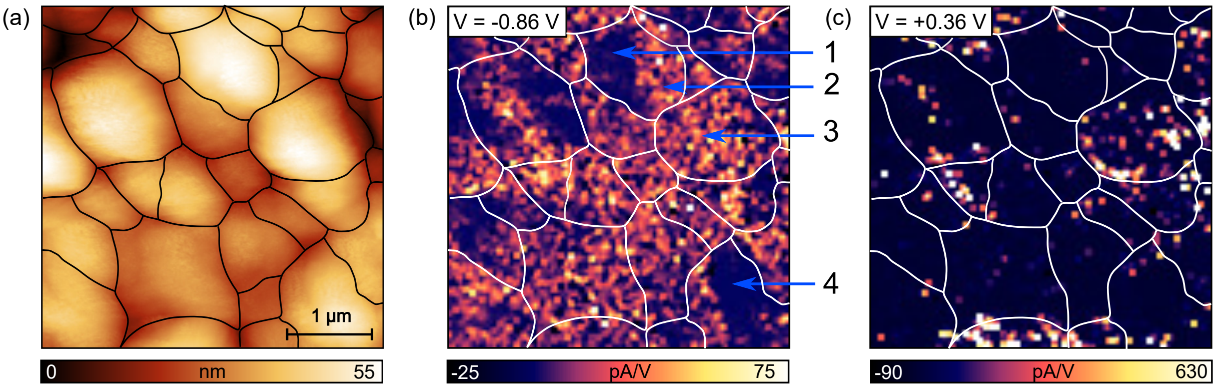

Figure 4.6: (a) STM topography with the grain boundaries defined by the black lines. (b,c) Associated dI/dV or conductance maps at -0.86 V and +0.36 V respectively with the grains boundaries defined with white lines.

At negative voltages, visual fluctuations in the conductance map were directly observed, where some grains appeared to be more conductive than others. Most importantly, different conductance were also discerned within single grains (see regions 1 and 2 of the same grain in Figure 4.6b). The grain boundaries themselves did not present a different contrast in conductance compared to the grains, which could also be attributed here to a limitation in the resolution of 40nm, originating from the scan size divided by the number of pixels used during the measurements. At positive voltages, homogeneity within a single grain seemed to be re-established but not between different grains. As an example, the grain depicted in the region 3 had now a much higher conductance than the grain represented by the regions 1 and 2 (Figure 4.6c), which was not the case at negative voltages. From the STM topography and extracted line profiles, one can infer that the observed differences in conductance within one grain are related to different facets of that grain. As already discussed in this thesis, different facet orientations can result in different surface terminations and therefore electronic properties. In order to confirm this, the dI/dV curves of each regions were extracted and modelled for different situations, to see which parameters were defining the observed changes in conductance within and between grains.

The dI/dV curves of the regions are depicted in Figure 4.7a together with the average conductance. At both negative and positive voltages, variations in the conductance of the regions were observed. The biggest visible changes were attributed to the regions 1 and 4, where at negative voltages, the conductance shifted to much lower values compared to regions 2 and 3, and the average dI/dV curve. To link these changes to electronic properties, two sets of simulations were performed. In Figure 4.7b, the CPD between tip and sample was varied from -0.35 V to -0.65 V, which represents a change of the sample's WF, linked to multiple parameters as previously discussed in section 1.3.5, but which could well be due to different surface terminations and surface dipoles. The simulation showed that varying the CPD by about 300 mV shifted the dI/dV curves to lower conductance values for both negative and positive voltages and with similar magnitudes. However, this cannot solely explain the differences observed in the experimental dI/dV curves for the different regions as unsymmetrical variations of the conductance depending on applied bias were observed.

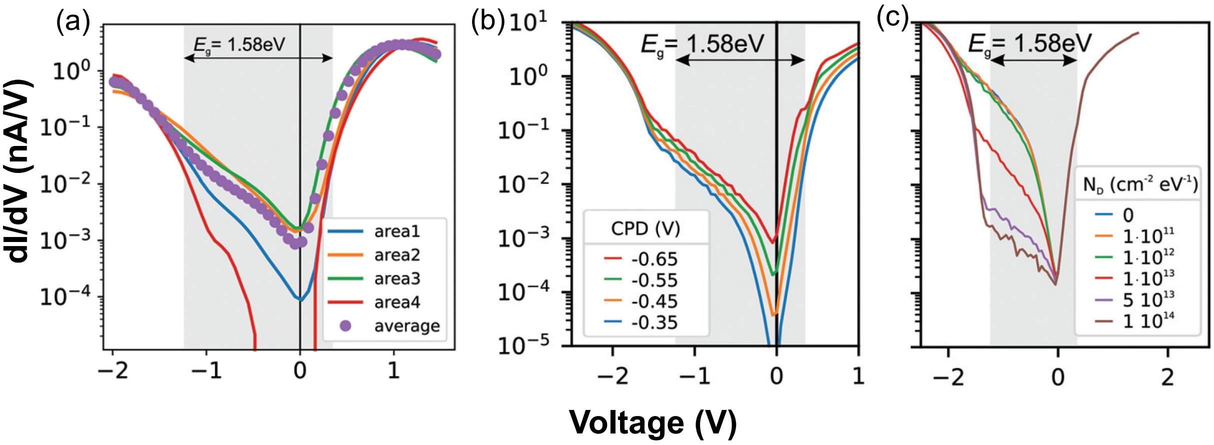

Figure 4.7: (a) Extracted dI/dV curves for each regions presented in Figure 4.6 and averaged dI/dV curve. (b,c) Simulated dI/dV curves with a varying CPD between -0.35 V to -0.65 V, and with a varying density of surface states between 0 and 1 × 10^{14} cm^{-2}eV^{-1} respectively. Courtesy of Alex Redinger.

The influence of solely varying the density of surface states from 0 to 1 × 10^{14} cm^{-2}eV^{-1} (Figure 4.7c) was then modelled. This resulted in a different observation, as no change could be observed for the onset of the conductance at positive voltages, whereas at negative voltages, large variations, similar to the one measured experimentally, could be visible.

The experimental dI/dV curves extracted from the regions therefore reflected both a change in density of states but also in CPD, as asymmetric fluctuations occurred, with large conductance drops at negative voltages and much lower conductance drops at positive voltages, depending on the region of interest. One has to note however that a change in density of surface states, such as the one presented in Figure 4.7, will also induce in turn a change in CPD due to a change of the surface dipole (strongly linked to the WF). In the previous simulation, this effect is not taken into account, as only one parameter was varied, thus the constant trend at positive voltages for Figure 4.7c. From these simulations, one can therefore infer that the observed changes in the dI/dV spectra for each region can be correlated to a different density of surface states, which induce a change of the CPD (or WF) value.

4.4 Grain boundary properties in MAPI absorbers

One crucial feature of polycristalline $MAPbI_3$ is the grain boundary and it is then important to determine if the density of surface states there is different from the one observed at the adjacent grains. To that end, CITS on a smaller scale (1.2 x 1.2 µm^2) was performed to resolve with a higher resolution the GBs (10 nm resolution). Note that better resolution down to 1-2 nm should be preferred to really observe the intrinsic feature of the GBs, but this would also induce larger thermal drift in the obtained images. In Figure 4.8, a STM topography of several grains and GBs and the associated CITS at -0.6, 0 and +0.6 V are represented. Dark and white lines are used to define the grains and approximate the regions of the boundaries but an image without the lines can be found Figure D.3 in the Appendix Chapter 4D.5. From the dI/dV images at the different voltages, no clear change in conductance at the GBs could be distinguished, but rather as previously observed, different density of surface states within single grains.

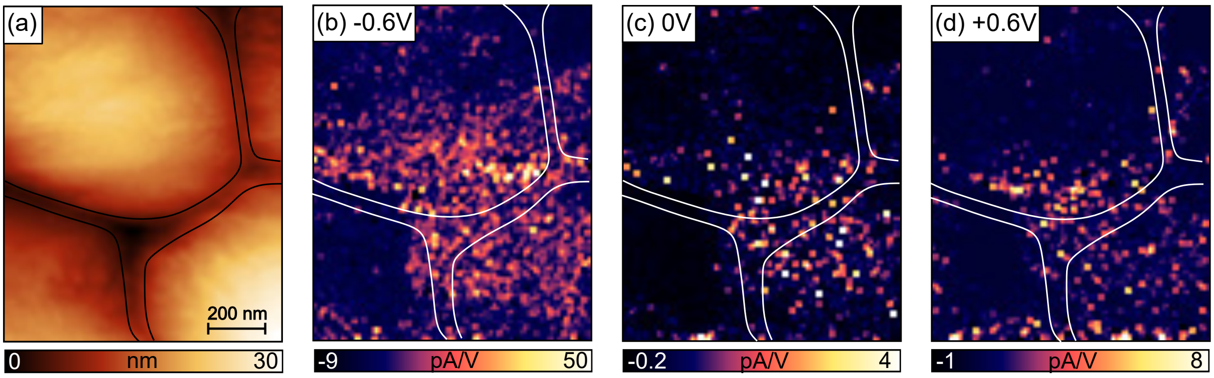

Figure 4.8: (a) STM topography on a smaller scale to resolve the grain boundaries. (b,c,d) highly-resolved dI/dV map at -0.6, 0 and +0.6 V respectively. The dark and white lines give a rough estimation of the position of the GBs.

The average I(V) curves at the grain boundaries and at the grains were therefore extracted and derived to access the average dI/dV curves and the resulting normalized $(dI/dV)/\overline{I/V}$ curves (Figure 4.9). From the latter, a bandgap of 1.65 eV for both the grains and the GBs was extracted, which is within the previous range observed (1.62 ± 0.5 eV). From the raw dI/dV curves, not much difference between grains and GBs was observed, except from a slight shift to lower conductance values for the grains, which can be attributed to a slightly higher CPD value compared to the GBs of about 22 mV when using simulation. This would indicate that the grains would have a WF lower by 22 meV compared to the GBs, which is insignificant and lower than kT at room temperature, but a magnitude which has often been observed in this thesis for several other types of perovskite absorbers using KPFM.

These observations, indicating an excellent passivation at the GBs as well as insignificant changes in WF, are not in line with most of the literature, where band bending, either downward or upward, from grains to GBs, is often reported. Most of the time reports conclude that these variations at the GBs cause either a worsening of the device performance due to barriers for charge carrier or improvement of the performances due to passivation at the GBs [18, 84, 337]. As previously discussed, the different use of solvents, but also air exposure of the sample or the use of light can already alter the surface properties and specifically the GBs, thus the sample's history has to be known.

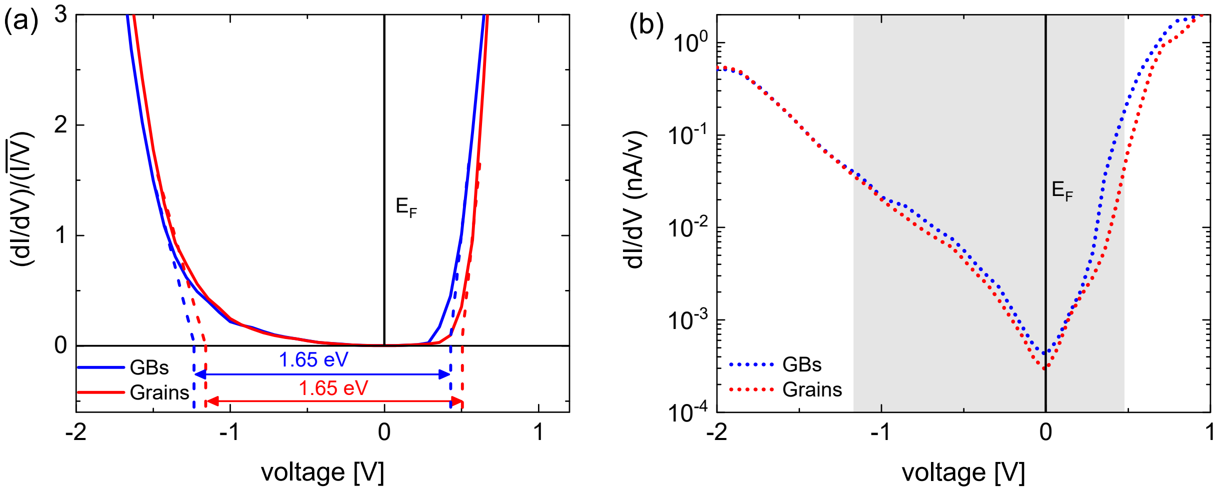

Figure 4.9: (a) Normalized $(\mathrm{dI/dV})/\overline{I/V}$ curves representing the grains and GBs and the extracted bandgaps. (b) dI/dV curves displaying a small shift in CPD.

4.5 Origin of the facet-dependent density of surface states

Previous reports already demonstrated that Fermi-level pinning could be caused by a high amount of Pb^0 at the surface of a perovskite absorber [338, 339] and additional n-type doping. However appearance of metallic lead has only been observed in UHV when light is used during XPS. The measurements presented in this chapter were only performed in the dark and only a low intensity light-emitting diode was used to move the sample around the UHV chamber and to approach the sample close to the tip. It is therefore not possible to fully discard that light did not alter the surface or the studied solution-based $MAPbI_3$. Besides, the absorbers were transferred from a glovebox to the UHV chamber by an inert gas suitcase, which does not entirely exclude the alteration of the surface of the absorber but this remains the most relevant option as solution-based solar cells are often fabricated in nitrogen-filled gloveboxes. The previous results obtained for $MAPbI_3$ absorbers showed that a high density of surface states was present and induced Fermi level pinning.

The high density of Pb^0 at the surface of perovskite is often attributed to metallic lead [338, 339] and directly linked to the decomposition of $MAPbI_3$ by first transitioning to PbI_2. However, the measured and extracted surface bandgap were also in accordance with the optical bandgap of perovskite, and did not increase, which would be the case in the presence of PbI_2, which has a bandgap value between 2.3 and 2.5 eV [340, 341, 342, 343]. Besides, if metallic lead was to be present at the surface, this would introduce additional states in the bandgap, as metallic behavior would be expected and observable, which was not the case here. Therefore the variations in the conductance, density of surface states and induced change in surface dipole can be attributed to an intrinsic property of the $MAPbI_3$ surface, stemming from different surface terminations, possibly modified by nitrogen exposure, as already reported by Leblebici et al. [145] and deQuilettes et al. [143]. In their work, they correlated carrier lifetimes with the variation of the Cl/(Cl + I) concentration, as chlorine is present in their absorber, which is also the case for the previously studied absorbers. In order to confirm that individual facets have distinct concentration of halide elements, correlative STM and composition measurements would need to be performed, in addition to photoluminescence mapping for instance.

4.6 Density of states at the surface of mixed-cation mixed-halide perovskites

Currently, the most efficient perovskite solar cells are based on mixed-cation and mixed-halide composition, therefore, it is interesting to look at how their surfaces differ from the ones of $MAPbI_3$ and if their surface properties can be linked to their improved device efficiencies. To that end, CITS measurements on $FAPbI_3$-rich perovskite, namely $FA_{0.97}MA_{0.03}PbI_{2.97}Br_{0.03}$ spin-coated on mesoporous TiO_2 and provided by Anurag Krishna [344], were carried out, where FA is the cation formamidinium and Br is the bromine halide. Devices made with these absorbers resulted in efficiencies above 21% and the parameters related to the efficiency can be found in the Figure D.4 of the appendix of Chapter 3D.6 and in the work of Anurag et al. [344]. Once again, the perovskite absorbers were analyzed without air exposure after their deposition and using UHV STM.

4.6.1 Inter-grain variations of the conductance

The STM topography together with the conductance maps at different voltages are represented in Figure 4.10. Just from the visual inspection, clear fluctuations in the dI/dV maps depending on the grains could be observed, as depicted by the grains 1,2,3 and 4.

The average dI/dV curve for each of the previously cited grains were extracted and plotted in semi-logarithmic scales (Figure 4.11b). The broadening method was also used to access the surface bandgap via the $(dI/dV)/\overline{I/V}$ (Figure 4.11a). From the extracted curves, different surface bandgaps, attributed to the different grains (Figure 4.11a), were first noticed. While the large grains (3 and 4) had their bandgap determined to be around 1.57 eV ± 0.5 eV, in accordance with the optical bandgap of the perovskite, the smaller grains (1 and 2) had much lower bandgaps (0.78 and 1.18 eV respectively). Such low bandgaps in Pb-based perovskite are not feasible and PbI_2 secondary phase compounds have much higher bandgap than the 1.57 eV of this absorber.

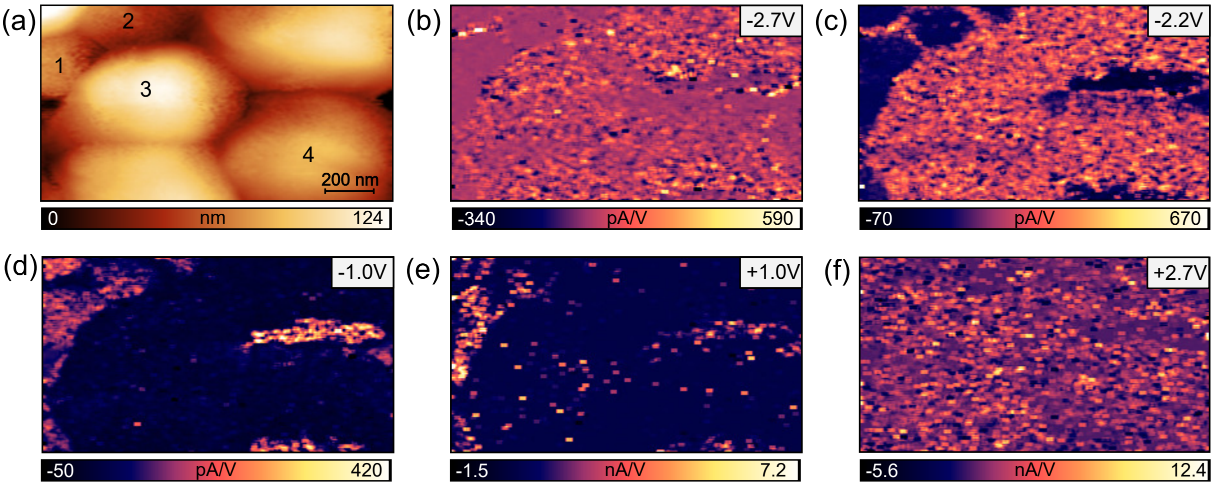

Figure 4.10: (a) STM topography of the surface of a $FA_{0.97}MA_{0.03}PbI_{2.97}Br_{0.03}$ absorber. (b, c, d, e, f) Corresponding conductance (dI/dV) maps at -2.7, -2.2, -1, +1 and +2.7 V respectively.

The dI/dV curves depicted on a semi-logarithmic scale (Figure 4.11b) further highlighted the variations in the conductance between the grains. At large negative voltages, the smaller grains had a lower conductance than the larger grains but this reversed when the tip voltage overcame -1.5 V. The asymmetric changes in the dI/dV curves at negative and positive voltages and the large change of the conductance in the near-zero voltage region suggested that the smaller grains had both a much different density of surface states as well a different CPD (WF) than the larger grains. For example, the smaller grains displayed an increased CPD, and WF, by about 0.3 to 1 eV compared to the larger grains.

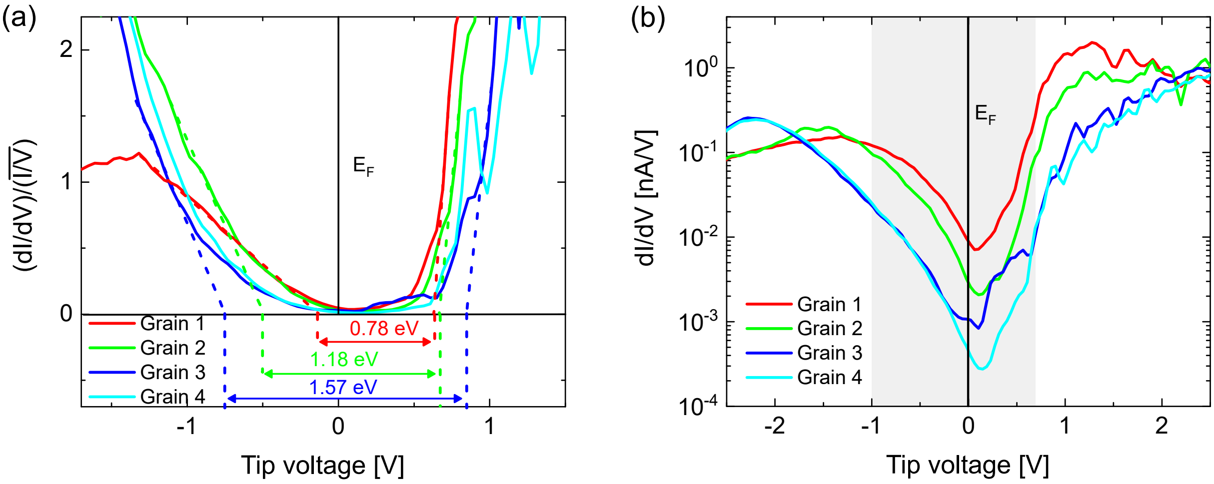

Figure 4.11: (a) (dI/dV)/$\overline{I/V}$ curves of the different grains and (b) dI/dV curves on a semi-log scale.

4.6.2 Intra-grain variations of the conductance

In addition to the fluctuations in the conductance observed between different grains, the similar aptitude between different facets of one grain was also noticed, as displayed in

Figure 4.12. Grain 1 (G_1) and grain 2 (G_2) present two different types of conductance, which are referred to here as facets F1 and F2 for each grain. Similarly to the previous case, the facets F_2 of each grains have lower conductance at large negative voltages compared to the facets F_1 (Figure 4.13), but after -1.7 V, the trend reverses until the conductance for each facet meet up at high positive voltage (+2.5 V).

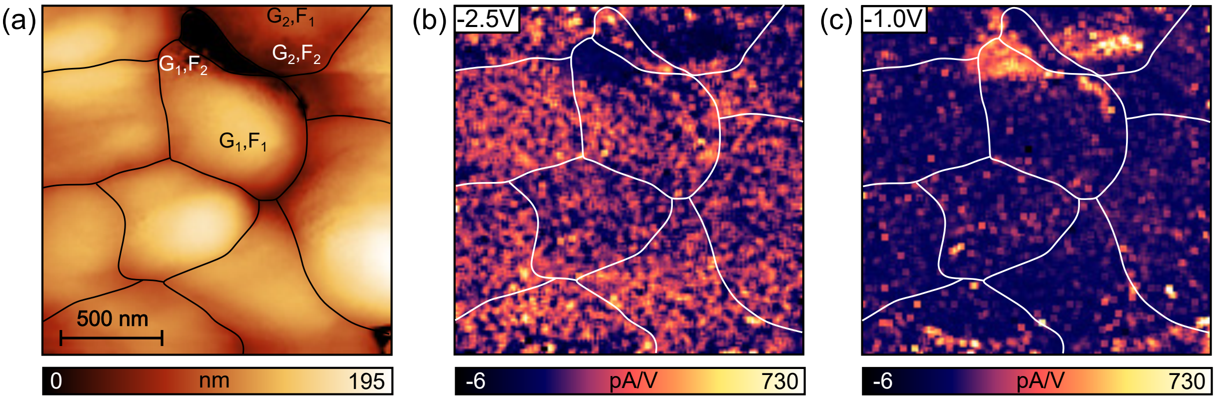

Figure 4.12: (a) STM topography of the same mixed cation-halide perovskite absorber. (b,c) Corresponding dI/dV images at -2.5 V and -1 V respectively. G_x,F_y represents the facet y of the grains x.

The average dI/dV curves of each facets were therefore extracted and plotted in Figure 4.13. The study started with the already discussed analysis of the surface bandgap for each facet (Figure 4.13a), which showed that the facets with the higher conductance displayed a much lower bandgap than the other regions (0.9 - 1.3 eV), that are in majority present at the surface of the absorber (1.57 eV ± 0.5 eV). Additionally, both facets presenting the lower bandgap had a non-zero, slightly positive conductance at 0 V, with an increase of the conductance magnitude scaling up with the reduction of the bandgap.

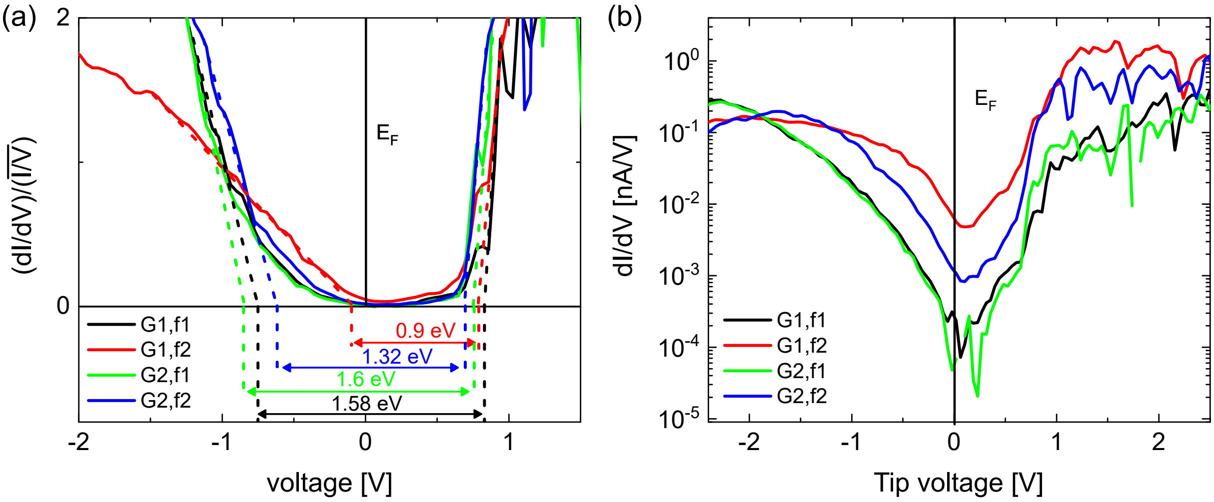

Figure 4.13: $(\mathrm{dI/dV})/\overline{I/V}$ curves of the different facets of grains 1 and 2 on and (b) dI/dV curves on a semi-log scale.

The extracted dI/dV curves on a semi-logarithmic scale were analyzed such that the different features of the facets appearing in the conductance curves could be clearly distinguished. The facets F_1 exhibited similar curves, whereas the facets F_2 presented what was previously simulated in the case of $MAPbI_3$ absorbers as both an increase in CPD and a change in density of states, which could be suggested from the asymmetric changes at positive and negative voltages. Even more interesting was that the magnitude of the changes in density of states (decrease) and CPD (decrease) scaled with the reduction of the bandgap. The exact same behavior were actually also observed when inter-grains (Figure 4.11b) were analyzed.

4.7 Origin of the low bandgap and defect signature

The combined increase of the WF (decrease of the CPD), decrease of the surface bandgap and decrease of the density of surface states therefore suggest the occurrence of metallic lead (Pb^0) due to partial degradation of the mixed cation-halide perovskite absorber, either caused by the UHV, or in combination with the light studies performed beforehand using KPFM. A higher density of metallic lead Pb^0 on some grains would introduce states in the bandgap and reduce the latter, towards a metallic behavior. Degradation of perovskite towards Pb^0 has already been reported to happen in UHV in combination with light [338]. In addition X-ray photoelectron spectroscopy (XPS) on this sample revealed the presence of metallic lead and scanning electron microscopy (SEM) showed the occurrence of PbI_2 grains [344]. Besides, after the UHV measurements, photoluminescence and time-resolved photoluminescence were carried out and compared to the measurements before the UHV exposure. The luminescence had decreased by ~ 1.5 and the effective lifetime had dropped from 570 ns to 380 ns, suggesting a degradation of the absorber's performances after UHV and light exposure (Figure D.5 in appendix of chapter 3). However, the possibility that the lowered bandgap and increased conductance are the results of trap states in the bandgap cannot be ruled out. Shallow traps can for example introduce discrete energy levels or disorder-induced acceptor-like and donor-like tail states in the bandgap, which will be visible in the DOS as a narrowing of the bandgap [345, 346, 347]. Density functional theory (DFT) or defect formation energy (DFE) calculations would be ideal tools to complement these STS measurements.

An average dI/dV curves was extracted from all the grains of the performed CITS. In Figure 4.14, the conductance is depicted in a semi-logarithmic scale to better visualize a bump in the dI/dV curve at +0.5 V.

This bump in the conductance is suggested to be the signature of a surface defect, as it vanished when passivation layers were used (see section 7.3 of Chapter 7). The origin of the defect could not be accessible with STS and therefore DFE computations were used and proposed that among the possible surface defects, lead-iodine antisite (Pb_I DFE = 0.59 eV) was likely to form on a PbI_2-rich mixed cation-halide perovskite surface [192, 348]. Using DFT calculations, the most stable configurations of the molecules used in the passivation layer (and discussed in section 7.3) that would interact with a Pb_I defect were modelled and led to the finding of an interaction energy of -0.98 eV, confirming a favorable interaction with the antisite defect [344]. It stemmed from the STS and computations that a defect was present in the surroundings of the conduction band, which can be the reason of the reduced intrinsic stability, the degradation of the absorber in UHV and/or upon illumination, which led to the appearance of potential metallic lead or shallow trap states.

Similarly to the case of $MAPbI_3$, the LDOS of the GBs were investigated and compared to the grains but did not exhibit large differences except from slight shifts that were in coherence with KPFM measurements later presented. This was discussed in a bit more

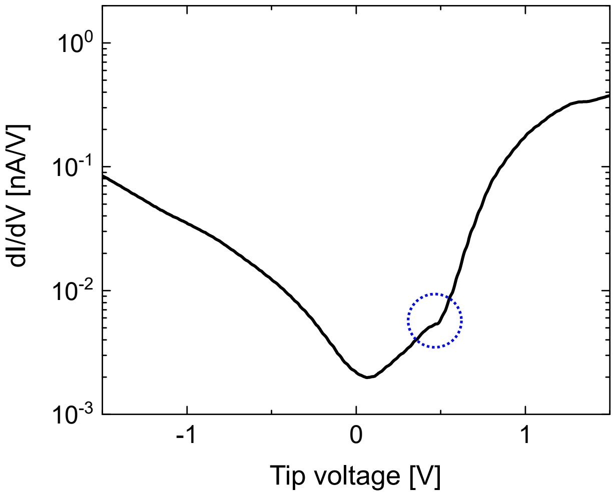

Figure 4.14: Average dI/dV curve extracted from a large amount of grains at the surface of the mixed cation-halide perovskite. The blue dotted circle represents the region with a potential defect signature.

details in section D.8 of the appendix of chapter 4. However, overall, CITS remains a very qualitative tool for GBs characterization when, as in this case, the resolution lies between 8 to 10 nm and the adjacent grains might contribute to some tunneling of current to the tip. FM-KPFM is therefore preferred and recommended to study these features.

4.8 Summary of Chapter 4

In this chapter, current imaging tunneling spectroscopy was used to access the local density of surface states of solution-based $MAPbI_3$ and $FA_{0.97}MA_{0.03}PbI_{2.97}Br_{0.03}$. Measuring the local conductance at the surface was shown to be a useful tool to access the density of surface states when low applied voltages were used. Different types of features, associated to the band structure of the perovskite, could be observed on a simple average dI/dV curve, as well as clear differences in conductance by solely looking at the CITS images. Air-exposure was circumvented to avoid any change at the surface related to external factors such as oxygen and moisture.

$MAPbI_3$ absorbers were used as a case study, where first the dI/dV curve were extracted and normalized by a broadened I/V, enabling the extraction of the surface bandgap of 1.62 ± 0.5 eV by using the extrapolation of the band edges in the $(\mathrm{dI/dV})/\overline{I/V}$ curve. Two cases were simulated, one without intrinsic surface states and one with a high density of surface states, and compared to the experimental results. It was observed that the $MAPbI_3$ absorbers had a high density of surface state of about 1×10^{13} $\mathrm{cm^{-2}eV^{-1}}$, which pinned the Fermi level and made the surface of the absorber non disrupted by tip-induced band bending.

Local fluctuations in conductance between grains and within single grains were observed, and modelling was used to understand their origin. It resulted that they were caused by a different amount of surface states depending on a facet of a grain, which also induced a change in the surface dipole, linked to the contact potential difference. The grain boundaries were also studied but no variations could be discerned compared to the grain interiors, except from a small change of the WF by 20 meV, which was insignificant due to its value being lower than kT.

The same procedure was used on a solution-based $FA_{0.97}MA_{0.03}PbI_{2.97}Br_{0.03}$ mixed halide perovskites. A defect signature could be resolved in the conduction band, at positive voltages, which density functional theory suggested to be a lead iodide antisite defect. CITS images revealed that different grains were again behaving differently than others but contrarily to the case of $MAPbI_3$, where degradation and Pb^0 formation were excluded, the reduced surface bandgap of these grains, as well as their increased conductance and increased WF, led to the suggestion of a degraded absorber. This could potentially lead to the formation of metallic lead or trap states, that would change the surface properties locally on the absorber. A similar behavior was observed within single grains. However shallow trap states creating acceptor or donor-like tail states in the DOS could not be excluded. Lastly, the grain boundaries again did not vary much compared to the grains, except from some minor variations in the density of surface states and potentially WF, which however are always difficult to resolve using scanning tunneling spectroscopy.

The overview of current imaging tunneling spectroscopy showed that density of surface states vary locally, in combination with other electronic properties such as surface dipole or WF, between distinct grains and between facets of a single grain, and this independently of the composition of the absorber. However, the commonly idea that grain boundaries are worsening the surface of the absorber was not demonstrated here, as they showed similar behavior than the grains. The aforementioned fluctuations in the conductance however impose another degree of complexity to the fabrication of devices as extraction layers are often relying on homogeneous interfaces to yield efficient solar cells.

Chapter 5

Co-evaporated MAPI and the impact of different growth conditions

As already presented in the SPM review in section 2.4 of Chapter 2, the SPM literature of perovskites is mostly, if not only, based on films fabricated by solution processes or by measuring perovskite films in ambient environments, thereby exposing their surfaces to solvents, oxygen and water. Therefore, there is a clear need to measure the intrinsic surface properties of perovskites in order to understand them and find optimal passivation strategies or fabrication designs to further improve the perovskite solar cell efficiencies.

To that end, thermal evaporation can be used to deposit $MAPbI_3$ thin films without the use of solvents and without oxygen and water contamination. They can also be evaporated on a large scale, due to the ease of controlling the composition, thickness and uniformity. However, as explained in section 3.5 of Chapter 3, the organic compound MAI of $MAPbI_3$ makes it challenging to control the evaporation rate through the evaporation temperature, and therefore the MAI partial pressure has to be used. Using thermal evaporation and KPFM in UHV, one therefore can wonder how the intrinsic bulk and surface properties of $MAPbI_3$ are affected by the MAI partial pressure.

This chapter therefore focuses on the intrinsic properties of $MAPbI_3$ films and how fabrication parameters affect their phase purity, their photostriction and their intrinsic stability. It is largely based on the work [349]. Section 5.1 will introduce the ability to tune the composition of $MAPbI_3$ via the control of the partial pressure of the organic compound. It will be shown that increasing the MAI pressure results in a transition from a PbI_2-rich $MAPbI_3$ film to a MAI-rich film. Section 5.2 will then discuss how correlative PL and TRPL can be used to compare the optoelectronic properties of $MAPbI_3$ with different compositions but also how to access their doping densities. The results will demonstrate that increasing the MAI pressure leads to an increase of the PL yield and the lifetime as well as the doping density. Section 5.3.1 will use KPFM measurements on two types of $MAPbI_3$ films with different compositions, and will present clear variations of their surface properties and different behaviors against annealing. The results will show that over-stoichiometric $MAPbI_3$ display low WF regions which can be linked to low-dimensional perovskites, that can disappear upon annealing but degrade the $MAPbI_3$ surface. Section 5.4 will focus on the changes of the lattice and the stability of the electronic properties upon illumination. It will present how over-stoichiometric $MAPbI_3$ films exhibit photostriction and how their intrinsic stability against light considerably reduces compared to near-stoichiometric films.

5.1 Tuning of the composition and structure via the MAI partial pressure

As previously discussed in section 3.1, the organic compound methylammonium iodide (MAI) is highly volatile, and therefore its partial pressure is used as one of the control parameters for the deposition of $MAPbI_3$ absorbers, similarly to other works [302, 307, 314, 315]. Throughout all this chapter, the total chamber pressure will be referred to as p and will be a measure of the MAI flux during the growth. Varying the partial pressure of MAI therefore influences its evaporation rate, which raises the question of a potential variation of the absorber's composition or morphology as a function of the pressure used. Therefore p was varied by an order of magnitude, from 1×10^{-6} mbar to 1×10^{-5} mbar, while the evaporation rate of PbI_2 was kept constant and techniques such as X-ray diffraction (XRD), energy dispersive X-ray spectroscopy (EDX), photoluminesnce (PL) and time-resolved PL (TRPL) were used to determine if any change in the absorber quality would occur.

EDX measurements were performed on different spots of $MAPbI_3$ films grown at different pressures and showed that by gradually increasing the pressure p, the I/Pb ratio was also increasing, as described by the table 5.1. At the lowest pressure, $p = p_{min} = 1 \times 10^{-6}$, the I/Pb ratio is of 2.6, lower than the stoichiometry of 3 of the chemical formula $CH_3NH_3PbI_3$, which would suggest a Pb-rich composition. In addition, in table 5.1, the PbI_2/(110) ratio is presented, which relates the ratio of the peak of the PbI_2 secondary phase in the XRD to the (110) peak of the tetragonal $MAPbI_3$.

p [mbar]	I/Pb ratio	PbI_2/(110)
1×10^{-6}	2.6	0.68
3×10^{-6}	2.9	0
5×10^{-6}	3.0	0
1×10^{-5}	3.9	0

Table 5.1: I/Pb ratio obtained by EDX and PbI_2/(110) extracted from XRD

As can be observed, only at the lowest pressure $p = p_{min} = 1 \times 10^{-6}$ mbar is the ratio non-zero, which correlated well with the previously mentioned non-stoichiometric value of 2.6, and can be attributed to the presence of a PbI_2 secondary phase, visible in Figure 5.1a. By increasing p, the ratio also increased to reach 3 at $p = 5 \times 10^{-6}$ mbar, but ultimately increased to an even larger value, of 3.9, at $p = 1 \times 10^{-5}$ mbar, which was surprising. Indeed, attaining values above the stoichiometric value of 3 is uncommon, but has already been reported in the literature [309]. Therefore, despite that EDX measurements suffer from a number of systematic errors [350] it can be safely concluded that the MAI partial pressure during growth allowed the tuning of the MAI content in the absorber layer. In addition, the EDX suggested that a considerable amount of iodine was in excess when the highest pressure was used. Several groups already reported that MAI grew in a Volmer Weber mode when thermal evaporation was used [315, 351, 352] but the XRD measurements performed (Figure 5.1a) did not show any trace of MAI precipitation in the diffractogram of the high MAI pressure sample (only after a storage of several months, see section E.1 of appendix Chapter 5). In addition, the PbI_2 secondary phase, which was present for the lowest pressure, could not be observed anymore for higher pressures, which corroborated that the MAI pressures used were enough to fully convert the evaporated

PbI_2 into the perovskite phase. There were however some subtle changes in the crystal structure when increasing the MAI partial pressure, which could be first depicted by zooming in near the (220) peak (Figure 5.1b).

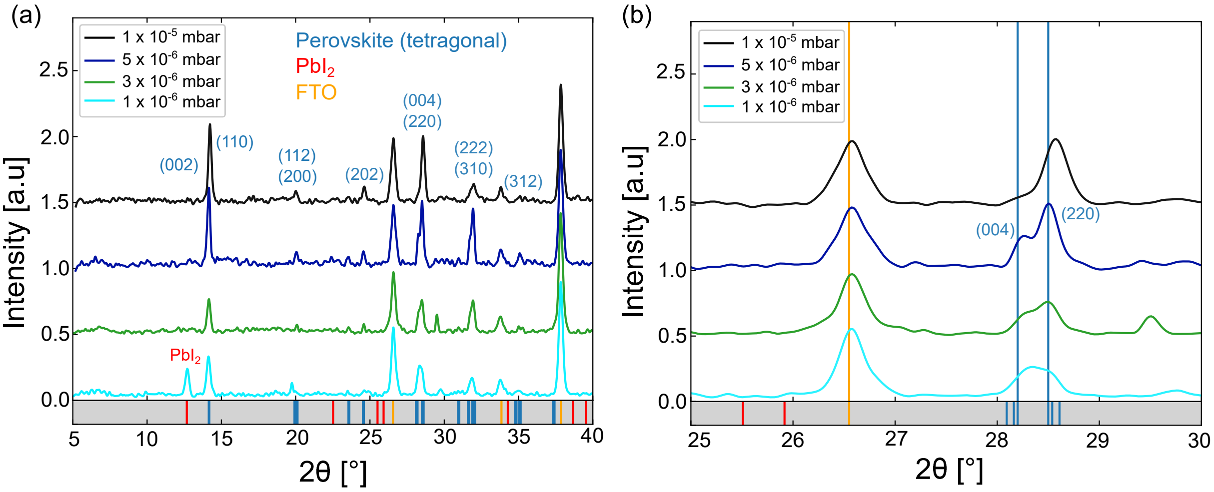

Figure 5.1: (a) Diffractograms of $MAPbI_3$ absorbers grown at different partial pressures, which are linked to different compositions. For the lowest pressure, a PbI_2 residual could be observed. For a better resolution, (b) represents a zoom of (a) near the (220) peak. For the identification of XRD peaks, PDF 00-007-0235 (ICDD,1957) for PbI_2 and PDF 01-084-7607 (ICDD, 2018) for tetragonal $MAPbI_3$ were used.

First, at the lowest pressure, a broad peak could be observed for the (220) reflection, presumably due to either the smaller grain size in these absorber layers or the presence of smaller features from the PbI_2 secondary phase, as can be observed with the SEM images of Figure E.2a of appendix Chapter 5E.2. By increasing p, the splitting of the peak into the (002) and (110) reflections, linked to the tetragonal crystal structure, was clearly observed and the grain size also increased with the increase of the I/Pb ratio (Figure E.2b of appendix Chapter 5E.2). When p_{max} was used, the broadening of the peaks reappeared, which this time did not go with an apparent reduction of the grain size (Figure E.2c of appendix Chapter 5E.2). Additionally, the full width at half maximum (FWHM) of the XRD peaks were higher for the lowest and highest pressure. In other materials, an increase of the FWHM has been reported to have multiple causes, such as an increase in stacking faults and structural disorder [353], a higher residual stress due to a higher density of grain distortion and dislocations at the surface [354] or also an increase in the density of point defects [355]. From the SEM images, the increase of the FWHM could be understandable for the lowest pressure due to the presence of smaller features caused by the PbI_2 secondary phase. However, as the grain size did not decrease for $MAPbI_3$ grown at the highest pressure, the increase of the FWHM could be the consequence of a worse crystal structure compared to the stoichiometric case, due to one of the previous reasons. Further high-resolution XRD should be carried out to unveil the origins of these differences.

Lastly, at p_{max}, a shift of the (220) peak to higher 2θ values was observed. A peak shift in XRD can be the result of a non-stoichiometry, which induces different interatomic spacing. In addition, strain, either from annealing or light, has been reported to shift peaks in the XRD diffractogram of perovskite [356, 357] indicating a different strain induced by the excess of MAI in the lattice. In this case, no annealing was performed and the illumination conditions were the same for all samples. Zhu et al. have reported that films experiencing compressive strain demonstrated peak shifts to higher 2θ values [357]. In addition, Song et al. have studied the phase transition of $MAPbI_3$ when varying the amount of MAI in the lattice. They concluded that over-stoichiometric films presented other crystal structure than the tegragonal one. When going over the stoichiometric point (I/Pb = 3), stacked perovskite sheets would occur as a new phase in the diagram, due to the introduction of stacking faults. They did not say whether the phase was more cubic or tetragonal but the introduction of stacked perovskite sheets, and in higher stoichiometries of low-dimensional perovskite, could induce additional strain in the lattice and shift the XRD peak. This phase diagram will be discussed in more details later in this chapter (Figure 5.8 and section 5.3). From the simple combination of XRD and EDX analysis, it can be concluded that using a relatively low MAI pressure of 3 to 5×10^{-6} mbar allowed to obtain a non-strained crystal structure without secondary phases and a clear tetragonal structure due to a near-stoichiometry composition.

High-resolution XRD was also carried out in the vicinity of the (110) and (220) orientation planes to confirm the previously observed trends (Figure 5.2). The samples were all the same except at the highest pressure where another sample was used. In comparison to the low-resolution scans, two observations were visible: this time the peak was not shifted to higher 2θ values, and there was a splitting of the peaks, which was not visible in the low-resolution scans. These differences between the previous low-resolution scan and the high-resolution scan could be linked to different degree of air exposure, which could slightly alter the crystal structure differently, or could be due to a lack of resolution for the first graph.

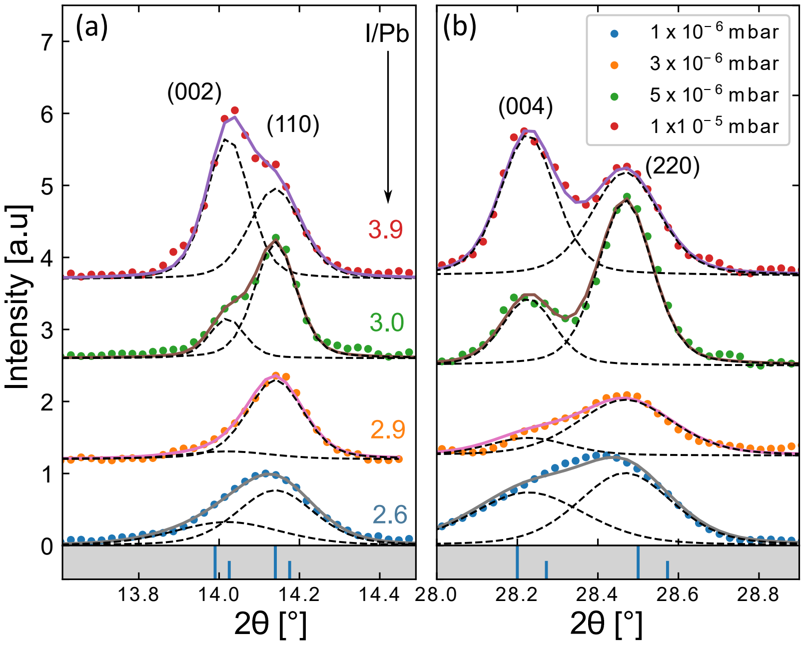

Figure 5.2: High-resolution XRD scans for $MAPbI_3$ absorbers evaporated using different MAI partial pressure near the (a) (110) and (b) (220) peaks. The I/Pb ratio depicted were extracted from EDX measurements.

The tetragonal splitting of the (110)/(002) and (220)/(004) peaks therefore appeared with the increase of the MAI partial pressure, which was synonym of an improved crystal quality. A main difference still occurred between the stoichiometric samples and the over-stoichiometric one (at p_{max} with an I/Pb of 3.9). For the latter, an inversion of the peak intensities happened. This behavior appeared on both fresh and aged samples, which excluded compositional changes due to a different storage time in the nitrogen-filled glovebox. A similar phenomena has already been reported in literature [358, 359, 360, 361, 362]. Kavadiya et al. electrosprayed MAI on top of spin-coated PbI_2 and observed a preferred orientation of grains with the [002] direction due to the growth process, visible by a higher intensity for the (002) peak compared to the (110) one [362]. Emara et al. have in their case reported such behavior when increasing the content of MAI in their perovskite. The XRD results obtained from the sample grown at the highest MAI partial pressure were in line with these reports, which could suggest that the excess of MAI initially used during growth and incorporated in the lattice (visible in the I/Pb ratio of 3.9) induced a different texturing and preferred grain orientation compared to when using near-stoichiometric conditions. However one has to note that even if the inversion of the peak intensities of the (110)/(002) and (220)/(004) was present in most of the high-pressure samples, sometimes some samples did not display it, and the reason why remains unanswered so far. Future work should focus on measuring samples with different pressures without exposing them to air. Nevertheless, it still remains to understand what could possibly induce the crystal structure to deviate from its original one when using high MAI content.

5.2 Variations in luminescence, lifetime and doping

In order to see if the change in the crystal structure related to the different MAI partial pressure had either a negative or a positive effect on the absorber properties, PL and TRPL in nitrogen were first used for the optical characterization (Figure 5.3) of $MAPbI_3$ grown on FTO. The first observation was that the PL quantum yield (PLQY) increased with the MAI partial pressure, and even more when using p_{max}, which displayed a greater surge in yield (Figure 5.3a). The extracted bandgap (via an asymmetric function fit) slightly varied (Table 5.2) from 1.61 eV for the Pb-rich absorber (p_{min}) to 1.6 eV for the near stoichiometric samples and 1.65 eV for the over-stoichiometric I-rich samples. In addition to the 50 meV blue-shift at p_{max}, the PL spectrum itself was broader, either due to the setup used and the wavelength resolution of the optical filter or an additional physical phenomenon. To confirm or refute the observed shift and broadening, several other samples were analyzed, on FTO but also on different other substrates and in the great majority, both blue-shift and PL broadening could be observed when varying the pressure from 3×10^{-6} mbar to 1×10^{-5} mbar.

Homogeneous or inhomogeneous broadening of the PL can be related to crystallinity disorder (defects-induced disorder) [363], local bandgap fluctuations caused by for example chemical or electrostatic potential variations, such as doping. FWHM broadening can also be the consequence of inhomogeneities in the material, linked to crystal size or shape [364, 365]. In perovskite literature, several causes were reported to be the consequence of PL broadening, as for example hot carriers with unexpectedly long lifetimes [366] or a strong phonon coupling [367]. Broad line width in PL, in addition to strong Stokes blue-shift, were also noticed in low-dimensional perovskites like the Ruddlesden–Popper ones where a broad emission near the 1.7 eV was measured, related to in-gap trap states or potential iodide-based defects [368]. Several other studies observed similar broadening in 2D perovskites, for instance on 200 nm-thick polycrystalline films [369] or for different

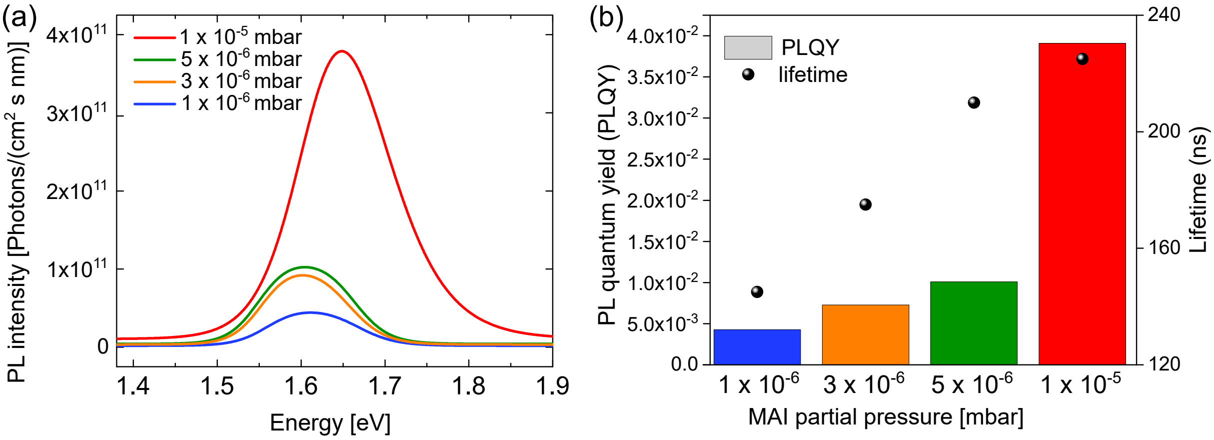

Figure 5.3: (a) Photoluminescence spectrum measured in a nitrogen-filled box TRPL measured for the same specific pressure series but using non-air exposed samples with a pulsed laser power density of 2.6×10^{-4} W cm^{-2} and a frequency of 1 MHz, corresponding to an injected carrier density of 1.15×10^{14} cm^{-3}. (b) Calculated PL yield and extracted effective lifetime from TRPL measurements.

compositions of low-dimensional perovskites [370, 371], which found its root in either free excitons, self-trapped excitons or distortion of the perovskite lattice. Lastly, the PL spectrum broadening was also observed in 2D-3D perovskite, prepared by vapor-assisted solution processes. Li et al. varied the concentration of phenylethylammonium (PEAI) in the PbI_2 precursor and used a solid–vapor reaction between the spin-coated PEAI-doped PbI_2 film and an MAI vapor under controlled pressure to obtain mixed 2D PEAI-3D $MAPbI_3$ films, which presented broader peaks than pure 3D $MAPbI_3$ films. They additionally reported a slight blue-shift when incorporating further PEAI 2D perovskite inside $MAPbI_3$ [372], which was in coherence with the observed broadening and blue-shift of the PL for the samples at MAI high pressure.

In addition to the PL yield increase and broadening when using higher MAI partial pressure, the effective lifetime measured via TRPL also improved (Figure 5.3b). Both PLQY and lifetimes were calculated using equations available in section 3.2 of Chapter 3. Using a laser power density of 2.6×10^{-4} W cm^{-2} and a frequency of 1MHz, which corresponds to an injected carrier density of 1.15×10^{14} cm^{-3}, the effective lifetime increased from about 145 ± 10 ns to 225 ± 10 ns from p_{min} to p_{max}. Both PL and TRPL were also carried out on $MAPbI_3$ grown on glass substrates for two sets of pressure (3×10^{-6} mbar and 1×10^{-5} mbar), in order to avoid any contribution from a hole or electron extraction layer in the determination of the PL yield or effective lifetime (Figure E.3 of appendix E.3 chapter 4). The observation that the optical properties improved from a low pressure to p_{max} was indifferent of the substrate, correlating that this was based on the intrinsic properties of the absorber and not due to a potential barrier formed by the junction between ETL/HTL and absorber.

Due to the dependence of the lifetime and the PL yield with the laser power density, and in order to have more statistics, measurements with a larger set of samples were performed for two pressures (3×10^{-6} mbar and 1×10^{-5} mbar), and this at different laser power densities (due to updates of the PL setup). These samples were grown throughout the time of this thesis. The trend remained the same as previously observed, such that the PLQY and τ_{eff} increased with the MAI partial pressure, highlighting an improvement of the optical properties of the absorber, which could suggest a potential better passivation

	p	bandgap	PLQY	effective lifetime	doping density
unit	mbar	eV	a.u	ns	cm^{-3}
	1×10^{-6}	1.61	4.3×10^{-3}	145	1.4×10^{16}
	3×10^{-5}	1.60	7.3×10^{-3}	175	2.0×10^{16}
	5×10^{-5}	1.60	1.0×10^{-2}	210	2.3×10^{16}
	1×10^{-5}	1.65	3.9×10^{-2}	225	8.7×10^{16}

Table 5.2: Bandgap, PLQY, effective lifetime and doping density calculated for different MAI partial pressures and measured under nitrogen.

of bulk or surface defects, as excess MAI has been reported to reduce MAI vacancies and promote iodine and MAI interstitials [373].

By using the same optical setup for PL and TRPL, with the same laser frequency and power, a correlation between the PLQY and τ_{eff} can be used to access the bulk doping density of the material, as explained in section 3.2 of Chapter 3. The calculated doping densities showed certain variations but a clear and large increase of the doping density, by almost an order of magnitude, from the low to the high pressure could be noticed. Such a change in doping can already play a role in solar cell performances, due to slight variations in carrier mobility, recombination rates or Fermi energy level, which impact V_{OC}, J_{SC} and FF. Fabricating devices was then useful to see if the improvement of the optical properties observed at the highest MAI partial used could be translated into more efficient devices.

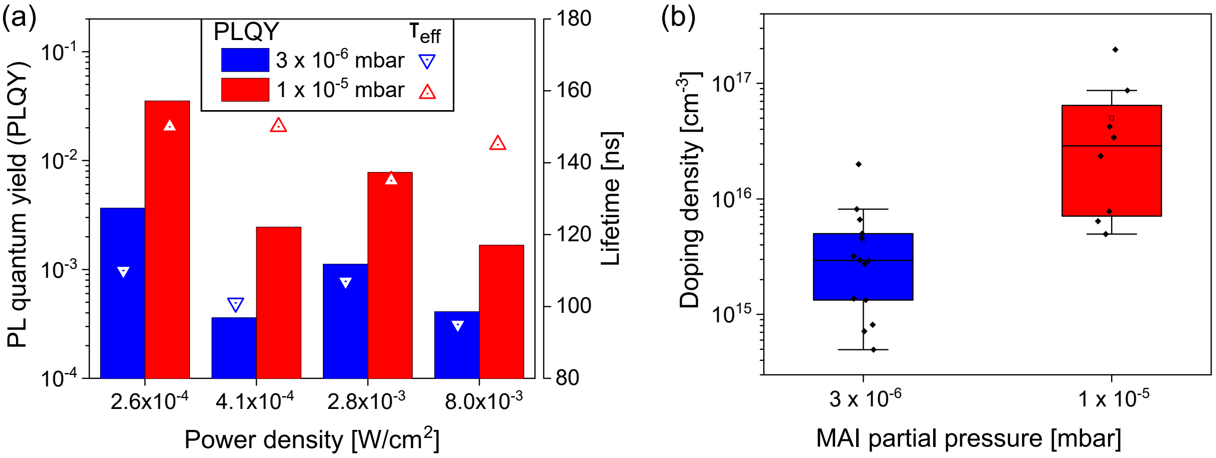

Figure 5.4: (a) Average external quantum efficiencies, effective lifetimes and (b) box chart of doping density for different pressures and laser power density.

Due to different fabrication constraints, and the following highly time-consuming KPFM measurements, absorbers at pressure of 3×10^{-6} mbar, which will now be referred to as p_{low}, and 1×10^{-5} mbar (p_{high}) were the only ones converted to devices and will be the only ones discussed extensively in the next sections of this chapter. The fabrication procedure was carried out at the Karlsruhe Institute of Technology by Tobias Abzieher, and is explained in section E.4 of appendix chapter 5. The 3×10^{-6} mbar was the one chosen over the other two pressures as the optical properties did not vary that much between 1×10^{-6} mbar and 5×10^{-6} mbar and due to an already extensive study of KPFM over annealing time performed on that one. The J-V curves and performances of the devices (V_{OC}, J_{SC}, FF and PCE) are depicted in Figure 5.5a. Interestingly, the best performing devices were not the ones with a $\mathrm{MAPbI_3}$ absorber grown with p_{high} even though they initially had much higher PLQY and better effective lifetimes. The low pressure samples achieved an average PCE of 14.5 % with average $\mathrm{V_{OC}}$, $\mathrm{J_{SC}}$ and FF of 1.05 V, 18.2 mA/cm^2 and 76 % respectively whereas the high pressure sample saw its PCE decreased by a factor 2 (6.6 %) with reduced $\mathrm{V_{OC}}$, $\mathrm{J_{SC}}$ and FF (0.97 V, 15.2 mA/cm^2 and 45 % respectively). In addition to that, devices made at p_{high} showed clear presence of hysteresis (represented by the large difference in the J-V curves in forward or backward scans) whereas very small differences could be discerned for devices made at p_{low}.

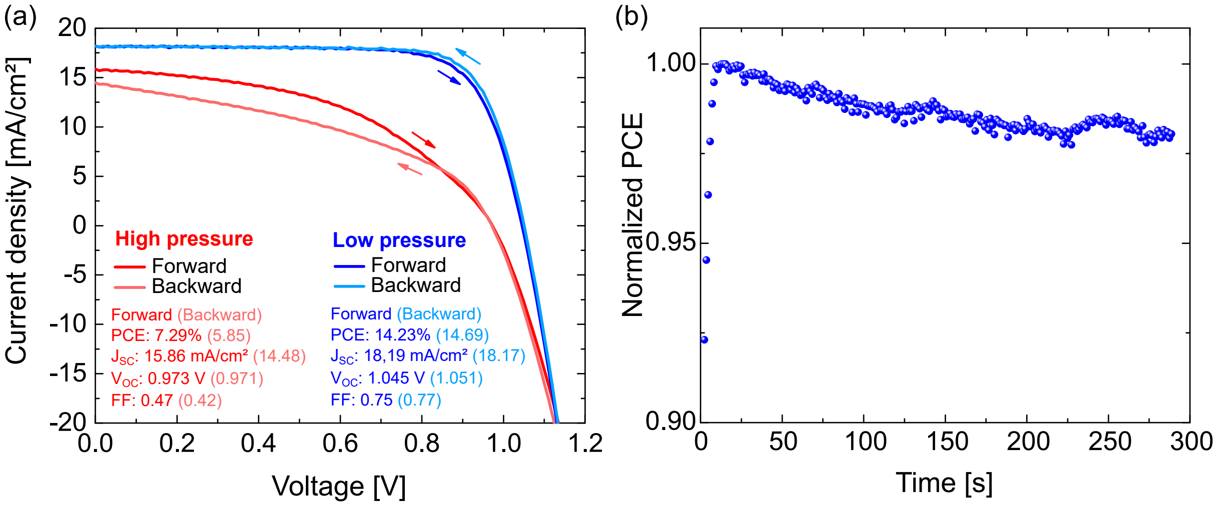

Figure 5.5: (a) J-V curves of the best solar cells made with absorbers at p_{low} (blue) and p_{high} (red). The device stack is glass/ITO/PTAA/$\mathrm{MAPbI_3}$/$\mathrm{C_{60}}$/BCP/Au. The inset represents the associated device performances. (b) Maximum Power Point tracking for the best solar cells (p_{low}).

The maximum power point tracking was used to observe the stability and quality of the best performing devices, in this case the low pressure samples. After 5 minutes of tracking, the PCE had already dropped by about 2 %, which could already point towards some stability issues even for the best co-evaporated devices made. On a side note, no optimization of the device fabrication was made, either in terms of absorber thickness or on the device side (choice and thickness of ETL / HTL and electrodes), which highlighted the potential for improvement in terms of efficiency. The reduced performances for the high pressure devices together with the observed hysteresis, often linked to ionic mobility, could have multiple causes, such as degradation of the absorber during the device fabrication or a worse energetic alignment between this specific absorber and the HTL and ETL for instance. As some of the bulk properties had already been investigated, the surface of absorbers grown at p_{low} and p_{high} were analyzed via KPFM.

5.3 Excess of MAI: surface and lattice variations

5.3.1 Surface variations of the electronic landscape

$\mathrm{MAPbI_3}$ absorbers grown on FTO at p_{low} and p_{high} were transferred from the PVD to the KPFM analysis chamber without breaking inert or vacuum environment, to prevent the surface from changing due to air or moisture exposure. The FTO substrate was again used here due to the need of a conductive bottom layer and to be coherent with the previously discussed XRD, EDX, PL and TRPL measurements. Figure 5.6(a,b) represent the AFM topography for the low and high pressure absorbers respectively, and give an indication of the average grain size and roughness. In coherence with the SEM measurements, larger and less homogeneous grains were observed at the surface of the high pressure sample ($\approx$ 95 nm) compared to the low pressure sample ($\approx$ 80 nm). The surface electronic properties were studied by means of KPFM and the contact potential difference maps (CPD), associated to the topography maps are displayed in Figure 5.6(c,d). The CPD is here associated to the difference between the workfunction (WF) of the sample and the WF of the KPFM tip, divided by the elementary charge e (see section 2.2 of Chapter 2), and for all of KPFM measurements of this thesis, the potential was applied to the sample, making an increase of the CPD, an increase of the sample WF.

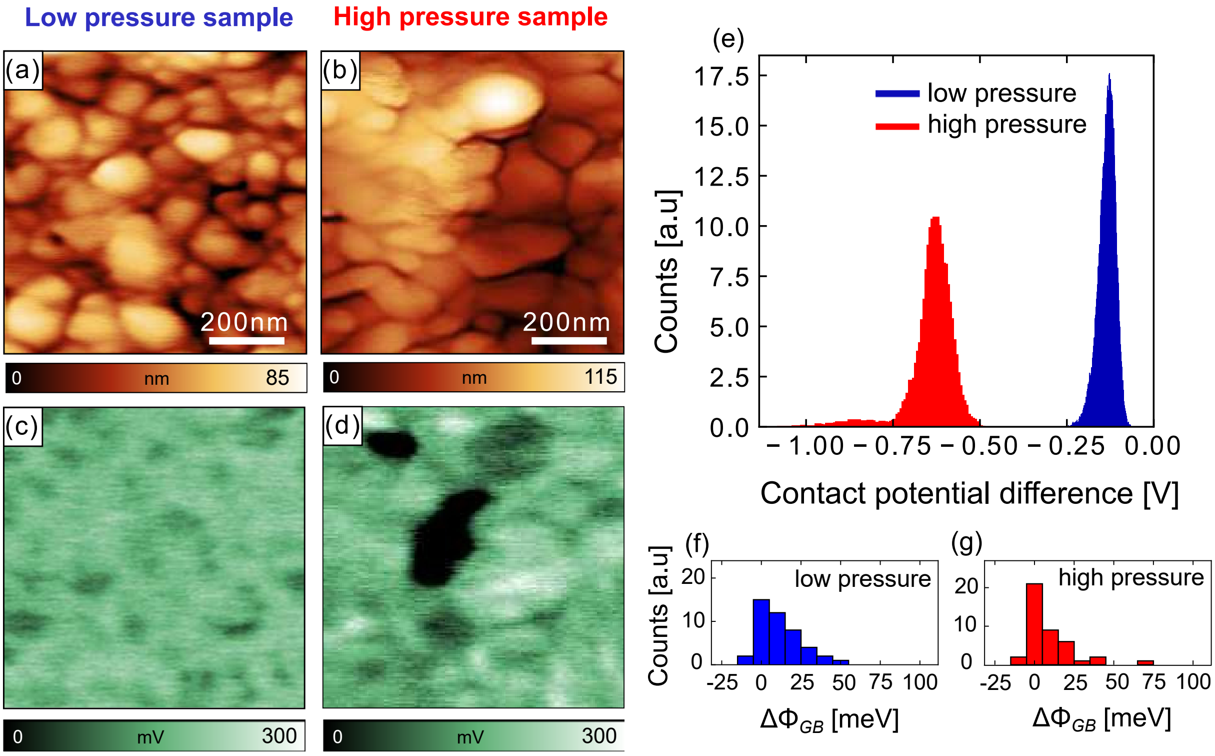

Figure 5.6: Topography of $MAPbI_3$ absorbers grown at (a) p_{low} and (b) p_{high} and their respective contact potential difference maps (c,d). The same scale bars have been used for ease of comparison. (e) Distribution of the CPD extracted from (c) and (d). (f,g) Grain boundary (GB) band bending for (f) p_{low} and (g) p_{high}, obtained via extraction of line profile from the CPD map. Δ_{GB} corresponds to the difference between the average CPD of two adjacent grains and the CPD of the GB that separate them.

The CPD map of the p_{low} absorbers did not show much variations with a relatively homogeneous surface, electronically speaking. Some darker regions could be observed but only limited to a difference in WF of about 50 meV, which is small and should not have an impact on the local band alignment with the top extraction layer. In comparison, the p_{high} absorbers presented a much less homogeneous surface, with regions having much lower WF (or CPD) compared to the rest of the absorber's surface (represented by the dark large patches in Figure 5.6b). The difference ranged from a hundred meV to several hundreds of meV (350 meV in average), which can become problematic when thinking about the deposition of an extraction layer with defined energetics on top of this surface. The CPD distribution of both absorbers can also be used to depict the observed differences

(Figure 5.6). The FWHM at p_{high} was on average 1.8 smaller than at p_{low}, indicative of the homogeneity, and a long tail at low CPD values could be discerned for the high pressure sample, which corroborated the existence of a bi-modal distribution of the WF at p_{high}. From a large set of samples, the regions exhibiting much lower WF than the rest of the surface represented $\sim$ 10 % of the $MAPbI_3$ surface (where the threshold was defined as CPD values smaller than 150 mV compared to the average CPD of the surface). From the previous EDX and XRD measurements, the KPFM measurements indicated that the formation of these low WF regions were related to the excess of MAI in the chamber, the high I/Pb ratio (iodine in excess) and the additional strain incorporated in the lattice. However, such large variations in WF can originate from different chemical or physical variations. Assuming a homogeneous surface bandgap, a reduced WF can stem from a higher doping, a different number of surface sates or surface dipoles, linked to different surface terminations or surface defects. A lower WF can also be linked to a low electron affinity and therefore two distinct materials at the surface (see section 1.3 of Chapter 1 for more details).

As the absorbers grown at p_{high} presented much higher PLQY and longer effective lifetimes, possibly arising from a passivation within the bulk or at the surface, the grain boundary (GB) band bending (BB) was studied. To do so, the CPD difference between multiple grains (between 50 to 100) and their adjacent GB was extracted from the line profiles of the CPD maps (Δ_{GB}). A positive value would be synonym of downward BB from grains to GB, and a negative value would be synonym of upward BB. An example of how Δ_{GB} was extracted is presented in Figure E.4 in the appendix chapter 5 E.5. One has to note that even if Δ_{GB} was extracted with great caution, it remains a qualitative value and an upper bound of the grain boundary band bending. The two GB band bending are depicted in Figure 5.6(f,g) for the low and high pressure case respectively. Most of the grain boundaries did not have a measurable BB for both samples, as the resolution limit of the KPFM is $\sim$ 10 mV. The maximum observed variation was in the order of 50 mV and a preference for downward BB was observed. The low BB (90 % of Δ_{GB} lies within $\pm$ 25 mV) is insignificant and cannot cause electronic barriers to prevent charge carriers to recombine at the GBs, as kT at room temperature is already in the order of 25 meV. Therefore, the better optoelectronic performances did not stem from a passivation of the grain boundaries at the surface due to the excess of MAI in the chamber at p_{high}, but most likely to better bulk properties.

5.3.2 MAI pressure-induced structural changes

The origin and nature of the observed low WF regions together with the reason why the fabricated devices did not perform according to the measured optoelectronic properties are still yet to be understood. To that end, high-resolution XRD was performed on a thicker high pressure sample, which was $\sim$ 870 nm-thick compared to the rest of the samples which were $\sim$ 400 nm-thick (as measured by profilometer). If the low WF regions should arise from a secondary phase, increasing the thickness should lead to a better signal-to-noise ratio when performing XRD. Figure 5.7(a,b) represents the KPFM images (topography and CPD maps) of the thicker p_{high} absorber, where the same low WF regions could again be discerned but with what appeared to be a better crystallinity and more facetting as they could be closely linked to grains in the AFM map.

The high resolution X-ray diffractogram of this thicker sample is depicted in Figure 5.7c together with the XRD measurements of the thinner absorber previously discussed in the KPFM section (Figure 5.6b).

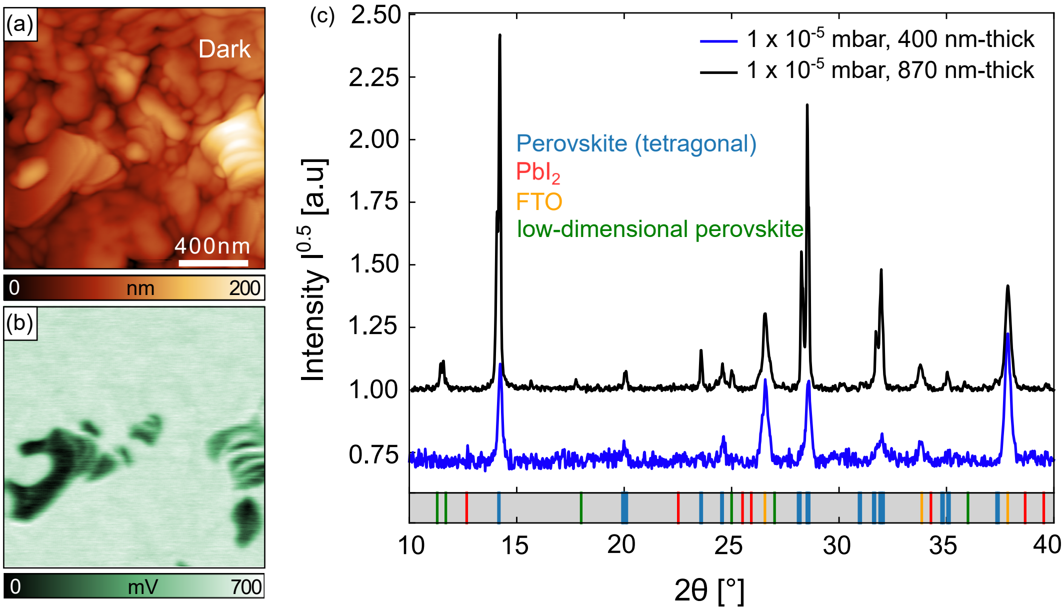

Figure 5.7: (a) AFM topography of a thick (~ 870 nm) absorber grown at p_{high} and its (b) associated CPD map. (c) X-ray diffractogram of the absorber depicted in (a) and the thinner (~ 400 nm) absorber presented in Figure 5.6b. The peak were identified using PDF 01-084-7607 (ICDD, 2018) for tetragonal $CH_3NH_3PbI_3$ and reference [374] for the LDPs.

The color-coded lines under the x-axis was added to indicate the position of the perovskite, substrate (FTO) and of possible secondary phases' reflexes. Independent of the thickness, all tetragonal peaks of $MAPbI_3$ were identified and no secondary PbI_2 could be discerned, suggesting fully-converted perovskite thin films. However, the thicker p_{high} absorber presented reflections that were not coherent with the tetragonal structure of $MAPbI_3$ but which were in excellent agreement with XRD results discussed by Song et al. [374]. In their work, they investigated the structural properties of $MAPbI_3$ by varying the compositions of MAI and PbI_2 and proposed a phase diagram (Figure 5.8a). Around a corresponding I/Pb ratio of 2.9 to 3.1, the tetragonal $I4/mcm$ (β) phase of $MAPbI_3$ is dominant (Figure 5.8b) until temperatures of 60°C, where the quasi-cubic (α) phase takes over. As the MAI concentration increases, so does the I/Pb ratio and, between values of 3.2 and 3.5, the excess of MAI creates stacking faults within the perovskite, which still remains as a 3D crystal but this phase ($\alpha\,'$) is indistinguishable from the tetragonal and quasi-cubic (β and α) phases in XRD.

When the MAI concentration is further increased, the $(PbI_6)^{4-}$ units can build up into 2D perovskite sheets (as well as 1D chains and 0D quantum dots if it is even more increased). These 2D perovskite sheets can also be referred to as low-dimensional perovskites (LDPs, δ phase) (Figure 5.8c) and as they are separated by a monolayer of MA^+ cations, some XRD peaks shift to lower angles, which enables their identification via XRD. From the work of Song et al. [374], it can be suggested that the p_{high} absorbers, with an excess of MAI and an over-stoichiometric I/Pb ratio, present traces of LDPs around 2θ angles of 11°, 25° and 36° (green lines in x-axis of Figure 5.7c). As the SPSs cannot be distinguished from the $MAPbI_3$ 3D cyrstal structure, it can be assumed that the p_{high} absorbers lie in the $\alpha\,' + \delta$ phase depicted in Figure 5.8a where both SPSs and LDPs co-exist in a 3D-2D mixed crystal structure.

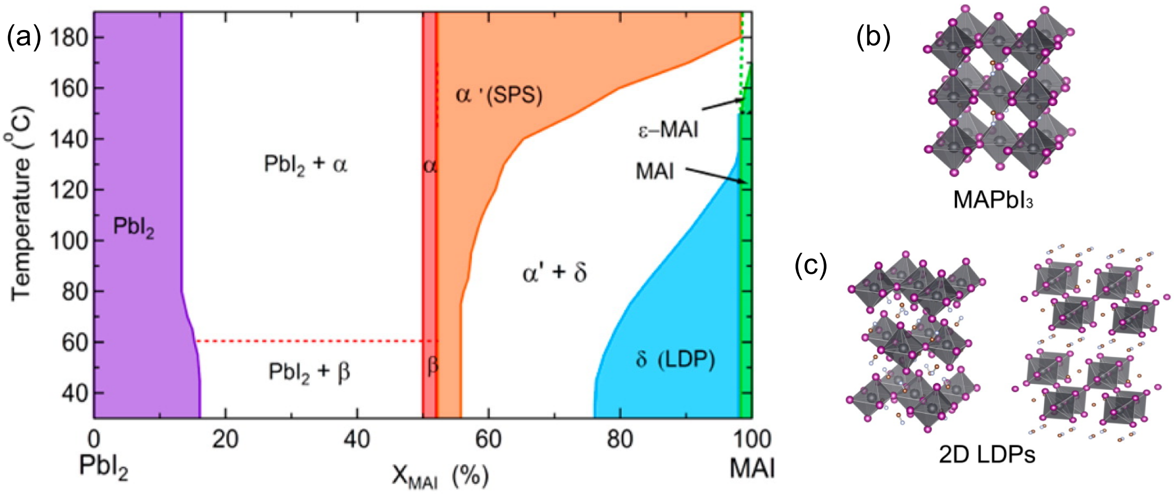

Figure 5.8: (a) Phase diagram for $MAPbI_3$ proposed by Song et al. (b) Crystal structure of $MAPbI_3$ perovskites (3D) and (c) 2D low dimensional perovskites (LDPs). The α phase refers to tetragonal $P4mm$ phase, β corresponds to the tetragonal $I4/mcm$ phase, α' is the stacked perovskite sheet (SPS) phase, δ is the LDP phase and ϵ the evaporation of MAI. Reproduced in part with permission from [374], Copyright 2015, American Chemical Society.

The observations of LDPs in the XRD pattern together with the KPFM measurements displaying low WF regions covering 10 % of the surface therefore suggest that these low WF areas are the signature of LDPs condensed on top and probably in the bulk of the p_{high} $MAPbI_3$ absorbers due to the excess of MAI concentration when using a high MAI vapor partial pressure during growth. As a way to verify that the low WF regions are linked to LDPs, one could reduce the I/Pb ratio such that the LDPs assemble completely into the 3D crystal structure and the δ phase vanishes. This is already observable when lowering the MAI partial pressure to p_{low} where no low WF regions in the KPFM and traces of LDPs in the XRD could be noticed. However, another option is to take a sample grown at p_{high} and anneal it at various temperatures to remove the MAI in excess and reduce the I/Pb ratio, triggering a phase change. This will be discussed in the next subsection together with an extensive study on the degradation effects caused by annealing in the case of p_{low} and p_{high} absorbers.

5.3.3 Annealing-induced variations in the absorbers

After the KPFM measurements on the as-grown samples (both low and high pressure), the samples were transferred back to the N_2-filled glovebox without air exposure and annealed at different temperatures in a nitrogen environment, and therefore without a surrounding MAI vapor pressure. The temperature was measured via a thermocouple attached to the surface of a dummy FTO substrate, placed next to the $MAPbI_3$ samples. The annealing environment is important to note as the perovskite composition will be altered differently depending on this environment. For example annealing in a methylamine environment has been reported to reduce surface impurities at the GBs, resulting in reduced recombination and better device performances [185]. Air annealing has also been demonstrated to be more efficient than nitrogen annealing, due to an improved crystallization with enlarged grains and removal of water upon annealing [375]. On the other hand, high temperatures (sometimes already at 100 °C) can degrade $MAPbI_3$ thin films by evaporating CH_3I and NH_3 and leaving residual PbI_2 [95, 376].

Figure 5.9 represents the KPFM topography and CPD maps of the p_{low} $MAPbI_3$ absorber at various stages: room temperature, and after nitrogen-annealing at 100 °C, 120 °C and 130 °C. Annealing at 100 °C did not increase the grain size and the electronic landscape remained the same, with relatively homogeneous surfaces. After annealing at 120 °C, the surface changed and larger grains with slightly higher WFs started to form (which appeared brighter in the CPD map of Figure 5.6f). The bi-modal distribution of grains indicated the start of the degradation of the sample but only a PbI_2 secondary phase could be observed in the XRD measurements after the annealing at 130 °C (Figure E.5a of appendix chapter 5 E.6). At that temperature, the KPFM topography and CPD maps (Figure 5.6(g,h)) exhibited a deterioration of the surface of the p_{low} absorber without clear observable grains. Higher annealing temperature (150 °C) resulted in a completely deteriorated surface, with the absorber turning into a yellow color and the disappearance of the $MAPbI_3$ peaks in the XRD together with the only occurrence of the PbI_2 peaks, therefore suggesting MAI evaporation.

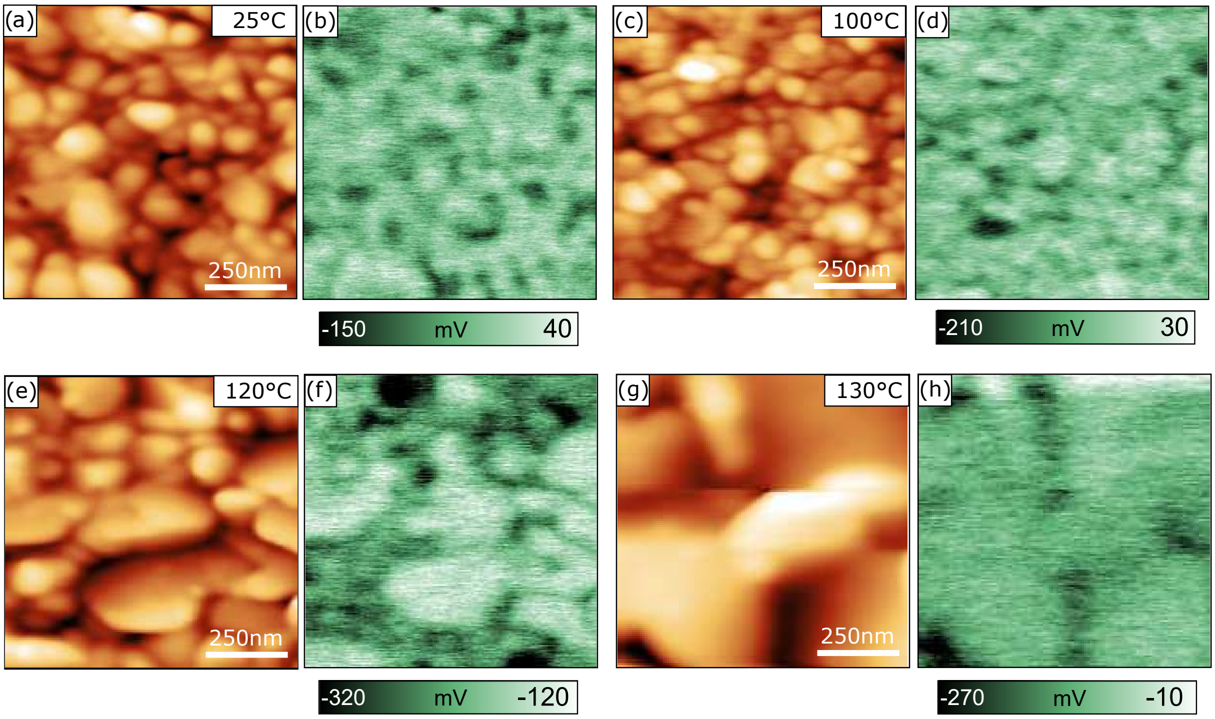

Figure 5.9: AFM topography (a,c,e,g) and CPD maps (b,d,f,h) of a p_{low} absorber at room temperature and after nitrogen-annealing at 100 °C, 120 °C and 130 °C respectively.

Concerning the high pressure sample (p_{high}), an increase of the grain size was noticed (Figure 5.10(a,c,e)) and EDX showed a reduction of the I/Pb ratio from 3.9 for the as-grown sample to 3.4 after the annealing step at 120 °C, which should lead the absorber to be within the α' phase where SPSs would still be present but the LDPs non-existent because converted into 3D $MAPbI_3$. The grain growth is often reported to be triggered by the use of vapor upon annealing [185, 377, 378]. However, in the present case, the MAI was incorporated during the co-evaporation procedure and the annealing performed only under nitrogen atmosphere. As the enlargement of the grains was not noticed for the p_{low} absorbers, the suggestion is that the excess of MAI introduced for the p_{high} samples acted as a flux agent for recrystallization, due to the splitting off of the iodine and methylamine upon external stimuli such as heat. This indicated a relatively low barrier for atomic motion and grain coarsening in those p_{high} absorbers, indicating potential adverse effects on the intrinsic stability of these absorbers.

After the 100 °C annealing (Figure 5.10b), the CPD maps still exhibited traces of low WF areas related to LDPs but they were only covering about 3 % of the surface (compared to 10 % at room temperature). After the annealing step at 120 °C, they had completely vanished and dark regions observed in the CPD map (Figure 5.10d) were within the 50 mV range, already observable in the p_{low} absorbers. At higher temperatures, such as the 130 °C image presented in Figure 5.10f, a mixed phase appeared, where MAPbI$_3$ probably coincided with PbI$_2$, only perceived in the X-ray diffractograms at 140 °C (Figure E.5b of appendix chapter 5E.6), and a bi-modal distribution of the grains could be detected, with the appearance of elongated grains in an overall noisy acquisition signal.

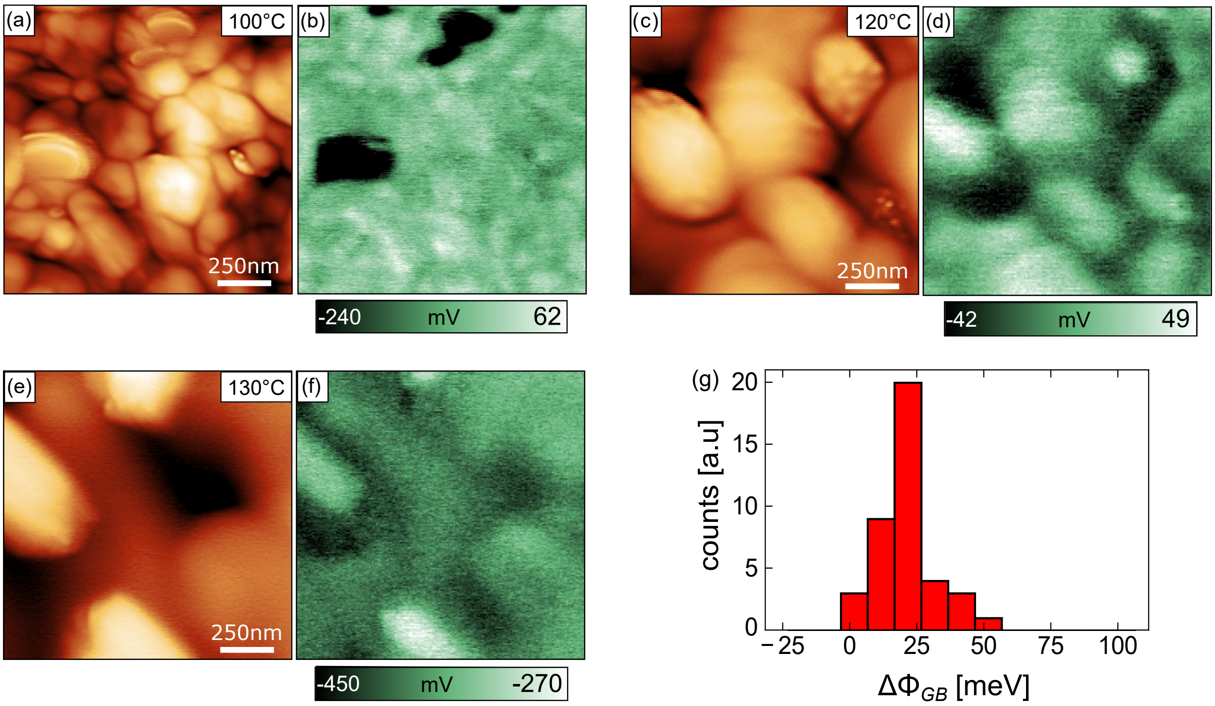

Figure 5.10: AFM topography (a,c,e) and CPD maps (b,d,f) of a p_{high} absorber after nitrogen-annealing at 100 °C, 120 °C and 130 °C respectively. (g) Grain boundary band bending of a p_{high} absorber at 120 °C.

Δ_{GB}, referring to the GB band bending, was again measured throughout all annealing steps. While no clear band bending could be observed for the as-grown p_{high} absorber, after the 120 °C annealing, a majority of grains displayed GB downward BB (also visible in Figure 5.10g), with an average value centered at 25 mV but also much more values exceeding 40 mV. This could potentially have adverse effects on charge extraction due to either preferential pathways for electrons to recombine non-radiatively or barriers for holes.

Generally speaking, nitrogen-annealing showed to be degrading both p_{low} and p_{high} MAPbI$_3$ films, which could be anticipated as no methylamine vapor was used during the annealing steps to make up for the continuous loss of evaporated MAI and reduction of MAPbI$_3$ towards PbI$_2$. Nevertheless, the intrinsic stability of the absorbers had to be studied in order to determine how the LDPs and SPSs, introduced by the MAI in excess, influence the quality of the p_{high} films. Initially showing better optoelectronic properties, even though stacking faults were introduced in the lattice, annealing at temperature above 120 °C demonstrated the possibility to remove the low WF areas associated to the LDPs.

TRPL measurements in air were also performed on both p_{low} and p_{high} absorbers after each annealing step and are presented in Figure 5.11. The absorbers presented are sibling samples to the ones used for the KPFM annealing study, i.e., they were grown during the same deposition run, which enabled for good complementary information even though the characterization environments used were different (UHV for KPFM and air for TRPL). The p_{low} absorbers exhibited a continuous drop of the effective lifetime over the different annealing steps (Figure 5.11a), which coincided with the visible degradation of the absorber in the KPFM images, which would clearly induce an increase in surface defects and therefore a higher degree of non-radiative recombination. However, even after 130 °C, $MAPbI_3$ films grown at p_{low} still retained an effective lifetime of a few tens of nanoseconds.

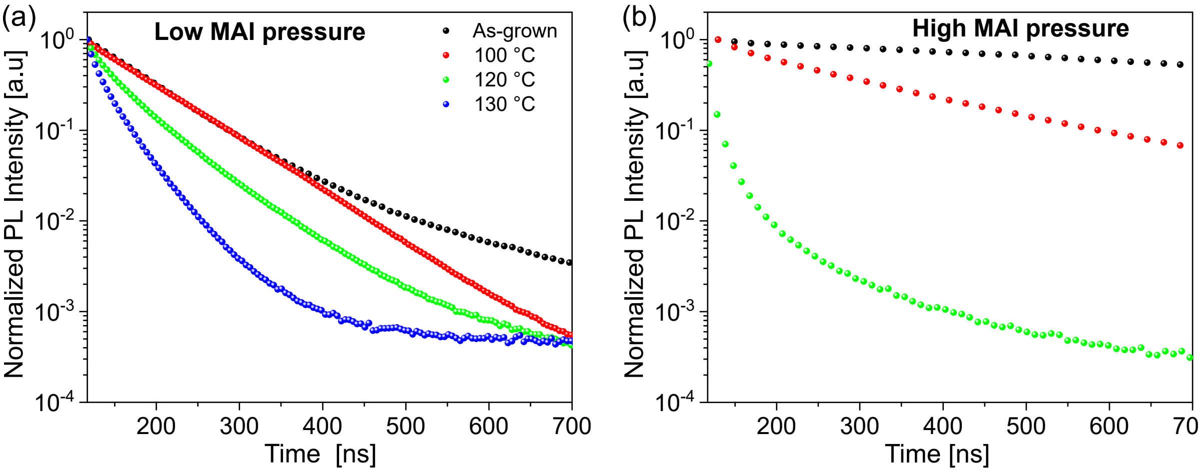

Figure 5.11: TPRL measurements in air for the different annealing steps for (a) p_{low} and (b) p_{high} absorbers, measured with laser power densities of 8.4×10^{-4} cm^{-2} (500 kHz) and 2.3×10^{-4} cm^{-2} (250 kHz) respectively, corresponding to charge carrier injections of 7.4×10^{14} cm^{-3} and 4.0×10^{14} cm^{-3}, which are relatively close to each other.

On the other hand, the high pressure sample displayed a different behavior (Figure 5.11b). Initially, the effective lifetime reduced slightly after the 100 °C annealing step, as it was the case at p_{low}. But the second annealing at 120 °C induced a much larger drop and after the 130 °C, the TRPL signal was barely measurable, indicating poor optoelectronic properties upon annealing. Fresher samples were fabricated and measured in nitrogen (Figure E.6a of appendix chapter 5E.7) and reflected the exact same behavior, where already at 120 °C, p_{high} absorbers would exhibit a drastic drop of their lifetime. PL measurements were in addition performed at the same injection as the TRPL measurements in nitrogen and revealed a clear drop of the PL yield together with a blue-shift upon annealing, from 1.60 eV at room temperature to 1.65 eV at 100 °C to finally reach 1.68 eV at 120 °C. The combination of the reduced effective lifetime, PL yield and blue-shift upon annealing coincided nicely with the appearance of the PbI_2 secondary phase in the XRD patterns and the degradation at the surface of the sample. Again this is coherent with the fact that annealing was performed with a lack of an MAI reservoir, which resulted in partial evaporation of the MAI and reduction towards PbI_2.

In addition to the previously-discussed qualitative KPFM analysis, calibration of the tip WF was carried out at each step in order to access the WF of the samples after annealing. HOPG was measured before and after each measurement of the studied sample, which led to the visible error bars in Figure 5.12. For the p_{low} absorber, the WF remained mainly the same from the as-grown conditions until the annealing step at 130 °C ($\sim$ 4.1 eV). The last annealing step at 150 °C led to a clear increase of the WF, which is assumed to be due to the evaporation of the MAI and transformation of $MAPbI_3$ towards PbI_2, which is a material with a higher bandgap (between 2.3 and 2.5 eV [340, 341, 342, 343]) and WF (6.35 eV from [138] (UPS), 4.6 eV from [379] (UPS), 5.2 eV from [380] (UPS), 5 eV from [381] (KPFM)) and which was also observed in XRD (Figure E.5b of appendix chapter 5E.6).

On the other hand, the p_{high} absorber exhibited an almost direct increase of its WF after annealing, from 4.2 eV at room temperature to 4.5 eV at 120 °C, proving that the surface energetics, comprised of surface terminations, defects and dipoles, varied considerably, which made the surface of the p_{high} absorber much less stable than the one grown at p_{low}. This was reflected by the TRPL measurements where a drastic drop of the effective lifetime was observed, potentially induced by an increase of the type of surface defects as well as density of surface states, which go hand in hand with an increase of the non-radiative recombination (SRH recombination for example).

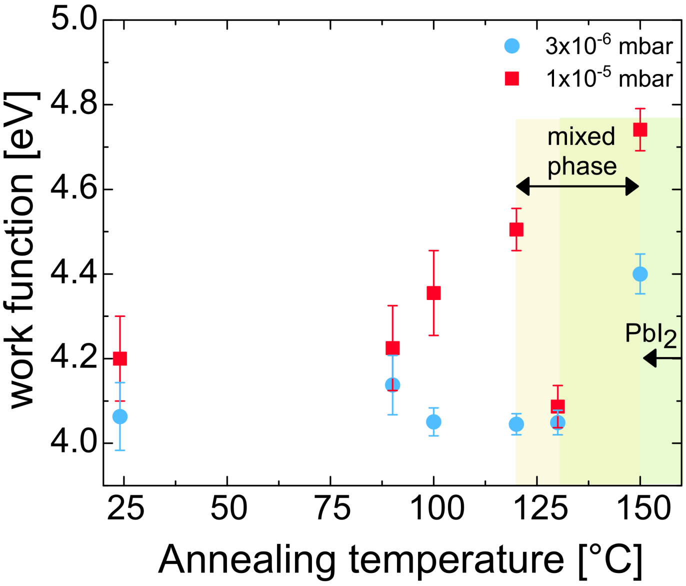

Figure 5.12: Calibrated workfunction of p_{low} and p_{high} absorbers for each annealing step.

An increase of the WF upon annealing can arise from multiple phenomena. If the surface was to remain intact (surface dipole and states), the bulk doping could induce variations in the WF. Annealing has already been reported to induce n-type doping [85], but this would come as a decrease of the WF. Calibrated PL and TRPL performed from room temperature to 120 °C at the same carrier injection (Figure E.7 of appendix chapter 5E.7) showed that the doping changed from 6.4×10^{15} cm^{-3} at room temperature, to around 1.0×10^{16} cm^{-3} after the 100 °C and 120 °C annealing steps, which goes in the same direction as Wang et al. [85]. However this observed change of the doping density is only responsible for a change of the Fermi level (E_C-E_F) (in the bulk and at the surface) of about 20 meV (obtained by using the doping equation 1.7 of Chapter 1). Therefore it is clear that variations of the bulk doping cannot explain the increase of the WF by 300 meV. The grain coarsening, removal of the LDPs together with the drop in the PLQY and effective lifetime upon annealing bring it to three possible origins:

- A change in the type of surface states, induced by different surface terminations as the LDPs are removed and the excess of MAI is used as a flux agent for recrystallization.
- An increase of the density of surface defects, due to the evaporation of MAI and visible via the drastic drop of the effective lifetime and PLQY.
- A change in the surface dipole induced by the previously listed causes.
- An increase of the electron affinity, due to a different phase or material at the surface of the absorber.

The latter stated origin is relevant as LDPs, mostly produced by the excess of MAI in the lattice, were removed upon annealing, which should alter the average electron affinity. Besides, photoemission measurements performed by Emara et al. on $MAPbI_3$ thin films with various composition showed that reducing the I/Pb ratio resulted in an increase of the ionization potential, which also induces an increase of the electron affinity when the bandgap is assumed unchanged [361]. This was coherent with the change in the I/Pb ratio from 3.9 to 3.4 after annealing at 120 °C. The likeliest situation however remains that all the aforementioned effects contribute to the variations of the WF upon annealing the p_{high} absorbers.

Interestingly after the 130 °C annealing step, the p_{high} absorber's WF dropped back to 4.1 eV, reaching the same value as for p_{low}, which could be explained by a complete change of both the electron affinity together with a change of the surface states. This coincided very well with the microscopic degradation visible in the KPFM measurements for both low and high pressure samples but also macroscopic degradation such as a change of color of the samples. At higher temperatures, the WF of both p_{low} and p_{high} absorbers increased, indicating a decomposition towards PbI_2, which has a higher WF. The difference between the WF at this specific temperature can be presumably assumed to be due to a different degree of decomposition.

From the previous set of experiments, it became clear that the excess of MAI resulting in the incorporation of low dimensional perovskites and stacked perovskite sheets into the 3D $MAPbI_3$ lattice had adverse effects on the stability on the absorber. Nevertheless, most of the previous experiments were performed in the dark (KPFM) or for a short period of illumination (PL, TRPL, XRD). As the studied films were to be part of a solar cell, the effect of prolonged illumination had to be investigated.

5.4 Pressure-dependent stability upon illumination

5.4.1 Topological and electronic stability

All the previously-discussed KPFM measurements were performed in the dark to preserve the samples and their surface from being altered, as light is known to cause structural variations in $MAPbI_3$ [382], such as degradation and iodine depletion [338, 383] but also redistribution of ions [384] that could skew the electronic surface landscape of the studied thin films. Nevertheless, as light is the essence of solar devices, the effects of illumination via a white LED ($\sim$ 10 mW cm^{-2}) on both the morphology and the contact potential difference were studied for a prolonged time after the dark measurements. Figure 5.13 represents the case of a p_{high} absorber first measured in the dark and where some LDPs can be visible as low WF areas (Figure 5.13b). The white LED was then switched on in Figures 5.13(c,d) and an intriguing phenomenon occurred.

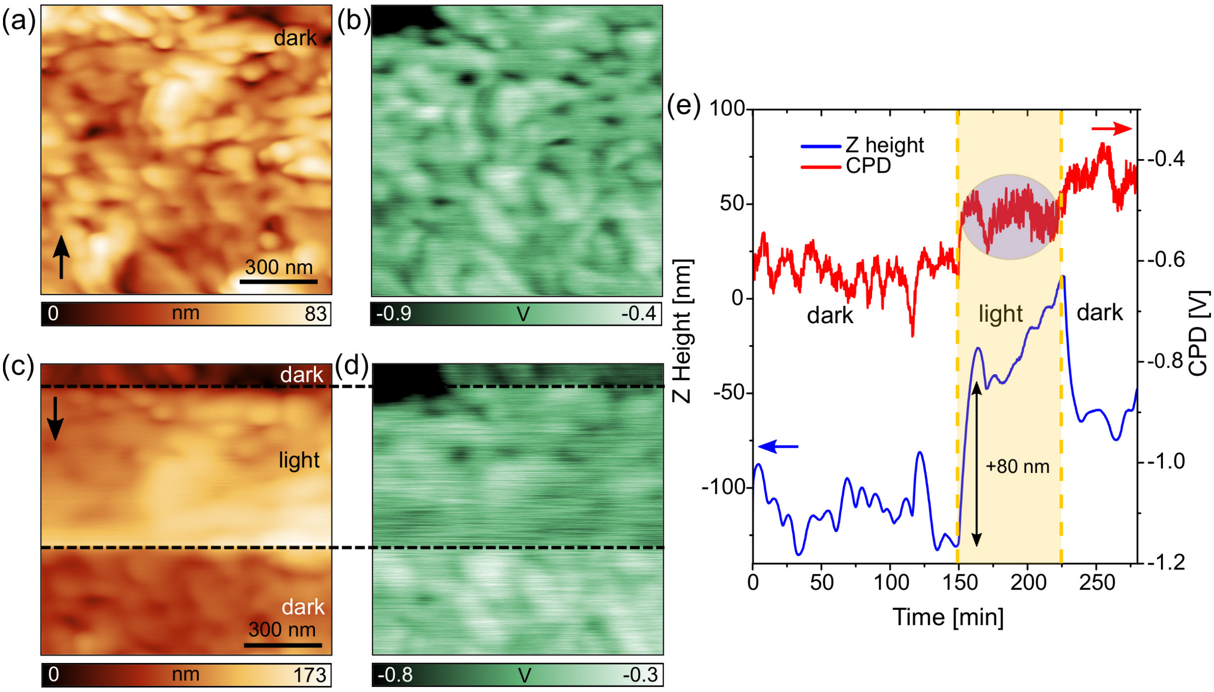

Figure 5.13: (a) AFM topography of a p_{high} absorber in the dark with its (b) associated CPD map. (c) AFM topopaphy on the same spot, in the dark, then upon illumination, and in the dark again. (d) Corresponding CPD map, the dashed lines represent the moment where the light was switched on and off. The arrows on the AFM topography maps represent the direction of the KPFM scan (e) Average extracted line profiles of (a,b,c,d) as a function of scanning time.

The AFM topography became blurry and displayed a fast change in the Z signal, corresponding to a change in the measured height of the sample. The latter changed by approximately 80 nm in a 3 minutes timespan before gradually increasing in a slower pace (Figure 5.13e). Variations of the Z signal upon illumination can originate from KPFM elements or electronics, even though 80 nm was a very large increase. Nevertheless to confirm or refute that the observed change in height was sample-related and not due to experimental artifacts, the same procedure was applied on samples composed of different materials, namely highly-oriented pyrolytic graphite (HOPG), gold, Cu(In,Ga)Se$_2$ and CuInSe$_2$. AFM and CPD maps, together with extracted line profiles of the samples studied, are presented in Figure E.8 of the appendix chapter 5E.8. For these different samples, a change of height between 10 to 20 nm has been observed, which remained considerably low compared to the 80 nm for the p_{high} MAPbI$_3$ thin film. This light-induced change in the Z signal visible for all samples was attributed to the direct and indirect heating of the cantilever, which expanded and resulted in a change of its resonance frequency, yielding in a shift of the Z component. Light was not directed on the tip, which therefore led to the suggestion that the reflectivity and roughness of the sample were responsible for the different magnitudes observed for the different materials, which was proved by seeing the largest change in height for the gold sample (Au:K), which has much higher reflectivity than p_{high} $MAPbI_3$.

The heating of the cantilever therefore did not induce such large changes in height, but other effects could cause this phenomenon, such as a redistribution of ions that would affect this electrostatic force. However, KPFM measurements in this thesis were always carried out with an active KPFM regulation, excluding this to happen. The last effect to take into consideration is the contamination of the tip due to a decomposition of the sample upon illumination, with adsorption of evaporated species by the KPFM tip. Zhang et al. have for example reported emissions of species like Br_2 and I_2 emitted from 2D and 3D perovskites when exposed to different wavelengths of laser, which resulted in a change of the WF of the tip in UHV [385]. In the different measurements performed throughout this thesis, the tip WF did change before and after illumination within the order of 50 to 100 meV, which is discussed extensively in the next chapter. However it seems non-realistic that adsorption of volatile species would yield such large changes in height, as light-induced variations in height also came without change of the topography and CPD quality (Figure E.9 of appendix chapter 5E.8).

Several groups have however reported the occurrence of a light-induced effect called photostriction in $MAPbI_3$ [116], MA-based films [202] and single crystals [386] but also mixed halide perovskites [387], which was however later subject to comment and response on whether or not photostriction was taking place in these thin films [388, 389]. Photostriction is referred to as a non-thermal phenomenon leading to a change of the lattice constant when a material is exposed to light. This would result in a change in height (and therefore Z signal) when measuring with AFM. The origin of photostriction depends on the material category [390], but a brief review can be found in section E.9 of appendix Chapter 5. As $MAPbI_3$ is an organic-inorganic semiconductor and because hydrogen bonding has been reported to exist between the amine group and the halide ions in perovskites [391, 392, 393], Zhou et al. proposed the following mechanism to interpret the photostriction in $MAPbI_3$. Upon above-band-gap illumination, a charge transfer will occur from the hybridized Pb 6s–I 5p orbital to the Pb 6p orbital, inducing the formation of weakly-bound excitons. This will result in the reduction of the electron density on the I site and will reduce its Coulomb interaction with the amine group, which will lead in the straightening of the Pb–I–Pb bond and a larger interatomic spacing. The latter will in the end be the cause of the deformation of the lattice upon illumination [116].

In addition to the fast increase in height upon illumination, a second, gradual but much slower, component can be discerned in the extracted line profile of the topography (Figure 5.13e), corresponding to the continuous heating of the KPFM system (cantilever and sample), which was measured to be at a rate of 1.2 nm/min in the Z direction for this specific sample. A similar value, 1.3 nm/min, was measured in the Y direction (bottom to top Figure 5.13c), which confirmed thermal drift in lateral directions as well, resulting in slightly elongated features. After the white LED was turned off, the fast component related to photostriction was almost entirely reversible, whereas the heating-induced component was recovering on a much longer timescale, resulting in a different height before and directly after illumination.

Therefore the previous discussions and experiments led to the conclusion that photostriction was occurring in the p_{high} absorbers and that the cause was most likely due to a weakening of the hydrogen bonding by the photo-generated carriers [116]. By measuring several different p_{high} absorbers under illumination with the white LED, an average height change of 70 ± 10 nm was measured and correlated to lattice expansion. Similarly, the response of p$_{low}$ absorbers to light was measured by KPFM. Figure 5.14 depicts the AFM topography and CPD map of the low pressure absorber, together with the extracted average line profiles. The exact same protocol of p_{high} was applied here and the position where the light was switched on and off is visible by the dashed lines. A much less pronounced increase of the height was observed here. As an example, illumination of this specific p_{low} absorber led to an increase of $\sim$ 20 nm. By performing this protocol on a multitude of low pressure samples, an average value of 12 ± 8 nm was obtained. It could be concluded that the samples grown at p_{low} only suffered from the previously discussed light-induced heating of the KPFM cantilever, as the magnitude was in the order of the one observed for all other materials (HOPG, gold, CISe).

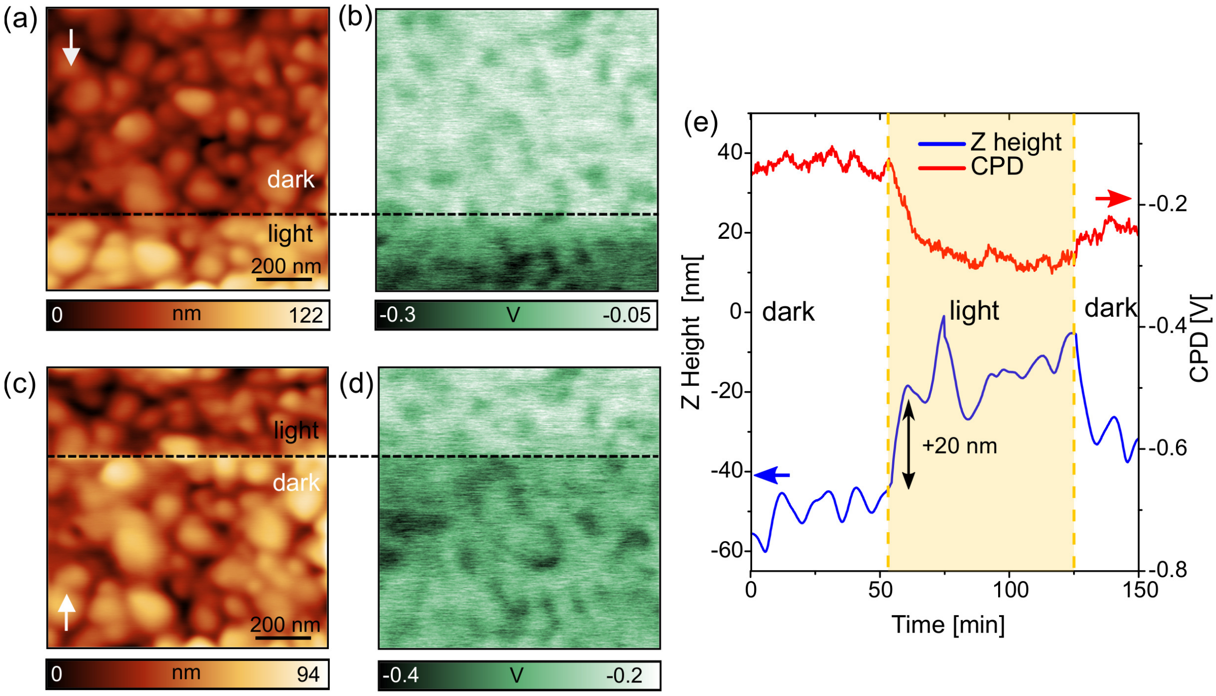

Figure 5.14: (a) AFM topography of a p_{low} absorber in the dark and under illumination with its (b) associated CPD map. (c) AFM topopaphy on the same spot, upon illumination then in the dark again. (d) Corresponding CPD map, the dashed lines represent the moment where the light was switched on and off. The arrows on the AFM topography maps represent the direction of the KPFM scan. (e) Average extracted line profiles of (a,b,c,d) as a function of scanning time.

By solely looking at the AFM topography maps, it can be foreseen that the LDPs, resulting from the initial excess of MAI during co-evaporation, induced the observed photostriction. It is however difficult to conclude that only the LDPs are the sole responsible for such photostriction. They were the only secondary phases observed in the XRD patterns but as already discussed, stacked perovskite sheets do not distinguish themselves from the MAPbI$_3$ 3D crystal structure but are highly likely to co-exist wit the LDPs in the p_{high} absorbers. The stacking faults introduced by the SPSs when two organic cation bilayers sandwich a variable number of metal halide layers could well be the dominant factor of photostriction in these MAI-rich thin films. When MAI is exclusively bound to the 3D perovskite lattice, as it is the case for the near-stoichiometric p_{low} absorbers, the photostriction effect does not exist.

Another interesting aspect of illuminating samples while carrying out KPFM measurements is the monitoring of the WF as a function of dark/light conditions but also illumination time. The two previous figures (Figure 5.13 and Figure 5.14) depicted the CPD maps for p_{high} and p_{low} absorbers in the different conditions and average line profiles were extracted and assembled next to each other in Figure 5.15. In both cases, two components were again observed as a function of illumination time. A very fast, almost instantaneous increase or decrease of the CPD, followed by a much longer increase or decrease. The first one can be associated to surface photovoltage (SPV), which is defined as the difference of the CPD directly after illumination and the CPD in the dark, and is related to the reduction of the surface band bending, due to the compensation of surface states by the photogenerated carriers, already discussed in sub-section 1.3.6 of Chapter 1. Different groups have already reported the build-up of SPV and resulting change in WF upon illumination [18, 19, 202, 263, 385] but a multitude of effects could produce the observed slow transients during illumination and after the illumination period (Figure 5.15), and will be discussed extensively in the next chapter, where an origin will be suggested.

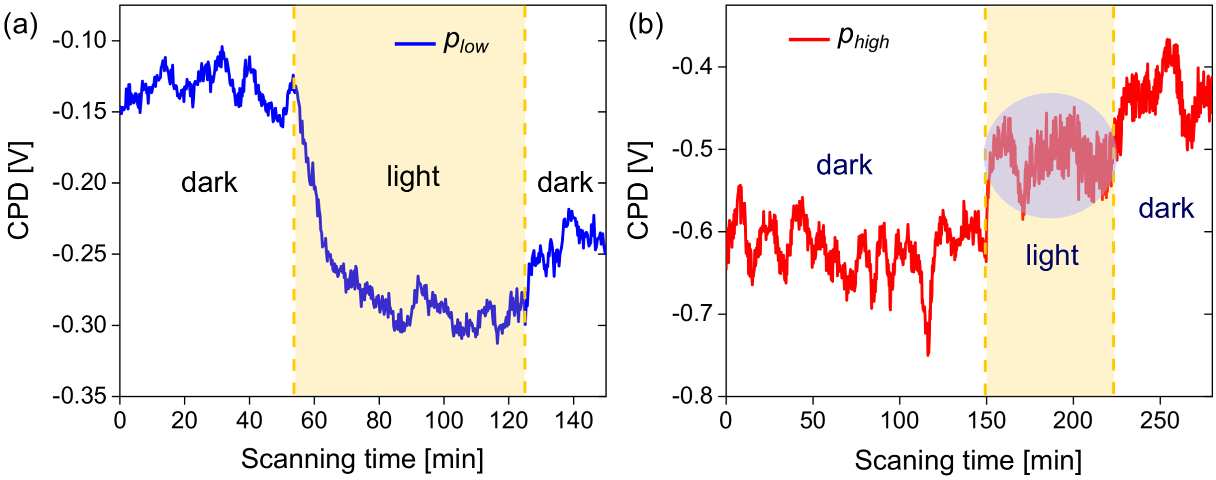

Figure 5.15: Extracted average line profiles from CPD maps of a (a) p_{low} absorber and (b) p_{high} absorber. The extraction comes from the images of Figure 5.14 and Figure 5.13 respectively. The yellow region represents the illumination timespan and the blue ellipse the region of noisy signal in the high pressure sample.

Nevertheless, differences can be noticed between the p_{high} and p_{low} samples. For the following results, the SPV will be calculated by subtracting the CPD value in the dark to the CPD value after a few seconds of illumination. Both the sign and magnitude of the SPV were different when using a low or high pressure. For p_{low} (Figure 5.15a), a small positive SPV of a few mV was measured, followed by a slow negative decay until saturation or equilibrium. For the p_{high} absorber (Figure 5.15b), a larger positive SPV of about +100 mV was measured, followed by a slow increase but almost instantaneous stabilization. These differences in the magnitude of the SPV indicate a different degree of surface band bending, strongly linked to surface defect states (acceptors and donors) and their density. This correlates well with the previously-discussed differences in WF, PL yield and effective lifetime. As already explained, the slower components in both absorbers are challenging to explain and require further experiments that will be performed in the next chapter.

In addition, the p_{high} absorber provided a CPD map and signal of much worse quality, depicted by the blurry and noisy image in Figure 5.13d and the noise highlighted by the blue circle in Figure 5.15b. The CPD signal (and topography) improved again directly after the light was switched on and these observations could not be made for the p_{low} samples. As all the scan parameters were constant, this noise level in the images can be attributed to a light-induced effect. From these measurements and the fact that similar behavior did not occur for p_{low} absorbers for the sample tip-sample distance, it can be suggested that the worsening of the KPFM quality upon illumination was most likely related to an increased ionic mobility caused by a reduced intrinsic stability of the p_{high} absorbers.

5.4.2 Optoelectronic stability

As solar cells are exposed to light for hours, it is essential to study the stability of the optoelectronic properties of perovskite upon prolonged exposure to illumination. As already discussed in section 1.2.5 of Chapter 1, light can be the cause of degradation depending on the environment used. In air, it has often been reported to promote the decomposition of $MAPbI_3$ into several compounds, like metallic Pb^0, followed by PbI_2 [107, 112, 113, 114]. In inert atmosphere, the optoelectronic properties often remain mainly the same [107, 112]. On the other hand, other works demonstrated the beneficial effect on the device performance of perovskite solar cells by light-soaking [103, 104].

To that end, the stability of p_{low} and p_{high} absorbers were investigated upon prolonged illumination with an above-bandgap laser illumination (532 nm). Both PL and TRPL were carried out on co-evaporated $MAPbI_3$ films on FTO substrate at a laser power density of 2.81×10^{-3} W cm^{-2} with a repetition rate of 1 MHz, corresponding to a carrier injection for TRPL of 1.24×10^{15} cm^{-3}. After approximately 15 minutes of measurements (several laser power densities for TRPL), the samples were exposed with a continuous illumination at a much higher intensity (3.4×10^{-2} W cm^{-2}) for 10 minutes and re-measured. The same procedure was repeated by gradually increasing the exposure time, to 25, 35, 45 and 55 minutes, which resulted in cumulative illumination times of 10, 35, 70, 115 and 170 minutes. As between each step, PL and TRPL were performed, this also added an estimated illumination time of $15 \times 6 = 90$ minutes in the end. Nevertheless, for the following discussion, the cumulative illumination time at the highest laser power density (3.4×10^{-2} W cm^{-2}) will be taken as reference. Figure 5.16 represents these measurements undertaken in a nitrogen-filled box for p_{low} and p_{high} absorbers that did not see other environment nor prior illumination. The PL measurements of the p_{low} sample (Figure 5.16a) displayed a very slight decrease in yield after the first 10 minutes of illumination but which was recovered upon further illumination and even ended up in a slightly higher PL yield in the end (170 minutes - pink). The TRPL measurements confirmed that the p_{low} sample was very stable upon prolonged laser exposure as only a negligible drop of the effective lifetime was observed (Figure 5.16b).

On the other hand, large variations in PL yield and TRPL transients were observed on the p_{high} absorbers. First, after 10 minutes of illumination, the PL yield almost dropped by a factor 3 and a shoulder peak around 1.62 eV appeared. Further illumination resulted in a partial recovery of the PL yield but with a clear aggravation of the shoulder peak together with a blue-shift of the main peak (towards 1.67 eV). Multi-band PL has been commonly observed in the perovskite community and different origins were reported, such as the coexistence of direct and indirect bandgaps [394, 395], differences within the bulk and surface electronic structures [233, 396, 397], or self-absorption amplified by internal reflection [398, 399]. Lastly, it is common to observe a blue-shift when lowering the

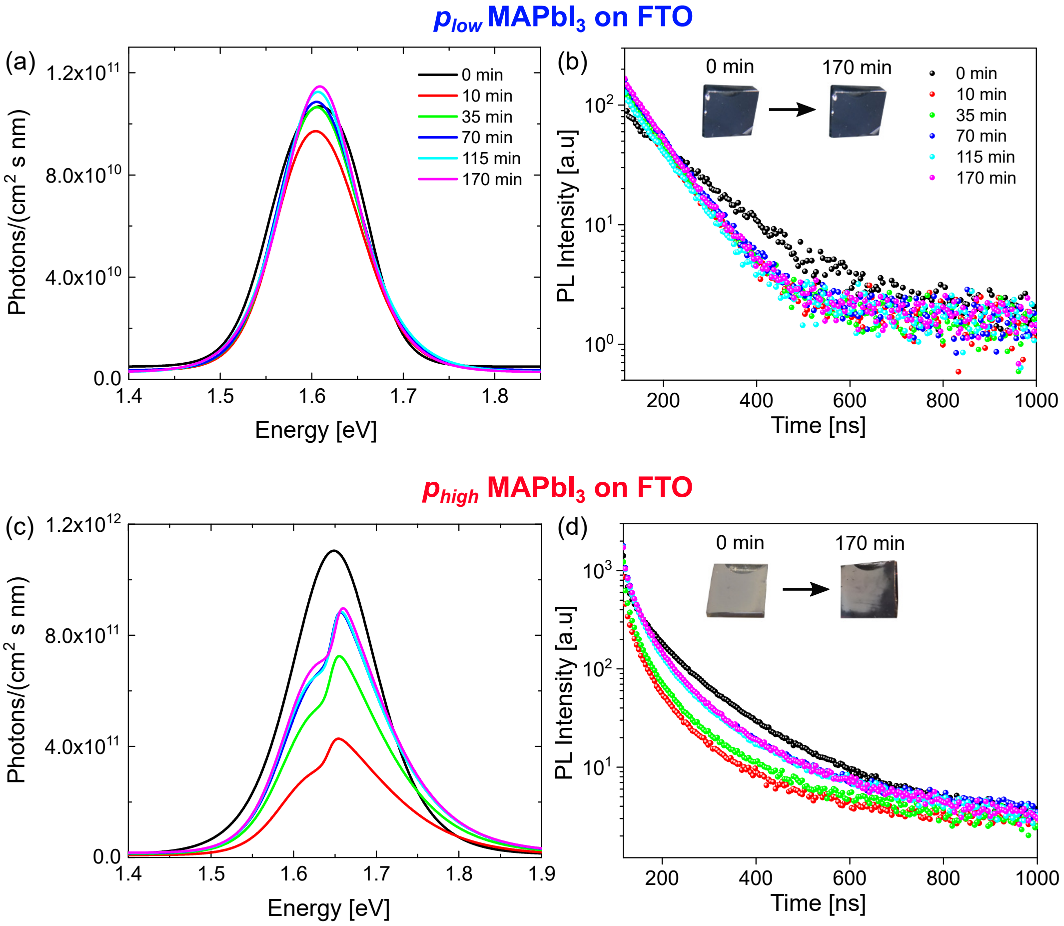

Figure 5.16: (a) PL and (b) TRPL measurements of the p_{low} absorber on an FTO substrate, performed in a nitrogen-filled box, at a laser power density of 2.81×10^{-3} W cm^{-2} with a repetition rate of 1 MHz, corresponding to a carrier injection for TRPL of 1.24×10^{15} cm^{-3}. The samples were first measured without prior light exposition and then were exposed for prolonged times using a laser power density of 3.4×10^{-2} W cm^{-2}. (c) PL and (d) TRPL for the p_{high} absorber under the same conditions as stated before. The insets represent the visible degradation of the samples upon prolonged illumination.

dimension of perovskite (quantum confinement) [400]. Two-dimensional perovskites have been reported to have higher PL peaks in the region of 600 to 740 nm (therefore a higher bandgap than the bulk $MAPbI_3$) [401] with 2D-layered $MAPbI_3$ nanosheets incuding PL peaks in a range of 514 to 763 nm [402]. Li et al. also proposed that the visible multi-band spectrum and the blue-shit observed on their $MAPbI_3$ films were the consequence of the presence of low-dimensional perovskite structures [403].

In the present case, the appearance of the double peaks in the p_{high} absorber only occurred after prolonged illumination and therefore could potentially be caused by light-induced degradation that would bring out the features of the LDPs and SPSs. However, no conclusion can be drawn from the sole PL spectra. TRPL measurements highlighted a continuous change of the TRPL transient, but mostly originating by the previously-discussed drop in the PL yield, as the extracted effective lifetime only sensibly dropped from 135 ns to 120 ns before recovering, and the transients' shape looked similar. As a side note, TRPL measurements were also performed on p_{low} and p_{high} films deposited on glass substrates, to remove the potential influence of an extraction layer (Figure E.10

of appendix chapter 5E.10). The laser power density used was slightly lower but the trend remained exactly the same, with this time a clearer initial reduction of the effective lifetime after 5 and 15 minutes, before recovery. This permitted to set aside any effect of charge accumulation, which could increase the effective lifetime, due to charge extraction layers. However, the shape of the curves for the high-pressure sample changed to a multi-exponential one upon prolonged illumination, which suggests an increase of the non-radiative recombination mechanisms [321].

From the previous set of measurements, it results that the intrinsic stability of $MAPbI_3$ thin films against light depends on its composition and structure. The near-stoichiometric p_{low} absorbers display a much better stability with quasi-constant PL yield, decay transient and effective lifetime, whereas large variations in all three can be discerned on the p_{high} absorbers, where an excess of MAI, LDPs and SPSs are present. Additionally, the insets of Figure 5.16(b,d) reinforce this idea, as macroscopic degradation at the surface of the high-pressure sample was visible after the illumination study whereas the one of the low pressure sample remained intact. At the position of the laser spot, and even on a larger portion of the p_{high} samples, the perovskite color changed, which suggested drastic changes in the absorber properties, which was again visible when performing the illumination study on glass substrates with a lower power density (insets of Figure E.10 of appendix chapter 5E.10).

As a complement, since these measurements were performed on a calibrated system using the same laser power density and on the same sample, doping could be extracted from the combination of PLQY and effective lifetime. Figure 5.17 depicts the summary of all three quantities for the two types of absorbers.

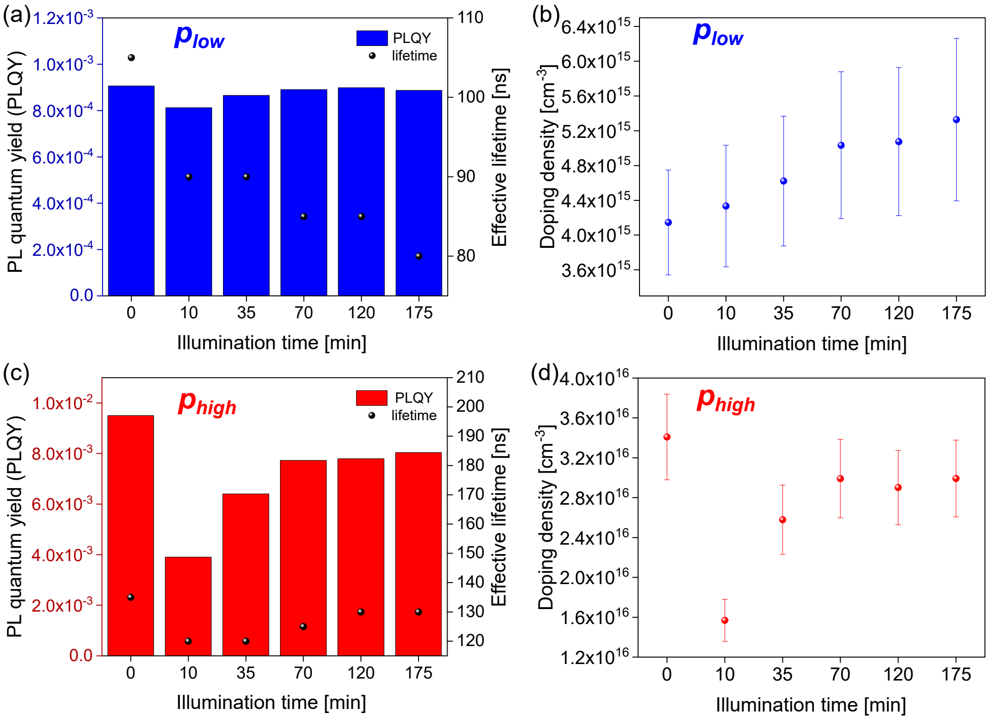

Figure 5.17: (a) PLQY, effective lifetime and (b) doping density for p_{low} $MAPbI_3$ absorber as a function of illumination time in a nitrogen environment. (c) PLQY, effective lifetime and (d) doping density for p_{high} $MAPbI_3$ absorber as a function of illumination time in a nitrogen environment.

The PLQY and effective lifetimes have already been discussed but have been displayed here to present the calculated and extracted values. The doping density stemming from the combination of these two quantities exhibit a negligible increase from 4.2×10^{15} cm^{-3} to 5.4×10^{15} cm^{-3} upon prolonged illumination for the p_{low} absorber. For the high-pressure case, the doping density slightly dropped from 3.4×10^{16} cm^{-3} to 1.6×10^{16} cm^{-3} after the first 10 minutes but recovered upon further illumination, following the trend of the PLQY and the effective lifetime. This showed again the difference in doping between the two types of absorbers (almost an order of magnitude) but also that the doping was sensitively the same with continuous light exposure in a nitrogen environment, which is primordial for the proper operation of encapsulated solar cells.

As already discussed, the optoelectronic behavior of $MAPbI_3$ thin films highly depends on its environment, and as the intrinsic stability of the absorbers against prolonged light exposure was studied in an inert environment (nitrogen), it felt necessary to investigate how these films performed under a more aggressive environment, i.e., in air with a standard relative humidity, where people have reported both an improvement or a worsening of the optoelectronic properties of $MAPbI_3$. Therefore sibling samples grown in the same deposition run as the previous ones were used and first measured in nitrogen to make sure they had comparable properties (PL yield and lifetime). They were then exposed to air and the exact same illumination procedure was applied for one p_{low} and one p_{high} sample.

Figure 5.18 represents the PL spectra and decay transients of these absorbers upon prolonged illumination in air. There were some clear deviations from the nitrogen study. First, the PL yield of the p_{low} absorber slightly increased after 10 minutes of illumination but even more after further light-soaking time. In addition, a shoulder peak could also be observed at 70 minutes and 170 minutes together with a blue-shift of the main peak. Similarly, the PL yield of the p_{high} absorber increased by a factor 3 after 170 minutes of illumination, with however a much pronounced deformation and broadening of the PL spectra, which still remains questionable as to what it is caused by, but the reader can read section E.10 of appendix Chapter 5 for a discussion about potential origins.

The TRPL decay transients of the p_{high} samples exhibited an up-shift with an improved effective lifetime (125 ns to 180 ns), coinciding with the previously observed improvement of the PL yield. Shin et al. reported that oxygen had an additional role of passivating agent of the metallic Pb-related surface states. After prolonged illumination in UHV to force the formation of these states (visible by a band bending in the UPS data), they exposed their $MAPbI_3$ sample to oxygen, and observed the recovery of its pristine energetic properties before the illumination [404]. Therefore, it can be suggested that the p_{high} absorbers have a higher density (or different types) of surface states, that get passivated by oxygen molecules or the formation of an oxygen superoxide [405], which resulted in the discernible improvement in effective lifetime. On the other hand, the p_{low} absorbers initially had few surface defects, and therefore the TRPL transients and effective lifetime did not change much upon exposure to air as no additional passivation was needed. This also agreed with the previous observations that the high-pressure samples had larger surface photovoltage than the low-pressure case, suggesting a higher surface band bending due to more surface defects or a higher density of surface states, which would be passivated and compensated by the oxygen treatment.

Once again, this proved the better intrinsic stability of the near-stoichiometric p_{low} $MAPbI_3$ films, which, upon combined oxygen and light exposure, could sustain their optoelectronic properties to a certain degree, while much larger variations in PL yield and effective lifetime were observed when a higher MAI partial pressure was used in the sample (p_{high}). The doping densities were not discussed here as they were only proving the points of other reports claiming that oxygen exposure induces p-type doping (linked to the increase of the PL yield) and that a reversibility could be achieved when storing the sample in an inert environment [114, 404, 406]. However if interested, the reader is directed to the detailed discussion in section E.10 of appendix Chapter 5.

p_{low} MAPbI$_3$ on FTO

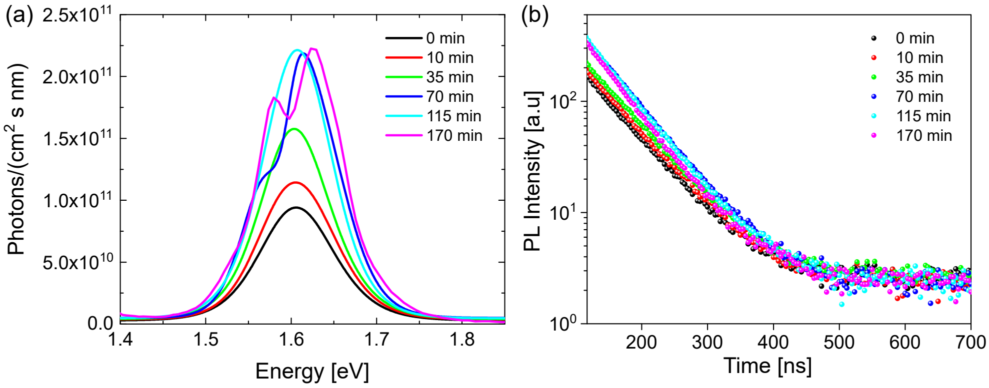

p_{high} MAPbI$_3$ on FTO

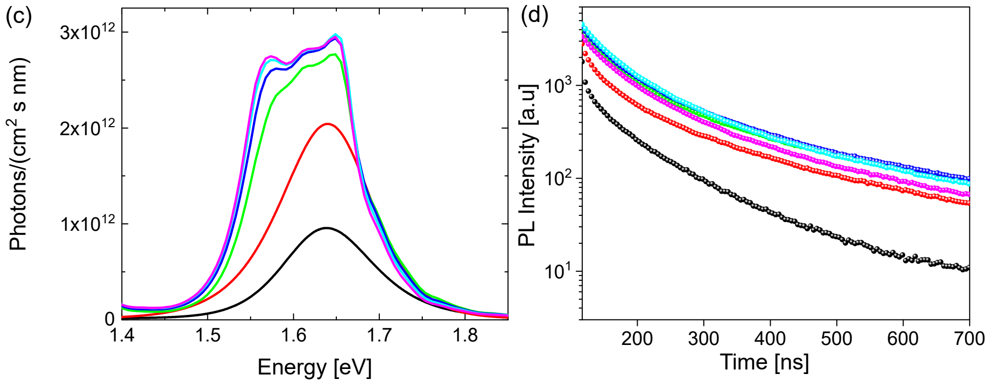

Figure 5.18: (a) PL and (b) TRPL measurements of the p$_{low}$ absorber on an FTO substrate, performed in air, at a laser power density of 2.81×10^{-3} W cm^{-2} with a repetition rate of 1 MHz, corresponding to a carrier injection for TRPL of 1.24×10^{15} cm^{-3}. The samples were first measured without prior light exposition and then were exposed for prolonged times using a laser power density of 3.4×10^{-2} W cm^{-2}. (c) PL and (d) TRPL for the p_{high} absorber under the same conditions as stated before.

5.5 Summary of Chapter 5

In this chapter, the effect of the MAI partial pressure on the intrinsic properties of co-evaporated $MAPbI_3$ was studied. By keeping a constant amount of PbI_2 and solely varying this pressure, it was demonstrated that the composition of $MAPbI_3$ absorbers could be tuned, from under-stoichiometric films to over-stoichiometric films. Structural fluctuations were revealed, with the presence of a PbI_2 secondary phase and broad peaks in the XRD diffractogram of Pb-rich films, and the appearance of the tetragonal splitting when stoichiometry was approached. Increasing further the MAI pressure resulted in the occurrence of strain in the lattice structure combined with additional texturing.

The optoelectronic properties were also shown to vary with the increase of MAI partial pressure, with a visible improvement in both, the PLQY and effective lifetime, induced by better bulk or surface properties. The calculated doping density also exhibited large variations from the near-stoichiometric absorbers (p_{low}) to the over-stoichiometric ones (p_{high}), with almost an order of magnitude of difference. However, the p_{high} absorber with better optoelectronic properties did not translate into better-performing solar devices and therefore the surface properties were cautiously studied.

KFPM measurements combined with high-resolution XRD revealed that using a higher MAI partial pressure led to the formation of low-dimensional perovskites (LDPs) and stacked perovskite sheets (SPSs), which introduced stacking faults in the 3D perovskite lattice. These LDPs were discernible by their much lower WF compared to the rest of the surface. Annealing at various temperatures of the samples were performed to study how the removal of these LDPs, by means of phase transition, would translate into variations of the surface energetics. It was shown that the p_{low} near-stoichiometric absorber had a much better intrinsic stability against temperature, while the p_{high} absorbers with incorporated-LDPs and SPS proved to have a poor stability. In addition, the optoelectronic properties of the p_{high} absorber worsen much faster than the ones of p_{low}.

The effect of light was investigated with KPFM and demonstrated that the excess of MAI in the form of LDPs promoted the occurrence of a photostriction effect, or lattice expansion upon illumination, as well as non-reversible changes in the surface energetics. The intrinsic stability upon light exposure was further studied by monitoring the optoelectronic properties of the different absorbers upon prolonged laser illumination. When measured in an inert environment, in nitrogen, the p_{low} absorber retained a constant PLQY and effective lifetime over several hours, while the PLQY and effective lifetime of the p_{high} absorber varied greatly. In air, the observed different trends in effective lifetime (slight decrease for p_{low} and increase for p_{high}) were most likely attributed to a larger amount of surface states for the high pressure sample, that were passivated by the oxygen molecules.

Overall, it was demonstrated that the intrinsic stability as well as the surface homogeneity and energetics strongly depend on the fabrication parameters used and the composition of the absorber. An excess of MAI in a $MAPbI_3$ absorber can initially induce better optoelectronic properties, but does not always yield higher efficiencies for devices. In this specific case, this was caused by the formation of LDPs and SPSs that promote higher doping, photostriction, ionic mobility, poor thermal and light stability as well as variations in the energetic landscape. These results highlight that the preparation method and composition need to always be taken into consideration when characterizing perovskites.

Chapter 6

Surface photovoltage, band bending and doping in MAPI

As observed in the previous chapter and reported in the literature, surface energetics of $MAPbI_3$, such as its WF, can be altered by light exposure. Upon illumination, surface photovoltage (SPV) occurs, which was already detailed in section 1.3.6 of Chapter 1. Measuring the SPV is interesting and can lead to the calculation of the surface band bending, when using different illumination intensities [204, 207].

Interestingly $MAPbI_3$ perovskites do not exhibit a simple fast SPV that takes place within micro-seconds but rather a multi-component SPV, where fast and slow transients succeed one another and can range from seconds to minutes, even hours. Several groups have observed this phenomena and correlated it to a combination of interfacial trap states and ionic migration [202, 203, 208, 209, 210]. In addition, the signs, magnitude and time-dependence of the CPD variations upon illumination were reported to be highly dependent on the substrate chemistry and its type (n- or p-type), as the latter can lead to different degrees of photo-conductivity [407], substrate-induced doping or substrate/perovskite interfacial band bending [169, 170, 171, 404]. However, most of the time, only one surface-sensitive technique is used to investigate the multi-component SPV, and an inert environment is critical to find the real cause. There is therefore a clear need to determine the origin of the multi-component SPV of non air-exposed $MAPbI_3$ by using several techniques in a clean environment.

Kelvin probe force microscopy (KPFM) and X-ray photoelectron spectroscopy (XPS) are two surface-sensitive methods that access different surface energetic quantities, the WF and the core level binding energies (BE) respectively. They are complementary and useful techniques, even if their detection depth differs (atoms at the surface for KPFM and a 10 nm-depth for XPS). On the other hand, the presence of surface dipole renders the KPFM interpretation difficult, and radiation from X-rays is well known to degrade hybrid halide perovskites [408, 409, 410].

In the first section 6.1 of this chapter, KPFM and XPS will be used on $MAPbI_3$ on different substrates (n and p-type) to shed light on the origin of the very long variations of the WF upon illumination, which was previously observed in Chapter 5. The calibration of the KPFM tip, the decrease of the CPD and of the BEs of the core elements will show that the photo-induced degradation of $MAPbI_3$ and evaporation of I_2 is the responsible for the multi-component SPV.

In the second section 6.2.3, the dependence of the SPV on the substrate will be studied to quantify the surface band bending. The combination of calibrated PL and TRPL will complement the previous measurements to demonstrate that $MAPbI_3$ cannot be highly n-type and that bending of the bands need to happen. Lastly, KPFM and calibrated PL and TRPL on $MAPbI_3$ with varying thicknesses and substrates will be used to investigate the substrate/perovskite interfacial band bending and draw energy band diagrams.

6.1 Origin of light-induced changes of the workfunction

6.1.1 Kelvin probe force microscopy investigation

In Chapter 5, KPFM measurements in dark and light conditions exhibited the presence of light-induced changes of the WF with fast and slow transients, suggesting that different physical phenomena were taking place in the $MAPbI_3$ perovskite films upon illumination. As mentioned in the introduction of this chapter 6, several groups have already linked it to different effects, but only using either KPFM or XPS, which renders the interpretation quite difficult due to the complex interplay between composition variations, ionic mobility, band bending...

To that end, near-stoichiometric $MAPbI_3$ absorbers with a thickness of about 400 nm were co-evaporated on 4 n-type substrates: fluorine-doped tin oxide (FTO), titanium oxide (TiO_2), tin oxide (SnO_2) and aluminum-doped zinc oxide (AZO), and 2 p-type substrates: nickel oxide (NiO) and poly(triaryl amine) (PTAA). Most of these substrates were provided by Tobias Abzieher [307]. These absorbers were referred to as p_{low} in the previous chapter and showed good intrinsic stability. Therefore the changes of their WF upon and after prolonged illumination were analyzed by UHV KPFM without exposure to air. Figure 6.1 depicts the topography and corresponding contact potential difference (CPD) maps obtained by KPFM in the dark of $MAPbI_3$ deposited on these 6 absorbers. The first observation concerned the morphology, with grain sizes that were mainly the same independent of the extraction layer used, with the exception of FTO and AZO which presented slightly larger grains. In addition, the roughness of the perovskite films was similar to the roughness of the substrate, where substrate with rougher surfaces (TiO_2 and FTO) yielded rougher $MAPbI_3$ films. The second observation was related to the CPD map, with the WF distributed within a range of $\sim$ 100 meV for all the samples (min: 90, max: 130), which led to rather homogeneous surfaces. In addition, no low WF areas, which were related to an excess of MAI and low-dimensional perovskites in Chapter 5, could be perceived, which was a first indication of the absorbers not being too over-stoichiometric (I/Pb ratio not above 3.3). All these KPFM measurements were calibrated by measuring a reference sample of highly ordered pyrolytic graphite (HOPG) with a WF of 4.6 ± 0.1 eV.

After imaging the previous samples in the dark, illumination with a white light-emitting diode (LED) with an estimated power density of 10 mW cm^{-2} was used to study the influence of the light on the WF for a prolonged time. Figure 6.2 represents the average CPD, extracted from the whole CPD map, of the different samples under different conditions: dark, followed by illumination and dark again after the illumination was turned off. The dashed lines represent the separation between the different conditions, and the yellow areas surrounding the CPD highlight the CPD regions where the light was

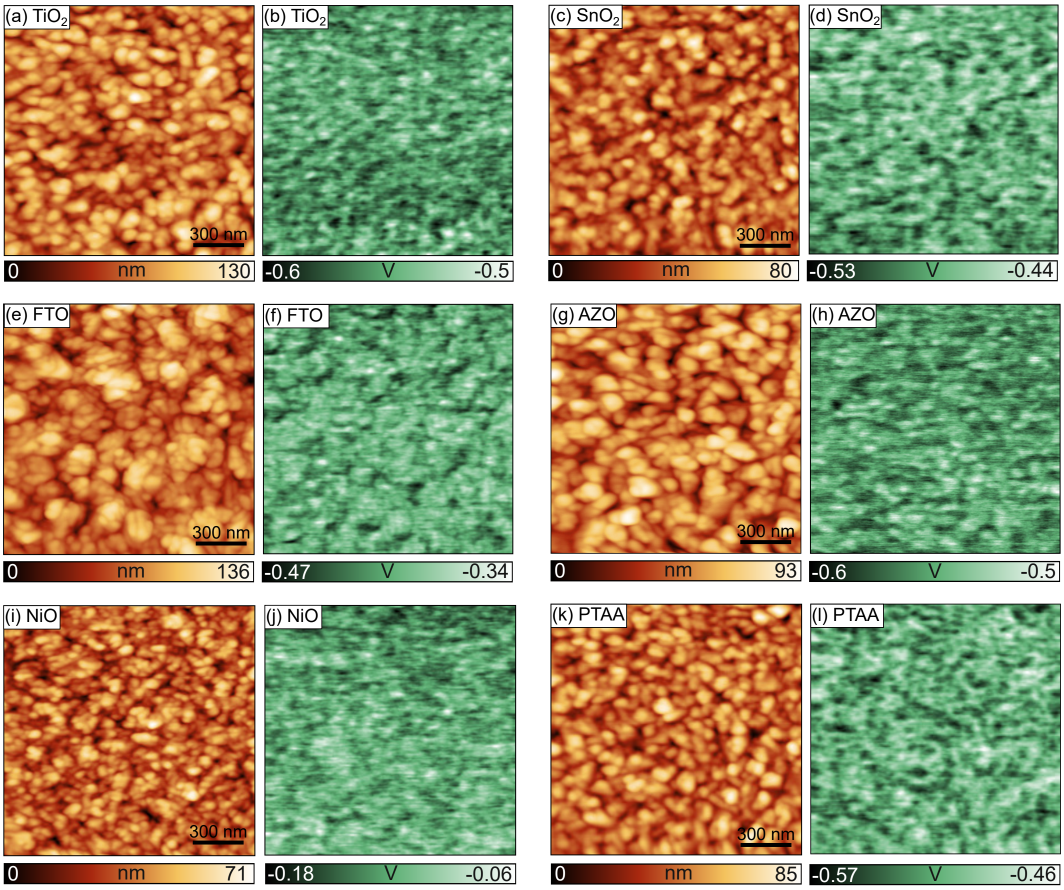

Figure 6.1: AFM topography measurements of $MAPbI_3$ absorbers grown on (a) TiO_2, (c) SnO_2, (e) FTO, (g) AZO, (i) NiO, (k) PTAA. (b,d,f,h,j,l) Corresponding CPD maps of (a,c,e,g,i,k).

switched on. The CPD of each sample in the dark was set to 0 V for better visibility and an easier comparison of the samples.

Firstly, a direct observation could be made: different components, or transients, existed upon illumination, with a first very fast change in the CPD, commonly known as surface photovoltage (SPV) and associated to the screening of the surface states by photogenerated carriers, and a second very slow-changing transient. Each individual evolution of the CPD upon illumination time can be found in Figure F.1 of appendix chapter 6F.1 for a better perspective of the different components. Upon switching the light off, the opposite effects were visible, i.e., fast and slow CPD changes but with the opposite sign.

The second observation concerned the sign of the SPV. For SnO_2 and TiO_2 (Figure 6.2a), the SPV was positive, suggesting an increase of the WF, coherent with the reduction of a downward band bending (BB). This reduction is caused by the compensation of a majority of donor-like surface states (positively-charged) by photogenerated carriers in an n-type or p-type semiconductor (see section 1.3.6 of Chapter 1). For the two other n-type substrates, FTO and AZO, the SPV was negligible, which could suggest that the intensity used did not permit to compensate either donor or acceptor states. It is important to note that both surface acceptors and donors can simultaneously exist [131], even if only one type of band bending is visible. For $MAPbI_3$ deposited on the p-type substrates (Figure 6.2b), NiO and PTAA, a positive SPV was easily discerned, leading again towards a reduction of a downward BB due to a majority of donor-like surface states.

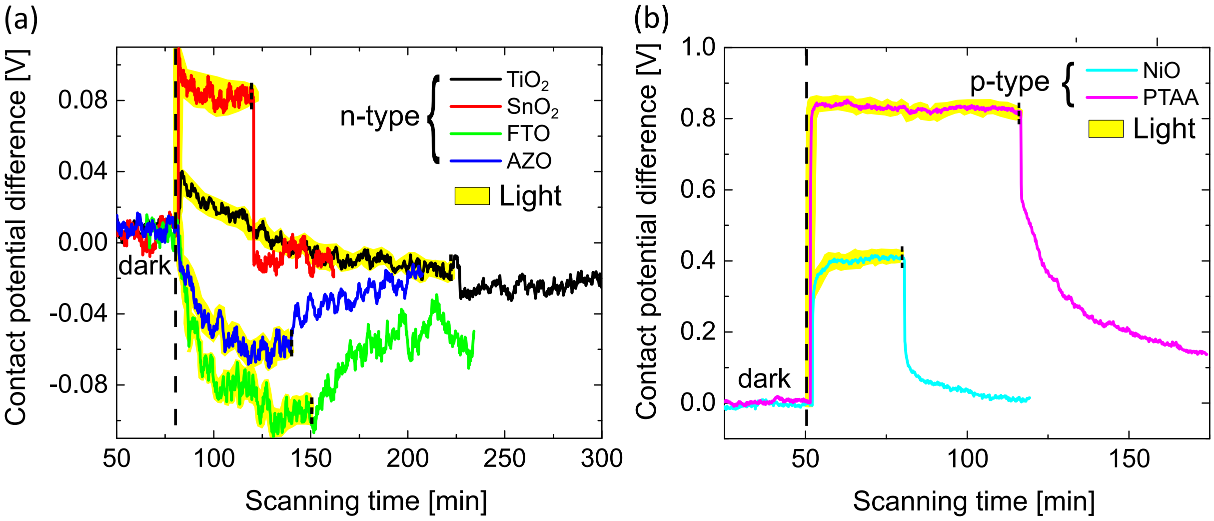

Figure 6.2: Extracted average contact potential difference (CPD) in the dark, upon illumination and after illumination for MAPbI$_3$ deposited on (a) n-type substrates and (b) p-type substrates. The dashed lines represent the moment were the light was switched on and off, and the yellow regions depict the illumination period. All the initial CPD values in the dark were set to 0 V for a better visibility of the trends and easier comparisons between samples.

Besides the sign of the SPV, which referred to the type of band bending occurring at the surface when the doping type is known, the magnitude of the latter was different for MAPbI$_3$ deposited on the substrates. To extract the SPV with the best precision possible, the raw data of the CPD maps were taken (Figure 6.3) instead of the average profile, leading to hundred of thousands of data points, but giving rise to a resolution between 10 to 30 ms (depending on the parameters used during the KPFM measurements), which was far greater than the 15 s step size of the average profile. The SPV values were extracted by taking the difference between the CPD after a few tens of milliseconds of illumination and the CPD in the dark, prior to any light exposure.

The extracted values of the SPV are reported in table 6.1. For the n-type substrates, the SPV values measured were relatively low, with a maximum of 65 mV extracted for SnO$_2$, 25 mV for TiO$_2$ and negligible values for FTO and AZO as the CPD change upon illumination was within the noise level or peak-to-peak ratio of the CPD signal. On the other hand, for the p-type substrates, the SPV values extracted were much greater, with 440 mV for PTAA and 215 mV for NiO. The difference in magnitude between MAPbI$_3$ deposited on n- an p-type substrates is interesting but can be explained by the fact that SPV takes into account multiple aspects such as light absorption and photo-generation of charge carriers, charge separation and transport, as well as recombination, trapping and emission of charge carriers. However, the magnitude of the different SPV would indicate a different degree of surface band bending, related to the type and density of surface states.

Abzieher et al. have reported that different crystallization mechanisms occur between MAPbI$_3$ grown on TiO$_2$, SnO$_2$ and MAPbI$_3$ grown on NiO, PTAA, which are the exact same substrates as in this study (as they were provided by their group). The first ones (n-type) had a preferred orientation (100) crystal planes whereas the latter ones (p-type) had preferred orientation along (110) and (111) planes. In the same work, they also demonstrated the consequence of these different orientations, such as the varying incorporation of MAI in the crystal lattice, which could result in larger segregation of PbI$_2$

Substrate	SPV (mV)
TiO_2	+25
SnO_2	+65
FTO	negligible
AZO	negligible
NiO	+215
PTAA	+440

Table 6.1: SPV for $MAPbI_3$ co-evaporated on different substrates, measured by KPFM using a white LED with a power of $\sim$ 10 mW cm^{-2}.

for TiO_2 and SnO_2 compared to NiO and PTAA, among other phenomena [307]. These results can also help in explaining the observed differences in SPV between n-type and p-type substrates, as different surface terminations, due to different grain orientations, will induce different surface band bending.

The third observation that one could retrieve out of the prolonged illumination KPFM study (Figure 6.2) was the difference in sign and magnitude of the CPD directly after the SPV component. For all n-type substrates (Figure 6.2a), the second slow-changing transient was a slow decay of the CPD with illumination time, followed by a plateau where the CPD seemed to have reached its equilibrium value under illumination. The decay time and magnitude before the plateau depended on the substrate, where for example FTO/$MAPbI_3$ showed to be the sample where the decay was the largest (-80 mV in 80 minutes) whereas TiO_2/$MAPbI_3$ had the longest decay (-60 mV in 145 minutes). Contrarily to the n-type, both p-type substrates presented a direct increase of the CPD after the SPV component, followed again by a plateau (with a distinction for PTAA, which will be discussed later on).

Zoom-in regions of the high-precision CPD measurements of SnO_2 and PTAA are depicted in Figure 6.3 and shed a bit more light on the different components present in the CPD signal upon illumination, with a millisecond resolution. Note that these two samples are representative of all combined substrates, except for the magnitude and the time. In both cases, the region labelled 1 represented the SPV component, which was clear due to the spike of the CPD within tens of milliseconds. The region labelled 2 referred to in all cases, if not negligible due do the CPD peak-to-peak signal, a direct residual increase of the CPD in the order of a second, which could not be interpreted just with KPFM. The last region, labelled 3, depended on the substrate type and extended from the end of region 2 until the stabilization of the CPD under illumination. For n-type substrates, and the example of SnO_2 (Figure 6.3a), region 3 corresponded to a long decay of the CPD, with a constant rate until stabilization occurred. For the case of p-type substrates, and the example of PTAA (Figure 6.3b), the CPD kept on increasing until it stabilized out.

A slow increase of the CPD upon illumination in vacuum has previously been reported in GaN to be caused by photo-induced desorption of negatively charged oxygen species [411]. However, all samples have seen similar fabrication, storage and transfer conditions and therefore should all present desorption of oxygen if that were to happen. Ionic migration has been found to be a slow process and could also induce a slow change of CPD upon illumination time [174, 202, 412]. The decrease or increase of the CPD could be induced by a different type of ionic species between n- and p- type due to different electric-

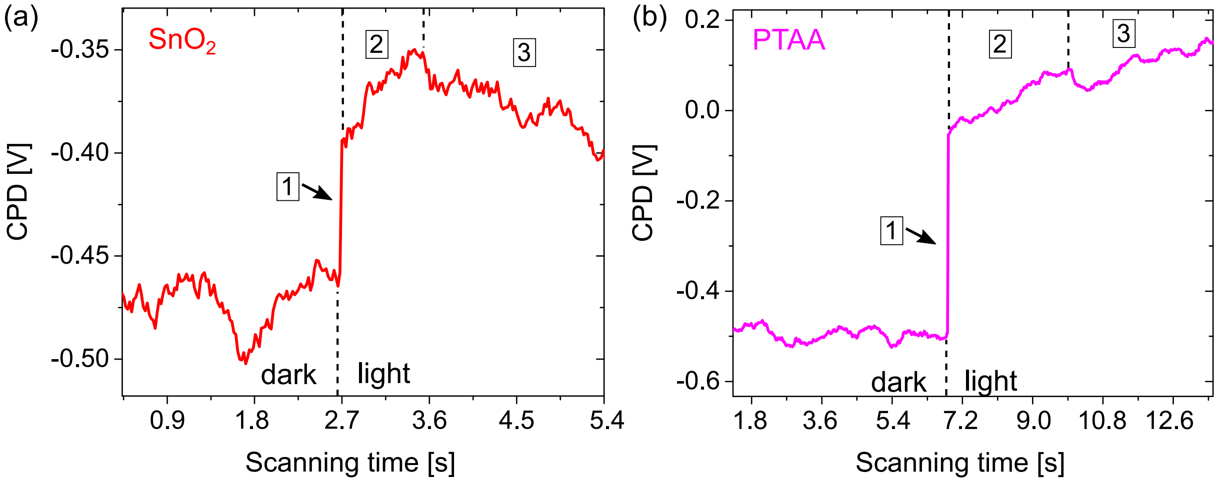

Figure 6.3: Zoom-in regions of the CPD near the beginning of the illumination process for (a) SnO_2 and (b) PTAA. The 1, 2 and 3 numbers label the different components of the CPD under illumination.

field induced by the substrate's type. Slow degradation of the perovskite could also change the WF of the sample or the WF of the tip due to desorption of species and adsorption from the tip, as Zhang et al. have already reported [385]. The difference between increase and decrease of the CPD upon illumination could therefore mean different evaporation of species from the surface.

The latter case is highly probable due to the use of a white LED source, which covers supra- and sub- bandgap energies. This should already be visible when measuring the CPD in the dark after the light is switched off. Figure 6.4 represents the CPD profile of TiO_2 and PTAA under illumination. The red dashed lines correspond to the average CPD value in the dark before and after illumination (CPD_{loss}). On TiO_2/$MAPbI_3$ (Figure 6.4a), and for the other n-type substrates, the CPD in the dark after illumination was always lower compared to the initial value in the dark. For PTAA and NiO, the CPD after illumination was either higher or equal to the initial CPD measured in the dark before the light study.

Table 6.2 gives the value CPD_{loss} corresponding to the CPD difference between initial dark and dark after illumination. As the difference of the measured CPD in the dark after illumination was always different from the initial value in the dark, either the WF of the sample had changed or the WF of the tip had changed. Therefore, the calibration of the tip before and after each sample's illumination study was performed. $\Delta_{CPD,HOPG}$ of Table 6.2 refers to the difference of the measured CPD on the HOPG reference sample, using the same tip, before and after the illumination studies (sometimes more than one), and gives an indication of how the tip WF had changed.

The values of $\Delta_{CPD,HOPG}$ for each sample studied are given in table 6.2 and match quite well with the CPD_{loss} as an error bar of ± 5 mV can be estimated for each value. This suggests the CPD_{loss} (loss of CPD between initial dark and dark after illumination) to be induced by a change in the tip WF and not a change in the WF of $MAPbI_3$ due to light exposure. However a change of the $MAPbI_3$ WF cannot be ruled out entirely as discrepancies exist. For example for $MAPbI_3$/PTAA, a large difference in magnitude between CPD_{loss} and $\Delta_{CPD,HOPG}$ can be discerned, which can be attributed to an effect only occurring on PTAA substrates (see section F.2 of appendix Chapter 6) and made challenging the comparison between CPD_{loss} and $\Delta_{CPD,HOPG}$, where the discrepancy was

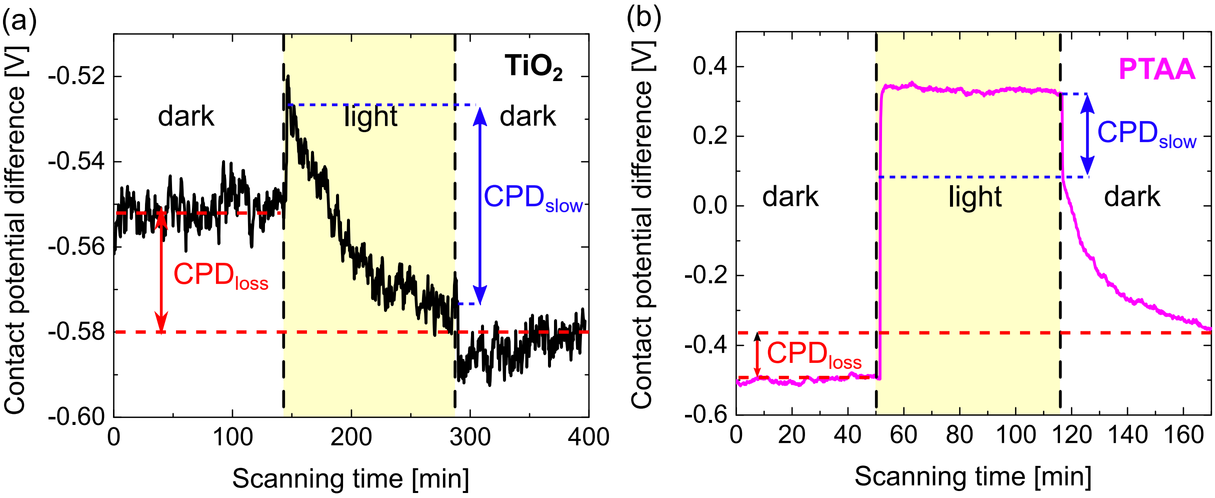

Figure 6.4: Average CPD profile of (a) TiO_2 and (b) PTAA. The red dashed lines represent the average CPD value in the dark prior to the illumination and in the dark after the illumination (CPD_{loss}). CPD_{slow} depicts the slow variation of CPD upon illumination.

Substrate	CPD_{loss} (mV)	$\Delta_{CPD,HOPG}$ (mV)	CPD_{slow} (mV)
TiO_2	-40	-40	-50
SnO_2	-25	-5	-20
FTO	-100	-110	-90
AZO	-30	-30	-55
NiO	+80	+100	+180
PTAA	+150	+25	+290

Table 6.2: CPD_{loss} refers to the CPD difference **in the dark** before and after illumination for $MAPbI_3$ deposited on the different substrates. CPD_{slow} refers to the slow change of the CPD under illumination, taken after the SPV value (fast CPD change). $\Delta_{CPD,HOPG}$ refers to the CPD difference measured on the reference sample HOPG before and after the illumination studies of $MAPbI_3$ samples on the different substrates. This gives an indication of how the tip WF changed.

the largest (+150 mV vs +25 mV). Nevertheless, the outcome of this extended KPFM study led to the suggestion that the tip WF had been changed, due to the illumination of $MAPbI_3$ upon prolonged illumination. Zhang et al. have already reported that in UHV, illumination with different laser wavelength induced the desorption of halide species, bromine and iodine for different types of perovskite, and induced a contamination of the tip by these evaporated species, which resulted in a change of the tip WF [385]. For the n-type substrates, the decrease of the CPD on HOPG, synonym of increase of the tip WF, was consistent with the study of Zhang et al., however for the p-type substrates an increase of the CPD on HOPG, or decrease of the tip WF, was observed, which could indicate a different contamination of the tip or another physical phenomenon.

Lastly, the value of the CPD change upon the prolonged illumination was calculated and labelled as CPD_{slow} (Table 6.2). It was determined by taking the difference in CPD values just before the light was switched off and just after the SPV extraction (represented in Figure 6.4). Figure 6.4 might not reflect the values of Table 6.2 because the figure displays the average CPD profile while the raw data were used for the table in order to have the precise starting and ending CPD values. Calculating CPD_{slow} was carried out to verify if the change of the tip WF could be correlated with the continuous change of the CPD upon prolonged light exposure. Table 6.2 exhibits the CPD_{slow} values for the different samples. A quite good agreement between CPD_{slow} and CPD_{loss} can be noticed for all n-type substrates, and therefore also match the $\Delta_{CPD,HOPG}$ values, which would indicate that all three values are interlinked and that the light-induced slow-changing CPD could be correlated with the desorption of halide species, contributing to the contamination of the tip WF. On the other hand, CPD_{slow} values for p-type substrates were much larger than the CPD_{loss} and $\Delta_{CPD,HOPG}$ measured, which would suggest an additional effect, independent of the desorption of species. In order to confirm or refute these assumptions, XPS was performed in different conditions on similar samples.

6.1.2 X-ray photoelectron spectroscopy characterization

Chemical variations at the surface were therefore investigated by XPS without air exposure, in the dark, after X-rays radiation, upon and after prolonged illumination. The equipment, procedure and parameters used can be found in appendix chapter 6F.3 and the measurements were carried out by Mathieu Fregnaux and Damien Aureau at IPVF. It has to be noted that MAPbI_3/FTO was the only one exposed to air, for a few minutes, due to faulty clamping of the sample and therefore its XPS results might be altered. However as XPS is sensitive to the first 10 nanometers and not entirely to the first atomic layer, as is KPFM, it is likely that the short exposure to oxygen did not skew the following results. First, the survey and core levels spectra in the dark were carried out and used as a reference measurement, followed directly by a second scan of the three main core levels (I3d, Pb4f and N1s) representing $\text{CH}_3\text{NH}_3\text{PbI}_3$, and used to estimate the effect of the X-ray beam radiation on the surface of MAPbI_3 for all substrates.

The I/Pb ratio was measured after each step, by using the atomic percentage obtained after fitting the peaks of $\text{Pb4f}_{7/2}$ and $\text{I3d}_{5/2}$ by first using a Shirley-based background deconvolution and a mixed Lorentz/Gaussian peak fit function with a ratio of 1/3. In addition, the factors used for the calculation of the atomic percentage of each element were taken directly from the Al Thermofisher library associated with the machine, which took into consideration the escape depth of the electrons.

As can be displayed in Table 6.3, the I/Pb ratio for the different samples were relatively close to each other and were in good agreement with their respective position on the sample holder, which did not rotate and led to slight but negligible co-evaporation inhomogeneities. For example, PTAA and NiO were the closest to the MAI source, which could be the reason why they have higher I/Pb ratio, but it could also be linked to the better incorporation of MAI into the crystal lattice and the better perovskite transformation, as reported by Abzieher et al. [307]. MAPbI_3/FTO was the only sample that did not fit well, which could either be due to a difference in adhesion, contact angle [307] or just the fact that the sample had been exposed to air.

It is also important to note that there is a 0.1 atomic% error in the calculated atomic percentage values, which would make insignificant the second digit after the decimal of the I/Pb ratio if taken alone. However, the second digits have here been kept, as the I/Pb trends upon illumination will be investigated. After the first scan and the X-rays beam exposure, the second scan led to the observation that the I/Pb ratio had almost not changed, suggesting a good stability against quick X-ray exposure. Again the MAPbI_3/FTO sample showed the largest change (from 3.1 to 3.2), which could have been

Substrate	I/Pb (dark)	I/Pb (after X-ray radiation)
TiO_2	3.19	3.22
SnO_2	3.19	3.19
FTO	3.1	3.2
AZO	3.13	3.1
NiO	3.25	3.21
PTAA	3.28	3.29

Table 6.3: I/Pb ratio in the dark and after the first scan to estimate the effect of the X-ray beam radiation.

caused by the formation of a small oxide altering the surface, but potentially removed after the first XPS scan, giving rise to a coherent value of 3.2, in agreement with the rest of the measurements. In addition to the I/Pb ratio, the presence of Pb^0 was noticed for three samples: $MAPbI_3$ on TiO_2, FTO and PTAA as depicted in Figure 6.5, which could indicate a poorer stability compared to the other substrates where no Pb^0 was discerned.

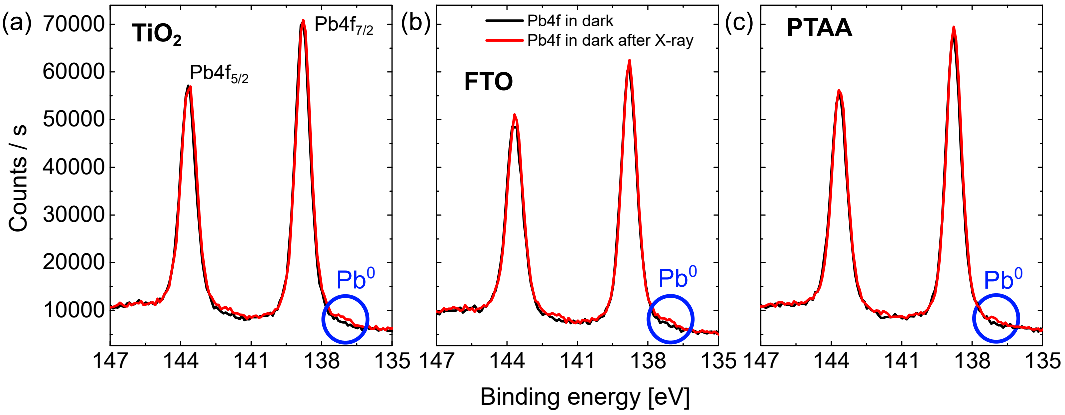

Figure 6.5: Successive XPS scans in the dark near the Pb4f core levels to estimate the effect of X-rays radiation, for (a) $MAPbI_3/TiO_2$, (b) $MAPbI_3$/FTO and (c) $MAPbI_3$/PTAA. The blue circle represents the formation of Pb^0 after X-rays exposure.

The presence of metallic lead Pb^0 has already been discussed in the section 1.2.5 of chapter 1 but is basically resulting from the degradation of $MAPbI_3$ into PbI_2 and the further dissociation into Pb^{2+}, that can easily reduce into Pb^0, and the gaseous species such as HI. In addition, after X-rays exposure and the very subtle change in peak intensity, linked to the I/Pb ratio, the binding energies (BE) of the three main core elements ($I3d_{5/2}$, $Pb4f_{7/2}$ and N1s) exhibited shifts of different magnitudes and signs, potentially due to the reduction of the surface band bending, as X-rays induce photo-generated carriers. This change in binding energies could also be linked to chemical variations (secondary phases such as PbI_2) or transfer of charges from one species to another. These changes in binding energies will be discussed and investigated with the illumination study.

To that end, an illumination cycle was designed to measure alternatively the different samples within one run. Figure 6.6 represents the iteration process used to study the different samples under illumination. First, the light was switched on and XPS measurements on the three main core levels were carried out fast enough on $MAPbI_3/SnO_2$ to minimize the impact of X-ray to a maximum (scan time of 68 s). The intensity of the light was not measured but the same LED as for KPFM was used outside a UHV chamber and therefore the intensities used between KPFM and XPS should not be greatly different. Directly after the measurement of $MAPbI_3/SnO_2$, XPS was performed on $MAPbI_3/NiO$, and so on... Note that all the samples were illuminated at the same time, and therefore the first measurement time (t_0) is different for all samples, which could induce slight discrepancies. 6 iterations of this cycle were performed, with an iteration time of 300 s for one individual sample, which led to measuring the samples under light exposure for about 30 minutes. In addition, $MAPbI_3/FTO$ was measured alone due to a malfunctioning metallic clamp and therefore had an iteration time of 300 s to mimic the same cycle as the other samples.

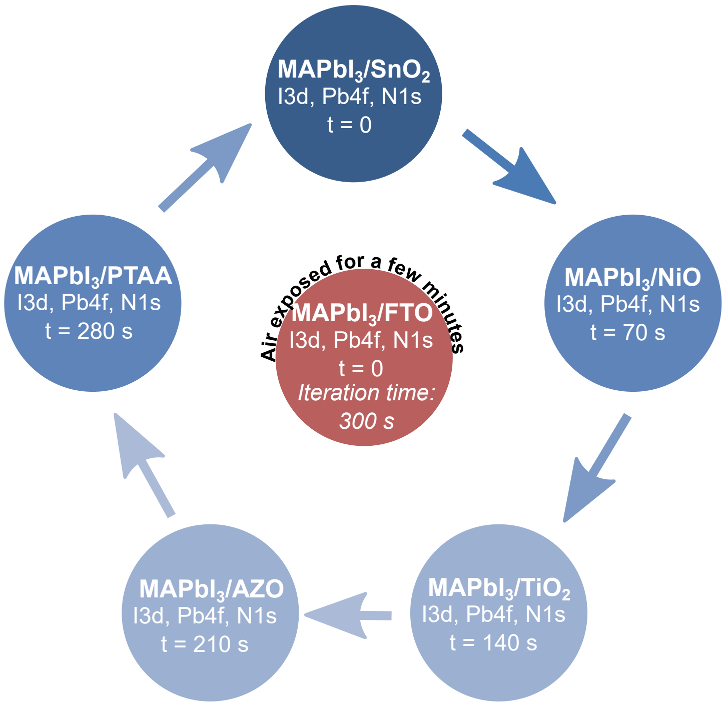

Figure 6.6: Diagram representing the illumination iteration used to study the different samples with XPS. First, the white LED was switched on, illuminating all the samples. Then $MAPbI_3/SnO_2$ was measured with XPS (main core levels). At the end of the scan (68 s), $MAPbI_3/NiO$ was put in place and measured with XPS, and so on until all the samples were measured once. Then, a new cycle began until 6 full cycles were performed (about 30 minutes). Due to the clamping problem of $MAPbI_3/FTO$, the sample was measured alone after a brief exposure to air for fixing the clamp. The iteration time was kept at 300 s to reproduce the same cycle as the other samples.

For the following discussion, the N1s core level will not be taken into consideration due to the low intensity and highly noisy signal, which could lead to erroneous interpretation. For a clear picture of how surface band bending and binding energies are correlated, Figure 6.7 was drawn and depicts the evolution of the WF and BE on an energy band diagram when light exposure is used for the case of $MAPbI_3/SnO_2$. To that end, the previous KPFM measurements were used to suggest the type of surface band bending, which was essentially the same for all samples and a weak n-type bulk doping was suggested due to the influence of the n-type substrate.

In the dark, the position of the charge neutrality level (CNL) with respect to the Fermi level induces the appearance of positively-charged donor surface states, which can be the

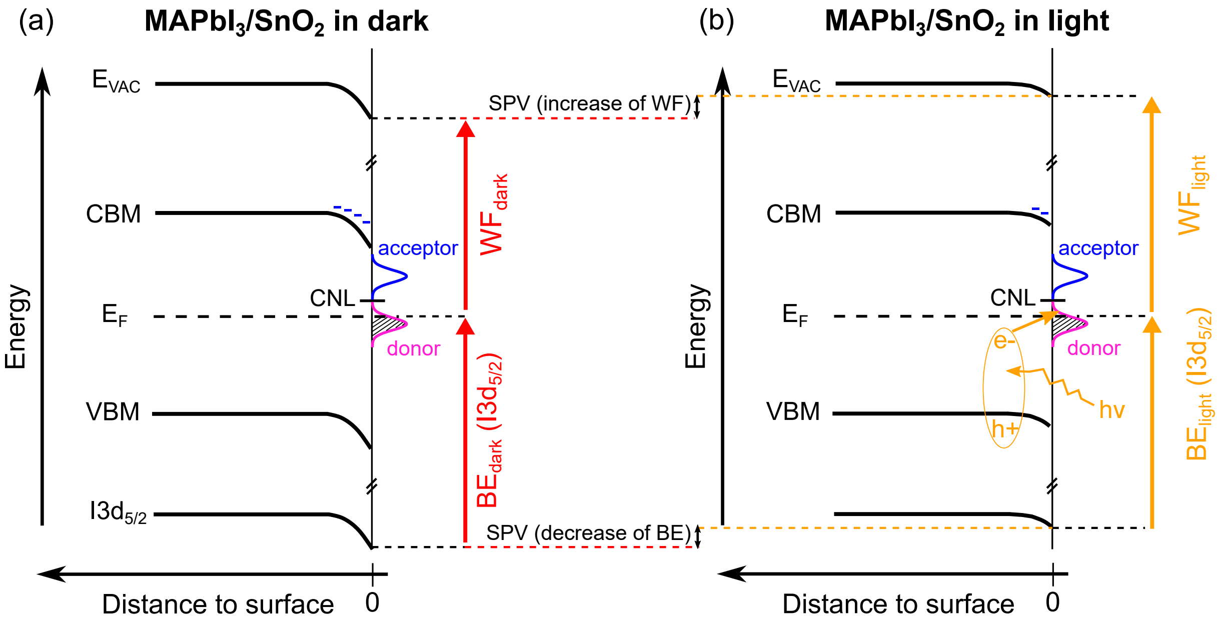

Figure 6.7: Energy band diagram representing the example of $MAPbI_3/SnO_2$ in the (a) dark and (b) under illumination. In the dark, due to the position of the charge neutrality level with respect to the Fermi level, there is the appearance of positively-charged donor surface states. In order to reach charge neutrality in the perovskite film, downward band bending occurs with an electron accumulation in the underneath surface space charge region. Upon low illumination, photogenerated electrons partially screen the positively-charged surface states, which reduces the band bending, increasing the WF and decreasing the binding energies of the core levels (example given with $I3d_{5/2}$).

case for a weakly doped n-type semiconductor or any p-type semiconductor. In order to reach charge neutrality in the perovskite film, downward band bending occurs with an accumulation of electrons in the underneath surface space charge region (see section 1.3.6 of Chapter 1). Upon low illumination, photogenerated electrons partially screen the positively-charged surface states, which reduces the band bending, increasing the WF and decreasing the binding energies of the core levels (with the example given here of $I3d_{5/2}$). If upward band bending was present at the surface (acceptor states), the WF upon illumination would decrease and the BE would increase. Therefore, the occurrence of SPV will always exhibit itself with an opposite sign when measuring changes in WF or BE between dark and illumination conditions.

Figure 6.8 depicts the changes in BE of the main investigated core levels (except N1s) upon prolonged illumination of two substrates SnO_2 (n-type) and NiO (p-type), but which are quite representative of all the other n- and p-type substrates. Their individual BE variations can be found in Figure F.4 of appendix chapter 6F.4.

Directly following the illumination, the BE of the I3d and Pb4f core levels decreased by 100 meV and 30 meV respectively, which could be coherent with the appearance of the surface photovoltage, which would reduce the surface downward band bending and therefore the value of the BE. These values of the shifted BE should ideally be equal when discussing collective shift and reduction of surface band bending. However the measurements of the core levels were successive, which led to more illumination time for one compared to the other. The decrease of the BE was in line with the observed SPV value of +65 meV determined using KPFM. For the NiO case, the BE energies of both

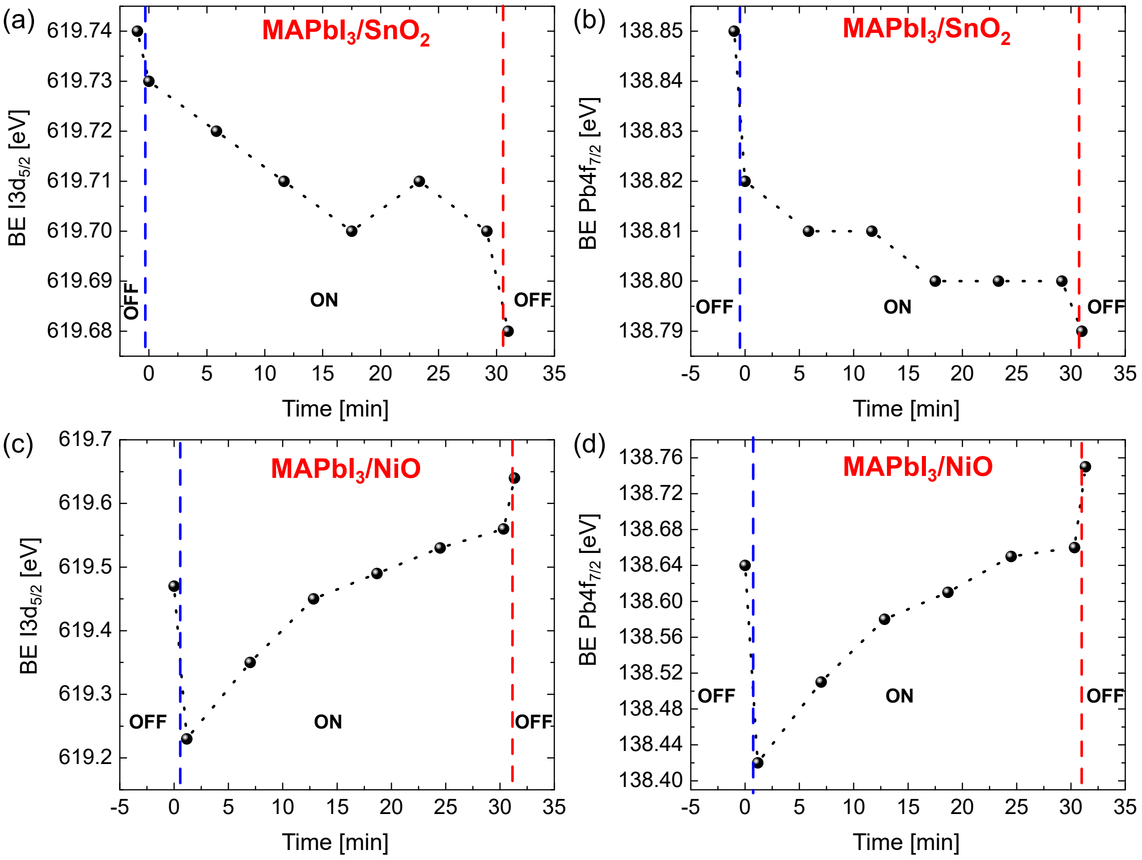

Figure 6.8: Changes in binding energies for the I3d$_{5/2}$ and Pb4f$_{7/2}$ core levels upon prolonged illumination for (a,b) $MAPbI_3/SnO_2$ and (c,d) $MAPbI_3$/NiO.

core levels decreased by 240 meV for I3d and 220 meV for Pb4f, which again agreed well with the calculated SPV value of +215 meV extracted from KPFM. It has however to be noted that, while the reduction of the BE for SnO_2 was directly measured after the light was switched on, the reduction of the BE for NiO was only measured after 70 s of illumination due to the iteration cycle of the XPS measurements.

Table 6.4 summarizes the BE changes for the first measurement after light exposure for all samples, together with the SPV measured from KPFM. There was a relatively good agreement between the measured SPV from the KPFM and the one measured from the XPS, to a certain degree concerning the different samples. As already explained, the opposite sign of the changes in WF and BE was coherent and indicated a reduction of the surface band bending. In the case of samples measured quite rapidly after illumination (SnO_2, FTO and NiO), the magnitude matched much more than for samples where the first XPS spectra was measured more than 2 minutes (t_0) after the light was switched on (TiO_2, AZO and PTAA). The discrepancies observed could also originate from the slight difference in the light intensity used between KPFM and XPS or to the fact that the samples measured with KPFM were from a different batch than the ones measured with XPS, and therefore very small inhomogeneities between deposition processes can occur.

After the first fast decrease of the BE upon illumination, linked to the SPV, the BE for SnO_2 continued to decay until stabilization at about -25 meV (BE$_{slow}$ of Table 6.5) after 17 minutes (t$_{stab,XPS}$, Table 6.5) of illumination (Figure 6.8). The KPFM measurements also showed that the CPD decreased by about 20 meV (CPD$_{slow}$ of Table 6.5) and stabilized after about 15 minutes ($t_{stab,CPD}$). This also was the case for all n-type substrates with

Substrate	SPV (mV)	ΔBE (I3d) (meV)	ΔBE (Pb4f) (meV)	t_0
TiO_2	+25	0	+10	140 s
SnO_2	+65	-100	-30	0 s
FTO	negligible	-30	-20	0 s
AZO	negligible	-20	-10	210 s
NiO	+215	-240	-220	70 s
PTAA	+440	-170	-50	280 s

Table 6.4: SPV, changes in BE for the main core levels with their associated t_0 time (measurement time after illumination) for $MAPbI_3$ co-evaporated on different substrates, measured by KPFM and XPS using a white LED with a power of $\sim$ 10 mW cm^{-2}.

different decay magnitudes and stabilization times, all presented in Table 6.5. The fact that both CPD and BE decreased, and therefore had the same sign, corroborated that this was due to a different effect than SPV and the reduction of surface band bending. In addition, the stabilization times ($t_{stab,XPS}$ and $t_{stab,CPD}$) and values (BE_{slow} and CPD_{slow}) matched quite well and therefore would suggest a physical effect that would both decrease the WF and the BE of the core elements. It still remained to investigate if the desorption of halide species could induce these simultaneous consequences.

On the other hand, the BE for NiO displayed, after the fast positive SPV, a continuous increase of the BE before stabilizing after about 30 minutes ($t_{stab,XPS}$, Table 6.5) of illumination at 330 and 240 meV for I3d and Pb4f respectively (BE_{slow}, Table 6.5). The KPFM measurements on NiO also exhibited a slow increase of the CPD reaching a final value of 180 meV after about 25 minutes ($t_{stab,CPD}$ and CPD_{slow}, Table 6.5) which showed again the very close corroboration between WF and BE variations upon prolonged illumination. PTAA also displayed an increase of BE (Table 6.5) with a smaller amplitude, much smaller than the CPD_{loss} measured previously, which could be shadowed by the previously-discussed unique effect affecting $MAPbI_3$/PTAA (see KPFM measurements). Therefore, the differences in sign and amplitude compared to the n-type substrates would indicate another effect occurring for the p-type substrates, which could be induced by a different degradation mechanism resulting from non-identical growth processes as reported by Abzieher et al. when co-evaporating $MAPbI_3$ on TiO_2, SnO_2 and NiO, PTAA [307].

In addition to the good correlation between the changes of BE after prolonged illumination and the slow-changing CPD values, all samples exhibited the appearance of a Pb^0 peak (Figure 6.9a), synonym of degradation of the perovskite, as it decomposes towards PbI_2 and HI, and where Pb^{2+} can easily reduce to metallic lead Pb^0 and I_2 can evaporate.

In Figure 6.9a, only the XPS measurements of the Pb4f core level of $MAPbI_3/SnO_2$ and NiO are depicted but the rest of the series can be found in Figure F.5 of appendix chapter 6F.5. Figure 6.9b summarizes the calculated Pb^0/Pb for each sample as a function of their respective illumination time. Greater degradation can be observed for $MAPbI_3$ co-evaporated on TiO_2 and FTO substrates, where the $Pb0^0$/Pb ratio reaches values close to 0.1 at the end of the illumination study. The rest of the samples have similar trends, which would also indicate a lower degradation.

Previous studies already reported the poorer crystallinity of $MAPbI_3$ on TiO_2, as amorphous $MAPbI_3$ gets introduced when using TiO_2 as an ETL, which contributes to a higher degree of trap density [413, 414]. Abzieher et al. have also demonstrated that TiO_2, and to a larger extent non-polar oxide substrates, lead to non-columnar growth, which

Substrate	BE_{slow} (I3d) (meV)	BE_{slow} (Pb4f) (meV)	$t_{stab,XPS}$ (min)	CPD_{slow} (mV)	$t_{stab,CPD}$ (min)
TiO_2	-70	-30	8	-50	115
SnO_2	-30	-20	17	-20	15
FTO	-60	-30	[5-15]	-90	35
AZO	-70	-50	27	-55	30
NiO	+330	+240	30	+180	25
PTAA	+110	+30	-	+290	-

Table 6.5: Slow changes in BE and CPD upon prolonged illumination, extracted after the occurrence of the SPV for $MAPbI_3$ co-evaporated on different substrates, together with their stabilization time (time it takes for the BE and CPD to be constant with prolonged illumination).

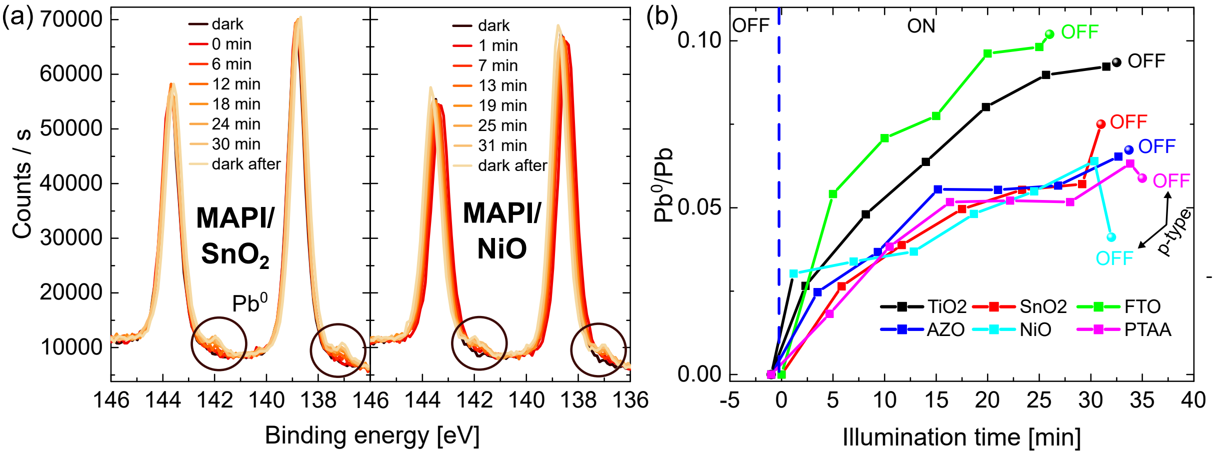

Figure 6.9: (a) XPS measurements of the Pb4f core level for $MAPbI_3/SnO_2$ and $MAPbI_3/NiO$ as a function of illumination time. (b) Pb^0/Pb ratio calculated from the extracted atomic % for all samples as a function of illumination time.

would in the end introduce more defects. They clearly showed that $MAPbI_3$ deposited on the same TiO_2 substrate as this study led to worse device performances, induced by non-ideal grain growth and poorer MAI incorporation in the perovskite lattice [307]. Lastly, Climent-Pascual et al. have reported that the roughness and chemical nature of the substrate layer have large implications concerning lattice parameters and preferred orientations of grains. They showed that when using an oxide substrate with a higher roughness (in their case FTO and TiO_2), a shrinking of the pseudocubic lattice parameters occurs and that $MAPbI_3$ co-evaporated on FTO and TiO_2 substrates transformed into PbO_x upon illumination, later degrading into PbI_2 if water was involved [415].

These reports are in line with the larger Pb^0 fraction observed in the XPS measurements for TiO_2 and FTO substrates in this thesis upon prolonged illumination. Besides, the roughness (root mean square, RMS) of $MAPbI_3$ on both TiO_2 and FTO was measured with AFM and was of $\sim$ 12 nm and $\sim$ 15 nm respectively, which was two to three times higher than the rest of the samples (6 nm in average), which proved that substrate roughness, together with its chemical nature and polar behavior, can strongly influence the properties and degradation mechanism of the following co-evaporated perovskite.

In addition to the degree of degradation, measured by the Pb^0/Pb ratio, the I/Pb ratios were monitored upon the illumination study to observe if the composition at the surface changed upon long light exposure. Table 6.6 depicts the I/Pb ratio around the very first minutes of illumination and at the end of the illumination study before the light was switched off.

Substrate	I/Pb (start illumination)	I/Pb (end illumination)	ΔI/Pb
TiO_2	3.13	2.98	-0.15
SnO_2	3.25	3.09	-0.16
FTO	3.07	2.92	-0.15
AZO	3.08	3.0	-0.08
NiO	3.20	3.15	-0.05
PTAA	3.24	3.22	-0.02

Table 6.6: Values of the I/Pb ratio at the beginning and at the end of the illumination study for $MAPbI_3$ co-evaporated on different substrates. $\Delta_{I/Pb}$ refers to the difference of the I/Pb ratio at the beginning and at the end of the illumination study.

It can be observed that independent of the type of the substrates, all I/Pb ratio decrease, which could suggest a reduction of the iodine concentration. The evaporation of iodine has previously been discussed and formerly reported to be existing in ultra-high-vacuum [385]. However, the changes in I/Pb ratio (denoted as ΔI/Pb in Table 6.6) are slightly higher for n-type substrates (-0.15 overall) compared to p-type substrates (-0.05 and -0.02).

Taking all the previous XPS observations into account, it becomes clear that surface reactions happen at the surface of the perovskite upon prolonged illumination. First, the slow changes in binding energies, even if collective for different core levels, can be caused by chemical shifts associated to different oxidation states or a change in the chemical bonding of the elements. Cappel et al. have reported the exact same behavior for a mixed halide perovskite, namely $(FAPbI_3)_{0.85}(MAPbBr_3)_{0.15}$ deposited by solution processes on an FTO/TiO_2 substrate [383]. They linked the observable continuous decrease of the BE of both the I4d and Pb5d core levels upon laser illumination to chemical changes resulting from photo-induced reactions at the surface. They additionally observed an increase of the amount of Pb^0 together with a reduced I/Pb ratio, which was connected to a reduced peak intensity for I4d and Pb5d. In the present case, most of the samples exhibited decrease in I3d and Pb4f peak intensities to a certain extent when comparing spectra in the dark and at the end of the illumination study, as displayed in Figure F.6 of appendix chapter 6F.6, which is in line with what Cappel et al. showed [383]. However the decrease observed was not as severe as the one reported from the latter, except for $MAPbI_3$/PTAA, and could still be within the measurement error. Nevertheless, a large increase of the Pb^0/Pb ratio and reduction of the I/Pb ratio together with the shift of the BE to lower values were observed here, which was in excellent agreement with the work of Cappel et al. [383].

They attributed these phenomena to a combination of effects, starting with ionic migration, followed by the reduction of perovskite to Pb^0 due to a photo-induced electron-transfer reaction between I^- and Pb^{2+} that could be translated in the case of this work by reaction 6.1 occurring at the surface:

$$MAPbI_3 + light \rightarrow Pb + I_2 + MAI \tag{6.1}$$

The formation of I_2 species leaves the film directly through sublimation, and can be picked up by the KPFM tip, thus the observed decrease of the CPD, but cannot be detected by XPS measurements. This might induce a small decrease in I^- and I/Pb ratio. The effect of heating can be ruled out as the nitrogen peak intensity remained the same during the illumination study [416]. Das et al. have also reported the same behavior for $MAPbI_3$ deposited on TiO_2 and attributed it to the same decomposition mechanism with further details [108]. The mechanism that they depict, and which is probable to happen here as well, is the following (Figure 6.10).

First, in the dark, donor-like surface states lead to a positive net charge at the surface, which is compensated by a downward band bending for charge neutrality (Figure 6.10a). In addition, the ultra-high-vacuum creates iodine vacancies (V_I) at the surface of $MAPbI_3$. Upon direct illumination, photogenerated electrons screen the positive surface states (drawn as Gaussian curves on the surface of $MAPbI_3$), giving rise to the SPV (Figure 6.10b). At the same time (Figure 6.10c), $MAPbI_3$ first degrades towards PbI_2 and other volatile species (HI, CH_3NH_2) and photogenerated electrons are then trapped by the iodine vacancies, and either recombine or are transferred to the Pb^{2+} states (resulting from the $PbI_2 \leftrightarrow Pb^{2+} + 2I^-$). The acquisition of the electrons by the Pb^{2+} states results in their reduction into Pb^0, and the formation of lead vacancies V_{Pb}. Simultaneously the photogenerated holes can be trapped by these latter vacancies and can either recombine or be transferred to adjacent I^- anions (Figure 6.10d), which will lead to their oxidation and the formation of I_2, which will leave the surface through sublimation (Figure 6.10e).

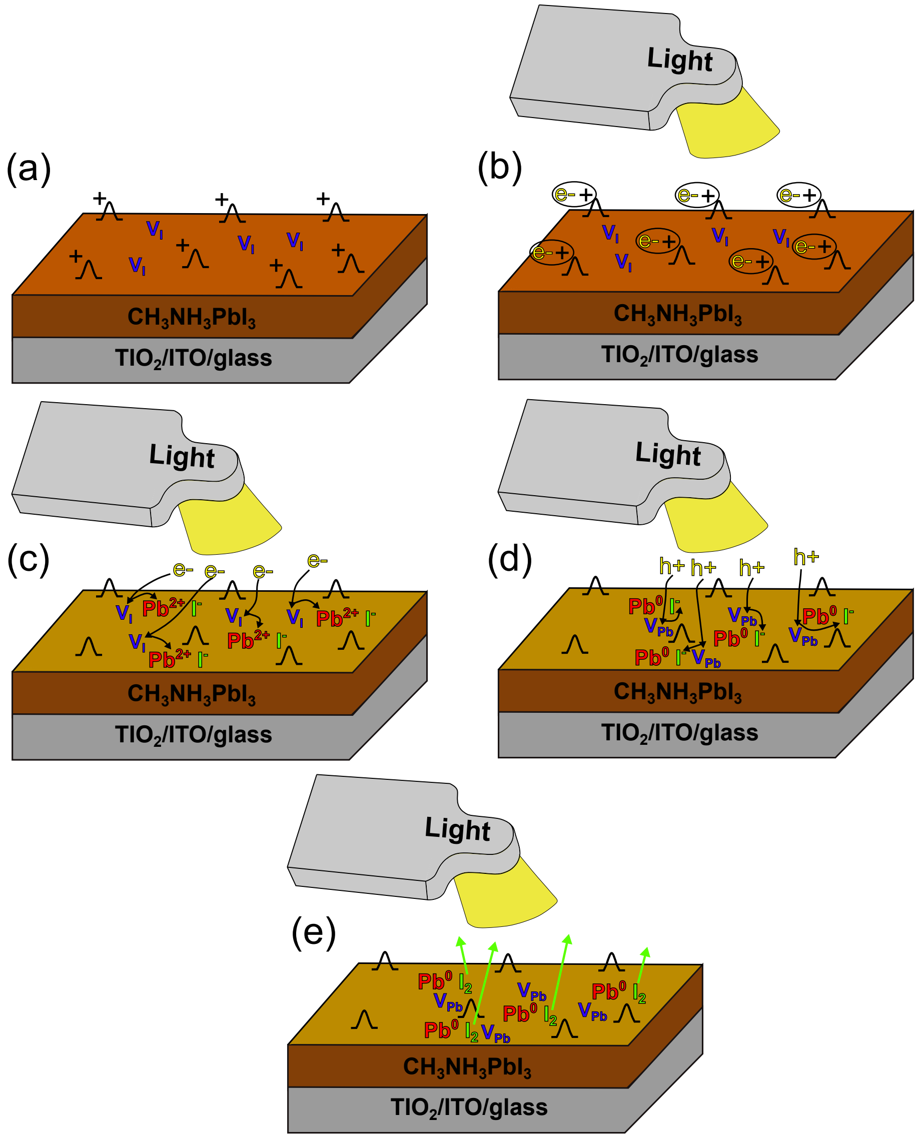

Figure 6.10: Sketches representing (a) the MAPbI$_3$ surface in the dark with its positive surface states ad iodine vacancies and (b) the compensation of these states by photogenerated electrons upon illumination, giving rise to the surface photovoltage. (c) At the same time, iodine vacancies trap photogenerated electrons and transfer them to adjacent Pb^{2+} states, which are reduced into Pb^0 and form Pb vacancies. (d) Holes can therefore be trapped by these vacancies and be transferred to I$^-$ anions which are oxidized into I$_2$ and leave the surface through sublimation.

In addition, XPS measurements in the dark after the illumination on the same spot and on a fresh spot were performed for each sample. The measurements led to some suggestions concerning the stability of the different substrates but were not relevant for this study. If interested, the reader is directed to section F.7 of appendix Chapter 6.

Therefore the previous complementary XPS and KPFM measurements led to the conclusion that the slow CPD transient observed via KPFM on co-evaporated $MAPbI_3$ under illumination were the consequence of the photo-induced degradation of the perovskite film and the iodine evaporation towards the KPFM tip. This is different from what has been reported in the literature where ionic migration, interfacial trap states were mostly reported to be the cause [202, 203, 208, 209, 210]. However this interpretation is coherent with the observable photo-induced evaporation of halide species from perovskite in UHV [108, 383, 385, 416]. Additionally, these measurements proved that the type of the substrate induced different degradation mechanisms for the evaporated perovskite layer on top, where n-type would result in evaporation of iodine but which would not be specifically the case for p-type substrates, or at least with an additional effect occurring, which requires further investigation. This could be linked to the distinct growth mechanisms reported by Abzieher et al. [307], which induce different surface terminations and surface states, and thereafter a different degree of surface band bending, as observed in this work. This is a highly important notion to consider when discussing interface alignment for the optimization of full perovskite devices. In addition, different ionic migration or built-in field when using a hole or extraction layer as the bottom layer could well be the cause of such differences. Studying such effect is of great importance to further understand which structure (n-i-p or p-i-n) to use to fabricate highly-stable solar cells for large-area industrial solar panels.

6.2 Band bending at the interface substrate/MAPI

After having extensively discussed the surface of the perovskite depending on its substrate, it also becomes important to shed some light on what happens at the interface of the latter, in terms of band alignment. To that end, KPFM measurements were used to first determine the WF of $MAPbI_3$ depending on its substrate, but also depending on its thickness. In addition, calibrated PL and TRPL were used to determine the doping density of $MAPbI_3$ for different thicknesses and for different substrates, which provided further information about the band bending from the first few nanometers to the surface of the perovskite.

6.2.1 Substrate-induced change in WF

The previous section 6.1.1 presented the measurements of $MAPbI_3$ co-evaporated on different absorbers (n- and p-type) in the dark and upon prolonged illumination. For each measurement in the dark, the tip was calibrated before on an HOPG reference sample in order to retrieve the WF. In addition, the WF of the underlying substrate was also extracted from KPFM measurements performed in UHV and without air exposure. As can be observed in Table 6.7, the WF of $MAPbI_3$ remains mainly the same for all substrates, between 4.09 and 4.19 eV, except for $MAPbI_3$/NiO where the WF was measured to be 4.48 eV, very close to the NiO substrate WF of 4.43 eV.

Substrate	Substrate WF (ev)	$MAPbI_3$/substrate WF (eV)
TiO_2	4.07	4.15
SnO_2	4.49	4.19
FTO	4.56	4.14
AZO	4.3	4.09
NiO	4.43	4.48
PTAA	4.81	4.17

Table 6.7: workfunction values for each substrate and $MAPbI_3$ co-evaporated on them, measured by KPFM after tip calibration with an HOPG reference sample.

As no high-resolution XPS near the valence band regions and no UPS were performed for the substrates, the electron affinities, ionization potentials and bandgaps of each substrate were used from various reports from the literature and are given in Table 6.8. Note that even if these values are taken from specific studies, they reflect most of the values reported in most of the works from the literature.

Substrate	WF (eV)	EA (eV)	IP (eV)	bandgap (eV)
TiO_2	4.07	4 [10]	7.2 [10]	3.2 [10]
SnO_2	4.49	4.5 [10]	8.0 [10]	3.5 [10]
FTO	4.56	4.4 [417]	7.6 [417]	3.2 [417]
AZO	4.3	4.3 [418]	7.7 [418]	3.4 [418]
NiO	4.43	1.8 [59]	5.4 [59]	3.6 [59]
PTAA	4.81	1.8 [59]	5.1 [59]	3.3 [59]

Table 6.8: Measured WF values from KPFM, and EA, IP and bandgap values from different sources in the literature.

Lastly, the electron affinity of $MAPbI_3$ was taken to be 3.9 eV, as values for EA are often reported to lie between 3.8 and 4.1 eV when using UPS [332, 419, 420, 421, 422, 423] and PL was used to measure the optical bandgaps, given in Table 6.9.

Substrate	$MAPbI_3$ WF (eV)	$MAPbI_3$ bandgap (eV)
TiO_2	4.15	1.61
SnO_2	4.19	1.61
FTO	4.14	1.60
AZO	4.09	1.61
NiO	4.48	1.62
PTAA	4.17	1.61

Table 6.9: Measured WF values from KPFM and optical bandgap from PL for $MAPbI_3$ co-evaporated on different substrates.

By taking all the previously discussed values into consideration as well as the SPV values from the previous section suggesting surface band bending, and assuming no bending of the bands (VBM, CBM, E_{VAC}) from the first layers to the bulk, it is possible to come up with the simplified energy band diagrams depicted in Figure 6.11. The shaded region (yellow with brown stripes) represents the substrate-$MAPbI_3$ interface, and the grey region the first few layers of $MAPbI_3$ where band bending are not defined. The SPV was taken into consideration to evaluate the band bending, but as the intensity used during the illumination study was relatively low (10 mW/cm^2) compared to a 1-sun illumination, it was assumed that the surface band bending was not fully compensated upon light exposure, i.e. no flat bands, leaving some remaining downward band bending during illumination (red surface band bending in the diagrams).

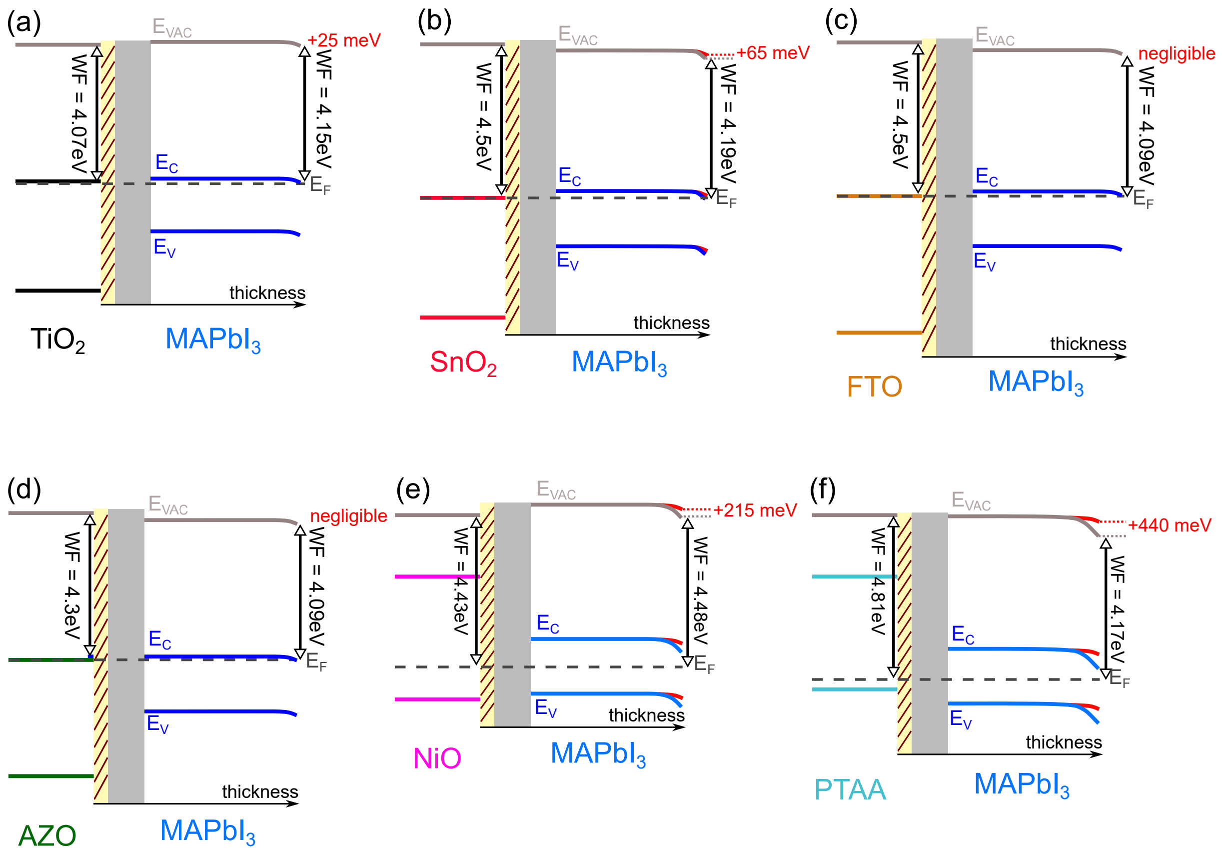

Figure 6.11: Energy band diagrams for $MAPbI_3$ co-evaporated on (a) TiO_2, (b) SnO_2, (c) FTO, (d) AZO, (e) NiO and (f) PTAA. The shaded region (yellow with brown stripes) refers to the interface region between the substrate and $MAPbI_3$ and the grey region to the first few layers of $MAPbI_3$ where the band bending is undefined. The red surface band bending corresponds to the light case and was used to estimate the band bending in the dark, supposing no flat bands under light conditions due to the low intensity of the white LED used.

From the sole use of the EA, WF and bandgaps of the different substrates and $MAPbI_3$, and with the assumption that the bands were constant from the underlying surface until deep in the bulk, it could be observed that the apparent doping of $MAPbI_3$ was very different when using n-type or p-type substrates. For the n-type ones, strong n-type bulk doping could be discerned whereas for p-type substrates, intrinsic or low p-type doping could be noticed. However $MAPbI_3$ was often reported to be low-doped and more intrinsic (see section 1.2.3 of Chapter 1), which is why they are used in a n-i-p or p-i-n configuration. In addition, the surface downward band bending is caused by positively-charged donor-like surface states (see section 1.3.6 of Chapter 1) and requires either p-type doping or weakly n-type doping as donor surface states are closer to the valence band than the conduction band. These explanation would not be coherent with what is drawn in a simplified way for the n-type substrates in Figure 6.11. Therefore, the doping densities for $MAPbI_3$ on the different substrates were extracted and are displayed in Figure 6.12 by using calibrated PL and TRPL measurements on these samples (see section 3.2 of Chapter 3).

The first observation was that $MAPbI_3$ on n-type substrates led to higher PL quantum yield (PLQY) (Figure 6.12a), extracted from the measured PL spectra (Figure F.8 of the appendix chapter 6F.8), as compared to p-type substrates. In addition, $MAPbI_3$ deposited on n-type substrates all showed higher lifetime than on p-type substrates. The use of extraction layers always renders the interpretation of PL and TRPL challenging due to the introduction of different interface regions and defects, which can change the surface lifetime. In addition, if the growth is substrate-dependent [307], then the non-radiative recombination mechanisms can also vary. Therefore the cause of the differences in PLQY and lifetime will not be discussed.

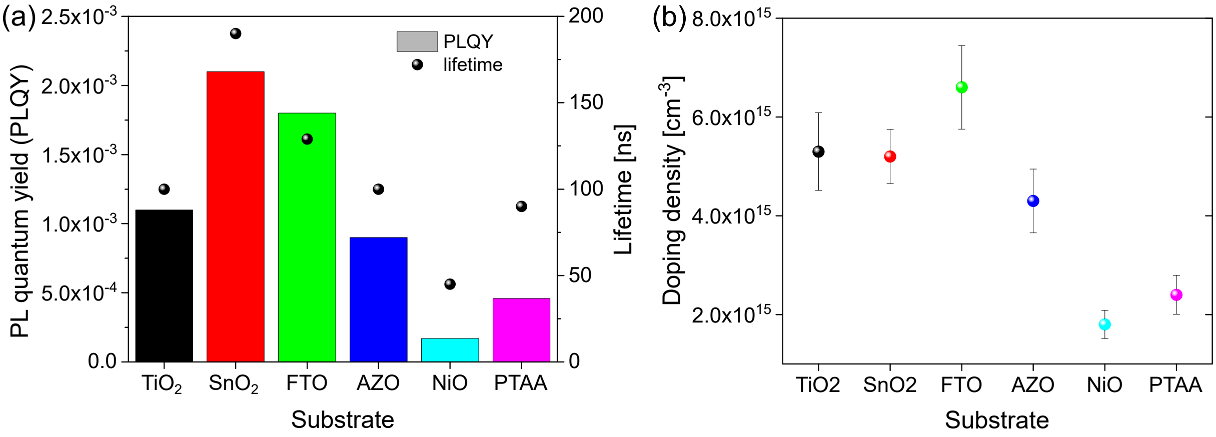

Figure 6.12: (a) External quantum efficiencies and lifetime and (b) calculated doping density for $MAPbI_3$ co-evaporated on different substrates. The laser power density used was 2.81×10^{-3} W/cm^2 with a frequency of 1MHz, yielding an injection of carriers of 1.2×10^{15} cm^{-3} for TRPL.

From the PLQY and lifetime values, the doping density for each sample was calculated and is presented in Figure 6.12b. It can be observed that the doping ranges from 1.8×10^{15} cm^{-3} (NiO) to 6.6×10^{15} cm^{-3} (FTO). Most of the $MAPbI_3$ absorbers co-evaporated on n-type substrates have a doping around 4-5$\times10^{15}$ cm^{-3}, with the exception of FTO, and a doping around 2×10^{15} cm^{-3} when using a p-type substrate. This shows that the doping density is mainly the same for all samples, with a slightly higher doping when using FTO, which is a highly n-doped semiconductor, and with a slightly lower doping when using p-type substrates. This therefore proved that the assumptions of strong n-type doping for $MAPbI_3$ on n-type substrates and the flat bands from the underlying surface of $MAPbI_3$ until deep in the bulk cannot be true.

6.2.2 Thickness-dependent workfunction

To estimate the band bending occurring after the first few layers of $MAPbI_3$ until the surface, $MAPbI_3$ was co-evaporated on an FTO substrate with different thicknesses, and the samples were then transferred without air exposure inside the UHV KPFM to measure their WF. Figure 6.13 depicts the energy band diagram obtained by using the different WF as a function of the thickness of the deposited perovskite film. It can be observed that the WF increased with the thickness, with a value of 3.85 eV for a film of about 300 nm and 4.25 eV for a film of 870 nm. This ultimately resulted in a bending of the bands inducing the Fermi level to be further away from the conduction band near the surface. Of course such a band bending supposes a similar surface at each thickness, otherwise the different WF obtained could have come from different surface terminations or dipoles. SPV was measured at each step and was always negligible, independent of the thickness (within the peak-to-peak CPD signal), which could indicate similar surface states.

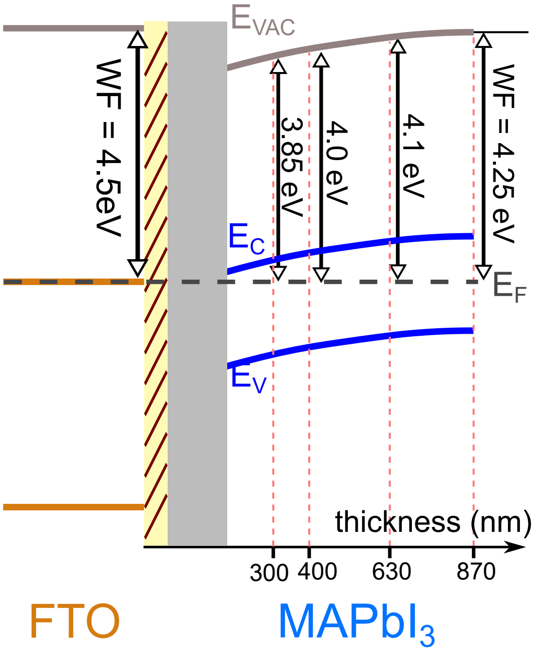

Figure 6.13: Energy band diagram of $MAPbI_3$ co-evaporated on an FTO substrate, by taking into consideration the different measured workfunction as a function of the thickness.

In this case, surface band bending was purposely omitted for visual clarity but it should be noted that additional bending of the bands occur at the surface, and also in the undefined regions, which are the first few layers of $MAPbI_3$ and the interface between the substrate. For the first one, further KPFM measurements at very small thicknesses should be carried out to investigate how the WF varies close to the substrate. For example Olthof et al. have reported either continuous bending or flattening out of the bands depending on the substrate when measuring film thicknesses between 3 to 30 nm [169]. Lastly, the Fermi level was taken to be around mig-gap to represent the case of a low-doped semiconductor, and to avoid the Fermi level to go over E_C at very low thicknesses, which would indicate a degenerated behavior deep in the bulk and which would not make sense. The position of the Fermi level ultimately reduced the electron affinity compared to the one taken from the literature, and also supposed a constant electron affinity independent of the film thickness. The KPFM measurements therefore suggest that the WF and therefore the doping, if the surface is considered unchanged at different film thicknesses, are changing with thickness. From the bending of the bands, this would result in a relatively higher doping densities when using thin $MAPbI_3$ films. On that account, calibrated PL and TRPL measurements were carried out using additional thicknesses in order to access the doping density.

6.2.3 Thickness-dependent doping density

$MAPbI_3$ was then co-evaporated on an FTO substrate with thicknesses varying from 5 to 200 nm and each absorber was measured with calibrated PL and TRPL in order to access the doping density at each step. Figure 6.14 depicts the calculated PLQY and lifetime and resulting doping density at different thicknesses. Interestingly, the PLQY was the highest for the thinnest sample, exceeding PLQY values of 10%, which was impressive. By increasing the thickness, the PLQY decreased which went against the general idea that the number of absorbed photons increases with thickness, resulting in incomplete absorption for thin samples. In addition, the lifetime increased with the thickness and was linked to a predominance of the surface lifetime for the thinnest samples, which reduced the overall effective lifetime. The discussion of these phenomena are further discussed in the work of Poeira et al. [424]. Figure 6.14b represents the calculated doping density for each thickness. For a 200 nm-thick film, the doping density reached a value of 7.5×10^{15} cm^{-3}, which was in good agreement with the doping density of 6.6×10^{15} cm^{-3} calculated for the $MAPbI_3$ film with a thickness of 400 nm (Figure 6.12b). However, when decreasing the film thickness, the doping density strongly increased to ultimately reach 9.8×10^{18} cm^{-3} for the 5 nm-thick film, which corresponds to very high doping in semiconductors. On a side note, the PL peak position was observed to blue-shift from 1.59 to 1.66 eV when reducing the absorber thickness (Figure F.9 of appendix chapter 6F.9).

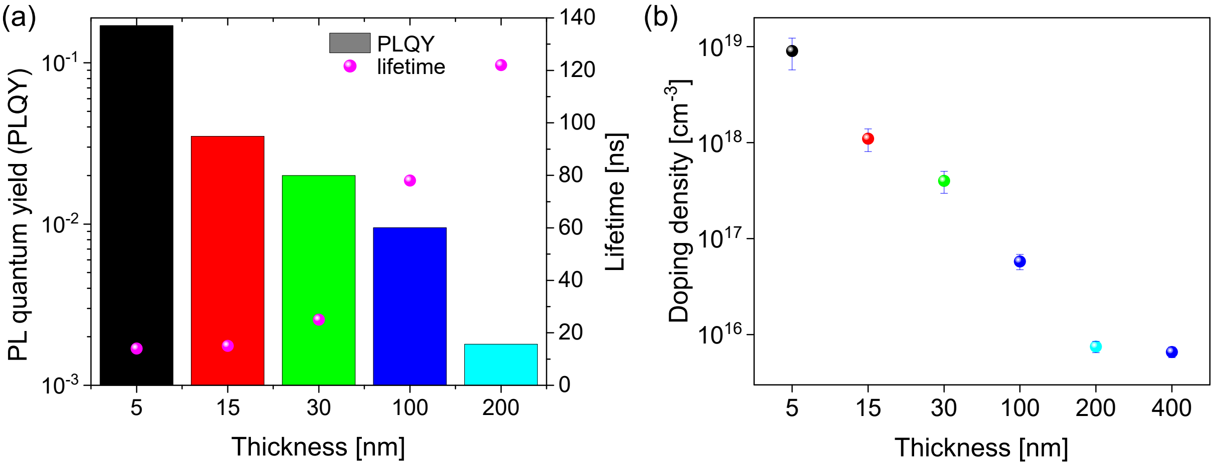

Figure 6.14: (a) Calculated EQE and lifetime from calibrated PL and TRPL measurements and (b) resulting doping density for $MAPbI_3$ co-evaporated on an FTO substrate at different thicknesses.

The increase of the doping density when reducing the thickness of the perovskite absorber correlated nicely with the decrease of the WF measured with KPFM, which showed that the Fermi level was getting closer to the CBM at low thicknesses, synonym of higher n-type doping. Poeira et al. have carried out similar experiments on different substrates, and for all them, the doping density increased when reducing the thickness, independent of the type (n or p), but with different magnitudes [424]. The previous measurements therefore showed that independent of the substrate type, the general trend was that the doping increased by reducing the thickness of the $MAPbI_3$ absorber. The magnitude of the bending of the bands, which depended on the nature and type of the substrate, remains unclear and would require systematic investigations. It is likely that it strongly varies upon the substrate nature (oxide or not), intrinsic doping (highly doped or not) and other parameters [169]. In addition, the growth conditions of $MAPbI_3$ due to the substrate would likely change the bending. The reported columnar growth in the (110) and (111) directions from the first few layers for $MAPbI_3$ co-evaporated on NiO and PTAA could for instance induce less variations in doping than the non-uniform and defective growth happening on TiO_2 and SnO_2 [307]. Future experiments should therefore focus on performing systematic thickness-dependent calibrated PL and TRPL on perovskite co-evaporated on different substrates, to estimate the band bending from the first few layers until the underlying surface. KPFM and UPS measurements could help complement these measurements to draw energy band diagrams with a greater precision.

For the following summarizing Figure 6.15, the bending behavior for FTO will be taken as a standard for the other substrates, but further characterization would be required to clarify these assumptions. From these presumed energy band diagrams, it can be noticed that band diagrams on the studied n-type substrates barely changed, except from the previously discussed surface band bending. For the case of the p-type substrates, in order to remain within similar doping density (and near the intrinsic doping level for high thicknesses), the electron affinity (and ionization potentials) had to stay close to the value of 3.9 eV taken at the beginning, from the literature. In addition, the surface band bending clearly indicated in the depicted situations that the surface of $MAPbI_3$ was n-type, as often reported in the literature [169, 332, 333] and even more so when co-evaporated on p-type substrates, due to stronger bending of the bands at the surface. Finally, the displayed bending of the bands would look favorable for charge extraction of electrons in the case of $MAPbI_3$ on n-type substrates, but would also favorably repel electrons at the interface p-type substrate/$MAPbI_3$ due to a larger energy barrier.

These complementary measurements (KPFM, SPV, calibrated PL and TRPL) show how the energy levels in $MAPbI_3$ can differ depending on the substrate used. Differently from Olthof et al. [169], the Fermi energy was close to the CB near the substrate/$MAPbI_3$ interface and gradually moved away from the CB when getting closer to the surface. However further measurements, such as calibrated PL and TRPL with KPFM, UPS and XPS, at different thicknesses and for all substrates should be performed and the results investigated to estimate with a higher degree of precision the band bending behavior from the first few layers of co-evaporated $MAPbI_3$ until the surface. Care should be taken such that the same environment should prevail when performing these measurements, in order to assume similar surface states. In the previous work, KPFM was performed in UHV while PL and TRPL were performed under nitrogen. At least air exposure was prevented but the environments slightly differed even though it can be assumed that measurements in vacuum and in the dark did not alter much the surface terminations of the perovskite film.

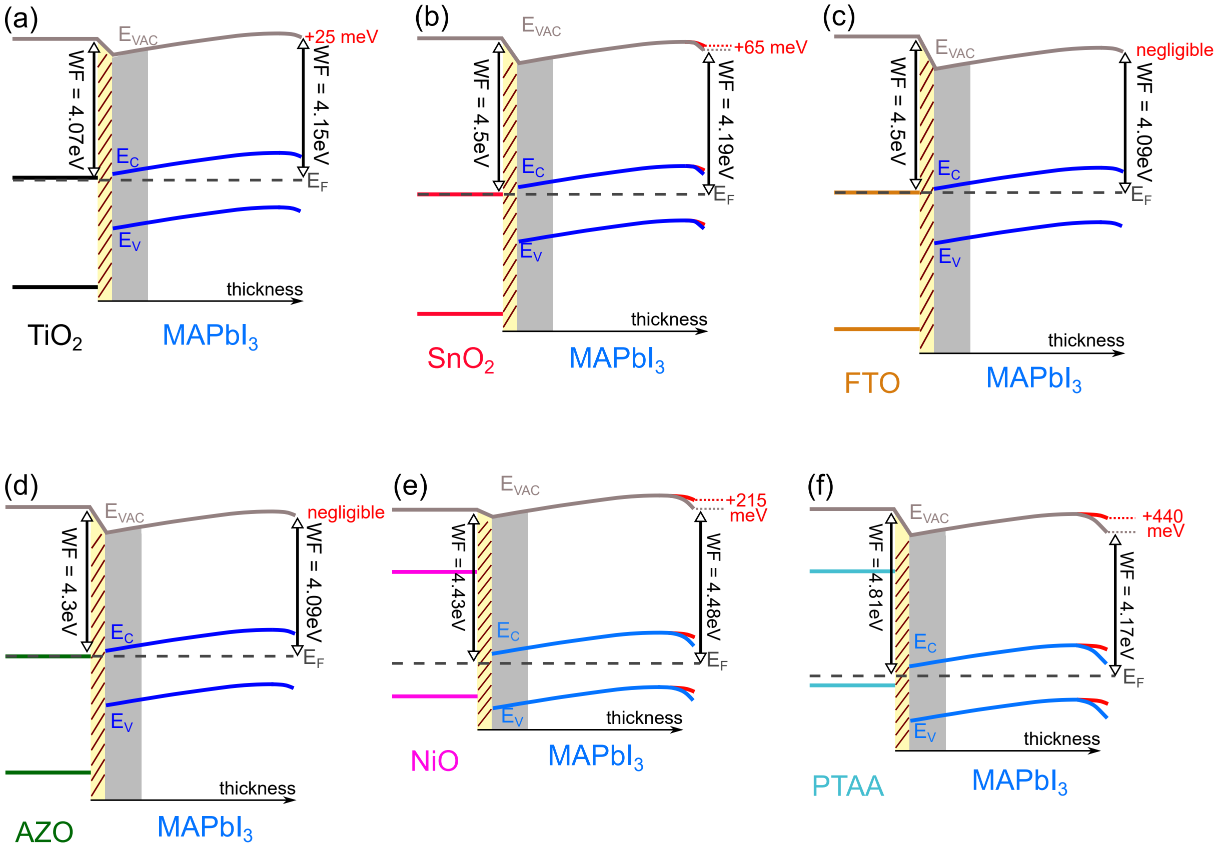

Figure 6.15: Summarizing energy band diagrams for $MAPbI_3$ co-evaporated on (a) TiO_2, (b) SnO_2, (c) FTO, (d) AZO, (e) NiO and (f) PTAA. Both surface band bending using SPV and band bending in the bulk are depicted here using the previous discussions. The shaded region (yellow with brown stripes) refers to the interface region between the substrate and $MAPbI_3$ and the grey region to the first few layers of $MAPbI_3$ where the band bending are undefined. The red surface band bending corresponds to the light case and was used to estimate the band bending in the dark, supposing no flat bands under light conditions due to the low intensity of the white LED used.

6.3 Summary of Chapter 6

In this chapter, the origin of the multi-component variations of the CPD upon light exposure for co-evaporated $MAPbI_3$ was investigated. The first fast increase of the CPD was linked with the screening of surface states by photogenerated electrons, reducing a downward surface band bending for all substrates. After the appearance of the SPV, the samples displayed a slow decrease (n-type) or a slow increase (p-type) of their CPD over prolonged illumination times. Upon switching off the light source, the CPD would partially recover, leading to different CPD value in the dark than from the original one.

This difference in values was correlated with the slow photo-induced change of the CPD and with a change of the tip's WF, which was calibrated before and after each measurement. This suggested a photo-induced contamination of the tip from the perovskite sample. XPS measurements in the dark and upon prolonged illumination were performed to investigate the chemical variations at the surface of $MAPbI_3$. On n-type substrate, the continuous decrease of the $MAPbI_3$ binding energies (I3d and Pb4f), the decrease of the I/Pb ratio and the increase of metallic lead Pb^0 over illumination time suggested a degradation of $MAPbI_3$ upon the combined effect of light and X-rays. A degradation mechanisms was given in which, upon illumination, $MAPbI_3$ decomposed into PbI_2 and other species, resulting in the reduction of Pb^{2+} into Pb^0 and the transformation of I^- into I_2. The latter species would eventually desorb and be adsorbed by the KPFM tip, altering its WF, in coherence with what was also reported in the literature.

For $MAPbI_3$ on p-type substrates, the KPFM and XPS measurements also highlighted variations at the surface due to the illumination, but did not permit to find the cause. Degradation and dissociation into PbI_2 and other species is likely to happen, but different species than I_2 might be evaporating and altering the tip WF. Additionally, other effects such as ion migration or redistribution, or trapping and detrapping of photogenerated charges in defects, might induce the observed variations in CPD and binding energies. Further characterization such as elemental mapping or high-resolution X-rays could be used to identify decomposition pathways.

Lastly, the KPFM of $MAPbI_3$ on different substrates, combined with calibrated PL and TRPL, were used to have a first estimation of the band bending occurring in $MAPbI_3$, from the surface to the first few layers in the bulk. SPV measured by KPFM was used to estimate the surface band bending. By using literature values for the electron affinities and bandgaps of all substrates, and for $MAPbI_3$, and by using the calibrated WFs measured by KPFM, a first drafts of energy band diagrams were drawn. Flat bands in the bulk were assumed, which resulted in a high n-type doping for $MAPbI_3$ on n-type substrates and close to intrinsic doping when using p-type substrates. However, the surface downward band bending (donor-like surface states) and the calibrated PL and TRPL measurements showed that the doping densities were mainly the same for all substrates, which suggested a bending of the bands in the bulk of the perovskite. KPFM and calibrated PL and TRPL were therefore carried out for different $MAPbI_3$ thicknesses and demonstrated a continuous increase of the doping when reducing the thickness, leading to strong bending of the bands. Using these information, final energy band diagrams were drawn. As these energy band diagrams are based on a lot of assumptions (electron affinities taken from literature and assumed constant with the thickness, similar bending for all substrates...), future measurements should focus on combining calibrated KPFM, PL and TRPL for different substrates and different thicknesses to have a better estimation of the band bending occurring in $MAPbI_3$ absorbers.

Chapter 7

Surface sensitivity and treatment of MAPI and mixed perovskites

The previous chapters focused on investigating the bare surface of co-evaporated $MAPbI_3$ absorbers, depending on their composition (use of low or high MAI partial pressure), and also depending on the thickness or the substrate they were fabricated on. Variations in WF but also surface photovoltage, surface band bending and stability against different conditions, such as light and heat, were discussed. It resulted that $MAPbI_3$ perovskites were relatively sensible to external factors and environment, even when near-stoichiometry was achieved to improve stability. The SPM literature on hybrid halide perovskite is already large and more groups should use these techniques to understand their surfaces. However the surface characterization are often carried out without taking into consideration the sample's conditioning history, such as the use of solvents or the exposure to ambient environments. This often leads to misleading interpretations of the surface properties of perovskites. Therefore, a clear tracking of the sample conditioning history (storage environment, contamination and post-treatments) is crucial when using surface-sensitive techniques. This chapter will focus on demonstrating the sensitivity of $MAPbI_3$ and mixed halide perovskites and how their surface properties can easily be altered by extrinsic factors. In addition, as surface passivation is becoming more and more common in the perovskite community, it will be shown how passivation treatments change the surface of mixed halide perovskites.

The first section 7.1 will use KPFM to demonstrate the sensitivity of the surface of $MAPbI_3$ when in contact with different environment or treatments. Oxygen exposure and dipping in solvents will result in the variation of the WF, the suppression of facet contrast and changes of the surface states, as measured by SPV. Section 7.2 will then present one option on how to improve the efficiency and stability of $MAPbI_3$ solar cells: the use of mixed cations-halides perovskites and how their surface differs from $MAPbI_3$'s surface. The surface of these mixed halide perovskites will be shown to be very different from co-evaporated $MAPbI_3$, with a pronounced GB band bending and large variations of WF between grains, some linked to PbI_2 grains. In section 7.3 and 7.4, KPFM and STM/STS will show how optimization strategies, such as surface passivation and varying the bottom extraction layer, alter the surface properties of these mixed perovskites. The results will demonstrate how ligand or 2D materials can be used to suppress surface defects, optimize the GB band bending, lower the WF and increase the surface bandgap to minimize hole barriers at the GBs and reduce interface recombination.

7.1 Surface sensitivity and treatment of MAPI

Investigating the properties of $MAPbI_3$ in different environment is essential as in-lab fabrication of solar cells often requires to expose the samples to various environments. Additionally, testing the stability of bare perovskites without layers on top or encapsulation can give a first overview of the quality of the absorber and its intrinsic resistance against different environments. One of the first experiments can be to study the effect of air exposure on the surface of $MAPbI_3$ using KPFM. Decomposition of the perovskite towards PbI_2 has already been reported to happen upon prolonged air exposure [99], which should be visible when performing KPFM. Koocher et al. also demonstrated the adsorption of water molecules depending on the surface terminations [425], which could induce different surface states and therefore a different WF. However Mosconi et al. have demonstrated that even though water molecules infiltrate the perovskite lattice, leading to a hydrated phase, it did not lead to electronic disorder and therefore variations of the surface energetics.

To that end, a $MAPbI_3$ film was co-evaporated on an FTO substrate and was first measured with KPFM in UHV without prior air exposure (Figure 7.1). The surface looked rather inhomogeneous with observable features in the CPD map related to different grains or facets.

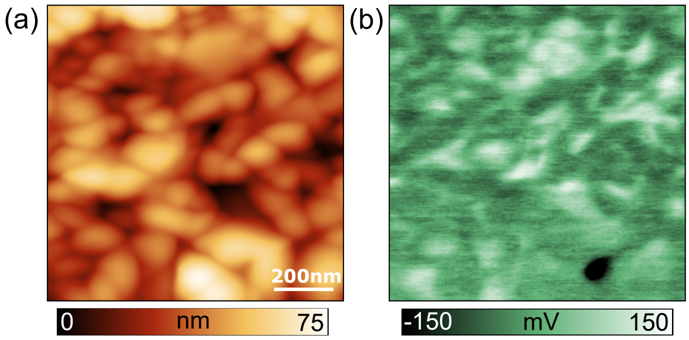

Figure 7.1: (a) Topography and (b) contact potential difference maps of a non-air exposed $MAPbI_3$ co-evaporated on FTO, measured with UHV FM-KPFM.

The average CPD distribution (Figure 7.2a) confirmed the previous observation by presenting a broad distribution peak and large variations in the CPD values from -0.1 V to 0.1 V. Furthermore Figure 7.2b displays an example of different WF values along different facets of a grain to give evidence of the facet-dependent contrast. In addition, no clear CPD contrast at the grain boundaries was visible and therefore the extraction of line profiles was needed to evaluate the variations of CPD between grains and GBs. Figure 7.2c presents the distribution of the CPD between grains and their adjacent GB, denoted as $\Delta CPD_{Grain-GB}$, extracted from 26 different line profiles from the CPD map of Figure 7.1b. A positive value would indicate a downward band bending from the grain to the grain boundary whereas a negative value would refer to an upward BB. As can be noticed, the distribution is centered at 0 mV, with 85 % of the values in a range of 0 ± 40 mV, which is negligible. Therefore there is no clear predominant band bending for this non-air exposed sample.

Then the sample was air exposed to air for a few hours and was taken back into the UHV FM-KPFM to be measured after its contamination. The acquired CPD map (Figure 7.3b) presented no visible feature but the CPD was still distributed within a 200 mV range

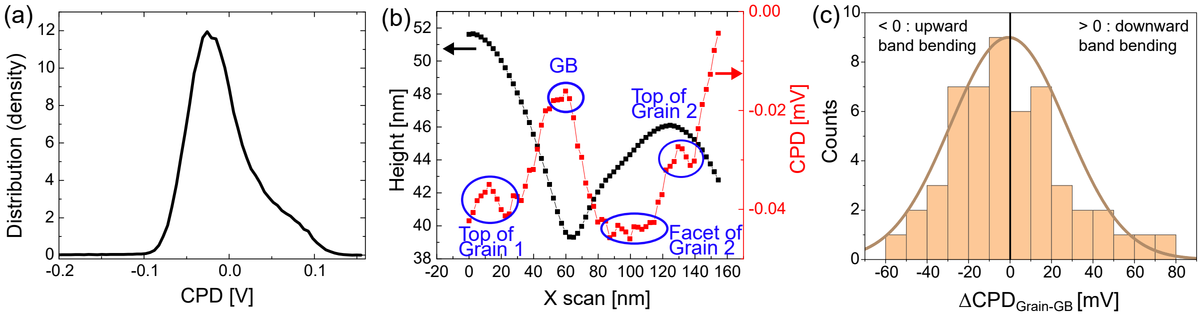

Figure 7.2: (a) Extracted average CPD distribution of the CPD map of Figure 7.1b. (b) Extracted topography and CPD lines profiles to highlight the different CPD on facets. (c) Distribution of the $\Delta CPD_{Grain-GB}$ calculated from line profiles, representing the grain boundary band bending behavior at the surface of this specific image of the $MAPbI_3$ absorber.

(Figure 7.4a), similar to the one observed for the as-grown $MAPbI_3$ absorber measured in UHV without air exposure. At first sight, it seemed that there was a preference for downward BB at the grain boundaries. To make sure, $\Delta CPD_{Grain-GB}$ was again calculated for this specific image, and the results are displayed in Figure 7.4b and as can be observed, the $\Delta CPD_{Grain-GB}$ was distributed over both positive and negative values, with 93 % of the values between 0 ± 40 mV, which again referred to a negligible band bending.

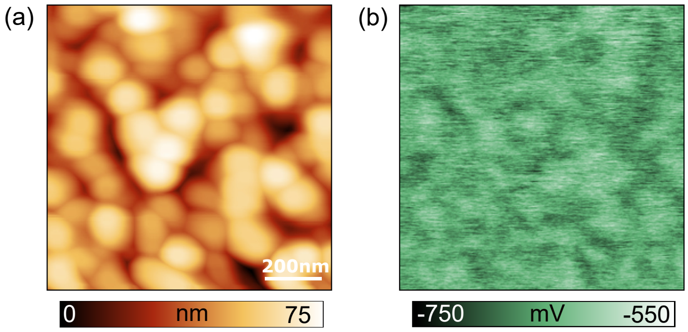

Figure 7.3: (a) Topography and (b) CPD maps of the previously air-exposed $MAPbI_3$ co-evaporated on FTO, measured with FM-KPFM in UHV.

However, the distribution also depicted a predominance towards downward band bending where 70% was calculated, while the as-grown sample displayed a 50/50 distribution (upward/downward). Therefore from such an image, it could be assumed that air exposure altered the surface in a non-reversible way which led to a loss of the original features and a predominance in the grain boundary BB. It is also important to note that the air exposure led to a more challenging scan of the sample, with the occurrence of multiple tip jumps due to tip-sample interaction, which could potentially come from a contaminated surface.

Similarly, $MAPbI_3$ was co-evaporated on two NiO substrates. One sample was transferred to the UHV KPFM without air exposure whereas the other one was exposed to a limited quantity of air, defined as the capacity in the pre-loading chamber of the UHV KPFM, for about 10 minutes. Figure 7.5 depicts topography and WF map images of the two samples. Some differences in topography were visible, where slightly smaller features could be visible for the as-grown sample together with a less rough surface, with a root

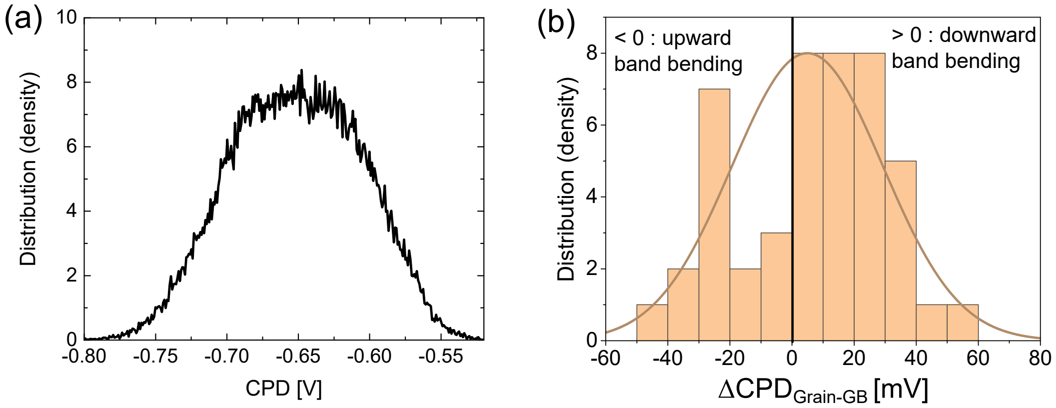

Figure 7.4: (a) Average CPD distribution extracted from the CPD map in Figure 7.3. (b) Distribution of the $\Delta\mathrm{CPD}_{Grain-GB}$ calculated from lines profiles, representing the grain boundary band bending behavior at the surface of this specific image of the $MAPbI_3$ absorber after being air exposed.

mean square (RMS) of 9 nm, compared to 12 nm for the perovskite exposed to air. The WF maps, which are only calibrated CPD maps, looked very similar, with a relatively homogeneous surface potential with the appearance of features with either lower or higher WF than the majority of the surface, representing facets or grain boundaries. This was also visible in the distribution of the WF for both samples (Figure 7.5e), where rather narrow single peaks were observed with similar magnitude. However, there was a clear difference in the average WF values, where the as-grown sample displayed a WF of 4.48 eV, and the air-exposed sample a WF of 4.13 eV, suggesting very different surfaces, most likely resulting from additional surface states induced by oxygen or water molecules.

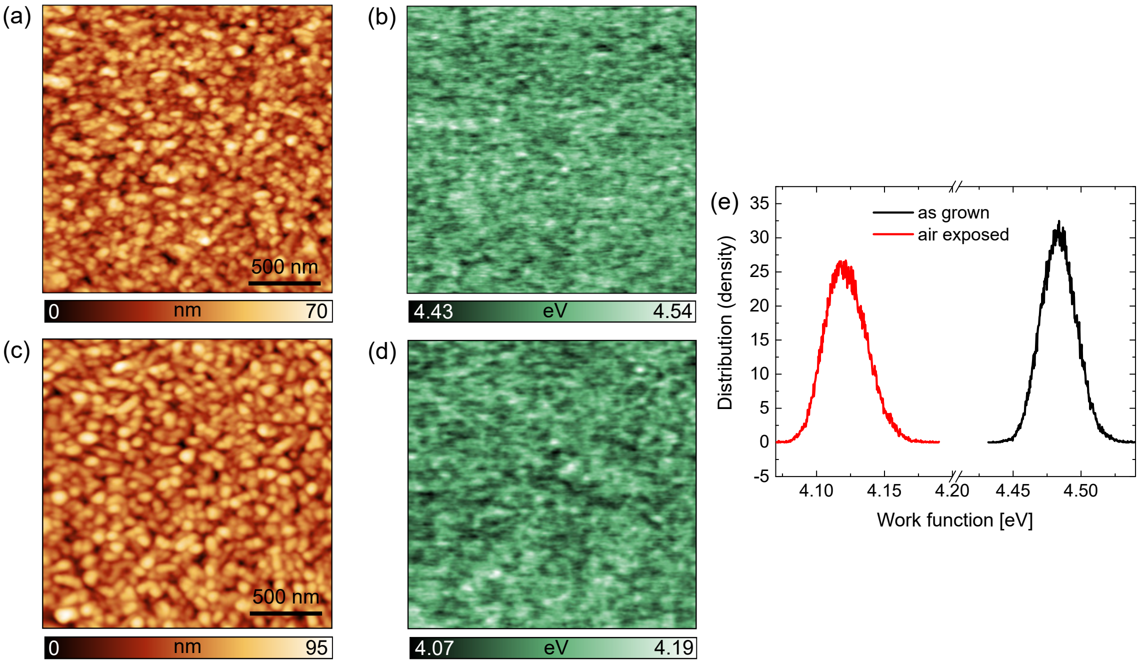

Figure 7.5: (a) Topography and (b) WF maps of as-grown $MAPbI_3$ co-evaporated on a NiO substrate. (c) Topography and (d) WF maps of air-exposed $MAPbI_3$ co-evaporated on a NiO substrate. (e) WF distribution of the two samples.

An additional useful step to study the effect of air exposure was to determine the surface photovoltage and the behavior of the WF upon prolonged illumination. A white LED illumination (~ 10 mW/cm^2) was used outside the UHV chamber and directed towards the samples. Figure 7.6 represents the CPD and the Z signal (height) of the two samples measured first in the dark, upon illumination and in the dark again. The first observation was that the SPV was different from the two samples, with +215 mV for the as-grown MAPbI$_3$ and +350 mV for the air-exposed one. The adsorption of water or oxygen molecules on the MAPbI$_3$ surface could introduce different type of surface states as well as a higher density of surface states, leading to a larger surface band bending, resulting in a higher SPV. Additionally, while the CPD of the as-grown sample stabilized after about 15 minutes of illumination, suggesting it had reached its equilibrium, the CPD of the air-exposed sample kept on increasing, reaching values higher than 500 mV compared to the initial value in the dark, with no visible stabilization. As already demonstrated in the previous Chapter 6, this increase correlates with a higher degree of combined degradation, ion migration and potentially defect trapping and detrapping, suggesting that the air exposure reduced the intrinsic stability of the absorber by enabling the incorporation of oxygen or water-based defects [114, 404, 406]. After the light was switched off, the CPD of the as-grown sample managed to reach back its original value in the dark whereas it was not the case of the air-exposed MAPbI$_3$, suggesting either that it would take more time to reach the original value or that the surface had changed, as the value of the tip WF did not change afterwards. On the other hand, no photostriction, i.e. lattice expansion upon illumination, was observed for the sample exposed to air, which showed the same behavior as the as-grown sample (Figure 7.6b), and which would suggest that oxygen incorporation did not alter the lattice constant of the perovskite.

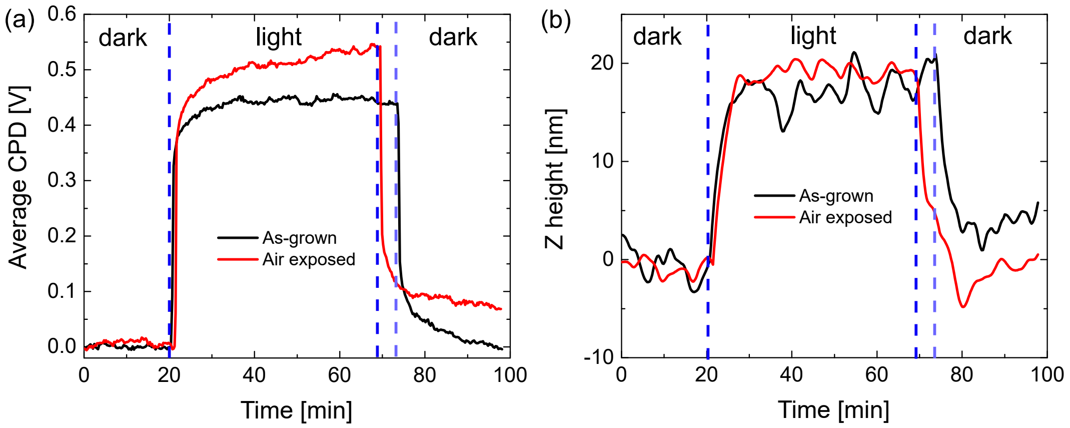

Figure 7.6: (a) CPD and (b) Z signal (height) of as-grown and air-exposed MAPbI$_3$/NiO, measured upon different conditions: dark, upon illumination and dark again after the light was switched off.

Other experiments were carried out and proved the clear alteration of the surface by exposing the sample to air, by using for example post-annealing treatments on air-exposed and non-air exposed samples (see appendix Chapter 7G.1). In addition, the previous samples were almost entirely measured in a UHV environment, which enabled the MAPbI$_3$ surface to retain its properties over long scanning times. On the other hand, when measuring MAPbI$_3$ for prolonged days in an ambient environment, the CPD signal was highly unstable in the dark. Figure 7.7 depicts the variations of the CPD for two samples, one measured in UHV and one in ambient conditions for 24 hours and for multiple days respectively. As can be observed, the CPD in the dark for the sample measured in

UHV is almost constant whereas the one for the sample measured in air gradually increases until reaching out a quasi-stagnation value after days of measurements, suggesting that the surface energetics would greatly change due to the combination of air exposure, light and measurement-induced interactions. Indeed it has to be noted that for the measurements in air, the laser used was in the absorption range of $MAPbI_3$, whereas this was not the case for the measurements in UHV, which could always result in laser-assisted degradation of the perovskite in air.

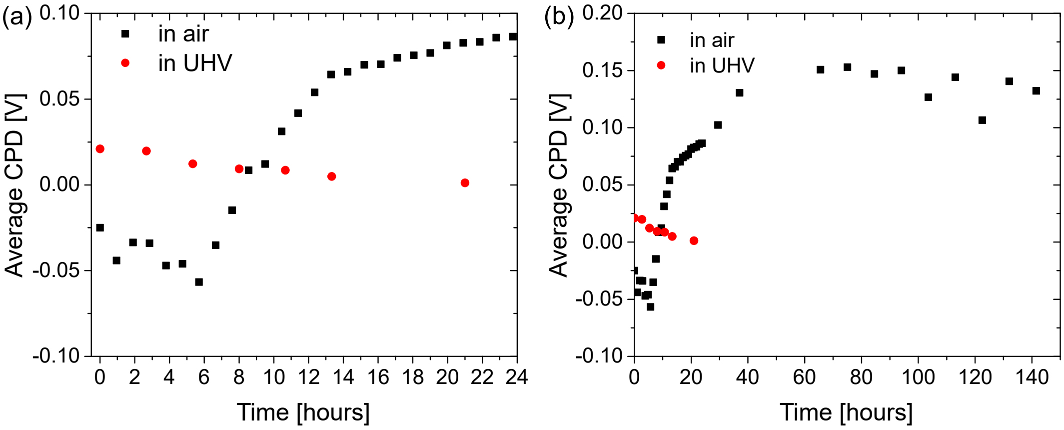

Figure 7.7: Average measured CPD values of both samples, measured in UHV and in air for (a) 24 hours and (b) multiple days.

Alternatively to air exposure, post-fabrication treatments can also alter the surface properties of $MAPbI_3$. Annealing in an nitrogen environment was already investigated in Chapter 5 and demonstrated that depending on the composition of the absorber, annealing in N_2 could irreversibly change the WF of $MAPbI_3$, as well as induce grain coarsening and sample degradation. In addition, the use of solvents is most of the time used in perovskite fabrication, and necessary when using solution-based processes. Isopropanol (IPA) for example has been a solvent used to help forming a perovskite phase by dissolving PbI_2 or MAI or other perovskite-based compounds and spin-coating the solution [337, 426, 427, 428] on substrates. Abzieher et al. [429, 430, 431] observed that IPA improved and helped washing out unreacted MAI via the use of IPA, which yielded more homogeneous perovskite surfaces. An increase of the power conversion efficiency from 9% to 18% resulted from the use of a 30 s IPA-solvent treatment on their co-evaporated $MAPbI_3$. After 60 s they however observed the peeling off of the perovskite, synonym of macroscopic degradation. It is therefore interesting to study the influence of dipping a perovskite absorber into IPA has on its surface.

In the following, the surface of their co-evaporated $MAPbI_3$ sample was compared after growth, and after treatment in a IPA solution for 30 s and 60 s. As a side note, it has to be noted that all samples had to be air exposed for transfer between the PVD chamber and the glovebox but no further air exposure occurred after the IPA-treatment as the samples were transferred from the glovebox to the UHV KPFM via an inert gas transfer suitcase. As already presented by T. Abzieher through SEM images [431], the IPA treatment for 30 s did not seem to change the topography of the $MAPbI_3$ absorber, and the measured grain size with KPFM remained the same and the roughness mainly similar (RMS of 9 nm for the as-grown sample compared to 7 nm for the 30s-IPA-treated sample). Slightly smaller grains with the appearance of higher and larger features came with a 60s-IPA treatment even though the roughness remained the same (RMS of 9 nm).

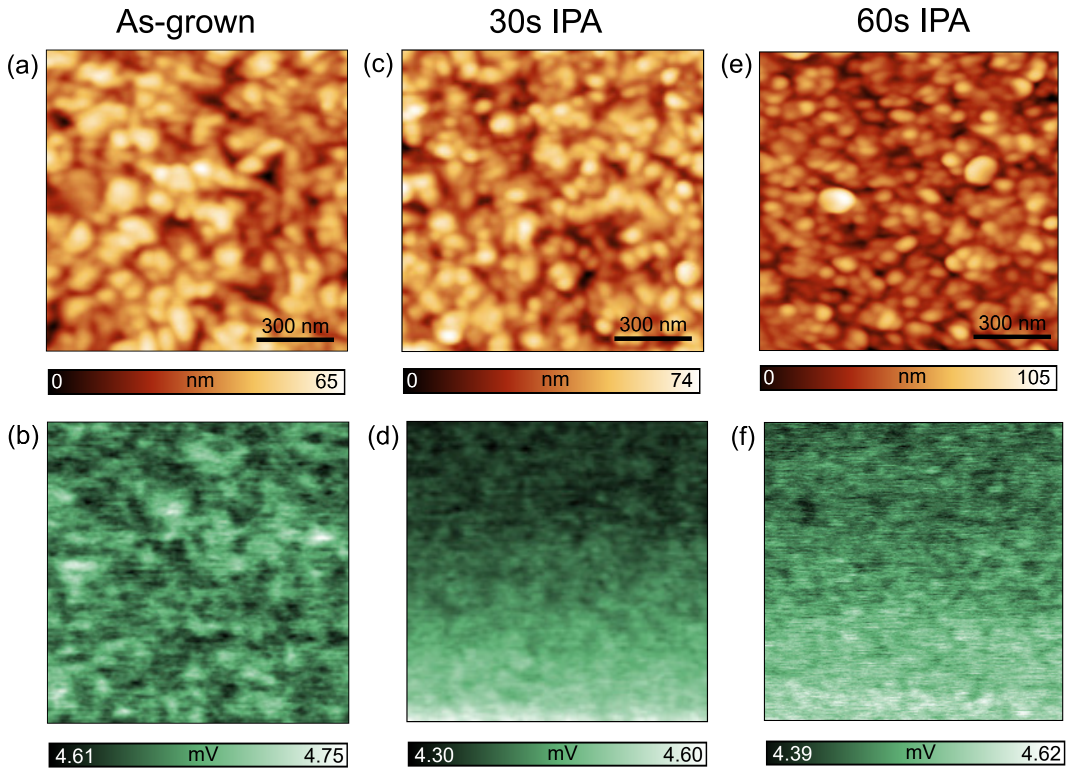

Figure 7.8: AFM topography of (a) as-grown but air exposed $MAPbI_3$ co-evaporated on PTAA, (c) post-treated with a IPA solution for 30 s in a nitrogen-filled glovebox and (e) post-treated with a IPA solution for 60 s in a nitrogen-filled glovebox. (b,d,f) Corresponding workfunction maps of (a,c,e).

Differences are however visible in the WF maps. For the as-grown sample, the WF map resembled the one already presented in many KPFM map of this thesis, with a rather homogeneous surface with some features with lower and higher WF but within an energy range of 140 meV, with an average WF of 4.68 eV. After 30 s of IPA bath, the WF map displayed a continuous decrease of its CPD signal until stabilization, a behavior which was already observed for $MAPbI_3$ co-evaporated on PTAA in Chapter 6 but only after illumination. This decay of the CPD signal could either come from a prior illumination of the sample as light is always needed to approach the KPFM tip close to the sample, or from the continuous desorption of species from the surface to the UHV but this cannot be confirmed as the tip's WF changed also due to interaction with the surface. Out-gassing of the IPA solution or a surface charging effect due to the IPA could also be potential causes of the CPD decrease. The WF values at the very beginning was of 4.6 eV and stabilized at 4.34 eV. Similarly, after the 60s-IPA treatment, the WF dropped from 4.61 eV to a stabilized value of 4.42 eV. The large variations of the WF made it a bit more challenging to interpret the energetic properties of $MAPbI_3$ after treatment. If the stabilized values are taken into account, then the WF after the IPA treatment of 30 s decreased by about 340 meV and by 260 meV for the 60s-IPA treatment, which does change considerably the interface band alignment and could help understand why the PCE increases with a 30s-IPA treatment.

The behavior of the WF was also studied upon illumination for all three samples (Figure 7.9). The CPD in all cases increased under light exposure but with different magnitude, with a SPV of +140 mV for the as-grown sample, a SPV of +375 mV for the

30s-IPA-treated sample and a SPV of +450 mV for the 60s-IPA-treated sample. These differences in SPV suggest an increase of the surface band bending when treating the sample with the IPA solution. In addition, as depicted in Figure 7.9, after the SPV, all samples observed a decay of their CPD followed by its stabilization. On the other hand, the 60s-IPA-treated sample did not stabilize in the same timespan, suggesting further degradation of $MAPbI_3$, as already discussed in Chapter 6.

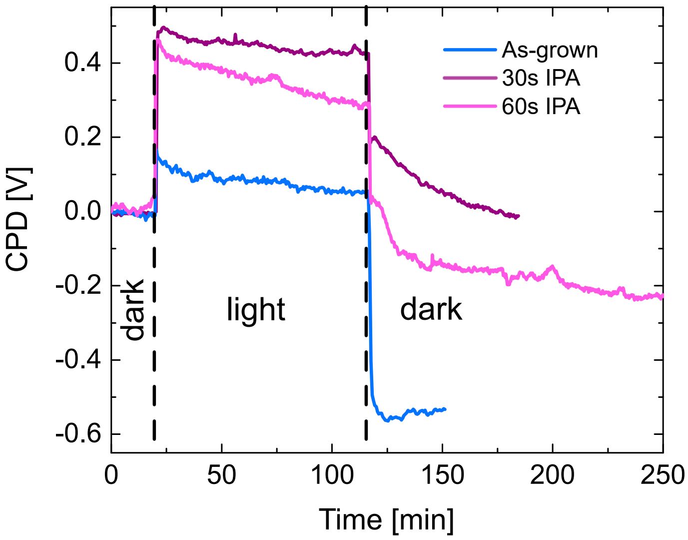

Figure 7.9: CPD of the as-grown $MAPbI_3$, 30s-IPA-treated $MAPbI_3$ and 60s-IPA-treated $MAPbI_3$ absorbers in the dark, upon illumination and in the dark again.

Lastly, after the light was switched off, only the 30s-IPA-treated sample showed an almost recovery of its original CPD value in the dark, whereas the as-grown sample exhibited a large sudden decrease of its CPD, not specifically correlated with a change of the tip WF, and the 60s-IPA-treated sample exhibited a continuous decrease of its CPD, without reaching its original CPD value in the dark. The previous qualitative study clearly indicates that the use of solvent in perovskite alters its surface, by varying the CPD stability but also the surface states and dipole, inducing different magnitude of surface band bending. These variations will have an influence in the extraction or repelling of charge carriers and thereafter device efficiencies. These observation reflect that most of the solution-based processes using solvents are unintentionally changing the surface energetics of perovskite thin films.

The previous experiments therefore indicated that the interpretation of KPFM measurements should take into consideration the sample's history, such as its fabrication (use of solvents) and exposure to different environment (oxygen). The surface of $MAPbI_3$ will most likely interact with its environment, which will result in the alteration of its surface by changing its surface states or surface dipole. This will lead to potential erroneous interpretation of the measured CPD, WF or behavior upon illumination.

7.2 Variations of surface properties of mixed halide perovskites

One of the most efficient ways reported to improve the efficiency of perovskite solar cells is to change the methylammonium (MA) cation with other larger or smaller cations as previously discussed in section 1.1.2 of Chapter 1. In addition, combining halides (bromide (Br), chloride (Cl) and iodide (I)) and cations (cesium (Cs), formamidinium (FA), MA) resulted in the record perovskite power conversion efficiencies [8, 301], which exceeds the highest PCE reachable with the $MAPbI_3$ composition. In the following section, the surface of high-efficient solution-based mixed perovskites will be investigated via KPFM and will be compared to the co-evaporated $MAPbI_3$ of this thesis.

The two investigated samples have different compositions: $FA_{0.97}MA_{0.03}PbI_{2.91}Br_{0.09}$ and $Rb_{0.03}Cs_{0.05}MA_{0.05}FA_{0.90}PbI_3$, which will be referred to as $Pero_{Br}$ and $Pero_{Rb,Cs}$ respectively as these are the elements not in common. They were fabricated and sent for characterization by Anurag Krishna and Yong Ding from Ecole polytechnique de Lausanne respectively [344, 432]. As can be observed, the first sample is composed of several halide ions (I^- and Br^-) and the basic FA^+ and MA^+ cations whereas the second sample displays one halide ion (I^-) and four cations (Cs^+, MA^+, FA^+ and Rb^+). Their fabrication procedure can be found in [344] and [432] respectively. Devices made from these perovskite absorbers exhibited similar efficiencies, with 22.4 % when using $Pero_{Br}$ and 22.7% when using $Pero_{Rb,Cs}$, with an almost similar device configuration. However their topographies and surface energetics looked rather different as depicted in Figure 7.10.

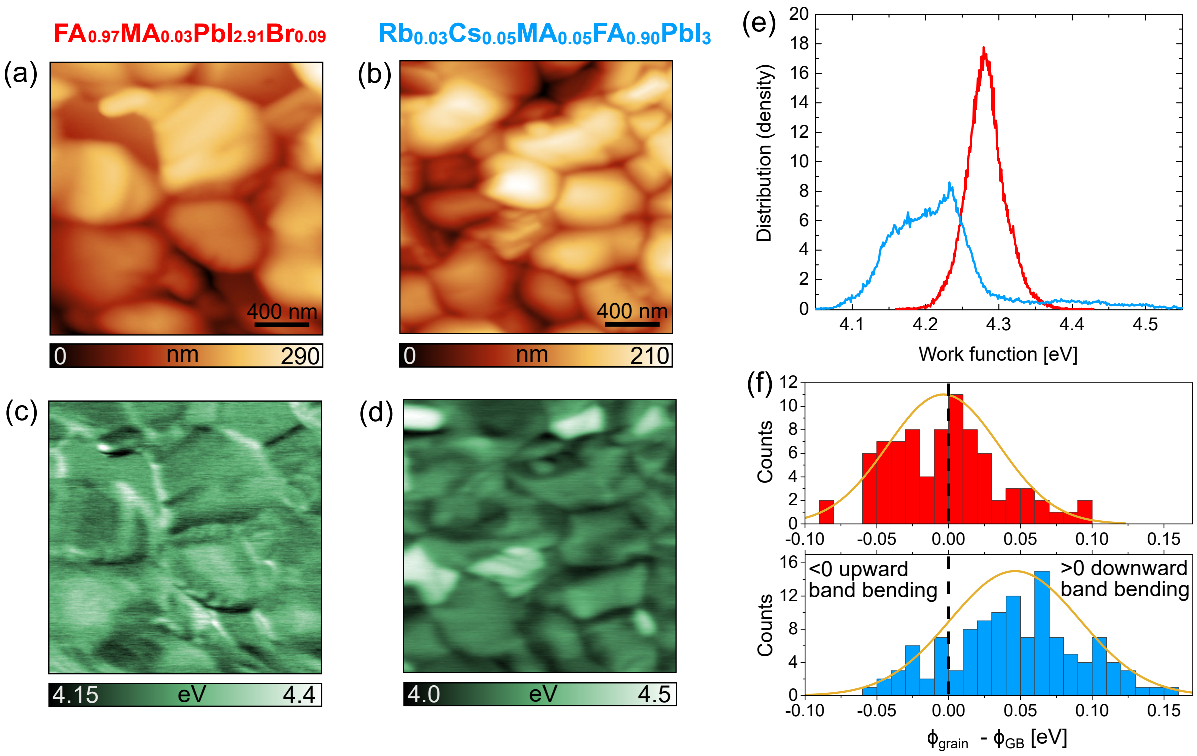

Figure 7.10: AFM topography of solution-based (a) $FA_{0.97}MA_{0.03}PbI_{2.91}Br_{0.09}$ and (b) $Rb_{0.03}Cs_{0.05}MA_{0.05}FA_{0.90}PbI_3$ with their respective workfunction maps in (c) and (d). (e) workfunction distribution of the workfunction maps and (f) grain boundary band bending for the two samples.

Both samples were not exposed to air after their deposition on their substrates and were transferred to the UHV KPFM without air exposure, avoiding their surface from being altered in any way. The AFM topography displayed a slight difference in the grain sizes with the Pero_{Br} exhibiting large grains than the $\text{Pero}_{Rb,Cs}$ (660 nm vs 460 nm in average) but both absorbers also presented smaller grains or features. Their WF maps (Figure 7.10(c,d)) showed even more differences even though their extracted average WF were mainly the same (4.28 eV and 4.21 eV respectively). As depicted in their distribution profiles (Figure 7.10e), $\text{Pero}_{Rb,Cs}$ provided a much broader distribution of its WF, of about 500 meV while Pero_{Br} displayed a much narrower one of 250 meV. The differences can be attributed to the visible brighter grains with a much larger WF in Figure 7.10d. These grains had WF on average 340 meV higher than the rest of the surface and covered 7% of the perovskite surface. These grains could be PbI_2 grains, as the latter have a higher bandgap, WF and display p-type characteristics [138, 420, 433]. Previous KPFM measurements performed on $FAPbI_3$-based mixed perovskites already uncovered the existence of the PbI_2 distributed all over the surface when an excess of PbI_2 was used [434, 435]. Gharibzadeh et al. have demonstrated the existence of PbI_2 grains in a $Cs_{0.18}FA_{0.82}PbI_3$ with a 10% excess of PbI_2 as these grains presented higher WF (higher by 110-230 meV) in the KPFM map but lower cathodoluminescence intensities [435]. Chen et al. have observed PbI_2-rich grains in the KPFM map of a $(FAPbI_3)_{0.85}(MAPbBr_3)_{0.15}$ mixed perovskite, which presented WF higher by more than 30 meV and higher lifetimes compared to the rest of the grains [434].

In addition to the WF distribution, the grain boundary band bending (GB-BB) was measured by extracting line profiles between grain boundaries and their adjacent grains. As displayed in Figure 7.10f, both samples exhibited both upward and downward BB but different distribution profiles. Pero_{Br} displayed a rather broad distribution of $\pm$ 100 meV, which could induce both electrons and hole barriers, reducing the efficiency to extract holes and limiting the overall device power conversion efficiency. On the other hand, $\text{Pero}_{Rb,Cs}$ exhibited a much larger predominance for downward BB (90%) with 50% of its values exceeding 40 meV, indicating a rather strong barrier for holes, which could limit the extraction efficiency of holes towards the hole transport layer. The 10% remaining upward band bending was within a 40 meV range, which is close to kT using the temperature of a solar cell under standard operating conditions ($\sim$ 30 meV) and therefore should not be detrimental to the device performances.

Compared to the co-evaporated $MAPbI_3$ of most of this thesis, the first observation was that the grains of the mixed perovskite were much larger, which could be attributed to the fabrication procedure where most of the time annealing, vector of grain enlargement, is used after spin-coating of a perovskite solution on a substrate. Much more contrast could also be observed at the grain boundaries for the mixed perovskites compared to co-evaporated $MAPbI_3$ where most of the variations were noticed at grain facets. However the enhanced contrast at the grain boundaries could also be the consequence of the enlarged grains, which made the visualization of the grain boundaries easier. While the measured GB band bending for the co-evaporated samples was almost always within a 0 ± 40 meV range, which was negligible and not detrimental to device performances, the GB-BB for the mixed-perovskites was much more pronounced and could affect the extraction efficiency or induce recombination at the GBs. Upon illumination, the mixed perovskites studied did not present a visible SPV using the 15 ms resolution of the KPFM while the $MAPbI_3/TiO_2$ displayed a slight increase of its WF. A more detailed discussion for the reader can be found in section G.2 of appendix Chapter 7.

This first qualitative study therefore showed that two $FAPbI_3$-based perovskites yielding similar efficiencies could exhibit large differences on their surfaces depending on the fabrication procedure and the additional elements used. Preliminary investigations of the absorber via surface-sensitive measurements, in this case KPFM, is useful to find routes of improvement for the future device. As an example, it is crucial to determine the nature of the high-WF grains and the pronounced GB downward BB of $\text{Pero}_{Rb,Cs}$ and their effect, either beneficial or harmful, on the perovskite absorber.

Therefore, Helium Ion Microscopy-Secondary Ion Mass Spectrometry (HIM-SIMS) was used as it enables the element mapping at the surface of a sample [256]. Figure 7.11b depicts the morphology image taken via the helium ion microscope and Figure 7.11(a,c) represent the elemental mapping of ^{133}Cs and ^{208}Pb at the surface of $\text{Pero}_{Rb,Cs}$. As can be observed the distribution of the Cs element was not uniform at the surface, whereas inhomogeneities could be also discerned for the Pb element but with much less clarity. The dark regions of Figure 7.11 are Cs-deficient regions and were linked to the small grains of the helium microscope image. The coverage of these Cs-deficient grains was calculated to be around 7%, matching the coverage of the high WF regions of the WF map in Figure 7.10d. As Cs should be uniformly distributed in the perovskite lattice and the Cs-deficient grains exhibited much larger WF than the rest of the surface, these grains were suggested to be PbI_2 or PbI_2-rich grains. This correlated nicely with the fact that $\text{Pero}_{Rb,Cs}$ was purposely fabricated with an enrichment of PbI_2, proven via XRD measurements [432].

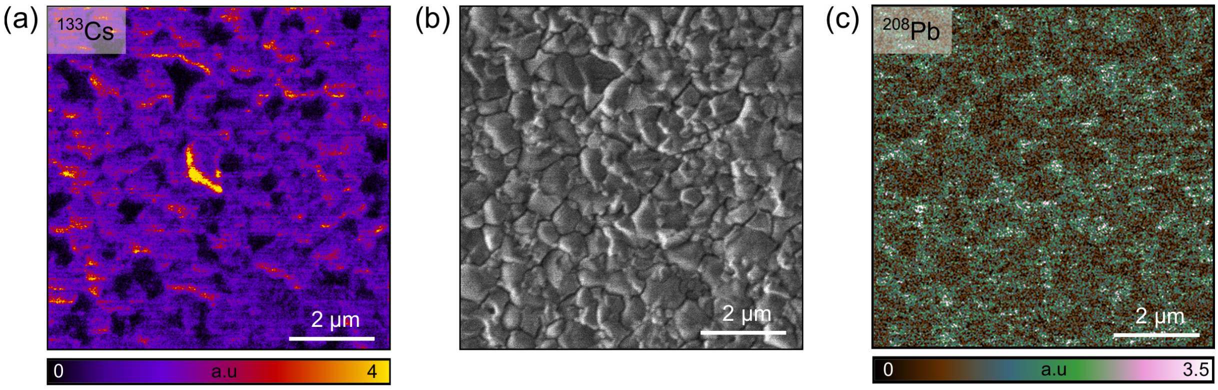

Figure 7.11: (a) Mapping of the ^{133}Cs element at the surface of $\text{Pero}_{Rb,Cs}$. (b) Helium microscope image of $\text{Pero}_{Rb,Cs}$ surface and (c) mapping of the ^{208}Pb element at the surface of $\text{Pero}_{Rb,Cs}$. Adapted with permission from [432]

In addition an overlay of the ^{133}Cs distribution and the surface morphology was made and is depicted in Figure G.4 of appendix chapter 7G.3. This further proved the link between specific grains and Cs-deficient regions but it also showed that higher Cs content was accumulating at certain grain boundaries. Addition of Cs into a $FAPbI_x$ rich perovskite has already been reported to reduce the trap density in the bulk and potentially at the grain boundaries [436], which are known to include a higher density of defect sites [437, 438]. Besides, the KPFM measurements presented a pronounced downward band bending at the grain boundaries (Figure 7.10), which could therefore be one of the consequences of the Cs accumulation at the grain boundaries.

The previous section gave an overview of the surfaces of mixed halide perovskites. These composition are the basis of highly efficient devices due to the substitution of MA by FA and the incorporation of different cations such as Cs and Rb and halide such as Br. It showed that preliminary studies of the surface properties can help in finding the routes for optimization towards even higher performances. As an example, Pero$_{Br}$ exhibited large grain boundary band bending, which could reduce the charge transport and extraction and therefore one possibility would be to passivate the grain boundaries or the surface by means of an additional layer on top of the perovskite, which will be discussed in the next section.

7.3 Surface passivation of mixed halide perovskites

Even if Pero$_{Br}$ exhibited a high efficiency of 22.4% with good device performances, the solar cell lacked of stability under standard operating conditions [344]. Passivation via tailored molecular modulators using Lewis acids and bases and other chemistry-based techniques proved to be successful for multiple groups [188, 189, 190, 439]. Therefore a multifunctional ligand 2,5-Thiophenedicarboxylic acid, which is rigid, and highly thermally stable, was spin-coated on top of the Pero$_{Br}$ perovskite. From now on, the as-grown Pero$_{Br}$ will be referred to as **control** while the same sample treated with the ligand solution will be referred to as **target**. More information concerning the ligand and its deposition procedure can be found in [344].

KPFM measurements of the target sample were carried out and compared to the already discussed control sample (Figure 7.10(a,c)). Figure 7.12(b,d) represent the topography and WF maps of the target sample. The grain size remains overall the same but very small features (dot-like) appear on the ligand-treated target sample, most likely resulting from the spin-coated solution.

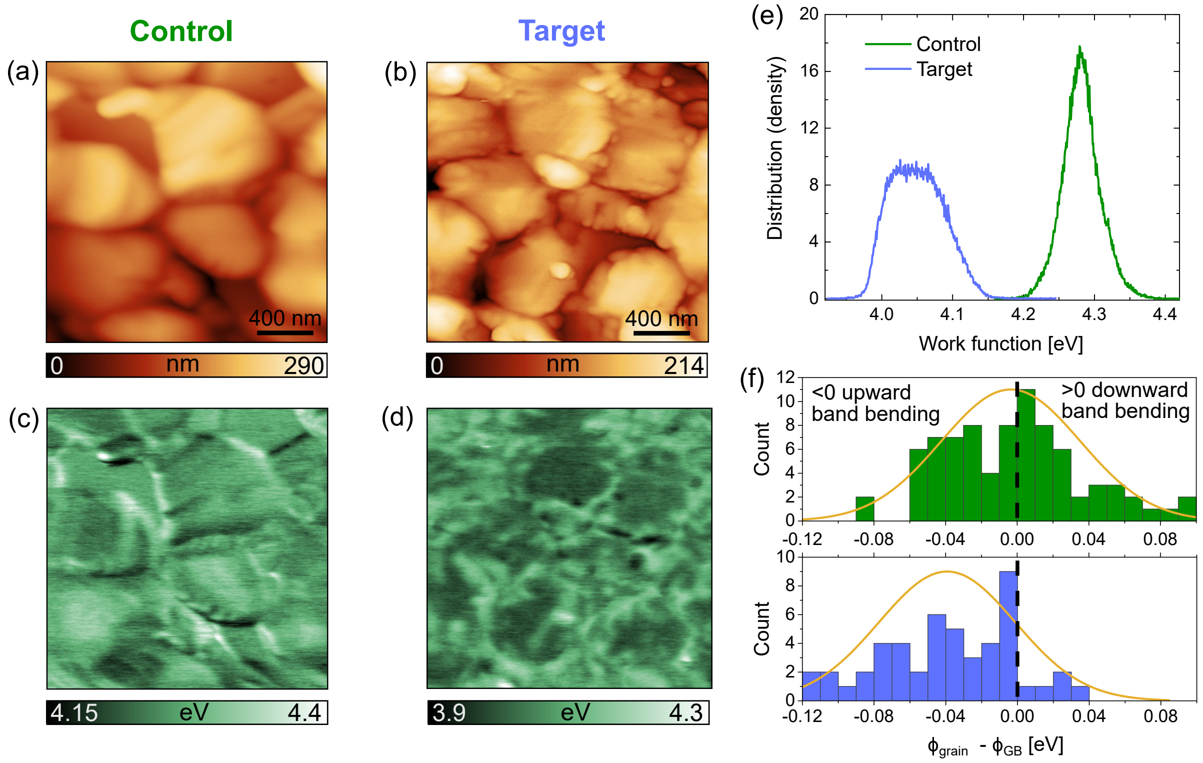

Figure 7.12: AFM topography of solution-based (a) control sample and (b) target with their respective WF maps in (c) and (d). (e) WF distribution of the WF maps and (f) GB band bending for the two samples.

Compared to the surface of the control perovskite, which exhibited variations of its

WF by ~ 250 meV, the target sample with the ligand deposited on top provided a slightly broader distribution (~ 350 meV), as suggested also by the visible WF map, where different contrasts could be discerned within single grains. Besides, the deposition of the ligand had the effect of decreasing the overall WF of the sample, from 4.28 eV for the control to 4.05 eV for the target. This variation in WF was also observed in the UPS measurements and could play a role in the interfacial alignment with the top hole extraction layer, spiro-OMeTAD (either better hole extraction or electron repelling).

Additionally, the GB-BB was measured (Figure 7.12f) for the two samples. While, the control perovskite presented a 50/50 distribution of upward/downward BB with a range of ± 100 meV, the target perovskite displayed almost exclusively upward band bending (90%) with a residual 10% of downward BB with a range of 0-40 meV, which made it negligible. The upward band bending however extended from 0 to 120 meV and was synonym of an accumulation of negative charge at the GBs, which can also be referred to as a small electron barrier. Therefore the surface treatment with the ligand enabled to suppress the previously-observed hole extraction barrier of the control sample, which should be beneficial and improve the hole extraction at the interface perovskite/spiro-OMeTAD.

Scanning tunneling spectroscopy (STS) is also of great use to study a purposely-altered surface (see Chapter 4). Therefore current imaging tunneling spectroscopy (CITS) was carried out on both samples in UHV. The case of the control perovskite was already discussed in the section 4.6 of Chapter 4 but as a reminder, the surface bandgap of the control sample was extracted to be 1.6 eV ± 0.1 from the broadened $(\mathrm{dI/dV})/\overline{I/V}$. Besides, a defect signature (likely a Pb_I antisite) was discerned in the conduction band (positive voltages) as $(\mathrm{dI/dV})/\overline{I/V}$ is a representative measure of the local density of states (LDOS) (Figure 7.13).

By comparison, the logarithmic $(\mathrm{dI/dV})/\overline{I/V}$ (inset of Figure 7.13) of the target sample did not present the defect signature of the control sample. Density functional theory (DFT) calculations were then used to model the most stable configurations of the ligand molecule interacting with the Pb_I defect. The passivating ligand showed an interaction energy of -0.98 eV confirming a favorable interaction with the surface antisite defect, which suggested an improvement of the surface thermodynamical properties after spin-coating the ligand on top of the control sample. Also the removal of a defect at this interface would reduce the surface recombination velocity and result in an improvement of the V_{OC}, which was the case [344].

In addition, the $(\mathrm{dI/dV})/\overline{I/V}$ of the target sample exhibited a larger surface bandgap of 1.9 eV ± 0.1 compared to the surface bandgap of the control sample. An increased surface bandgap can suppress interfacial recombination at the perovskite/HTL interface and was already identified as one of the key properties of high-efficiency $\mathrm{Cu(In,Ga)Se_2}$ solar cells [440, 441]. On a side note, the down-shift (lower conductance) of the logarithmic $(\mathrm{dI/dV})/\overline{I/V}$ of the target sample (inset) was coherent with the reduction of the WF observed in the KPFM measurements. In complement to the KPFM and STS measurements, PL and TRPL were carried out as means of rapid stability tests. After the UHV measurements that lasted a few days, both the PL yield and the lifetime (Figure G.5(a,c) of Appendix G.4) of the control sample decreased (from 570 ns to 380 ns) whereas the PL yield of the target sample, treated with the ligand, increased and the decay curve (Figure G.5(b,d) of Appendix G.4) remained mainly the same (450 ns to 440 ns). This proved that the stability of the target sample was improved due to the passivation with the ligand.

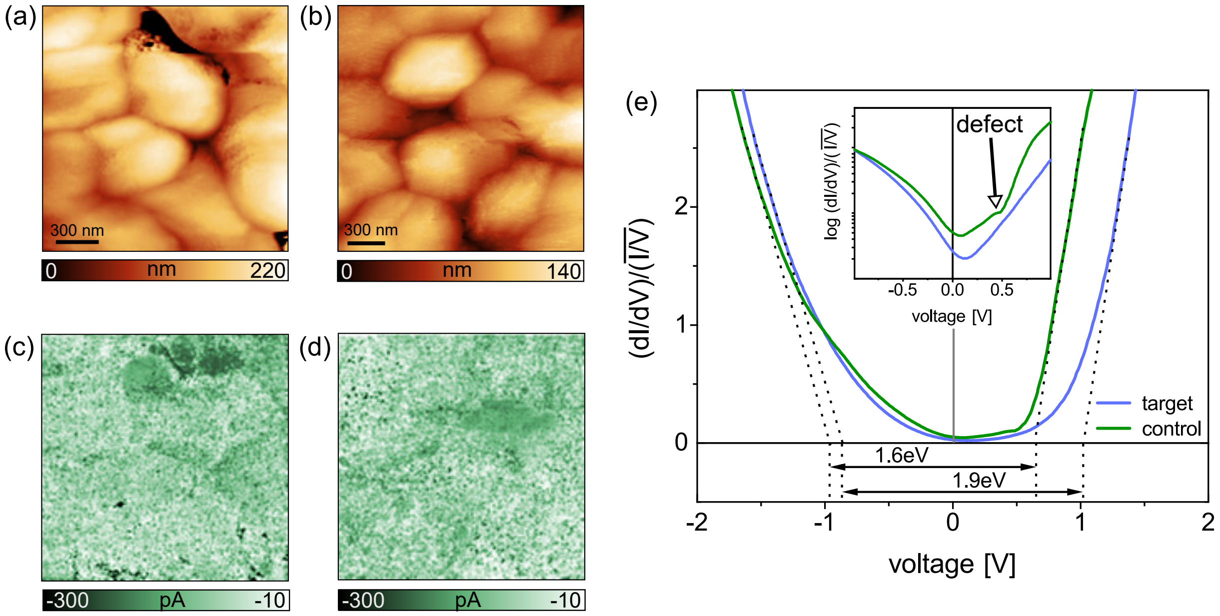

Figure 7.13: STM topography of solution-based (a) control sample and (b) target with their respective conductance (dI/dV) maps obtained with a voltage of -2V in (c) and (d). (e) Average broadened conductance curves of the control and target sample. The linear extrapolations of the curves (dotted lines) depict different bandgaps for the different samples. The inset represents the same curves plotted on a logarithmic scale. The control sample shows a defect response at a positive applied voltage.

Therefore, the treatment of the mixed perovskite surface with a spin-coated ligand enabled the suppression of surface defects in the vicinity of the conduction band, homogenized the grain boundary band bending by yielding a sole electron barrier resulting in an effective extraction of the charges towards the hole extraction layer and lastly increased the surface bandgap, which reduced the interface recombination between the perovskite and the extraction layer. These passivation techniques led to an increase in device efficiency and an improvement of the long-term operational stability as shown by Anurag et al. [344]. This proves that a thorough investigation of the surface is essential and that improvement of the devices can thereby be carried out through surface treatment and passivation.

Similarly, the passivation of the surface of the same control perovskite (Pero$_{Br}$) can originate from the use of different materials. As an example, a Rubidium complex (Rb^{+}) was incorporated in Pero$_{Br}$ through a gradient configuration (from the surface to deeper into the bulk). In addition, further surface passivation was performed by coating a two-dimensional halide salt, namely phenylethylammonium iodide (PEAI), which is a bulk cation with a large radius whose purpose is to isolate the anionic layers of the 3D perovskite structure and transform it into a 2D perovskite [442]. The Rb and Rb/PEAI passivation both led to a reduction of the WF, a suppression of the GB downward BB, a suppression of the defect visible in STS and an increase surface bandgap. The reader can find the results and discussions in details in section G.5 of appendix Chapter 7 but the results resemble the ones from the ligand passivation previously discussed.

7.4 Varying the bottom layer to improve the efficiency

As discussed in section 1.3.5 of Chapter 1, the bottom layer is also a crucial part of the perovskite solar cell. Its nature will structure the perovskite lattice and growth conditions, which can eventually result in reduced defects for certain grain orientations and thereby higher efficiencies [307]. In addition, the choice of the bottom layer should reduce the resistive losses and number of defects, in order to reduce interfacial recombination. Mesoporous and planar TiO_2 are the most used electron transport layers for high-efficiency perovskite solar cells but resistive losses are still present [432, 443] and reproducing the efficiencies of small area (lab-scale) perovskite devices on larger areas, either for mini-module or module, remains challenging using these electron transport layer [444, 445, 446].

To remedy this issue, TiO_2 nanoparticles (NP) and single-crystalline TiO_2 rhombus-like nanoparticles (SC) with higher conductivity and fewer trap states were used and their effect on the surface of $Pero_{Rb,Cs}$ were investigated using KPFM and other techniques, the latter being discussed extensively in the work of Yong Ding, who provided the samples [432]. Compared to the commercially-available and commonly-used NP-TiO_2, devices using SC-TiO_2 yielded PCE up to 24.05% compared to 22.7% for the NP-TiO_2. In addition, the SC-TiO_2 presented exposed (001) facets while the NP-TiO_2 (101) facets [432], and it was therefore interesting to study whether this difference in facet orientation could alter the surface of the perovskite spin-coated on top.

The substrates were first measured using KPFM in UHV to access their WF as depicted in Figure 7.14. The SC-TiO_2 exhibited a WF of 4.25 eV, which was higher by 150 meV compared to the WF of NP-TiO_2, which was of 4.1 eV. This change in WF could potentially be linked to the different surface terminations. Besides, a change of 150 meV could additionally benefit the interface alignment with $Pero_{Rb,Cs}$ either by improving electron extraction or hole repelling.

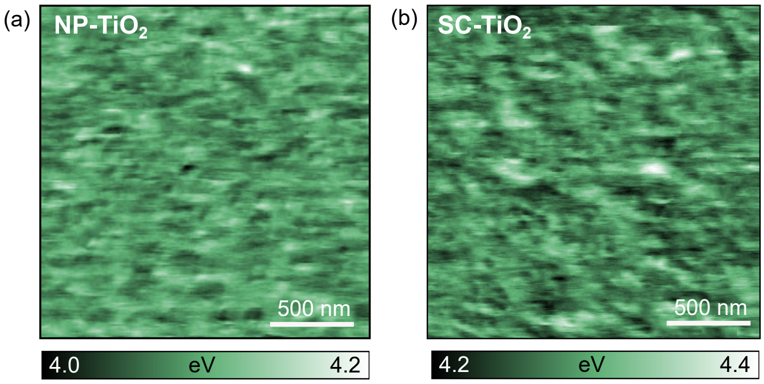

Figure 7.14: workfunction maps of (a) SC-TiO_2 and (b) NP-TiO_2 using KPFM.

$Pero_{Rb,Cs}$ was then spin-coated on top of each substrate, following the procedure of [432] and the samples were measured using UHV KPFM without air exposure. At first sight, both samples looked very similar, in terms of grain size (Figure 7.15(a,d)) but also concerning their WF maps (Figure 7.15(b,e)). In both cases, they exhibited grains with much higher WF than the rest of the surface (about 8% coverage for both samples), which was already discussed before and attributed to PbI_2- rich or PbI_2 grains using HIM-SIMS.

However, some differences could also be observed, such as a slightly rougher sample when the perovskite was spin-coated on the NP-TiO_2 (RMS of 27 ± 6 nm) compared to

Sc-TiO_2 (RMS of 22 ± 5 nm). The HIM-SIMS also revealed that Cs accumulation (very bright/yellow signal in Figure 7.15c) at the grain boundaries did not seem to be present when $Pero_{Rb,Cs}$ was fabricated on the SC-TiO_2.

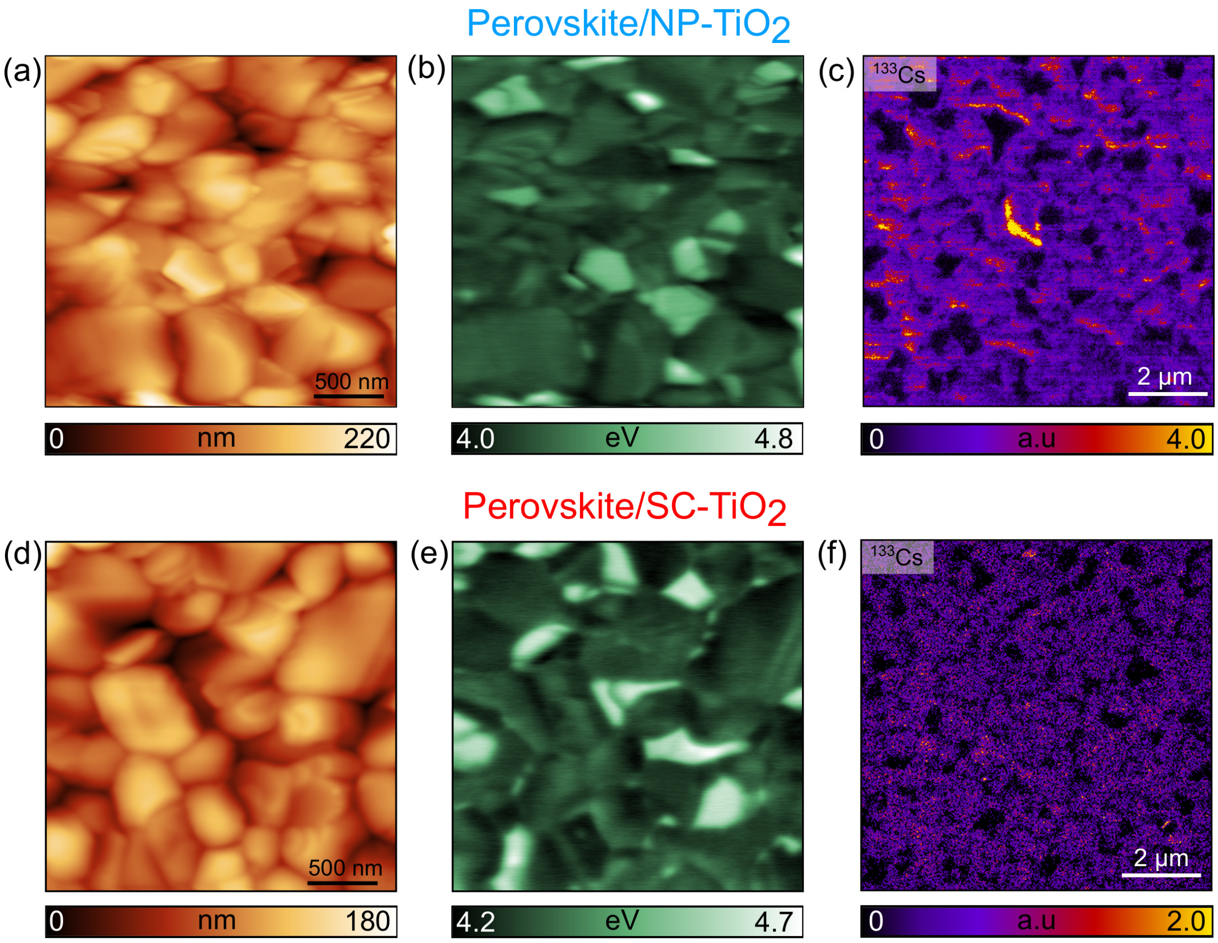

Figure 7.15: (a) AFM topography, (b) KPFM workfunction map and (c) HIM-SIMS ^{133}Cs elemental map of $Pero_{Rb,Cs}$ deposited on NP-TiO_2. (d), (e) and (f) are the same measurements carried out on $Pero_{Rb,Cs}$ deposited on SC-TiO_2.

Most importantly, the WF increased from 4.21 eV to 4.36 eV when changing the substrate from NP- to SC-TiO_2. This difference of about 150 meV was already observed for the substrates themselves and could be the consequence of either a substrate-induced doping, as already reported in the literature [169, 332], or the different facet orientation of the substrates, that induced different growth and thereby different surface terminations of the perovskite. Besides the change in WF, the distribution also varied as is better highlighted by Figure 7.16a. Both samples displayed a similar distribution, with a major peak associated to more than 50% of their surface, and a long tail in the positive values, associated to the PbI_2-rich or PbI_2 grains. However, the WF range of the Perovskite/NP was of 800 meV, much larger than the one of the Perovskite/SC (close to 500 meV). A careful analysis of all acquired images revealed that in average, the PbI_2-rich grains had a WF 340 meV higher compared to the rest of the surface for the Perovskite/NP while it was only of 260 meV for the Perovskite/SC. Additionally, the Perovskite/NP had only 37% of its WF centered at its average value ± 0.03 eV whereas it was 52% for the Perovskite/SC. These numbers showed a better homogeneity of the grains when using SC-TiO_2 instead of NP-TiO_2.

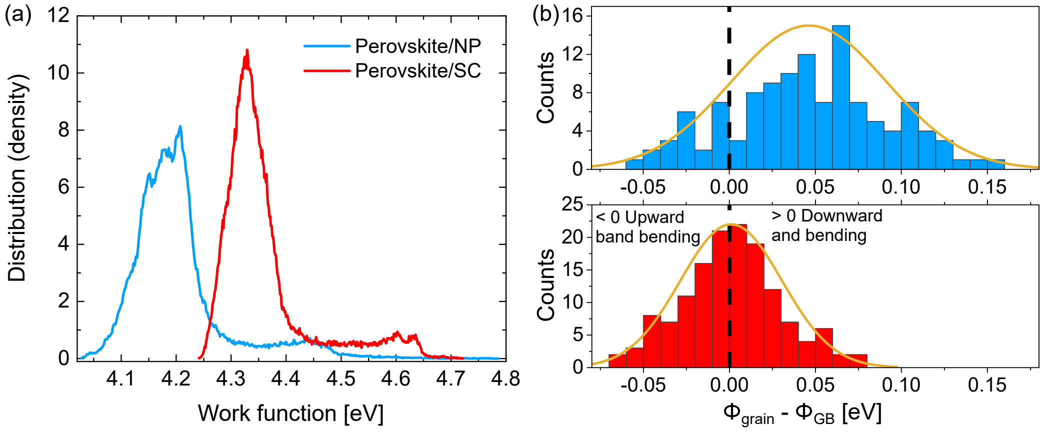

Figure 7.16: (a) Distribution of the workfunction and (b) grain boundary band bending for Pero$_{Rb,Cs}$ spin-coated on NP-TiO$_2$ and SC-TiO$_2$.

The grain boundary band bending was measured for both samples. The NP/perovskite exhibited a large predominance of downward BB (more than 80%) with 50% of its values exceeding 40 meV, which suggested a hard barrier for holes, which could severely reduce the extraction efficiency of the charges towards the hole transport layer. On the other hand, the use of SC-TiO$_2$ resulted in the large reduction of this downward BB. As depicted in Figure 7.16b, the BB was homogeneous with an almost 50/50 distribution of both types of BB and with 80% of the overall BB in a 0 ± 40 meV range, which is negligible. It remains however to investigate whether the Cs accumulation at the grain boundaries observed for the NP/perovskite is responsible for the pronounced downward band bending, as it was not visible on the HIM-SIMS mapping of the SC/perovskite. If that would be the case, a following question would be to understand if the change of facet orientation, induced by the change of the substrate from NP-TiO$_2$ to SC-TiO$_2$, promoted a better incorporation of Cs into the lattice, avoiding this accumulation at the GBs.

In addition, the Pero$_{Rb,Cs}$ did not present a surface photovoltage when illumination was used during the KPFM measurements but a continuous decay of its CPD upon prolonged illumination (Figure 7.17a) when the NP-TiO$_2$ was used as a substrate.

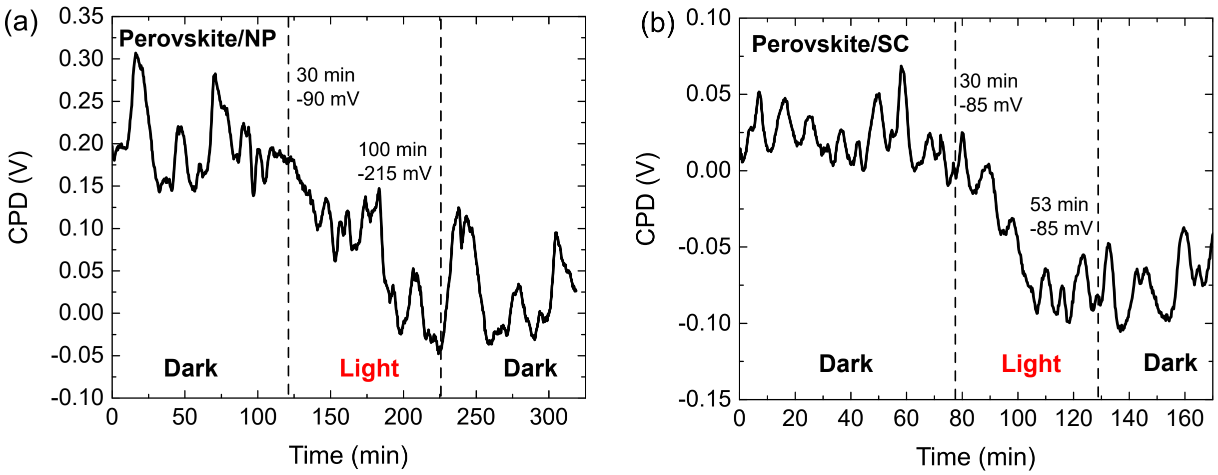

Figure 7.17: CPD in the dark, upon illumination and in the dark again for the (a) SC/perovskite and (b) NP/perovskite.

This is synonym of desorption of halide species towards the vacuum, caused by the light-induced degradation of the surface. On the other hand, the use of SC-TiO_2 led to a stabilization of the CPD decay upon prolonged illumination after about 30 minutes as depicted in Figure 7.17b, which proved the better stability of the structure compared to the Perovskite/SC. These results were in coherence with the stability tests performed on the unencapsulated devices, where the SC-based devices retained 90% of their initial efficiency for 1400 hours at maximum power point under continuous AM1.5G light illumination, while the NP-based devices dropped to 60% of their initial efficiency [432]. This also proved that testing the stability of the CPD upon prolonged illumination with KPFM can be a preliminary stability test for perovskite absorbers.

Lastly, the Perovskite/SC sample was air exposed for approximately 24 hours to investigate the influence of oxygen and water exposure on the surface properties of the mixed perovskite compared to the previously discussed case of air-exposed co-evaporated $MAPbI_3$. Figure 7.18(a,b) represent the topography of both non air-exposed and air-exposed samples, where no change could be observed in terms of grain size but the air-exposed sample displayed a slightly rougher surface (RMS of 31 ± 6 nm) compared to the non air-exposed case (RMS of 22 ± 5 nm) as was also the case for the co-evaporated $MAPbI_3$ and was most likely the result of contamination. The air exposure however increased the average WF of the Perovskite/SC by about 140 meV (4.36 eV compared to 4.5 eV after air exposure), which is in accordance with oxygen-induced p-doping, already reported in the literature [114, 404, 406].

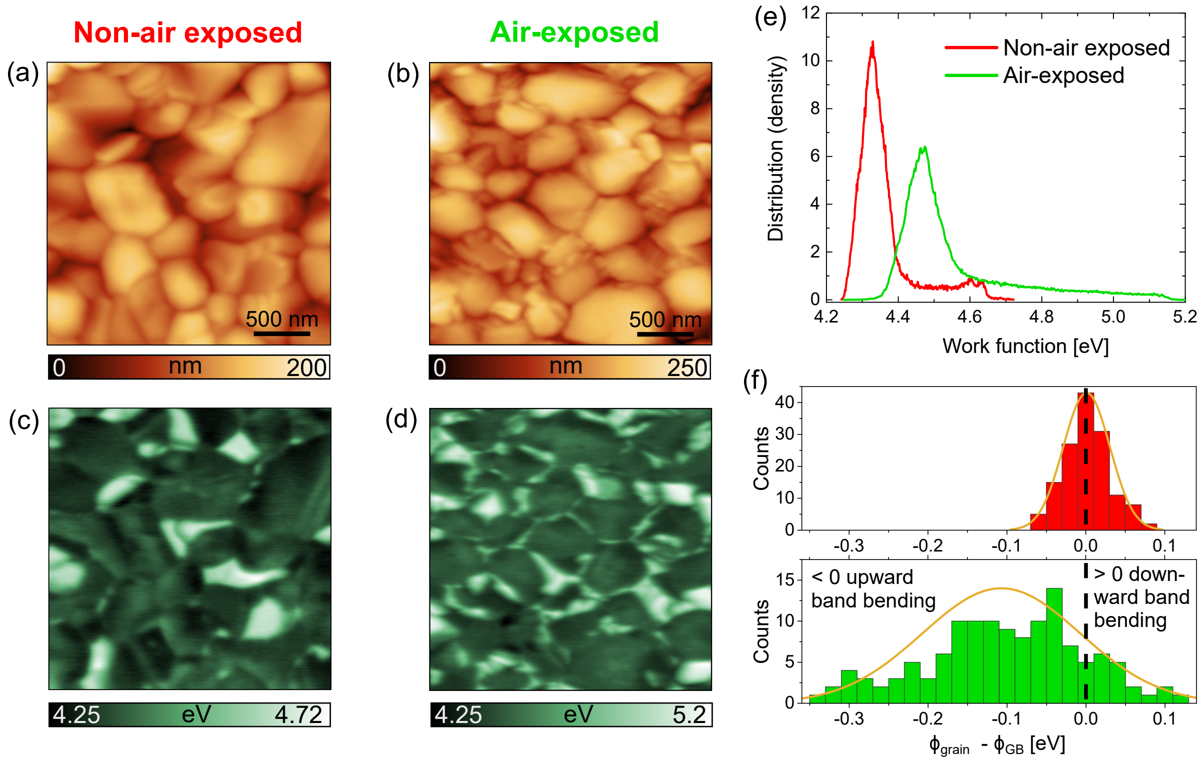

Figure 7.18: AFM topography of (a) non-air exposed Perovskite/SC and (b) air-exposed Perovskite/SC with their respective workfunction maps in (c) and (d). (e) workfunction distribution of the workfunction maps and (f) grain boundary bending for the two samples.

Besides the increase of the WF, its distribution drastically increased as well from a 500 meV range to 950 meV range, related to a much longer tail in the high WF values, as depicted in Figure 7.18e. High WF grains, linked to PbI_2-rich grains were still present after air exposure, however an additional feature appeared specifically after the air exposure. As displayed in Figure 7.18d, the grain boundaries almost all presented a much higher WF than their adjacent grains. This is even more visible in the large-area images of Figure G.10 of the appendix Chapter 7G.7. Therefore an analysis of the GB band bending was carried out (Figure 7.18f). While the non-air exposed Perovskite/SC presented negligible band bending with 80% of its BB within 0 ± 40 meV, the air exposure had for effect to completely change that behavior. The air-exposed sample exhibited a predominance of upward band bending (more than 90%) with values ranging from only a few meV to hundreds of meV, and as depicted by the distribution, an average value close to 100 meV. The direct consequence is a strong barrier for electrons at the surface and potential pathways at the GBs for holes either for efficient charge extraction or recombination. The oxygen exposure in that specific case could be a potential passivation technique and be beneficial for the device performances as previous reports discussed the benefits of a small amount of moisture, which improved the film quality [100, 101, 102]. However to confirm or refute this, further measurements with the light switched on should also be carried out in order to determine if the air exposure also induced surface states that would take part in the creation of a SPV, which was not the case for the non-air exposed one (using a light intensity of 10 mW/cm^2).

Once again, these last results proved how essential the knowledge of the sample conditioning, such as the use of solvents or the exposure to air, and the sample composition, PbI_2-rich or MAI-rich for example, were in order to understand the observed features and their impact on the solar cell performances.

7.5 Summary of Chapter 7

In this chapter the sensitivity of the surfaces of $MAPbI_3$ and mixed perovskites was investigated through KPFM in the dark but also under different stimuli such as light, air-exposure or solvent-treatment. For co-evaporated $MAPbI_3$, air-exposure proved to alter its WF, the facet contrast, the density and/or type of surface states, as demonstrated by the large change in surface photovoltage, and the stability upon prolonged illumination. The use of solvent was also demonstrated to seriously alter the surface of co-evaporated $MAPbI_3$ by affecting its WF as well as its surface photovoltage, synonym of potential variations of the surface band bending and interface alignment.

Solution-based mixed perovskites were also studied as they are one of the ways to improve the overall device efficiency. Compared to the methylammonium tri-iodide perovskites, a much greater contrast at the grain boundaries was discerned. Depending on the composition, a type of grain boundary band bending was predominant, resulting in either hole or electron barrier, potential reducer of charge extraction or inducer of recombination, limiting the solar cell's performances. Therefore passivation methods were used in order to overcome these limitations. Deposition of a ligand, a rubidium complex and a 2D material (PEAI) on top of the surface were carried out. They resulted in the change of the WF together with, either a reduction of the grain boundary band bending or a predominance towards a beneficial band bending. Scanning tunneling spectroscopy additionally unveiled that these passivation techniques suppressed potential surface defects and increased the surface bandgap, reducing the interfacial recombination. Surface passivation were therefore demonstrated to be effective ways to improve the power conversion efficiency of mixed perovskites.

Alternatively, varying the bottom layer, where the mixed perovskite directly forms onto, proved to also influence the surface. The use of single crystal-based TiO_2 substrates, with higher mobility and reduced trap densities, compared to the commonly used nanoparticles-based TiO_2 was demonstrated to change the WF, suppress harmful grain boundary band bending and improve the absorber stability upon illumination. Lastly, KPFM combined with elemental mapping through HIM-SIMS enabled the discernment of PbI_2-rich grains. The air exposure of the mixed perovskites led to a change of the average WF, in coherence with a p-type induced doping from oxygen and a large upward band bending from the grains to the grain boundaries, potentially further passivating the surface.

These results highlighted the importance of monitoring the conditioning history of the sample after fabrication, such as the use of solvents, air exposure or post-treatments (annealing or light-quenching) as they will ultimately alter the surface properties of perovskites, such as their surface states and WF, or their stability. Determining the intrinsic surface properties of perovskites is crucial in order to understand the interaction of its surface with the extraction layer deposited on top, to further optimize these interfaces through passivation techniques for example, and to improve the perovskite solar cell efficiencies.

Conclusion and Outlook

Hybrid organic-inorganic perovskites (HOIPs) have been for the last ten years the most studied material system in the photovoltaic community, due to their promising solar cell efficiencies. Besides, their association with silicon in a tandem configuration is most likely bound to be the next generation of commercialized solar panels. Several routes to improve the efficiency of HOIP solar cells have been investigated, such as mixing the elements (cations and anions) in the composition, varying the extraction layers or using surface passivation strategies. For the latter, a clear understanding of the intrinsic surface properties is required. However, researchers have mainly focused on using solution-based fabrication techniques due to their low cost and practicability. Two issues stem from such methods: the impossibility to upscale them for the fabrication of large-area solar cells, and the use of solvents, that can be toxic, and are incompatible with large-scale manufacturing and alter the intrinsic surface properties of HOIPs.

The thesis had two aims: the first one was to grow HOIPs with a scalable technique that would not alter their intrinsic surface properties, which was achieved using physical vapor deposition (PVD). The second one was to characterize the HOIP intrinsic surface properties using scanning probe microscopy (SPM) techniques to understand how the HOIP surfaces differ from other semiconductors and find ways to control and optimize these surfaces. To avoid oxygen and water contamination, the HOIPs were evaporated in a nitrogen-filled glovebox and ultra-high-vacuum (UHV) SPM as well as an inert-gas transfer suitcase were used. On a side note, solution-based samples were still studied in this thesis as the evaporated ones, via PVD, proved to be unfit for scanning tunneling microscopy (STM), and also to compare different fabrication techniques and HOIP compositions.

In the first part of this thesis, the local density of states (LDOS) of solution-based HOIPs, both $MAPbI_3$ and mixed halide perovskites, were investigaed through STM and scanning tunneling spectroscopy (STS). The surface band gap was first extracted using the normalized dI/dV curves and a broadening technique, and presented a similar value as reported in the literature. The lateral variations of the LDOS of $MAPbI_3$ on the nanometer scale were first investigated and combined with simulations of the dI/dV curves, that led to a quantification of the density of surface states. The simulations demonstrated an average density of surface states of 10^{13} cm^{-2} eV^{-1}, that pinned the Fermi level at the surface. Additionally, these simulations proved that both the density of surface states and the workfunction (WF) varied between grains and for different facets of a grain. These surface fluctuations were attributed to different surface terminations and not to the degradation of $MAPbI_3$ in a UHV environment. The grain boundaries, which are often referred to as centers of non-radiative recombinations and detrimental to solar cells, did not show any differences in terms of density of surface states and band bending compared to the grains, which differed from what is often reported in the literature. Lastly, as mixed halide HOIPs are currently the record efficiency holders, they were similarly analyzed and also displayed lateral variations of their density of surface states and WFs but also surface bandgaps, which was this time attributed to a degradation of the perovskite towards metallic Pb (Pb^0).

The second part of this thesis focused on the intrinsic surface properties and degradation of co-evaporated $MAPbI_3$ thin films using both surface-sensitive and bulk characterization techniques. The volatile nature of the organic compound methylammonium iodine (MAI) of $MAPbI_3$ created challenges in using the evaporation temperature as a control parameter in the PVD set-up. The growth of the HOIP films was therefore controlled by the chamber pressure, dominated by the MAI partial pressure. The effects of varying this pressure on the bulk and surface properties of $MAPbI_3$ were investigated. Increasing the MAI partial pressure proved to change the composition (I/Pb ratio) of $MAPbI_3$ from a PbI_2-rich composition to a MAI-rich composition (over-stoichiometric). This increase of MAI partial pressure also induced a structural transition from a $MAPbI_3$ crystal structure with PbI_2 secondary phases at low pressures to a differently textured structure with additional strain at high pressures. The use of a high MAI pressure led to better optoelectronic performances but worse solar cell efficiencies, thus the surface properties were characterized with Kelvin probe force microscopy (KPFM).

KPFM demonstrated the occurrence of areas with much lower WF compared to the rest of the surface when over-stoichiometric (high MAI pressure) samples were grown. In comparison, the WF maps of near-stoichiometric samples were homogeneous. X-ray diffraction and literature reports linked these low WF areas to the incorporation of low dimensional (2D) perovskites (LDPs) and stacked perovskite sheets (SPSs) in the 3D $MAPbI_3$ structure. Annealing at different temperatures were carried out to remove these LDPs from the $MAPbI_3$ lattice, which was successful but severely degraded the over-stoichiometric samples. On the other hand, the near-stoichiometric $MAPbI_3$ were much more stable. Illuminating the over-stoichiometric $MAPbI_3$ films led to a photostriction effect, i.e. a lattice expansion, which is not desirable, and does not exist for near-stoichiometric films. Using high MAI pressure also resulted in a noisy KPFM signal when using light, which was linked to an increased ion migration. Lastly, prolonged illumination on over-stoichiometric films led to their degradation in both nitrogen and ambient environments, while the near-stoichiometric ones proved to be highly stable. Therefore the use of high MAI partial pressure, that led to the introduction of LDPs and SPSs in the $MAPbI_3$ lattice, was demonstrated to be detrimental to the perovskite performances and to reduce its stability against heat and light.

X-ray photoelectron spectroscopy (XPS) and KPFM were then combined on near-stoichiometric $MAPbI_3$ films to determine the origin of the multi-component variations of the WF upon prolonged illumination. Several substrates (n- and p- types) were used to additionally observe how these variations differ on different device configurations. The first fast increase of the WF was attributed to the surface photovoltage effect (SPV), in which photo-generated charge carriers screen the surface states and reduce the surface band bending. This increase of the WF was coherent with an observed fast collective decrease of the binding energies (BE) of $MAPbI_3$ core elements. The second slow transient of the WF upon prolonged illumination was either a slow decrease for $MAPbI_3$ on n-type substrates or a slow increase on p-type substrates. XPS measurements showed a similar behavior with a slow decrease of the BE and a slow increase of the BE of the core elements on n- and p-type substrates respectively. The interpretation of the calibrated KPFM and the XPS measurements led to the conclusion that photo-induced degradation occurred at the surface of $MAPbI_3$, which resulted in the evaporation of I_2 in the vacuum, contaminating the KPFM tip and inducing chemical variations as well as an increased formation of Pb^0. For $MAPbI_3$ on p-type substrates, other phenomena should exist and further measurements should be carried out to explain the continuous increase of the WF and BEs upon prolonged illumination.

KPFM of $MAPbI_3$ on these different substrates was also used in conjunction with calibrated PL and time-resolved PL (TRPL) for different thicknesses to draw band diagrams. The surface band bending, via SPV measurements, proved to be much higher on p-type substrates than on n-type substrates. This led to a downward band bending, indicative of surface donors and either weak n-type doping or p-type doping, which did not work with flat band conditions. The WF extracted from KPFM and the doping densities calculated from combining PL and TRPL led to the conclusion that the conduction and valence bands had to bend within the bulk of $MAPbI_3$. This part of the thesis would require further measurements to confirm the trends on each substrate.

The last part of this thesis investigated the sensitivity of co-evaporated $MAPbI_3$ films and solution-based mixed halide HOIP films. KPFM and STM/STS were used to study the effects of extrinsic factors such as oxygen exposure, solvents or passivation layers on the workfunction, GB band bending (BB), surface bandgap and LDOS on the surface of these different HOIPs. Oxygen exposure was demonstrated to change the average WF and suppress the initially observable facet features of as-grown $MAPbI_3$ films, and to completely alter the GB-BB of mixed halide perovskites. The use of solvents on co-evaporated $MAPbI_3$ altered the average WF but also the surface states, depicted by large variations of the SPV for different dipping times. The surface of mixed halide perovskite was shown to be quite different from co-evaporated $MAPbI_3$ with either large variations of WF between grains, linked to PbI_2 grains, or pronounced GB band bending. STM and STS demonstrated the existence of a surface defect, and that surface passivation strategies were used to suppress it. The latter also completely changed the GB band bending towards a more beneficial one (reduction of the hole barrier) and increased the surface bandgap close to 2 eV, which reduced the interface recombinations. Lastly, the use of different substrates with different surface terminations also resulted in observable surface variations of the GB band bending and average WF values. This part of the thesis proved the need to know the sample conditioning history (use of solvents, air exposure...) before interpreting data acquired from surface-sensitive measurements.

In addition, this thesis demonstrated that a clear understanding of the intrinsic surface properties of HOIPs is crucial in order to optimize the solar cell stack via the use of charge transport layers or passivation strategies for example. Besides, the intrinsic stability of HOIPs can already be tested through techniques such as KPFM, PL and TRPL.

As any work, this thesis brought its share of questions and perspectives. First, solution-based fabrication processes do not look viable as scalable methods for the fabrication of large-area solar cells, yet their efficiencies exceed the ones of perovskites made from thermal evaporation, which is more likely to be used in a manufacturing company. Therefore, the research should intensify on the thermal evaporation of mixed halide perovskites, which present a much higher intrinsic stability compared to $MAPbI_3$, and on lead-free perovskites. Secondly, as a general note, great care should be taken when interpreting results from surface-sensitive measurements such as KPFM, STM/STS, XPS. The sample's history, such as the fabrication method used, how it was stored and if it was exposed to different environments, has to be clearly laid out to facilitate a common understanding of the surface properties of HOIPs.

The STM/STS measurements presented in this thesis showed that lateral variations of the surface properties existed, both on $MAPbI_3$ and mixed halide HOIPs. It would be interesting to investigate how these lateral fluctuations affect the interface with a charge-transport layer. As an example, calculations could be used to simulate how a change of the density of surface states from one facet of a grain to another translate into different interaction energies with molecules from the top layer, and which surface termination would be the most favorable. When this is known, one could vary the fabrication parameters in order to reduce these lateral variations, if they were found to be detrimental. Besides, further STM/STS measurements should be performed to study and clarify the role of the GBs in HOIPs, which are still highly debated. In this thesis, no extrinsic factor such as oxygen or water molecules were used during STM/STS, but it would be crucial to see if the density of surface states at the GBs vary with an intentional contamination. In addition, STM/STS on co-evaporated HOIPs, which was not successful in this thesis, would be highly interesting to observe how the surface differ from solution-based HOIPs.

Concerning the co-evaporated $MAPbI_3$, one question that remains to be answered is how the low-dimensional perovskites, introduced in the lattice with a high MAI partial pressure, alter the structure and stability of $MAPbI_3$. To that end, density functional theory (DFT) calculations or other techniques could be used to model the interactions between the 3D and 2D perovskites. 2D perovskite are often reported to improve devices efficiencies as they offer a certain degree of passivation or can be used to strengthen the perovskite structure, but this was not the case in this thesis. It would be interesting to know if these non-intentionally formed 2D perovskites could be used in a different way such that they improve the intrinsic stability of $MAPbI_3$ and not the opposite. In addition, AFM showed to be a reasonable technique to observe if photostriction exists in perovskite films and should used more extensively, such that it can finally be understood whether photostriction is beneficial or detrimental for the PV performances.

XPS and KPFM measurements showed the occurrence of photo-induced degradation of co-evaporated $MAPbI_3$. However further characterization using other techniques should be used to disentangle this from any other phenomena, such as ion migration or surface trapping/detrapping via defect states, especially on p-types substrates where no conclusion could be drawn. Besides, combining KPFM, calibrated PL and TRPL proved to be efficient in defining a first simplified draft of the energy band diagram of $MAPbI_3$ on an extraction layer. However, these techniques have to be used systematically and the effect of such bending of the bands should be investigated by simulating the electric field in such structures and observed how it affects for example the transport of charges carriers, their recombinations and the migration of ions.

Lastly, passivation strategies seem to be one of the best solutions to improve device efficiencies. This work has proved that using passivation layers, the GB band bending was changed and the surface band gap increased. Simulations and computations would need to be used to see how such changes impact the recombination mechanisms and the transport of charge carriers. Models could therefore be defined on how to actually improve the surface such that they do not stay the limiting factor in the improvement of the efficiency of perovskite solar cells.

A lot of topics are still to be investigated, and every day, tens to hundreds of new questions arise, but the ultimate goal to keep in mind for all researchers is to make the commercialization of perovskite solar cells possible rapidly, and make it such that recycling them remains doable.

Appendix A

Appendix Chapter 1

A.1 Structure and working principle of a solar cell

A solar cell is itself subdivided in different layers that have all different purposes. To generate an electrical power, a photovoltaic device needs first to absorb light, convert it into charge carriers (electrons and holes) and transport these charge carriers towards electrodes, leading to the creation of a current. To that end, the most classical architecture of a solar cell uses a combination of an n-type semiconductor with a p-type semiconductor of the same material, which leads to the formation of a so-called p-n homojunction when brought in contact together. A simplified energy band diagram is depicted in Figure A.1a when the two doped semiconductors are not in contact and their respective Fermi energy levels are close to the CB for the n-type and close to the VB for the p-type.

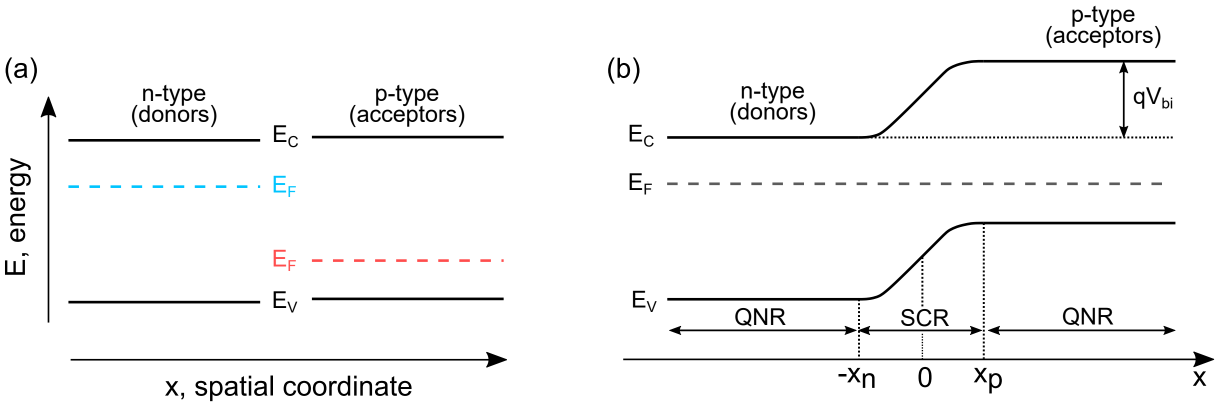

Figure A.1: (a) Energy band diagram of an n-type semiconductor and a p-type semiconductor, with their respective Fermi energy level before the formation of a contact. (b) Formation of a p-n homojunction inducing alignment of the Fermi energy levels, bending of the conduction and valence bands at the interface, formation of a space charge region (SCR) and quasi neutral regions (QNR), and formation of a built-in voltage (V_{bi}).

In Figure A.1b, when the semiconductors are brought in contact, free electrons from the n-type semiconductor diffuse into the p-type semiconductor and recombine with holes in the p-type semiconductors. Similarly, free holes in the p-type semiconductor diffuse into the n-type side and recombine with electrons. The ionized impurities on both side cannot diffuse as they are bound to the crystal lattice. After diffusion, the Fermi energy level align and there is the formation of a depleted region in both semiconductors, near the junction. In the n-type side, a positively charged region is created while in the p-type side, a negatively charged region is formed. The outcome is the creation of an electric field within the region, which is also called space charge region (SCR) or depletion layer. Ultimately a built-in voltage V_{bi} is formed at the junction due to the electric field, and the drift current derived from it is opposite to the diffusion current. In thermal equilibrium, the majority of the electrons stay in the n-type side and similarly for the holes in the p-type side, forming quasi-neutral regions (QNR).

The built-in potential is either a barrier or facilitator for carriers and can be either reduced or increased by for example applying an external voltage V_a (forward or reverse bias), which will also change the total width w of the space region, as follows:

$$w = |-x_n| + |x_p| = \sqrt{\frac{2\epsilon\epsilon_0}{q}\left(\frac{1}{N_A} + \frac{1}{N_D}\right)(V_{bi} - V_a)} \tag{A.1}$$

-x_n and x_p are respectively the space charge regions in the n-side and the p-type, ϵ and ϵ_0 are the dielectric constants of the material and of the vacuum respectively. The total net current density across the junction, combining the drift and diffusion currents of both holes and electrons is defined by equation (A.2):

$$j = j_0\left(\exp\left(\frac{qV_a}{Ak_BT}\right) - 1\right) \tag{A.2}$$

j_0 is the saturation current density and A the diode quality factor. Not only external voltages can vary the built-in potential, but also other external stimuli, such as illumination from the light. Photons coming into the junction with an energy $h\nu \geq E_g$ can be absorbed and electrons-hole pairs are created (electrons from the VB have enough energy to go to the CB leaving a hole behind). There is consequently an additional concentration of electrons Δn and holes Δp. It stems from this generation of extra charge carriers, that the minority-carrier densities on each side of the pn junction are changed but the majority carrier densities remain the same (except if the illumination used induces a generation of holes and electrons superior to the majority carrier densities). Therefore the product $np = (n_0 + \Delta n)(p_0 + \Delta p)$ is no longer equal to n_i^2. The explanation is that as both the electrons and holes are represented in quasi-thermal equilibrium by a Fermi-Dirac distribution, two Fermi energy levels have to be defined, and this as follows:

$$\begin{aligned} n &= n_i \exp\left(\frac{E_{F,n} - E_i}{k_BT}\right) \\ p &= n_i \exp\left(\frac{E_i - E_{F,p}}{k_BT}\right) \end{aligned} \tag{A.3}$$

$E_{F,n}$ and $E_{F,p}$ are the quasi Fermi-level for the electrons and holes respectively, and the product np then becomes:

$$np = n_i^2 \exp\left(\frac{E_{F,n} - E_{F,p}}{k_BT}\right) \tag{A.4}$$

$E_{F,n} - E_{F,p} = \Delta\mu$ is called the quasi-Fermi level splitting (QFLS) and can be used to describe the maximum energy that can be extracted from the system, and is used as an upper limit for the performance for the open-circuit voltage of a solar cell, that will be defined later.

So far the main part of a solar cell, the p-n junction, where the absorption of photons and the generation of electrons-holes pairs take place have been discussed. To finish up the solar cell, electrodes are needed on each side of the p-n junction in order to collect the photo-generated charge carriers. Several other layers are used in order to optimize a solar cell. Figure A.2 displays for example the common structure of an exemplary silicon solar cell, which is the most used material nowadays to fabricate a photovoltaic device. The emitter is the front semiconductor layer forming the p-n junction (often n-type for silicon solar cells). It will absorb most of the photons and is fabricated thin enough that it can reduce charge recombination, which will be discussed later. The front electrodes do not fully cover the n-side to let the light come in, and an additional anti-reflection coating is deposited on top to avoid reflection of light and loss of incoming photons inside the p-n junction. The commercialized solar cells have now a much more complex structure than the one here, with further layers used to improve the overall efficiency of the devices, such as the passivated emitter and rear contact (PERC) configuration [447] or the heterojunction with intrinsic thin layer (HIT) configuration [448].

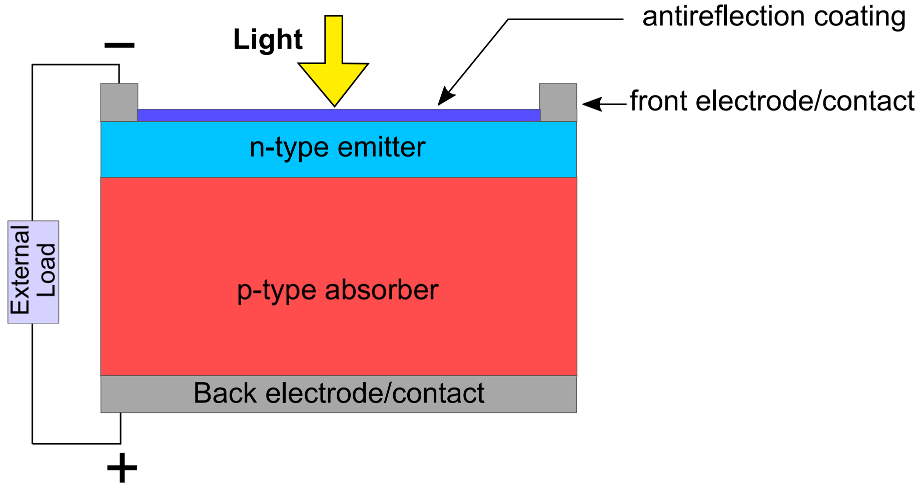

Figure A.2: Structure of a classic solar cell, for example a silicon-based one.

Upon illumination, the current across the solar cell changes from the one in equation (A.2). If the photo-generated holes and electrons are efficiently collected by the electrode (which depends on several factors), then an additional photocurrent density J_{ph} is generated and flows in the opposite direction of the current calculated in the dark. Therefore j becomes:

$$j = j_0 \left(\exp \left(\frac{qV_a}{Ak_BT} - 1 \right) \right) - j_{ph} \tag{A.5}$$

When an external load is connected to the above-mentioned structure, a potential builds up between the two terminals. Without that load, but only with connected electrodes, a short-circuit occurs, and ultimately a short-circuit current J_{SC} is created. From the equation A.5, one can see that in that case, when $V = 0$, $J = J_{SC} = J_{ph}$. Additionally, when no current density flows throughout the device, the device is in a situation known to be as open-circuit and the resulting voltage is called open-circuit voltage, following equation (A.6):

$$V_{OC} = \frac{Ak_BT}{q} \ln \left(\frac{j_{ph}}{j_0} + 1 \right) \tag{A.6}$$

Both the open-circuit voltage V_{OC} and the short-circuit current J_{SC} are crucial parameters when discussing solar cell performances. Measuring the current density as a function of the applied voltage is therefore one of the main measurements to determine the solar cell efficiency, and both the V_{OC} and the J_{SC} can be extracted from the commonly called J-V (current density-voltage) curves, as depicted in Figure A.3.

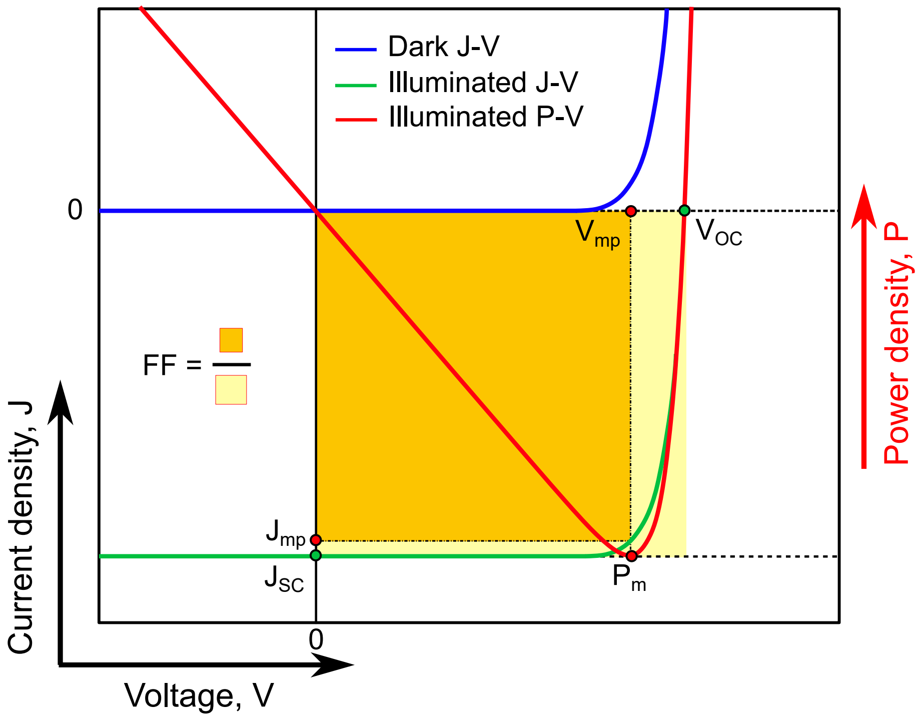

Figure A.3: Sketch of a current density - voltage (J-V) curve of a solar cell in the dark and under illumination, as well as the powder-density - voltage (P-V) curve. The fill factor (FF) is also depicted as the fraction of the two yellow zones.

In addition to the J-V curve, it is important and interesting to look at the power density (current density × voltage) as a function of the applied voltage, that is the P-V curve, as it gives access to the maximum power density the solar cell can deliver. This maximum, P_m, comes with the characteristic pair (J_{mp},V_{mp}). This introduces the last figure of merit of the JV curve, that is the fill factor (FF), which is a measure of the "squareness" of the J-V curve. With all these parameters, it becomes possible to calculate the power conversion efficiency η of a solar cell. The latter corresponds to the ratio between the power it can deliver and the power it collected initially through the light and can be written as follows:

$$\eta = \frac{P_{mp}}{P_{in}} = \frac{J_{mp}\,V_{mp}}{P_{in}} = \frac{FF\,J_{SC}\,V_{OC}}{P_{in}} \tag{A.7}$$

The solar cell efficiency therefore depends on the fill factor FF, the V_{OC}, the J_{SC} and the P_{in} which can all be deduced when performing J-V measurements and knowing the incoming power. As the power conversion efficiency (PCE) also varies with the incoming illumination power, it was for the best interest of all to have a standardized value so that solar cells could be easily compared. A complete set of standard testing conditions have actually emerged, where the illumination used is the so-called AM1.5 solar spectrum with a power density of 1000 W/m^2 with a cell temperature of 25°C. The highest PCE to date for a single p-n junction solar cell without light concentration is of 29.1% for an epitaxially-grown GaAs-based thin film by Alta Devices [301]. Better efficiencies can be obtained by stacking solar cells with different materials. The overall record efficiency to date is of 47.1% by using 6 p-n junctions and concentrating light [449]. A detailed list of the record efficiencies over the years can be found on the NREL best efficiency chart [8] and the current highest PCE for each technology can also be found in the solar cell efficiency tables by Green et al. [301]. Converting light from electricity is therefore far away from being 100%, and this because of multiple types of losses in solar cells, which will be discussed thereafter.

A.2 Fundamental losses in a solar cell

Firstly, all the photons from the solar radiation spectrum do not reach the device as absorption bands from oxygen, hydrogen or carbon dioxide reduce the spectral irradiance and therefore the incoming photons. A few fundamental solar cell losses then occur and the efficiency drops quite rapidly. In terms of thermodynamics, the solar cells acts as a Carnot engine and therefore the PCE drops by a few percent. Boltzmann losses then come into place to further reduce the PCE due to angular inequality of incident and emitted radiation. Then all photons with a lower energy than the bandgap are not absorbed and all photons with energy greater than the bandgap create carriers with high kinetic energies, which are called hot electrons and holes, and which induce thermalization losses [450]. These losses are represented in Figure A.4a.

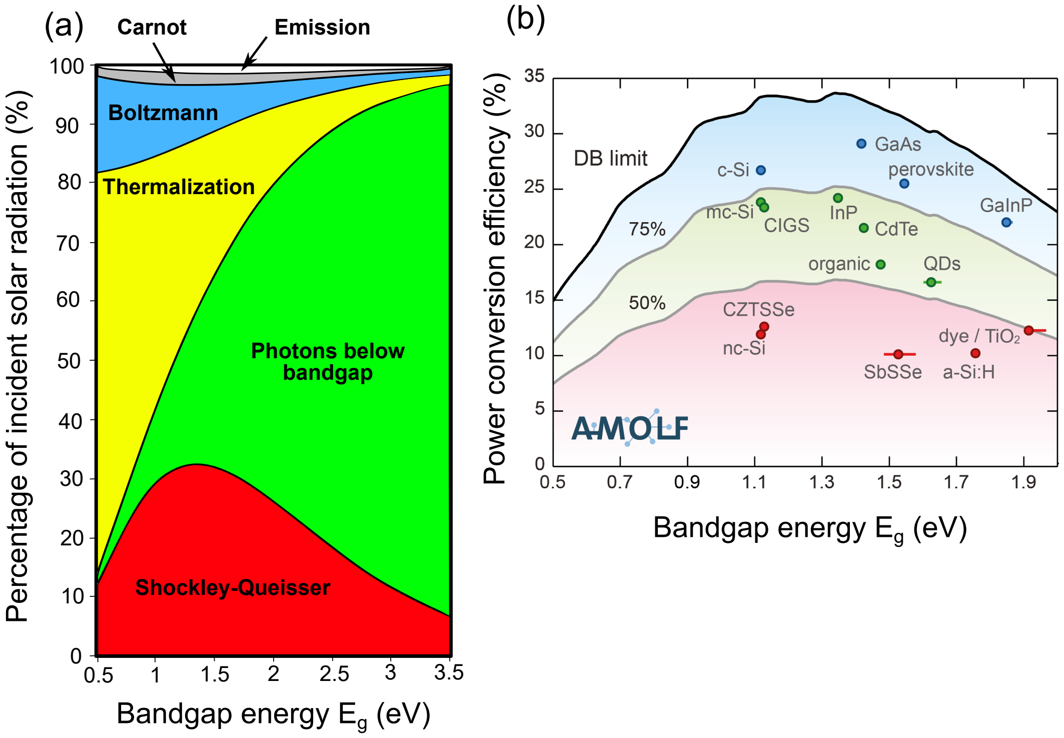

Figure A.4: (a) Representation of the losses in a solar cell from the starting point of incident photons to the Shockley-Queisser limit. Adapted from Nelson et al. with permission from the Royal Society of Chemistry. (b) Shockley-Queisser limit (black line) as a function of the bandgap energy. Some characteristic efficiencies of different material systems are also plotted. Reprinted from [451].

In addition, calculations have been performed in order to find the maximum and ideal PCE of a solar cell depending on its bandgap. The model is called the Shockley-Queisser

(SQ) model and takes into consideration that the solar cell acts as a grey body where all the photons equal or above the bandgap are absorbed, that each of these photons create one electron-hole pair and that all generated carriers are collected by the electrical contacts. Lastly, the model assumes only one type of recombination as discussed in the following. When an electron is excited in the conduction band and has reached its lower energy position, it will eventually stabilize to a lower energy position in the valence band and move into an empty valence band state, which removes a hole. This whole process is called recombination and is sub-divided into different recombination processes. However the SQ model only takes into consideration the radiative recombination, that is when an electron and a hole recombine and emit a photon with the associated bandgap energy. This gives an upper limit of the PCE as depicted in Figure A.4b [451, 452]. As previously mentioned, the SQ model gives the maximum PCE a solar cell can have depending on the material used, or an upper limit for an ideal single-junction solar cell. The bandgap of $\mathrm{MAPbI_3}$ is of $\sim$ 1.6 eV, which directly gives a SQ efficiency of 30.14% [86].

A.3 Recombination mechanisms, rates and lifetimes

Radiative recombination

Radiative recombination, which cannot be avoided, comes with a recombination rate R_{rad} in $\mathrm{cm^{-3}s^{-1}}$, which is a material property, determined by the radiative coefficient k_{rad} and the doping density. R_{rad} is a key value that defines how fast and efficiently the charge carrier collection needs to be before carriers recombine. It is defined as follows [321]:

$$R_{rad} = R_{ill} - R_{rad}^0 = k_{rad}(1 - p_r)(np - n_i^2) \tag{A.8}$$

k_{rad} is specific to $\mathrm{MAPbI_3}$. R_{rad}^0 is the radiative recombination rate at equilibrium, R_{ill} the radiative recombination rate when the perovskite is excited with light and p_r is the reabsorption probability of photons emitted for radiative recombination and are re-absorbed in the active area. $n = \Delta n + n_0$ and $p = \Delta p - p_0$ are the electron and holes densities with Δn and Δp the photo-generated charge carriers densities. When the number of photogenerated carriers does not exceed the doping, called low-injection regime, and assuming a p-type $\mathrm{MAPbI_3}$, it results in $p \approx p_0$ and $p_0 \gg n$ and the radiative recombination rate becomes:

$$R_{rad} = k_{rad}(1 - p_r)p_0\Delta n = \frac{\Delta n}{\tau_{rad}} \tag{A.9}$$

This equation introduces the radiative lifetime τ_{rad} which gives the average time before a charge carrier recombines radiatively and is not the limiting factor in a poly-cristalline solar cell. Typical radiative lifetime for $\mathrm{MAPbI_3}$ ranges from a few nanoseconds when the doping density is very high to microseconds, and is usually the longest for single-crystal perovskites. Dang et al. have for example reported lifetimes exceeding 80 µs for single-crystal $\mathrm{MAPbI_3}$ using techniques such as transient photovoltaic (TPV) and impedance spectroscopy (IS) [453]. As this type of recombination is defined by the material properties and is fixed, it is not the type of recombination that limits the device performance. However other types of recombination exist that can reduce the performance of the perovskite solar cell, they are called non-radiative recombinations.

Auger recombination

Auger recombination is a process involving three charge carriers. The recombination of an electron-hole pair does not yield to the creation of a photon, additional heat to the systems or a phonon but it excites a third electron of the CB. Therefore this electron will thermalize again to its lower energy level in the CB. Auger recombination happens mostly in highly-doped semiconductors or under high injection of charge carriers, and is therefore often neglected in low-injection regime. The Auger recombination rate can be described by the following equation [321]:

$$R_{Aug} = (C_n n + C_p p)(np - n_i^2) \tag{A.10}$$

C_n and C_p are the Auger coefficients for the electrons and holes respectively.

Shockley-Read-Hall recombination
When defect states are introduced within the bandgap of the absorber, the charge carriers can get trapped in that state and can recombine with a hole moving up to the same energy state before the electron has a possibility to be re-emitted thermally in the CB. This type of non-radiative recombination is called Shockley-Read-Hall (SRH) recombination and comes with a recombination rate denoted R_{SRH} and depends on different aspects of a defect, which are its energy level and activation energy. The reader is brought to read section A.4 of Appendix Chapter 1 for a discussion of points defects in $MAPbI_3$. The recombination rate is written as follows [321]:

$$R_{SRH} = \frac{(np - n_i^2)}{(n + n_1)\tau_p + (p + p_1)\tau_n} \tag{A.11}$$

n_1 and p_1 are the carrier densities that describe their emission from the defect state situated at the energy level E_T. τ_n and τ_p represent the SRH lifetime for electrons and holes respectively with $\tau_{SRH} = \tau_n + \tau_p$. Again, in the case of a p-type $MAPbI_3$ with $p_0 \gg n$, in the low-injection regime, and considering only deep defects as recombination centers (and $np > n_i^2$), R_{SRH} becomes [321]:

$$R_{SRH} = \frac{\Delta n}{\tau_n} \tag{A.12}$$

In the bulk, τ_n can be associated to a recombination cross section σ_{th}, an electron thermal velocity v_{th} and the trap density N_T at the energy state E_T, as follows:

$$\tau_n = \frac{1}{\sigma_n v_t h N_T} \tag{A.13}$$

Typical values for the product of the capture cross-section and the defect density for $MAPbI_3$ ranges from $\sim 10^1$ to 10^{-4} cm^{-1} [454]. SRH lifetimes vary from a few hundreds of nanoseconds to a few microseconds depending on the doping and defect densities of the perovskite [455].

Total bulk recombination
Combining all these recombination rates and assuming only deep defects, a total recombination rate R_{tot} can be obtained as follows [321]:

$$R_{tot} = \left[k_{rad}(1 - p_r) + \frac{1}{n\tau_p + p\tau_n} + C_n n + C_p p\right](np - n_i^2) \tag{A.14}$$

When assuming, as in the previous cases, a p-type $MAPbI_3$ in a low-injection regime, equation A.14 becomes [321]:

$$R_{tot} = \left[k_{rad}(1 - p_r)p_0 + \frac{1}{\tau_n} + C_p p_0^2\right] \Delta n = \left(\frac{1}{\tau_{rad}} + \frac{1}{\tau_{SRH}} + \frac{1}{\tau_{Aug}}\right) \Delta n = \frac{\Delta n}{\tau_{bulk}} \quad (A.15)$$

This introduces the bulk lifetime τ_{bulk} which combines all the different lifetimes in the bulk. In addition to the bulk lifetime, bare surfaces are also prone to defects and the deposition of layers on top can also induce interface defects or recombination.

Surface and interface recombination

The last types of recombination are the ones occurring at the surfaces or interfaces with the layers, and they are most of the time the ones limiting the overall lifetime of a device. A simplified definition of the surface lifetime, assuming a p-type $MAPbI_3$ and a low-injection regime, is described following equation A.16

$$\tau_s = \frac{d}{S_p + S_n} + \frac{d^2}{D_n \pi^2} \quad (A.16)$$

S_p and S_n are the surface recombination velocities at the interface $MAPbI_3$/HTL and $MAPbI_3$/ETL respectively, d is the thickness of the absorber and D_n the diffusion constant. S_p and S_n fulfill a similar role as the inverse electron and hole lifetimes in bulk SRH recombination. $S_{p,n}$ mainly depend on the density of surface defects that can act as recombination centers [456]. This makes the surface recombination mainly defect-driven but, in addition, interface recombination can happen as depicted by R_I in Figure 1.13 of Chapter 1, which represents the recombination of a charge within the transport layer with a charge of the absorber. These interface recombinations are also referred to as front and back recombination, depending on where they happen. Additionally to the intrinsic point defects and the back/front recombination, dangling bonds and grain boundaries are also sources of non-radiative recombination centers and the extraction layers and electrodes have much more complex role and effects in the effective lifetime.

Finally, the total lifetime, which takes into account both bulk and surface lifetimes can be written as follows:

$$\frac{1}{\tau_{tot}} = \frac{1}{\tau_{bulk}} + \frac{1}{\tau_s} \quad (A.17)$$

A.4 Point defetcs of MAPI

SRH recombination in $MAPbI_3$ is linked to intrinsic point defects that exist in this perovskite lattice. First-principles calculations like DFT are tools that can reveal the defect levels and defect formation energies of these point defects, that can occur as vacancies, antisites, interstitials. Yin et al. were one of the first groups to look into these point defects and reported that the dominant defects with the lowest formation energies, namely lead vacancy (V_{Pb}) and MA interstitial (MA_i) were mostly forming shallow traps within 0.05 eV of the bands [373]. In recent studies however, it has been reported that spin-orbit coupling (SOC) in DFT calculations should be used to simulate the point defects and that the latter also strongly depend on the processing conditions and composition of the perovskite (I-rich/I-poor, MA-rich...). For instance, the fact that perovskite can self-dope to either n- or p-type depending on its composition (I-rich / MA-rich) can be the consequence of intrinsic point defects acting as electron acceptor or hole donor. In any case, this led to various reports suggesting for example that iodide vacancy (V_I), iodide interstitial (I_i) and lead substitution by iodide (I_{Pb}) were forming deep traps with low formation energies [457, 458, 459]. Figure A.5 depicts one of the pioneer studies by Yin et al. [373] and more recent calculations by Meggiolaro et al. [460].

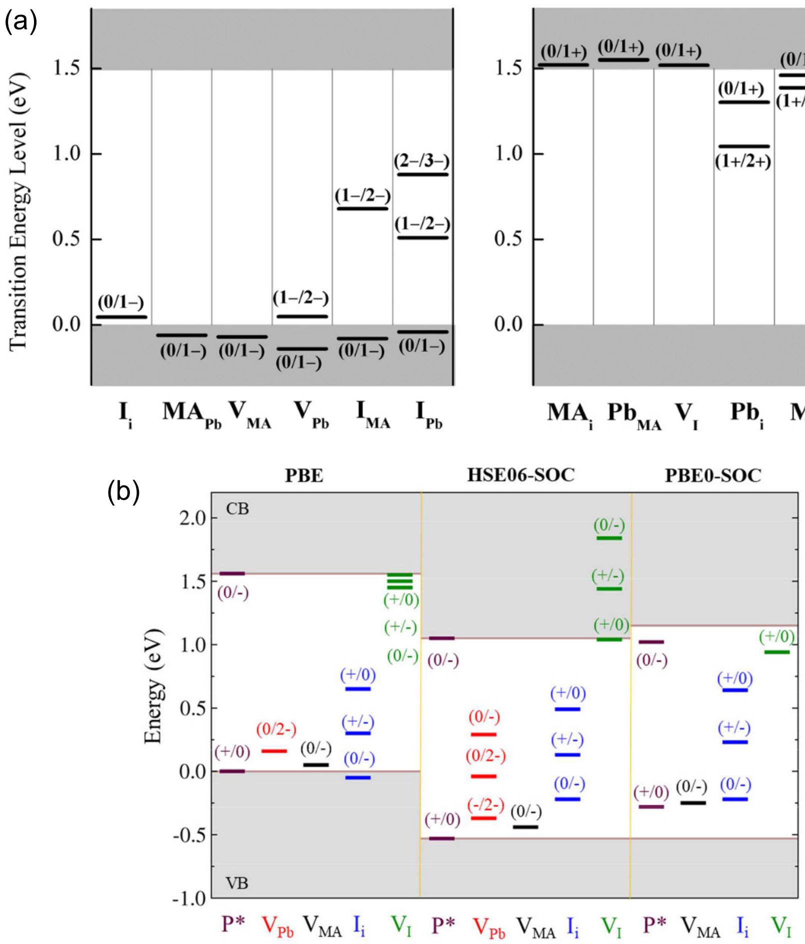

Figure A.5: (a) Transition level of point defects in $MAPbI_3$ from DFT calculations with intrinsic acceptors (left) and donors (right). Reprinted from [373], with the permission of AIP Publishing. (b) Thermodynamic ionization levels calculated at the PBE, HSE06-SOC and PBE0-SOC levels of theory for the most stable defects. Reprinted with permission from [460]. Copyright 2021 American Chemical Society.

The nature of the intrinsic point defects in $MAPbI_3$ is important as they contribute to the electrical doping. As an example, in perovskites, there is a large amount of shallow defects, which are known to ionize more easily at room temperature and therefore can act as efficient dopants.

A.5 Water-intercalated and mono-hydrated phase of MAPI

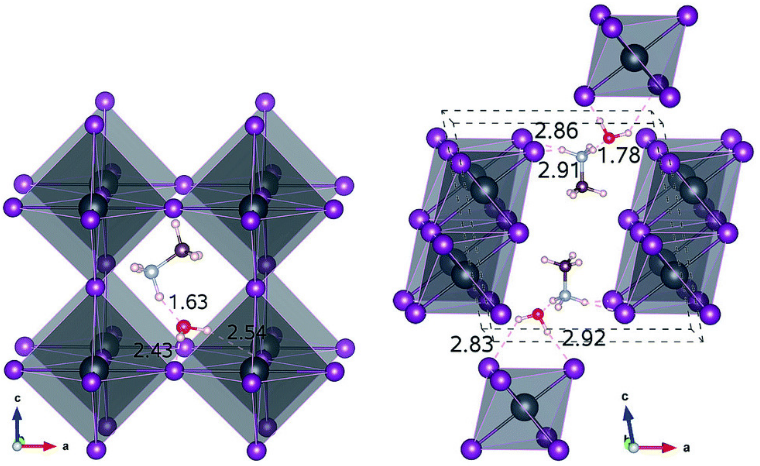

(a) (b)

Figure A.6: Polyhedral view of (a) water intercalated phase $MAPbI_3\_H_2O$ and (b) mono-hydrated phase $MAPbI_3{\cdot}H_2O$. Hydrogen bonds are marked with dotted lines and the bond lengths are presented in units of angstrom (dark grey: Pb; purple: I; brown: C; light blue: N; red: O; light pink: H). Reprinted from [461] under a Creative Commons Attribution 3.0 Unported Licence. Copyright The Royal Society of Chemistry 2018.

A.6 The debate behind the hysteresis of perovskite

Li et al. have reported that migration of iodine ions and interstitials are the main causes for hysteresis without however completely ruling out the MA cation [172], but several reports have demonstrated the role of I^- and MA^+ in the migration process [462, 463]. Azpiroz et al. have on the other hand suggested that migration of iodine defects was too fast and could not explain the slow hysteresis response, and that MA and Pb vacancies could be responsible for this behavior [464]. The channel for these species to migrate are multiple, from bulk point defects, to surface defects and grain boundaries, as well as local lattice distortion and strains [462]. For ease of understanding, Figure A.7 reprinted from [465] depicts the working principle of hysteresis caused by ion migration and charge accumulation.

In the case of a forward scan (Figure A.7a), where no bias is applied ($V = 0$) as the pre-scan condition is short-circuit, ions migrate and accumulate at the interfaces due to the driving force of the built-in field. The direct consequence from that accumulation of ionic charges is the screening of the former built-in field, reducing the extraction efficiency of the photogenerated charge carriers and thus the fill factor and open-circuit voltage, and also increasing the recombination of photogenerated carriers at the wrong interface. However in the reverse scan (Figure A.7b), where there is a pre-bias which overcomes the built-in potential ($V \geq V_{OC}$), the ions will migrate in the opposite direction, which will reinforce the built-in field and improve charge carrier extraction. Additionally, this reduces non-radiative recombination at the wrong interface and this ionic accumulation can induce local doping at the interfaces resulting in improvement of the interface energetics and

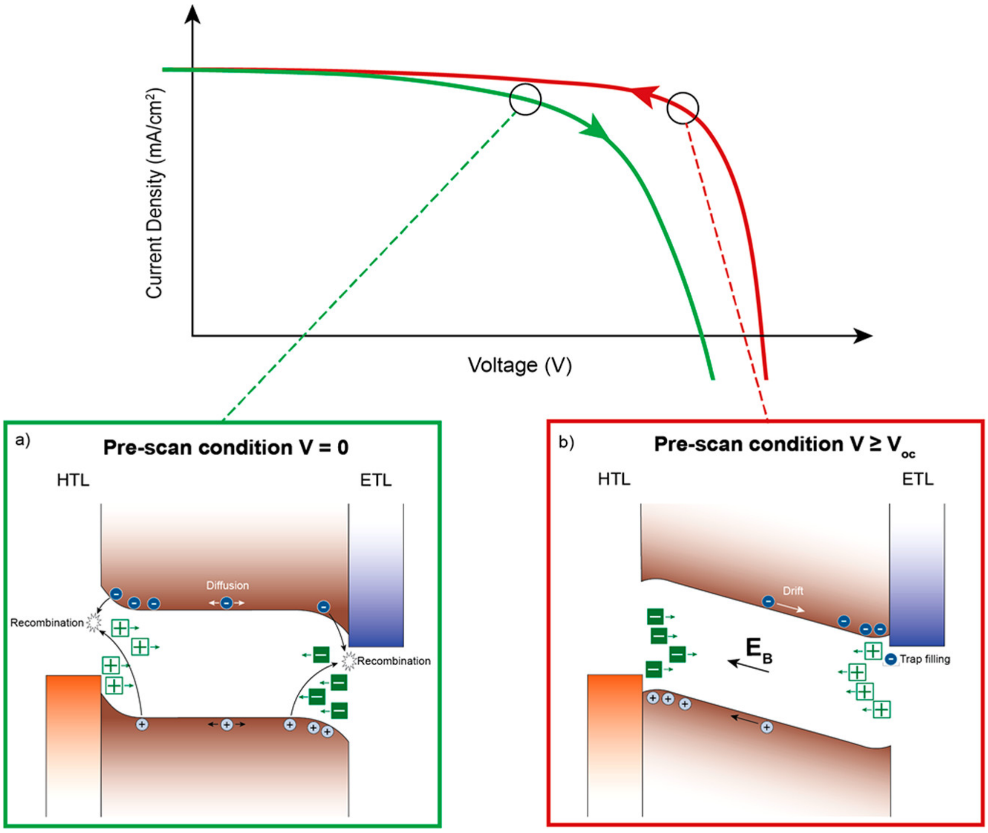

Figure A.7: Explanation of hysteresis. (a) In the case of a forward scan, with a short-circuit as a pre-scan condition. (b) In the case of a reverse scan, with an applied bias as a pre-scan condition. Reprinted with permission from [465]. Copyright 2021 American Chemical Society.

beneficial trap filling [465]. In any case, hysteresis is still highly controversial and even if most groups have found that ion migration and reduction of charge carrier efficiency are the dominant causes, one cannot underrate the effects of modification of the interface band alignment, alteration of the chemical surface, trapping and detrapping via defect sites, ferroelectricity... Reducing hysteresis could therefore be performed by changing the device architecture, where new HTM and ETL would passivate these trap states, or improve the interface alignment. It could also be enabled by improving the material quality and stability by the incorporation of mixed cations and anions structure. However, when no hysteresis is visible, it does not mean that ion migration has been suppressed, but rather that the charge extraction is not affected by the redistribution of ions. Ion migration is not only activated by applying a bias, but can also be photo-induced and linked to changes in electric field due to filling of traps by photogenerated carriers and migrations of iodine [384], or can also be thermally-activated [466, 467].

A.7 Grain boundaries in semiconductors used in solar cells

In semiconductors used for solar cells, it is known that GBs are regions where recombination is high due to the introduction of defect states in the bandgap. In addition, transport of carriers can be affected as GBs can block the lateral carrier flow and can also provide shunt paths for current flows in a device. If carriers get trapped at the grain boundaries, a potential energy barrier can build up which can result in a reduction of carriers from grain to grain. In that sense, increasing the grain size to limit the number of GBs seems to be the way forward, but it was also recently reported that using smaller grains in silicon solar cells could reduce the stress at the GBs, which would in the end lead to less electrically active defects and less recombination [468]. Passivation of grain boundaries has also been one of the goals to improve device performances. In cadmium telluride (CdTe) absorbers, heat treatment with $CdCl_2$ can be for example used to segregate Cl atoms into the GBs, changing the doping and helping carrier collection [469, 470]. The improved collection at the GBs in this technology actually makes it better than its single-crystal counterpart [471]. In copper indium gallium diselenide (CIGSe), Nicoara et al. have demonstrated that heavy alkali elements can induce better passivation at the grain boundaries by reducing the density of charged defects [472]. Even though it sometimes occurs that grain boundaries lead to improvement of the final device, it is in general not the case and thus care must be taken to investigate these interfaces and understand the role they play in the absorber and solar cell stack. In the end, the questions to be answered are whether grain boundaries are beneficial and if not, how can one reduce or suppress their effect of acting as recombination centers or altering the material properties such as band edge positions [473].

A.8 HTL and ETL improvement

TiO_2 was originally used as an ETL for the bottom layer due to its high conductivity, however it introduced a high trap-state density. Therefore, [6,6]-phenyl-C61-butyric acid methyl ester (PCBM) was inserted in between to act as the ETL and had the effect of mitigating the TiO_2 trap states, reducing the non-radiative recombination channel [474, 475]. Not only did PCBM reduce the trap states on the TiO_2 surface, it was also reported to passivate the iodine-rich trap sites at the grain and grain boundaries of the $MAPbI_3$, making it also useful as a top ETL in a p-i-n architecture [476, 477]. In terms of HTM, spiro-OMeTAD was one of the first organic layers to be used due to its ease of deposition. However, it was also noticed that this HTM was inducing degradation at the interface with the perovskite at high temperature, which made it not desirable for a stable and commercial-friendly solar cells [466, 478]. The polymer layer poly(3,4-ethylenedioxythiophene):poly(styrenesulfonate) (PEDOT:PSS) has also been one of the most used HTM in perovskite devices due to its good processibility, high thermal stability, transparency and suitable energy levels [479, 480, 481]. Poly(bis(4-phenyl)(2,4,6-trimethylphenyl)amine) (PTAA) was then preferred due to its even better thermal stability compared to PEDOT:PSS [482]. Ultra-thin layers of PTAA were also reported to suppress interfacial recombination and accelerate hole transfer at the interface perovskite/PEDOT:PSS [483].

When using the ETL as a bottom layer, one of the strategies used to passivate the potential defective surface was through the deposition of self-assembled monolayers (SAMs). Zuo et al. have for example used 3-aminopropanoic acid self-assembled monolayers (C3-SAM) to reduce the pin-holes and interface recombination with the ZnO ETL [484]. More recently, Al-Ashouri et al. have used 2PACz and MeO-2PACz as SAMs on ITO to both create an optimal energy alignment as well as suppress non-radiative losses at the interface [419]. SAMs can also be used on top of bottom HTM as well, as demonstrated by Bai et al. where a diethanolamine SAM was deposited on top of an NiO substrate to yield pinhole-free perovskite [485].

A.9 The techniques to characterize the surface properties of MAPI

Surface-sensitive techniques can be divided in different categories: structural, chemical, electronic and optical characterization. As perovskite absorber have typically a microstructure, their surface features range from several microns (sometimes tens or hundreds of micrometers) to atomic scale. Therefore the techniques used require spatial resolution enabling the observations of such small features. The following discussion is based on review papers from Xue et al. [136], Hidalgo et al. [486] and Rothmann et al. [487] if not referenced otherwise. For a detailed overview of all the techniques, the readers are referred to the books by Abou-Ras et al. [488] and Pazoki et al. [489].

Structural

Scanning electron microscopy (SEM) and atomic force microscopy (AFM) are the most known techniques to access the surface morphology of perovskite thin films as they can retrieve information about homogeneity, grain size, grain and grain boundaries population, surface roughness, and they are already a first good step to optimize the absorber fabrication process. The lateral resolution for these techniques is around a few nanometers (for AFM it depends on the tip apex) and the limitations are mostly the degradation of the perovskite due to the high-energy electron-beam for SEM and distortion due to lateral forces as well light-induced degradation due to absorption of the laser emission for the AFM (depending on the bandgap of the perovskite and the wavelength of the laser). Compared to AFM, SEM only gives information on a two-dimensional level, and therefore roughness and depth profile cannot be accessed using this technique. AFM can also be used to observe if the surface does not present differences in mechanical properties, using the phase signal. In order to get atomic resolution of the perovskite surface, scanning tunneling microscopy (STM) can be used as it has the highest spatial resolution, however roughness is the limitation as only ultra-smooth surfaces can be resolved at the atomic scale. STM can nevertheless also be used on rough samples for topography measurements but AFM is often preferred as STM requires conductive samples and is based on tunnelling of charges into either occupied or unoccupied states, which differs from AFM (see Chapter 2 for more information on these techniques). Transmission electron microscopy (TEM) and high-resolution TEM (HRTEM) enable a much higher resolution than SEM. Besides, atomic-scale imaging can also be achieved but the degradation of the surface is also enhanced due to the transmitted electron-beam. In addition, the crystal structure of the perovskite surface can be determined using grazing-incidence X-ray scattering (GIXS), giving additional information on the crystallographic orientation of the crystal lattice. Compared to X-ray diffraction (XRD) technique, small incident angles of the incoming X-rays are used. Besides, using varying the incident angles during the measurement, as with grazing-incidence wide-angle X-ray scattering (GIWAXS), depth profile of the lattice structure from the surface down can be carried out. However the surface sensitivity of such techniques is relatively low as the detection depth ranges from 50 to 500 nm.

Chemical

Often used combined with SEM or TEM, energy-dispersive X-ray spectroscopy (EDX or EDS) enables the determination of the elemental distribution in the perovskite material. Mostly referred to as a bulk technique, surface-sensitivity can be approached by using low energy electrons but this requires a machine with high-resolution. Similarly, electron energy-loss spectroscopy (EELS) can provide chemical information depending on the energy used. The surface chemistry is however mostly studied by X-ray photo-electron spectroscopy (XPS), which not only gives information about the elemental distribution within the first 10 nm of the surface, but also indicates molecular interaction amongst other properties based on the shift of the binding energy of core levels. Like EDX, the analysis of XPS is quantitative and damage can be dealt on the sample due to X-ray exposure. Secondary ion mass spectroscopy (SIMS) is also another technique to measure the composition at the surface by sputtering the surface using a focused ion beam (FIB) and by collecting the ejected secondary electrons. Time-of-flight SIMS (ToF-SIMS) is usually the standard type of mass analyzer of ionized species sputtered from the surface. Depth profile can also be carried out. Helium ion microscope SIMS (HIM-SIMS) is a recently-developed instrument enabling to image with great spatial resolution the composition at the surface, which enables to obtain chemical information at the micrometer and nanometer scale [490]. These techniques are however qualitative and limited by the destruction of the perovskite samples by the FIB. Lastly, synchrotron infrared nanospectroscopy (nano-FTIR) is another scanning probe technique to retrieve information about molecular structures and chemical information spatially-resolved, with however a lower resolution than STM.

Optical

Photoluminescence (PL) mapping can be of use to determine critical features of a surface, such as grain boundaires, pin holes or secondary phases present at the surface, that would have a different luminescence of energy bandgap. Similarly, time-resolved PL (TRPL) mapping can be used in the same way to determine the carrier dynamics (lifetime), which is more electronic-related. However, to study features down the micro- or nano-scale, micro-PL mapping is preferred and enable by the use of focusing lenses. PL and TRPL mapping are most of the time useful for surface characterization when combined with topography measurements such as SEM or AFM, and have a limited spatial resolution and a large contribution from the bulk. Cathodoluminesnce (CL) mapping can also be mentioned as the working principle are very close to PL with a subtle difference concerning the excitation source, which is based on electrons rather than photons. Lastly, transient absorption (TA) mapping, or pump-probe spectroscopy is used to retrieve information about absorption and transmittance data of the perovskite spatially and in time, and is also used to understand carrier dynamics. However, once again all these techniques are of much better use as a surface technique when combined with microstructure characterization techniques (SEM, AFM) or chemical and electronic techniques that involve mapping.

Electronic

In addition to XPS, ultraviolet photoelectron spectroscopy (UPS) and inverse photoemission spectroscopy (IPES) can be used to determine quantitatively the electronic-energy levels at the surface of perovskite, such as WF, electron affinity and electronic states above E_F. No spatial resolution can be achieved (strictly-speaking) and the resolution depth of these techniques is within 1 to 5 nm. However, the extraction of the VBM and CBM is not extremely reliable and damage to the perovskite sample is often observed. X-ray beam induced current (XBIC) and electron beam induced current (EBIC) are useful for strudying the current collection at surfaces but also between interfaces.

Appendix B

Appendix Chapter 2

B.1 Working principle of PID controller

The principle of the PID controller is that it continuously calculates error signal in SPM and applies a correction based on the proportional (P), integral (I), and derivative (D) terms. The P component depends on the difference between I_{meas} and I_{set} and uses a P gain to determine the ratio of the output response to the error signal. If I_{meas} is 10 times greater than I_{set} and the P gain is set to 5, this will lead to a proportional response of 50. Increasing the P gain has for effect to increase the response of the feedback unit and therefore results in a faster change in tip-sample distance. However increasing the P gain too much can result in larger oscillation of the measured current and instability of the control system. The I component is the integral and sums the error term over time, and therefore the goal of the I component is to drive the steady state error to zero. Increasing or reducing too much the I gain will result in an increase of the error. Lastly, the D component has, for example, for role to decrease the output of the feedback loop if the I_{meas} increases rapidly. However most systems do not use D gains as it is highly sensitive to noise in I_{meas} but use a combination of P and I [491].

B.2 STM auto-approach working principle

In the auto-approach mode, the electronics measured the tunneling current flowing between tip and sample and adjusted the tip-sample distance in a step by step approach in order to reach the set value for the tunneling current. To that end, the Z piezo was expanded to its maximum and the current was continuously measured. If the measured current was lower than the set value, the electronics would move the piezodrive closer to the tip by about a micrometer and again simultaneously expand the piezo while measuring the current. These steps were carried out until the measured value equaled the set value.

B.3 CITS working principle

For current imaging tunneling spectroscopy (CITS), more parameters were required as displayed by the diagram in Figure B.1. First, as the goal is to image the tunneling current at different voltages, a voltage range has to be set (V_{start} and V_{end}). As CITS delivers a map of I for different V, a grid (x lines by y pixels) has to be set as well, which can be the same as the topography resolution or different. For example, a I-V curve could be acquired every two pixels and every two lines instead of every pixel and line for a gain of time.

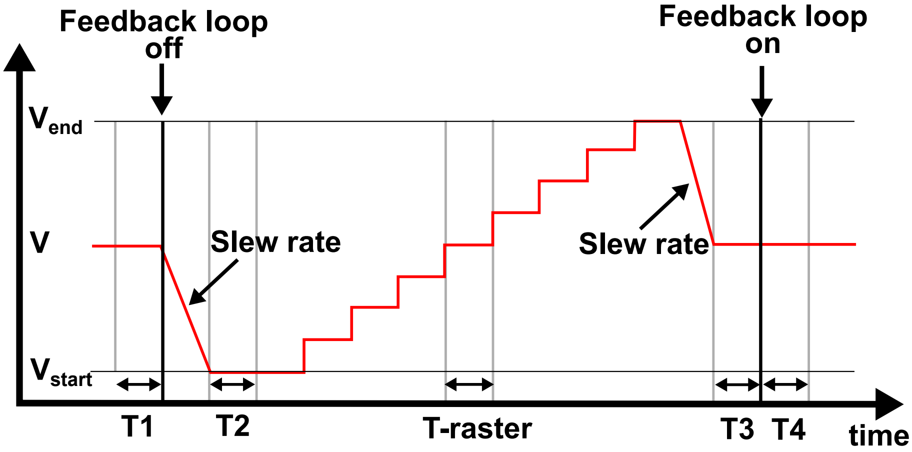

Figure B.1: Principle and important parameters for STS in a VT-AFM from Scienta Omicron.

The CITS then works as follows: the first x line(s) are scanned to acquire topography, where x depends on the grid resolution from the CITS. At the end of the x topography line, the tip is brought back to the beginning of this line and the feedback loop (used for keeping a constant current during topography) is turned off in order for the system to not change the tip-sample distance during the I-V spectroscopy. A time **T1** is then waited before the gap voltage **V**, set for the topography, changes to V_{start} with a certain slew rate (in V/s). Afterwards, a time T2 is waited before the beginning of the I-V spectroscopy. These values are important to give a bit of time for the system to stabilize and not induce artifact at the beginning of the spectroscopy. The current is then measured at the voltage $V = V_{start}$, then the voltage is changed to the next value (which depends on the step size defined by the user) and then a time **T-raster** is waited before measuring the tunneling current at this new value. The same procedure is applied until V reaches V_{end}. Afterwards the system changes the voltage back from V_{end} to V. A time **T3** is waited before the feedback loop is turned on and an additional time **T4** is waited before the tip moves to the next pixel where the same previous procedure will be performed again.

V_{start} V	V_{end} V	Slew rate V/s	Points a.u	T-raster μs	T1 ms	T2 ms	T3 ms	T4 ms
-2.7	2.7	20	130	600	20	2	2	300

Table B.1: CITS parameters used to scan perovskite thin films.

This enables the acquisition of tunneling current maps at different voltages, which can then be extracted pixel by pixel, area by area or in average for the whole image in order to obtain an I-V curve, which can be further exploited as dI/dV or normalized dI/dV curves for the determination of the local density of states. An example of working CITS parameters for perovskite is given in table B.1

Appendix C

Appendix Chapter 3

C.1 PCE losses of perovskites when upscaling solution based techniques

The losses of PCE when upscaling solution-based techniques are mostly linked to three factors: resistances, dead areas and inhomogeneity [492]. Resistive losses are commonly arising from the semi-transparent electrodes, which have lower conductivity than metallic contacts and induce energy losses through heat. Dead areas are also common to modules as they require the reduction of the active area due to device patterning. These first two factors can be dealt with by using highly transparent conductive layers and laser patterning for example [492]. However, the inhomogeneity is the most crucial factor when considering commercial-scale modules, as each layer should be homogeneous (in thickness and material properties) within a certain specifications range. However, spin-coating, which is the method currently used for the highest-efficient lab-scale devices, does not enable the deposition of a fully-homogeneous perovskite absorber layer on areas above 4 cm^2. To date, the highest efficiency for a perovskite solar cell is 25.5% [8, 301] with a 0.095 cm^2 active area and is based on solution processes. The highest achievable PCE for an area larger than 1 cm^2 is 22.6% [301, 493], the highest PCE for a mini-module is 20.1% with an area of 63.98 cm^2 [301, 494] and the largest PCE for a non-concentrating module is 17.9% for an area of 804 cm^2 achieved by inkjet printing [301, 495], which is still quite far away from the 24.4% of the Si-crystalline standard modules [301, 496], the 19% of the thin-film CdTe large modules [301, 497] or the 19.2 % of the thin-film CIGS small modules [301, 498]. From blade coating and spray coating to slot die coating and hot casting, the methods used to deposit high-quality perovskite absorbers on large areas are numerous [499, 274] but still did not yield modules that are comparable with other technologies in terms of efficiency.

C.2 PVD, turbo pump and protective baffle

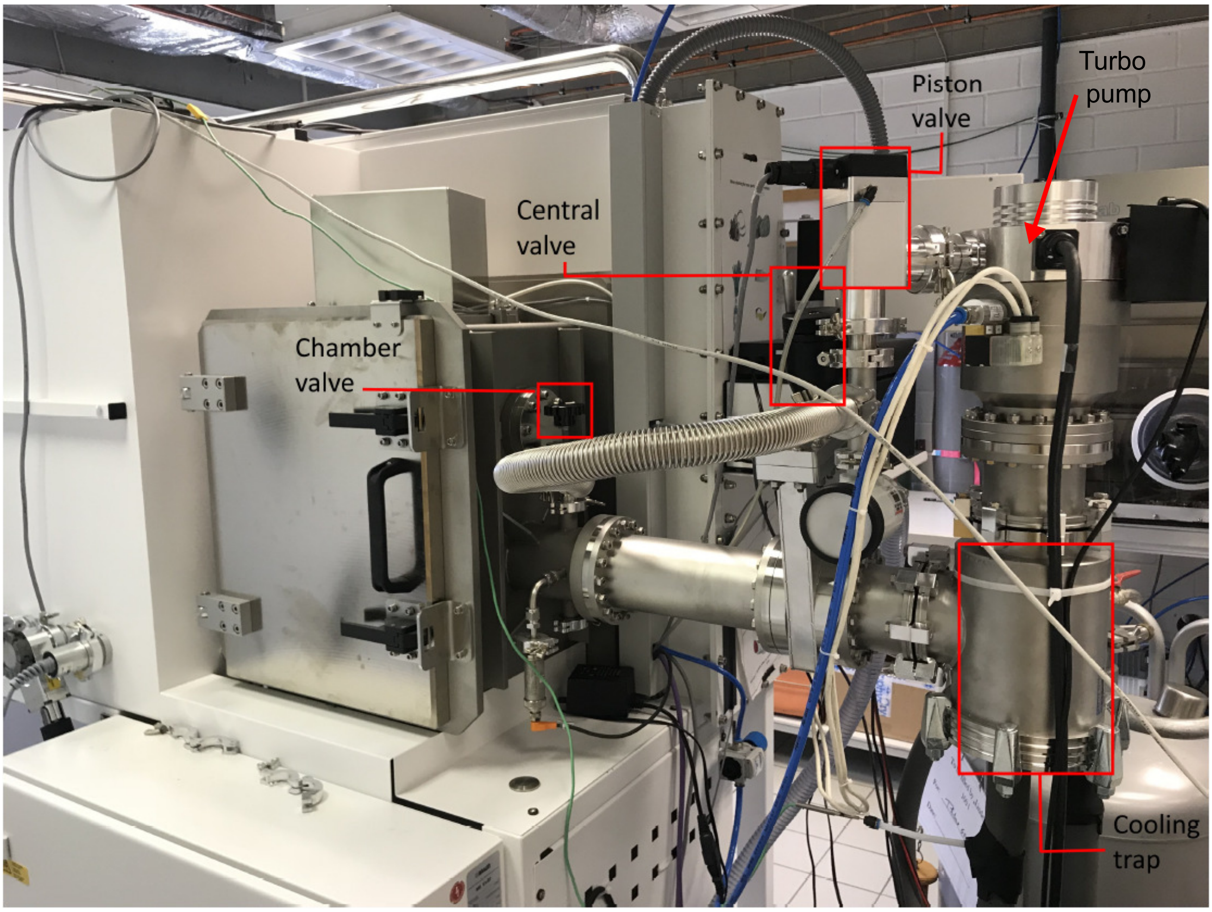

Figure C.1: Picture of the backside of the PVD with the turbo pump and the protective baffle. Courtesy of Ricardo Poeira.

Appendix D

Appendix Chapter 4

D.1 Synthesis of the MAPbI samples

All chemicals used were purchased from Sigma Aldrich except for $PbAc_2$, which was synthesized. The perovskite films were processed on 8 x 8 mm^2 indium tin oxide (ITO) coated substrates (10 Ohm/sq., Präzisions Glas & Optik GmbH, Germany). The substrates were cleaned and afterwards ozone-treated before use. The solution for the perovskite layer was prepared by dissolving 0.8 mmol of $PbAc_2$, 0.2 mmol of $PbCl_2$ and 3 mmol of methylammonium iodide (MAI) to 1.66 ml of DMF. The solution was stirred at 70 °C for 30 mins and then filtered (0.45 µm PTFE) before use. The films were formed via spin coating at 4000 rpm for 60 s and subsequently annealed at 80 °C for 10 mins. The samples were then stored inside a glovebox (0.4 ppm of H_20 and <0.1 ppm of O_2) where they were mounted on a custom-made sample holder suitable for an Omicron VT SPM machine. They were then transferred under inert gas inside a “suitcase”. The final step was the transfer of the sample from the latter suitcase to the SPM under ultra-high vacuum.

D.2 Measurement parameters for the CITS

V_{gap}	I_{set}	Scan speed	V_{ramp}	T1	T2	T3	T4	Slew rate	T-raster
V	pA	nm/s	V	ms	ms	ms	ms	V/s	ms
-2	10 to 200	600 to 1000	-2 to +2	400	20	20	950	100	35

Table D.1: Standard CITS parameters.

D.3 SEM images of the solution-based MAPI

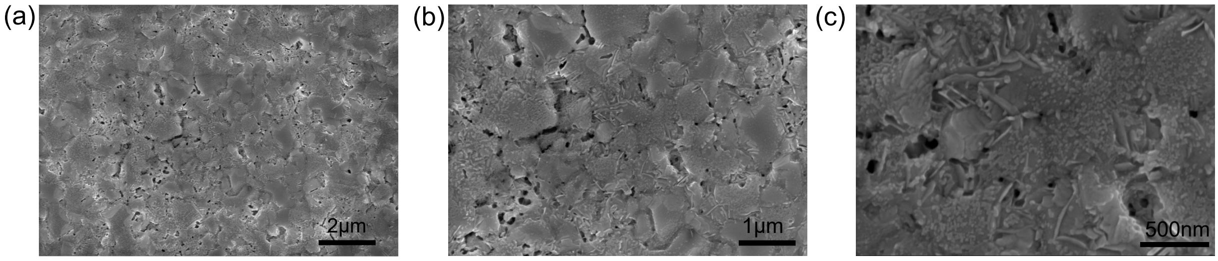

Figure D.1: SEM of solution-based MAPI at 7 kV with (a) x10,(b) x20 and (c) x50 zoom.

D.4 Photoluminescence and time-resolved Photoluminescence

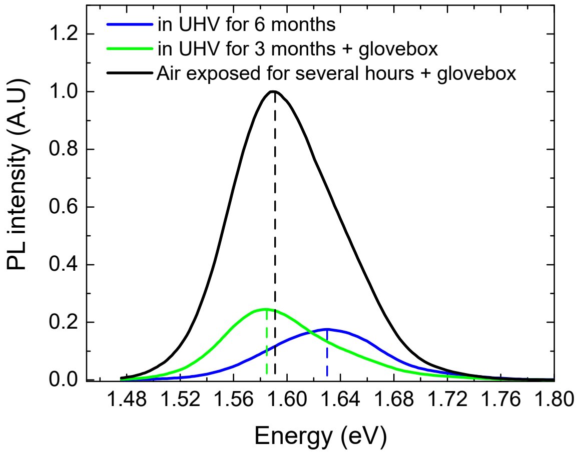

Figure D.2: PL spectra of the same $MAPbI_3$ absorber stored under different conditions.

D.5 STM of poylcrystalline MAPI and its GBs

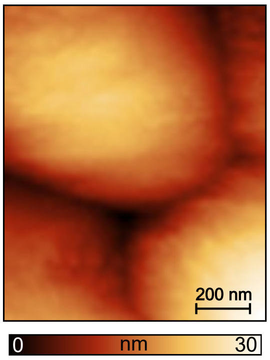

Figure D.3: STM topography at a smaller scale to resolve the grain boundaries.

D.6 Efficiency of mixed cation-halide perovskites

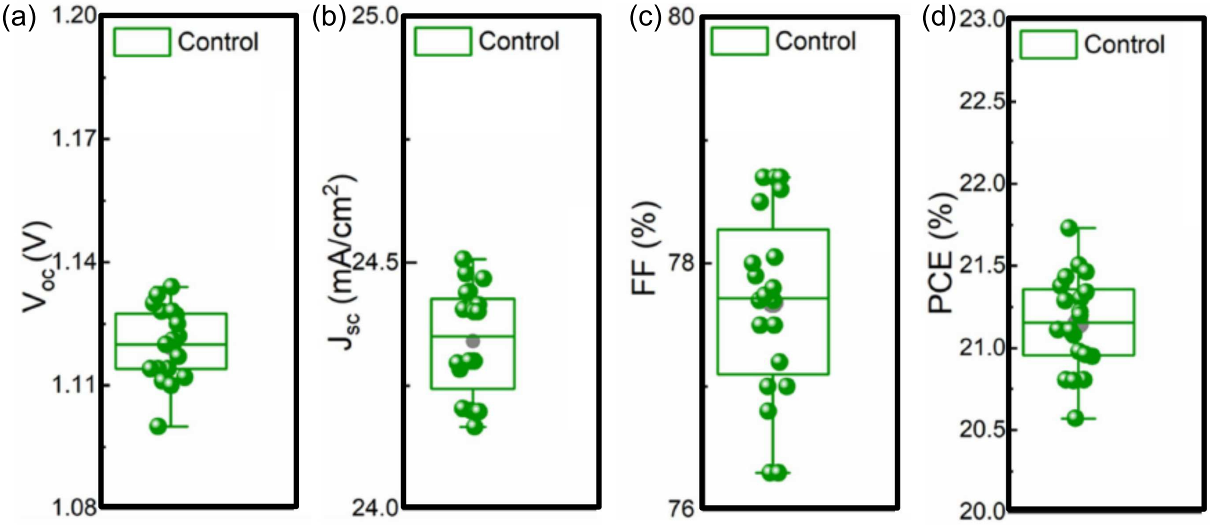

Figure D.4: Summary of photovoltaic metric of the mixed cation-halide perovskite from two best batches (without anti-reflection coating) [344]. (a) Open-circuit voltage (V_{OC}), (b) short-circuit current (J_{SC}), (c) fill factor (FF), (d) power conversion efficiency (PCE). Reproduced with permission from [344] under a Creative Commons Attribution-NonCommercial 3.0 Unported Licence.

D.7 Effect of UHV SPM on the PL of mixed halide perovskites

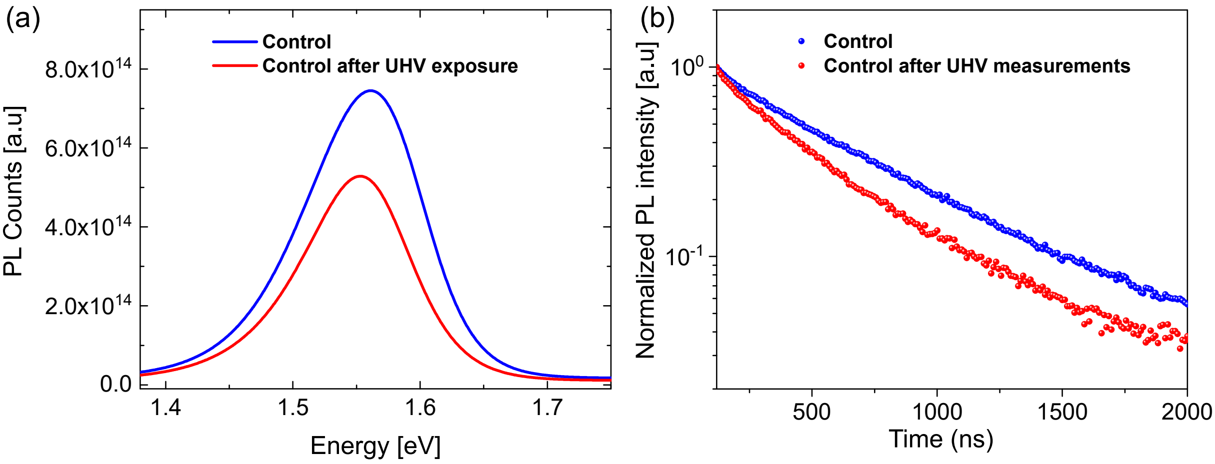

Figure D.5: (a) Photoluminescence and (b) time-resolved photoluminescence before and after UHV measurements of the mixed cation-halide perovskite absorber.

D.8 Conductance at the grain boundaries of mixed perovskites

The investigation of the GBs was performed to determine if any fluctuations in the density of states would be visible, compared to the grains. To that end, a scan resolution of 8-10 nm per pixel for the spectroscopy was used to access, if not the GBs themselves, the close vicinity of the GBs. The surface bandgap (Figure D.6a) at the GBs did not differ from the one extracted at the average grains (and by excluding the low bandgap grains). In addition, the visible defect or bump in the conduction band at the grains was not observed at the GBs, which are often referred to as recombination centers due to the high probability of defect formation there. In comparison to the $MAPbI_3$ absorber, the GBs of the mixed cation-halide perovskite did exhibit a slight shift of the valence band compared to the grains and a very subtle decrease of the WF, which would indicate a very low upward band bending, which was also corroborated with KPFM measurements presented in this thesis, where 60% of upward band bending and 40% of downward band bending were observed (see section 7.2). The small asymmetry in the variation of the dI/dV of the GBs suggests a weak change in the density of surface states, combined with the aforementioned change in WF. However, overall, CITS remains a very qualitative tool for GBs characterization when, as in this case, the resolution lies between 8 to 10 nm and the adjacent grains might contribute to some tunneling of current to the tip. FM-KPFM is therefore preferred and recommended to study these features.

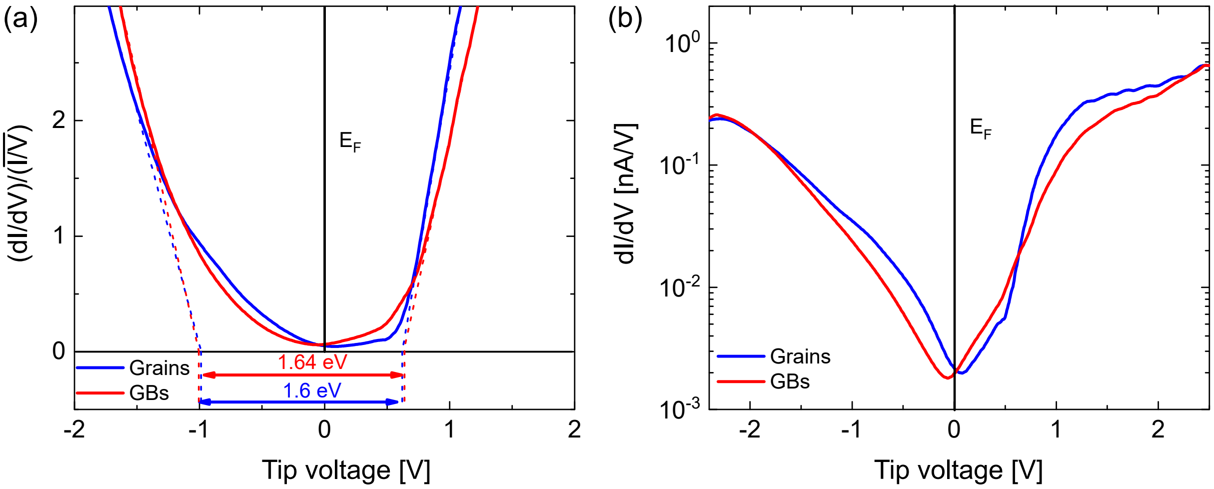

Figure D.6: (a) (dI/dV)/$\overline{I/V}$ curves at the grains and at the GBs and (b) dI/dV curves on a semi-log scale.

Appendix E

Appendix Chapter 5

E.1 Presence of MAI precipitation in XRD after long storage

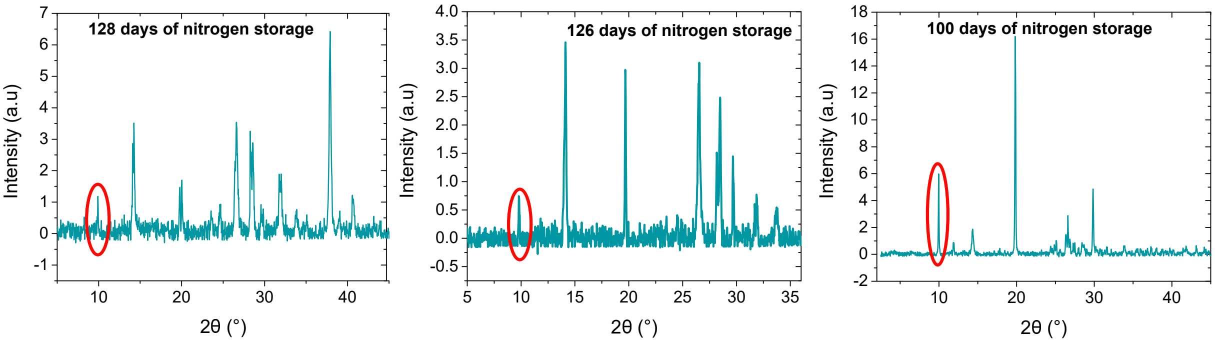

Figure E.1: Occurrence of MAI precipitation near the 2θ angle at 10° after long storage in the nitrogen glovebox.

E.2 SEM and XRD of samples with different I/Pb ratios

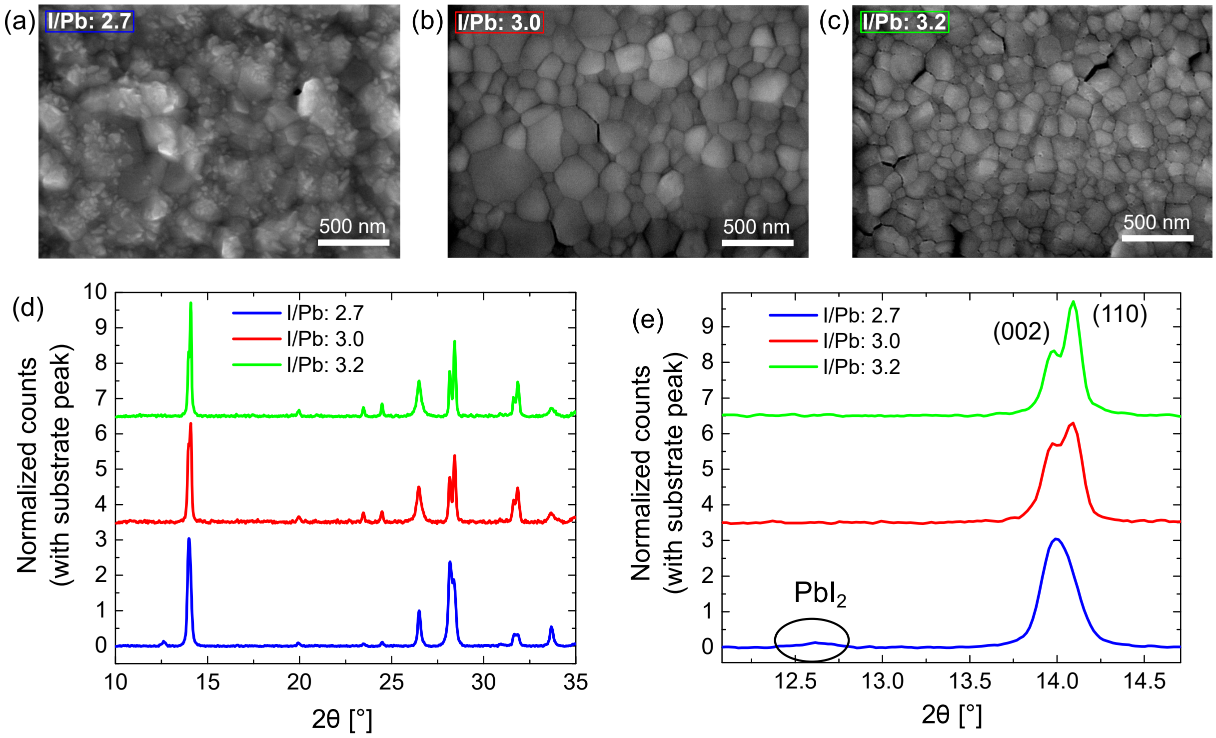

Figure E.2: SEM images of MAPbI$_3$ samples with an I/Pb ratio of (a) 2.7, (b) 3.0 and (c) 3.2. (d) XRD diffractogram of the same samples and (d) zoom-in near the (002) and (110) peaks.

E.3 TRPL of samples grown at different pressures on glass substrates

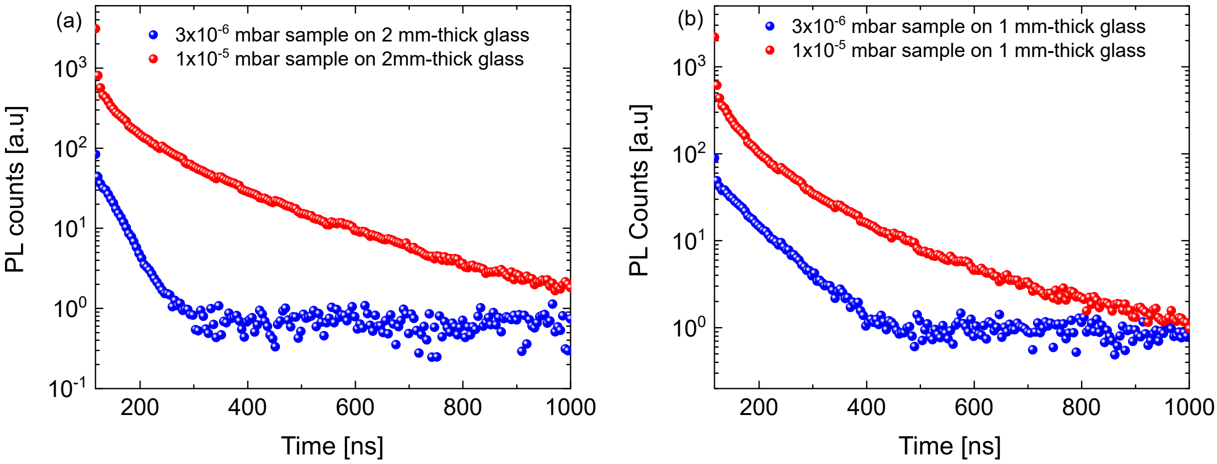

Figure E.3: TRPL of $MAPbI_3$ on (a) 2 mm-thick and (b) 1 mm-thick glass substrates with a laser power density of 1.8×10^{-3} W cm^{-2} and a frequency of 1MHz, corresponding to an injected carrier density of 7.9×10^{14} cm^{-3}.

E.4 Fabrication and characterization of MAPI solar cells

For the fabrication of devices, the hole transport layer PTAA was spin-coated on 16x16 mm^2 glass substrates covered by pre-patterned ITO (Luminescence Technology) and used as the bottom electrode. $MAPbI_3$ films of about 400 nm were then co-evaporated with a constant temperature of 330 °C applied to the PbI_2 crucible and the chamber pressure was kept constant either at 3×10^{-6} mbar or 1×10^{-5} mbar, corresponding to p_{low} and p_{high} respectively. The absorbers deposited on the hole transport layer were then transferred into a glovebox where they were treated in an IPA bath for 30 s. 25 nm of C_{60} with a rate of 0.2 angstroms/s followed by 3 nm of BCP with a rate of 0.25 angstroms/s were then thermally evaporated on top of the IPA-treated perovskites. Scribing of the samples was then performed to access the bottom ITO electrodes by using a small amount of dimethylformamide (DMF) on a cotton bud and the isopropanol (IPA) to dry the solvent and stop the etching reaction. The samples were then transferred to a thermal evaporator where 75 nm of gold was evaporated at a rate of 2 angstroms/s using a mask to obtain an L-shape gold contact. The characterization of the devices was performed in a nitrogen-filled glovebox, using a solar simulator and automated pins to measure the 4 cells per sample (active area of about 4 cm^2). The voltages used ranged from -0.2 V to 1.2 V, and backward then forward bias scans were performed to study the hysteresis, with a sweeping rate of 0.6 V/s and samples kept at 25 °C. Maximum power point (MPP) tracking was only performed for the best two devices for 5 minutes.

E.5 Extracting band bending at the GBs

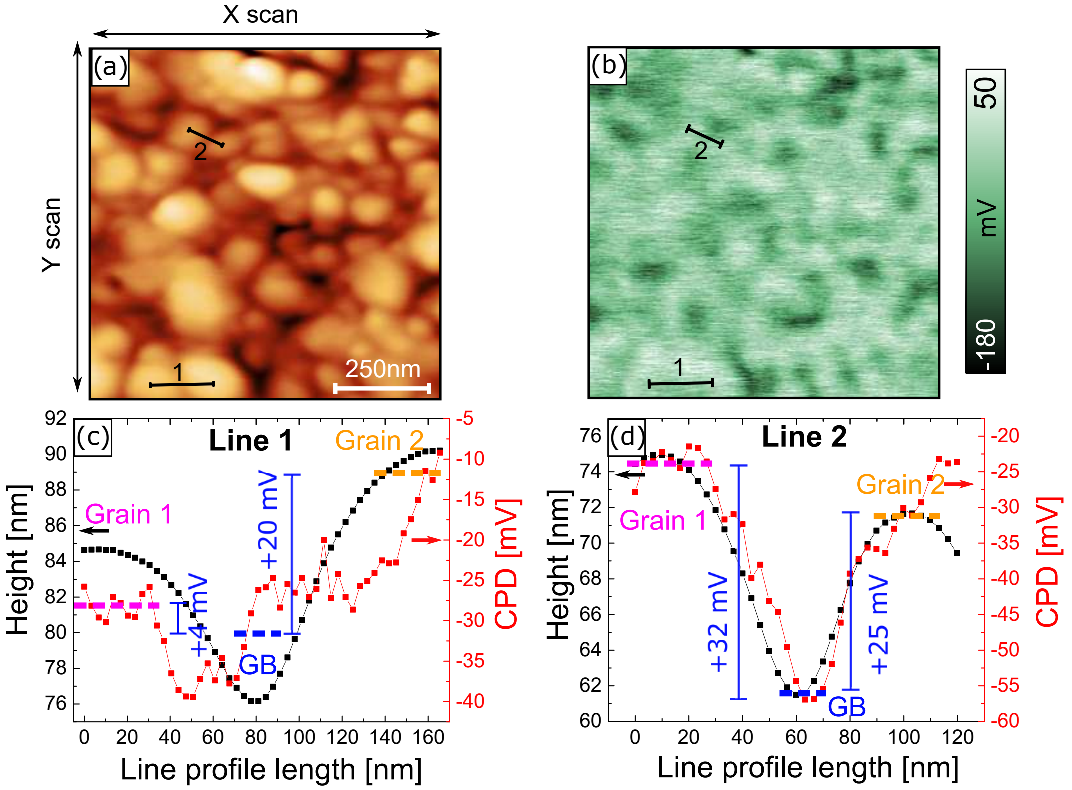

Figure E.4: Representation of the method used to extract the average CPD of two adjacent grains and the CPD of the GB that separates them to calculate the grain boundary band bending Δ_{GB}.

As can be observed, sometimes the CPD signal aligns perfectly with the topography (Figure E.4b) such that at the GB a minimum (or maximum) is found. However, other extraction of curves indicated either that the CPD minimum or maximum was not at the GB itself but for example at a facet, or that a shift existed between the signal of the CPD and the topography (Figure E.4a). A visible shift between the CPD and the topography could have different reasons. First, if the scan speed is set to high values and the feedback loop of the setpoint is not adjusted correctly (see section 2.2 of Chapter 2), the pre-amplifier used to access the CPD will have difficulty in acquiring the CPD values exactly at the topography position and a delay could occur. However in the images, the shift would not always appear and therefore other reasons should prevail. A second reason could be that depending on the dimensions of the grain boundary, which are the slope of the GB (its steepness), its width and its depth, the contribution of the KPFM tip differs. It has already been reported that in frequency-modulated KPFM (FM-KPFM), the apex of the KPFM tip contributes to 75-95% of the CPD signal, while the cone contributes to 5-25% [500, 227]. But, depending on the dimensions of the GB studied, the cone-facet distance could be smaller than the apex-GB distance, which would induce a stronger electrostatic contribution of the cone and therefore a shift in the CPD signal compared to the topograhy. Even if Δ_{GB} was extracted with great caution, it remains a qualitative value and an upper bound of the grain boundary band bending.

E.6 XRD of low and high pressure absorbers after annealing

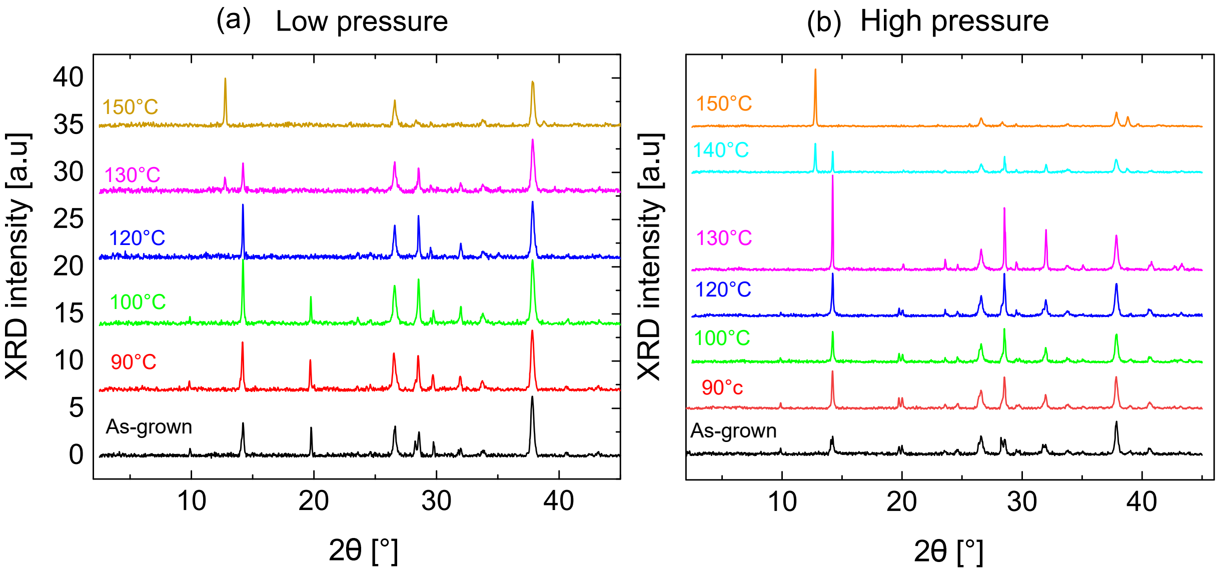

Figure E.5: XRD measurements as a function of annealing temperature for the (a) low and (b) high pressure absorbers.

E.7 TRPL and PL of high pressure samples in nitrogen after annealing

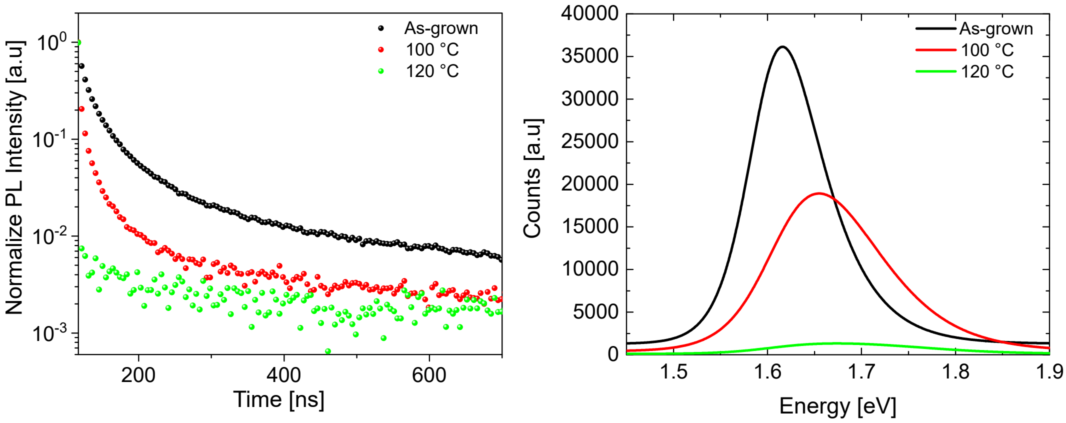

Figure E.6: (a) TRPL and (b) PL measurements of a p_{high} MAPbI$_3$ absorber performed under nitrogen after different annealing steps. The laser power density used was 8.0×10^{-3} cm^{-2} with a frequency of 1 MHz, corresponding to a charge carrier injection of 3.5×10^{15} cm^{-3}.

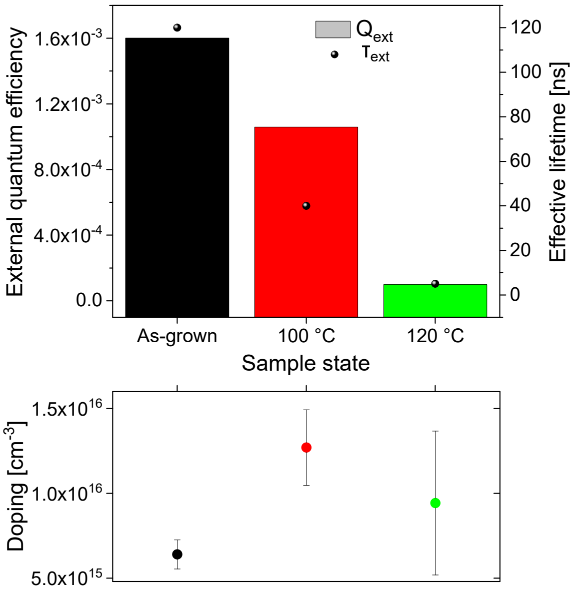

Figure E.7: External quantum efficiency, effective lifetime and doping density at room temperature and after annealing at 100 °C and 120 °C. The laser power density used was 8.0×10^{-3} cm^{-2} with a frequency of 1 MHz, corresponding to a charge carrier injection of 3.5×10^{15} cm^{-3}.

E.8 Change of height upon illumination studied with KPFM

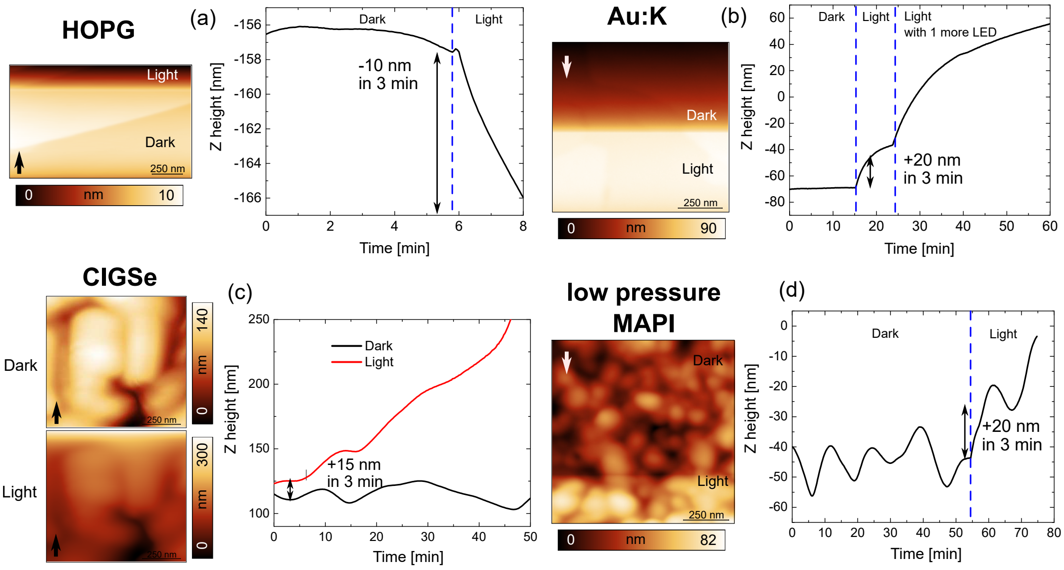

Figure E.8: AFM topography and extracted average line profiles in dark and light conditions for (a) HOPG, (b) post-deposited potassium on gold (Au:K), CIGSe and low pressure MAPbI$_3$. The arrows represent the direction of the AFM scan and the dashed lines the moment where the light was switched on and off, unless written otherwise.

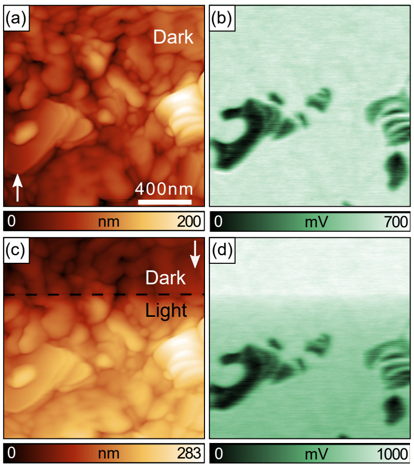

Figure E.9: (a) AFM topography and (b) CPD map of the 870 nm p_{high} MAPbI$_3$ absorber measured in the dark. (c) AFM topography and (d) CPD map at the same position under white LED illumination. The arrows represent the direction of the scan and the dashed lines the moment where the light was switched on and off.

E.9 Short review of the origins of photostriction

Photostriction is the lattice expansion upon illumination and has already been observed in perovskites [116, 202, 386, 387]. Tsai et al. reported that lattice expansion upon illumination had a positive effect on the device performance of their mixed halide-cation perovskites [387]. B. Kundys has reviewed the different causes of photostriction for several material categories (ferroelectric, polar and non-polar semiconductors and organic polymercs) [390]. For example, the volume of a semiconductor, like germanium (Ge), can vary depending on the occupation of its electronic energy levels, i.e. in the conduction and valence bands. The illumination of a semiconductor (with an energy exceeding the bandgap energy) induces the generation of electron-hole pairs, and their separation in both conduction and valence bands. The electrons in the conduction band can contribute to the atomic bonding energy while the holes in the valence band will decrease the energy of the covalent bonds. As the photo-generated charges will change the occupation of the electronic energy levels, the volume of the semiconductor can change, resulting in the effect called photostriction [390]. In non-polar semiconductors, this photostriction, and its sign (dilation or contraction) depends on the pressure susceptibility of the energy gap. For organic materials, the deformation of the lattice upon illumination was related to the light-induced movement of a photosensitive cluster of atoms which induces a change in chemical bonding and the production of a twist in a polymer chain, which results in a nematic order-disorder transition [115]. Zhou et al. have simplified the explanation for organic materials, saying that the photostriction was the consequence of the variations of intermolecular spacing as polymer chains are glued by hydrogen bonds and van der Waals interaction [116].

E.10 TRPL degradation of absorbers on glass

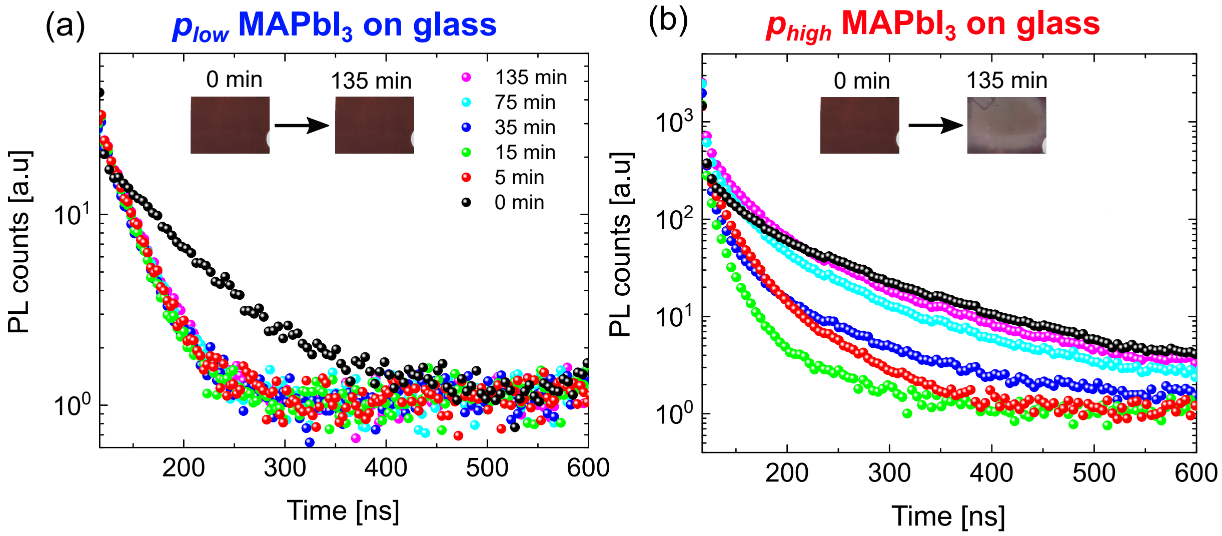

Figure E.10: TRPL measurements of (a) p_{low} and (b) p_{high} absorbers co-evaporated on glass substrates, performed at a laser power density of 4.65×10^{-4} W cm^{-2} with a repetition rate of 1 MHz, corresponding to a carrier injection of 2.0×10^{14} cm^{-3}. The samples were first measured without prior light exposition and then were exposed for prolonged times using a laser power density of 6.0×10^{-3} W cm^{-2}s. The insets represent the visible degradation of the samples after laser exposition.

E.11 PLQY, lifetime and doping in air and after nitrogen storage

The features observed in Figure 5.18 of Chapter 5 (double peak) are often observed in low-temperature PL measurements when transitioning through different phases of MAPbI$_3$, which was not the case here. This could however be caused by the resolution of the liquid crystal wavelength filter and the step size of the PL measurements. In any case, exposure to oxygen demonstrated the improvement of the PL yield, as already reported by several groups [501, 405, 502]. The origin of the light-induced improvement in the PL has been debated, some referring to a deactivation of deep hole traps, caused by iodine interstitials [502], or the formation of a superoxide (O_2^-) at the perovskite surface, due to the capture of electrons by oxygen molecules, together with the migration of halide interstitials in the bulk which will reduce the non radiative trap density [405]. Lastly others have reported that diffusion of O_2 in the bulk was already possible in the dark but accelerated upon illumination, occupying iodide vacancy sites and reducing non-radiative recombination [114, 405, 503]. However, the increase in the PL yield, which could be the consequence of the reduction of the non-radiative recombination due to a potential oxygen-induced passivation, did not translate into an increase of the effective lifetime for the p_{low} absorbers, where the transients remained mainly the same upon the whole illumination time series, with a negligible continuous decrease in the effective lifetime from 90 ns to 60 ns.

In addition, the calculated PLQY and extracted effective lifetime were combined to access the doping density for each step of the illumination study carried out in air (Figure

E.11). For the p_{low} absorber, prolonged illumination resulted in a doping density that more than tripled (from 4.1×10^{15} cm^{-3} to 1.4×10^{16} cm^{-3}), whereas it more than doubled for the p_{high} absorber (from 3.3×10^{16} cm^{-3} to 8.6×10^{16} cm^{-3}).

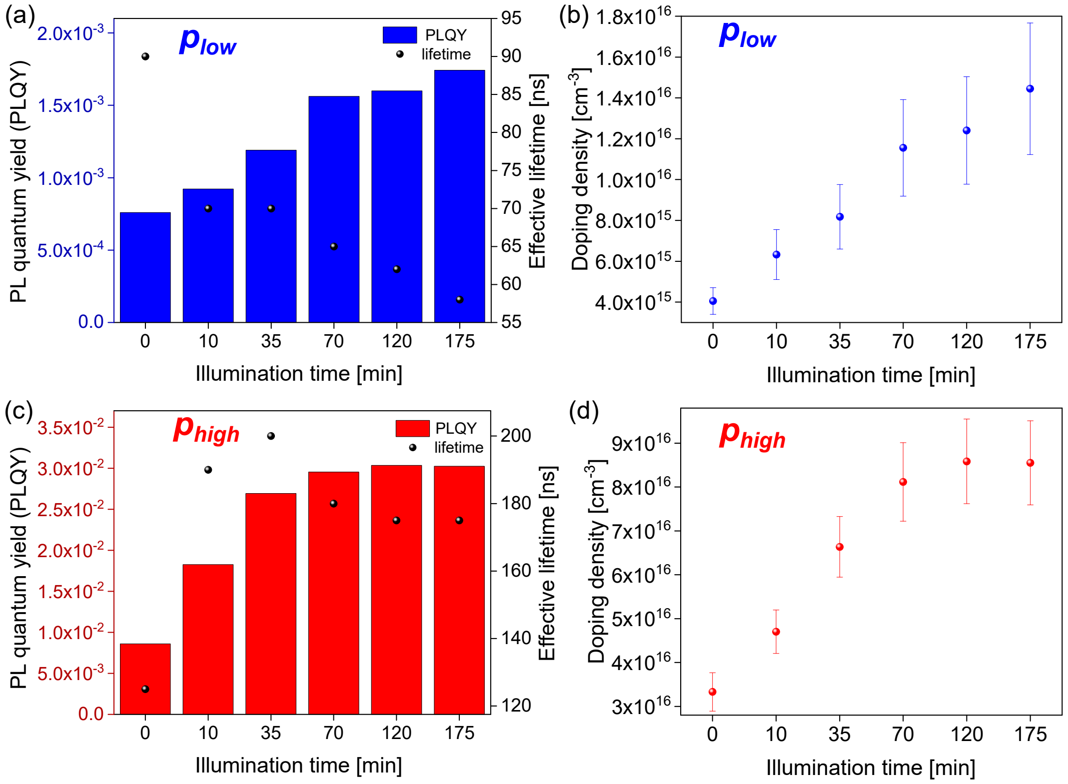

Figure E.11: (a) PLQY, effective lifetime and (b) doping density for p_{low} MAPbI$_3$ absorber as a function of illumination time in air. (c) PLQY, effective lifetime and (d) doping density for p_{high} MAPbI$_3$ absorber as a function of illumination time in air.

Szemjonov et al. have reported that oxygen promoted p-type doping in triple-cation halide perovskites and caused the occupation of iodide vacancies by the oxygen molecules, which resulted in acceptor-like states. They additionally observed increase of the PL yield upon air exposure, and that upon high vacuum conditions, the WF of the perovskite, measured by KPFM, decreased, reversing the p-doping into the intrinsic behavior of the perovskite [406]. Senocrate et al. also demonstrated that when oxygen is introduced in the MAPbI$_3$ lattice, which can be accelerated by illumination, the molecule acts as an acceptor dopant by substituting I$^-$ by O^{2-} [114]. More recently, Shin et al. studied the impact of different environments on the bulk and surface properties of MAPbI$_3$ using UPS and DFT calculations. They showed that in nitrogen, MAPbI$_3$ is essentially intrinsic, whereas upon air and oxygen-controlled exposure, a clear p-type doping was occurring, due to diffusion of oxygen exposure in the bulk, which was reversible when exposing the sample in UHV, where the WF recovered its initial value before air exposure. They explained the intrinsic property due to the balance of both I vacancies (donors) and I interstitials (acceptors), and the oxygen-induced p-doping by the combination of oxygen molecules with I vacancies, which enhances the p-type behavior of MAPbI$_3$ [404]. The increased doping density calculated for both p_{low} and p_{high} absorbers therefore agrees with the previously-discussed work in the literature, and demonstrated the promotion of p-type doping when exposing the sample to air. The magnitude of the changes in PLQY and doping as a function of oxygen exposure and illumination time is approximately the same, but only the effective lifetime of the p_{high} absorber shows a clear increase.

In order to observe if the oxygen-induced p-type doping was reversible in the different $MAPbI_3$ absorbers, they were stored in a nitrogen-filled glovebox for 2 months, and re-measured with PL and TRPL at the same laser power density after this period. PL spectra and TRPL transients for the p_{low} and p_{high} samples measured in nitrogen and in air after deposition, after the illumination study and after the 2-month storage period, are depicted in Figure E.13 and E.14 of appendix chapter 5E.12. In addition, the calculated PLQY, extracted effective lifetime and calculated doping density after deposition, after each illumination step and after the 2-month storage are summarized in Figure E.12. The storage in nitrogen showed to be beneficial for the p_{low} absorber, independently of the environment conditions of the measurements (air or nitrogen). Both the PLQY and the effective lifetime clearly increased, with the improvement in lifetimes being substantial. For the p_{high} absorber, the PLQY in nitrogen was similar to the one measured at the end of the illumination study, and therefore quite close to the as-grown one. However after being exposed to air, the nitrogen storage enabled to recover partially the original as-grown sample's PLQY. Concerning the effective lifetime, it reduced after the storage for the non-air exposed sample, whereas it remained the same as after the illumination study for the air-exposed sample.

By combining these PLQY and effective lifetime values, the doping density was evaluated. For the p_{low} absorber, the doping density after storage of the non-air exposed sample was mainly the same as after deposition, while the doping density of the air-exposed sample managed to almost fully recover its initial value. For the p_{high} case, the non-air exposed sample saw its doping density continue to increase even after nitrogen storage, whereas it dropped for non air-exposed sample. These measurements are in good agreement with Shin et al. and show that the intrinsic doping of $MAPbI_3$ can be recovered after oxygen-induced p-type doping [404]. It is important to note that in this specific case only storage in nitrogen was carried out, which might explain the partial recovery of the doping, whereas UHV storage should potentially induce full recovery, due to an enhanced sublimation and out-diffusion of the oxygen molecules from the $MAPbI_3$ bulk.

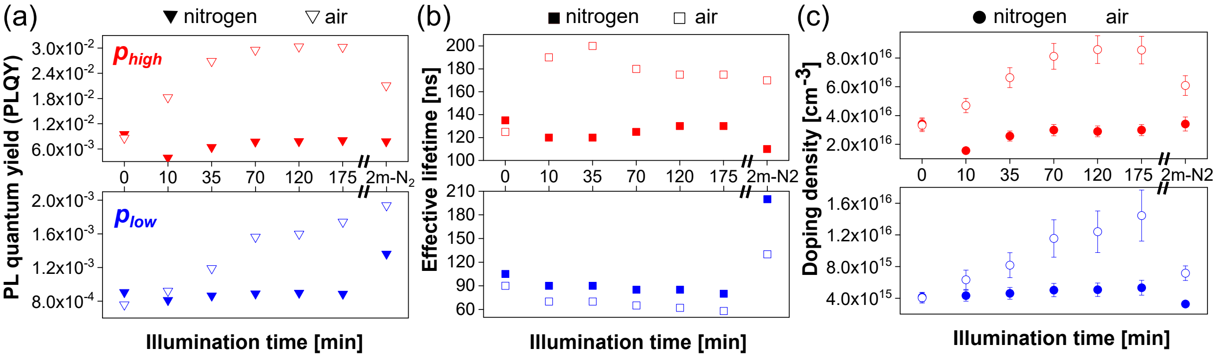

Figure E.12: (a) PLQY, (b) effective lifetime, (c) doping density for the p_{low} and p_{high} absorber, exposed to nitrogen or air, after deposition, after each illumination step and after the 2-month storage.

E.12 PL and TRPL after nitrogen storage

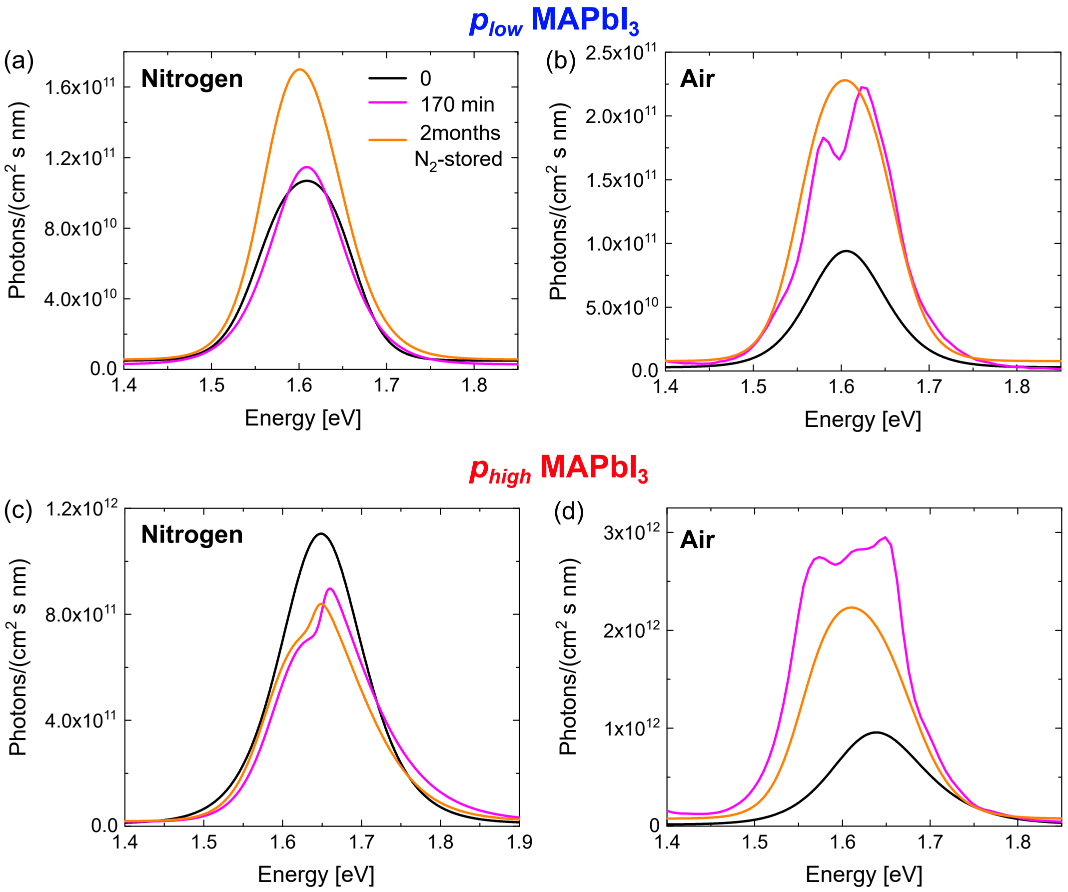

Figure E.13: PL measurements on p_{low} absorber in (a) nitrogen, (b) in air, and on p_{high} absorber in (c) nitrogen and (b) in air. The measurements were performed at a laser power density of 2.81×10^{-3} W cm^{-2} with a repetition rate of 1 MHz.

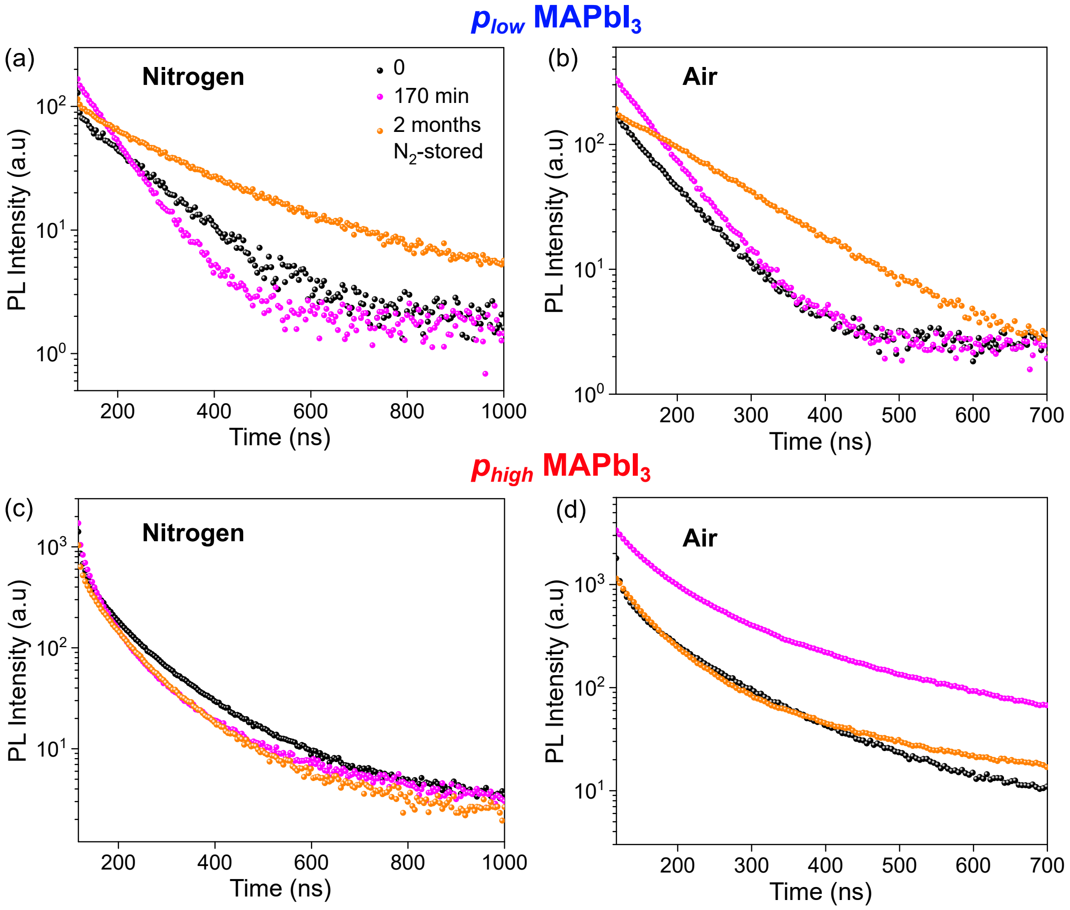

Figure E.14: TRPL measurements on p_{low} absorber in (a) nitrogen, (b) in air, and on p_{high} absorber in (c) nitrogen and (b) in air. The measurements were performed at a laser power density of 2.81×10^{-3} W cm^{-2} with a repetition rate of 1 MHz, corresponding to a carrier injection for TRPL of 1.24×10^{15} cm^{-3}.

Appendix F

Appendix Chapter 6

F.1 Individual CPD profile in the dark and illumination

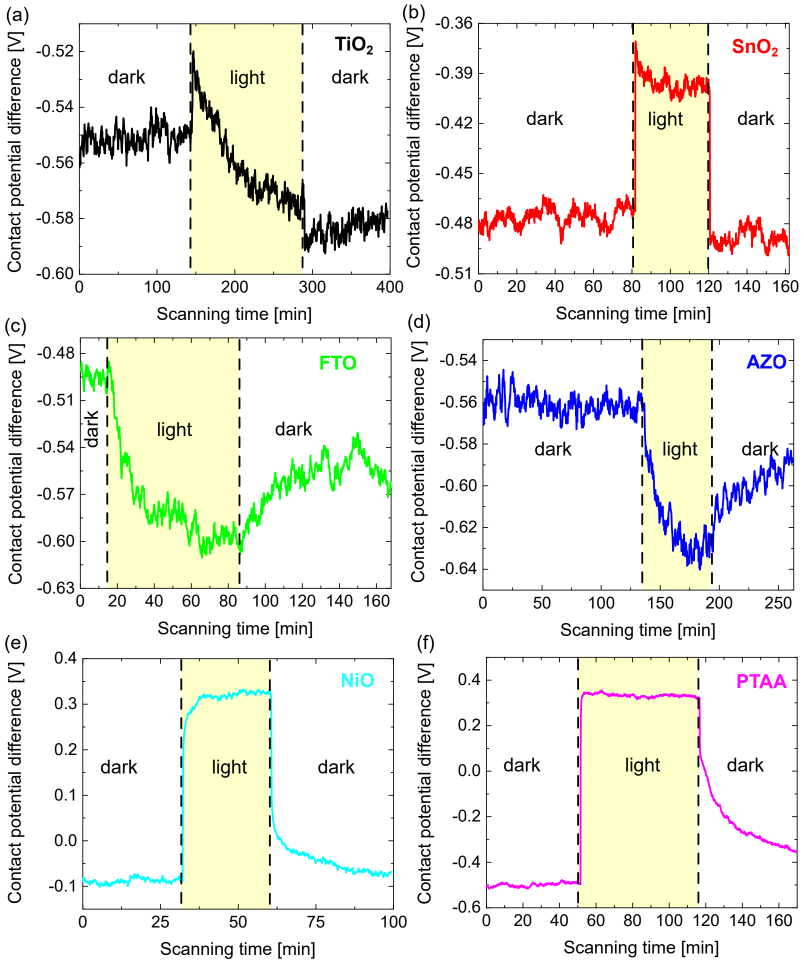

Figure F.1: Average CPD profile, extracted from a CPD map, of $MAPbI_3$ thin films under different conditions (light, dark, and light again) for different substrates: (a) TiO_2, (b) SnO_2, (c) FTO, (d) AZO, (e) NiO and (f) PTAA. The dashed lines represent the separation between dark and light periods and the light-yellow area depicts the illumination period.

F.2 CPD instability in the dark of PTAA after light exposure

Figure F.2 represents successive KPFM measurements of $MAPbI_3$/PTAA on different spots of the samples. The first one was already discussed with the illumination study (sub-section 6.1.1 of Chapter 6). At the end of the measurement in the dark, the CPD signal had still not reached an equilibrium state with a stabilized CPD. The measurement was ended and a new one was directly carried out on a new spot of the sample. Ideally, the CPD should have started either at the initial value in the dark or at the last value recorded in the last image, as the sample is homogeneous. However, the CPD value on the second spot was higher and kept on decreasing over time in the dark. After 45 minutes, the measurement was stopped, and the sample was kept at rest in the dark for 8 hours before measuring a new spot on the sample in the dark. The first CPD value was even higher than previously recorded, and decayed for a prolonged time until a potential stabilization. Interestingly in all cases the final CPD value seemed to reach a value of -0.36 V and could potentially be linked to a reached equilibrium after ionic migration due to the electric field induced by the KPFM tip, or a charging effect at the surface. This also indicated a worse intrinsic stability against light of $MAPbI_3$ co-evaporated on PTAA.

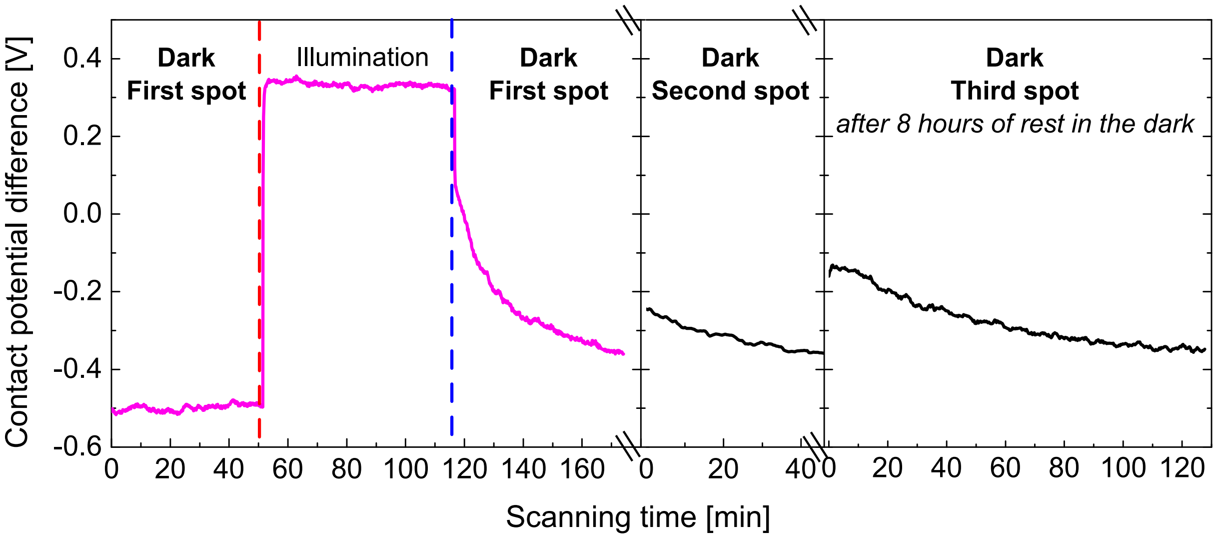

Figure F.2: CPD evolution of $MAPbI_3$ on PTAA for different consecutive spots or images. A continuous decay of the CPD is visible after having exposed the sample to illumination, which does not stabilize in the range of the scanning time.

F.3 XPS equipment, parameters and procedure

XPS spectra were acquired using a Thermofisher Scientific Nexsa Spectrometer in ultra-high vacuum with a mono-chromated X-ray source of Aluminium (Al $K_\alpha = 1486.68$ eV). The spot size was of 400 µm. For the survey spectra, the pass energy used was 200 eV with a dwell time of 50 ms and an energy step of 1 eV. For the studied core level spectra, a pass energy of 20 eV was used with a dwell time of 100 ms and an energy step of 0.1 eV. The first measurement in the dark was acquired in 3 min and 24 s and the second measurement to study the influence of the X-ray lasted 2 min and 02 s. The times for each core elements are detailed in table F.1.

Core levels	Scanning time (s)	Number of scans
I3d	30	1
Pb4f	20	1
N1s	72	4
C1s	114	6
O1s	80	4
Survey	68	1

Table F.1: List of the core elements (and survey) scanned together with the scanning time used.

The samples, after being co-evaporated, were sent in a nitrogen-filled sealed bag and opened in a nitrogen-filled glovebox where they were mounted in the XPS sample holder (Figure F.3) and electrically connected with a carbon tape for the back contact and a clip for the front contact. The sample holder was transferred to the load-lock of the XPS without air exposure.

A gold sample was used as the reference sample by measuring the $Au4f_{7/2}$ core level. The first measurement of the $MAPbI_3$ samples in the dark consisted in measuring all the spectra of the aforementioned core elements and the full spectra (survey). The second measurement in the dark consisted in measuring the core elements I3d, Pb4f and N1s just after the first measurement to estimate the X-ray beam effects on the binding energies.

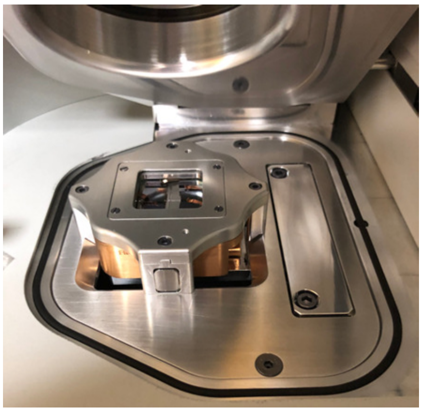

Figure F.3: The XPS sample holder with the 6 samples previously mounted in a nitrogen-filled glovebox and electrically connected by means of carbon tape for the back contact and clip for the front contact. The transfer between the glovebox and the XPS load lock was carried out without air exposure.

F.4 Changes in binding energies upon illumination

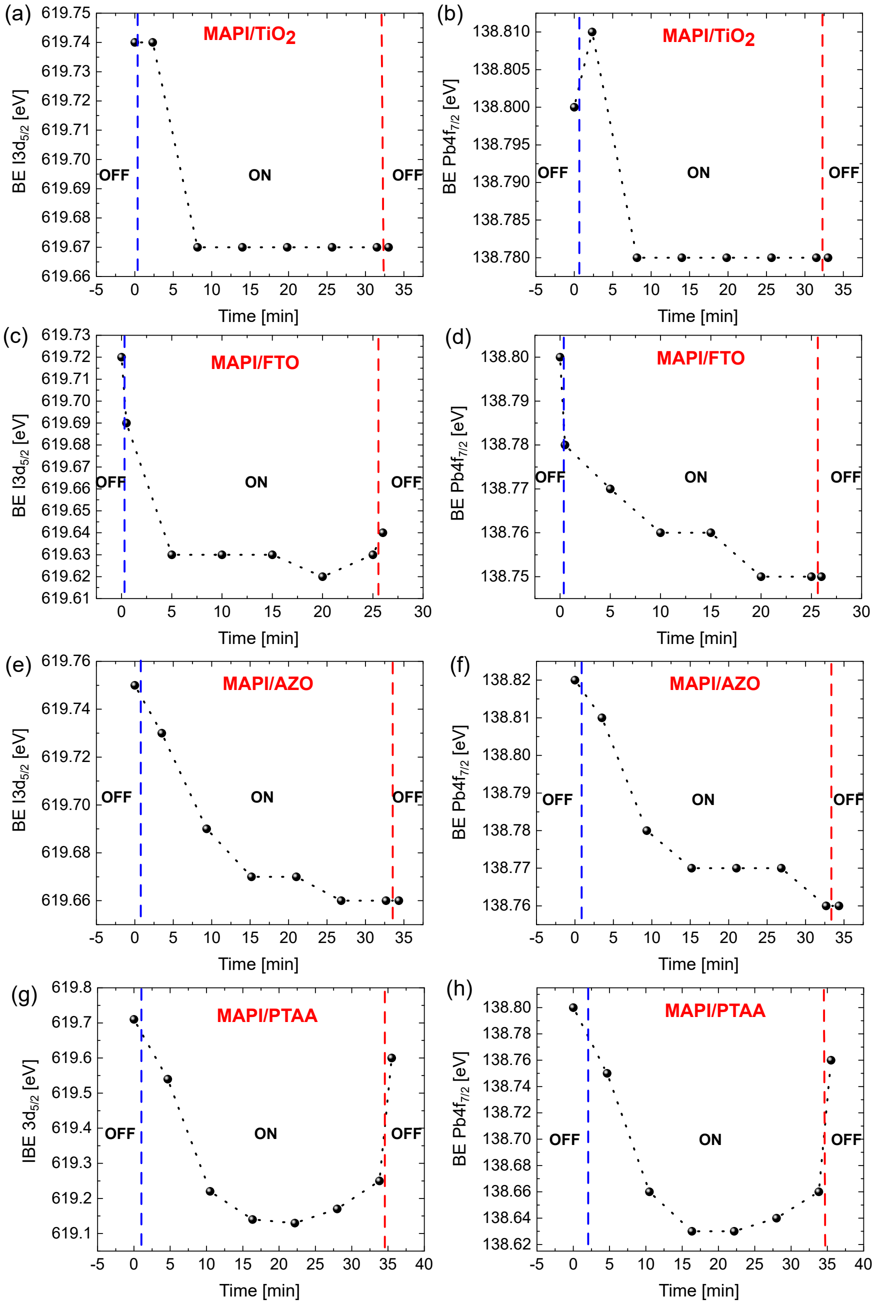

Figure F.4: Changes in binding energies for the $I3d_{5/2}$ and $Pb4f_{7/2}$ core elements of $MAPbI_3$ deposited on different substrates (a,b) TiO_2, (c,d) FTO, (e,f) AZO and (g,h) PTAA. The dashed lines represent the moment were the light was switched on and off.

F.5 Appearance of metallic lead as a function of time

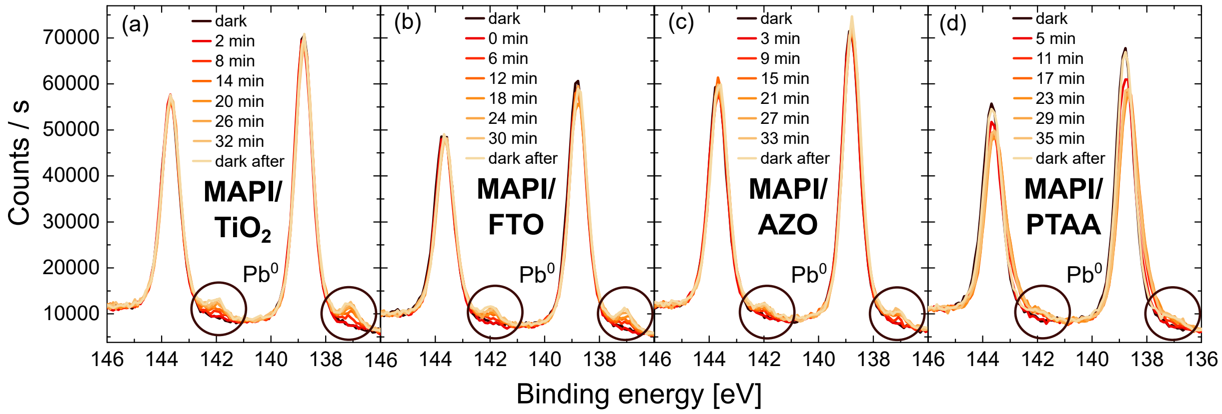

Figure F.5: XPS measurements of the Pb4f core level for (a) $MAPbI_3/TiO_2$, (b) $MAPbI_3$/FTO, (c) $MAPbI_3$/AZO and (d) $MAPbI_3$/PTAA as a function of illumination time.

F.6 Changes in peak intensities for I3d and Pb4f core levels with light

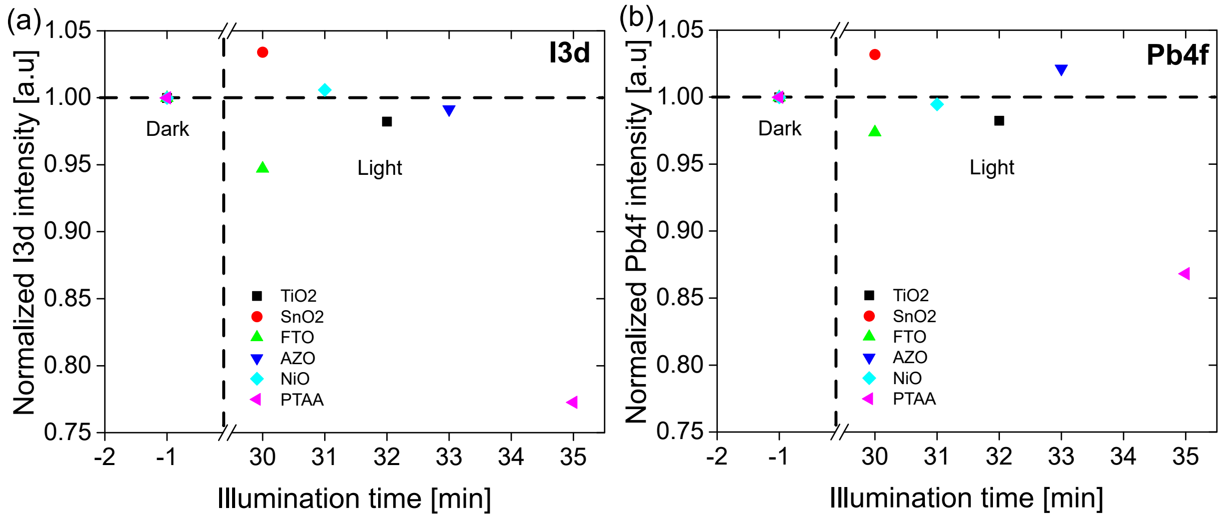

Figure F.6: Evolution of the peak intensities in the dark and after prolonged illumination for the core levels (a) $I3d_{5/2}$ and (b) $Pb4f_{7/2}$ for $MAPbI_3$ co-evaporated on different substrates.

F.7 XPS investigation in the dark after illumination

The Pb^0/Pb and I/Pb ratios were extracted on the same spot after the light was switched off, as well as on a fresh spot, close to the one used during the illumination study, which was exposed to light but not to X-rays. Figure F.7 represents the evolution of these ratios upon the different stages of the XPS measurements, starting with the first dark spectra.

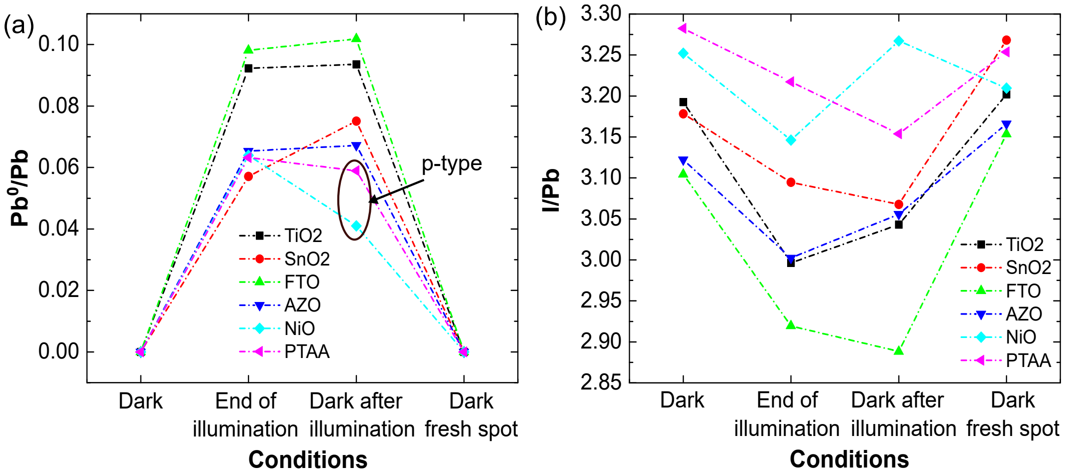

Figure F.7: (a) Pb^0/Pb ratio and (b) I/Pb ratio extracted from XPS measurements for $MAPbI_3$ co-evaporated on different substrates and for different conditions: in the dark, at the end of the illumination study, in the dark after the illumination study and in the dark on a fresh spot next to the one measured under illumination.

After the last light iteration cycle, the white LED was switched off and a new XPS spectrum, together with additional measurements at the main core levels, were performed again. The Pb^0/Pb ratio for $MAPbI_3$ deposited on n-type substrates further increased even if direct illumination was not present, suggesting that the use of X-rays was still enough to induce further degradation. On the other hand, the perovskite films deposited on p-type substrates displayed a direct decrease of their Pb^0/Pb ratio as soon as the light was switched off (circled region in Figure F.7b), which could indicate a better stability and resistance to degradation of $MAPbI_3$ on the p-type substrates, or a slower recovery or non-reversible degradation for $MAPbI_3$ deposited on n-type substrates. When measuring on a close spot, not exposed to X-rays but exposed to light, no Pb^0 was observed on all samples, suggesting that the light itself did not seem to produce Pb^0 but the combination of X-rays and light did.

Additionally, the I/Pb ratios were extracted but did not show trends that depended on the substrate's type, as some samples showed a further decrease of the I/Pb ratio (SnO_2, FTO and PTAA) whereas others an increase (TiO_2, AZO, NiO) when the light was switched off (Figure F.7b). However, when measured on a fresh spot, the I/Pb ratio of $MAPbI_3$ co-evaporated on n-type substrates were always higher than the initial I/Pb ratio in the dark, whereas they were lower for p-type substrates. One explanation could be that different lateral ion migrations occur, strongly linked to the degradation mechanism and the type of species lost from the surface in the vacuum upon illumination [384]. However, the measurement error in the determination of the atomic percentage of the elements is such that the second digit after the decimal can be neglected, and therefore the different I/Pb ratios on the fresh spots could just be caused by small inhomogeneities at the surface of the perovskite absorber.

F.8 PL and TRPL of MAPI on different substrates

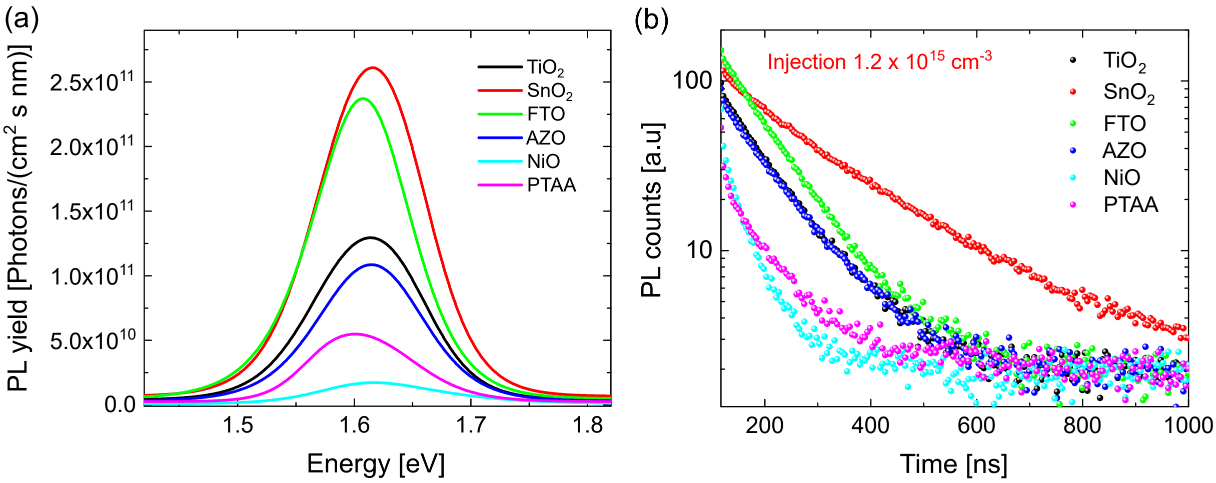

Figure F.8: (a) PL yield and (b) TRPL of MAPbI$_3$ co-evaporated on different substrates. The laser power used was 2.81×10^{-3} W/cm^2 with a pulsed laser at a frequency of 1 MHz, yielding an injection for the TRPL of 1.2×10^{15} carriers/cm^3.

F.9 PL bandgap of MAPI on FTO as a function of film thickness

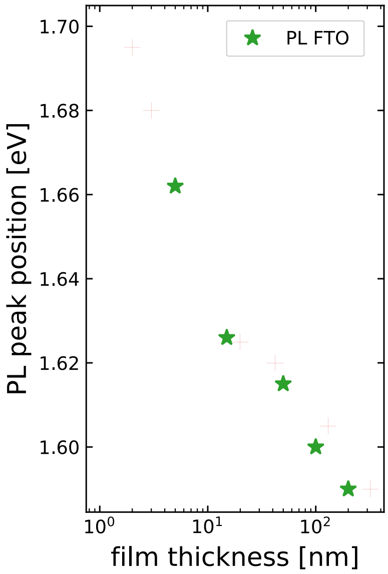

Figure F.9: PL peak position of MAPbI$_3$ co-evaporated on an FTO substrate with different absorber thicknesses. Reproduced with permission from [424].

Appendix G

Appendix Chapter 7

G.1 UHV KPFM images of MAPI after air exposure and annealing

A $MAPbI_3$ absorber co-evaporated on an FTO substrate was exposed to air for a few minutes, then introduced back in the glovebox where it was annealed under nitrogen atmosphere at 90 °C for 10 minutes. It was then introduced and measured in the UHV KPFM and compared to a sibling non-air exposed $MAPbI_3$ absorber, similarly annealed at 90 °C. As a side note, the samples were co-evaporated with a high MAI partial pressure, leading to the appearance of low-dimensional perovskites as low WF regions as depicted in Figure G.1b. The extraction of line profiles showed that these regions had CPD values of 110 mV lower than the rest of the surface for this specific features, and could not be specifically linked to a feature in the topography map. The occurrence of low-dimensional perovskites was extensively discussed in Chapter 5.

In comparison, the air-exposed and annealed sample directly presented visible large and high features on the topography map (Figure G.1d), about 150 nm higher than the rest of the surface, which were nicely linked to features with lower CPD in the CPD map (Figure G.1e). The CPD values of these features were almost 400 mV lower than the rest of the surface (at its lowest), suggesting by its large difference in WF and clear grain-like structure, a different material than $MAPbI_3$ at the surface.

Light was also used to observe how the air exposed and annealed sample would behave upon prolonged illumination. As a reminder (Figure F.1 of appendix chapter 6F.1), the non-air exposed annealed $MAPbI_3$ is likely to behave like the as-grown sample (without annealing), that is to have negligible SPV and a continuous decrease of the CPD upon illumination, as annealing of the as-grown sample did not lead to a change of its surface topography, its WF or its optoelectronic properties. For the air-exposed and annealed sample (Figure G.2), first a continuous decay of the CPD in the dark was observed, suggesting some instability at the surface, either due to continuous degradation and evaporation of halide species, or charging. Upon illumination, a SPV of -100 mV was calculated, followed by a further decrease of the CPD until a continuous prolonged increase of the CPD was observed. The cause of these effects will not be discussed here, but it clearly showed that the contamination of the sample in air before annealing is likely to induce additional and different surface states, resulting in a larger band bending and greater SPV magnitude but also instability of the absorber's surface, highlighted by the regions 1 and 3 in Figure G.2.

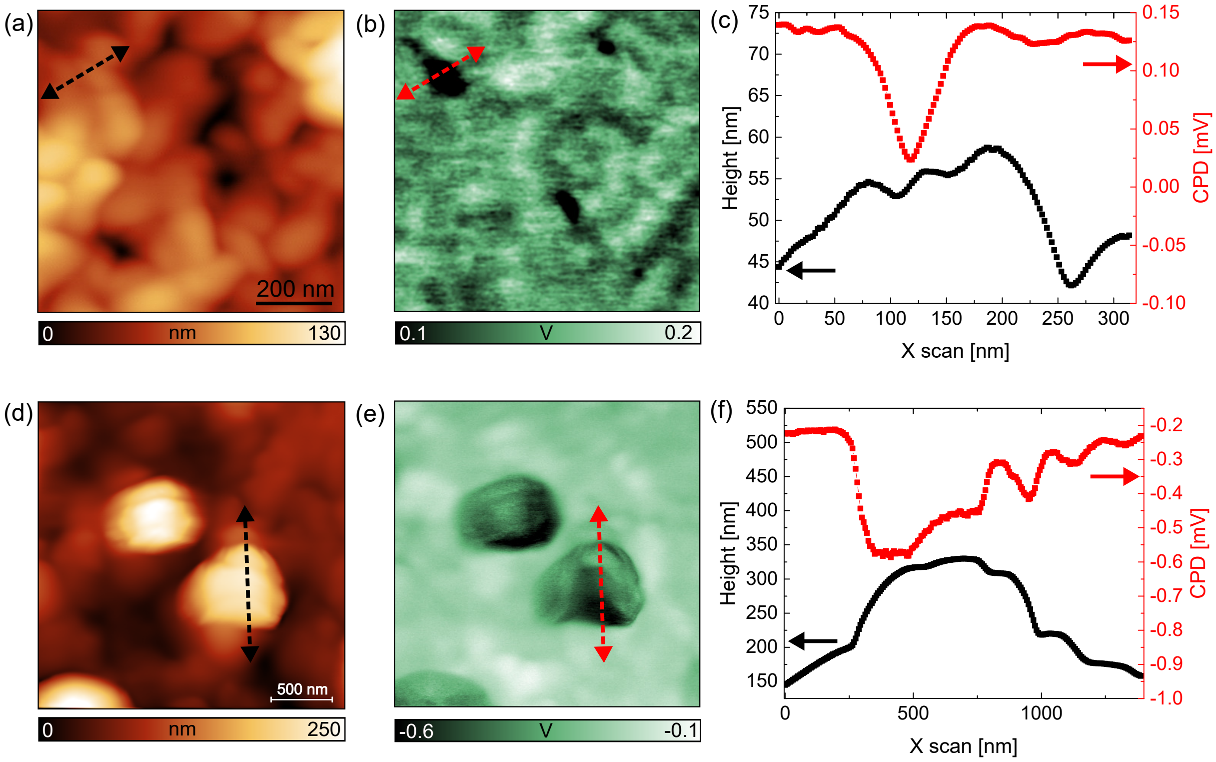

Figure G.1: (a) Topography and (b) CPD maps of a $MAPbI_3$ as-grown absorber co-evaporated on FTO and annealed for 10 minutes in a nitrogen environment at 90 °C. (c) Extracted height and CPD profiles from the black and red dashed lines of (a) and (b). (d) Topography and (e) CPD maps of a $MAPbI_3$ as-grown absorber co-evaporated on FTO, air exposed for a few minutes and annealed for 10 minutes in a nitrogen environment at 90 °C. (f) Extracted height and CPD profiles from the black and red dashed lines of (d) and (e).

G.2 SPV of mixed halide perovskites

Upon illumination, the mixed perovskites studied did not present a visible SPV using the 15 ms resolution of the KPFM where the $MAPbI_3/TiO_2$ displayed a slight increase of its WF followed by a further increase and continuous decrease of the CPD. As represented by the average CPD in dark and illuminated conditions of Figure G.3, no sudden change of the CPD could be discerned for the $Pero_{Rb,Cs}$ spin-coated on TiO_2, however after prolonged illumination a continuous decrease of the CPD was observed, coherent with a light-induced degradation of the perovskite and evaporation of I_2, altering the KPFM tip WF as discussed in Chapter 6. Similarly, $Pero_{Br}$ did not exhibit a sudden change of its WF upon illumination but the effect of prolonged illumination was not studied. The difference in SPV could be coming from a difference in the preparation of the solution-based TiO_2 but it has to be noted that when monitoring the **average** CPD upon illumination for co-evaporated $MAPbI_3$, there would always be a clear, visible and sudden change of the CPD independent of the substrates, whereas no change of the CPD was observed for both mixed perovskites. This could suggest reduced surface states (donor or acceptor-like) induced by the use of several cations or halides, as it has previously been reported that the proper elemental substitution (in this case Br) could reduce trap states [504], but could also be caused by the different polarization for FA^+ and Cs^+ compared to MA^+ [505, 506]. In addition, the use of Cs^+ and Rb^+ was demonstrated to promote the uniform distribution

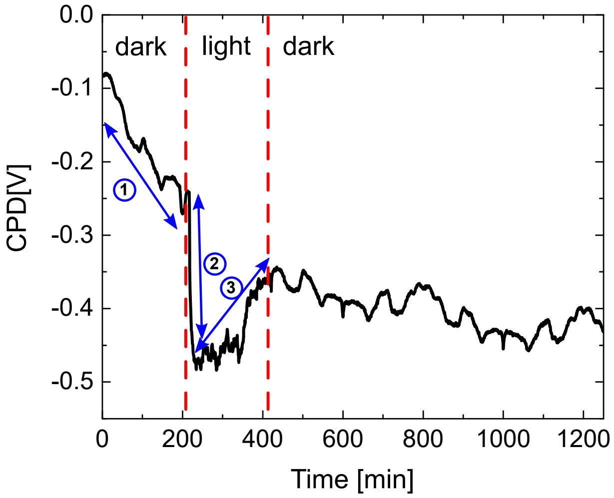

Figure G.2: Average extracted CPD in the dark, upon illumination and in the dark again. The region denoted 1 corresponds to the continuous decrease of the CPD in the dark. The region 2 corresponds to the SPV and the continuous decrease of the CPD directly after illumination. The region 3 corresponds to the continuous increase of the CPD upon prolonged illumination.

of halides, preventing the formation of segregated halide- or cation-rich phases [507] that would bring additional surface states and therefore a larger SPV.

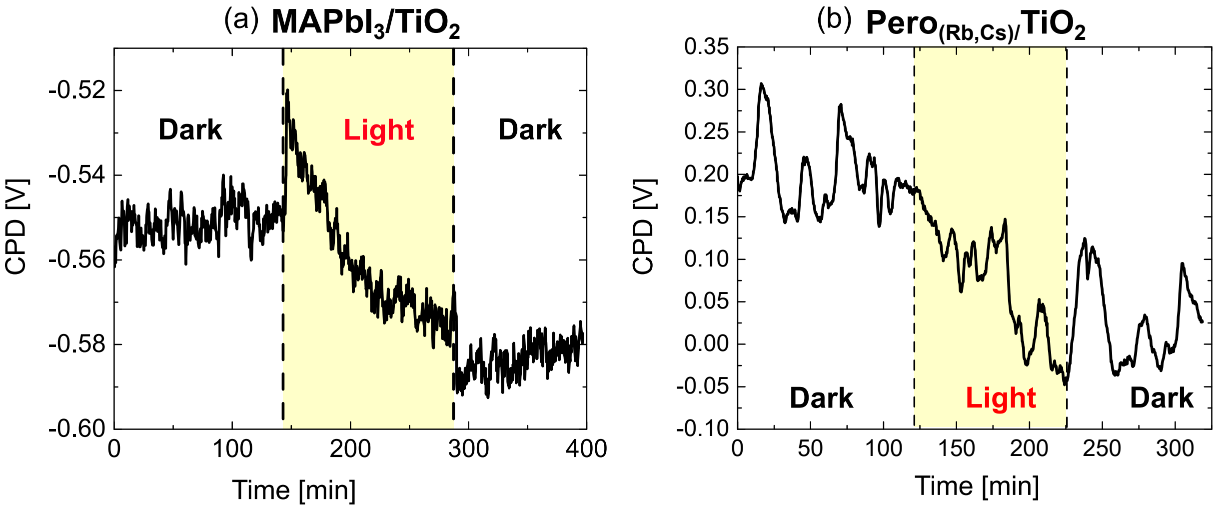

Figure G.3: CPD in different conditions: dark, during illumination and in the dark again for (a) $MAPbI_3$ co-evaporated on TiO_2 and (b) $Pero_{Rb,Cs}$ spin-coated on TiO_2.

G.3 HIM-SIMS overlay of the mixed perovskite

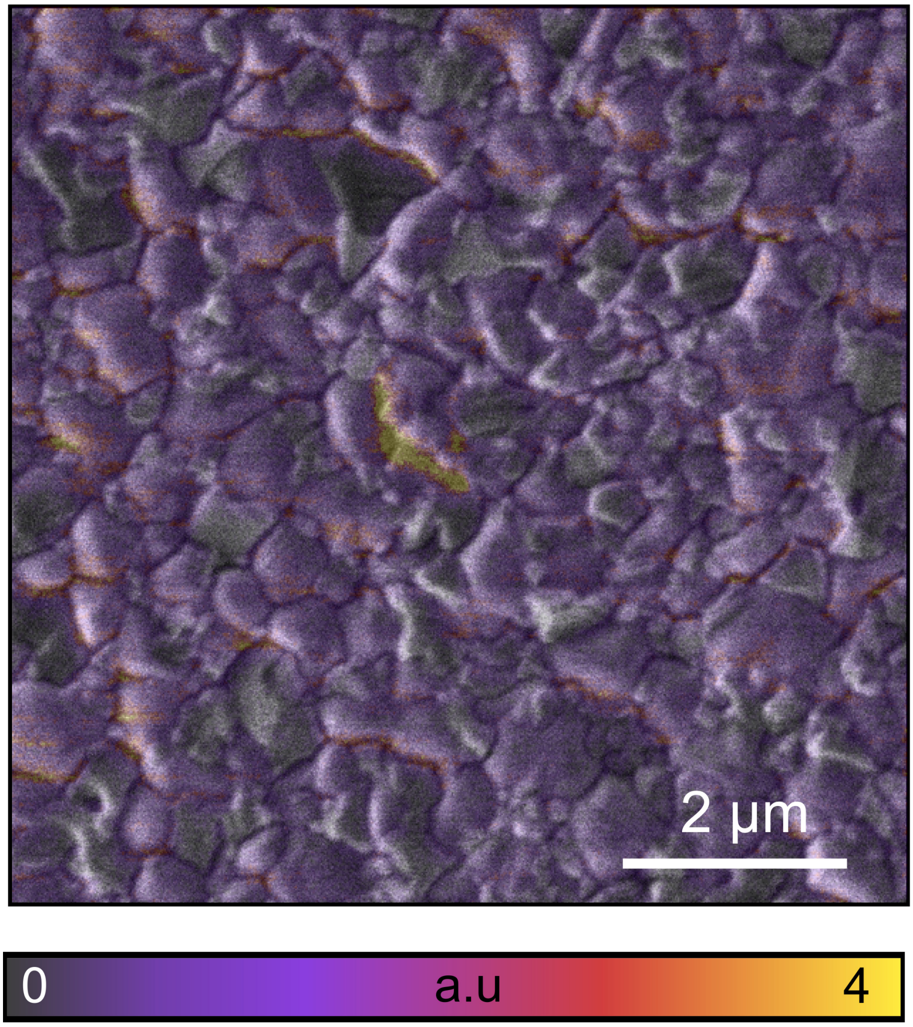

Figure G.4: Overlay of the elemental distribution of ^{133}C with its helium ion microscope morphology image at the surface of Pero$_{Rb,Cs}$

G.4 PL and TRPL measurements of control and target samples

In complement to the KPFM and STS measurements, PL and TRPL were carried out as means of rapid stability tests. After the UHV measurements that lasted a few days, both the PL yield and the lifetime (Figure G.5(a,c)) of the control sample decreased (from 570 ns to 380 ns) whereas the PL yield of the target sample, treated with the ligand, increased and the decay curve (Figure G.5(b,d)) remained mainly the same (450 ns to 440 ns). The second test was a 45 minutes exposure to a laser with a power density of 2.8×10^{-3} W/cm^2. Both samples presented an increase of their PL yield with the same magnitude, suggesting the quenching of defects by photogenerated carriers.

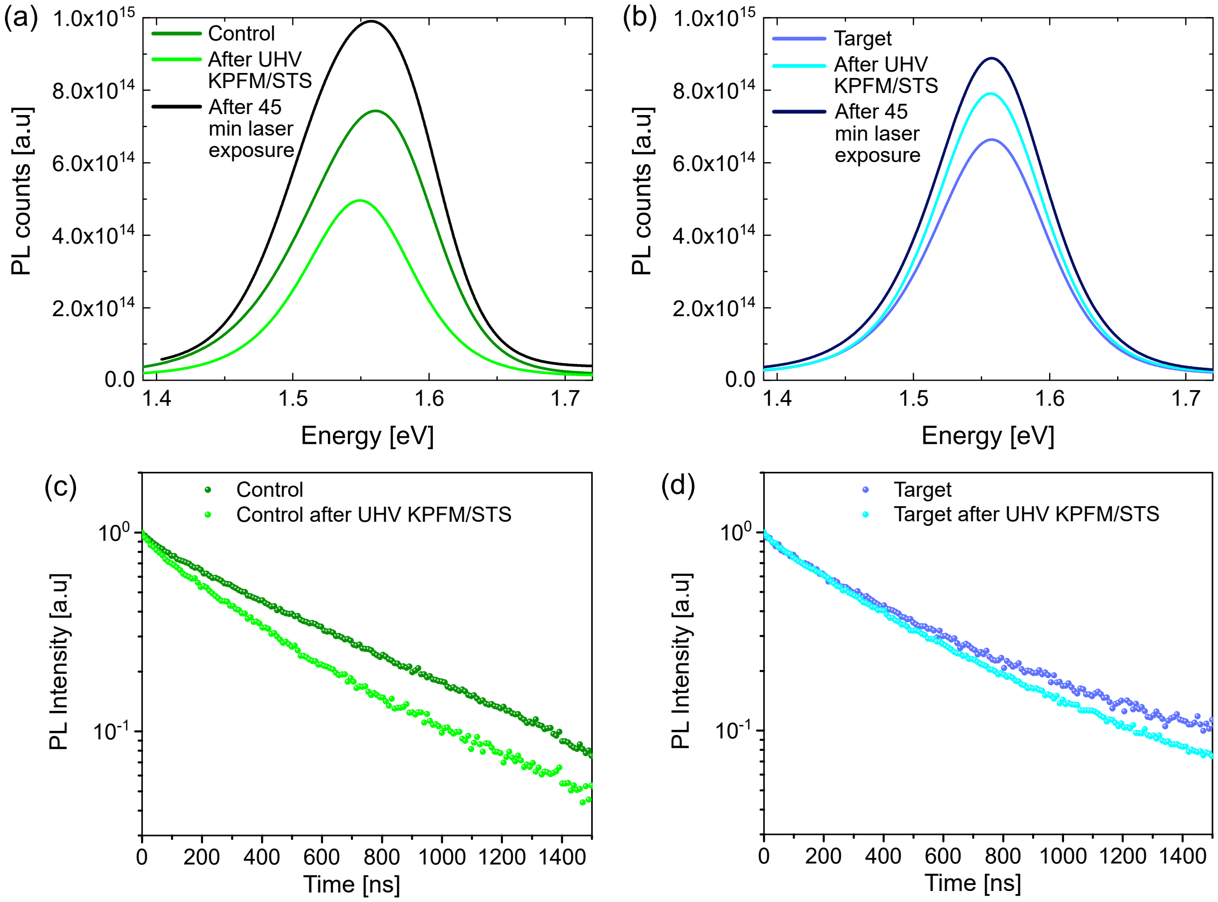

Figure G.5: (a,b) PL measurements for the control and target samples before, after the UHV measurements and after a 45 min laser-exposure. (c,d) TRPL measurements for the control and target samples before and after the UHV measurements.

G.5 Passivation of perovskite with Rb and Rb/PEAI

The first sample will be referred to as **Rb-passivated** and the second as **Rb/PEAI-passivated**. KPFM and STS measurements were carried out to determine the differences in the surface energetics and local density of states of both samples compared to the control sample.

After both treatments (Rb complex only or the Rb complex and the PEAI solutions), small elongated grains appeared on top of the larger original grains in the AFM topography (red dotted circles or spheres in Figure G.6(b,c)). These smaller grains displayed on both WF maps a much lower WF than the rest of the surface (160 meV lower for the Rb-passivated perovskite and 200 meV lower for the Rb/PEAI-passivated perovskite).

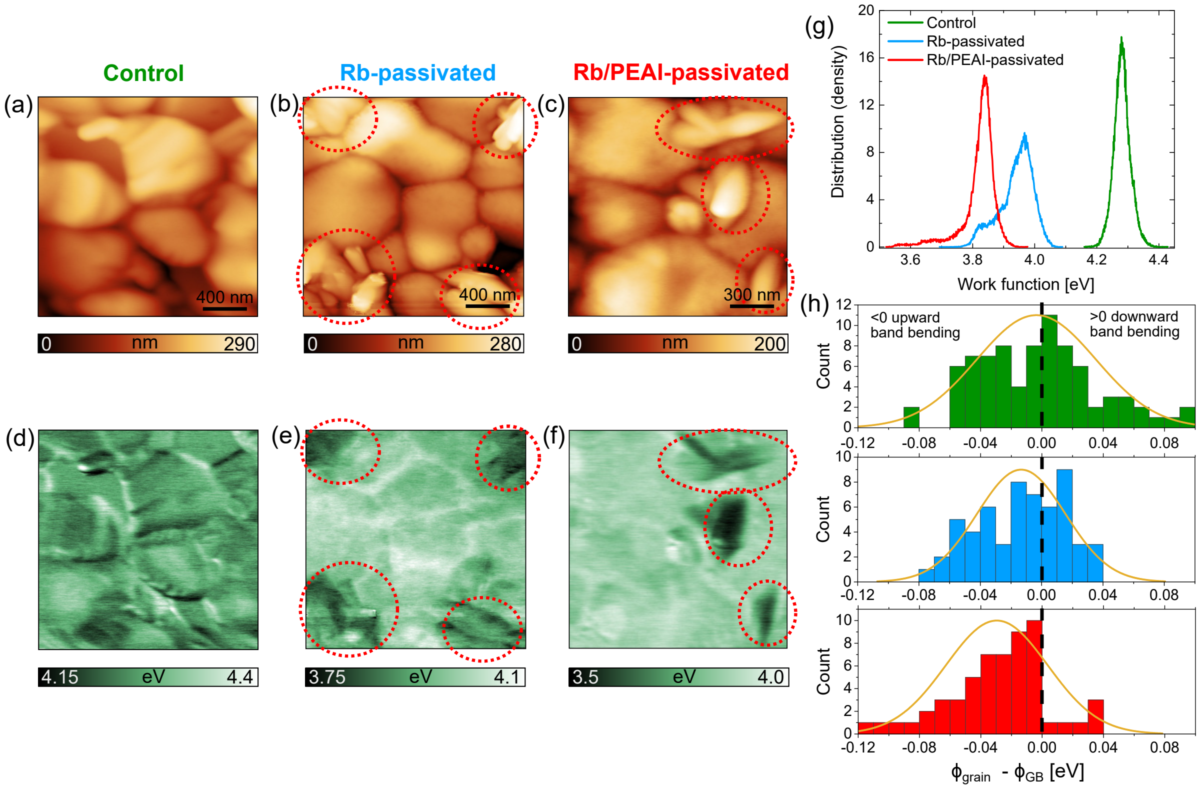

Figure G.6: AFM topography of (a) the control perovskite, (b) post-treated with the Rb complex and (c) post-treated with the Rb complex and the PEAI 2D layer. (d), (e), (f) are the respective workfunction maps of (a), (b), (c). (g) Distribution of the workfunction for all samples. (h) Grain boundary band bending distribution for all three samples. The red dotted circles represent the smaller elongated grains on top of the large grains appearing after the post-deposition treatments.

The distribution of the WF complemented this visual approach with a double-peak and longer tails in the negative WF values (Figure G.6g). These grains were most likely resulting either from a Rb-perovskite secondary phase or from the result of the formation of low dimensional perovskite when the PEAI molecules interacted with the Rb-passivated perovskite surface (for the last sample). Grazing-incidence wide-angle X-ray scattering (GIWAXS) and elemental mapping at the surface would be ideal characterization techniques in order to determine the exact nature of these grains. There was an observable difference between the average WF values after the different treatments, with a WF of 4.28 eV for the control sample that decreased to 3.96 eV for the Rb-passivated perovskite to 3.82 eV for the Rb/PEAI-passivated perovskite. This change of the WF could already help by either inducing better hole extraction or electron repelling at the interface perovskite/HTL. XPS and UPS measurements would help complement these findings. In addition, the GB band bending was measured for the treated perovskite and compared to the control sample. As already discussed, the control sample exhibited both hole and electron barriers at the grain boundaries (upward and downward BB), which was counterproductive with respect to hole extraction. The Rb-passivated perovskite displayed 60% of upward BB and 40% of downward BB (compared to the 50/50 of the control sample) but the major point was the reduction in the magnitude as all the values of the downward BB were below or equal to 40 meV, which is negligible. The Rb/PEAI-passivated perovskite on the other hand almost entirely exhibited upward band bending (90%) and again with the 10 remaining percent of downward BB in the 40 meV range. Therefore, the KPFM measurements again demonstrated that the passivation with either the Rb complex or the combination of Rb^+ and PEAI solutions enables the suppression of the hole barrier at the grain boundaries, by only keeping the electron barrier.

CITS maps were then acquired for each sample and are depicted in Figure G.7(a to f). The (dI/dV)/$\overline{I/V}$ again showed that by using passivation techniques, the surface bandgap could be increased. The Rb-passivation induced a shift of the LDOS, at the conduction band onset, which resulted in an increased surface bandgap of 2.11 ± 0.1 eV compared to the 1.6 ± 0.1 eV of the control sample.

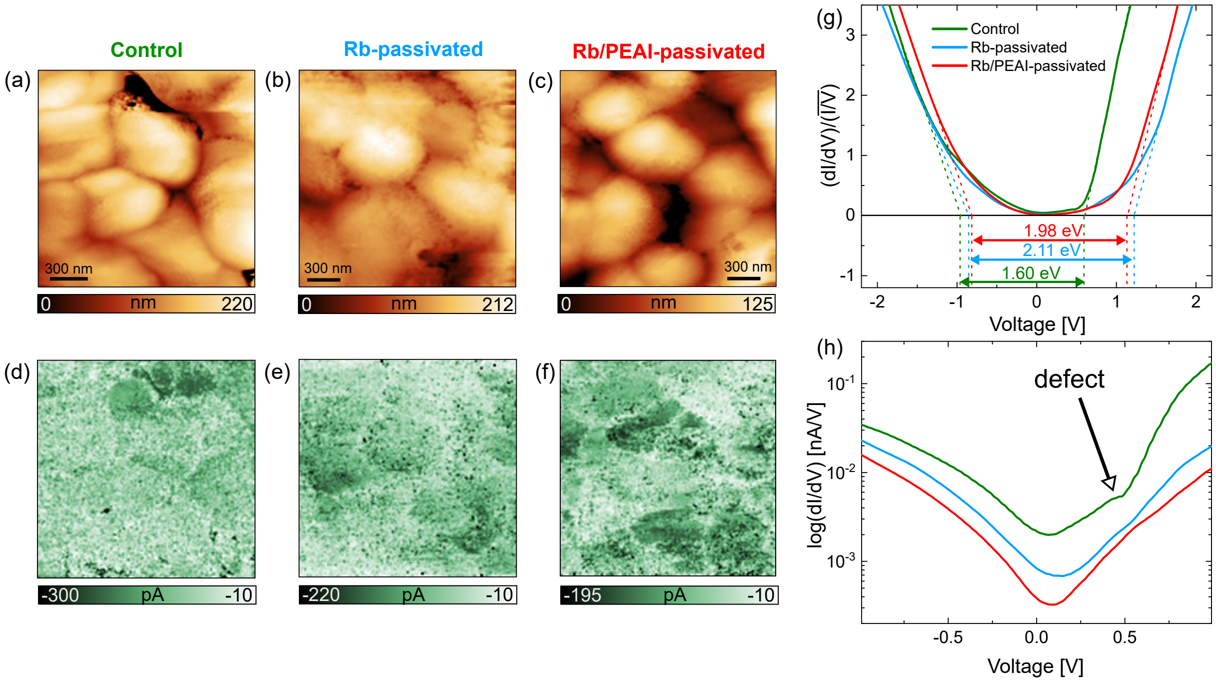

Figure G.7: STM topography of the (a) control sample, (b) Rb-passivated sample and (c) Rb/PEAI-passivated sample with their respective conductance (dI/dV) maps obtained with a voltage of -2V in (d),(e) and (f). (g) Average broadened conductance curves of the control and target samples. The linear extrapolations of the curves (dotted lines) depict different bandgaps for the different samples. (h) represents the same curves plotted on a logarithmic scale. The control sample shows a defect response at a positive applied voltage.

On the other hand the Rb/PEAI passivation led to the shift of both valence and conduction bands onsets and resulted in a surface bandgap of 1.98 ± 0.1 eV. In addition, the logarithmic plots of the dI/dV curves again demonstrated that the use of the different passivation techniques suppressed the defect signature observed for the control sample near the conduction band (positive voltages). Lastly, the overall down shift of the conductance (to lower conductance values) for the Rb-passivated perovskite and even futher down for the Rb/PEAI-passivated perovskite were coherent with the reduction of the WF previously measured with KPFM.

The previous STS measurements once again proved that the use of passivation agents after the fabrication of perovskite can be used to reduce interfacial recombination by increasing the surface bandgap, remove potential surface defects by enabling the favorable interaction between for example organic or inorganic molecules and the lead iodide antisite in this specific case. In addition, the KPFM measurements proved that the grain boundary band bending could be altered in a favorable way, such that only the occurrence of an electron barrier would prevail, improving the hole extraction towards the HTL. Lastly, reducing the WF could help in the interface alignment by either improving the hole extraction or repelling electrons in a more efficient way, which remained to be proved.

These surface passivations led to an overall improvement of the device performance. Combining the incorporation of a Rb complex through a gradient configuration followed by the deposition of a 2D material on top led to a change in efficiency of 22.4% to 25.01%. Both the V_{OC} and the FF exhibited improvement (1.13 V to 1.19 V and 78.5% to 82.6%) which were the proof of a reduction of surface and interface recombination and an improved carrier extraction and collection. In addition, the surface treatment also induced an improvement of the absorber stability as depicted in Figure G.8 and G.9 of appendix Chapter 7G.6 where the PL yield of the Rb/PEAI sample improved after the UHV exposure and almost did not change after the 45 minutes illumination, suggesting for the latter a potential reduction of defects that would ohterwise contribute to the quenching of the PL upon prolonged light exposure. In addition, the TRPL decay curves were very stable compared to the rest of the samples. The device stability should follow these trends and will need to be further investigated under different standard conditions and stimuli.

G.6 PL and TRPL of Rb- and Rb/PEAI-passivated perovskites

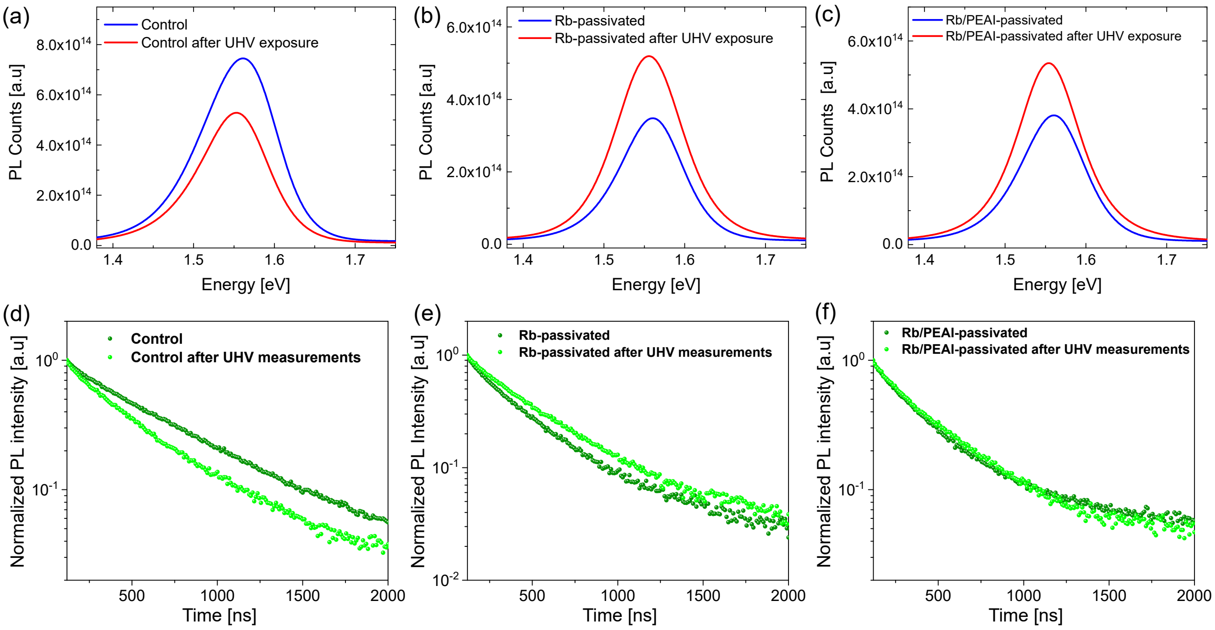

Figure G.8: PL before and after UHV KPFM/STS of (a) control Pero$_{Br}$, (b) control perovskite treated with the Rb complex and (c) control perovskite treated with the Rb complex and the PEAI 2D material. (e), (f) and (g) are the TRPL measurements of the same samples under the same conditions. The laser power density used was 2.8×10^{-3} W/cm^2 at 1 MHz, corresponding to an injection of 1.2×10^{15} carriers/c^3 for the TRPL.

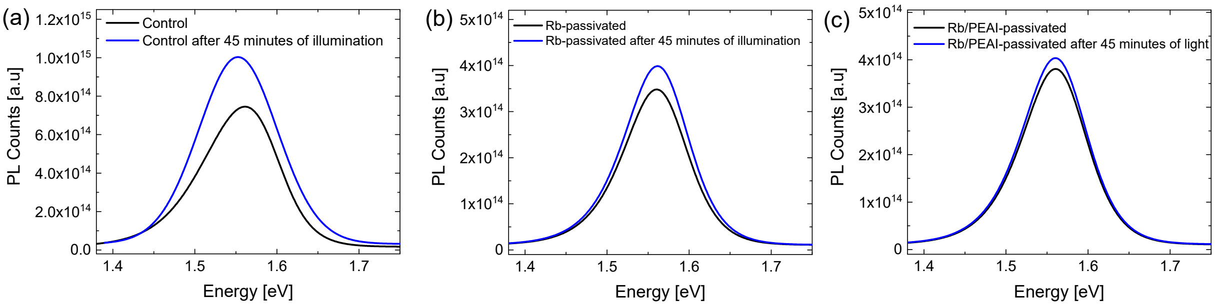

Figure G.9: PL before and after 45 minutes continuous laser exposure of (a) control Pero$_{Br}$, (b) control perovskite treated with the Rb complex and (c) control perovskite treated with the Rb complex and the PEAI 2D material. The laser power density used was 2.8×10^{-3} W/cm^2 at 1 MHz.

G.7 Large-area KPFM images of air-exposed mixed perovskites

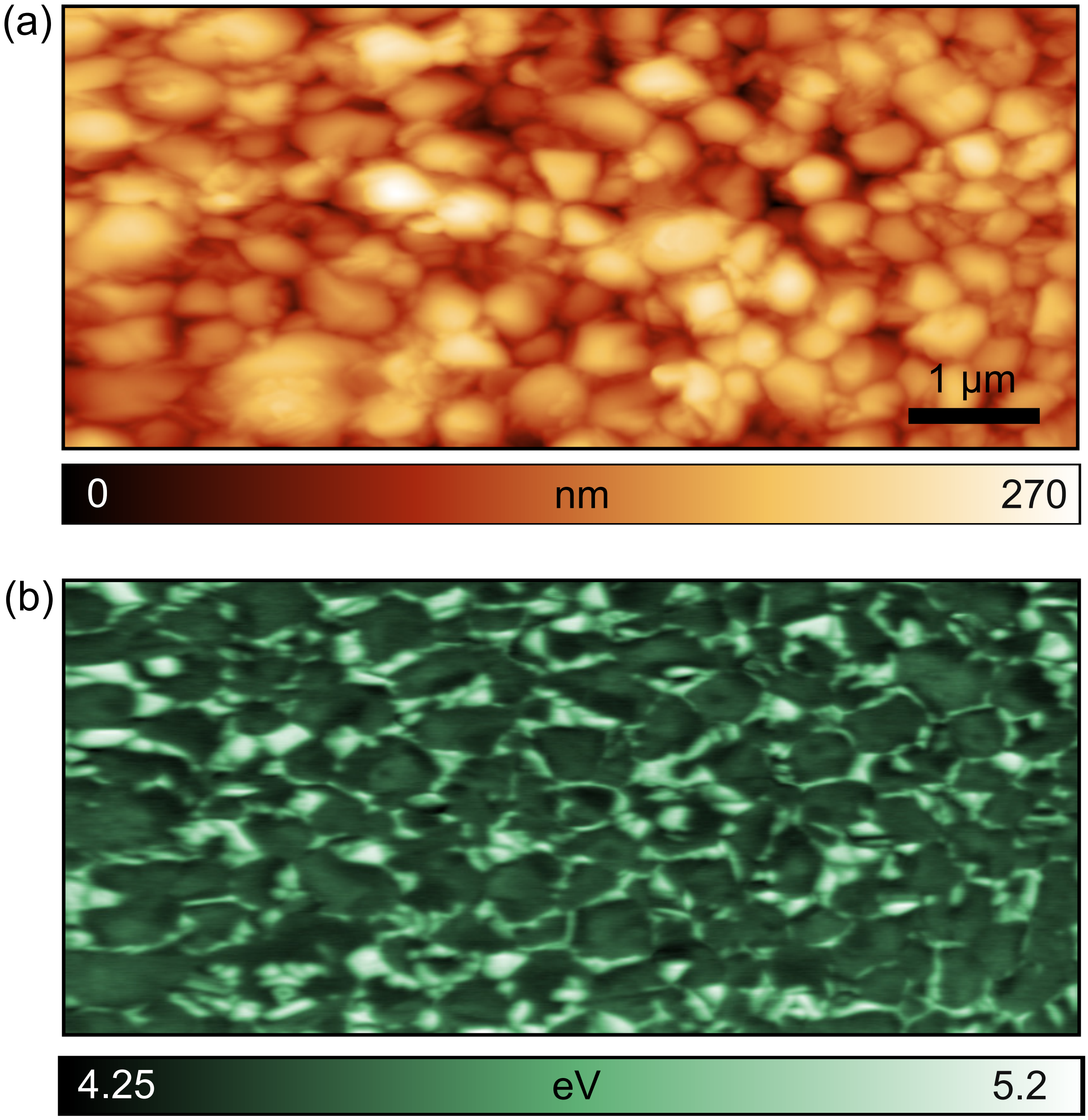

Figure G.10: Large area (a) AFM topography and (b) workfunction map of the air exposed Perovskite/SC.

Publications and Presentations

List of publications

First author

T. Gallet, D. Grabowski, T. Kirchartz, and A. Redinger, “Fermi-level pinning in methylammonium lead iodide perovskites”, *Nanoscale*, 11, 36, 16828–16836 (2019)

T. Gallet, E. M. Lanzoni, and A. Redinger, “Effects of Annealing and Light on Co-evaporated Methylammonium Lead Iodide Perovskites using Kelvin Probe Force Microscopy in Ultra-High Vacuum”, *2019 IEEE 46th Photovoltaic Specialists Conference Proceedings*, 1477–1482 (2019)

T. Gallet, R. G. Poeira, E. M. Lanzoni, T. Abzieher, U. W. Paetzold, and A. Redinger, “Co-evaporation of $CH_3NH_3PbI_3$: How Growth Conditions Impact Phase Purity, Photostriction, and Intrinsic Stability”, *ACS Applied Materials & Interfaces*, 13, 2, 2642–2653 (2021)

Co-author

E. M. Lanzoni, **T. Gallet**, C. Spindler, O. Ramirez, C. K. Boumenou, S. Siebentritt and A. Redinger, “The impact of Kelvin probe force microscopy operation modes and environment on grain boundary band bending in perovskite and Cu(In,Ga)Se2 solar cells”, *Nano Energy*, 88, 106270 (2021)

A. Krishna, H. Zhang, Z. Zhou, **T. Gallet**, M. Dankl, O. Ouellette, F. T. Eickemeyer, F. Fu, M. Mensi, S. M. Zakeeruddin, U. Rothlisberger, G. N. M. Reddy, A. Redinger, M. Grätzel and A. Hagfeldt, “Nanoscale interfacial engineering enables highly stable and efficient perovskite photovoltaics”, *Energy & Environmental Science*, 14, 5552-5562 (2021)

Y. Ding, B. Ding, H. Kanda, J. O. Usiobo, **T. Gallet**, Z. Yang, Y. Liu, H. Huang, J. Sheng, C. Liu, Y. Yang, V. I. E. Queloz, X. Zhang, J.-N. Audinot, A. Redinger, W. Dang, E. Mosconic, W. Luo, F. De Angelis, M. Wang, P. Dörflinger, M. Armer, V. Schmid, R. Wang, Keith G. Brooks, J. Wu, V. Dyakonov, G. Yang, S. Dai, P. J. Dyson and M. K. Nazeeruddin, “Efficient and Stable Perovskite Solar Cells and Modules Incorporating Single-crystalline TiO_2 Nanoparticles Achieve a Record Fill Factor”, *Nature Nanotechnology*, accepted (2022)

R. G. Poeira, J. Seil, **T. Gallet**, T. P. Weiss, C. Pauly and A. Redinger, “Origin of near-unity photoluminescence quantum yields in ultra-thin $CH_3NH_3PbI_3$ absorbers”, *Physical Review Letters*, submitted (2021)

List of presentations

T. Gallet, E. M. Lanzoni, M. Melchiorre and A. Redinger, “Co-evaporation of Methylammonium Lead Iodide Perovskite Absorbers and Their Optical and Structural Properties”, 35th EUPVSEC, Brussels, Belgium, 2018. Poster presentation

T. Gallet, E. M. Lanzoni and A. Redinger, “Effects of Annealing and Light on Co-evaporated Methylammonium Lead Iodide Perovskites using Kelvin Probe Force Microscopy in Ultra-High Vacuum”, 46th IEEE PVSC, Phoenix, 2019. Oral presentation

T. Gallet, E. M. Lanzoni, A. Redinger, “The importance of knowing your surface in perovskites: when methylammonium iodide content alters the structural, surface, electronic and ionic properties of $CH_3NH_3PbI_3$”, PVSchool 2020, Les Houches, France, 2020. Poster presentation

T. Gallet, E. M. Lanzoni and A. Redinger, “The Importance of Knowing Your Surface in Perovskites—When Methylammonium Iodide Content Alters the Structural, Surface, Electronic and Ionic Properties of $CH_3NH_3PbI_3$”, 2020 MRS Spring & Fall Meeting, Boston (virtual), USA, 2020. Oral presentation

Acknowledgments

The writing of this thesis is obviously not the product of a single person, but the contribution of many people within the Scanning Probe Microscopy (SPM) group, the University of Luxembourg but also external partners and most importantly the people that share my life.

First, I would like to thank Alex Redinger, my supervisor and mentor. I have been lucky enough that he trusted me back in 2017 to be the first PhD student of his newly-formed group, and for that I will be eternally grateful. His guidance, reliability and support throughout these four years have shaped my researcher mind and I could not have asked for a better advisor and manager. Despite his very busy schedule and his family, his door was always open for discussions, and his love for physics and solar cells as well as his relentless desire to understand everything have made his group prosper internationally. The things I have learned and the development of my critical mind are in a major part thanks to him and I am happy to have spent these four years alongside him and helped in the development of his group.

I would also like to thank Phil Dale and Thomas Unold for being part of my PhD committee, and their sharp and useful advice at the different meetings we attended together. In addition, a big thanks to Philip Schulz and Mael Guennou who accepted to be part of my PhD defense committee. Thank you also Philip for helping out with the XPS measurements and I hope that future collaborations with Alex will be fruitful.

Another thank you to Anurag Krishna, Hong Zhang, Jennifer Usiobo and Yong Ding from EPFL for their trust in my work and the fruitful collaborations. I hope these collaborations on perovskites will be the first of many for the SPM group! Similarly, a big thank you to Tobias Abzieher and Ulrich Wilhelm Paetzold from KIT for their help in fabricating my first solar cells. Thank you Tobias for having taken a full day to show me how the devices were made and for your contribution to my first 14.5% device efficiency. Thanks to Thomas Kirchatz and David Grabowski for providing my first perovkite samples. Lastly, thank you to Michele Melchiorre for helping me with different measurements or depositions, despite your busy calendar.

After Alex comes the rest of the SPM group. A big thank you to the Ulrich Siegel, Robert Wagener, Nicolas Tournier and Bernd Uder. Uli was the first one in the group and I cannot thank him enough for his constant technical assistance, reliability and his knowledge on everything. It was a pleasure working with him and thank you for inviting the SPM group to your house for a little Christmas party. Thank you Robert for the long and interesting discussions. Merci Nicolas for bringing such skills into the team, and for the fun discussions we had. Thanks Bernd for teaching me about SPM, and for the constant knowledge you can provide.

Another thank you to a crucial member of the group, Astrid Tobias and for the administrative tasks we gave you, that you put up with and you dealt with great speed. Also thank you for always asking news about my family and for the fun discussions we had. I wish you great success with your plans.

A big thank you to all the members of the SPM group: Christian, Evandro, Jonathan, Ricardo, Joé, Himanshu, Joana, Jérémy and Ajay. As the first member of the group, I was lucky enough to have known all of you.

Chrisitan, we shared a common project and I am grateful to know you. Your kindness and altruism were always contagious and I am happy to have spent these 4 years next to you, in the same office, and to have learned your story and your culture. I wish you great success in your career and happiness with your family.

Similarly to Christian, I have spent almost all my thesis working with Evandro. Thank you for your continuous help in either explaining KPFM, measuring my samples or helping me reboot my computer on a Saturday during my multiple remote sessions. More than that, thank you for being a friend and for the numerous fun and serious discussions we had during these years. Your unlimited generosity make you and Monica good friends that one should keep and I cannot wait to explore Brazil with you one day!

Thank you Jonathan and Himanshu for being great and fun people to talk to and always very helpful and available when needed. Thank you Joé for trusting me in advising you during your Master thesis, that you mastered like a chief. You are the first one to have fabricated in-house perovskite cells in Luxembourg, don't forget that! A big thank you to Ricardo for coding the PL imaging software we are still using, and for helping me measure some of my samples. I am happy that you found a place in Phil's group even though you would have been better in our group (joke)! Thank you to Joana for bringing that feminine spark we all needed in our group, you are a talented and brilliant woman and you should never lack confidence in your potential.

A quick round of thank you to the people from the LPV and LEM groups: Alberto, Conrad, Max, Finn, Thomas, Sudhanshu, Damilola, Nayia, Mohit, Daniel and Susanne, and also to the people I have enjoyed discussing with and that have made my 4 years at the university better: Shameek, Sharif, Larry, Giordano, Mathias, Hakam...

Last but not least, I want to thank my family that has always encouraged and supported me throughout these years. My parents, first, as they have made me the person I am, but also my brother and sister, whom I could always rely on. Also thank you Armand for reading a part of my thesis, I know how hard it was for you!

Most importantly, the biggest thank you would go to my partner, Julie, who has always been very supportive and understanding even though I sometimes had to work during weekends or at night. She has re-shaped me entirely and thanks to her I have become a much better person. In times where I would be swamped with work, she would willingly take care of everything, the food, our son Liox and more, and for that I am forever grateful. Without her, both this PhD thesis and this dissertation would not have been possible. You even read my full thesis and corrected it! Thank you and I love you.

Similarly to the rest of this thesis, the acknowledgements were very long and I have most likely forgotten some people. If you are reading this and have not been acknowledged, please forgive me and send me a text, I will offer you a drink of your choice.

Bibliography

[1] I. P. on Climate Change, "Climate change widespread, rapid, and intensifying." https://www.ipcc.ch/2021/08/09/ar6-wg1-20210809-pr. (accessed: 16.10.2021).

[2] W. W. Fund, "Driving the transition from fossil fuels to efficient, renewable and sustainable energy." https://wwf.panda.org/discover/our_focus/climate_and_energy_practice/what_we_do/changing_energy_use. (accessed: 16.10.2021).

[3] I. E. Agency, "Energy efficiency is the cornerstone for building a secure and sustainable energy system." https://www.iea.org/news/energy-efficiency-is-the-cornerstone-for-building-a-secure-and-sustainable-energy-system. (accessed: 16.10.2021).

[4] I. E. Agency, "Snapshot 2021." https://iea-pvps.org/snapshot-reports/snapshot-2021/. (accessed: 16.10.2021).

[5] F. I. for Solar Energy Systems, "Photovoltaics report." https://www.ise.fraunhofer.de. (accessed: 16.10.2021).

[6] I. R. E. Agency, "Solar energy." https://www.irena.org/solar. (accessed: 16.10.2021).

[7] I. E. Agency, "Solar pv report." https://www.iea.org/reports/solar-pv. (accessed: 16.10.2021).

[8] N. R. E. Laboratory, "Best research-cell efficiency chart." https://www.nrel.gov/pv/cell-efficiency.html. (accessed: 09.03.2021).

[9] A. Kojima, K. Teshima, Y. Shirai, and T. Miyasaka, "Organometal halide perovskites as visible-light sensitizers for photovoltaic cells," *Journal of the American Chemical Society*, 2009.

[10] K. Mahmood, S. Sarwar, and M. T. Mehran, "Current status of electron transport layers in perovskite solar cells: materials and properties," 2017.

[11] M. Jung, S.-G. Ji, G. Kim, and S. I. Seok, "Perovskite precursor solution chemistry: from fundamentals to photovoltaic applications," *Chemical Society Reviews*, vol. 48, no. 7, pp. 2011–2038, 2019.

[12] R. Wang, M. Mujahid, Y. Duan, Z. Wang, J. Xue, and Y. Yang, "A Review of Perovskites Solar Cell Stability," *Advanced Functional Materials*, vol. 29, p. 1808843, nov 2019.

[13] F. Xu, T. Zhang, G. Li, and Y. Zhao, "Mixed cation hybrid lead halide perovskites with enhanced performance and stability," *Journal of Materials Chemistry A*, vol. 5, no. 23, pp. 11450–11461, 2017.

[14] L. She, M. Liu, and D. Zhong, "Atomic Structures of CH 3 NH 3 PbI 3 (001) Surfaces," *ACS Nano*, vol. 10, pp. 1126–1131, jan 2016.

[15] J. Hieulle, X. Wang, C. Stecker, D. Y. Son, L. Qiu, R. Ohmann, L. K. Ono, A. Mugarza, Y. Yan, and Y. Qi, "Unraveling the Impact of Halide Mixing on Perovskite Stability," *Journal of the American Chemical Society*, 2019.

[16] J. Hieulle, S. Luo, D. Y. Son, A. Jamshaid, C. Stecker, Z. Liu, G. Na, D. Yang, R. Ohmann, L. K. Ono, L. Zhang, and Y. Qi, "Imaging of the Atomic Structure of All-Inorganic Halide Perovskites," *Journal of Physical Chemistry Letters*, vol. 11, no. 3, pp. 813–823, 2020.

[17] M. C. Shih, S. S. Li, C. H. Hsieh, Y. C. Wang, H. D. Yang, Y. P. Chiu, C. S. Chang, and C. W. Chen, "Spatially Resolved Imaging on Photocarrier Generations and Band Alignments at Perovskite/PbI2 Heterointerfaces of Perovskite Solar Cells by Light-Modulated Scanning Tunneling Microscopy," *Nano Letters*, vol. 17, no. 2, pp. 1154–1160, 2017.

[18] J. S. Yun, A. Ho-Baillie, S. Huang, S. H. Woo, Y. Heo, J. Seidel, F. Huang, Y. B. Cheng, and M. A. Green, "Benefit of grain boundaries in organic-inorganic halide planar perovskite solar cells," *Journal of Physical Chemistry Letters*, 2015.

[19] J. S. Yun, J. Seidel, J. Kim, A. M. Soufiani, S. Huang, J. Lau, N. J. Jeon, S. I. Seok, M. A. Green, and A. Ho-Baillie, "Critical Role of Grain Boundaries for Ion Migration in Formamidinium and Methylammonium Lead Halide Perovskite Solar Cells," *Advanced Energy Materials*, 2016.

[20] J. J. Li, J. Y. Ma, Q. Q. Ge, J. S. Hu, D. Wang, and L. J. Wan, "Microscopic Investigation of Grain Boundaries in Organolead Halide Perovskite Solar Cells," *ACS Applied Materials and Interfaces*, 2015.

[21] N. Adhikari, A. Dubey, D. Khatiwada, A. F. Mitul, Q. Wang, S. Venkatesan, A. Iefanova, J. Zai, X. Qian, M. Kumar, and Q. Qiao, "Interfacial Study To Suppress Charge Carrier Recombination for High Efficiency Perovskite Solar Cells," *ACS Applied Materials & Interfaces*, vol. 7, pp. 26445–26454, dec 2015.

[22] B. Chen, P. N. Rudd, S. Yang, Y. Yuan, and J. Huang, "Imperfections and their passivation in halide perovskite solar cells," *Chemical Society Reviews*, vol. 48, no. 14, pp. 3842–3867, 2019.

[23] G. Rose, "Beschreibung einiger neuen Mineralien des Urals," *Annalen der Physik*, 1839.

[24] V. M. Goldschmidt, "Die Gesetze der Krystallochemie," *Die Naturwissenschaften*, 1926.

[25] M. Johnsson and P. Lemmens, "Crystallography and Chemistry of Perovskites," in *Handbook of Magnetism and Advanced Magnetic Materials*, Wiley, 2007.

[26] A. Ihalage and Y. Hao, "Analogical discovery of disordered perovskite oxides by crystal structure information hidden in unsupervised material fingerprints," *npj Computational Materials*, 2021.

[27] R. Jacobs, G. Luo, and D. Morgan, "Materials Discovery of Stable and Nontoxic Halide Perovskite Materials for High-Efficiency Solar Cells," *Advanced Functional Materials*, 2019.

[28] Q. Tao, P. Xu, M. Li, and W. Lu, "Machine learning for perovskite materials design and discovery," 2021.

[29] A. M. Glazer, "The classification of tilted octahedra in perovskites," *Acta Crystallographica Section B Structural Crystallography and Crystal Chemistry*, 1972.

[30] T. He, Q. Huang, A. P. Ramirez, Y. Wang, K. A. Regan, N. Rogado, M. A. Hayward, M. K. Haas, J. S. Slusky, K. Inumara, H. W. Zandbergen, N. P. Ong, and R. J. Cava, "Superconductivity in the non-oxide perovskite MgCNi3," *Nature*, vol. 411, pp. 54–56, may 2001.

[31] J. Zhang, W. J. Ji, J. Xu, X. Y. Geng, J. Zhou, Z. B. Gu, S. H. Yao, and S. T. Zhang, "Giant positive magnetoresistance in half-metallic double-perovskite Sr2CrWO6 thin films," *Science Advances*, 2017.

[32] J. N. Wilson, J. M. Frost, S. K. Wallace, and A. Walsh, "Dielectric and ferroic properties of metal halide perovskites," *APL Materials*, 2019.

[33] W. Yu, F. Li, L. Yu, M. R. Niazi, Y. Zou, D. Corzo, A. Basu, C. Ma, S. Dey, M. L. Tietze, U. Buttner, X. Wang, Z. Wang, M. N. Hedhili, C. Guo, T. Wu, and A. Amassian, "Single crystal hybrid perovskite field-effect transistors," *Nature Communications*, 2018.

[34] W. Hu, H. Cong, W. Huang, Y. Huang, L. Chen, A. Pan, and C. Xue, "Germanium/perovskite heterostructure for high-performance and broadband photodetector from visible to infrared telecommunication band," *Light: Science and Applications*, 2019.

[35] X. K. Liu, W. Xu, S. Bai, Y. Jin, J. Wang, R. H. Friend, and F. Gao, "Metal halide perovskites for light-emitting diodes," 2021.

[36] J. Y. Kim, J. W. Lee, H. S. Jung, H. Shin, and N. G. Park, "High-Efficiency Perovskite Solar Cells," 2020.

[37] Q. A. Akkerman and L. Manna, "What Defines a Halide Perovskite?," 2020.

[38] F. Demartin, I. Campostrini, C. Castellano, and M. Russo, "Parascandolaite, KMgF3, a new perovskite-type fluoride from Vesuvius," *Physics and Chemistry of Minerals*, 2014.

[39] C. Li, X. Lu, W. Ding, L. Feng, Y. Gao, and Z. Guo, "Formability of ABX 3 (X = F, Cl, Br, I) halide perovskites," *Acta Crystallographica Section B: Structural Science*, 2008.

[40] C. J. Bartel, C. Sutton, B. R. Goldsmith, R. Ouyang, C. B. Musgrave, L. M. Ghiringhelli, and M. Scheffler, "New tolerance factor to predict the stability of perovskite oxides and halides," *Science Advances*, 2019.

[41] C. C. Stoumpos and M. G. Kanatzidis, "The Renaissance of Halide Perovskites and Their Evolution as Emerging Semiconductors," *Accounts of Chemical Research*, 2015.

[42] W. Li, Z. Wang, F. Deschler, S. Gao, R. H. Friend, and A. K. Cheetham, "Chemically diverse and multifunctional hybrid organic-inorganic perovskites," 2017.

[43] R. D. Shannon, "Revised effective ionic radii and systematic studies of interatomic distances in halides and chalcogenides," *Acta Crystallographica Section A*, 1976.

[44] G. Kieslich, S. Sun, and A. K. Cheetham, "An extended Tolerance Factor approach for organic-inorganic perovskites," *Chemical Science*, 2015.

[45] J. P. Correa-Baena, M. Saliba, T. Buonassisi, M. Grätzel, A. Abate, W. Tress, and A. Hagfeldt, "Promises and challenges of perovskite solar cells," 2017.

[46] D. B. Mitzi, C. A. Feild, Z. Schlesinger, and R. B. Laibowitz, "Transport, optical, and magnetic properties of the conducting halide perovskite ch3nh3sni3," *Journal of Solid State Chemistry*, 1995.

[47] A. M. Salau, "Fundamental absorption edge in PbI2:KI alloys," *Solar Energy Materials*, 1980.

[48] C. R. Kagan, D. B. Mitzi, and C. D. Dimitrakopoulos, "Organic-inorganic hybrid materials as semiconducting channels in thin- film field-effect transistors," *Science*, 1999.

[49] P. Würfel, *Physics of Solar Cells: From Principles to New Concepts*. WILEY-VCH, 2007.

[50] S. Sze and K. K. Ng, *Physics of Semiconductor Devices*. John Wiley & Sons, 2006.

[51] H. S. Kim, C. R. Lee, J. H. Im, K. B. Lee, T. Moehl, A. Marchioro, S. J. Moon, R. Humphry-Baker, J. H. Yum, J. E. Moser, M. Grätzel, and N. G. Park, "Lead iodide perovskite sensitized all-solid-state submicron thin film mesoscopic solar cell with efficiency exceeding 9%," *Scientific Reports*, 2012.

[52] S. D. Stranks, G. E. Eperon, G. Grancini, C. Menelaou, M. J. Alcocer, T. Leijtens, L. M. Herz, A. Petrozza, and H. J. Snaith, "Electron-hole diffusion lengths exceeding 1 micrometer in an organometal trihalide perovskite absorber," *Science*, 2013.

[53] G. Xing, N. Mathews, S. Sun, S. S. Lim, Y. M. Lam, M. Grätzel, S. Mhaisalkar, and T. C. Sum, "Long-range balanced electron-and hole-transport lengths in organic-inorganic CH3NH3PbI3," *Science*, 2013.

[54] J. H. Heo, S. H. Im, J. H. Noh, T. N. Mandal, C. S. Lim, J. A. Chang, Y. H. Lee, H. J. Kim, A. Sarkar, M. K. Nazeeruddin, M. Grätzel, and S. I. Seok, "Efficient inorganic-organic hybrid heterojunction solar cells containing perovskite compound and polymeric hole conductors," *Nature Photonics*, 2013.

[55] O. J. Sandberg, J. Kurpiers, M. Stolterfoht, D. Neher, P. Meredith, S. Shoaee, and A. Armin, "On the Question of the Need for a Built-In Potential in Perovskite Solar Cells," *Advanced Materials Interfaces*, 2020.

[56] M. M. Lee, J. Teuscher, T. Miyasaka, T. N. Murakami, and H. J. Snaith, "Efficient hybrid solar cells based on meso-superstructured organometal halide perovskites," *Science*, 2012.

[57] J. Y. Jeng, Y. F. Chiang, M. H. Lee, S. R. Peng, T. F. Guo, P. Chen, and T. C. Wen, "CH3NH3PbI3 perovskite/fullerene planar-heterojunction hybrid solar cells," *Advanced Materials*, 2013.

[58] M. Liu, M. B. Johnston, and H. J. Snaith, "Efficient planar heterojunction perovskite solar cells by vapour deposition," *Nature*, 2013.

[59] C. C. Chueh, C. Z. Li, and A. K. Jen, "Recent progress and perspective in solution-processed Interfacial materials for efficient and stable polymer and organometal perovskite solar cells," 2015.

[60] Z. Hu, W. Fu, L. Yan, J. Miao, H. Yu, Y. He, O. Goto, H. Meng, H. Chen, and W. Huang, "Effects of heteroatom substitution in spiro-bifluorene hole transport materials," *Chemical Science*, 2016.

[61] W. C. Lai, K. W. Lin, T. F. Guo, P. Chen, and Y. Y. Liao, "Perovskite-based solar cells with inorganic inverted hybrid planar heterojunction structure," *AIP Advances*, 2018.

[62] T. B. Abzieher, *Thermische Koverdampfung von hybriden Perowskit-Halbleitern für den Einsatz in Solarzellen.* PhD thesis, Karlsruher Institut für Technologie (KIT), 2020.

[63] Z. Wang, Z. Shi, T. Li, Y. Chen, and W. Huang, "Stability of Perovskite Solar Cells: A Prospective on the Substitution of the A Cation and X Anion," 2017.

[64] C. Motta, F. El-Mellouhi, S. Kais, N. Tabet, F. Alharbi, and S. Sanvito, "Revealing the role of organic cations in hybrid halide perovskite CH3 NH3PbI3," *Nature Communications*, 2015.

[65] J. W. Lee, D. J. Seol, A. N. Cho, and N. G. Park, "High-efficiency perovskite solar cells based on the black polymorph of HC(NH2)2PbI3," *Advanced Materials*, 2014.

[66] F. Wang, H. Yu, H. Xu, and N. Zhao, "HPbI3: A new precursor compound for highly efficient solution-processed perovskite solar cells," *Advanced Functional Materials*, 2015.

[67] G. E. Eperon, G. M. Paternò, R. J. Sutton, A. Zampetti, A. A. Haghighirad, F. Cacialli, and H. J. Snaith, "Inorganic caesium lead iodide perovskite solar cells," *Journal of Materials Chemistry A*, 2015.

[68] R. J. Sutton, G. E. Eperon, L. Miranda, E. S. Parrott, B. A. Kamino, J. B. Patel, M. T. Hörantner, M. B. Johnston, A. A. Haghighirad, D. T. Moore, and H. J. Snaith, "Bandgap-Tunable Cesium Lead Halide Perovskites with High Thermal Stability for Efficient Solar Cells," *Advanced Energy Materials*, 2016.

[69] L. K. Ono, E. J. Juarez-Perez, and Y. Qi, "Progress on Perovskite Materials and Solar Cells with Mixed Cations and Halide Anions," 2017.

[70] Q. Jiang, Y. Zhao, X. Zhang, X. Yang, Y. Chen, Z. Chu, Q. Ye, X. Li, Z. Yin, and J. You, "Surface passivation of perovskite film for efficient solar cells," *Nature Photonics*, 2019.

[71] J. J. Yoo, G. Seo, M. R. Chua, T. G. Park, Y. Lu, F. Rotermund, Y.-K. Kim, C. S. Moon, N. J. Jeon, J.-P. Correa-Baena, V. Bulović, S. S. Shin, M. G. Bawendi, and J. Seo, "Efficient perovskite solar cells via improved carrier management," *Nature*, vol. 590, pp. 587–593, feb 2021.

[72] R. E. Wasylishen, O. Knop, and J. B. Macdonald, "Cation rotation in methylammonium lead halides," *Solid State Communications*, 1985.

[73] A. A. Bakulin, O. Selig, H. J. Bakker, Y. L. Rezus, C. Müller, T. Glaser, R. Lovrincic, Z. Sun, Z. Chen, A. Walsh, J. M. Frost, and T. L. Jansen, "Real-Time Observation of Organic Cation Reorientation in Methylammonium Lead Iodide Perovskites," *Journal of Physical Chemistry Letters*, 2015.

[74] N. Onoda-Yamamuro, O. Yamamuro, T. Matsuo, and H. Suga, "p-T phase relations of CH3NH3PbX3 (X = Cl, Br, I) crystals," *Journal of Physics and Chemistry of Solids*, 1992.

[75] M. T. Weller, O. J. Weber, P. F. Henry, A. M. Di Pumpo, and T. C. Hansen, "Complete structure and cation orientation in the perovskite photovoltaic methylammonium lead iodide between 100 and 352 K," *Chemical Communications*, 2015.

[76] C. Eames, J. M. Frost, P. R. Barnes, B. C. O'Regan, A. Walsh, and M. S. Islam, "Ionic transport in hybrid lead iodide perovskite solar cells," *Nature Communications*, 2015.

[77] P. Umari, E. Mosconi, and F. De Angelis, "Relativistic GW calculations on CH3 NH3 PbI 3 and CH3 NH3 SnI3 Perovskites for Solar Cell Applications," *Scientific Reports*, 2014.

[78] T. Umebayashi, K. Asai, T. Umebayashi, K. Asai, T. Kondo, T. Kondo, and A. Nakao, "Electronic structures of lead iodide based low-dimensional crystals," *Physical Review B - Condensed Matter and Materials Physics*, 2003.

[79] W. K. Chong, D. Giovanni, and T.-C. Sum, *Halide Perovskites Photovoltaics, Light Emitting Devices, and Beyond.* Wiley-VCH, 2018.

[80] I. Studenyak, M. Kranj, and M. Kurik, "Urbach Rule in Solid State Physics," *International Journal of Optics and Applications*, 2014.

[81] S. De Wolf, J. Holovsky, S. J. Moon, P. Löper, B. Niesen, M. Ledinsky, F. J. Haug, J. H. Yum, and C. Ballif, "Organometallic halide perovskites: Sharp optical absorption edge and its relation to photovoltaic performance," *Journal of Physical Chemistry Letters*, 2014.

[82] C. W. Greeff and H. R. Glyde, "Anomalous Urbach tail in GaAs," *Physical Review B*, 1995.

[83] R. B. Wehrspohn, S. C. Deane, I. D. French, I. G. Gale, M. J. Powell, and R. Brüggemann, "Urbach energy dependence of the stability in amorphous silicon thin-film transistors," *Applied Physics Letters*, 1999.

[84] Y. Li, W. Yan, Y. Li, S. Wang, W. Wang, Z. Bian, L. Xiao, and Q. Gong, "Direct Observation of Long Electron-Hole Diffusion Distance in CH 3 NH 3 PbI 3 Perovskite Thin Film," *Scientific Reports*, 2015.

[85] Q. Wang, Y. Shao, H. Xie, L. Lyu, X. Liu, Y. Gao, and J. Huang, "Qualifying composition dependent p and n self-doping in CH3NH3PbI3," *Applied Physics Letters*, 2014.

[86] S. Rühle, "Tabulated values of the Shockley-Queisser limit for single junction solar cells," *Solar Energy*, 2016.

[87] J. Jiang, X. Yang, Y. Huang, M. Li, Q. Tao, M. Fei, H. L. Cai, F. M. Zhang, and X. S. Wu, "Improvement in solar cell efficiency based on the MAPbI3films extracted by a mixed anti-solvent," *Applied Physics Letters*, 2020.

[88] B. Gao, J. Meng, J. Lu, and R. Zhao, "CH3NH3PbI3 perovskite solar cells with efficiency over 22Letters, 2020.

[89] P. Holzhey and M. Saliba, "A full overview of international standards assessing the long-term stability of perovskite solar cells," 2018.

[90] K. Wu, A. Bera, C. Ma, Y. Du, Y. Yang, L. Li, and T. Wu, "Temperature-dependent excitonic photoluminescence of hybrid organometal halide perovskite films," *Physical Chemistry Chemical Physics*, 2014.

[91] A. Poglitsch and D. Weber, "Dynamic disorder in methylammoniumtrihalogenoplumbates (II) observed by millimeter-wave spectroscopy," *The Journal of Chemical Physics*, 1987.

[92] B. Brunetti, C. Cavallo, A. Ciccioli, G. Gigli, and A. Latini, "On the Thermal and Thermodynamic (In)Stability of Methylammonium Lead Halide Perovskites," *Scientific Reports*, 2016.

[93] A. Alberti, I. Deretzis, G. Mannino, E. Smecca, S. Sanzaro, Y. Numata, T. Miyasaka, and A. La Magna, "Revealing a Discontinuity in the Degradation Behavior of CH3NH3PbI3 during Thermal Operation," *Journal of Physical Chemistry C*, 2017.

[94] B. Conings, J. Drijkoningen, N. Gauquelin, A. Babayigit, J. D'Haen, L. D'Olieslaeger, A. Ethirajan, J. Verbeeck, J. Manca, E. Mosconi, F. De Angelis, and H. G. Boyen, "Intrinsic Thermal Instability of Methylammonium Lead Trihalide Perovskite," *Advanced Energy Materials*, 2015.

[95] N. K. Kim, Y. H. Min, S. Noh, E. Cho, G. Jeong, M. Joo, S. W. Ahn, J. S. Lee, S. Kim, K. Ihm, H. Ahn, Y. Kang, H. S. Lee, and D. Kim, "Investigation of Thermally Induced Degradation in CH3NH3PbI3 Perovskite Solar Cells using In-situ Synchrotron Radiation Analysis," *Scientific Reports*, 2017.

[96] Y. Reyna, M. Salado, S. Kazim, A. Pérez-Tomas, S. Ahmad, and M. Lira-Cantu, "Performance and stability of mixed FAPbI3(0.85)MAPbBr3(0.15) halide perovskite solar cells under outdoor conditions and the effect of low light irradiation," *Nano Energy*, vol. 30, pp. 570–579, dec 2016.

[97] N. J. Jeon, J. H. Noh, W. S. Yang, Y. C. Kim, S. Ryu, J. Seo, and S. I. Seok, "Compositional engineering of perovskite materials for high-performance solar cells," *Nature*, vol. 517, pp. 476–480, jan 2015.

[98] M. Saliba, T. Matsui, J.-Y. Seo, K. Domanski, J.-P. Correa-Baena, M. K. Nazeeruddin, S. M. Zakeeruddin, W. Tress, A. Abate, A. Hagfeldt, and M. Grätzel, "Cesium-containing triple cation perovskite solar cells: improved stability, reproducibility and high efficiency," *Energy and Environmental Science*, vol. 9, no. 6, pp. 1989–1997, 2016.

[99] Y. H. Kye, C. J. Yu, U. G. Jong, Y. Chen, and A. Walsh, "Critical Role of Water in Defect Aggregation and Chemical Degradation of Perovskite Solar Cells," *Journal of Physical Chemistry Letters*, 2018.

[100] M. K. Gangishetty, R. W. Scott, and T. L. Kelly, "Effect of relative humidity on crystal growth, device performance and hysteresis in planar heterojunction perovskite solar cells," *Nanoscale*, 2016.

[101] L. Ling, S. Yuan, P. Wang, H. Zhang, L. Tu, J. Wang, Y. Zhan, and L. Zheng, "Precisely Controlled Hydration Water for Performance Improvement of Organic–Inorganic Perovskite Solar Cells," *Advanced Functional Materials*, 2016.

[102] M. Lv, X. Dong, X. Fang, B. Lin, S. Zhang, X. Xu, J. Ding, and N. Yuan, "Improved photovoltaic performance in perovskite solar cells based on CH3NH3PbI3 films fabricated under controlled relative humidity," *RSC Advances*, 2015.

[103] Y. Deng, Z. Xiao, and J. Huang, "Light-induced self-poling effect on organometal trihalide perovskite solar cells for increased device efficiency and stability," *Advanced Energy Materials*, 2015.

[104] C. Zhao, B. Chen, X. Qiao, L. Luan, K. Lu, and B. Hu, "Revealing Underlying Processes Involved in Light Soaking Effects and Hysteresis Phenomena in Perovskite Solar Cells," *Advanced Energy Materials*, 2015.

[105] A. M. Leguy, J. M. Frost, A. P. McMahon, V. G. Sakai, W. Kochelmann, C. Law, X. Li, F. Foglia, A. Walsh, B. C. O'Regan, J. Nelson, J. T. Cabral, and P. R. Barnes, "The dynamics of methylammonium ions in hybrid organic-inorganic perovskite solar cells," *Nature Communications*, 2015.

[106] X. Wu, L. Z. Tan, X. Shen, T. Hu, K. Miyata, M. Tuan Trinh, R. Li, R. Coffee, S. Liu, D. A. Egger, I. Makasyuk, Q. Zheng, A. Fry, J. S. Robinson, M. D. Smith, B. Guzelturk, H. I. Karunadasa, X. Wang, X. Zhu, L. Kronik, A. M. Rappe, and A. M. Lindenberg, "Light-induced picosecond rotational disordering of the inorganic sublattice in hybrid perovskites," *Science Advances*, 2017.

[107] X. Tang, M. Brandl, B. May, I. Levchuk, Y. Hou, M. Richter, H. Chen, S. Chen, S. Kahmann, A. Osvet, F. Maier, H. P. Steinrück, R. Hock, G. J. Matt, and C. J. Brabec, "Photoinduced degradation of methylammonium lead triiodide perovskite semiconductors," *Journal of Materials Chemistry A*, 2016.

[108] C. Das, M. Wussler, T. Hellmann, T. Mayer, and W. Jaegermann, "In situ XPS study of the surface chemistry of MAPI solar cells under operating conditions in vacuum," *Physical Chemistry Chemical Physics*, 2018.

[109] J. Yang, Q. Hong, Z. Yuan, R. Xu, X. Guo, S. Xiong, X. Liu, S. Braun, Y. Li, J. Tang, C. Duan, M. Fahlman, and Q. Bao, "Unraveling Photostability of Mixed Cation Perovskite Films in Extreme Environment," *Advanced Optical Materials*, 2018.

[110] R. P. Xu, Y. Q. Li, T. Y. Jin, Y. Q. Liu, Q. Y. Bao, C. O'Carroll, and J. X. Tang, "In Situ Observation of Light Illumination-Induced Degradation in Organometal Mixed-Halide Perovskite Films," *ACS Applied Materials and Interfaces*, 2018.

[111] Z. Song, C. Wang, A. B. Phillips, C. R. Grice, D. Zhao, Y. Yu, C. Chen, C. Li, X. Yin, R. J. Ellingson, M. J. Heben, and Y. Yan, "Probing the origins of photodegradation in organic-inorganic metal halide perovskites with time-resolved mass spectrometry," *Sustainable Energy and Fuels*, 2018.

[112] D. Bryant, N. Aristidou, S. Pont, I. Sanchez-Molina, T. Chotchunangatchaval, S. Wheeler, J. R. Durrant, and S. A. Haque, "Light and oxygen induced degradation limits the operational stability of methylammonium lead triiodide perovskite solar cells," *Energy and Environmental Science*, 2016.

[113] N. H. Nickel, F. Lang, V. V. Brus, O. Shargaieva, and J. Rappich, "Unraveling the Light-Induced Degradation Mechanisms of CH3NH3PbI3 Perovskite Films," *Advanced Electronic Materials*, 2017.

[114] A. Senocrate, T. Acartürk, G. Y. Kim, R. Merkle, U. Starke, M. Grätzel, and J. Maier, "Interaction of oxygen with halide perovskites," *Journal of Materials Chemistry A*, 2018.

[115] S. Kundu and T. L. Kelly, "In situ studies of the degradation mechanisms of perovskite solar cells," *EcoMat*, 2020.

[116] Y. Zhou, L. You, S. Wang, Z. Ku, H. Fan, D. Schmidt, A. Rusydi, L. Chang, L. Wang, P. Ren, L. Chen, G. Yuan, L. Chen, and J. Wang, "Giant photostriction in organic-inorganic lead halide perovskites," *Nature Communications*, 2016.

[117] Y. B. Lu, W. Y. Cong, C. Guan, H. Sun, Y. Xin, K. Wang, and S. Song, "Light enhanced moisture degradation of perovskite solar cell material CH3NH3PbI3," *Journal of Materials Chemistry A*, 2019.

[118] H. J. Snaith, A. Abate, J. M. Ball, G. E. Eperon, T. Leijtens, N. K. Noel, S. D. Stranks, J. T. W. Wang, K. Wojciechowski, and W. Zhang, "Anomalous hysteresis in perovskite solar cells," *Journal of Physical Chemistry Letters*, 2014.

[119] W. Tress, N. Marinova, T. Moehl, S. M. Zakeeruddin, M. K. Nazeeruddin, and M. Grätzel, “Understanding the rate-dependent J-V hysteresis, slow time component, and aging in CH3NH3PbI3 perovskite solar cells: The role of a compensated electric field,” *Energy and Environmental Science*, 2015.

[120] B. Chen, M. Yang, S. Priya, and K. Zhu, “Origin of J-V Hysteresis in Perovskite Solar Cells,” 2016.

[121] S. Van Reenen, M. Kemerink, and H. J. Snaith, “Modeling Anomalous Hysteresis in Perovskite Solar Cells,” *Journal of Physical Chemistry Letters*, 2015.

[122] P. Calado, A. M. Telford, D. Bryant, X. Li, J. Nelson, B. C. O’Regan, and P. R. Barnes, “Evidence for ion migration in hybrid perovskite solar cells with minimal hysteresis,” *Nature Communications*, 2016.

[123] J. Barbé, V. Kumar, M. J. Newman, H. K. Lee, S. M. Jain, H. Chen, C. Charbonneau, C. Rodenburg, and W. C. Tsoi, “Dark electrical bias effects on moisture-induced degradation in inverted lead halide perovskite solar cells measured by using advanced chemical probes,” *Sustainable Energy and Fuels*, 2018.

[124] B. Xu, W. Wang, X. Zhang, H. Liu, Y. Zhang, G. Mei, S. Chen, K. Wang, L. Wang, and X. W. Sun, “Electric Bias Induced Degradation in Organic-Inorganic Hybrid Perovskite Light-Emitting Diodes,” *Scientific Reports*, 2018.

[125] R. L. Hoye, P. Schulz, L. T. Schelhas, A. M. Holder, K. H. Stone, J. D. Perkins, D. Vigil-Fowler, S. Siol, D. O. Scanlon, A. Zakutayev, A. Walsh, I. C. Smith, B. C. Melot, R. C. Kurchin, Y. Wang, J. Shi, F. C. Marques, J. J. Berry, W. Tumas, S. Lany, V. Stevanović, M. F. Toney, and T. Buonassisi, “Perovskite-Inspired Photovoltaic Materials: Toward Best Practices in Materials Characterization and Calculations,” *Chemistry of Materials*, 2017.

[126] K. Motoki, Y. Miyazawa, D. Kobayashi, M. Ikegami, T. Miyasaka, T. Yamamoto, and K. Hirose, “Degradation of CH3NH3PbI3 perovskite due to soft x-ray irradiation as analyzed by an x-ray photoelectron spectroscopy time-dependent measurement method,” *Journal of Applied Physics*, 2017.

[127] H. Yuan, E. Debroye, K. Janssen, H. Naiki, C. Steuwe, G. Lu, M. Moris, E. Orgiu, H. Uji-I, F. De Schryver, P. Samorì, J. Hofkens, and M. Roeffaers, “Degradation of Methylammonium Lead Iodide Perovskite Structures through Light and Electron Beam Driven Ion Migration,” *Journal of Physical Chemistry Letters*, 2016.

[128] C. Xiao, Z. Li, H. Guthrey, J. Moseley, Y. Yang, S. Wozny, H. Moutinho, B. To, J. J. Berry, B. Gorman, Y. Yan, K. Zhu, and M. Al-Jassim, “Mechanisms of Electron-Beam-Induced Damage in Perovskite Thin Films Revealed by Cathodoluminescence Spectroscopy,” *Journal of Physical Chemistry C*, 2015.

[129] C. Bracher, B. G. Freestone, D. K. Mohamad, J. A. Smith, and D. G. Lidzey, “Degradation of inverted architecture CH3NH3PbI3-xClx perovskite solar cells due to trapped moisture,” *Energy Science and Engineering*, 2018.

[130] R. Liu, L. Wang, Y. Fan, Z. Li, and S. Pang, “UV degradation of the interface between perovskites and the electron transport layer,” *RSC Advances*, 2020.

[131] W. Mönch and N. J. Dinardo, “Semiconductor Surfaces and Interfaces,” *Physics Today*, 1994.

[132] H. Uratani and K. Yamashita, “Charge Carrier Trapping at Surface Defects of Perovskite Solar Cell Absorbers: A First-Principles Study,” *Journal of Physical Chemistry Letters*, 2017.

[133] J. Haruyama, K. Sodeyama, L. Han, and Y. Tateyama, “Surface Properties of CH3NH3PbI3 for Perovskite Solar Cells,” 2016.

[134] J. Haruyama, K. Sodeyama, L. Han, and Y. Tateyama, “Termination dependence of tetragonal CH3NH3PbI 3 surfaces for perovskite solar cells,” *Journal of Physical Chemistry Letters*, 2014.

[135] C. Quarti, F. De Angelis, and D. Beljonne, “Influence of Surface Termination on the Energy Level Alignment at the CH3NH3PbI3 Perovskite/C60 Interface,” *Chemistry of Materials*, 2017.

[136] J. Xue, R. Wang, and Y. Yang, “The surface of halide perovskites from nano to bulk,” 2020.

[137] Q. Chen, H. Zhou, T. B. Song, S. Luo, Z. Hong, H. S. Duan, L. Dou, Y. Liu, and Y. Yang, “Controllable self-induced passivation of hybrid lead iodide perovskites toward high performance solar cells,” *Nano Letters*, 2014.

[138] D. H. Cao, C. C. Stoumpos, C. D. Malliakas, M. J. Katz, O. K. Farha, J. T. Hupp, and M. G. Kanatzidis, “Remnant PbI2, an unforeseen necessity in high-efficiency hybrid perovskite-based solar cells?,” *APL Materials*, 2014.

[139] B. wook Park, N. Kedem, M. Kulbak, D. Y. Lee, W. S. Yang, N. J. Jeon, J. Seo, G. Kim, K. J. Kim, T. J. Shin, G. Hodes, D. Cahen, and S. I. Seok, “Understanding how excess lead iodide precursor improves halide perovskite solar cell performance,” *Nature Communications*, 2018.

[140] P. Schulz, D. Cahen, and A. Kahn, “Halide Perovskites: Is It All about the Interfaces?,” 2019.

[141] A. Torres and L. G. Rego, “Surface effects and adsorption of methoxy anchors on hybrid lead iodide perovskites: Insights for spiro-MeOTAD attachment,” *Journal of Physical Chemistry C*, 2014.

[142] E. Mosconi, J. M. Azpiroz, and F. De Angelis, “Ab Initio Molecular Dynamics Simulations of Methylammonium Lead Iodide Perovskite Degradation by Water,” *Chemistry of Materials*, 2015.

[143] D. W. DeQuilettes, S. M. Vorpahl, S. D. Stranks, H. Nagaoka, G. E. Eperon, M. E. Ziffer, H. J. Snaith, and D. S. Ginger, “Impact of microstructure on local carrier lifetime in perovskite solar cells,” *Science*, 2015.

[144] C. G. Bischak, E. M. Sanehira, J. T. Precht, J. M. Luther, and N. S. Ginsberg, “Heterogeneous Charge Carrier Dynamics in Organic-Inorganic Hybrid Materials: Nanoscale Lateral and Depth-Dependent Variation of Recombination Rates in Methylammonium Lead Halide Perovskite Thin Films,” *Nano Letters*, 2015.

[145] S. Y. Leblebici, L. Leppert, Y. Li, S. E. Reyes-Lillo, S. Wickenburg, E. Wong, J. Lee, M. Melli, D. Ziegler, D. K. Angell, D. F. Ogletree, P. D. Ashby, F. M. Toma, J. B. Neaton, I. D. Sharp, and A. Weber-Bargioni, “Facet-dependent photovoltaic efficiency variations in single grains of hybrid halide perovskite,” *Nature Energy*, 2016.

[146] Y. Ma, P. M. Hangoma, W. I. Park, J. H. Lim, Y. K. Jung, J. H. Jeong, S. H. Park, and K. H. Kim, “Controlled crystal facet of MAPbI3 perovskite for highly efficient and stable solar cell via nucleation modulation,” *Nanoscale*, 2019.

[147] W. Zhu, Q. Wang, W. Chai, D. Chen, D. Chen, J. Chang, J. Zhang, C. Zhang, and Y. Hao, “Tailored interfacial crystal facets for efficient CH3NH3PbI3 perovskite solar cells,” *Organic Electronics*, 2020.

[148] L. A. Muscarella, E. M. Hutter, S. Sanchez, C. D. Dieleman, T. J. Savenije, A. Hagfeldt, M. Saliba, and B. Ehrler, “Crystal Orientation and Grain Size: Do They Determine Optoelectronic Properties of MAPbI3 Perovskite?,” *Journal of Physical Chemistry Letters*, 2019.

[149] A. Sutton and R. Balluffi, “Interfaces in Crystalline Materials Clarendon,” *Monographs on the physics and chemistry of materials*, 1995.

[150] W. J. Yin, T. Shi, and Y. Yan, “Unique properties of halide perovskites as possible origins of the superior solar cell performance,” *Advanced Materials*, 2014.

[151] W. J. Yin, H. Chen, T. Shi, S. H. Wei, and Y. Yan, “Origin of High Electronic Quality in Structurally Disordered CH3NH3PbI3 and the Passivation Effect of Cl and O at Grain Boundaries,” *Advanced Electronic Materials*, 2015.

[152] M. Yang, Y. Zeng, Z. Li, D. H. Kim, C. S. Jiang, J. Van De Lagemaat, and K. Zhu, “Do grain boundaries dominate non-radiative recombination in CH3NH3PbI3 perovskite thin films?,” *Physical Chemistry Chemical Physics*, 2017.

[153] Z. Chu, M. Yang, P. Schulz, D. Wu, X. Ma, E. Seifert, L. Sun, X. Li, K. Zhu, and K. Lai, “Impact of grain boundaries on efficiency and stability of organic-inorganic trihalide perovskites,” *Nature Communications*, 2017.

[154] Z. Xiao, Q. Dong, C. Bi, Y. Shao, Y. Yuan, and J. Huang, “Solvent Annealing of Perovskite-Induced Crystal Growth for Photovoltaic-Device Efficiency Enhancement,” *Advanced Materials*, 2014.

[155] B. Yang, O. Dyck, J. Poplawsky, J. Keum, A. Puretzky, S. Das, I. Ivanov, C. Rouleau, G. Duscher, D. Geohegan, and K. Xiao, “Perovskite Solar Cells with Near 100% Internal Quantum Efficiency Based on Large Single Crystalline Grains and Vertical Bulk Heterojunctions,” *Journal of the American Chemical Society*, 2015.

[156] W. Zhang, S. Pathak, N. Sakai, T. Stergiopoulos, P. K. Nayak, N. K. Noel, A. A. Haghighirad, V. M. Burlakov, D. W. Dequilettes, A. Sadhanala, W. Li, L. Wang, D. S. Ginger, R. H. Friend, and H. J. Snaith, “Enhanced optoelectronic quality of perovskite thin films with hypophosphorous acid for planar heterojunction solar cells,” *Nature Communications*, 2015.

[157] R. Long, J. Liu, and O. V. Prezhdo, "Unravelling the Effects of Grain Boundary and Chemical Doping on Electron-Hole Recombination in CH3NH3PbI3 Perovskite by Time-Domain Atomistic Simulation," *Journal of the American Chemical Society*, 2016.

[158] Y. Wang, W. H. Fang, R. Long, and O. V. Prezhdo, "Symmetry Breaking at MAPbI 3 Perovskite Grain Boundaries Suppresses Charge Recombination: Time-Domain ab Initio Analysis," *Journal of Physical Chemistry Letters*, 2019.

[159] T. S. Sherkar, C. Momblona, L. Gil-Escrig, J. Ávila, M. Sessolo, H. J. Bolink, and L. J. A. Koster, "Recombination in Perovskite Solar Cells: Significance of Grain Boundaries, Interface Traps, and Defect Ions," *ACS Energy Letters*, 2017.

[160] S. Shao, M. Abdu-Aguye, T. S. Sherkar, H. H. Fang, S. Adjokatse, G. ten Brink, B. J. Kooi, L. J. A. Koster, and M. A. Loi, "The Effect of the Microstructure on Trap-Assisted Recombination and Light Soaking Phenomenon in Hybrid Perovskite Solar Cells," *Advanced Functional Materials*, 2016.

[161] J. W. Lee, S. H. Bae, N. De Marco, Y. T. Hsieh, Z. Dai, and Y. Yang, "The role of grain boundaries in perovskite solar cells," 2018.

[162] A. F. Castro-Méndez, J. Hidalgo, and J. P. Correa-Baena, "The Role of Grain Boundaries in Perovskite Solar Cells," 2019.

[163] D. Cahen and A. Kahn, "Electron energetics at surfaces and interfaces: Concepts and experiments," *Advanced Materials*, 2003.

[164] A. Kahn, "Fermi level, work function and vacuum level," 2016.

[165] R. W. Strayer, W. Mackie, and L. W. Swanson, "Work function measurements by the field emission retarding potential method," *Surface Science*, 1973.

[166] Z. Zhang and J. T. Yates, "Band Bending in Semiconductors: Chemical and Physical Consequences at Surfaces and Interfaces," *Chemical Reviews*, vol. 112, pp. 5520–5551, oct 2012.

[167] A. Zangwill, *Physics at Surfaces.* Cambridge University Press, 1988.

[168] H. Lüth, "Space-Charge Layers at Semiconductor Inferfaces," in *Surfaces and Interfaces of Solids*, Springer-Verlag Berlin Heidelberg, 1993.

[169] S. Olthof and K. Meerholz, "Substrate-dependent electronic structure and film formation of MAPbI 3 perovskites," *Scientific Reports*, 2017.

[170] E. M. Miller, Y. Zhao, C. C. Mercado, S. K. Saha, J. M. Luther, K. Zhu, V. Stevanović, C. L. Perkins, and J. Van De Lagemaat, "Substrate-controlled band positions in CH3NH3PbI3 perovskite films," *Physical Chemistry Chemical Physics*, 2014.

[171] P. Schulz, L. L. Whittaker-Brooks, B. A. Macleod, D. C. Olson, Y. L. Loo, and A. Kahn, "Electronic Level Alignment in Inverted Organometal Perovskite Solar Cells," *Advanced Materials Interfaces*, 2015.

[172] C. Li, S. Tscheuschner, F. Paulus, P. E. Hopkinson, J. Kießling, A. Köhler, Y. Vaynzof, and S. Huettner, "Iodine Migration and its Effect on Hysteresis in Perovskite Solar Cells," *Advanced Materials*, 2016.

[173] H. Lee, S. Gaiaschi, P. Chapon, A. Marronnier, H. Lee, J. C. Vanel, D. Tondelier, J. E. Bourée, Y. Bonnassieux, and B. Geffroy, "Direct experimental evidence of halide ionic migration under bias in CH3NH3PbI3-xClx-based perovskite solar cells using GD-OES analysis," *ACS Energy Letters*, 2017.

[174] K. Domanski, B. Roose, T. Matsui, M. Saliba, S. H. Turren-Cruz, J. P. Correa-Baena, C. R. Carmona, G. Richardson, J. M. Foster, F. De Angelis, J. M. Ball, A. Petrozza, N. Mine, M. K. Nazeeruddin, W. Tress, M. Grätzel, U. Steiner, A. Hagfeldt, and A. Abate, "Migration of cations induces reversible performance losses over day/night cycling in perovskite solar cells," *Energy and Environmental Science*, 2017.

[175] C. Wang, C. Wang, X. Liu, J. Kauppi, Y. Shao, Z. Xiao, C. Bi, J. Huang, and Y. Gao, "Electronic structure evolution of fullerene on CH3NH3PbI3," *Applied Physics Letters*, 2015.

[176] P. Zhao, B. J. Kim, and H. S. Jung, "Passivation in perovskite solar cells: A review," 2018.

[177] J. Kim, A. Ho-Baillie, and S. Huang, "Review of Novel Passivation Techniques for Efficient and Stable Perovskite Solar Cells," 2019.

[178] L. Fu, H. Li, L. Wang, R. Yin, B. Li, and L. Yin, "Defect passivation strategies in perovskites for an enhanced photovoltaic performance," 2020.

[179] S. Akin, N. Arora, S. M. Zakeeruddin, M. Grätzel, R. H. Friend, and M. I. Dar, "New Strategies for Defect Passivation in High-Efficiency Perovskite Solar Cells," 2020.

[180] C. Li, H. Li, Z. Zhu, N. Cui, Z. Tan, and R. Yang, "Perovskite Passivation Strategies for Efficient and Stable Solar Cells," 2021.

[181] M. Abdi-Jalebi, Z. Andaji-Garmaroudi, S. Cacovich, C. Stavrakas, B. Philippe, J. M. Richter, M. Alsari, E. P. Booker, E. M. Hutter, A. J. Pearson, S. Lilliu, T. J. Savenije, H. Rensmo, G. Divitini, C. Ducati, R. H. Friend, and S. D. Stranks, "Maximizing and stabilizing luminescence from halide perovskites with potassium passivation," *Nature*, 2018.

[182] F. Zheng, W. Chen, T. Bu, K. P. Ghiggino, F. Huang, Y. Cheng, P. Tapping, T. W. Kee, B. Jia, and X. Wen, "Triggering the Passivation Effect of Potassium Doping in Mixed-Cation Mixed-Halide Perovskite by Light Illumination," *Advanced Energy Materials*, 2019.

[183] J. P. Correa-Baena, Y. Luo, T. M. Brenner, J. Snaider, S. Sun, X. Li, M. A. Jensen, N. T. P. Hartono, L. Nienhaus, S. Wieghold, J. R. Poindexter, S. Wang, Y. S. Meng, T. Wang, B. Lai, M. V. Holt, Z. Cai, M. G. Bawendi, L. Huang, T. Buonassisi, and D. P. Fenning, "Homogenized halides and alkali cation segregation in alloyed organic-inorganic perovskites," *Science*, 2019.

[184] D. Y. Son, J. W. Lee, Y. J. Choi, I. H. Jang, S. Lee, P. J. Yoo, H. Shin, N. Ahn, M. Choi, D. Kim, and N. G. Park, "Self-formed grain boundary healing layer for highly efficient CH3 NH3 PbI3 perovskite solar cells," *Nature Energy*, 2016.

[185] Y. Jiang, E. J. Juarez-Perez, Q. Ge, S. Wang, M. R. Leyden, L. K. Ono, S. R. Raga, J. Hu, and Y. Qi, "Post-annealing of MAPbI3 perovskite films with methylamine for efficient perovskite solar cells†," *Materials Horizons*, 2016.

[186] F. Cai, Y. Yan, J. Yao, P. Wang, H. Wang, R. S. Gurney, D. Liu, and T. Wang, "Ionic Additive Engineering Toward High-Efficiency Perovskite Solar Cells with Reduced Grain Boundaries and Trap Density," *Advanced Functional Materials*, 2018.

[187] W. Zhou, D. Li, Z. Xiao, Z. Wen, M. Zhang, W. Hu, X. Wu, M. Wang, W. H. Zhang, Y. Lu, S. Yang, and S. Yang, "Zwitterion Coordination Induced Highly Orientational Order of CH3NH3PbI3 Perovskite Film Delivers a High Open Circuit Voltage Exceeding 1.2 V," *Advanced Functional Materials*, 2019.

[188] G. Yang, P. Qin, G. Fang, and G. Li, "A Lewis Base-Assisted Passivation Strategy Towards Highly Efficient and Stable Perovskite Solar Cells," *Solar RRL*, 2018.

[189] F. Zhang, D. Bi, N. Pellet, C. Xiao, Z. Li, J. J. Berry, S. M. Zakeeruddin, K. Zhu, and M. Grätzel, "Suppressing defects through the synergistic effect of a Lewis base and a Lewis acid for highly efficient and stable perovskite solar cells," *Energy and Environmental Science*, 2018.

[190] S. Wang, A. Wang, X. Deng, L. Xie, A. Xiao, C. Li, Y. Xiang, T. Li, L. Ding, and F. Hao, "Lewis acid/base approach for efficacious defect passivation in perovskite solar cells," 2020.

[191] D. Bi, X. Li, J. V. Milić, D. J. Kubicki, N. Pellet, J. Luo, T. LaGrange, P. Mettraux, L. Emsley, S. M. Zakeeruddin, and M. Grätzel, "Multifunctional molecular modulators for perovskite solar cells with over 20% efficiency and high operational stability," *Nature Communications*, 2018.

[192] R. Wang, J. Xue, K. L. Wang, Z. K. Wang, Y. Luo, D. Fenning, G. Xu, S. Nuryyeva, T. Huang, Y. Zhao, J. L. Yang, J. Zhu, M. Wang, S. Tan, I. Yavuz, K. N. Houk, and Y. Yang, "Constructive molecular configurations for surface-defect passivation of perovskite photovoltaics," *Science*, 2019.

[193] X. Zheng, Y. Deng, B. Chen, H. Wei, X. Xiao, Y. Fang, Y. Lin, Z. Yu, Y. Liu, Q. Wang, and J. Huang, "Dual Functions of Crystallization Control and Defect Passivation Enabled by Sulfonic Zwitterions for Stable and Efficient Perovskite Solar Cells," *Advanced Materials*, 2018.

[194] G. Grancini, C. Roldán-Carmona, I. Zimmermann, E. Mosconi, X. Lee, D. Martineau, S. Narbey, F. Oswald, F. De Angelis, M. Graetzel, and M. K. Nazeeruddin, "One-Year stable perovskite solar cells by 2D/3D interface engineering," *Nature Communications*, 2017.

[195] J. Fan, Y. Ma, C. Zhang, C. Liu, W. Li, R. E. Schropp, and Y. Mai, "Thermodynamically Self-Healing 1D–3D Hybrid Perovskite Solar Cells," *Advanced Energy Materials*, 2018.

[196] N. Yang, C. Zhu, Y. Chen, H. Zai, C. Wang, X. Wang, H. Wang, S. Ma, Z. Gao, X. Wang, J. Hong, Y. Bai, H. Zhou, B. B. Cui, and Q. Chen, "An: In situ cross-linked 1D/3D perovskite heterostructure improves the stability of hybrid perovskite solar cells for over 3000 h operation," *Energy and Environmental Science*, 2020.

[197] S. Yang, S. Chen, E. Mosconi, Y. Fang, X. Xiao, C. Wang, Y. Zhou, Z. Yu, J. Zhao, Y. Gao, F. De Angelis, and J. Huang, "Stabilizing halide perovskite surfaces for solar cell operation with wide-bandgap lead oxysalts," *Science*, 2019.

[198] J. S. Godding, A. J. Ramadan, Y. H. Lin, K. Schutt, H. J. Snaith, and B. Wenger, "Oxidative Passivation of Metal Halide Perovskites," *Joule*, 2019.

[199] E. H. Jung, N. J. Jeon, E. Y. Park, C. S. Moon, T. J. Shin, T. Y. Yang, J. H. Noh, and J. Seo, "Efficient, stable and scalable perovskite solar cells using poly(3-hexylthiophene)," *Nature*, 2019.

[200] L. Kronik and Y. Shapira, "Surface photovoltage phenomena: Theory, experiment, and applications," *Surface Science Reports*, 1999.

[201] R. Chen, F. Fan, T. Dittrich, and C. Li, "Imaging photogenerated charge carriers on surfaces and interfaces of photocatalysts with surface photovoltage microscopy," 2018.

[202] Y. Almadori, D. Moerman, J. L. Martinez, P. Leclère, and B. Grévin, "Multimodal noncontact atomic force microscopy and Kelvin probe force microscopy investigations of organolead tribromide perovskite single crystals," *Beilstein Journal of Nanotechnology*, 2018.

[203] J. L. Garrett, E. M. Tennyson, M. Hu, J. Huang, J. N. Munday, and M. S. Leite, "Real-Time Nanoscale Open-Circuit Voltage Dynamics of Perovskite Solar Cells," *Nano Letters*, 2017.

[204] M. A. Reshchikov, M. Foussekis, and A. A. Baski, "Surface photovoltage in undoped n-type GaN," *Journal of Applied Physics*, 2010.

[205] P. Granitzer, K. Rumpf, Y. Strzhemechny, and P. Chapagain, "Transient surface photovoltage studies of bare and Ni-filled porous silicon performed in different ambients," *Nanoscale Research Letters*, 2014.

[206] L. Collins, M. Ahmadi, J. Qin, Y. Liu, O. S. Ovchinnikova, B. Hu, S. Jesse, and S. V. Kalinin, "Time resolved surface photovoltage measurements using a big data capture approach to KPFM," *Nanotechnology*, 2018.

[207] A. Winnerl, R. N. Pereira, and M. Stutzmann, "Kinetics of optically excited charge carriers at the GaN surface," *Physical Review B - Condensed Matter and Materials Physics*, 2015.

[208] V. W. Bergmann, Y. Guo, H. Tanaka, I. M. Hermes, D. Li, A. Klasen, S. A. Bretschneider, E. Nakamura, R. Berger, and S. A. Weber, "Local Time-Dependent Charging in a Perovskite Solar Cell," *ACS Applied Materials and Interfaces*, 2016.

[209] M. Daboczi, J. Kim, J. Lee, H. Kang, I. Hamilton, C. T. Lin, S. D. Dimitrov, M. A. McLachlan, K. Lee, J. R. Durrant, and J. S. Kim, "Towards Efficient Integrated Perovskite/Organic Bulk Heterojunction Solar Cells: Interfacial Energetic Requirement to Reduce Charge Carrier Recombination Losses," *Advanced Functional Materials*, 2020.

[210] T. Leijtens, G. E. Eperon, A. J. Barker, G. Grancini, W. Zhang, J. M. Ball, A. R. S. Kandada, H. J. Snaith, and A. Petrozza, "Carrier trapping and recombination: The role of defect physics in enhancing the open circuit voltage of metal halide perovskite solar cells," *Energy and Environmental Science*, 2016.

[211] D. Toth, B. Hailegnaw, F. Richheimer, F. A. Castro, F. Kienberger, M. C. Scharber, S. Wood, and G. Gramse, "Nanoscale Charge Accumulation and Its Effect on Carrier Dynamics in Tri-cation Perovskite Structures," *ACS Applied Materials & Interfaces*, vol. 12, pp. 48057–48066, oct 2020.

[212] M. V. Salapaka and S. M. Salapaka, "Scanning Probe Microscopy," *IEEE Control Systems*, vol. 28, pp. 65–83, apr 2008.

[213] K. Bian, C. Gerber, A. J. Heinrich, D. J. Müller, S. Scheuring, and Y. Jiang, "Scanning probe microscopy," *Nature Reviews Methods Primers*, vol. 1, p. 36, dec 2021.

[214] S. A. Parsons and B. Jefferson, "Chapter 15: Adhesion analysis of scaling systems," in *Interface Science and Technology*, Elsevier, 2006.

[215] G. Binnig, H. Rohrer, C. Gerber, and E. Weibel, "Surface Studies by Scanning Tunneling Microscopy," *Physical Review Letters*, vol. 49, pp. 57–61, jul 1982.

[216] C. J. Chen, *Introduction to Scanning Tunneling Microscopy.* Oxford University Press, mar 2021.

[217] G. Binnig and H. Rohrer, "Scanning tunneling microscopy," *Surface Science*, vol. 152-153, pp. 17–26, apr 1985.

[218] B. Voigtländer, *Scanning Probe Microscopy.* NanoScience and Technology, Berlin, Heidelberg: Springer Berlin Heidelberg, 2015.

[219] J. Bardeen, "Tunnelling from a Many-Particle Point of View," *Physical Review Letters*, vol. 6, pp. 57–59, jan 1961.

[220] J. Tersoff and D. R. Hamann, "Theory and Application for the Scanning Tunneling Microscope," *Physical Review Letters*, vol. 50, pp. 1998–2001, jun 1983.

[221] C. J. Chen, "Tunneling matrix elements in three-dimensional space: The derivative rule and the sum rule," *Physical Review B*, vol. 42, pp. 8841–8857, nov 1990.

[222] R. Feenstra, J. A. Stroscio, and A. Fein, "Tunneling spectroscopy of the Si(111)2 × 1 surface," *Surface Science*, vol. 181, pp. 295–306, mar 1987.

[223] R. M. Feenstra, "Tunneling spectroscopy of the (110) surface of direct-gap III-V semiconductors," *Physical Review B*, vol. 50, pp. 4561–4570, aug 1994.

[224] G. Binnig, C. F. Quate, and C. Gerber, “Atomic Force Microscope,” *Physical Review Letters*, vol. 56, pp. 930–933, mar 1986.

[225] Israelachvili,Jacob , “Intermolecular and Surface Forces,” in *Intermolecular and Surface Forces*, Elsevier, 2011.

[226] W. Melitz, J. Shen, A. C. Kummel, and S. Lee, “Kelvin probe force microscopy and its application,” *Surface Science Reports*, vol. 66, pp. 1–27, jan 2011.

[227] E. M. Lanzoni, T. Gallet, C. Spindler, O. Ramírez, C. K. Boumenou, S. Siebentritt, and A. Redinger, “The impact of Kelvin probe force microscopy operation modes and environment on grain boundary band bending in perovskite and Cu(In,Ga)Se2 solar cells,” *Nano Energy*, 2021.

[228] NanosurfLab, “Omicron variable-temperature scanning tunnelling microscope.” https://nanosurf.fzu.cz/tools.php. (accessed: 04.10.2021).

[229] S. Omicron, “Vt spm, outstanding spm performance with maximum flexibility.” https://scientaomicron.com/en/Components/SPMs/VT-SPM. (accessed: 04.10.2021).

[230] R. Ohmann, L. K. Ono, H.-S. Kim, H. Lin, M. V. Lee, Y. Li, N.-G. Park, and Y. Qi, “Real-Space Imaging of the Atomic Structure of Organic–Inorganic Perovskite,” *Journal of the American Chemical Society*, vol. 137, pp. 16049–16054, dec 2015.

[231] Y. Liu, K. Palotas, X. Yuan, T. Hou, H. Lin, Y. Li, and S. T. Lee, “Atomistic Origins of Surface Defects in CH3NH3PbBr3 Perovskite and Their Electronic Structures,” *ACS Nano*, vol. 11, no. 2, pp. 2060–2065, 2017.

[232] H. C. Hsu, B. C. Huang, S. C. Chin, C. R. Hsing, D. L. Nguyen, M. Schnedler, R. Sankar, R. E. Dunin-Borkowski, C. M. Wei, C. W. Chen, P. Ebert, and Y. P. Chiu, “Photodriven Dipole Reordering: Key to Carrier Separation in Metalorganic Halide Perovskites,” *ACS Nano*, vol. 13, no. 4, pp. 4402–4409, 2019.

[233] B. Murali, S. Dey, A. L. Abdelhady, W. Peng, E. Alarousu, A. R. Kirmani, N. Cho, S. P. Sarmah, M. R. Parida, M. I. Saidaminov, A. A. Zhumekenov, J. Sun, M. S. Alias, E. Yengel, B. S. Ooi, A. Amassian, O. M. Bakr, and O. F. Mohammed, “Surface Restructuring of Hybrid Perovskite Crystals,” *ACS Energy Letters*, 2016.

[234] D. Azulay, I. Levine, S. Gupta, E. Barak-Kulbak, A. Bera, G. San, S. Simha, D. Cahen, O. Millo, G. Hodes, and I. Balberg, “On the influence of multiple cations on the in-gap states and phototransport properties of iodide-based halide perovskites,” *Physical Chemistry Chemical Physics*, vol. 20, pp. 24444–24452, 2018.

[235] S. Wieghold, N. Shirato, V. Rose, and L. Nienhaus, “Investigating the effect of electric fields on lead halide perovskites by scanning tunneling microscopy,” *Journal of Applied Physics*, vol. 128, p. 125303, 2020.

[236] S. Sahare, P. Ghoderao, S. B. Khan, Y. Chan, and S.-L. Lee, “Recent progress in hybrid perovskite solar cells through scanning tunneling microscopy and spectroscopy,” *Nanoscale*, vol. 12, no. 30, pp. 15970–15992, 2020.

[237] J. Hieulle, C. Stecker, R. Ohmann, L. K. Ono, and Y. Qi, "Scanning Probe Microscopy Applied to Organic-Inorganic Halide Perovskite Materials and Solar Cells," *Small Methods*, vol. 2, p. 1700295, jan 2018.

[238] M. Telychko and J. Lu, "Recent advances in atomic imaging of organic-inorganic hybrid perovskites," *Nano Materials Science*, vol. 1, pp. 260–267, dec 2019.

[239] Z. Kang, H. Si, M. Shi, C. Xu, W. Fan, S. Ma, A. Kausar, Q. Liao, Z. Zhang, and Y. Zhang, "Kelvin probe force microscopy for perovskite solar cells," *Science China Materials*, vol. 62, pp. 776–789, jun 2019.

[240] C. Shakher Pathak, "Application of Atomic Force Microscopy in Organic and Perovskite Photovoltaics," in *Atomic Force Microscopy - Basic Principles to Advanced Applications [Working Title]*, IntechOpen, jun 2021.

[241] B. Grévin, "Kelvin Probe Force Microscopy Characterization of Organic and Hybrid Perovskite Solar Cells," in *Springer Series in Surface Sciences*, pp. 331–365, Springer, 2018.

[242] J. M. Howard, R. Lahoti, and M. S. Leite, "Imaging Metal Halide Perovskites Material and Properties at the Nanoscale," *Advanced Energy Materials*, vol. 10, p. 1903161, jul 2020.

[243] V. W. Bergmann, S. A. L. Weber, F. Javier Ramos, M. K. Nazeeruddin, M. Grätzel, D. Li, A. L. Domanski, I. Lieberwirth, S. Ahmad, and R. Berger, "Real-space observation of unbalanced charge distribution inside a perovskite-sensitized solar cell," *Nature Communications*, vol. 5, p. 5001, dec 2014.

[244] A. Dymshits, A. Henning, G. Segev, Y. Rosenwaks, and L. Etgar, "The electronic structure of metal oxide/organo metal halide perovskite junctions in perovskite based solar cells," *Scientific Reports*, vol. 5, p. 8704, aug 2015.

[245] Z. Li, C. Xiao, Y. Yang, S. P. Harvey, D. H. Kim, J. A. Christians, M. Yang, P. Schulz, S. U. Nanayakkara, C.-S. Jiang, J. M. Luther, J. J. Berry, M. C. Beard, M. M. Al-Jassim, and K. Zhu, "Extrinsic ion migration in perovskite solar cells," *Energy and Environmental Science*, vol. 10, no. 5, pp. 1234–1242, 2017.

[246] M. Cai, N. Ishida, X. Li, X. Yang, T. Noda, Y. Wu, F. Xie, H. Naito, D. Fujita, and L. Han, "Control of Electrical Potential Distribution for High-Performance Perovskite Solar Cells," *Joule*, vol. 2, pp. 296–306, feb 2018.

[247] S. Panigrahi, S. Jana, T. Calmeiro, D. Nunes, R. Martins, and E. Fortunato, "Imaging the Anomalous Charge Distribution Inside CsPbBr 3 Perovskite Quantum Dots Sensitized Solar Cells," *ACS Nano*, vol. 11, pp. 10214–10221, oct 2017.

[248] F. Lan, M. Jiang, and G. Li, "The characterization of defects states and charge injection barriers in perovskite solar cells," in *2017 IEEE 17th International Conference on Nanotechnology (IEEE-NANO)*, pp. 379–382, IEEE, jul 2017.

[249] J. Lee, J. Kong, H. Kim, S.-O. Kang, and K. Lee, "Direct observation of internal potential distributions in a bulk heterojunction solar cell," *Applied Physics Letters*, vol. 99, p. 243301, dec 2011.

[250] J. S. Yun, J. Kim, T. Young, R. J. Patterson, D. Kim, J. Seidel, S. Lim, M. A. Green, S. Huang, and A. Ho-Baillie, “Humidity-Induced Degradation via Grain Boundaries of HC(NH 2) 2 PbI 3 Planar Perovskite Solar Cells,” *Advanced Functional Materials*, vol. 28, p. 1705363, mar 2018.

[251] Y. Shao, Y. Fang, T. Li, Q. Wang, Q. Dong, Y. Deng, Y. Yuan, H. Wei, M. Wang, A. Gruverman, J. Shield, and J. Huang, “Grain boundary dominated ion migration in polycrystalline organic–inorganic halide perovskite films,” *Energy & Environmental Science*, vol. 9, no. 5, pp. 1752–1759, 2016.

[252] J. Song, Y. Zhou, N. P. Padture, and B. D. Huey, “Anomalous 3D nanoscale photoconduction in hybrid perovskite semiconductors revealed by tomographic atomic force microscopy,” *Nature Communications*, 2020.

[253] T.-X. Qin, E.-M. You, M.-X. Zhang, P. Zheng, X.-F. Huang, S.-Y. Ding, B.-W. Mao, and Z.-Q. Tian, “Quantification of electron accumulation at grain boundaries in perovskite polycrystalline films by correlative infrared-spectroscopic nanoimaging and Kelvin probe force microscopy,” *Light: Science & Applications*, vol. 10, p. 84, dec 2021.

[254] S. Y. Luchkin, A. F. Akbulatov, L. A. Frolova, S. A. Tsarev, P. A. Troshin, and K. J. Stevenson, “Spatially-resolved nanoscale measurements of grain boundary enhanced photocurrent in inorganic CsPbBr3 perovskite films,” *Solar Energy Materials and Solar Cells*, vol. 171, pp. 205–212, nov 2017.

[255] M. I. Saidaminov, K. Williams, M. Wei, A. Johnston, R. Quintero-Bermudez, M. Vafaie, J. M. Pina, A. H. Proppe, Y. Hou, G. Walters, S. O. Kelley, W. A. Tisdale, and E. H. Sargent, “Multi-cation perovskites prevent carrier reflection from grain surfaces,” *Nature Materials*, vol. 19, pp. 412–418, apr 2020.

[256] P. Gratia, G. Grancini, J. N. Audinot, X. Jeanbourquin, E. Mosconi, I. Zimmermann, D. Dowsett, Y. Lee, M. Grätzel, F. De Angelis, K. Sivula, T. Wirtz, and M. K. Nazeeruddin, “Intrinsic Halide Segregation at Nanometer Scale Determines the High Efficiency of Mixed Cation/Mixed Halide Perovskite Solar Cells,” *Journal of the American Chemical Society*, 2016.

[257] L. Lin, J. T.-W. Wang, T. W. Jones, M. Grigore, A. Cook, D. W. DeQuilettes, R. Brenes, B. C. Duck, K. F. Anderson, N. W. Duffy, B. Wenger, V. Bulović, J. Pu, J. Li, B. Chi, H. J. Snaith, and G. J. Wilson, “Bulk recrystallization for efficient mixed-cation mixed-halide perovskite solar cells,” *Journal of Materials Chemistry A*, vol. 7, no. 44, pp. 25511–25520, 2019.

[258] C. Xiao, F. Zhang, Z. Li, S. P. Harvey, X. Chen, K. Wang, C.-S. Jiang, K. Zhu, and M. Al-Jassim, “Inhomogeneous Doping of Perovskite Materials by Dopants from Hole-Transport Layer,” *Matter*, vol. 2, pp. 261–272, jan 2020.

[259] E. M. Tennyson, M. Abdi-Jalebi, K. Ji, J. L. Garrett, C. Gong, A. A. Pawlicki, O. S. Ovchinnikova, J. N. Munday, S. D. Stranks, and M. S. Leite, “Correlated Electrical and Chemical Nanoscale Properties in Potassium-Passivated, Triple-Cation Perovskite Solar Cells,” *Advanced Materials Interfaces*, vol. 7, p. 2000515, sep 2020.

[260] Y. Cho, A. M. Soufiani, J. S. Yun, J. Kim, D. S. Lee, J. Seidel, X. Deng, M. A. Green, S. Huang, and A. W. Y. Ho-Baillie, "Mixed 3D-2D Passivation Treatment for Mixed-Cation Lead Mixed-Halide Perovskite Solar Cells for Higher Efficiency and Better Stability," *Advanced Energy Materials*, vol. 8, p. 1703392, jul 2018.

[261] M. Zhang, J. S. Yun, Q. Ma, J. Zheng, C. F. J. Lau, X. Deng, J. Kim, D. Kim, J. Seidel, M. A. Green, S. Huang, and A. W. Y. Ho-Baillie, "High-Efficiency Rubidium-Incorporated Perovskite Solar Cells by Gas Quenching," *ACS Energy Letters*, vol. 2, pp. 438–444, feb 2017.

[262] Y. Yang, L. Wu, X. Hao, Z. Tang, H. Lai, J. Zhang, W. Wang, and L. Feng, "Beneficial effects of potassium iodide incorporation on grain boundaries and interfaces of perovskite solar cells," *RSC Advances*, vol. 9, no. 49, pp. 28561–28568, 2019.

[263] C. Yang, P. Du, Z. Dai, H. Li, X. Yang, and Q. Chen, "Effects of Illumination Direction on the Surface Potential of CH 3 NH 3 PbI 3 Perovskite Films Probed by Kelvin Probe Force Microscopy," *ACS Applied Materials and Interfaces*, 2019.

[264] S. P. Dunfield, A. Bojar, S. Cacovich, M. Frégnaux, T. Klein, R. Bramante, F. Zhang, D. Regaldo, V. Dufoulon, J.-B. Puel, G. Teeter, J. M. Luther, M. Bouttemy, D. Nordlund, K. Zhu, D. T. Moore, M. F. van Hest, J.-P. Kleider, J. J. Berry, and P. Schulz, "Carrier gradients and the role of charge selective contacts in lateral heterojunction all back contact perovskite solar cells," *Cell Reports Physical Science*, vol. 2, p. 100520, aug 2021.

[265] E. M. Tennyson, J. L. Garrett, J. A. Frantz, J. D. Myers, R. Y. Bekele, J. S. Sanghera, J. N. Munday, and M. S. Leite, "Nanoimaging of Open-Circuit Voltage in Photovoltaic Devices," *Advanced Energy Materials*, vol. 5, p. 1501142, dec 2015.

[266] X. Liu, Y. Liu, F. Gao, Z. Yang, and S. F. Liu, "Photoinduced surface voltage mapping study for large perovskite single crystals," *Applied Physics Letters*, vol. 108, p. 181604, may 2016.

[267] T. Zhang, N. Guo, G. Li, X. Qian, L. Li, and Y. Zhao, "A general non-CH 3 NH 3 X (X = I, Br) one-step deposition of CH 3 NH 3 PbX 3 perovskite for high performance solar cells," *Journal of Materials Chemistry A*, vol. 4, no. 9, pp. 3245–3248, 2016.

[268] J.-h. Im, I.-H. Jang, N. Pellet, M. Grätzel, and N.-G. Park, "Growth of CH3NH3PbI3 cuboids with controlled size for high-efficiency perovskite solar cells," *Nature Nanotechnology*, vol. 9, pp. 927–932, nov 2014.

[269] B.-E. Cohen, S. Gamliel, and L. Etgar, "Parameters influencing the deposition of methylammonium lead halide iodide in hole conductor free perovskite-based solar cells," *APL Materials*, vol. 2, p. 081502, aug 2014.

[270] J. Burschka, N. Pellet, S.-J. Moon, R. Humphry-Baker, P. Gao, M. K. Nazeeruddin, and M. Grätzel, "Sequential deposition as a route to high-performance perovskite-sensitized solar cells," *Nature*, vol. 499, pp. 316–319, jul 2013.

[271] N. J. Jeon, J. H. Noh, Y. C. Kim, W. S. Yang, S. Ryu, and S. I. Seok, "Solvent engineering for high-performance inorganic–organic hybrid perovskite solar cells," *Nature Materials*, vol. 13, pp. 897–903, sep 2014.

[272] A. D. Taylor, Q. Sun, K. P. Goetz, Q. An, T. Schramm, Y. Hofstetter, M. Litterst, F. Paulus, and Y. Vaynzof, “A general approach to high-efficiency perovskite solar cells by any antisolvent,” *Nature Communications*, vol. 12, p. 1878, dec 2021.

[273] Y. Vaynzof, “The Future of Perovskite Photovoltaics—Thermal Evaporation or Solution Processing?,” *Advanced Energy Materials*, vol. 10, p. 2003073, dec 2020.

[274] R. Swartwout, M. T. Hoerantner, and V. Bulović, “Scalable Deposition Methods for Large-area Production of Perovskite Thin Films,” *ENERGY & ENVIRONMENTAL MATERIALS*, vol. 2, pp. 119–145, jun 2019.

[275] H. Eggers, F. Schackmar, T. Abzieher, Q. Sun, U. Lemmer, Y. Vaynzof, B. S. Richards, G. Hernandez-Sosa, and U. W. Paetzold, “Inkjet-Printed Micrometer-Thick Perovskite Solar Cells with Large Columnar Grains,” *Advanced Energy Materials*, vol. 10, p. 1903184, feb 2020.

[276] J. E. Bishop, C. D. Read, J. A. Smith, T. J. Routledge, and D. G. Lidzey, “Fully Spray-Coated Triple-Cation Perovskite Solar Cells,” *Scientific Reports*, vol. 10, p. 6610, dec 2020.

[277] P. Fan, D. Gu, G.-X. Liang, J.-T. Luo, J.-L. Chen, Z.-H. Zheng, and D.-P. Zhang, “High-performance perovskite CH3NH3PbI3 thin films for solar cells prepared by single-source physical vapour deposition,” *Scientific Reports*, vol. 6, p. 29910, sep 2016.

[278] K. Hwang, Y.-S. Jung, Y.-J. Heo, F. H. Scholes, S. E. Watkins, J. Subbiah, D. J. Jones, D.-Y. Kim, and D. Vak, “Toward Large Scale Roll-to-Roll Production of Fully Printed Perovskite Solar Cells,” *Advanced Materials*, vol. 27, pp. 1241–1247, feb 2015.

[279] Z. Yang, C.-C. Chueh, F. Zuo, J. H. Kim, P.-W. Liang, and A. K. Jen, “High-Performance Fully Printable Perovskite Solar Cells via Blade-Coating Technique under the Ambient Condition,” *Advanced Energy Materials*, vol. 5, p. 1500328, jul 2015.

[280] M. R. Leyden, L. K. Ono, S. R. Raga, Y. Kato, S. Wang, and Y. Qi, “High performance perovskite solar cells by hybrid chemical vapor deposition,” *J. Mater. Chem. A*, vol. 2, no. 44, pp. 18742–18745, 2014.

[281] Q. Chen, H. Zhou, Z. Hong, S. Luo, H.-S. Duan, H.-H. Wang, Y. Liu, G. Li, and Y. Yang, “Planar Heterojunction Perovskite Solar Cells via Vapor-Assisted Solution Process,” *Journal of the American Chemical Society*, vol. 136, pp. 622–625, jan 2014.

[282] D. M. Mattox, *Handbook of Physical Vapor Deposition (PVD) Processing.* Elsevier, 2010.

[283] K. S. Sree Harsha, *Principles of Vapor Deposition of Thin Films.* Elsevier, 2006.

[284] PowerStream, “Vapor pressures of the chemical elements.” https://www.powerstream.com/vapor-pressure.htm. (accessed: 28.09.2021).

[285] H. Frey and H. R. Khan, *Handbook of Thin-Film Technology.* Berlin, Heidelberg: Springer Berlin Heidelberg, 2015.

[286] S. B. K. Moorthy, *Thin Film Structures in Energy Applications.* Cham: Springer International Publishing, 2015.

[287] J. Li, R. Gao, F. Gao, J. Lei, H. Wang, X. Wu, J. Li, H. Liu, X. Hua, and S. F. Liu, "Fabrication of efficient CsPbBr3 perovskite solar cells by single-source thermal evaporation," *Journal of Alloys and Compounds*, vol. 818, p. 152903, mar 2020.

[288] Z.-H. Zheng, H.-B. Lan, Z.-H. Su, H.-X. Peng, J.-T. Luo, G.-X. Liang, and P. Fan, "Single Source Thermal Evaporation of Two-dimensional Perovskite Thin Films for Photovoltaic Applications," *Scientific Reports*, vol. 9, p. 17422, dec 2019.

[289] A. Ng, Z. Ren, Q. Shen, S. H. Cheung, H. C. Gokkaya, G. Bai, J. Wang, L. Yang, S. K. So, A. B. Djurišić, W. W.-f. Leung, J. Hao, W. K. Chan, and C. Surya, "Efficiency enhancement by defect engineering in perovskite photovoltaic cells prepared using evaporated PbI 2 /CH 3 NH 3 I multilayers," *Journal of Materials Chemistry A*, vol. 3, no. 17, pp. 9223–9231, 2015.

[290] D. B. Mitzi, M. T. Prikas, and K. Chondroudis, "Thin Film Deposition of Organic-Inorganic Hybrid Materials Using a Single Source Thermal Ablation Technique," *Chemistry of Materials*, vol. 11, no. 3, pp. 542–544, 1999.

[291] C. Momblona, L. Gil-Escrig, E. Bandiello, E. M. Hutter, M. Sessolo, K. Lederer, J. Blochwitz-Nimoth, and H. J. Bolink, "Efficient vacuum deposited p-i-n and n-i-p perovskite solar cells employing doped charge transport layers," *Energy and Environmental Science*, 2016.

[292] J. Li, H. Wang, X. Y. Chin, H. A. Dewi, K. Vergeer, T. W. Goh, J. W. M. Lim, J. H. Lew, K. P. Loh, C. Soci, T. C. Sum, H. J. Bolink, N. Mathews, S. Mhaisalkar, and A. Bruno, "Highly Efficient Thermally Co-evaporated Perovskite Solar Cells and Mini-modules," *Joule*, 2020.

[293] J. Li, H. A. Dewi, H. Wang, J. Zhao, N. Tiwari, N. Yantara, T. Malinauskas, V. Getautis, T. J. Savenije, N. Mathews, S. Mhaisalkar, and A. Bruno, "Co-Evaporated MAPbI 3 with Graded Fermi Levels Enables Highly Performing, Scalable, and Flexible p-i-n Perovskite Solar Cells," *Advanced Functional Materials*, p. 2103252, jul 2021.

[294] D. Pérez-del Rey, P. P. Boix, M. Sessolo, A. Hadipour, and H. J. Bolink, "Interfacial Modification for High-Efficiency Vapor-Phase-Deposited Perovskite Solar Cells Based on a Metal Oxide Buffer Layer," *The Journal of Physical Chemistry Letters*, vol. 9, pp. 1041–1046, mar 2018.

[295] M. Roß, S. Severin, M. B. Stutz, P. Wagner, H. Köbler, M. Favin-Lévêque, A. Al-Ashouri, P. Korb, P. Tockhorn, A. Abate, B. Stannowski, B. Rech, and S. Albrecht, "Co-Evaporated Formamidinium Lead Iodide Based Perovskites with 1000 h Constant Stability for Fully Textured Monolithic Perovskite/Silicon Tandem Solar Cells," *Advanced Energy Materials*, vol. 11, p. 2101460, sep 2021.

[296] Y.-H. Chiang, M. Anaya, and S. D. Stranks, "Multisource Vacuum Deposition of Methylammonium-Free Perovskite Solar Cells," *ACS Energy Letters*, vol. 5, pp. 2498–2504, aug 2020.

[297] J. Li, J. Dagar, O. Shargaieva, M. A. Flatken, H. Köbler, M. Fenske, C. Schultz, B. Stegemann, J. Just, D. M. Többens, A. Abate, R. Munir, and E. Unger, "20.8% Slot-Die Coated MAPbI 3 Perovskite Solar Cells by Optimal DMSO-Content and Age of 2-ME Based Precursor Inks," *Advanced Energy Materials*, vol. 11, p. 2003460, mar 2021.

[298] H. Fan, F. Li, P. Wang, Z. Gu, J.-H. Huang, K.-J. Jiang, B. Guan, L.-M. Yang, X. Zhou, and Y. Song, "Methylamine-assisted growth of uniaxial-oriented perovskite thin films with millimeter-sized grains," *Nature Communications*, vol. 11, p. 5402, dec 2020.

[299] Z. Huang, D. Wang, S. Wang, and T. Zhang, "Highly Efficient and Stable MAPbI3 Perovskite Solar Cell Induced by Regulated Nucleation and Ostwald Recrystallization," *Materials*, vol. 11, p. 778, may 2018.

[300] Z. Chen, B. Turedi, A. Y. Alsalloum, C. Yang, X. Zheng, I. Gereige, A. AlSaggaf, O. F. Mohammed, and O. M. Bakr, "Single-Crystal MAPbI 3 Perovskite Solar Cells Exceeding 21Energy Letters, vol. 4, pp. 1258–1259, jun 2019.

[301] M. A. Green, E. D. Dunlop, J. Hohl-Ebinger, M. Yoshita, N. Kopidakis, and X. Hao, "Solar cell efficiency tables (Version 58)," *Progress in Photovoltaics: Research and Applications*, vol. 29, pp. 657–667, jul 2021.

[302] L. E. Polander, P. Pahner, M. Schwarze, M. Saalfrank, C. Koerner, and K. Leo, "Hole-transport material variation in fully vacuum deposited perovskite solar cells," *APL Materials*, 2014.

[303] J. Borchert, I. Levchuk, L. C. Snoek, M. U. Rothmann, R. Haver, H. J. Snaith, C. J. Brabec, L. M. Herz, and M. B. Johnston, "Impurity Tracking Enables Enhanced Control and Reproducibility of Hybrid Perovskite Vapor Deposition," *ACS Applied Materials & Interfaces*, vol. 11, pp. 28851–28857, aug 2019.

[304] O. Malinkiewicz, A. Yella, Y. H. Lee, G. M. Espallargas, M. Graetzel, M. K. Nazeeruddin, and H. J. Bolink, "Perovskite solar cells employing organic charge-transport layers," *Nature Photonics*, vol. 8, pp. 128–132, feb 2014.

[305] P. Pistor, J. Borchert, W. Fränzel, R. Csuk, and R. Scheer, "Monitoring the Phase Formation of Coevaporated Lead Halide Perovskite Thin Films by in Situ X-ray Diffraction," *The Journal of Physical Chemistry Letters*, vol. 5, pp. 3308–3312, oct 2014.

[306] C.-W. Chen, H.-W. Kang, S.-Y. Hsiao, P.-F. Yang, K.-M. Chiang, and H.-W. Lin, "Efficient and Uniform Planar-Type Perovskite Solar Cells by Simple Sequential Vacuum Deposition," *Advanced Materials*, vol. 26, pp. 6647–6652, oct 2014.

[307] T. Abzieher, T. Feeney, F. Schackmar, Y. J. Donie, I. M. Hossain, J. A. Schwenzer, T. Hellmann, T. Mayer, M. Powalla, and U. W. Paetzold, "From Groundwork to Efficient Solar Cells: On the Importance of the Substrate Material in Co-Evaporated Perovskite Solar Cells," *Advanced Functional Materials*, p. 2104482, jul 2021.

[308] J. C. Costa, J. Azevedo, J. P. Araújo, L. M. Santos, and A. Mendes, "High purity and crystalline thin films of methylammonium lead iodide perovskites by a vapor deposition approach," *Thin Solid Films*, vol. 664, pp. 12–18, oct 2018.

[309] J. Teuscher, A. Ulianov, O. Müntener, M. Grätzel, and N. Tétreault, "Control and Study of the Stoichiometry in Evaporated Perovskite Solar Cells," *ChemSusChem*, 2015.

[310] B.-S. Kim, M.-H. Choi, M.-S. Choi, and J.-J. Kim, "Composition-controlled organometal halide perovskite via CH 3 NH 3 I pressure in a vacuum co-deposition process," *Journal of Materials Chemistry A*, vol. 4, no. 15, pp. 5663–5668, 2016.

[311] S.-Y. Hsiao, H.-L. Lin, W.-H. Lee, W.-L. Tsai, K.-M. Chiang, W.-Y. Liao, C.-Z. Ren-Wu, C.-Y. Chen, and H.-W. Lin, "Efficient All-Vacuum Deposited Perovskite Solar Cells by Controlling Reagent Partial Pressure in High Vacuum," *Advanced Materials*, vol. 28, pp. 7013–7019, aug 2016.

[312] M. J. Bækbo, O. Hansen, I. Chorkendorff, and P. C. K. Vesborg, "Deposition of methylammonium iodide via evaporation – combined kinetic and mass spectrometric study," *RSC Advances*, vol. 8, no. 52, pp. 29899–29908, 2018.

[313] A. E. Williams, P. J. Holliman, M. J. Carnie, M. L. Davies, D. A. Worsley, and T. M. Watson, "Perovskite processing for photovoltaics: a spectro-thermal evaluation," *J. Mater. Chem. A*, vol. 2, no. 45, pp. 19338–19346, 2014.

[314] L. K. Ono, S. Wang, Y. Kato, S. R. Raga, and Y. Qi, "Fabrication of semi-transparent perovskite films with centimeter-scale superior uniformity by the hybrid deposition method," *Energy and Environmental Science*, 2014.

[315] S. Wang, L. K. Ono, M. R. Leyden, Y. Kato, S. R. Raga, M. V. Lee, and Y. Qi, "Smooth perovskite thin films and efficient perovskite solar cells prepared by the hybrid deposition method," *Journal of Materials Chemistry A*, 2015.

[316] S. J. Wolter, V. Steckenreiter, M. C. Tatarzyn, T. Wietler, R. Niepelt, and S. Kajari-Schröder, "Determination and influence evaluation of the acoustic impedance ratio for thermal co-evaporation," *Applied Physics Letters*, vol. 113, p. 013301, jul 2018.

[317] B.-S. Kim, L. Gil-Escrig, M. Sessolo, and H. J. Bolink, "Deposition Kinetics and Compositional Control of Vacuum-Processed CH 3 NH 3 PbI 3 Perovskite," *The Journal of Physical Chemistry Letters*, vol. 11, pp. 6852–6859, aug 2020.

[318] M. Saliba, J.-P. Correa-Baena, C. M. Wolff, M. Stolterfoht, N. Phung, S. Albrecht, D. Neher, and A. Abate, "How to Make over 20% Efficient Perovskite Solar Cells in Regular (n–i–p) and Inverted (p–i–n) Architectures," *Chemistry of Materials*, vol. 30, pp. 4193–4201, jul 2018.

[319] A. Redinger, S. Levcenko, C. J. Hages, D. Greiner, C. A. Kaufmann, and T. Unold, "Time resolved photoluminescence on Cu(In, Ga)Se 2 absorbers: Distinguishing degradation and trap states," *Applied Physics Letters*, vol. 110, p. 122104, mar 2017.

[320] P. Caprioglio, M. Stolterfoht, C. M. Wolff, T. Unold, B. Rech, S. Albrecht, and D. Neher, "On the Relation between the Open-Circuit Voltage and Quasi-Fermi Level Splitting in Efficient Perovskite Solar Cells," *Advanced Energy Materials*, vol. 9, p. 1901631, sep 2019.

[321] T. Kirchartz, J. A. Márquez, M. Stolterfoht, and T. Unold, "Photoluminescence-Based Characterization of Halide Perovskites for Photovoltaics," 2020.

[322] F. Staub, H. Hempel, J. C. Hebig, J. Mock, U. W. Paetzold, U. Rau, T. Unold, and T. Kirchartz, "Beyond Bulk Lifetimes: Insights into Lead Halide Perovskite Films from Time-Resolved Photoluminescence," *Physical Review Applied*, vol. 6, no. 4, pp. 1–13, 2016.

[323] J. Seil, "Characterization of perovskite solar cells for tandem applications via calibrated and time-resolved photoluminescence," Master's thesis, University of Luxembourg, 2021.

[324] A. Bercegol, F. J. Ramos, A. Rebai, T. Guillemot, D. Ory, J. Rousset, and L. Lombez, "Slow Diffusion and Long Lifetime in Metal Halide Perovskites for Photovoltaics," *The Journal of Physical Chemistry C*, vol. 122, pp. 24570–24577, nov 2018.

[325] E. V. Péan, S. Dimitrov, C. S. De Castro, and M. L. Davies, "Interpreting time-resolved photoluminescence of perovskite materials," *Physical Chemistry Chemical Physics*, vol. 22, no. 48, pp. 28345–28358, 2020.

[326] G. D. Tainter, M. T. Hörantner, L. M. Pazos-Outón, R. D. Lamboll, H. Āboliņš, T. Leijtens, S. Mahesh, R. H. Friend, H. J. Snaith, H. J. Joyce, and F. Deschler, "Long-Range Charge Extraction in Back-Contact Perovskite Architectures via Suppressed Recombination," *Joule*, vol. 3, pp. 1301–1313, may 2019.

[327] R. Poeira, "Growth of organic inorganic perovskite methylammonium lead triiodide by co-evaporation technique," Master's thesis, University of Luxembourg, 2020.

[328] J. M. Ball, S. D. Stranks, M. T. Hörantner, S. Hüttner, W. Zhang, E. J. W. Crossland, I. Ramirez, M. Riede, M. B. Johnston, R. H. Friend, and H. J. Snaith, "Optical properties and limiting photocurrent of thin-film perovskite solar cells," *Energy & Environmental Science*, vol. 8, no. 2, pp. 602–609, 2015.

[329] I. Schnitzer, E. Yablonovitch, C. Caneau, and T. J. Gmitter, "Ultrahigh spontaneous emission quantum efficiency, 99.7% internally and 72% externally, from AlGaAs/GaAs/AlGaAs double heterostructures," *Applied Physics Letters*, vol. 62, pp. 131–133, jan 1993.

[330] R. K. Ahrenkiel, "Chapter 2 Minority-Carrier Lifetime in III–V Semiconductors," in *Semiconductors and Semimetals*, pp. 39–150, Elsevier, 1993.

[331] T. Gallet, D. Grabowski, T. Kirchartz, and A. Redinger, "Fermi-level pinning in methylammonium lead iodide perovskites," *Nanoscale*, vol. 11, pp. 16828–16836, sep 2019.

[332] P. Schulz, E. Edri, S. Kirmayer, G. Hodes, D. Cahen, and A. Kahn, "Interface energetics in organo-metal halide perovskite-based photovoltaic cells," in *Energy and Environmental Science*, 2014.

[333] J. Endres, D. A. Egger, M. Kulbak, R. A. Kerner, L. Zhao, S. H. Silver, G. Hodes, B. P. Rand, D. Cahen, L. Kronik, and A. Kahn, "Valence and Conduction

Band Densities of States of Metal Halide Perovskites: A Combined Experimental-Theoretical Study," *Journal of Physical Chemistry Letters*, 2016.

[334] A. Zohar, I. Levine, S. Gupta, O. Davidson, D. Azulay, O. Millo, I. Balberg, G. Hodes, and D. Cahen, "What is the Mechanism of MAPbI3 p-Doping by I2? Insights from Optoelectronic Properties," *ACS Energy Letters*, 2017.

[335] N. Ishida, K. Sueoka, and R. M. Feenstra, "Influence of surface states on tunneling spectra of n -type GaAs(110) surfaces," *Physical Review B - Condensed Matter and Materials Physics*, 2009.

[336] R. M. Feenstra, Y. Dong, M. P. Semtsiv, and W. T. Masselink, "Influence of tip-induced band bending on tunnelling spectra of semiconductor surfaces," *Nanotechnology*, vol. 18, p. 044015, jan 2007.

[337] D. Kim, G. Y. Kim, C. Ko, S. R. Pae, Y. S. Lee, O. Gunawan, D. F. Ogletree, W. Jo, and B. Shin, "Effects of Postsynthesis Thermal Conditions on Methylammonium Lead Halide Perovskite: Band Bending at Grain Boundaries and Its Impacts on Solar Cell Performance," *Journal of Physical Chemistry C*, 2016.

[338] Y. Li, X. Xu, C. Wang, B. Ecker, J. Yang, J. Huang, and Y. Gao, "Light-Induced Degradation of CH3NH3PbI3 Hybrid Perovskite Thin Film," *Journal of Physical Chemistry C*, 2017.

[339] F. Zu, P. Amsalem, M. Ralaiarisoa, T. Schultz, R. Schlesinger, and N. Koch, "Surface State Density Determines the Energy Level Alignment at Hybrid Perovskite/Electron Acceptors Interfaces," *ACS Applied Materials and Interfaces*, 2017.

[340] R. Ahuja, H. Arwin, A. Ferreira da Silva, C. Persson, J. M. Osorio-Guillén, J. Souza de Almeida, C. Moyses Araujo, E. Veje, N. Veissid, C. Y. An, I. Pepe, and B. Johansson, "Electronic and optical properties of lead iodide," *Journal of Applied Physics*, vol. 92, pp. 7219–7224, dec 2002.

[341] Y. Wang, Y.-Y. Sun, S. Zhang, T.-M. Lu, and J. Shi, "Band gap engineering of a soft inorganic compound PbI 2 by incommensurate van der Waals epitaxy," *Applied Physics Letters*, vol. 108, p. 013105, jan 2016.

[342] R. Frisenda, J. O. Island, J. L. Lado, E. Giovanelli, P. Gant, P. Nagler, S. Bange, J. M. Lupton, C. Schüller, A. J. Molina-Mendoza, L. Aballe, M. Foerster, T. Korn, M. Angel Niño, D. P. de Lara, E. M. Pérez, J. Fernandéz-Rossier, and A. Castellanos-Gomez, "Characterization of highly crystalline lead iodide nanosheets prepared by room-temperature solution processing," *Nanotechnology*, vol. 28, p. 455703, nov 2017.

[343] D. Y. Lin, B. C. Guo, Z. Y. Dai, C. F. Lin, and H. P. Hsu, "Pbi2 single crystal growth and its optical property study," *Crystals*, 2019.

[344] A. Krishna, H. Zhang, Z. Zhou, T. Gallet, M. Dankl, O. Ouellette, F. T. Eickemeyer, F. Fu, S. Sanchez, M. Mensi, S. M. Zakeeruddin, U. Rothlisberger, G. N. Manjunatha Reddy, A. Redinger, M. Grätzel, and A. Hagfeldt, "Nanoscale interfacial engineering enables highly stable and efficient perovskite photovoltaics," *Energy and Environmental Science*, 2021.

[345] H. Jin, E. Debroye, M. Keshavarz, I. G. Scheblykin, M. B. J. Roeffaers, J. Hofkens, and J. A. Steele, “It’s a trap! On the nature of localised states and charge trapping in lead halide perovskites,” *Materials Horizons*, vol. 7, no. 2, pp. 397–410, 2020.

[346] H. F. Haneef, A. M. Zeidell, and O. D. Jurchescu, “Charge carrier traps in organic semiconductors: a review on the underlying physics and impact on electronic devices,” *Journal of Materials Chemistry C*, vol. 8, no. 3, pp. 759–787, 2020.

[347] A. M. Zeidell, T. Ren, D. S. Filston, H. F. Iqbal, E. Holland, J. D. Bourland, J. E. Anthony, and O. D. Jurchescu, “Organic Field-Effect Transistors as Flexible, Tissue-Equivalent Radiation Dosimeters in Medical Applications,” *Advanced Science*, vol. 7, p. 2001522, sep 2020.

[348] N. Liu and C. Y. Yam, “First-principles study of intrinsic defects in formamidinium lead triiodide perovskite solar cell absorbers,” *Physical Chemistry Chemical Physics*, 2018.

[349] T. Gallet, R. G. Poeira, E. M. Lanzoni, T. Abzieher, U. W. Paetzold, and A. Redinger, “Co-evaporation of CH3NH3PbI3: How growth conditions impact phase purity, photostriction, and intrinsic stability,” *ACS Applied Materials and Interfaces*, 2021.

[350] J. Goldstein, D. Newbury, D. Joy, C. Lyman, P. Echlm, E. Lifshin, L. Sawyer, and J. Micheal, “Scanning Electron Microscopy and X-ray Microanalysis - Third Edition,” *Springer*, 2003.

[351] J. Ávila, C. Momblona, P. P. Boix, M. Sessolo, and H. J. Bolink, “Vapor-Deposited Perovskites: The Route to High-Performance Solar Cell Production?,” 2017.

[352] L. K. Ono, M. R. Leyden, S. Wang, and Y. Qi, “Organometal halide perovskite thin films and solar cells by vapor deposition,” 2016.

[353] J.-M. Kim and H.-T. Chung, “Electrochemical characteristics of orthorhombic LiMnO2 with different degrees of stacking faults,” *Journal of Power Sources*, vol. 115, pp. 125–130, mar 2003.

[354] I. C. Noyan and J. B. Cohen, *Residual Stress.* New York, NY: Springer New York, 1987.

[355] H.-M. Tung, J.-H. Huang, D.-G. Tsai, C.-F. Ai, and G.-P. Yu, “Hardness and residual stress in nanocrystalline ZrN films: Effect of bias voltage and heat treatment,” *Materials Science and Engineering: A*, vol. 500, pp. 104–108, jan 2009.

[356] J. Zhao, Y. Deng, H. Wei, X. Zheng, Z. Yu, Y. Shao, J. E. Shield, and J. Huang, “Strained hybrid perovskite thin films and their impact on the intrinsic stability of perovskite solar cells,” *Science Advances*, vol. 3, p. eaao5616, nov 2017.

[357] C. Zhu, X. Niu, Y. Fu, N. Li, C. Hu, Y. Chen, X. He, G. Na, P. Liu, H. Zai, Y. Ge, Y. Lu, X. Ke, Y. Bai, S. Yang, P. Chen, Y. Li, M. Sui, L. Zhang, H. Zhou, and Q. Chen, “Strain engineering in perovskite solar cells and its impacts on carrier dynamics,” *Nature Communications*, vol. 10, p. 815, dec 2019.

[358] J. Borchert, H. Boht, W. Fränzel, R. Csuk, R. Scheer, and P. Pistor, “Structural investigation of co-evaporated methyl ammonium lead halide perovskite films during growth and thermal decomposition using different PbX2 (X = I, Cl) precursors,” *Journal of Materials Chemistry A*, 2015.

[359] A. Llanos, E. S. Thibau, and Z.-H. Lu, “Abnormal thin film structures in vapor-phase deposited methylammonium lead iodide perovskite,” *Journal of Vacuum Science & Technology A: Vacuum, Surfaces, and Films*, 2016.

[360] T. M. Brenner, Y. Rakita, Y. Orr, E. Klein, I. Feldman, M. Elbaum, D. Cahen, and G. Hodes, “Conversion of single crystalline PbI2 to CH3NH3PbI3: Structural relations and transformation dynamics,” *Chemistry of Materials*, 2016.

[361] J. Emara, T. Schnier, N. Pourdavoud, T. Riedl, K. Meerholz, and S. Olthof, “Impact of Film Stoichiometry on the Ionization Energy and Electronic Structure of CH3NH3PbI3 Perovskites,” *Advanced Materials*, 2016.

[362] S. Kavadiya, J. Strzalka, D. M. Niedzwiedzki, and P. Biswas, “Crystal reorientation in methylammonium lead iodide perovskite thin film with thermal annealing,” *Journal of Materials Chemistry A*, 2019.

[363] O. A. Ajayi, J. V. Ardelean, G. D. Shepard, J. Wang, A. Antony, T. Taniguchi, K. Watanabe, T. F. Heinz, S. Strauf, X.-Y. Zhu, and J. C. Hone, “Approaching the intrinsic photoluminescence linewidth in transition metal dichalcogenide monolayers,” *2D Materials*, vol. 4, p. 031011, jul 2017.

[364] D. Pal, V. G. Stoleru, E. Towe, and D. Firsov, “Quantum Dot-Size Variation and Its Impact on Emission and Absorption Characteristics: An Experimental and Theoretical Modeling Investigation,” *Japanese Journal of Applied Physics*, vol. 41, pp. 482–489, feb 2002.

[365] C. Meier, A. Gondorf, S. Lüttjohann, A. Lorke, and H. Wiggers, “Silicon nanoparticles: Absorption, emission, and the nature of the electronic bandgap,” *Journal of Applied Physics*, vol. 101, p. 103112, may 2007.

[366] H. H. Fang, S. Adjokatse, S. Shao, J. Even, and M. A. Loi, “Long-lived hot-carrier light emission and large blue shift in formamidinium tin triiodide perovskites,” *Nature Communications*, 2018.

[367] C. Wehrenfennig, M. Liu, H. J. Snaith, M. B. Johnston, and L. M. Herz, “Homogeneous emission line broadening in the organo lead halide perovskite CH3NH3PbI3-xClx,” *Journal of Physical Chemistry Letters*, 2014.

[368] S. Kahmann, E. K. Tekelenburg, H. Duim, M. E. Kamminga, and M. A. Loi, “Extrinsic nature of the broad photoluminescence in lead iodide-based Ruddlesden–Popper perovskites,” *Nature Communications*, 2020.

[369] V. S. Chirvony, I. Suárez, J. Rodríguez-Romero, R. Vázquez-Cárdenas, J. Sanchez-Diaz, A. Molina-Sánchez, E. M. Barea, I. Mora-Seró, and J. P. Martínez-Pastor, “Inhomogeneous Broadening of Photoluminescence Spectra and Kinetics of Nanometer-Thick (Phenethylammonium)2PbI4 Perovskite Thin Films: Implications for Optoelectronics,” *ACS Applied Nano Materials*, vol. 4, pp. 6170–6177, jun 2021.

[370] D. Cortecchia, S. Neutzner, A. R. S. Kandada, E. Mosconi, D. Meggiolaro, F. De Angelis, C. Soci, and A. Petrozza, “Broadband emission in two-dimensional hybrid perovskites: The role of structural deformation,” *Journal of the American Chemical Society*, 2017.

[371] C. Deng, G. Zhou, D. Chen, J. Zhao, Y. Wang, and Q. Liu, “Broadband Photoluminescence in 2D Organic-Inorganic Hybrid Perovskites: (C7H18N2)PbBr4 and (C9H22N2)PbBr4,” *Journal of Physical Chemistry Letters*, 2020.

[372] M. H. Li, H. H. Yeh, Y. H. Chiang, U. S. Jeng, C. J. Su, H. W. Shiu, Y. J. Hsu, N. Kosugi, T. Ohigashi, Y. A. Chen, P. S. Shen, P. Chen, and T. F. Guo, “Highly Efficient 2D/3D Hybrid Perovskite Solar Cells via Low-Pressure Vapor-Assisted Solution Process,” *Advanced Materials*, 2018.

[373] W. J. Yin, T. Shi, and Y. Yan, “Unusual defect physics in CH3NH3PbI3 perovskite solar cell absorber,” *Applied Physics Letters*, 2014.

[374] Z. Song, S. C. Watthage, A. B. Phillips, B. L. Tompkins, R. J. Ellingson, and M. J. Heben, “Impact of Processing Temperature and Composition on the Formation of Methylammonium Lead Iodide Perovskites,” *Chem. Mater.*, vol. 27, no. 13, pp. 4612–4619, 2015.

[375] S. R. Raga, M. C. Jung, M. V. Lee, M. R. Leyden, Y. Kato, and Y. Qi, “Influence of air annealing on high efficiency planar structure perovskite solar cells,” *Chemistry of Materials*, 2015.

[376] T. Du, C. H. Burgess, J. Kim, J. Zhang, J. R. Durrant, and M. A. McLachlan, “Formation, location and beneficial role of PbI2 in lead halide perovskite solar cells,” *Sustainable Energy and Fuels*, 2017.

[377] Z. Zhou, Z. Wang, Y. Zhou, S. Pang, D. Wang, H. Xu, Z. Liu, N. P. Padture, and G. Cui, “Methylamine-Gas-Induced Defect-Healing Behavior of CH3NH3PbI3 Thin Films for Perovskite Solar Cells,” *Angewandte Chemie - International Edition*, 2015.

[378] T. Seewald, E. R. Schütz, C. Ebenhoch, and L. Schmidt-Mende, “Curing perovskites — A way towards control of crystallinity and improved stability,” 2020.

[379] A. Calloni, A. Abate, G. Bussetti, G. Berti, R. Yivlialin, F. Ciccacci, and L. Duò, “Stability of Organic Cations in Solution-Processed CH 3 NH 3 PbI 3 Perovskites: Formation of Modified Surface Layers,” *The Journal of Physical Chemistry C*, vol. 119, pp. 21329–21335, sep 2015.

[380] E. S. Thibau, *Master Thesis: Photoemission Spectroscopy Studies of Methylammonium Lead Iodide Perovskite Thin Films and Interfaces*. PhD thesis, University of Toronto, Department of Materials Science and Engineering, 2016.

[381] S. Ding, X. Xiao, S. Liu, J. Wu, Z. Huang, X. Qi, and J. Li, “Detection of interfacial charge transfer in MoS2/PbI2 heterostructures via Kelvin probe force microscope,” *Applied Physics A*, vol. 125, p. 287, may 2019.

[382] D. Kim, J. S. Yun, P. Sharma, D. S. Lee, J. Kim, A. M. Soufiani, S. Huang, M. A. Green, A. W. Ho-Baillie, and J. Seidel, "Light- and bias-induced structural variations in metal halide perovskites," *Nature Communications*, 2019.

[383] U. B. Cappel, S. Svanström, V. Lanzilotto, F. O. Johansson, K. Aitola, B. Philippe, E. Giangrisostomi, R. Ovsyannikov, T. Leitner, A. Föhlisch, S. Svensson, N. Mårtensson, G. Boschloo, A. Lindblad, and H. Rensmo, "Partially Reversible Photoinduced Chemical Changes in a Mixed-Ion Perovskite Material for Solar Cells," *ACS Applied Materials and Interfaces*, 2017.

[384] D. W. DeQuilettes, W. Zhang, V. M. Burlakov, D. J. Graham, T. Leijtens, A. Osherov, V. Bulović, H. J. Snaith, D. S. Ginger, and S. D. Stranks, "Photo-induced halide redistribution in organic-inorganic perovskite films," *Nature Communications*, 2016.

[385] F. Zhang, F. Ullrich, S. Silver, R. A. Kerner, B. P. Rand, and A. Kahn, "Complexities of contact potential difference measurements on metal halide perovskite surfaces," *Journal of Physical Chemistry Letters*, vol. 10, no. 4, pp. 890–896, 2019.

[386] T. C. Wei, H. P. Wang, T. Y. Li, C. H. Lin, Y. H. Hsieh, Y. H. Chu, and J. H. He, "Photostriction of CH3NH3PbBr3 Perovskite Crystals," *Advanced Materials*, 2017.

[387] H. Tsai, R. Asadpour, J. C. Blancon, C. C. Stoumpos, O. Durand, J. W. Strzalka, B. Chen, R. Verduzco, P. M. Ajayan, S. Tretiak, J. Even, M. A. Alam, M. G. Kanatzidis, W. Nie, and A. D. Mohite, "Light-induced lattice expansion leads to high-efficiency perovskite solar cells," *Science*, 2018.

[388] N. Rolston, R. Bennett-Kennett, L. T. Schelhas, J. M. Luther, J. A. Christians, J. J. Berry, and R. H. Dauskardt, "Comment on "light-induced lattice expansion leads to high-efficiency perovskite solar cells"," 2020.

[389] H. Tsai, W. Nie, and A. D. Mohite, "Response to Comment on "light-induced lattice expansion leads to high-efficiency solar cells"," 2020.

[390] B. Kundys, "Photostrictive materials," *Applied Physics Reviews*, vol. 2, p. 011301, mar 2015.

[391] T. Glaser, C. Müller, M. Sendner, C. Krekeler, O. E. Semonin, T. D. Hull, O. Yaffe, J. S. Owen, W. Kowalsky, A. Pucci, and R. Lovrinčić, "Infrared Spectroscopic Study of Vibrational Modes in Methylammonium Lead Halide Perovskites," *The Journal of Physical Chemistry Letters*, vol. 6, pp. 2913–2918, aug 2015.

[392] I. Swainson, L. Chi, J.-H. Her, L. Cranswick, P. Stephens, B. Winkler, D. J. Wilson, and V. Milman, "Orientational ordering, tilting and lone-pair activity in the perovskite methylammonium tin bromide, CH 3 NH 3 SnBr 3," *Acta Crystallographica Section B Structural Science*, vol. 66, pp. 422–429, aug 2010.

[393] J.-H. Lee, N. C. Bristowe, P. D. Bristowe, and A. K. Cheetham, "Role of hydrogen-bonding and its interplay with octahedral tilting in CH 3 NH 3 PbI 3," *Chemical Communications*, vol. 51, no. 29, pp. 6434–6437, 2015.

[394] E. M. Hutter, M. C. Gélvez-Rueda, A. Osherov, V. Bulović, F. C. Grozema, S. D. Stranks, and T. J. Savenije, "Direct-indirect character of the bandgap in methylammonium lead iodide perovskite," *Nature Materials*, 2017.

[395] B. Wu, H. Yuan, Q. Xu, J. A. Steele, D. Giovanni, P. Puech, J. Fu, Y. F. Ng, N. F. Jamaludin, A. Solanki, S. Mhaisalkar, N. Mathews, M. B. Roeffaers, M. Grätzel, J. Hofkens, and T. C. Sum, "Indirect tail states formation by thermal-induced polar fluctuations in halide perovskites," *Nature Communications*, 2019.

[396] B. Murali, E. Yengel, C. Yang, W. Peng, E. Alarousu, O. M. Bakr, and O. F. Mohammed, "The Surface of Hybrid Perovskite Crystals: A Boon or Bane," 2017.

[397] S. T. Birkhold, E. Zimmermann, T. Kollek, D. Wurmbrand, S. Polarz, and L. Schmidt-Mende, "Impact of Crystal Surface on Photoexcited States in Organic–Inorganic Perovskites," *Advanced Functional Materials*, 2017.

[398] Y. Fang, H. Wei, Q. Dong, and J. Huang, "Quantification of re-Absorption and re-emission processes to determine photon recycling efficiency in perovskite single crystals," *Nature Communications*, 2017.

[399] K. Schötz, A. M. Askar, W. Peng, D. Seeberger, T. P. Gujar, M. Thelakkat, A. Köhler, S. Huettner, O. M. Bakr, K. Shankar, and F. Panzer, "Double peak emission in lead halide perovskites by self-absorption," *Journal of Materials Chemistry C*, 2020.

[400] J. A. Sichert, Y. Tong, N. Mutz, M. Vollmer, S. Fischer, K. Z. Milowska, R. García Cortadella, B. Nickel, C. Cardenas-Daw, J. K. Stolarczyk, A. S. Urban, and J. Feldmann, "Quantum Size Effect in Organometal Halide Perovskite Nanoplatelets," *Nano Letters*, 2015.

[401] J. Liu, Y. Xue, Z. Wang, Z. Q. Xu, C. Zheng, B. Weber, J. Song, Y. Wang, Y. Lu, Y. Zhang, and Q. Bao, "Two-Dimensional CH3NH3PbI3 Perovskite: Synthesis and Optoelectronic Application," *ACS Nano*, 2016.

[402] J. Liu, J. Leng, K. Wu, J. Zhang, and S. Jin, "Observation of internal photoinduced electron and hole separation in hybrid two-dimentional perovskite films," *Journal of the American Chemical Society*, 2017.

[403] J. Li, A. Dobrovolsky, A. Merdasa, E. L. Unger, and I. G. Scheblykin, "Luminescent Intermediates and Humidity-Dependent Room-Temperature Conversion of the MAPbI3 Perovskite Precursor," *ACS Omega*, 2018.

[404] D. Shin, F. Zu, A. V. Cohen, Y. Yi, L. Kronik, and N. Koch, "Mechanism and Timescales of Reversible p-Doping of Methylammonium Lead Triiodide by Oxygen," *Advanced Materials*, 2021.

[405] M. Anaya, J. F. Galisteo-López, M. E. Calvo, J. P. Espinós, and H. Míguez, "Origin of Light-Induced Photophysical Effects in Organic Metal Halide Perovskites in the Presence of Oxygen," *Journal of Physical Chemistry Letters*, 2018.

[406] A. Szemjonov, K. Galkowski, M. Anaya, Z. Andaji-Garmaroudi, T. K. Baikie, S. Mackowski, I. D. Baikie, S. D. Stranks, and M. S. Islam, "Impact of Oxygen

on the Electronic Structure of Triple-Cation Halide Perovskites," *ACS Materials Letters*, 2019.

[407] A. M. Tirmzi, J. A. Christians, R. P. Dwyer, D. T. Moore, and J. A. Marohn, "Substrate-Dependent Photoconductivity Dynamics in a High-Efficiency Hybrid Perovskite Alloy," *Journal of Physical Chemistry C*, 2019.

[408] W. C. Lin, W. C. Lo, J. X. Li, Y. K. Wang, J. F. Tang, and Z. Y. Fong, "In situ XPS investigation of the X-ray-triggered decomposition of perovskites in ultrahigh vacuum condition," *npj Materials Degradation*, 2021.

[409] F. Lang, O. Shargaieva, V. V. Brus, H. C. Neitzert, J. Rappich, and N. H. Nickel, "Influence of radiation on the properties and the stability of hybrid perovskites," *Advanced Materials*, 2018.

[410] J. D. McGettrick, K. Hooper, A. Pockett, J. Baker, J. Troughton, M. Carnie, and T. Watson, "Sources of Pb(0) artefacts during XPS analysis of lead halide perovskites," *Materials Letters*, 2019.

[411] M. Foussekis, A. A. Baski, and M. A. Reshchikov, "Comparison of surface photovoltage behavior for n-type versus p-type GaN," *Journal of Vacuum Science & Technology B, Nanotechnology and Microelectronics: Materials, Processing, Measurement, and Phenomena*, 2011.

[412] M. Daboczi, I. Hamilton, S. Xu, J. Luke, S. Limbu, J. Lee, M. A. McLachlan, K. Lee, J. R. Durrant, I. D. Baikie, and J. S. Kim, "Origin of Open-Circuit Voltage Losses in Perovskite Solar Cells Investigated by Surface Photovoltage Measurement," *ACS Applied Materials and Interfaces*, 2019.

[413] J. B. Patel, J. Wong-Leung, S. Van Reenen, N. Sakai, J. T. W. Wang, E. S. Parrott, M. Liu, H. J. Snaith, L. M. Herz, and M. B. Johnston, "Influence of Interface Morphology on Hysteresis in Vapor-Deposited Perovskite Solar Cells," *Advanced Electronic Materials*, 2017.

[414] R. C. Shallcross, S. Olthof, K. Meerholz, and N. R. Armstrong, "Impact of Titanium Dioxide Surface Defects on the Interfacial Composition and Energetics of Evaporated Perovskite Active Layers," *ACS Applied Materials and Interfaces*, 2019.

[415] E. Climent-Pascual, B. C. Hames, J. S. Moreno-Ramírez, A. L. Álvarez, E. J. Juarez-Perez, E. Mas-Marza, I. Mora-Seró, A. De Andrés, and C. Coya, "Influence of the substrate on the bulk properties of hybrid lead halide perovskite films," *Journal of Materials Chemistry A*, 2016.

[416] B. Philippe, B. W. Park, R. Lindblad, J. Oscarsson, S. Ahmadi, E. M. Johansson, and H. Rensmo, "Chemical and electronic structure characterization of lead halide perovskites and stability behavior under different exposures-A photoelectron spectroscopy investigation," *Chemistry of Materials*, 2015.

[417] M. G. Helander, M. T. Greiner, Z. B. Wang, W. M. Tang, and Z. H. Lu, "Work function of fluorine doped tin oxide," *Journal of Vacuum Science and Technology A: Vacuum, Surfaces, and Films*, 2011.

[418] D. B. Khadka, Y. Shirai, M. Yanagida, J. W. Ryan, and K. Miyano, "Exploring the effects of interfacial carrier transport layers on device performance and optoelectronic properties of planar perovskite solar cells," *Journal of Materials Chemistry C*, 2017.

[419] A. Al-Ashouri, A. Magomedov, M. Roß, M. Jošt, M. Talaikis, G. Chistiakova, T. Bertram, J. A. Márquez, E. Köhnen, E. Kasparavičius, S. Levcenco, L. Gil-Escrig, C. J. Hages, R. Schlatmann, B. Rech, T. Malinauskas, T. Unold, C. A. Kaufmann, L. Korte, G. Niaura, V. Getautis, and S. Albrecht, "Conformal monolayer contacts with lossless interfaces for perovskite single junction and monolithic tandem solar cells," *Energy and Environmental Science*, 2019.

[420] M. Caputo, N. Cefarin, A. Radivo, N. Demitri, L. Gigli, J. R. Plaisier, M. Panighel, G. Di Santo, S. Moretti, A. Giglia, M. Polentarutti, F. De Angelis, E. Mosconi, P. Umari, M. Tormen, and A. Goldoni, "Electronic structure of MAPbI3 and MAPbCl3: importance of band alignment," *Scientific Reports*, 2019.

[421] K. T. Butler, J. M. Frost, and A. Walsh, "Band alignment of the hybrid halide perovskites CH3NH3PbCl3, CH3NH3PbBr3 and CH3NH3PbI3," *Materials Horizons*, 2015.

[422] Q. D. Ou, C. Li, Q. K. Wang, Y. Q. Li, and J. X. Tang, "Recent Advances in Energetics of Metal Halide Perovskite Interfaces," *Advanced Materials Interfaces*, 2017.

[423] A. K. Jena, A. Kulkarni, and T. Miyasaka, "Halide Perovskite Photovoltaics: Background, Status, and Future Prospects," *Chemical Reviews*, 2019.

[424] R. G. Poeira, J. Seil, T. Gallet, T. P. Weiss, C. Pauly, and A. Redinger, "Origin of near-unity photoluminescence quantum yields in ultra-thin CH3NH3PbI3 absorbers," *Physical Review Letters*, 2021.

[425] N. Z. Koocher, D. Saldana-Greco, F. Wang, S. Liu, and A. M. Rappe, "Polarization Dependence of Water Adsorption to CH3NH3PbI3 (001) Surfaces," *Journal of Physical Chemistry Letters*, 2015.

[426] X. J. She, C. Chen, G. Divitini, B. Zhao, Y. Li, J. Wang, J. F. Orri, L. Cui, W. Xu, J. Peng, S. Wang, A. Sadhanala, and H. Sirringhaus, "A solvent-based surface cleaning and passivation technique for suppressing ionic defects in high-mobility perovskite field-effect transistors," *Nature Electronics*, 2020.

[427] M. Yang, T. Zhang, P. Schulz, Z. Li, G. Li, D. H. Kim, N. Guo, J. J. Berry, K. Zhu, and Y. Zhao, "Facile fabrication of large-grain CH3 NH3 PbI3-x Brx films for high-efficiency solar cells via CH3NH3 Br-selective Ostwald ripening," *Nature Communications*, 2016.

[428] M. B. Johansson, L. Xie, B. J. Kim, J. Thyr, T. Kandra, E. M. Johansson, M. Göthelid, T. Edvinsson, and G. Boschloo, "Highly crystalline MAPbI3 perovskite grain formation by irreversible poor-solvent diffusion aggregation, for efficient solar cell fabrication," *Nano Energy*, 2020.

[429] X. Wang, X. Li, G. Tang, L. Zhao, W. Zhang, T. Jiu, and J. Fang, “Improving efficiency of planar hybrid CH3NH3PbI3-xClx perovskite solar cells by isopropanol solvent treatment,” *Organic Electronics*, 2015.

[430] T. Abzieher, F. Mathies, M. Hetterich, A. Welle, D. Gerthsen, U. Lemmer, U. W. Paetzold, and M. Powalla, “Additive-Assisted Crystallization Dynamics in Two-Step Fabrication of Perovskite Solar Cells,” *Physica Status Solidi (A) Applications and Materials Science*, 2017.

[431] T. B. Abzieher, *Thermische Koverdampfung von hybriden Perowskit-Halbleitern für den Einsatz in Solarzellen.* PhD thesis, Karlsruher Institut für Technologie (KIT), 2020.

[432] Y. Ding, B. Ding, H. Kanda, J. Usiobo Onovbaramwen, T. Gallet, Z. Yang, Y. Liu, H. Huang, J. Sheng, C. Liu, Y. Yang, V. Queloz, X. Zhang, J.-N. Audinot, A. Redinger, W. Dang, E. Mosconi, W. Luo, F. De Angelis, M. Wang, P. Wu, G. Yang, S. Dai, P. Dyson, and M. Khaja Nazeeruddin, “Single-crystalline TiO_2 Nanoparticles for Narrowing the Scalability Gap towards Stable and Efficient Perovskite Modules,” *Researchsquare*, 2021.

[433] R. A. Street, S. E. Ready, F. Lemmi, K. S. Shah, P. Bennett, and Y. Dmitriyev, “Electronic transport in polycrystalline Pbl2 films,” *Journal of Applied Physics*, 1999.

[434] S. Chen, X. Wen, J. S. Yun, S. Huang, M. Green, N. J. Jeon, W. S. Yang, J. H. Noh, J. Seo, S. I. Seok, and A. Ho-Baillie, “Spatial Distribution of Lead Iodide and Local Passivation on Organo-Lead Halide Perovskite,” *ACS Applied Materials and Interfaces*, 2017.

[435] S. Gharibzadeh, P. Fassl, I. M. Hossain, P. Rohrbeck, M. Frericks, M. Schmidt, T. Duong, M. R. Khan, T. Abzieher, B. A. Nejand, F. Schackmar, O. Almora, T. Feeney, R. Singh, D. Fuchs, U. Lemmer, J. P. Hofmann, S. A. L. Weber, and U. W. Paetzold, “Two birds with one stone: dual grain-boundary and interface passivation enables ¿22% efficient inverted methylammonium-free perovskite solar cells,” *Energy and Environmental Science*, vol. 28, no. 11, pp. 3384–3392, 2021.

[436] Y. Hu, E. M. Hutter, P. Rieder, I. Grill, J. Hanisch, M. F. Aygüler, A. G. Hufnagel, M. Handloser, T. Bein, A. Hartschuh, K. Tvingstedt, V. Dyakonov, A. Baumann, T. J. Savenije, M. L. Petrus, and P. Docampo, “Understanding the Role of Cesium and Rubidium Additives in Perovskite Solar Cells: Trap States, Charge Transport, and Recombination,” *Advanced Energy Materials*, 2018.

[437] I. Grill, K. Handloser, F. C. Hanusch, N. Giesbrecht, T. Bein, P. Docampo, M. Handloser, and A. Hartschuh, “Controlling crystal growth by chloride-assisted synthesis: Towards optimized charge transport in hybrid halide perovskites,” *Solar Energy Materials and Solar Cells*, 2017.

[438] H. D. Kim, H. Ohkita, H. Benten, and S. Ito, “Photovoltaic Performance of Perovskite Solar Cells with Different Grain Sizes,” *Advanced Materials*, 2016.

[439] S. Wu, J. Zhang, Z. Li, D. Liu, M. Qin, S. H. Cheung, X. Lu, D. Lei, S. K. So, Z. Zhu, and A. K. Jen, “Modulation of Defects and Interfaces through Alkylammonium Interlayer for Efficient Inverted Perovskite Solar Cells,” *Joule*, 2020.

[440] R. Scheer and H.-W. Schock, *Chalcogenide Photovoltaics.* John Wiley and Sons, 2011.

[441] T. Dullweber, O. Lundberg, J. Malmström, M. Bodegård, L. Stolt, U. Rau, H. W. Schock, and J. H. Werner, “Back surface band gap gradings in Cu(In,Ga)Se2 solar cells,” *Thin Solid Films*, 2001.

[442] K. T. Cho, G. Grancini, Y. Lee, E. Oveisi, J. Ryu, O. Almora, M. Tschumi, P. A. Schouwink, G. Seo, S. Heo, J. Park, J. Jang, S. Paek, G. Garcia-Belmonte, and M. K. Nazeeruddin, “Selective growth of layered perovskites for stable and efficient photovoltaics,” *Energy and Environmental Science*, 2018.

[443] Y. Wang, Y. Yue, X. Yang, and L. Han, “Toward Long-Term Stable and Highly Efficient Perovskite Solar Cells via Effective Charge Transporting Materials,” 2018.

[444] Z. Li, T. R. Klein, D. H. Kim, M. Yang, J. J. Berry, M. F. Van Hest, and K. Zhu, “Scalable fabrication of perovskite solar cells,” 2018.

[445] S. W. Lee, S. Bae, D. Kim, and H. S. Lee, “Historical Analysis of High-Efficiency, Large-Area Solar Cells: Toward Upscaling of Perovskite Solar Cells,” *Advanced Materials*, 2020.

[446] D. H. Kim, J. B. Whitaker, Z. Li, M. F. van Hest, and K. Zhu, “Outlook and Challenges of Perovskite Solar Cells toward Terawatt-Scale Photovoltaic Module Technology,” 2018.

[447] A. Blakers, “Development of the PERC Solar Cell,” *IEEE Journal of Photovoltaics*, 2019.

[448] M. Taguchi, A. Yano, S. Tohoda, K. Matsuyama, Y. Nakamura, T. Nishiwaki, K. Fujita, and E. Maruyama, “24.7% Record efficiency HIT solar cell on thin silicon wafer,” *IEEE Journal of Photovoltaics*, 2014.

[449] J. F. Geisz, R. M. France, K. L. Schulte, M. A. Steiner, A. G. Norman, H. L. Guthrey, M. R. Young, T. Song, and T. Moriarty, “Six-junction III–V solar cells with 47.1Nature Energy, 2020.

[450] C. A. Nelson, N. R. Monahan, and X. Y. Zhu, “Exceeding the Shockley-Queisser limit in solar energy conversion,” 2013.

[451] S. Tabernig, “Detailed balance charts, efficiencies relative to the detailed balance limit.” https://www.lmpv.nl/db/. (accessed: 31.08.2021).

[452] A. Polman, M. Knight, E. C. Garnett, B. Ehrler, and W. C. Sinke, “Photovoltaic materials: Present efficiencies and future challenges,” 2016.

[453] Q. Dong, Y. Fang, Y. Shao, P. Mulligan, J. Qiu, L. Cao, and J. Huang, “Electron-hole diffusion lengths ¿ 175 μm in solution-grown CH 3 NH 3 PbI 3 single crystals,” *Science*, vol. 347, pp. 967–970, feb 2015.

[454] A. A. B. Baloch, M. I. Hossain, N. Tabet, and F. H. Alharbi, "Practical Efficiency Limit of Methylammonium Lead Iodide Perovskite (CH 3 NH 3 PbI 3) Solar Cells," *The Journal of Physical Chemistry Letters*, vol. 9, pp. 426–434, jan 2018.

[455] L. Krückemeier, B. Krogmeier, Z. Liu, U. Rau, and T. Kirchartz, "Understanding Transient Photoluminescence in Halide Perovskite Layer Stacks and Solar Cells," *Advanced Energy Materials*, vol. 11, p. 2003489, may 2021.

[456] P. Schulz, "Interface Design for Metal Halide Perovskite Solar Cells," *ACS Energy Letters*, vol. 3, pp. 1287–1293, jun 2018.

[457] M. H. Du, "Efficient carrier transport in halide perovskites: Theoretical perspectives," 2014.

[458] M. L. Agiorgousis, Y. Y. Sun, H. Zeng, and S. Zhang, "Strong covalency-induced recombination centers in perovskite solar cell material CH3NH3PbI3," *Journal of the American Chemical Society*, 2014.

[459] A. Buin, P. Pietsch, J. Xu, O. Voznyy, A. H. Ip, R. Comin, and E. H. Sargent, "Materials processing routes to trap-free halide perovskites," *Nano Letters*, 2014.

[460] D. Meggiolaro and F. De Angelis, "First-Principles Modeling of Defects in Lead Halide Perovskites: Best Practices and Open Issues," *ACS Energy Letters*, 2018.

[461] U.-G. Jong, C.-J. Yu, G.-C. Ri, A. P. McMahon, N. M. Harrison, P. R. F. Barnes, and A. Walsh, "Influence of water intercalation and hydration on chemical decomposition and ion transport in methylammonium lead halide perovskites," *Journal of Materials Chemistry A*, vol. 6, no. 3, pp. 1067–1074, 2018.

[462] Y. Yuan and J. Huang, "Ion Migration in Organometal Trihalide Perovskite and Its Impact on Photovoltaic Efficiency and Stability," *Accounts of Chemical Research*, 2016.

[463] J. Haruyama, K. Sodeyama, L. Han, and Y. Tateyama, "First-principles study of ion diffusion in perovskite solar cell sensitizers," *Journal of the American Chemical Society*, 2015.

[464] J. M. Azpiroz, E. Mosconi, J. Bisquert, and F. De Angelis, "Defect migration in methylammonium lead iodide and its role in perovskite solar cell operation," *Energy and Environmental Science*, 2015.

[465] S. N. Habisreutinger, N. K. Noel, and H. J. Snaith, "Hysteresis Index: A Figure without Merit for Quantifying Hysteresis in Perovskite Solar Cells," *ACS Energy Letters*, 2018.

[466] G. Divitini, S. Cacovich, F. Matteocci, L. Cinà, A. Di Carlo, and C. Ducati, "In situ observation of heat-induced degradation of perovskite solar cells," 2016.

[467] J. Li, Q. Dong, N. Li, and L. Wang, "Direct Evidence of Ion Diffusion for the Silver-Electrode-Induced Thermal Degradation of Inverted Perovskite Solar Cells," *Advanced Energy Materials*, 2017.

[468] Y. M. Yang, A. Yu, B. Hsu, W. C. Hsu, A. Yang, and C. W. Lan, "Development of high-performance multicrystalline silicon for photovoltaic industry," *Progress in Photovoltaics: Research and Applications*, 2015.

[469] C. Li, G. Chen, W. Wang, J. Zhang, L. Wu, X. Hao, and L. Feng, "Grain boundary passivation by CdCl2 treatment in CdTe solar cells revealed by Kelvin probe force microscopy," *Journal of Materials Science: Materials in Electronics*, 2018.

[470] A. H. Munshi, J. M. Kephart, A. Abbas, A. Danielson, G. Gelinas, J. N. Beaudry, Barth, J. M. Walls, and W. S. Sampath, "Effect of CdCl2 passivation treatment on microstructure and performance of CdSeTe/CdTe thin-film photovoltaic devices," *Solar Energy Materials and Solar Cells*, 2018.

[471] C. Li, Y. Wu, J. Poplawsky, T. J. Pennycook, N. Paudel, W. Yin, S. J. Haigh, M. P. Oxley, A. R. Lupini, M. Al-Jassim, S. J. Pennycook, and Y. Yan, "Grain-boundary-enhanced carrier collection in CdTe solar cells," *Physical Review Letters*, 2014.

[472] N. Nicoara, R. Manaligod, P. Jackson, D. Hariskos, W. Witte, G. Sozzi, R. Menozzi, and S. Sadewasser, "Direct evidence for grain boundary passivation in Cu(In,Ga)Se2 solar cells through alkali-fluoride post-deposition treatments," *Nature Communications*, 2019.

[473] D. Keller, S. Buecheler, P. Reinhard, F. Pianezzi, B. Bissig, R. Carron, F. Hage, Q. Ramasse, R. Erni, and A. N. Tiwari, "Band gap widening at random CIGS grain boundary detected by valence electron energy loss spectroscopy," *Applied Physics Letters*, 2016.

[474] K. Wojciechowski, S. D. Stranks, A. Abate, G. Sadoughi, A. Sadhanala, N. Kopidakis, G. Rumbles, C. Z. Li, R. H. Friend, A. K. Jen, and H. J. Snaith, "Heterojunction modification for highly efficient organic-inorganic perovskite solar cells," *ACS Nano*, 2014.

[475] G. Xing, B. Wu, S. Chen, J. Chua, N. Yantara, S. Mhaisalkar, N. Mathews, and T. C. Sum, "Interfacial Electron Transfer Barrier at Compact TiO2/CH3NH3PbI3 Heterojunction," *Small*, 2015.

[476] Y. Shao, Z. Xiao, C. Bi, Y. Yuan, and J. Huang, "Origin and elimination of photocurrent hysteresis by fullerene passivation in CH3NH3PbI3 planar heterojunction solar cells," *Nature Communications*, 2014.

[477] J. Xu, A. Buin, A. H. Ip, W. Li, O. Voznyy, R. Comin, M. Yuan, S. Jeon, Z. Ning, J. J. McDowell, P. Kanjanaboos, J. P. Sun, X. Lan, L. N. Quan, D. H. Kim, I. G. Hill, P. Maksymovych, and E. H. Sargent, "Perovskite-fullerene hybrid materials suppress hysteresis in planar diodes," *Nature Communications*, 2015.

[478] A. K. Jena, Y. Numata, M. Ikegami, and T. Miyasaka, "Role of spiro-OMeTAD in performance deterioration of perovskite solar cells at high temperature and reuse of the perovskite films to avoid Pb-waste," *Journal of Materials Chemistry A*, 2018.

[479] Y. Xia, K. Sun, J. Chang, and J. Ouyang, "Effects of organic inorganic hybrid perovskite materials on the electronic properties and morphology of poly(3,4-ethylenedioxythiophene):poly(styrenesulfonate) and the photovoltaic performance of planar perovskite solar cells," *Journal of Materials Chemistry A*, 2015.

[480] K. Sun, P. Li, Y. Xia, J. Chang, and J. Ouyang, "Transparent Conductive Oxide-Free Perovskite Solar Cells with PEDOT:PSS as Transparent Electrode," *ACS Applied Materials and Interfaces*, 2015.

[481] C. G. Wu, C. H. Chiang, Z. L. Tseng, M. K. Nazeeruddin, A. Hagfeldt, and M. Grätzel, "High efficiency stable inverted perovskite solar cells without current hysteresis," *Energy and Environmental Science*, 2015.

[482] J. Kim, N. Park, J. S. Yun, S. Huang, M. A. Green, and A. W. Ho-Baillie, "An effective method of predicting perovskite solar cell lifetime–Case study on planar CH3NH3PbI3 and HC(NH2)2PbI3 perovskite solar cells and hole transfer materials of spiro-OMeTAD and PTAA," *Solar Energy Materials and Solar Cells*, 2017.

[483] M. Wang, H. Wang, W. Li, X. Hu, K. Sun, and Z. Zang, "Defect passivation using ultrathin PTAA layers for efficient and stable perovskite solar cells with a high fill factor and eliminated hysteresis," *Journal of Materials Chemistry A*, 2019.

[484] L. Zuo, Z. Gu, T. Ye, W. Fu, G. Wu, H. Li, and H. Chen, "Enhanced photovoltaic performance of CH3NH3PbI3 perovskite solar cells through interfacial engineering using self-assembling monolayer," *Journal of the American Chemical Society*, 2015.

[485] Y. Bai, H. Chen, S. Xiao, Q. Xue, T. Zhang, Z. Zhu, Q. Li, C. Hu, Y. Yang, Z. Hu, F. Huang, K. S. Wong, H. L. Yip, and S. Yang, "Effects of a Molecular Monolayer Modification of NiO Nanocrystal Layer Surfaces on Perovskite Crystallization and Interface Contact toward Faster Hole Extraction and Higher Photovoltaic Performance," *Advanced Functional Materials*, 2016.

[486] J. Hidalgo, A. F. Castro-Méndez, and J. P. Correa-Baena, "Imaging and Mapping Characterization Tools for Perovskite Solar Cells," 2019.

[487] M. U. Rothmann, W. Li, J. Etheridge, and Y. B. Cheng, "Microstructural characterisations of perovskite solar cells – From grains to interfaces: Techniques, features, and challenges," *Advanced Energy Materials*, 2017.

[488] D. Abou-Ras, T. Kirchartz, and U. Rau, *Advanced Characterization Techniques for Thin Film Solar Cells: Second Edition.* Wiley-VCH Verlag GmbH and Co, 2016.

[489] M. Pazoki, A. Hagfeldt, and T. Edvinsson, *Characterization techniques for perovskite solar cell materials.* Elsevier, 2019.

[490] T. Wirtz, P. Philipp, J. N. Audinot, D. Dowsett, and S. Eswara, "High-resolution high-sensitivity elemental imaging by secondary ion mass spectrometry: From traditional 2D and 3D imaging to correlative microscopy," *Nanotechnology*, 2015.

[491] N. Instruments, "Pid theory explained." https://www.ni.com/en-us/innovations/white-papers/06/pid-theory-explained.html. (accessed: 15.09.2021).

[492] G. Tregnago, “Losses at large,” *Nature Energy*, vol. 4, pp. 529–529, jul 2019.

[493] J. Peng, D. Walter, Y. Ren, M. Tebyetekerwa, Y. Wu, T. Duong, Q. Lin, J. Li, T. Lu, M. A. Mahmud, O. L. C. Lem, S. Zhao, W. Liu, Y. Liu, H. Shen, L. Li, F. Kremer, H. T. Nguyen, D. Y. Choi, K. J. Weber, K. R. Catchpole, and T. P. White, “Nanoscale localized contacts for high fill factors in polymer-passivated perovskite solar cells,” *Science*, 2021.

[494] S. N. E. o. T. Anu Bhambhani, “20.5% record efficiency for perovskite module.” http://taiyangnews.info/technology/20-5-world-record-efficiency-for-perovskite-solar-module/. (accessed: 06.07.2021).

[495] D. Li, D. Zhang, K. S. Lim, Y. Hu, Y. Rong, A. Mei, N. G. Park, and H. Han, “A Review on Scaling Up Perovskite Solar Cells,” 2021.

[496] K. Yoshikawa, H. Kawasaki, W. Yoshida, T. Irie, K. Konishi, K. Nakano, T. Uto, D. Adachi, M. Kanematsu, H. Uzu, and K. Yamamoto, “Silicon heterojunction solar cell with interdigitated back contacts for a photoconversion efficiency over 26%,” *Nature Energy*, 2017.

[497] F. Solar, “First solar series 6^{th} advanced thin film solar technology.” https://www.firstsolar.com/en-AU/-/media/First-Solar/Technical-Documents/Series-6-Datasheets/Series-6-Datasheet.ashx. (accessed: 03.09.2021).

[498] S. Frontier, “Solar frontier cis thin-film submodule achieves highest efficiency world record of 19.2%.” https://www.solar-frontier.com/eng/news/2017/0227_press.html. (accessed: 03.09.2021).

[499] L. Qiu, S. He, L. K. Ono, S. Liu, and Y. Qi, “Scalable Fabrication of Metal Halide Perovskite Solar Cells and Modules,” 2019.

[500] T. Wagner, H. Beyer, P. Reissner, P. Mensch, H. Riel, B. Gotsmann, and A. Stemmer, “Kelvin probe force microscopy for local characterisation of active nanoelectronic devices,” *Beilstein Journal of Nanotechnology*, vol. 6, pp. 2193–2206, nov 2015.

[501] Y. Tian, M. Peter, E. Unger, M. Abdellah, K. Zheng, T. Pullerits, A. Yartsev, V. Sundström, and I. G. Scheblykin, “Mechanistic insights into perovskite photoluminescence enhancement: Light curing with oxygen can boost yield thousandfold,” *Physical Chemistry Chemical Physics*, 2015.

[502] D. Meggiolaro, E. Mosconi, and F. De Angelis, “Mechanism of Reversible Trap Passivation by Molecular Oxygen in Lead-Halide Perovskites,” *ACS Energy Letters*, 2017.

[503] N. Aristidou, C. Eames, I. Sanchez-Molina, X. Bu, J. Kosco, M. Saiful Islam, and S. A. Haque, “Fast oxygen diffusion and iodide defects mediate oxygen-induced degradation of perovskite solar cells,” *Nature Communications*, 2017.

[504] L. Xie, P. Song, L. Shen, J. Lu, K. Liu, K. Lin, W. Feng, C. Tian, and Z. Wei, “Revealing the compositional effect on the intrinsic long-term stability of perovskite solar cells,” *Journal of Materials Chemistry A*, 2020.

[505] Q. Li, Z. Chen, I. Tranca, S. Gaastra-Nedea, D. Smeulders, and S. Tao, "Compositional effect on water adsorption on metal halide perovskites," *Applied Surface Science*, 2021.

[506] L. Zhou, C. Katan, W. Nie, H. Tsai, L. Pedesseau, J. J. Crochet, J. Even, A. D. Mohite, S. Tretiak, and A. J. Neukirch, "Cation Alloying Delocalizes Polarons in Lead Halide Perovskites," *Journal of Physical Chemistry Letters*, 2019.

[507] H. X. Dang, K. Wang, M. Ghasemi, M. C. Tang, M. De Bastiani, E. Aydin, E. Dauzon, D. Barrit, J. Peng, D. M. Smilgies, S. De Wolf, and A. Amassian, "Multi-cation Synergy Suppresses Phase Segregation in Mixed-Halide Perovskites," *Joule*, 2019.